Super-Earths throw theorists for a loop *p. 438*

Molecular defenses in warring plants *pp. 442 & 478*

Positive discrimination in France *p. 474*

Science

$15
29 JULY 2016
sciencemag.org

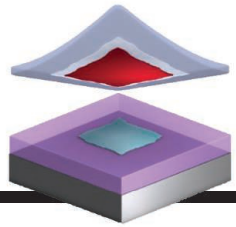
AAAS



LICHEN SYMBIOSIS

Two fungal partners, not one *p. 488*

CONTENTS



461
Two-dimensional frontiers

29 JULY 2016 • VOLUME 353 • ISSUE 6298



434

NEWS

IN BRIEF

428 News at a glance

IN DEPTH

432 OBSTACLES LOOM ALONG PATH TO THE END OF AIDS
International meeting highlights clash between ambitious goals and wobbly funding *By J. Cohen*

433 CHIMPANZEE SANCTUARIES OPEN DOOR TO MORE RESEARCH
Collaboration aims to beef up science at retirement centers *By D. Grimm*

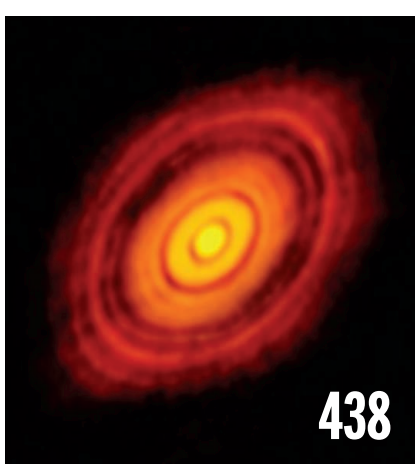
434 RETHINKING THE NORTH AMERICAN WOLF
Genome sequencing suggests two endangered wolf species are coyote hybrids *By V. Morell*
▸ *SCIENCE ADVANCES* RESEARCH ARTICLE BY B. M. VONHOLDT *ET AL.*

436 AFTER FAILED COUP, TURKEY'S ACADEMICS FEEL REGIME'S WRATH
Thousands of researchers and university officials fired, suspended, or told to return home immediately *By J. Bohannon*

437 UNCERTAINTY REIGNS IN BREXIT BRITAIN
As U.K. universities counsel their E.U. staff, researchers see first signs of fallout *By E. Stokstad*

FEATURE

438 FORBIDDEN PLANETS
How the zoo of exoplanets has turned planet formation theory upside down *By D. Clery*



438

INSIGHTS

PERSPECTIVES

442 PARASITIC PLANTS—A CURE FOR WHAT AILS THEE
A parasitic plant is perceived by its host plant in a similar manner to microbes *By V. Ntoukakis and S. Gimenez-Ibanez*
▸ REPORT P. 478

444 ON THE RECORD WITH *E. COLI* DNA
DNA can be engineered for cells to record events in real time *By O. Borkowski* et al.
▸ RESEARCH ARTICLES PP. 462 & 463

445 THE SMOKING GUN FOR ATLANTIC CIRCULATION CHANGES
Deep-sea sediments record changes in ocean circulation during the last glacial age *By A. Schmittner*
▸ REPORT P. 470

446 PLANT EXTINCTIONS TAKE TIME
Many plant species may already be functionally extinct *By Q. Cronk*

POLICY FORUM

448 COUNTERING IMPRECISION IN PRECISION MEDICINE
Better coordination is needed to study complex interventions *By S. P. Hey and A. S. Kesselheim*

BOOKS *ET AL.*

450 I CONTAIN MULTITUDES
By E. Yong, reviewed by S. Perkins

451 HISTORY WITHIN
By M. Sommer, reviewed by M. Meloni

LETTERS

452 CLARIFYING SAMPLES IN ZIKA ANALYSES
By J. R. M. de Oliveira and D. A. P. Moura

452 ANIMAL-BASED ANTIBODIES: OBSOLETE
By A. C. Gray et al.

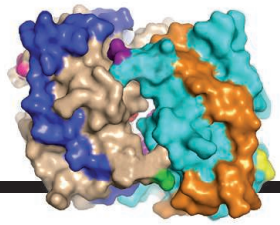
453 THE LINE BETWEEN SCIENCE AND POLITICS
By M. Weintraub

453 TECHNICAL COMMENT ABSTRACTS

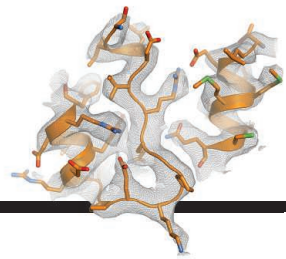
Downloaded from http://science.sciencemag.org/ on July 28, 2016

PHOTO: (TOP) ROLAND SEITRE/MINDEN PICTURES

Published by AAAS



503
A Zika drug target



506
HIV assembly

RESEARCH

IN BRIEF

458 From *Science* and other journals

REVIEW

461 **APPLIED PHYSICS**
2D materials and van der Waals heterostructures *K. S. Novoselov* et al.
REVIEW SUMMARY; FOR FULL TEXT:
dx.doi.org/10.1126/science.aac9439

RESEARCH ARTICLES

462 **CELL LINEAGE TRACING**
Whole-organism lineage tracing by combinatorial and cumulative genome editing *A. McKenna* et al.
RESEARCH ARTICLE SUMMARY; FOR FULL TEXT:
dx.doi.org/10.1126/science.aaf7907
▸ PERSPECTIVE P. 444

463 **SYNTHETIC BIOLOGY**
Molecular recordings by directed CRISPR spacer acquisition *S. L. Shipman* et al.
RESEARCH ARTICLE SUMMARY; FOR FULL TEXT:
dx.doi.org/10.1126/science.aaf1175
▸ PERSPECTIVE P. 444

REPORTS

464 **OPTICS**
Orbital angular momentum microlaser *P. Miao* et al.

467 **ELECTROCHEMISTRY**
Nanostructured transition metal dichalcogenide electrocatalysts for CO_2 reduction in ionic liquid *M. Asadi* et al.

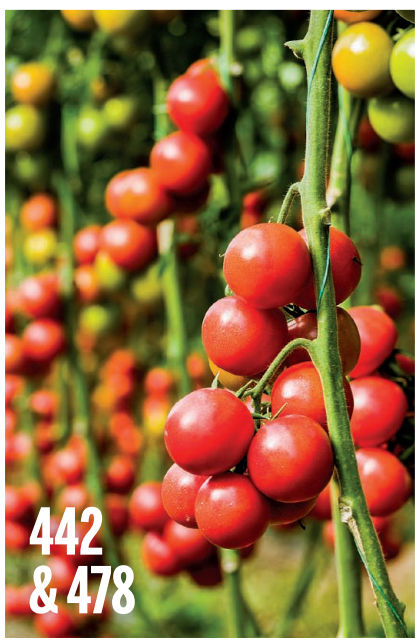
470 **PALEOCEANOGRAPHY**
North Atlantic ocean circulation and abrupt climate change during the last glaciation *L. G. Henry* et al.
▸ PERSPECTIVE P. 445

474 **EDUCATION**
Teaching accreditation exams reveal grading biases favor women in male-dominated disciplines in France *T. Breda and M. Hillion*

478 **PARASITIC PLANTS**
Detection of the plant parasite *Cuscuta reflexa* by a tomato cell surface receptor *V. Hegenauer* et al.
▸ PERSPECTIVE P. 442

482 **PLANT ECOLOGY**
Rapid evolution accelerates plant population spread in fragmented experimental landscapes *J. L. Williams* et al.

485 **PLANT DEVELOPMENT**
Arabidopsis transcriptional repressor VAL1 triggers Polycomb silencing at *FLC* during vernalization *J. I. Qüesta* et al.



488 **SYMBIOSIS**
Basidiomycete yeasts in the cortex of ascomycete macrolichens *T. Spribille* et al.
▸ VIDEO

492 **INFECTION**
Increased plasmid copy number is essential for *Yersinia* T3SS function and virulence *H. Wang* et al.

495 **EPIGENETICS**
Early-life nutrition modulates the epigenetic state of specific rDNA genetic variants in mice *M. L. Holland* et al.

499 **HUMAN GENETICS**
Early Neolithic genomes from the eastern Fertile Crescent *F. Broushaki* et al.

503 **STRUCTURAL BIOLOGY**
Crystal structure of Zika virus NS2B-NS3 protease in complex with a boronate inhibitor *J. Lei* et al.

506 **STRUCTURAL BIOLOGY**
An atomic model of HIV-1 capsid-SP1 reveals structures regulating assembly and maturation *F. K. M. Schur* et al.

DEPARTMENTS

427 **EDITORIAL**
Intentional equity
By France A. Córdova

514 **WORKING LIFE**
Growth from failure
By Tenaya K. Vallery

ON THE COVER



Hypogymnia imshaugii, a macrolichen common in northwestern North America. Lichens were previously thought to contain two parts: an ascomycetous fungus and a photosynthetic alga. Spribille *et al.* show that a third element—a basidiomycete yeast—is part of the lichen cortex in the largest group of macrolichens. See page 488. *Photo: Timothy B. Wheeler/ timwheelerphotography.com*

Science Staff 426
News & Notes 455
New Products 509
Science Careers 510

SCIENCE (ISSN 0036-8075) is published weekly on Friday, except the last week in December, by the American Association for the Advancement of Science, 1200 New York Avenue, NW, Washington, DC 20005. Periodicals mail postage (publication No. 484460) paid at Washington, DC, and additional mailing offices.

Copyright © 2016 by the American Association for the Advancement of Science. The title SCIENCE is a registered trademark of the AAAS.

Domestic individual membership and subscription (51 issues): $165 ($74 allocated to subscription). Domestic institutional subscription (51 issues): $1522; Foreign postage extra: Mexico, Caribbean (surface mail) $55; other countries (air assist delivery) $89. First class, airmail, student, and emeritus rates on request. Canadian rates with GST available upon request, GST #1254 88122. Publications Mail Agreement Number 1069624. **Printed in the U.S.A.**
Change of address: Allow 4 weeks, giving old and new addresses and 8-digit account number. **Postmaster:** Send change of address to AAAS, P.O. Box 96178, Washington, DC 20090–6178. **Single-copy sales:** $15.00 current issue, $20.00 back issue prepaid includes surface postage; bulk rates on request. **Authorization to photocopy** material for internal or personal use under circumstances not falling within the fair use provisions of the Copyright Act is granted by AAAS to libraries and other users registered with the Copyright Clearance Center (CCC) Transactional Reporting Service, provided that $35.00 per article is paid directly to CCC, 222 Rosewood Drive, Danvers, MA 01923. The identification code for *Science* is 0036-8075. *Science* is indexed in the *Reader's Guide to Periodical Literature* and in several specialized indexes.

Published by AAAS

Downloaded from http://science.sciencemag.org/ on July 28, 2016

353 (6298)
(July 29, 2016)
Science **353** (6298), 427-514.

Editor's Summary

This copy is for your personal, non-commercial use only.

Article Tools Visit the online version of this article to access the personalization and article tools:
http://science.sciencemag.org/content/353/6298

Permissions Obtain information about reproducing this article:
http://www.sciencemag.org/about/permissions.dtl

Science (print ISSN 0036-8075; online ISSN 1095-9203) is published weekly, except the last week in December, by the American Association for the Advancement of Science, 1200 New York Avenue NW, Washington, DC 20005. Copyright 2016 by the American Association for the Advancement of Science; all rights reserved. The title *Science* is a registered trademark of AAAS.

Downloaded from http://science.sciencemag.org/ on July 28, 2016

Science
AAAS
1200 New York Avenue, NW, Washington, DC 20005
Clarendon House, Clarendon Road, Cambridge, UK CB2 8FH

Editor-in-Chief Jeremy Berg
Executive Editor Monica M. Bradford **News Editor** Tim Appenzeller
Managing Editor, Research Journals Katrina L. Kelner
Deputy Editors Lisa D. Chong, Andrew M. Sugden(UK), Valda J. Vinson, Jake S. Yeston

Research and Insights

DEPUTY EDITOR, EMERITUS Barbara R. Jasny **SR. EDITORS** Caroline Ash(UK), Gilbert J. Chin, Julia Fahrenkamp-Uppenbrink(UK), Pamela J. Hines, Stella M. Hurtley(UK), Paula A. Kiberstis, Marc S. Lavine(Canada), Kristen L. Mueller, Ian S. Osborne(UK), Beverly A. Purnell, L. Bryan Ray, Guy Riddihough, H. Jesse Smith, Jelena Stajic, Peter Stern(UK), Phillip D. Szuromi, Sacha Vignieri, Brad Wible, Nicholas S. Wigginton, Laura M. Zahn **ASSOCIATE EDITORS** Brent Grocholski, Keith T. Smith **ASSOCIATE BOOK REVIEW EDITOR** Valerie B. Thompson **LETTERS EDITOR** Jennifer Sills **LEAD CONTENT PRODUCTION EDITORS** Harry Jach, Lauren Kmec **CONTENT PRODUCTION EDITORS** Jeffrey E. Cook, Chris Filiatreau, Cynthia Howe, Barbara P. Ordway, Catherine Wolner **SR. EDITORIAL COORDINATORS** Carolyn Kyle, Beverly Shields **EDITORIAL COORDINATORS** Aneera Dobbins, Joi S. Granger, Lisa Johnson, Maryrose Madrid, Anita Wynn **PUBLICATIONS ASSISTANTS** Jeffrey Hearn, Dona Mathieu, Le-Toya Mayne Flood, Shannon McMahon, Scott Miller, Jerry Richardson, Alice Whaley(UK), Brian White **EXECUTIVE ASSISTANT** Anna Bashkirova **ADMINISTRATIVE SUPPORT** Janet Clements(UK), Lizanne Newton(UK)

News

NEWS MANAGING EDITOR John Travis **INTERNATIONAL EDITOR** Richard Stone **DEPUTY NEWS EDITORS** Robert Coontz, Elizabeth Culotta, David Grimm, David Malakoff, Leslie Roberts **CONTRIBUING EDITOR** Martin Enserink(Europe) **SR. CORRESPONDENTS** Daniel Clery(UK), Jeffrey Mervis, Elizabeth Pennisi **NEWS WRITERS** Adrian Cho, Jon Cohen, Jennifer Couzin-Frankel, Carolyn Gramling, Eric Hand, Jocelyn Kaiser, Catherine Matacic, Kelly Servick, Robert F. Service, Erik Stokstad(Cambridge, UK), Emily Underwood **INTERNS** Patrick Monahan **CONTRIBUTING CORRESPONDENTS** John Bohannon, Warren Cornwall, Ann Gibbons, Mara Hvistendahl, Sam Kean, Eli Kintisch, Kai Kupferschmidt(Berlin), Andrew Lawler, Christina Larson(Beijing), Mitch Leslie, Charles C. Mann, Eliot Marshall, Virginia Morell, Dennis Normile(Shanghai), Heather Pringle, Tania Rabesandratana(London), Gretchen Vogel(Berlin), Lizzie Wade(Mexico City) **CAREERS** Donisha Adams, Rachel Bernstein(Editor) **COPY EDITORS** Julia Cole, Dorie Chevlen, Jennifer Levin (Chief) **ADMINISTRATIVE SUPPORT** Jessica Adams

Executive Publisher Rush D. Holt
Publisher Bill Moran **Chief Digital Media Officer** Rob Covey

BUSINESS OPERATIONS AND PORTFOLIO MANAGEMENT DIRECTOR Sarah Whalen **PRODUCT DEVELOPMENT DIRECTOR** Will Schweitzer **PRODUCT DEVELOPMENT ASSOCIATE** Hannah Heckner **BUSINESS SYSTEMS AND FINANCIAL ANALYSIS DIRECTOR** Randy Yi **MANAGER OF FULFILLMENT SYSTEMS** Neal Hawkins **SYSTEMS ANALYST** Nicole Mehmedovich **DIRECTOR, BUSINESS OPERATIONS & ANALYSIS** Eric Knott **MANAGER, BUSINESS OPERATIONS** Jessica Tierney **SENIOR BUSINESS ANALYST** Cory Lipman **BUSINESS ANALYSTS** David Garrison, Michael Hardesty Meron Kebede, Sandy Kim **FINANCIAL ANALYST** Drew Sher **DIRECTOR, COPYRIGHTS LICENSING SPECIAL PROJECTS** Emilie David **PERMISSIONS ASSOCIATE** Elizabeth Sandler **RIGHTS, CONTRACTS, AND LICENSING ASSOCIATE** Lili Kiser **RIGHTS & PERMISSIONS ASSISTANT** Alexander Lee

MARKETING DIRECTOR Elise Swinehart **ASSOCIATE MARKETING DIRECTOR** Stacey Burke Bowers **MARKETING ASSOCIATE** Steven Goodman **CREATIVE DIRECTOR** Scott Rodgerson **SENIOR ART ASSOCIATES** Paula Fry **ART ASSOCIATE** Kim Huynh

FULFILLMENT SYSTEMS AND OPERATIONS membership@aaas.org **MANAGER, MEMBER SERVICES** Pat Butler **SPECIALISTS** Terrance Morrison, Latasha Russell **MANAGER, DATA ENTRY** Mickie Napoleoni **DATA ENTRY SPECIALISTS** Brenden Aquilino, Fiona Giblin **MARKETING ASSOCIATE** Isa Sesay-Bah

PUBLISHER RELATIONS, EASTERN REGION Keith Layson **PUBLISHER RELATIONS, WESTERN REGION** Ryan Rexroth **SALES RESEARCH COORDINATOR** Aiesha Marshall **MANAGER, SITE LICENSE OPERATIONS** Iquo Edim **SENIOR OPERATIONS ANALYST** Lana Guz **FULFILLMENT ANALYST** Judy Lillibridge

WEB TECHNOLOGIES PORTFOLIO MANAGER Trista Smith **TECHNICAL MANAGER** Chris Coleman **PROJECT MANAGER** Nick Fletcher **DEVELOPERS** Ryan Jensen, Jimmy Marks, Brandon Morrison

DIGITAL MEDIA DIRECTOR OF ANALYTICS Enrique Gonzales **DIGITAL REPORTING ANALYST** Eric Hossinger **SR. WEB PRODUCER** Sarah Crespi **WEB PRODUCER** Alison Crawford **VIDEO PRODUCER** Nguyen Nguyen **SOCIAL MEDIA PRODUCER** Brice Russ

DIRECTOR OF OPERATIONS PRINT AND ONLINE Lizabeth Harman **DIGITAL/PRINT STRATEGY MANAGER** Jason Hillman **QUALITY TECHNICAL MANAGER** Marcus Spiegler **PROJECT ACCOUNT MANAGER** Tara Kelly **DIGITAL PRODUCTION MANAGER** Lisa Stanford **ASSISTANT MANAGER DIGITAL/PRINT** Rebecca Doshi **SENIOR CONTENT SPECIALISTS** Steve Forrester, Antoinette Hodal, Lori Murphy, Anthony Rosen **CONTENT SPECIALISTS** Jacob Hedrick, Kimberley Oster

DESIGN DIRECTOR Beth Rakouskas **DESIGN EDITOR** Marcy Atarod **SENIOR DESIGNERS** Garvin Grullón, Chrystal Smith **GRAPHICS MANAGING EDITOR** Alberto Cuadra **SENIOR SCIENTIFIC ILLUSTRATORS** Chris Bickel, Katharine Sutliff **SCIENTIFIC ILLUSTRATOR** Valerie Altounian **INTERACTIVE GRAPHICS EDITOR** Jia You **SENIOR GRAPHICS SPECIALISTS** Holly Bishop, Nathalie Cary **PHOTOGRAPHY MANAGING EDITOR** William Douthitt **SENIOR PHOTO EDITOR** Christy Steele **PHOTO EDITOR** Emily Petersen

DIRECTOR, GLOBAL COLLABORATION, CUSTOM PUBLICATIONS, ADVERTISING Bill Moran **EDITOR, CUSTOM PUBLISHING** Sean Sanders: 202-326-6430 **ADVERTISING MARKETING MANAGER** Justin Sawyers: 202-326-7061 science_advertising@aaas.org **ADVERTISING SUPPORT MANAGER** Karen Foote: 202-326-6740 **ADVERTISING PRODUCTION OPERATIONS MANAGER** Deborah Tompkins **SR. PRODUCTION SPECIALIST/GRAPHIC DESIGNER** Amy Hardcastle **SR. TRAFFIC ASSOCIATE** Christine Hall **SALES COORDINATOR** Shirley Young **ASSOCIATE DIRECTOR, COLLABORATION, CUSTOM PUBLICATIONS/CHINA/TAIWAN/KOREA/SINGAPORE** Ruolei Wu: +86-186 0082 9345, rwu@aaas.org **COLLABORATION/CUSTOM PUBLICATIONS/JAPAN** Adarsh Sandhu + 81532-81-5142 asandhu@aaas.org **EAST COAST/E. CANADA** Laurie Faraday: 508-747-9395, FAX 617-507-8189 **WEST COAST/W. CANADA** Lynne Stickrod: 415-931-9782, FAX 415-520-6940 **MIDWEST** Jeffrey Dembski: 847-498-4520 x3005, Steven Loerch: 847-498-4520 x3006 **UK EUROPE/ASIA** Roger Goncalves: TEL/FAX +41 43 243 1358 **JAPAN** Katsuyoshi Fukamizu(Tokyo): +81-3-3219-5777 kfukamizu@aaas.org **CHINA/TAIWAN** Ruolei Wu: +86-186 0082 9345, rwu@aaas.org

WORLDWIDE ASSOCIATE DIRECTOR OF SCIENCE CAREERS Tracy Holmes: +44 (0) 1223 326525, FAX +44 (0) 1223 326532 tholmes@science-int.co.uk **CLASSIFIED** advertise@sciencecareers.org **U.S. SALES** Tina Burks: 202-326-6577, Nancy Toema: 202-326-6578 **EUROPE/ROW SALES** Sarah Lelarge **SALES ASSISTANT** Kelly Grace **JAPAN** Hiroyuki Mashiki(Kyoto): +81-75-823-1109 hmashiki@aaas.org **CHINA/TAIWAN** Ruolei Wu: +86-186 0082 9345 rwu@aaas.org **MARKETING MANAGER** Allison Pritchard **MARKETING ASSOCIATE** Aimee Aponte

AAAS BOARD OF DIRECTORS, CHAIR Geraldine L. Richmond **PRESIDENT** Barbara A. Schaal **PRESIDENT-ELECT** Susan Hockfield **TREASURER** David Evans Shaw **CHIEF EXECUTIVE OFFICER** Rush D. Holt **BOARD** Cynthia M. Beall, May R. Berenbaum, Carlos J. Bustamante, Stephen P.A. Fodor, Claire M. Fraser, Michael S. Gazzaniga, Laura H. Greene, Elizabeth Loftus, Mercedes Pascual

SUBSCRIPTION SERVICES For change of address, missing issues, new orders and renewals, and payment questions: 866-434-AAAS (2227) or 202-326-6417, FAX 202-842-1065. Mailing addresses: AAAS, P.O. Box 96178, Washington, DC 20090-6178 or AAAS Member Services, 1200 New York Avenue, NW, Washington, DC 20005

INSTITUTIONAL SITE LICENSES 202-326-6730 **REPRINTS:** Author Inquiries 800-635-7181 **COMMERCIAL INQUIRIES** 803-359-4578 **PERMISSIONS** 202-326-6765, permissions@aaas.org **AAAS Member Services** 202-326-6417 or http://membercentral.aaas.org/discounts

Science serves as a forum for discussion of important issues related to the advancement of science by publishing material on which a consensus has been reached as well as including the presentation of minority of conflicting points of view. Accordingly, all articles published in *Science*—including editorials, news and comment, and book reviews—are signed and reflect the individual views of the authors and not official points of view adopted by AAAS or the institutions with which the authors are affiliated.

INFORMATION FOR AUTHORS See pages 624 and 625 of the 5 February 2016 issue or access www.sciencemag.org/authors/science-information-authors

SENIOR EDITORIAL BOARD
Gary King, *Harvard University,* **Susan M. Rosenberg,** *Baylor College of Medicine,*
Ali Shilatifard, *Northwestern University Feinberg School of Medicine*

BOARD OF REVIEWING EDITORS (Statistics board members indicated with **(S)**)

Adriano Aguzzi, *U. Hospital Zürich*
Takuzo Aida, *U. of Tokyo*
Leslie Aiello, *Wenner-Gren Foundation*
Judith Allen, *U. of Edinburgh*
Sonia Altizer, *U. of Georgia*
Sebastian Amigorena, *Institut Curie*
Kathryn Anderson, *Memorial Sloan-Kettering Cancer Center*
Meinrat O. Andreae, *Max-Planck Inst. Mainz*
Paola Arlotta, *Harvard U.*
Johan Auwerx, *EPFL*
David Awschalom, *U. of Chicago*
Clare Baker, *University of Cambridge*
Nenad Ban, *ETH Zurich*
Jordi Bascompte, *University of Zurich*
Franz Bauer, *Instituto de Astrofisica*
Ray H. Baughman, *U. of Texas, Dallas*
David Baum, *U. of Wisconsin*
Carlo Beenakker, *Leiden U.*
Kamran Behnia, *ESPCI-ParisTech*
Yasmine Belkaid, *NIAID, NIH*
Philip Benfey, *Duke U.*
May Berenbaum, *U. of Illinois*
Gabriele Bergers, *U. of California, San Francisco*
Bradley Bernstein, *Massachusettes General Hospital*
Peer Bork, *EMBL*
Bernard Bourdon, *Ecole Normale Supérieure de Lyon*
Chris Bowler, *École Normale Supérieure*
Ian Boyd, *U. of St. Andrews*
Emily Brodsky, *U. of California, Santa Cruz*
Ron Brookmeyer, *U. of California Los Angeles* **(S)**
Christian Büchel, *U. Hamburg-Eppendorf*
Joseph A. Burns, *Cornell U.*
Carter Tribley Butts, *U. of California, Irvine*
Gyorgy Buzsaki, *New York U. School of Medicine*
Blanche Capel, *Duke U.*
Mats Carlsson, *U. of Oslo*
Ib Chorkendorff, *U. of Denmark*
David Clapham, *Children's Hospital Boston*
Joel Cohen, *Rockefeller U., Columbia U.*
James J. Collins, *MIT*
Robert Cook-Deegan, *Duke U.*
Lisa Coussens, *Oregon Health & Science U.*
Alan Cowman, *Walter & Eliza Hall Inst.*
Robert H. Crabtree, *Yale U.*
Roberta Croce, *Vrije Universiteit*
Janet Currie, *Princeton U.*
Jeff L. Dangl, *U. of North Carolina*
Tom Daniel, *U. of Washington*
Frans de Waal, *Emory U.*
Stanislas Dehaene, *Collège de France*
Robert Desimone, *MIT*
Claude Desplan, *New York U.*
Dennis Discher, *U. of Pennsylvania*
Gerald W. Dorn II, *Washington U. School of Medicine*
Jennifer A. Doudna, *U. of California, Berkeley*
Bruce Dunn, *U. of California, Los Angeles*
William Dunphy, *Caltech*
Christopher Dye, *WHO*
Todd Ehlers, *U. of Tuebingen*
David Ehrhardt, *Carnegie Inst. of Washington*
Tim Elston, *U. of North Carolina at Chapel Hill*
Jennifer Elisseeff, *U. of N*
Gerhard Ertl, *Fritz-Haber-Institut, Berlin*
Barry Everitt, *U. of Cambridge*
Ernst Fehr, *Johns Hopkins U.*
Anne C. Ferguson-Smith, *U. of Cambridge*
Michael Feuer, *The George Washington U.*
Toren Finkel, *NHLBI, NIH*
Kate Fitzgerald, *U. of Massachusetts*
Peter Fratzl, *Max-Planck Inst.*
Elaine Fuchs, *Rockefeller U.*
Daniel Geschwind, *UCLA*
Karl-Heinz Glassmeier, *TU Braunschweig*
Ramon Gonzalez, *Rice U.*
Julia R. Greer, *Caltech*
Elizabeth Grove, *U. of Chicago*
Nicolas Gruber, *ETH Zurich*
Kip Guy, *St. Jude's Children's Research Hospital*
Taekjip Ha, *U. of Illinois at Urbana-Champaign*
Wolf-Dietrich Hardt, *ETH Zurich*
Christian Haass, *Ludwig Maximilians U.*
Sharon Hammes-Schiffer, *U. of Illinois at Urbana–Champaign*
Michael Hasselmo, *Boston U.*
Martin Heimann, *Max-Planck Inst. Jena*
Yka Helariutta, *U. of Cambridge*
James A. Hendler, *Rensselaer Polytechnic Inst.*
Janet G. Hering, *Swiss Fed. Inst. of Aquatic Science & Technology*
Kai-Uwe Hinrichs, *U. of Bremen*
David Hodell, *U. of Cambridge*
Lora Hooper, *UT Southwestern Medical Ctr. at Dallas*
Tamas Horvath, *Yale University*
Raymond Huey, *U. of Washington*
Fred Hughson, *Princeton U.*
Auke Ijspeert, *EPFL Lausanne*
Stephen Jackson, *USGS and U. of Arizona*
Steven Jacobsen, *U. of California, Los Angeles*
Kai Johnsson, *EPFL Lausanne*
Peter Jonas, *Inst. of Science & Technology (IST) Austria*
Matt Kaeberlein, *U. of Washington*
William Kaelin Jr., *Dana-Farber Cancer Inst.*
Daniel Kahne, *Harvard U.*
Daniel Kammen, *U. of California, Berkeley*
Abby Kavner, *U. of California, Los Angeles*
Hitoshi Kawakatsu, *U. of Tokyo*
Masashi Kawasaki, *U. of Tokyo*
V. Narry Kim, *Seoul National U.*
Robert Kingston, *Harvard Medical School*
Etienne Koechlin, *Ecole Normale Suprieure*
Alexander Kolodkin, *Johns Hopkins U.*
Thomas Langer, *U. of Cologne*
Mitchell A. Lazar, *U. of Pennsylvania*
David Lazer, *Harvard U.*
Thomas Lecuit, *IBDM*
Virginia Lee, *U. of Pennsylvania*
Stanley Lemon, *U. of North Carolina at Chapel Hill*
Ottoline Leyser, *Cambridge U.*
Wendell Lim, *U.C. San Francisco*
Marcia C. Linn, *U. of California, Berkeley*
Jianguo Liu, *Michigan State U.*
Luis Liz-Marzan, *CIC biomaGUNE*
Jonathan Losos, *Harvard U.*
Ke Lu, *Chinese Acad. of Sciences*
Christian Lüscher, *U. of Geneva*
Laura Machesky, *CRUK Beatson Inst. for Cancer Research*
Anne Magurran, *U. of St. Andrews*
Oscar Marin, *CSIC & U. Miguel Hernández*
Charles Marshall, *U. of California, Berkeley*
C. Robertson McClung, *Dartmouth College*
Rodrigo Medellin, *U. of Mexico*
Graham Medley, *U. of Warwick*
Tom Misteli, *NCI*
Yasushi Miyashita, *U. of Tokyo*
Mary Ann Moran, *U. of Georgia*
Richard Morris, *U. of Edinburgh*
Alison Motsinger-Reif, *NC State U.* **(S)**
Thomas Murray, *The Hastings Center*
Daniel Neumark, *U. of California, Berkeley*
Kitty Nijmeijer, *U. of Twente*
Helga Nowotny, *European Research Advisory Board*
Ben Olken, *MIT*
Rachel O'Reilly, *Warwick U.*
Joe Orenstein, *U. of California Berkeley & Lawrence Berkeley National Lab*
Harry Orr, *U. of Minnesota*
Pilar Ossorio, *U. of Wisconsin*
Andrew Oswald, *U. of Warwick*
Isabella Pagano, *Istituto Nazionale di Astrofisica*
Margaret Palmer, *U. of Maryland*
Steve Palumbi, *Stanford U.*
Jane Parker, *Max-Planck Inst. of Plant Breeding Research*
Giovanni Parmigiani, *Dana-Farber Cancer Inst.* **(S)**
John H. J. Petrini, *Memorial Sloan-Kettering Cancer Center*
Samuel Pfaff, *Salk Institute for Biological Studies*
Joshua Plotkin, *U. of Pennsylvania*
Albert Polman, *FOM Institute AMOLF*
Philippe Poulin, *CNRS*
Jonathan Pritchard, *Stanford U.*
Wim van der Putten, *Netherlands Instituut voor Ecologie*
David Randall, *Colorado State U.*
Felix Rey, *Institut Pasteur*
Trevor Robbins, *U. of Cambridge*
Jim Roberts, *Fred Hutchinson Cancer Research Ctr.*
Amy Rosenzweig, *Northwestern University*
Mike Ryan, *U. of Texas, Austin*
Mitinori Saitou, *Kyoto U.*
Shimon Sakaguchi, *Kyoto U.*
Miquel Salmeron, *Lawrence Berkeley National Lab*
Jürgen Sandkühler, *Medical U. of Vienna*
Alexander Schier, *Harvard U.*
Vladimir Shalaev, *Purdue U.*
Robert Siliciano, *Johns Hopkins School of Medicine*
Denis Simon, *Arizona State U.*
Uri Simonsohn, *U. of Pennsylvania*
Alison Smith, *John Innes Centre*
Richard Smith, *U. of North Carolina* **(S)**
John Speakman, *U. of Aberdeen*
Allan C. Spradling, *Carnegie Institution of Washington*
Jonathan Sprent, *Garvan Inst. of Medical Research*
Eric Steig, *U. of Washington*
Paula Stephan, *Georgia State U. and National Bureau of Economic Research*
Molly Stevens, *Imperial College London*
V. S. Subrahmanian, *U. of Maryland*
Ira Tabas, *Columbia U.*
Sarah Teichmann, *Cambridge U.*
John Thomas, *North Carolina State U.*
Shubha Tole, *Tata Institute of Fundamental Research*
Christopher Tyler-Smith, *The Wellcome Trust Sanger Inst.*
Herbert Virgin, *Washington U.*
Bert Vogelstein, *Johns Hopkins U.*
Cynthia Volkert, *U. of Göttingen*
David Wallach, *Weizmann Inst. of Science*
Ian Walmsley, *U. of Oxford*
Jane-Ling Wang, *U. of California, Davis* **(S)**
David Waxman, *Fudan U.*
Jonathan Weissman, *U. of California, San Francisco*
Chris Wikle, *U. of Missouri* **(S)**
Ian A. Wilson, *The Scripps Res. Inst.* **(S)**
Timothy D. Wilson, *U. of Virginia*
Rosemary Wyse, *Johns Hopkins U.*
Jan Zaanen, *Leiden U.*
Kenneth Zaret, *U. of Pennsylvania School of Medicine*
Jonathan Zehr, *U. of California, Santa Cruz*
Len Zon, *Children's Hospital Boston*
Maria Zuber, *MIT*

BOOK REVIEW BOARD
David Bloom, *Harvard U.,* **Samuel Bowring,** *MIT,* **Angela Creager,** *Princeton U.,*
Richard Shweder, *U. of Chicago,* **Ed Wasserman,** *DuPont*

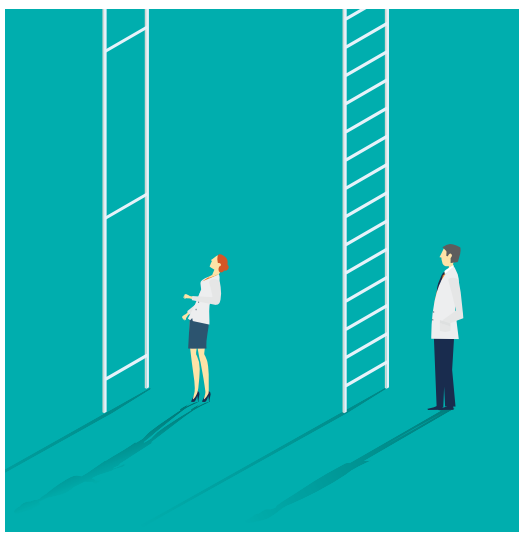
EDITORIAL

Intentional equity

Over a decade ago, when I was chief scientist at the U.S. National Aeronautics and Space Administration, I spoke at a conference called Women and Science: Celebrating Achievements, Charting Challenges. I lauded women working in astrophysics, government, and science policy in the United States and elsewhere, but said that progress was mixed—the veneer of success for women across the sciences, and in science leadership, was too thin across the globe. What has changed since then? Cultural barriers, a lack of enlightened policies, and the need for role models and support systems still exist worldwide. However, today there is good reason to be optimistic. The international scientific community is coming together intentionally to acknowledge and tackle gender equity.

This year, I made my first trip as the U.S. National Science Foundation (NSF) director to the Next Einstein Forum (NEF) in Africa, where I was on a panel discussing women in science, technology, engineering, and mathematics (STEM) fields. Scientists, engineers, and innovators from across the continent—women and men—all were hungry for change and fighting for equality. A resulting declaration committed to prioritizing the enrollment of women in STEM programs at the tertiary and postgraduate levels in Africa. I also was in India for the annual meeting of the Global Research Council (GRC), where heads of research funding agencies took up the issue of gender equity in STEM research. Even though I was the only woman (until then) on the 12-member governing board, everyone agreed to a statement of actions that countries could implement to further gender equity in STEM fields, including gender considerations in research design and analysis. The GRC board committed to collect and share data to chart progress.

The global economy, too, is now being viewed through a gender equity lens. Japan, host country of the May 2016 G7 Science and Technology Ministers' Meeting of leading industrial nations, is encouraging G7 nations to lead efforts in "inclusive innovation" to ensure that everyone accesses and benefits from science and technology. Further, the final G7 report encourages the development of "policy and working environments in which equal opportunity allows women to exert their abilities [and] advance their career prospects." Such changes help STEM equality and will attract and retain talented women in STEM careers.



"...global equity for women in science...is a call to action..."

What about the United States? Women now earn about half of all science and engineering bachelor's degrees, yet they account for only 30% of the U.S. science and engineering workforce. In some STEM fields, such as mechanical engineering, the percentage of women is in the single digits. NSF will continue to advance equity through data-driven decision-making. Our Career–Life Balance Initiative, for example, mitigates factors that can negatively affect women's ability to carry out research, especially during the early years of their careers. NSF's ADVANCE program encourages universities to use institutional data about recruitment and retention to develop structural changes to improve representation and advancement of women. These deliberate actions by NSF complement the research that NSF supports in the science and practice of STEM gender equity. Projects range from computer programming camps to encourage girls, to studies on creating classroom environments that attract and retain female students. One of our newest initiatives, NSF INCLUDES, is fostering innovative alliances and networks that can scale up effective methods for addressing shortages and broadening the participation of women and others who are underrepresented in STEM fields.

Ensuring global equity for women in science and engineering research requires personal commitment to action within one's own sphere of influence. It is a call to action we all must embrace.

–France A. Córdova



France A. Córdova is director of the U.S. National Science Foundation, Arlington, VA, USA.

Downloaded from http://science.sciencemag.org/ on July 28, 2016

IMAGES: (INSET) JOZEFMICIC ADAPTED BY G. GRULLÓN/*SCIENCE*; (TOP RIGHT) NSF/STEPHEN VOSS

10.1126/science.aah5898

Published by AAAS

NEWS

> “Let’s ask ourselves why haven’t we beaten this epidemic. Could it be because we don’t want to?”
>
> **South African–born actress and AIDS activist Charlize Theron**, in a speech last week at the International AIDS Conference in Durban. Theron suggested that society values some lives more than others, contributing to the virus’s spread.

IN BRIEF



The Norway rat is one of several predators that New Zealand wants to eliminate.

PHOTO: © TIM JAMES/MABEL GRAY/ALAMY STOCK PHOTO

New Zealand’s goal: Rat-free by 2050

An isolated archipelago, New Zealand once hosted almost 200 species of native birds, many of them flightless like the iconic kiwi. But introduced species—rats, possums, and a weaselike carnivore called a stoat—kill about 25 million of these native birds every year. This week, the country’s prime minister, John Key, announced a $20 million commitment of seed money to set up Predator Free New Zealand Ltd., a company that would lead the charge in getting rid of all of these predators by 2050. Until now, the country’s eradication efforts have focused on small islands; those efforts boast a 90% success rate, says James Russell, a conservation biologist at the University of Auckland in New Zealand. The new effort, Russell says, is “the modern equivalent to landing someone on Mars,” requiring new technologies and billions of dollars to succeed. But he is optimistic because local communities and organizations are on board. However, staying rat-free after 2050 might be the challenge, says Alberta Agriculture and Forestry conservation biologist Phil Merrill in Lethbridge. (That Canadian province is rat-free.) “They can do it if they can prevent the rats from jumping off the boats,” he predicts.

AROUND THE WORLD

Public wary of tech enhancements

WASHINGTON, D.C. | A new poll finds that Americans have serious questions about the use of new technologies to enhance the lives of healthy people. The Pew Research Center in Washington, D.C., asked 4726 U.S. adults for their views on editing genes in utero to reduce the prevalence of serious diseases, implanting brain chips into healthy individuals to augment their mental skills, and infusing fit people with synthetic blood to increase performance. The results, announced this week, show that Americans are much more comfortable with the idea of using those technologies to help correct existing problems or cope with a disability than to achieve a higher level of functioning. Those with strong religious beliefs are

Downloaded from http://science.sciencemag.org/ on July 28, 2016

Published by AAAS

especially troubled by the prospect of such enhancements, seeing them as meddling with nature, and women were significantly more wary than men. "The strength of differences based on religious commitment is one of the most surprising results," says Cary Funk, an associate director of research at Pew. "People were able to grasp the nuances of these different technologies," she added, "even though none has been put into practice."
http://bit.ly/techenhance

Accord nearer on HFCs

VIENNA | Nations have moved a step closer to a global agreement to curb the use of hydrofluorocarbons (HFCs), potent climate-warming compounds used in aerosols and for cooling. After days of meetings in Vienna, on 24 July negotiators from more than 150 nations reported substantial progress toward a deal that calls for richer nations to essentially end the use of HFCs by the 2030s, with poorer nations getting additional time to meet that goal. But negotiators must still resolve exact timetables, and how to fund the development and deployment of substitute technologies. Nations hope to sign a final deal in Kigali in October. Researchers estimate that phasing out HFCs, which became a widely used replacement for ozone-eating chlorofluorocarbons, could prevent as much as 0.5°C of planetary warming.

Gillnet ban aims to save vaquita

MEXICO CITY | Fishing with gillnets will soon be permanently banned in the northernmost part of the Gulf of California, Mexico's national fisheries commission announced on 19 July. The ban, which will begin in September, is intended to protect the vaquita, a small porpoise that lives only in those waters. The vaquita is listed as critically endangered, with just 60 individuals remaining; the mammals often die after becoming tangled in the vertical "walls" of netting. Fishing at night, when the rules are hardest to enforce, will also be prohibited, and fishing boats will have to depart from and return to specially designated docks. The ban focuses on the legal shrimp fishery, but gillnets are also used to illegally catch totoaba, an endangered fish whose swim bladder sells for $60,000 per kilogram in China. Enforcing the ban on new nets will be key to saving the vaquita, but "removing abandoned 'ghost' gillnets from vaquita habitat is the most immediate and urgent priority," says Omar Vidal, CEO of World Wildlife Fund Mexico in Mexico City.



A vaquita caught in fishing nets.

PHOTOS: (LEFT TO RIGHT) © FLIP NICKLIN/MINDEN PICTURES; COURTESY OF TEL AVIV UNIVERSITY



The cactus collection at the Tel Aviv University Botanical Garden in Israel.

Israeli botanical gardens face budget cuts

Israel's 11 botanical gardens are scrambling to cope with deep cuts in funding from the government's agricultural ministry. Spending on the gardens, which host research and education programs and are often associated with universities, is down by more than 50% this year, from about 4.5 million shekels ($1.1 million) in 2014 to 2 million shekels this year. That's a reprieve from a 98% cut that the ministry announced last year, but still a major blow for the gardens, which rely heavily on ministry funds to pay for basic operations. "There were times this year when we couldn't afford potting soil, or even printer paper," says Tal Levanony, curator of the garden associated with Tel Aviv University. http://bit.ly/Israeshekellgardens

'First-in-human' trials overhauled

LONDON | The European Union is beefing up protections for volunteers in phase I clinical trials in the wake of a disastrous clinical study in Rennes, France, that resulted in the death of one volunteer and the hospitalization of five others (*Science*, 12 February, p. 642). On 21 July, the European Medicines Agency (EMA) in London announced, in a "concept paper" written by an international group of experts, that it wants to improve strategies to identify and reduce risks in "first-in-human" (FIH) studies. The current guideline for FIH studies dates from 2007. EMA will seek in particular to reduce the risks of studies that combine different subtrials, which are becoming increasingly common; the trial in Rennes included subtrials using single and multiple dose administration, as well as trials on drug interactions with food and on pharmacodynamics, the study of a drug's biochemical and physiologic effects on the body. This increased complexity requires a new, structured approach, EMA says, in which decisions on each new step need to be based on the data collected at the previous one. EMA invites comments from stakeholders until 30 September, after which it will publish a draft revised guideline, probably later this year. http://bit.ly/_EMArules

A pan-European pension fund

MANCHESTER, U.K. | The European Union makes it easy for researchers to hop between member countries for research

Downloaded from http://science.sciencemag.org/ on July 28, 2016

Published by AAAS

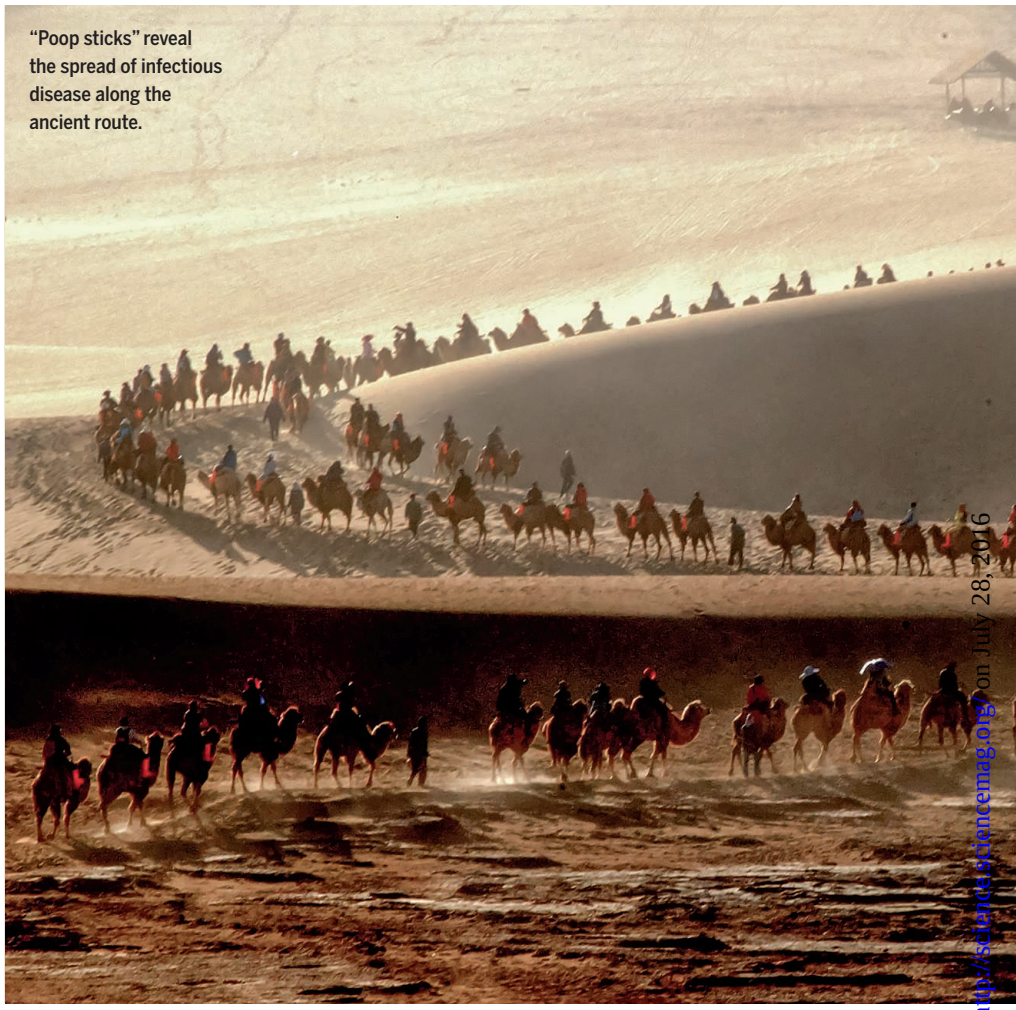
and training opportunities. Now, it is easing a practical concern linked to this mobility: securing a full retirement pension. Most European countries offer social security, but universities and institutions often provide "supplemental" pensions, which mobile researchers could lose out on. A pan-European pension plan called RESAVER that would allow researchers to carry supplemental pension benefits with them has been in the making since October 2014, and it is now up and running, organizers explained on 24 July at the EuroScience Open Forum in Manchester. Only three organizations, including a private university in Hungary and a research center in Italy, are ready to pay into the fund. But another 100 may join in the near future. In some countries, however, social and legal factors factors could limit the take-up of the plan.
http://bit.ly/RESAVER

Satellite shuffle for South Pole

SOUTH POLE | The National Science Foundation (NSF) last month decommissioned the oldest continuously operating satellite in the sky, the 38-year-old Geostationary Operational Environmental Satellite (GOES-3), because of its shrinking fuel supply. GOES-3 was originally a weather satellite, but for the past 21 years it has provided phone and internet service to NSF's Amundsen-Scott South Pole Station. Most communications satellites orbit at or near the equator, but GOES-3's orbit included a southerly oscillation that provided about a 6-hour window of visibility to the South Pole each day. (Several satellites provide visibility windows to the South Pole; with GOES-3, the total window was about 10 to 11 hours each day.) The decommissioning of GOES-3, in which the satellite was transferred to a "graveyard orbit" far from operating geostationary satellites and then shut down, was completed on 29 June. "Communication from Antarctica is hard by today's standards when you can pick up an iPhone and talk to someone in microseconds," says Pat Smith, program manager, technology development for NSF's U.S. Antarctic Program. The Defense Satellite Communications System phase III, vehicle B7 satellite is replacing GOES-3; it is more powerful and sophisticated, providing a higher data rate. It will also increase the daily visibility window for the South Pole to 14 to 15 hours, Smith says.



An artist's rendering of the GOES-3 satellite, which was moved into "graveyard orbit" last month.



"Poop sticks" reveal the spread of infectious disease along the ancient route.

World's deepest blue hole

SANSHA, PARACEL ISLANDS | Off the coast of the Paracel Islands in the South China Sea lies a dark blue, underwater cavern known as the "Dragon Hole." It's long been the stuff of local legend. Now, a team of Chinese researchers says it is officially the world's deepest known blue hole, plunging to a depth of about 300 meters—about 100 meters deeper than the previous recordholder, Dean's Blue Hole off the coast of the Bahamas. Blue holes occur on shallow carbonate platforms, such as the Bahama Banks, the Yucatán Peninsula, or the Paracel Islands; they are thought to have formed during past ice ages, when sea level was much lower and chemical weathering acted on the then-exposed, limestone-rich rock. The researchers began their exploration of the blue hole last August with the aid of an underwater robot, sonar scanners, deep-sea current meters, and underwater cameras. The team told a Chinese news agency last week that they had found more than 20 species of fish and marine life near the surface of the blue hole; below about 100 meters, however, the water contains too little oxygen to support life, they said. On 24 July, Sansha renamed the cavern the Sansha Yongle Blue Hole, and said it has plans to continue to study it. The Paracel Islands are among several disputed territories in the South China Sea; China and Vietnam have both laid claim to the island chain.

IMAGES: (LEFT TO RIGHT) NASA; CHINA DAILY/REUTERS/NEWSCOM

Downloaded from http://science.sciencemag.org/ on July 28, 2016

Published by AAAS



Sickness on the Silk Road

Travelers along the Silk Road toted a lot more than silk and spices. Fossilized intestinal parasites found in 2000-year-old human excrement from western China are offering the first evidence of the spread of infectious diseases along the Silk Road. In 1992, scientists working at the eastern edge of the Taklamakan Desert excavated a latrine at a Silk Road relay station where travelers likely slept and ate. The researchers found a number of "hygiene sticks," bamboo sticks with strips of cloth that were used to wipe the nether regions; the sticks were sent to a museum and forgotten about for decades. But last year, researchers at the University of Cambridge in the United Kingdom obtained the sticks and examined the ancient feces. They discovered eggs from four different parasites, including the Chinese liver fluke—a flatworm endemic to marshy areas. That parasite, the researchers suggested last week in the *Journal of Archaeological Science: Reports*, must have originally been picked up by travelers in modern-day Guangdong province, some 2000 kilometers away.

PHOTO: C.H. FAHAM/FLICKR

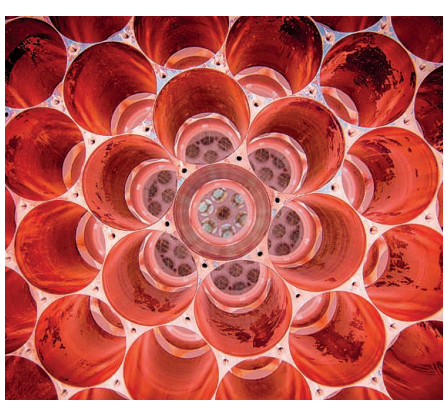
FINDINGS

New spin on an old ball game

In cricket, there are many ways that a bowler can outwit a batsman, but perhaps the one shrouded in the most mystery is spin bowling. Delivered at relatively low speed, like the knuckleball in baseball, the ball is given such extreme amounts of spin that it swerves while in the air and changes direction on the bounce. A pair of researchers has now shown that subtle spin combinations can produce the surprising and potentially game-changing results. In a paper in *Physica Scripta*, Ian Robinson of Victoria University in Melbourne, Australia, and Garry Robinson of the University of New South Wales, Canberra, describe a mathematical analysis of cricket balls in flight under the influence of three different directions of spin, plus gravity, drag, and lift. Topspin is known to make a ball bounce earlier; however, the researchers show that, if the total amount of spin is kept constant, a small amount of topspin added to a side-spinning ball makes it land 25 centimeters earlier, and a touch of sidespin added to a topspin delivery can produce 10 centimeters of sideways drift. The results, they say, could help cricket fans understand the underappreciated art of spin bowling.

Dark matter hunt comes up empty

The latest, most sensitive search for particles of dark matter—the invisible stuff whose gravity appears to bind the galaxies—has come up empty. The leading candidates for dark matter are so-called weakly interacting massive particles, or WIMPs. Since 2012, physicists working with the Large Underground Xenon (LUX) detector have searched for WIMPs bumping into the atomic nuclei in 370 kilograms of frigid liquid xenon. But the experiment, housed 1480 meters deep at the Sanford Underground Research Facility in Lead, South Dakota, ended its final run in May, and researchers found no evidence for such particles, they reported last week at a conference in Sheffield, U.K. The WIMP hunt will continue with newer detectors that will be even more sensitive: XENON1T, a detector at Italy's subterranean Gran Sasso National Laboratory that contains 3.5 metric tons of liquid xenon, and a rebuild of the LUX detector called LZ that would contain 10 metric tons of xenon and come online in 2020. But physicists' enthusiasm for WIMPs may be cooling—not just because they haven't found them yet, but also because the world's biggest atom smasher, Europe's Large Hadron Collider, has yet to blast such particles into existence, as theory suggests it should.



LUX's photomultiplier tubes watched in vain.

BY THE NUMBERS

156%

Average budget overrun for Olympic Games since 1960—the highest average cost overrun of any type of megaproject. All Games have had cost overruns (arXiv.org).

88%

Fraction of 628 physicians from 10 U.S. children's hospitals who said in a survey that they believe shaken baby syndrome is a valid diagnosis (*The Journal of Pediatrics*).

8

The United States's energy efficiency rank in 2016, up from 13 in 2014, according to the nonprofit American Council for an Energy-Efficient Economy. Germany is in first place.

Downloaded from http://science.sciencemag.org/ on July 28, 2016

Published by AAAS



PHOTO: INTERNATIONAL AIDS SOCIETY/ROGAN WARD

INFECTIOUS DISEASE

Obstacles loom along path to the end of AIDS

International meeting highlights clash between ambitious goals and wobbly funding

By **Jon Cohen**, *in Durban, South Africa*

The ambitious goal of "ending AIDS" is colliding with sobering realities. Researchers are convinced that if enough infected people can be put on antiretroviral (ARV) drugs, new infection rates will fall and AIDS will become a thing of the past. In 2014, the Joint United Nations Programme on HIV/AIDS (UNAIDS) embraced the goal, setting a 2030 target for identifying and treating everyone living with HIV. That would mean expanding the number of people on ARVs from 17 million today to nearly 37 million. But at the International AIDS Conference here last week, researchers and advocates highlighted disheartening trends: Funding is tight, infection rates remain high, drugs aren't getting cheaper, and infected people may not take the pills they are offered. "I'm scared," said UNAIDS head Michel Sidibé during the opening ceremony.

Last year, UNAIDS estimates that the world spent $19 billion on the HIV/AIDS response. It's a huge increase from the less than $2 billion spent in 2000, when the international AIDS meeting last took place here. But to "end AIDS," the agency calculates that funding must ramp up to $26.2 billion a year by 2020. And support is flat or declining. "If we continue with this trend, we'll not be able to end AIDS by 2030," Sidibé said. "We will have a rebound in the epidemic."

A new report from UNAIDS and the Kaiser Family Foundation shows that for the first time in 5 years, HIV/AIDS assistance from wealthy donor countries declined in 2015. Poorer countries have also cut domestic spending on treatment and prevention. And the two biggest purchasers of ARVs are deeply concerned about their budgets.

As part of its "replenishment" drive, the Global Fund to Fight AIDS, Tuberculosis and Malaria is asking donor countries to contribute $13 billion to cover grants to countries over the next 3 years—up from $12 billion raised at the last replenishment. "There's a huge uncertainty," given the political flux in the United States, the United Kingdom, and other leading European donor countries, says Michel Kazatchkine, a former Global Fund head who now is a special AIDS envoy for the United Nations secretary-general in Geneva, Switzerland. The U.S. President's Emergency Plan for AIDS Relief (PEPFAR) in Washington, D.C., which invests $4.7 billion a year on bilateral aid, has had a flat budget since 2009 and has been able to expand the number of people on treatment primarily because drug costs have declined. "Flat is the new increase," said PEPFAR's director of financial stability, Michael Ruffner.

South Africa feels the funding pinch acutely. The country has the world's largest epidemic and buys more ARVs than any other: Out of an estimated 6.6 million people infected, 3.4 million are on treatment. It now pays for 80% of its HIV/AIDS response, and the Global Fund and PEPFAR are cutting back support. But the country has had a declining gross domestic product for the last 5 years (*Science*, 1 July, p. 18), along with a currency devaluation that made drugs from foreign companies more expensive.

Meanwhile, the number of people around the world who become infected with HIV each year, nearly 2 million, has remained stubbornly stable for 5 years. In Eastern Europe and central Asia, the region with the fastest growing epidemic in the world, new infections jumped 57% between 2000 and 2015. Russia no longer receives Global Fund assistance because it's too wealthy, and support for Ukraine is also dwindling. Many of these countries have haphazard HIV/AIDS responses. For instance, only 18% of the HIV-infected people in Eastern European and central Asian countries currently receive ARVs.

Cheaper drugs could stretch funds and make the 2030 goal more attainable. Indian manufacturers of generic pills provide 76% of all the drugs used in low- and middle-income countries, charging as little as $100 per patient per year. But Anil Soni of generic drug titan Mylan Pharmaceuticals in Canonsburg, Pennsylvania, which has a large operation in

Downloaded from http://science.sciencemag.org/ on July 28, 2016

Published by AAAS

Street marches at the International AIDS Conference held in Durban, South Africa, last week rallied countries to offer treatment to all HIV-infected people.

Bengaluru, India, contends that generic drug prices for first-line treatment are already at rock bottom. He has warned the big buyers that companies will lose money if they cut prices much lower, and that they need more stable purchasing commitments to invest in the plants that will be required to more than double their production. "I don't think it's impressed upon anyone that treating 30 million people over 100 countries with 15,000 metric tons of drug has never been done," said Soni, who in earlier jobs sat on the other side of the table, negotiating lower prices when he worked at the Global Fund and the Clinton Health Access Initiative.

Peter Piot, the former director of UNAIDS who now heads the London School of Hygiene & Tropical Medicine, says he spent much of his career urging drug companies to lower prices, but he now agrees with Soni that they've hit the bottom. He talks of a "looming crisis of insufficient supply of ARVs" if generic companies decide that the profit margin is too small and that it's better business to produce Viagra or high blood pressure drugs.

UNAIDS's "ending AIDS" goal is also colliding with human behavior. Its cornerstone is what's known as 90-90-90: Ninety percent of HIV-infected people know their status, 90% of that group receives care, and 90% of people on treatment suppress the level of virus in their blood to undetectable levels. This both helps individuals and reduces the likelihood that they will transmit the infection, as a landmark study published in 2011 proved convincingly. But in the United States, only 30% of HIV-infected people fully suppress their virus, and the number is far lower in many countries.

A new study of 28,000 people in South Africa underscores the problem. The so-called Treatment as Prevention (TasP) study compared communities that started ARVs as soon as people learned they were infected with those that began treatment later, as per older government recommendations. The two cohorts had the same rate of new infections, probably because 53% of the people in the immediate treatment arm who were eligible for the drugs never followed up with a clinic visit within 12 months. Even among the 47% who did, not all opted to start treatment.

The TasP results emphasize that offering ARVs to every infected person is just one step forward and, absent intensive efforts to get people on treatment and help them stick with it, has little chance of bringing the epidemic to an end. ■

CREDITS: (GRAPHIC) A. CUADRA/*SCIENCE*; (DATA) CHIMPCARE

ANIMAL RESEARCH

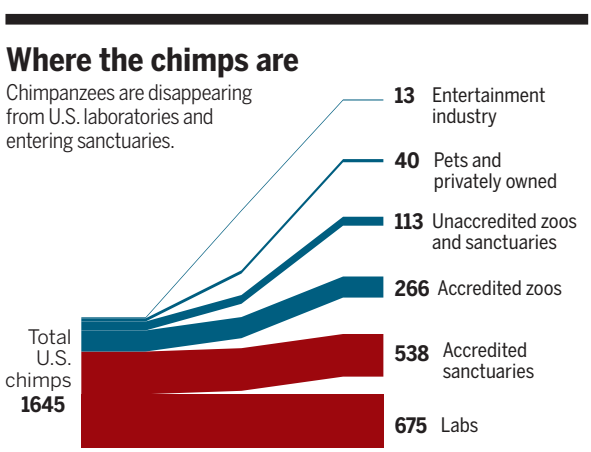
Chimpanzee sanctuaries open door to more research

Collaboration aims to beef up science at retirement centers

By **David Grimm**, *in Keithville, Louisiana*

The lab chimp is on the verge of extinction. Fewer than 700 remain in U.S. laboratories, and most are expected to move to sanctuaries over the next decade because of ethical and scientific concerns (*Science*, 19 June 2015, p. 1296). But a new opportunity may be opening up for studies of chimpanzee behavior and cognition: A first-of-its-kind partnership between a sanctuary and a research center, announced this month, is designed to bolster the scientific output of facilities that have until now primarily focused on the long-term care of their animals.

Proponents hope the agreement, between the Chimp Haven sanctuary here and a research arm of the Lincoln Park Zoo in Chicago, Illinois, will become a model for others. "I hope that this collaboration is the first step that sets a trend," says Gregg Tully, executive director of the Pan African Sanctuary Alliance, a network of 22 African sanctuaries based in Portland, Oregon.



But such partnerships won't be easy, because sanctuaries, particularly in the United States, have long had a fraught relationship with the research community. "They see science as a threat," says Brian Hare, an evolutionary anthropologist at Duke University in Durham, North Carolina, who has studied chimpanzee cognition in African sanctuaries for more than a decade. Scientists, meanwhile, have questioned whether important, quality studies can be done at facilities that allow little or no interaction between researchers and animals. The agreement between Chimp Haven and the zoo's Lester E. Fisher Center for the Study and Conservation of Apes is "a good first step," says Michael Beran, a psychologist at Georgia State University in Atlanta who has worked with lab chimps for more than 20 years. "But it's going to take a lot more work to see if this model establishes itself."

African sanctuaries, which mostly draw orphans from the bushmeat and pet trades rather than from labs, have been more amenable to research, notes Stephen Ross, director of the Fisher Center, who facilitated the new agreement. But projects only happen when a visiting scientist like Hare comes along, he says. "When the researcher goes away, the science goes away."

He wanted to build a stronger bridge between the sanctuary and scientific worlds. In addition to his zoo duties, he chairs the board of directors of Chimp Haven, which has more than 200 chimpanzees and is the designated retirement center for all federally owned chimps. Ross believed a partnership between the sanctuary, which was already doing some limited behavioral research, and the Fisher Center, where several Ph.D.s study chimp memory and tool use, could bolster Chimp Haven's research program while allowing zoo scientists access to more animals in a more natural setting. A $350,000 grant from the Arcus Foundation, which supports great ape conservation, launched the collaboration.

It also allowed the group to hire its first researcher, postdoc Bethany Hansen. Today, she's jotting notes on her iPad mini as she watches seven chimps in "The Courtyard"—a two-story caged enclosure about the size of a tennis court filled with hammocks, tire swings, and climbing platforms. She's tracking each chimp for about 10 minutes, and noting every 30 seconds what they're doing and who they're with. The goal is to see

Downloaded from http://science.sciencemag.org/ on July 28, 2016

Published by AAAS

how the presence of strangers affects their behavior, findings that may influence how much access sanctuaries allow the public.

Hansen is also studying how the chimps adapt to the sanctuary's environments, including corrals and a 2-hectare forest where the animals can climb trees and poke sticks into artificial termite mounds. At Chimp Haven, she has access to 10 times the number of chimpanzees she would at the zoo, and, unlike in the wild, there's no danger of losing track of an animal. "You're getting the best of both worlds," Ross says.

In return, the sanctuary gets a full-time scientist. Research director Amy Fultz says her team is lucky to collect 6 hours of data on the chimpanzees per week. Hansen can do 3 hours a day and tackle a variety of projects. "It enhances what we can do, and it enhances our mission," Fultz says.

Some biomedical studies may even be possible. Chimp Haven's president, Cathy Spraetz, says the sanctuary would consider sharing blood and other tissues collected during routine procedures with outside scientists. It has also agreed to donate the brains of deceased animals.

Still, sanctuary research faces big challenges. Most animals at Chimp Haven have spent their entire lives in labs, where some were injected with viruses like hepatitis and HIV and regularly had organs biopsied and blood drawn. That could complicate research on how normal chimps think and behave, says David Watts, a Yale University primatologist who has studied chimpanzees in Uganda for more than 20 years. "We see some puzzling findings with these [captive] animals in cognition research," he says, like chimps asking humans to do things for them—which would never happen in the wild.

But the biggest hurdles are cultural. Ross would like to eventually move on to more substantive studies of behavior and cognition at the sanctuary. That could include giving the animals touchscreens and puzzles to play with. Spraetz is open to such experiments, as long as they don't interfere with the animals' normal lives.

But Molly Polidoroff, who runs Save the Chimps—North America's largest chimpanzee sanctuary, based in Fort Pierce, Florida—is less comfortable with such work. "We don't test hypotheses with our chimps."

Given that resistance, Georgia State's Beran questions whether sanctuaries can do weighty science. "These facilities could have a very large impact on the field, but only if they can find a way to do this work without conflicting with their retirement mission," he says. "It would be a real shame if in 10 years the only research that was being done was, 'What diet should they be on?'"

And if Chimp Haven truly wants to beef up its research program, it will need to find more money. The National Institutes of Health owns most of the chimpanzees here and pays for their care, but it doesn't fund research on them. So the collaboration will have to expand its reliance on donors and private foundations. Ross also hopes that scientists who have lost their lab chimps will come to sanctuaries to continue their work—and bring their own money.

For now, sanctuaries seem open to the idea of conducting more research. Even Save the Chimps's Polidoroff has just hired a nationally known scientist to head up a formal behavioral research program. "We see the potential for doing more," she says. Hare is optimistic, too. "I think research on great apes will flourish," he says. "There's a happy page being turned here." ■



Bethany Hansen observes retired chimps in an outdoor play area at Chimp Haven in Keithville, Louisiana.

PHOTO: DAVID GRIMM

CONSERVATION BIOLOGY

Rethinking the North American wolf

Genome sequencing suggests two endangered wolf species are coyote hybrids

By **Virginia Morell**

When is a wolf a wolf? For more than 30 years, the question has dogged scientists, conservationists, and policymakers attempting to restore and protect the large wild canids that once roamed North America. Now, a study of the complete genomes of 28 canids reveals that despite differences in body size and behavior, North American gray wolves and coyotes are far more closely related than previously believed, and only recently split into two lineages. Furthermore, the endangered red and eastern wolves are not unique lineages with distinct evolutionary histories, but relatively recent hybrids of gray wolves and coyotes, the scientists report online this week in *Science Advances*.

That could be a problem for the wolves. The red wolf is currently protected under the U.S. Endangered Species Act (ESA), and some conservationists would like to see the eastern wolf listed as well. (It is protected in Canada.) But as hybrids, they may not qualify for protection under U.S. law. The study "helps with more data but hurts by giving less protection to [the] two wolf types," says Doug Smith, the leader of Yellowstone National Park's wolf restoration project in Mammoth, Wyoming.

The research team argues that red and eastern wolves should still be protected, and urges reconsideration of our black-and-white species concept. "People think that species should be genetically pure, that there should be tidy categories for 'wolf' and 'coyote.' That's not what we found," says Bridgett vonHoldt, an evolutionary biologist at Princeton University and the study's lead author. "The study shows that mixed ancestry is common, even in animals [in the western United States] we've traditionally identified as 'pure,'" adds Linda Rutledge, a postdoc in VonHoldt's lab who was not involved in the study and doesn't accept all its findings. "It shows how outdated the endangered species policy is with respect to hybrids."

Downloaded from http://science.sciencemag.org/ on July 28, 2016

Published by AAAS

Gray wolves (*Canis lupus*) and the smaller, narrow-snouted coyotes (*C. latrans*) have long been accepted as North America's two large canid species. But some scientists recognize two additional wolf species—the red (*C. rufus*), found in the southeastern United States, and the eastern wolf (*C. lycaon*), which ranges from the Great Lakes into eastern Canada (see map, below).

The United States Fish and Wildlife Service (FWS) counts both as species. It put the red wolf on the endangered list in 1973 and started a captive breeding program for it in 1980, but reintroducing the animals has proven difficult, because they readily mate with coyotes. The agency has not put the eastern wolf on the endangered list, although it is restricted to a small portion of its former range. (In a controversial move in 2012, FWS used the existence and range of the eastern wolf as a technicality that could invalidate the gray wolf's protections, because if the eastern wolf is a real species, then the gray's range in the original ESA filing was incorrect.)

Other researchers have suspected, however, that both "species" are, in fact, wolf-coyote hybrids that arose after the grays were hunted almost to extinction. To help sort out the North American wolves' muddled history, VonHoldt's team sequenced the whole genomes—nearly 3 billion bases each—of 28 large canids; they included wolves from Asia, Mexico, Canada, and the United States, plus coyotes, domesticated dogs, and a golden jackal. Comparing the genomes let them "look back in time at the canids' deep evolutionary history," VonHoldt explains, "and to find each species's closest relative, and when they diverged."

Using a molecular clock based on differences in the genomes to calculate when coyotes and gray wolves split, the team got a surprise: These canids separated from the Eurasian wolf and into two distinct lineages between 6000 and 117,000 years ago. Other researchers had previously dated this event to 1 million years ago using the fossil record. The recent date for the wolf-coyote split "is phenomenal," VonHoldt says. "They are very close relatives." Even western wolves that do not breed with coyotes still share some coyote genes.

But the team found even more coyote genes, of more recent origin, in red wolves and eastern wolves, including those from Algonquin Provincial Park in Canada where pure eastern wolves were thought to exist. The paper estimates that Algonquin wolves have about 32% coyote ancestry, and Quebec wolves more than 50%. The team concludes that neither the red nor the eastern wolf is a species. Instead, they suggest that both are hybrid populations that arose after Europeans arrived in North America, when gray wolves that managed to survive hunting and habitat loss mixed with expanding populations of coyotes. "There's nothing in their genome that's not gray wolf or coyote," says co-author Robert Wayne, an evolutionary biologist at the University of California, Los Angeles.

Rutledge and others, including conservation geneticist Paul Wilson, who studies the eastern wolf at Trent University in Peterborough, Canada, argue that researchers need to sequence more samples of *C. lycaon* before dumping that taxon. But others who have long questioned the status of eastern and red wolves welcome the work. "Wolf biologists and others have been waiting for this sort of definitive analysis for years," says Susan Haig, a wildlife ecologist at the United States Geological Survey in Corvallis, Oregon.

The loss of species status for the red and eastern wolves doesn't mean they should lose protection, Wayne and others say. Hybridization is "a natural and commonly occuring evolutionary event," Wayne says, noting that the ESA has successfully been used to protect hybrid species such as the Florida puma and western spotted owl. He thinks eastern and red wolves should be protected because they likely still carry genes from wolves that once inhabited these regions, and because they are evolving into animals better adapted to today's human-dominated landscapes. The team also argues that the agency's arguments for delisting the gray wolf are no longer valid.

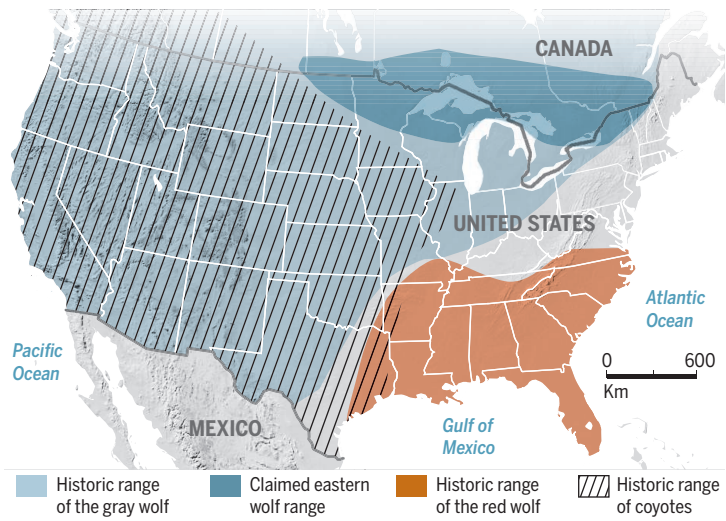
It's possible that eastern and red wolves—if regarded as grays—would still be protected, but FWS declined to comment on the details of the paper.

Other scientists say the messy natural biology revealed by the study clashes with society's need for clear legal definitions. "It's beautiful work and topflight science," says Mike Phillips, a restoration ecologist with the Turner Endangered Species Fund in Bozeman, Montana. "But from a practical standpoint, to do what they're asking [and consider the ecological benefits of hybrids], you'd have to amend the ESA."

He and others lament the possibility that red wolves might lose ESA protection because of the findings. That, they say, would be a sad irony for canids that likely evolved because of human disturbance in the first place. ■

A continent of canids

Opinions vary on wolf ranges and identities, but most researchers agree that the gray wolf once roamed across much of North America (including into Mexico, not shown) and that the coyote ranged across the west. A new genetic study finds that the red wolf and the eastern wolf (one from Quebec in Canada, bottom) arose later by mixing with coyotes as they expanded eastward.





CREDITS: (PHOTO) ROLAND SEITRE/MINDEN; (MAP) A. CUADRA/*SCIENCE*

Downloaded from http://science.sciencemag.org/ on July 28, 2016

Published by AAAS



Supporters of Turkey's government celebrate the failed coup on a bridge in Istanbul.

PHOTO: YAGIZ KARAHAN

TURKISH SCIENCE

After failed coup, Turkey's academics feel regime's wrath

Thousands of researchers and university officials fired, suspended, or told to return home immediately

By **John Bohannon**

Last week's failed coup attempt in Turkey lasted just a day, but the pain has only begun for Turkish academics. In a massive political purge, the government has suspended or fired thousands of professors and staff at universities, as well as employees of the nation's ministry of education. Officials have also ordered researchers who are affiliated with Turkish universities and working abroad to return home immediately—with an implied threat of treason charges for those who don't.

As a result of the moves, even Turkey's researchers who are still employed "have just lost this entire field and conference season," says Cagan Sekercioglu, an ecologist based at the University of Utah in Salt Lake City who, like other Turks who permanently left their country for academia abroad, is beyond the government's reach.

The 15 July coup attempt was short-lived. Rebel soldiers briefly seized key buildings, bridges, and roads, but Turkish President Recep Tayyip Erdoğan quickly reestablished his grip on power. Erdoğan then made an ominous announcement about his opponents: "They will pay a heavy price." Exactly who "they" are remains to be seen.

Many of the protest movements against Erdoğan over the years have originated among academics, which may be why they are one focus of his wrath. In the span of a few days, Erdoğan fired more than 45,000 civil servants in the military and judiciary, and 15,000 staff members of the ministry of education. Some 21,000 teachers lost their licenses, and more than 1500 university deans have reportedly resigned under pressure. Since then, officials have sacked hundreds more faculty and staff at some universities. It's not clear whether or when those removed from jobs might get them back. Universities have ground to a halt, say sources based in Turkey. On 21 July, Erdoğan tightened his grip by declaring a 3-month state of emergency, which allows him to set curfews, issue decrees, and make arrests without warrants.

The global scientific community is looking on with dismay. "[We are] alarmed by the repressive and excessive nature of recent measures against several public sectors in Turkey, including the academic and research community," reads an open letter published last week by the European Federation of Academies of Sciences and Humanities. The purge is not a proportional reaction, says Martin Chalfie, chair of the Committee on Human Rights at the U.S. National Academies of Sciences, Engineering, and Medicine in Washington, D.C. "Protecting national security should not be incompatible with safeguarding fundamental rule of law and human rights principles."

Turkish law does give Erdoğan broad authority over Turkey's 180 universities. Although each campus chooses its rector through a nominally democratic process in which faculty members vote for candidates, the ministry of education has the final say. "The university rarely gets its top choice," says Caghan Kizil, a Turkish molecular biologist based at the Dresden University of Technology in Germany. As a result, Erdoğan's allies occupy key slots, as the aftermath of the coup has made clear. "The university rectors asked their deans to resign and the implication was clear: Resign or you will be accused of treason and arrested," Kizil says.

For some Turkish academics, the government's response has mostly spelled inconvenience, at least so far. Graduate students have had to at least temporarily abandon visiting research posts that they had won through prestigious programs, such as the European Union's Erasmus Mundus scholarship. Postdoctoral researchers planning to travel abroad are in limbo. "A Turkish postdoc who was going to come to my lab had to cancel and lost a month's rent," Utah's Sekercioglu says. Turkish universities have been contacting their researchers abroad, but some are still waiting for any word. "Nobody has called me back yet," says a Turkish scientist on sabbatical at a U.S. university who requested anonymity. The purge troubles him, he says, but he is "very glad that the coup did not succeed."

Many academics fear the clampdown is just the beginning. It is a sign that "academic freedoms will no longer exist" in Turkey, predicts Sinem Arslan, a Turk doing doctoral work in political science at the University of Essex in the United Kingdom. The government has urged rectors to hand over the names of university members suspected of having ties to coup organizers, academics report; many fear the move will encourage ideological blacklisting. Government officials "want to take the universities under their full control," Arslan says. "I don't think that anybody will be able to work on research areas that are considered taboo by the government or write anything that criticizes the government." Erdoğan has been hostile to the women's rights movement, for example, and to academics who express support for the country's Kurdish minority (*Science*, 25 March, p. 1381).

Many see the purge as an opportunistic power grab by the ruling Justice and Development Party, and maintain that plans to quash dissent have been in the works for years. Critics of the government had hoped to find embarrassing evidence of those plans in nearly 300,000 internal government emails released by the organization WikiLeaks days after the coup. But the cache, which includes emails dating back 2010, has so far yielded little. ■

Downloaded from http://science.sciencemag.org/ on July 28, 2016

Published by AAAS

EUROPE

Uncertainty reigns in Brexit Britain

As U.K. universities counsel their E.U. staff, researchers see first signs of fallout

By **Erik Stokstad**, *in Manchester, U.K.*

Nothing has changed, yet everything has changed. In the weeks since the United Kingdom voted to leave the European Union, the U.K. government has made it clear that foreign residents won't be kicked out, and their legal rights remain intact—and that might only change after new treaties are forged, a process that could take years. But when the University of Oxford held an information session on Brexit this month, the meeting was packed and several hundred scientists and other staff crammed into an overflow room. "The general feeling was anxiety," says Ian Walmsley, pro-vice-chancellor for research and innovation at Oxford.

Researchers from other parts of the European Union, who make up 16% of academic staff at U.K. universities, are anxious about their status, and—like their U.K. colleagues—concerned about access to European grant funding and research facilities. Reassuring details are scarce. In a speech at the EuroScience Open Forum (ESOF), the largest general scientific meeting in Europe, held here from 23 to 27 July, a tired looking Jo Johnson, U.K. minister for universities and science, could only tell delegates: "I recognize the demand for further clarity on these issues and I'm working intensively with colleagues across government to provide it as soon as practicable." He took no questions.

After the 23 June referendum, the pressure group Scientists for EU asked researchers about their concerns. Among the 400 responses, 46 reported hearing about or experiencing xenophobia. And at least 84 people were planning to leave the United Kingdom or know someone who is. "We are very concerned about recruitment and retention of academic and research staff," says Paul Crowther, an astrophysicist at the University of Sheffield in the United Kingdom.

The U.K. government announced on 11 July that the referendum did not change the rights of E.U. nationals. Nevertheless, the message to foreign scientists must be stronger, says Venki Ramakrishnan, president of the Royal Society in London. "They need to be reassured, if they are here and employed, they're not suddenly going to be told that they have to apply for permission or leave."

Larger political developments have added to the anxiety. The new prime minister, Theresa May, did little to comfort university-based scientists when she formed her new cabinet earlier this month: Responsibility for universities was split from research and placed in a different department. Johnson, who was appointed minister for universities and science in May 2015 and remains in the role, now has to report to two departments.

Universities are starting to take matters into their own hands. At Imperial College London (ICL), where 25% of staff and 20% of students hail from other countries in the European Union, the human resources department has set up 10 sessions from now until September with a law firm to explain how to apply for residency and citizenship. The university has also offered interest-free loans to help cover the cost of applications. "The biggest risk to our science right now is uncertainty and misperception about studying and working in the U.K.," Maggie Dallman, associate provost of ICL, said in a statement. "We must keep shouting that U.K. science is open for business and help the government ensure that this remains the case."

As for participation in Horizon 2020, the European Union's giant, 7-year funding program, the E.U. directorate for research said on 4 July that U.K. scientists can still apply for and participate in grants while the United Kingdom remains part of the European Union. "No one should have any doubt about it," Carlos Moedas, the commissioner for research, told a large audience at ESOF. "Horizon 2020 projects will continue to be evaluated based on merit and not on nationality." There is anecdotal evidence, however, that some E.U. researchers and managers perceive that U.K. involvement might now pose a liability in an E.U. grant application. Among the Scientists for EU responses, 33 described disruptions in Horizon 2020 consortia, such as being asked not to participate. "It's a chilling effect on collaboration," says Kieron Flanagan, a science policy expert at the University of Manchester.

Some say the government should take steps to forestall discrimination against U.K. participants in Horizon 2020 grants. Before and during negotiations over Brexit, for example, it could guarantee to make up for any funding lost because of the separation. That way E.U. applicants would be assured that U.K. collaborators can bring money for the duration of a project. "We will continue to push for that," Ramakrishnan says.

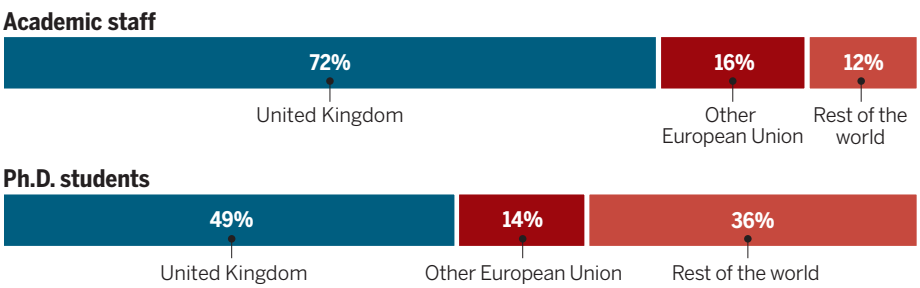
After the separation, the United Kingdom could buy into Horizon 2020 as an associate member, as some other non-E.U. nations have done. But some are skeptical that the government will replace much, if any, of the 10% of science funding that currently comes from the European Union. "I doubt if we will persuade the government to increase the money to make up for E.U. funds," Walmsley says.

The scientific community is gearing up to push for the best possible deal once the divorcing partners begin discussing terms. And Ramakrishnan says he's optimistic about future participation in E.U. science programs. "As one of the strongest science countries in Europe, we're also valuable to the rest of Europe," he says. Another reason for hope, according to James Wilsdon, a science policy expert at the University of Sheffield, is that in the difficult Brexit negotiations, participants will seek easy areas of agreement first—and science could be recognized as a mutual win. ■

With reporting by Tania Rabesandratana.

Open to the world

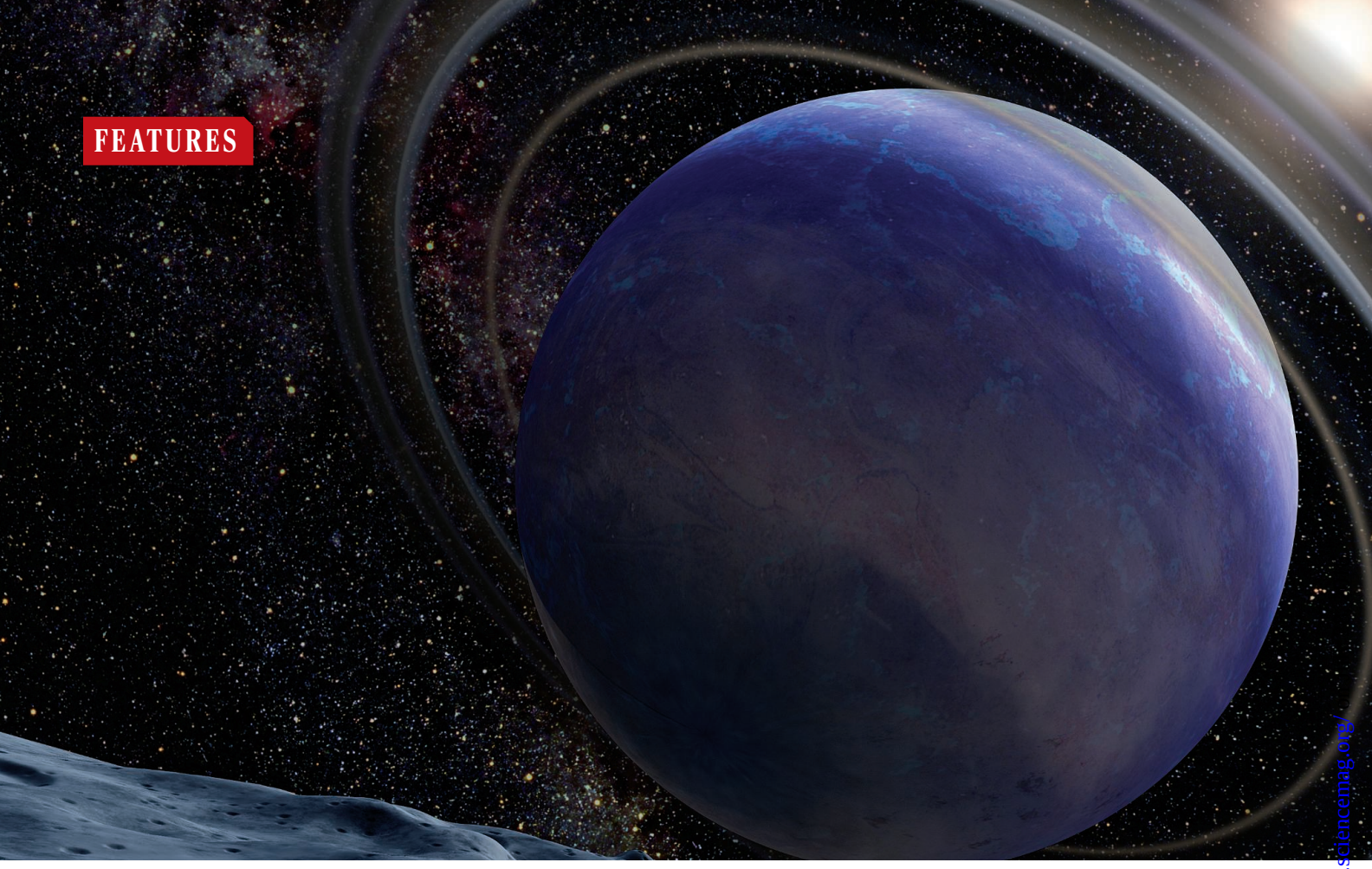
U.K. universities employ academic staff from all over the world, including nearly 32,000 from the rest of the European Union. The proportion of foreign Ph.D. students is even higher.



CREDITS: (GRAPHIC) A. CUADRA/*SCIENCE*; (DATA) HIGHER EDUCATION STATISTICS AGENCY

Downloaded from http://science.sciencemag.org/ on July 28, 2016

Published by AAAS



Downloaded from http://science.sciencemag.org/

FORBIDDEN PLANETS

How the zoo of exoplanets has turned planet formation theory upside down

By **Daniel Clery**

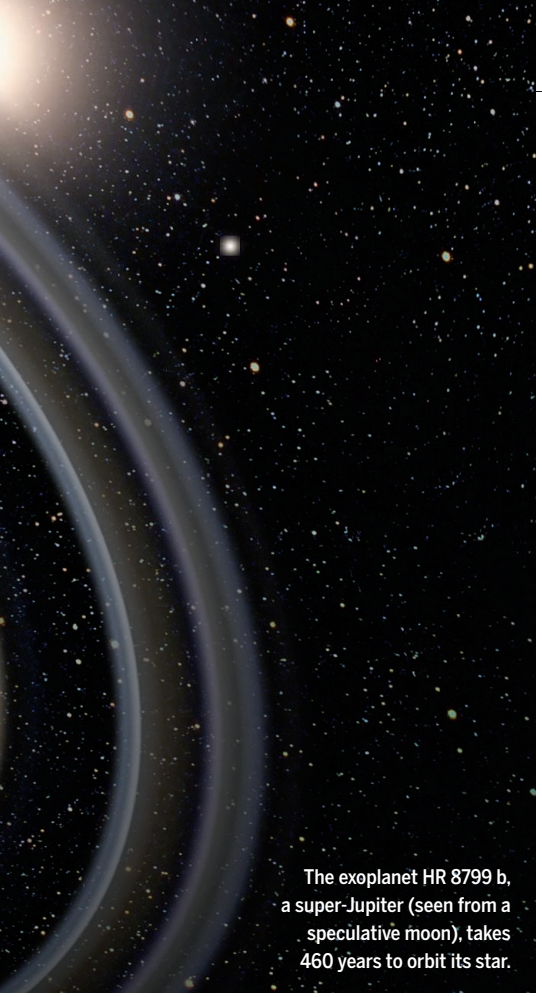
When astronomers discovered the first exoplanet around a normal star 2 decades ago, there was joy—and bewilderment. The planet, 51 Pegasi b, was half as massive as Jupiter, but its 4-day orbit was impossibly close to the star, far smaller than the 88-day orbit of Mercury. Theorists who study planet formation could see no way for a planet that big to grow in such tight confines around a newborn star. It could have been a freak, but soon, more "hot Jupiters" turned up in planet searches, and they were joined by other oddities: planets in elongated and highly tilted orbits, even planets orbiting their stars "backward"—counter to the star's rotation.

The planet hunt accelerated with the launch of NASA's Kepler spacecraft in 2009, and the 2500 worlds it has discovered added statistical heft to the study of exoplanets—and yet more confusion. Kepler found that the most common type of planet in the galaxy is something between the size of Earth and Neptune—a "super-Earth," which has no parallel in our solar system and was thought to be almost impossible to make. Now, ground-based telescopes are gathering light directly from exoplanets, rather than detecting their presence indirectly as Kepler does, and they, too, are turning up anomalies. They have found giant planets several times the mass of Jupiter, orbiting their star at more than twice the distance Neptune is from the sun—another region where theorists thought it was impossible to grow large planets. Other planetary systems looked nothing like our orderly solar system, challenging the well-worn theories that had been developed to explain it.

"It's been really obvious things didn't fit pretty much from day one," says Bruce Macintosh, a physicist at Stanford University in Palo Alto, California. "There has never been a moment when theory has

PHOTO: NASA/ESA/G. BACON (STSCI)

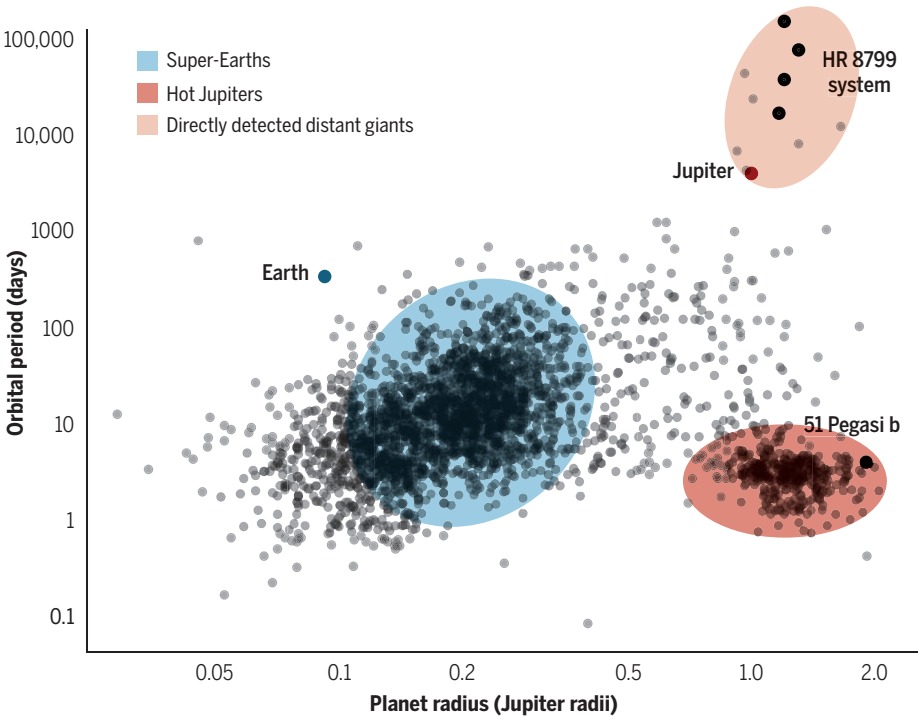
Published by AAAS



The exoplanet HR 8799 b, a super-Jupiter (seen from a speculative moon), takes 460 years to orbit its star.

Super-Earths rising

Hot Jupiters came first. The Kepler spacecraft then found super-Earths, also in close-in orbits, to be the most common type of exoplanet. Ground-based telescopes are now directly seeing distant giants like HR 8799 b.



caught up with observations."

Theorists are trying to catch up—coming up with scenarios for growing previously forbidden kinds of planets, in places once thought off-limits. They are envisioning how planets could form in much more mobile and chaotic environments than they ever pictured before, where nascent planets drift from wide to narrow orbits or get ricocheted into elongated or off-kilter paths by other planets or passing stars. But the ever-expanding zoo of exotic planets that observers are tallying means every new model is provisional. "You can discover something new every day," says astrophysicist Thomas Henning of the Max Planck Institute for Astronomy in Heidelberg, Germany. "It's a Gold Rush situation."

THE TRADITIONAL MODEL of how stars and their planets form dates back to the 18th century, when scientists proposed that a slowly rotating cloud of dust and gas could collapse under its own gravity. Most of the material forms a ball that ignites into a star when its core gets dense and hot enough. Gravity and angular momentum herd the leftover material around the protostar into a flat disk. Dust is key to transforming this disk into a set of planets. The dust, which accounts for a small fraction of the disk's mass, is made up of microscopic specks of iron and other solids. As they swirl in the roiling disk, the specks occasionally collide and stick together by electromagnetic forces. Over a few million years, the dust builds up into grains, pebbles, boulders, and, eventually, kilometer-wide planetesimals.

At that point gravity takes over, pulling in other planetesimals and vacuuming up dust and gas until planet-sized bodies take shape. By the time that happens in the inner part of the disk, most of its gas has been stripped away, either gobbled up by the star or blown away by its stellar wind. The dearth of gas means inner planets remain largely rocky, with thin atmospheres.

This growth process, known as core accretion, proceeds faster in the outer parts of the disk, where it is cold enough for water to freeze. The ice beyond this "snowline" supplements the dust, allowing protoplanets to consolidate more quickly. They build up a solid core five to 10 times the mass of Earth—quickly enough that the disk remains gas-rich and the core can pull in a thick atmosphere, producing a gas giant like Jupiter. (One of the goals of NASA's Juno spacecraft, which arrived at Jupiter earlier this month, is to see whether the planet really does have a massive core.)

This scenario naturally produces a planetary system just like our own: small, rocky planets with thin atmospheres close to the star, a Jupiter-like gas giant just beyond the snowline, and the other giants getting progressively smaller at greater distances because they move more slowly through their orbits and take longer to hoover up material. All the planets remain roughly where they formed, in circular orbits in the same plane. Nice and tidy.

But the discovery of hot Jupiters suggested something was seriously amiss with the theory. A planet with an orbit measured in days travels an extremely short distance around the star, which limits the amount of material it can scoop up as it forms. It seemed inconceivable that a gas giant could have formed in such a location. The inevitable conclusion was that it must have formed farther out and moved in.

Theorists have come up with two possible mechanisms for shuffling the planetary deck. The first, known as migration, requires there to be plenty of material left in the disk after the giant planet has formed. The planet's gravity distorts the disk, creating areas of higher density, which, in turn, exert a gravitational "drag" on the planet, causing it to gradually drift inward toward the star.

There is supporting evidence for the idea. Neighboring planets often end up in a stable, gravitational relationship known

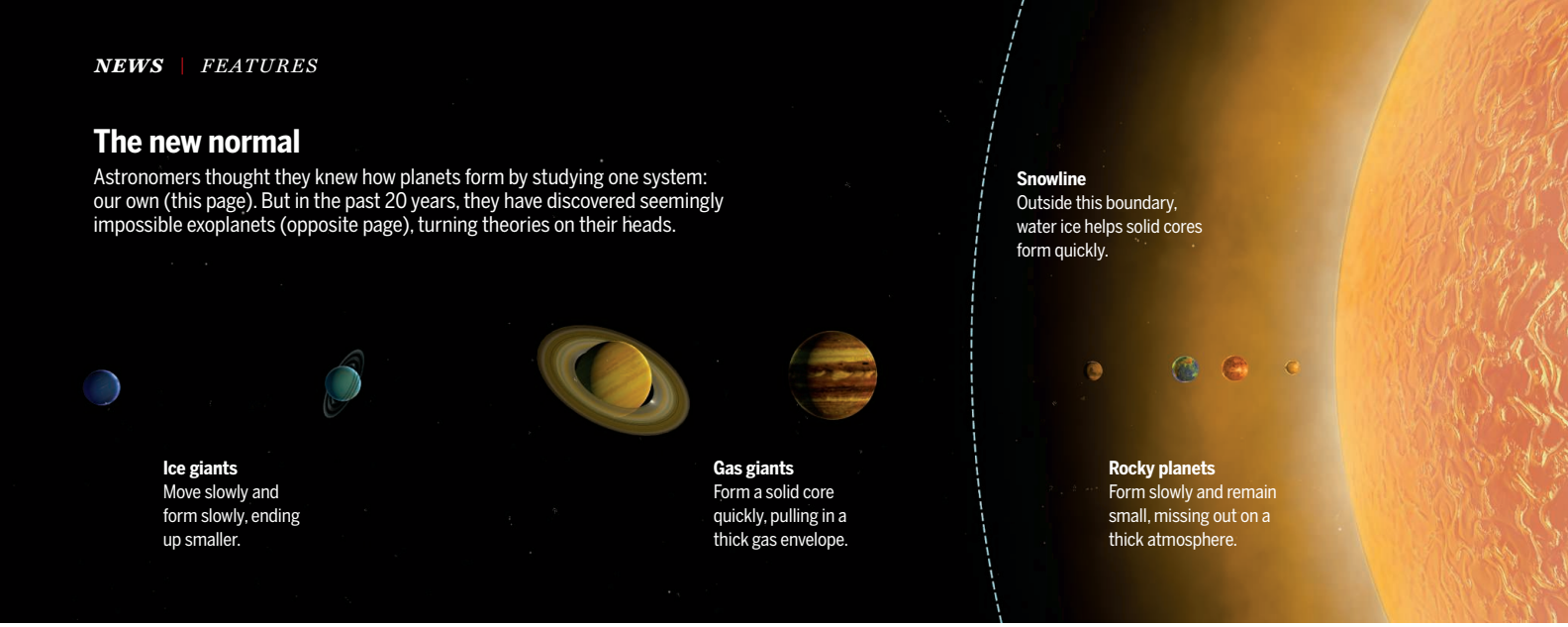
CREDITS: (GRAPHIC) J. YOU/*SCIENCE*; (DATA) EXOPLANETS.EU

Downloaded from http://science.sciencemag.org/ on July 28, 2016

Published by AAAS

The new normal

Astronomers thought they knew how planets form by studying one system: our own (this page). But in the past 20 years, they have discovered seemingly impossible exoplanets (opposite page), turning theories on their heads.



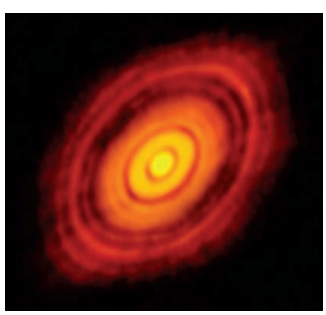
as orbital resonance. This happens when the lengths of their orbits are in a ratio of small whole numbers. Pluto, for example, orbits the sun two times for every three orbits of Neptune. It's highly unlikely that they just happened to form that way, so they must have drifted into that position, where they were locked in by the extra stability. Migration early in our solar system's history could account for other oddities, including the small size of Mars and the sparse, disrupted asteroid belt. To explain them, theorists have invoked a maneuver called the grand tack, in which Jupiter originally formed closer to the sun, drifted inward almost to the orbit of Earth, and then drifted out again to its current position.

Some modelers find such scenarios unnecessarily complex. "I do have faith in Occam's razor," says Greg Laughlin, an astronomer at the University of California (UC), Santa Cruz. Laughlin argues that planets are more likely to form in place and stay put. He says it's possible for large planets to form close to their star if protoplanetary disks contain much more material there than previously believed. Some movement of planets may still occur—enough to explain resonances, for example—but "it's a final subtle adjustment, not a major conveyor belt," Laughlin says.

But others say that there simply could not be enough material to form close-in planets like 51 Pegasi b and others that are even closer. "They cannot have formed in situ," physicist Joshua Winn of the Massachusetts Institute of Technology in Cambridge declares flatly. And the sizable fraction of exoplanets that appear to be in elongated, tilted, or even backward orbits also seems to imply some kind of planet shuffling.

For these oddballs, theorists invoke a gravitational melee rather than a sedate migration. A mass-rich disk could produce many planets close together, where gravitational tussles would fling them into the star, into weird orbits, or out of the system. Another potential disruptor is a companion star in an elongated orbit. Most of the time it would be too far away to have an influence, but occasionally it could swing in and stir things up. Or, if the parent star is a member of a tight-knit stellar cluster, a neighboring star might drift too close and wreak havoc. "There are a lot of ways to break a system," Winn says.

KEPLER'S SURPRISING FINDING that 60% of sunlike stars are orbited by a super-Earth, however, requires a whole new class of theories. Most super-Earths, thought to be largely solid rock and metal with modest amounts of gas, follow tighter orbits than Earth, and often a star has several. The Kepler-80 system, for example, has four super-Earths, all with orbits of 9 days or less. The traditional theory holds that inside the snowline core accretion is too slow to produce something so large. And super-Earths are rarely found in resonant orbits, suggesting that they haven't migrated, but formed where they sit.



An image of HL Tauri's protoplanetary disk. Are planets forming in the gaps?

Researchers are coming up with ways around the problem. One idea is to speed up accretion, through a process known as pebble accretion. The gas in a rich disk exerts a lot of drag on pebble-sized objects. This generally slows them down, causing them to drift in toward the star. If they pass a planetesimal along the way, their slow speed means they can be captured more easily, boosting accretion. But faster accretion and a gas-rich disk raise their own problem: The super-Earths ought to pull in a thick atmosphere once they exceed a certain size. "How do you keep them from becoming gas giants?" asks astrophysicist Roman Rafikov of the Institute for Advanced Study in Princeton, New Jersey.

Eugene Chiang, an astronomer at UC Berkeley, says there is no need to speed up accretion, so long as the disk is solid-rich and gas-poor. He says that an inner disk 10 times denser than the one that formed the solar system could easily produce one or more super-Earths. Chiang has his super-Earths avoid collecting too much residual gas by forming in the dying days of the disk when most of the gas has dissipated.

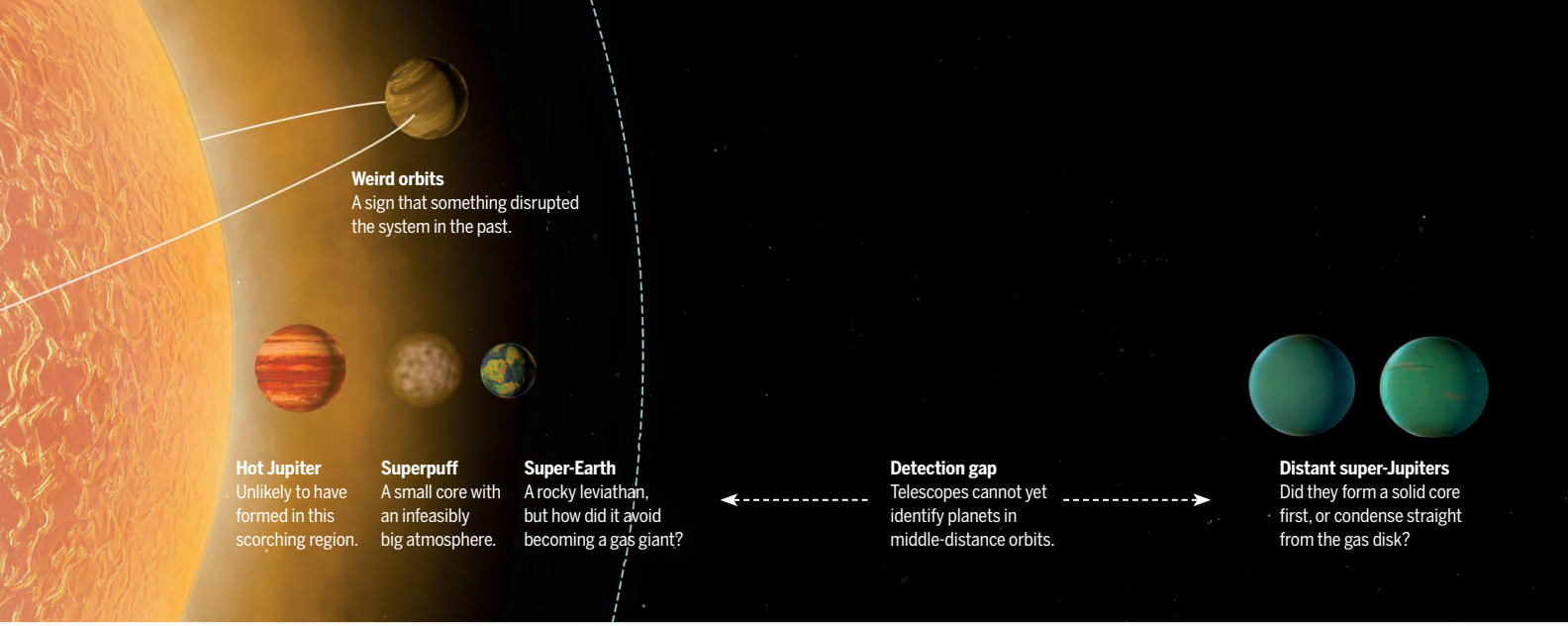
Some early observations from the Atacama Large Millimeter/submillimeter Array (ALMA), an international facility nearing completion in northern Chile, support this proposal. ALMA can map radio emissions from the warm dust and gravel in disks. The few it has studied so far seem to be relatively massive. But the observations aren't yet a smoking gun, because ALMA is not yet fully operational and it can only see the outer parts of disks, not the regions where super-Earths reside. "Getting close in, that's the trick," Chiang says—something that ALMA may perform when all 66 of its antennas are working.

Chiang also has an explanation for another discovery of Kepler's: superpuffs, a rare and equally problematic set of planets that have a smaller mass than super-Earths but appear huge, with a puffed-up atmosphere making up 20% of their mass. Such planets are thought to form in a gas-rich disk. But in the inner disk, warm gas would fight against the planet's weak gravity, so the cold and dense gas of the outer disk is the more likely womb.

Downloaded from http://science.sciencemag.org/ on July 28, 2016

CREDITS: (PHOTO) ALMA, (ESO/NAOJ/NRAO); (GRAPHIC) V. ALTOUNIAN/*SCIENCE*

Published by AAAS



Chiang invokes migration to explain their close orbits—a notion supported by the fact that superpuffs are often found locked in resonant orbits.

MOST OF THE ATTENTION in exoplanet research has so far focused on the inner parts of planetary systems, roughly within a distance equivalent to the orbit of Jupiter, for the simple reason that that's all existing detection methods can see. The two main methods—measuring the wobble of stars caused by the gravitational tug of an orbiting planet and measuring the periodic dimming of a star as a planet passes in front—both favor big planets in close orbits. Imaging the planets themselves is extremely difficult, because their faint light is all but swamped by the glare from their star, which can be a billion times brighter.

But by stretching the limits of the world's biggest telescopes, astronomers have seen a handful of planets directly. And over the past couple years, two new instruments designed specifically to image exoplanets have joined the hunt (*Science*, 21 February 2014, p. 833). Europe's Spectro-Polarimetric High-contrast Exoplanet REsearch (SPHERE) and the U.S.-backed Gemini Planet Imager (GPI) are attached to big telescopes in Chile and employ sophisticated masks, called coronagraphs, to block out the light of the star. Not surprisingly, planets far from their stars are the easiest targets.

One of the earliest and most astounding systems found by direct imaging is the one around the star HR 8799, where four planets range in orbits from beyond that of Saturn out to more than twice the distance of Neptune. What's most surprising is that all four are huge, more than five times the mass of Jupiter. According to theory, planets in such distant orbits move so slowly that they should grow at a glacial rate and top out at masses well short of Jupiter's before the disk disperses. Yet the planets' nice circular orbits suggest they weren't flung there from closer to their stars.

Such distant giants lend support to the most radical challenge to standard theory, in which some planets form not by core accretion, but by a process called gravitational instability. This process requires a gas-rich protoplanetary disk, which breaks up into clumps under its own gravity. These blobs of gas would collapse over time directly into giant planets without having to form a solid core first. Models suggest that the mechanism will only work in particular circumstances: The gas has to be cold, it mustn't be spinning too fast, and the contracting gas must be able to shed heat efficiently. Can it explain the planets of HR 8799? Only the outer two are distant and cold enough, Rafikov says. "It's still quite a puzzling system," he says.

In the past, radio telescope observations of protoplanetary disks have provided some support for gravitational instability. Sensitive to cold gas, the telescopes saw disks spattered with messy, asymmetrical blobs. But recent images from ALMA paint a different picture. ALMA is sensitive to shorter wavelengths that come from dust grains in the midplane of the disk, and its images of the star HL Tauri in 2014 and TW Hydrae this year showed smooth, symmetrical disks with dark circular "gaps" extending far beyond Neptune-like orbits (see picture, p. 440). "It was a tremendous surprise. The disk was not a mess, but has a nice, regular, beautiful structure," Rafikov says. These images, suggestive of planets sweeping their orbits clean as they grow by core accretion, were a blow to advocates of gravitational instability.

It's too early to tell what other surprises GPI and SPHERE may find in the outer reaches of planetary systems. But the region between those outlying neighborhoods and the close-in domains of hot Jupiters and super-Earths remains stubbornly out of reach: too close to the star for direct imaging, too far for indirect techniques relying on stellar wobbles or dimming. As a result, it is hard for theorists to get a full picture of what exoplanetary systems are like. "We're basing things on fragmentary and incomplete observations," Laughlin says. "Right now, everyone's probably wrong."

Astronomers won't have to wait long for better data. Next year, NASA will launch its Transiting Exoplanet Survey Satellite (TESS), and the following year the European Space Agency (ESA) is expected to launch the Characterizing Exoplanets Satellite (CHEOPS). Unlike Kepler, which surveyed a large number of stars in sparse detail to compile an exoplanetary census, TESS and CHEOPS will focus on bright, sunlike stars close to Earth, enabling researchers to explore the midorbit terra incognita. And because the targeted stars are nearby, ground-based telescopes should be able to assess the mass of their planets, allowing researchers to calculate the planets' density, indicating which are rocky or gassy.

The James Webb Space Telescope, due for launch in 2018 (*Science*, 19 February, p. 804), will go further, analyzing starlight that passes through an exoplanet's atmosphere to determine its makeup. "Composition is an important clue to formation," Macintosh says. For example, finding heavier elements in the atmospheres of super-Earths could suggest that a disk rich in such elements is needed to form planetary cores fast enough. And next decade, spacecraft such as NASA's Wide Field Infrared Survey Telescope and ESA's Planetary Transits and Oscillations will join the hunt, alongside a new generation of enormous ground-based telescopes with mirrors 30 meters across or more.

If the past is anything to go by, modelers will have to keep on their toes. "Nature is smarter than our theories," Rafikov says. ■

Downloaded from http://science.sciencemag.org/ on July 28, 2016

Published by AAAS



PLANT BIOLOGY

Parasitic plants—A CuRe for what ails thee

A parasitic plant is perceived by its host plant in a similar manner to microbes

By **Vardis Ntoukakis**[1] *and* **Selena Gimenez-Ibanez**[2]

Parasitic plants cause dramatic changes in ecosystems and represent a serious risk to agriculture by attacking crops of high economic importance. A highly conserved part of plant immune systems is the recognition of microbe-associated molecular patterns (MAMPs) by plasma membrane–localized pattern recognition receptors (PRRs) that initiate an effective immune response upon activation (*1*). Whether parasitic plants are also sensed as foes by these receptors was until now unknown. On page 478 of this issue, Hegenauer *et al.* report the identification of a canonical PRR that is required for responsiveness to a MAMP-like molecule from the parasitic plant *Cuscuta reflexa* and protects plants against parasitic attack (*2*). This finding opens the possibility of biotechnological applications for sustainable crop protection against these devastating parasites.

The ability of plants to store energy from sunlight makes them attractive targets for pests and parasites looking to exploit their carbohydrates, nutrients, and water. Not surprisingly, parasitic organisms, including microbes, insects, nematodes, and parasitic plants, attack plant hosts as their primary source of nutrition. The biological threat mounted by parasitic organisms can cause devastating agricultural loses and can profoundly influence natural ecosystems. Parasitic plants are estimated to cost billions of dollars annually in crop losses across five continents, with particular impact in Africa (*3*).

Seeds of parasitic plants survive in soil for years, but after germination they must find a susceptible host plant within a few days. Plants of the genera *Striga* and *Cuscuta* have sophisticated mechanisms to sense host plants by perceiving molecules exuded by the host—a strategy that dramatically increases the chances of a successful infection (*3*). Once in contact with the host, the survival of the parasite depends on the rapid formation of specialized feeding structures called haustoria that penetrate the host cell wall and siphon nutrients directly from vascular

[1]*Warwick Integrative Synthetic Biology Centre, School of Life Sciences, University of Warwick, Coventry CV4 7AL, UK.* [2]*Plant Molecular Genetics Department, Centro Nacional de Biotecnología–CSIC, 28049 Madrid, Spain. Email: v.ntoukakis@warwick.ac.uk; selena.gimenez@cnb.csic.es*

PHOTO: AZGAR DONMAZ/ISTOCKPHOTO.COM

Downloaded from http://science.sciencemag.org/ on July 28, 2016

Published by AAAS

tissue (*4*). Haustoria formation is a common pathogenicity strategy also used by fungi and oomycetes. Therefore, the virulence strategy of parasitic plants seems to share commonalities with parasitic microbes, raising the possibility that molecular aspects of host-parasite interaction may also be conserved.

Hegenauer *et al*. investigated the interaction between the plant stem parasite *C. reflexa* and cultivated tomato (*Solanum lycopersicum*), which is resistant to this parasite (*5*). They found that tomatoes respond to *C. reflexa* extracts with immune phenotypes similar to those associated with MAMP perception, which suggests that *C. reflexa* indeed produces a MAMP-like molecule. To identify the source of host perception associated with the Cuscuta factor, the authors screened a population of tomatoes differing in the ability to recognize the elicitor. They used a clever series of genetic tricks to assign Cuscuta factor responsiveness to a canonical host PRR. The new receptor contains external leucine-rich repeats and associates constitutively with protein kinases of the SOBIR (suppressor of BAK1-interacting receptor kinase) type (*6*), a hallmark of this type of PRR. The authors renamed this receptor CuRe1 (*Cuscuta* receptor 1), which becomes the first surface-localized receptor found to recognize a parasitic plant.

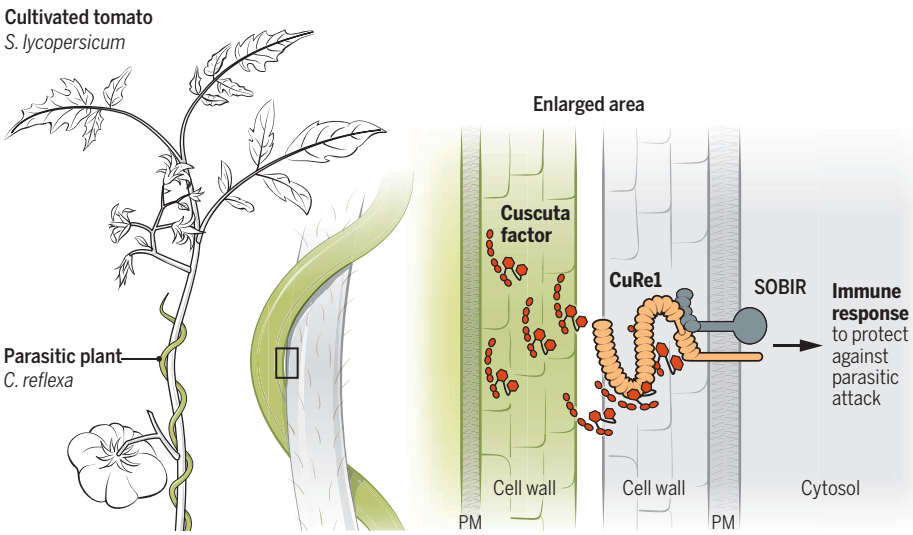
The authors could not identify the structure of the Cuscuta factor precisely, but it appears to be a small, potentially O-glycosylated peptide that is associated with, and possibly a structural component of, the *C. reflexa* cell wall. The Cuscuta factor is present in all *Cuscuta* species tested but is absent from the related nonparasitic species *Calystegia sepium* or from unrelated parasitic plants, which contrasts with the current paradigm that MAMPs are widely conserved in a given class of organisms (*7*)—in this case, plants themselves. This poses an obvious problem: If plants could respond to general plant factors, a predictable outcome might be autoimmunity. This implies that the Cuscuta factor precisely identifies members of this genus. It is tempting to speculate that the Cuscuta factor might be a cell wall component intimately associated with a parasitic lifestyle or a common cell wall protein with a specific posttranslational modification. The narrow distribution spectrum of the Cuscuta factor likely reflects the strong selection pressure against plants perceiving themselves as nonself.

PRRs can function when transferred across plant species barriers (*8*, *9*). To evaluate the potential of CuRe1 to protect susceptible plants from *C. reflexa* attack, the authors used genetic engineering techniques to transform the *CuRe1* gene into closely and distantly related susceptible plants. The CuRe1-transformed lines became sensitive to the Cuscuta factor and were more resistant to *C. reflexa* attack. Thus, CuRe1 has the potential to protect crop plants against infestation by *Cuscuta*.

Remarkably, Hegenauer *et al*. found that cultivated tomato has mechanisms of resistance against *C. reflexa* in addition to CuRe1. This accords with what is known about the multiple layers of incompatibility between parasitic *Striga* species and their hosts (*10*). For microbial pathogens, haustoria serve as secretion sites for virulence proteins called effectors that promote pathogenesis but may be recognized by intracellular host immune complexes encoded by resistance (*R*) genes, strongly reactivating immunity (*1*). Host resistance to *Striga* relies on classical R proteins (*11*); it therefore follows that parasitic plants may secrete their own effectors via haustoria, and that these in turn might be recognized by the host immune system in resistant hosts. In fact, the authors noted that tomato plants lacking CuRe1 were not susceptible to *Cuscuta* infection, implying further active resistance mechanisms in this species. Putative *Cuscuta* effectors would have to be very highly evolved so that they are active in the host but not within the parasitic plant.

The identification of CuRe1 represents a major breakthrough in understanding the strategies used by plants to sense danger from diverse origins. This work greatly advances our understanding of the mechanisms controlling plant resistance to parasitic plants while at the same time opening up new avenues of research. For example, we need to understand the nature of the Cuscuta factor and whether other parasitic plants are perceived by PRRs. Another outstanding question is whether parasitic plants inject effectors into their host and whether R proteins recognize these effectors, as in the case of parasitic microbes. We also need to know why these effectors are not active on their parasites of origin.

On the basis of these new results, interfamily transfer of CuRe1 emerges as a feasible strategy for crop protection. Furthermore, standardized bioengineering and gene editing approaches will accelerate the engineering of receptors with novel ligand specificities (*12*, *13*). This is the beginning of an exciting journey that will allow us to understand the intracellular dialog during parasitic plant-plant associations with broad applications in biology and agriculture. ■



Know your enemy. During infection, the tomato (*S. lycopersicum*) surface-localized immune receptor CuRe1 detects the presence of the Cuscuta factor released from the cell wall of the parasitic plant *C. reflexa*. CuRe1 contains external leucine-rich repeats and associates constitutively with SOBIR-type protein kinases. Heterologous expression of CuRe1 into closely and distantly related susceptible plants confers resistance against the attack of *C. reflexa*. PM, plasma membrane.

REFERENCES AND NOTES

1. J. D. Jones, J. L. Dangl, *Nature* **444**, 323 (2006).
2. V. Hegenauer *et al*., *Science* **353**, 478 (2016).
3. J. B. Runyon, J. F. Tooker, M. C. Mescher, C. M. De Moraes, *Sustain. Agric. Rev.* **1**, 13 (2009).
4. S. Yoshida, S. Cui, Y. Ichihashi, K. Shirasu, *Annu. Rev. Plant Biol.* **67**, 643 (2016).
5. B. Kaiser, G. Vogg, U. B. Furst, M. Albert, *Front. Plant Sci.* **6**, 45 (2015).
6. A. A. Gust, G. Felix, *Curr. Opin. Plant Biol.* **21**, 104 (2014).
7. B. P. Thomma *et al*., *Plant Cell* **23**, 4 (2011).
8. C. Zipfel, *Trends Immunol.* **35**, 345 (2014).
9. P. Y. Huang, L. Zimmerli, *Front. Plant Sci.* **5**, 624 (2014).
10. S. Yoshida, K. Shirasu, *New Phytol.* **183**, 180 (2009).
11. J. Li, M. P. Timko, *Science* **325**, 1094 (2009).
12. N. J. Patron *et al*., *New Phytol.* **208**, 13 (2015).
13. J. W. Woo *et al*., *Nat. Biotechnol.* **33**, 1162 (2015).

ACKNOWLEDGMENTS

We thank J. Rathjen for critical reading and valuable input into the manuscript. Supported by the Royal Society and by Biotechnology and Biological Science Research Council grant BB/M017982/1 (V.N.) and by Spanish Ministry for Science and Innovation grant BIO2014-55884-JIN (S.G.-I.).

10.1126/science.aag3111

GRAPHIC: K. SUTLIFF/*SCIENCE*

Downloaded from http://science.sciencemag.org/ on July 28, 2016

Published by AAAS

SYNTHETIC BIOLOGY

On the record with E. coli *DNA*

DNA can be engineered for cells to record events in real time

By **Olivier Borkowski,[1,2] Charlie Gilbert,[1,2] Tom Ellis[1,2]**

Synthetic biology uses DNA programs to add new functions into living cells. By expressing transcription factors, microbes such as *Escherichia coli* can be made to perform complex computational logic (*1*) and pass "memories" of selected events between generations (*2*). But DNA is more than just the source code for protein expression programs; DNA can be used as the storage medium for information. In synthetic biology, the use of DNA for in vivo information storage was first realized in 2009 with a synthetic genetic program that enabled *E. coli* to count events by using a recombinase to rearrange DNA in response to an input (*3*). With multiple recombinases, this technology could be used to store 1.375 bytes of information in a living *E. coli* (*4*). As reported by Shipman *et al.* (*5*) on page 463 of this issue, and by Roquet *et al.* (*6*), in vivo encoding of information into DNA is pushed even further, using either genome editing to store dozens of bytes of data, or employing multiple recombinases to realize "state machines" inside living cells.

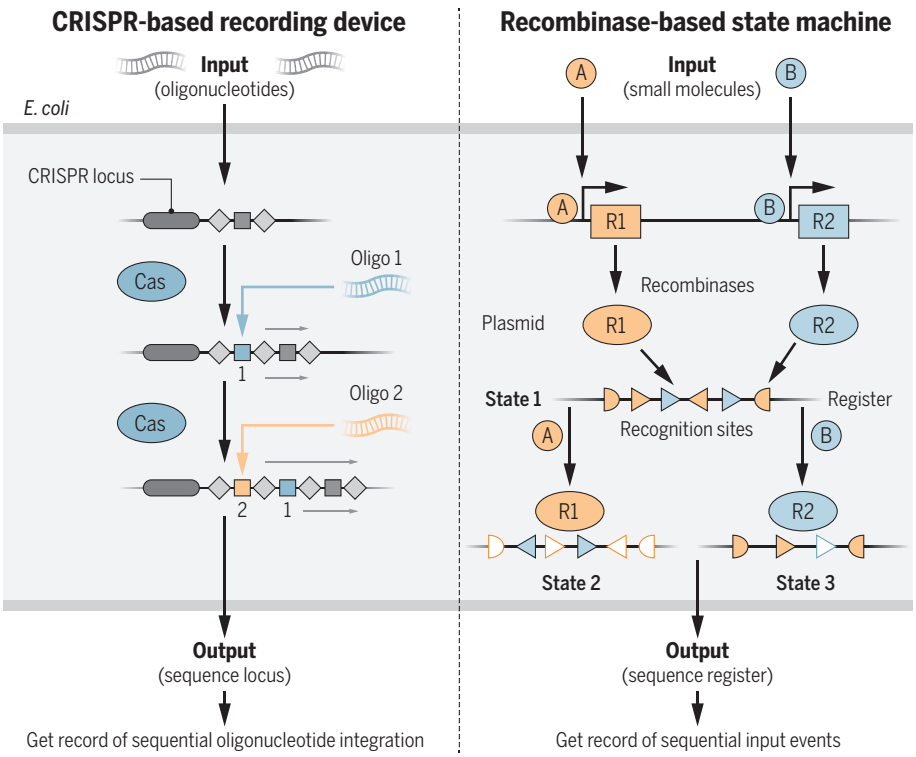
The clustered regularly interspaced short palindromic repeats (CRISPR)–Cas system is a prokaryotic adaptive immune system, in which CRISPR regions within the genome capture foreign DNA sequences during infections. These are later used by Cas9 to recognize and digest foreign DNA bearing the same sequence. The DNA sequences incorporated by CRISPR, called protospacers, form a memory of all previous infections encountered by the cell.

To create living cells engineered to record information into their DNA, Shipman *et al.* exploited the natural recording capacity of CRISPR-Cas using the native *E. coli* system to integrate multiple, user-defined protospacer sequences into CRISPR arrays. Using electroporation, bacteria take up oligonucleotides 35 base pairs (bp) in length and integrate this DNA as protospacers. Because the temporal order of protospacer acquisition events translates to a physical order in the CRISPR array, the record of what information (DNA sequences) was given to the cells at what time can be retrieved by sequencing the full CRISPR locus (see the figure). Shipman *et al.* integrated 3 sets of 5 oligonucleotide protospacers (15 elements) in this way.

To expand the data storage capacity of their system, Shipman *et al.* generated modified versions of Cas1 and Cas2 capable of integrating oligonucleotides in either forward or reverse orientations. Theoretically, this recording device can store between 20 and 100 bytes of DNA information in the genome of living *E. coli*. However, as CRISPR arrays are naturally capable of harboring hundreds of protospacers, it is likely that the storage capacity per cell could easily be increased.

Although the method of rearranging DNA with recombinases is unable to store similar amounts of information in vivo, it can be much more readily exploited by having it interact with native and synthetic gene expression programs. Roquet *et al.* used recombinase-based memory to build a classic motif from computation—the state machine. State machines perform order-dependent input processing, so that at any point the system can be interrogated and the identity and order of inputs deduced. In response to external inputs, multiple recombinases recorded memory into a DNA "register," a synthetic sequence hosted on a plasmid consisting of an array of nested recognition sites for the different recombinases. Depending on the inputs and thus on the order of activation of the different recombinases, the register is rearranged into distinct orientations (see the figure). With just three inputs controlling three recombinases, it is possible to build a 16-state machine in *E. coli*. Theoretically, with seven inputs and seven orthogonal recombinases, it would be possible to encode 13,700 distinct states.

To reveal the order and type of inputs received by any cell or population of cells,



Molecular recording devices. (**Left**) In the CRISPR-based recording device, short oligonucleotide sequences are integrated into a genomic CRISPR array between short spacer sequences (light gray diamonds) through the action of the Cas1-Cas2 complex. The order of sequential oligonucleotide integrations (colored squares) is preserved in the spatial arrangement of the CRISPR locus. The information recorded can then be retrieved by next-generation sequencing of the CRISPR locus. (**Right**) For the recombinase-based state machine, small molecules control the expression of recombinases. The recombinases act on a DNA register, consisting of nested recombinase recognition sites (orange and blue triangles and half-ellipses). Depending on the order of recombinase activation, the DNA register adopts different states that can be read by DNA sequencing (or by reporter-protein expression).

GRAPHIC: C. BICKEL/*SCIENCE*

[1]*Centre for Synthetic Biology and Innovation, Imperial College London, London SW7 2AZ, UK.* [2]*Department of Bioengineering, Imperial College London, London SW7 2AZ, UK. Email: t.ellis@imperial.ac.uk*

Downloaded from http://science.sciencemag.org/ on July 28, 2016

Published by AAAS

the DNA registers can simply be sequenced from the bacteria, or can also be quickly determined by quantitative polymerase chain reaction. Alternatively, the register sequences can be designed to contain genetic parts such as promoters and transcription factors. When these functional registers rearrange into certain states, they can trigger gene expression changes that lead to different *E. coli* phenotypes. Roquet *et al.* created a database of thousands of regulatory programs in which the cell's behavior is tied to the state of the register. Using these biological outputs means that the state machine can lead the cells to take actions in response to the appropriate string of inputs.

Currently, the inputs used by both the CRISPR and recombinase systems are simple molecules. Roquet *et al.* used small molecules to activate recombinase expression, whereas Shipman *et al.* transformed synthetic oligonucleotides into cells. However, both studies suggest ways to feed in complex cellular phenotypes as inputs. By replacing recombinase regulation with alternative genetic control systems, Roquet *et al.* propose that state machines could monitor environmental signals or gene expression. Similarly, Shipman *et al.* suggest using their device to capture gene expression information by converting native messenger RNA transcripts into protospacers through the action of reverse transcriptase. As both Shipman *et al.* and Roquet *et al.* suggest, these strategies could be used to generate intrinsic devices within cells that autonomously record the timing of complex and inaccessible processes, such as gene dysregulation in cancer or developmental gene regulatory cascades. As McKenna *et al.* (*7*) describe on page 462 of this issue, an autonomous method that continually mutates a genomic locus using CRISPR-Cas has provided valuable information for whole-organism genetic lineage tracing.

The methods used by Shipman *et al.* and by Roquet *et al.* represent new benchmarks in both in vivo information recording and biological computation, and show that DNA can be predictably edited over generations of living cells. Linking these DNA memories with the inherent power of cells to sense and act on their environments will no doubt lead to many exciting advances for synthetic biology. ■

REFERENCES

1. A. A. K. Nielsen *et al.*, *Science* **352**, aac7341 (2016).
2. J. W. Kotula *et al.*, *Proc. Natl. Acad. Sci. U.S.A.* **111**, 4838 (2014).
3. A. E. Friedland *et al.*, *Science* **324**, 1199 (2009).
4. L. Yang *et al.*, *Nat. Methods* **11**, 1261 (2014).
5. S. L. Shipman *et al.*, *Science* **353**, aaf1175 (2016).
6. N. Roquet *et al.*, *Science* **353**, aad8559 (2016).
7. A. McKenna *et al.*, *Science* **353**, aaf7907 (2016).

10.1126/science.aah4438

GRAPHIC: N. CARY/*SCIENCE*

CLIMATE CHANGE

The smoking gun for Atlantic circulation changes

Deep-sea sediments record changes in ocean circulation during the last glacial age

By **Andreas Schmittner**

The Atlantic meridional overturning circulation (AMOC) has long been implicated in rapid climate changes during the most recent ice age. However, convincing observational evidence from the deep ocean has remained limited. On page 470 of this issue, Henry *et al.* (*1*) present two independent records from a well-dated, high-resolution sediment core from Bermuda Rise in the North Atlantic (see the figure) that may be the smoking gun that paleoceanographers have been looking for.

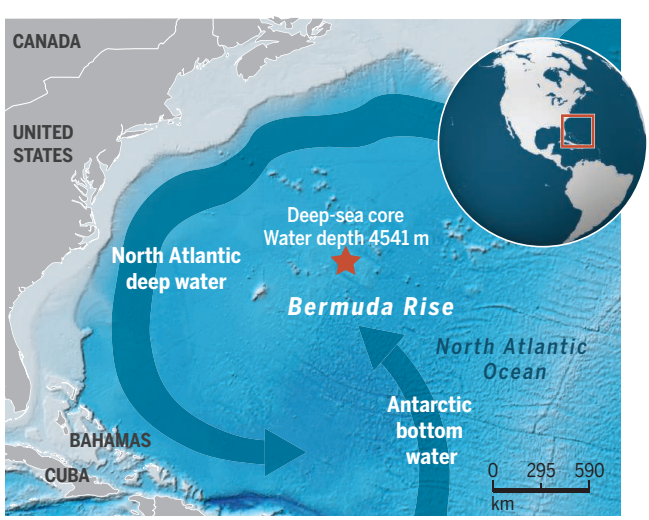
The AMOC is part of a system of currents that spans Earth's oceans (*2*). In the Atlantic, these currents flow northward near the surface from the southern hemisphere across the equator, via the Gulf Stream, and into the subpolar North Atlantic. There, the chilled and salty waters sink to depths of ~2 to 3 km and flow back south along the margin of the Americas into the Southern Ocean as North Atlantic deep water (see the figure). This flow pattern transports heat from the southern to the northern hemisphere and keeps the North Atlantic region warm and Antarctica cool (*3*).

During the most recent ice age, rapid and large climate changes occurred at time scales of several centuries to millennia. These Dansgaard-Oeschger (D-O) events were characterized by abrupt warming and cooling in the North Atlantic and more gradual temperature changes of the opposite sign around Antarctica (*4*). This asymmetric response of surface temperatures is consistent with disruptions to the interhemispheric heat transport by the AMOC. Theory and modeling suggests that rapid transitions between different AMOC states can be triggered by freshwater fluxes, which could cause the observed changes in surface temperatures (*5*).

Despite evidence from surface temperature reconstructions that support the idea of AMOC variability causing the D-O events, doubts have lingered because surface temperatures can be affected by many processes. Evidence from the deep sea would be more convincing because the AMOC is, after all, a deep-sea phenomenon. But few high-resolution, well-dated paleoceanographic records from the deep sea exist, hampering unequivocal attribution. Moreover, paleoceanographic reconstructions are indirect and rely on proxies, making it difficult to infer ocean circulation changes.

One such proxy is the ratio of two radioisotopes, protactinium and thorium (Pa/Th), which are produced constantly at a ratio of 0.093. Deviations from this ratio

College of Earth, Ocean, and Atmospheric Sciences, Oregon State University, Corvallis, OR 97331, USA. Email: aschmitt@coas.oregonstate.edu



Deep ocean changes. Based on data from a deep-sea core at Bermuda Rise, Henry *et al.* argue that particularly cold phases during the last glaciation were associated with reduced ocean circulation in the North Atlantic. The map depicts today's deep-sea circulation near the core (located at 33° 41.443′ N, 57° 34.559′ W).

Downloaded from http://science.sciencemag.org/ on July 28, 2016

Published by AAAS

have been interpreted as the effect of the AMOC, although other secondary processes also influence Pa/Th (*6*). Another AMOC proxy is the standardized carbon isotope ratio in the fossil shells of bottom-dwelling (benthic) foraminifera ($\delta^{13}C_{BF}$); these organisms record the carbon isotope ratios of dissolved inorganic carbon in the water column. $\delta^{13}C_{BF}$ is also affected by other processes, but those can be simulated in three-dimensional (3D) models (*7*) and differ from the secondary processes affecting Pa/Th.

Thus, if secondary processes dominated the variations of Pa/Th and/or $\delta^{13}C_{BF}$, we would not expect to see any correlation between them. However, Henry *et al.*'s Pa/Th and $\delta^{13}C_{BF}$ records are highly correlated both with each other and with sea surface temperature (SST) variations in a nearby sediment core. In their reconstruction, cold phases in the North Atlantic are ~2°C cooler in the subtropical North Atlantic. Pa/Th increases during these cold phases, approaching the production value, and $\delta^{13}C_{BF}$ decreases by ~0.5 per mil. In 3D climate model simulations, collapse and resumption of the AMOC caused by freshwater perturbations to the North Atlantic results in similar changes in SSTs and $\delta^{13}C_{BF}$ at the core location (*8*).

This agreement indicates that at least some of the ice age D-O events, particularly those accompanied by massive ice berg rafting, were associated with large AMOC changes and perhaps even AMOC collapses. But Henry *et al.*'s data also indicate a variety of responses, with other events showing smaller changes.

In the future, combining high-quality paleoceanographic reconstructions with 3D circulation models that directly simulate the proxies may allow AMOC changes to be quantified throughout the most recent ice age. This could help to better assess how AMOC changes affect ecosystems and societies, such as shifts in the intertropical convergence zone, ocean productivity, and carbon cycle, and how likely they are to occur in the future as a result of human-caused climate change (*9*). ■

REFERENCES

1. L. G. Henry *et al.*, *Science* **353**, 470 (2016).
2. T. Kuhlbrodt *et al.*, *Rev. Geophys.* **45**, RG2001 (2007).
3. T. J. Crowley, *Paleoceanography* **7**, 489 (1992).
4. C. Buizert *et al.*, *Nature* **520**, 661 (2015).
5. T. F. Stocker, S. J. Johnsen, *Paleoceanography* **18**, 1087 (2003).
6. C. T. Hayes *et al.*, *Deep Sea Res. II* **116**, 29 (2015).
7. A. Schmittner *et al.*, *Biogeosci.* **10**, 5793 (2013).
8. A. Schmittner, D. C. Lund, *Clim. Past* **11**, 135 (2015).
9. W. Cheng, J. C. H. Chiang, D. X. Zhang, *J. Climate* **26**, 7187 (2013).

10.1126/science.aag3156

ECOLOGY

Plant extinctions take time

Many plant species may already be functionally extinct

By **Quentin Cronk**

The recent *State of the World's Plants* report from the Royal Botanic Gardens, Kew (*1*) estimates that 50,000 of the ~390,000 known vascular plant species are at risk of extinction. Given the rarity of so many plants, coupled with widespread environmental destruction over the past quarter-century, we might expect that a lot of plants should have gone extinct. Indeed, estimates made in the early 1990s suggest that up to 30,000 species should have gone extinct by 2015 (*2*, *3*). Yet, the International Union for Conservation of Nature (IUCN) Red List of Threatened Species database for 2016 has fewer than 150 extinct species. How can we explain this discrepancy?

Proving an absence is an age-old problem in science. To prove the existence of an organism, one can collect a specimen and put it in a museum collection. Proving that an organism does not exist is more problematic. It is always possible that we have not looked hard enough. As a result, the answer to the seemingly simple question of how many plant species have become extinct in the Anthropocene is that no one really knows. But this does not mean that there is no problem. Many plant species may be on an inevitable path to extinction, even though isolated specimens can survive for decades or more.

> ***"...we [may be] facing slow-creeping biodiversity loss on a large scale."***

To derive global plant extinction rates expected by 2015, multiple studies in the early 1990s estimated likely species losses based on the habitat area expected to be lost (*2*, *3*). This species-area model is potentially problematic (*4*). But even if the model is flawed, the underlying concept is uncontroversial: less habitat, fewer species. The studies arrived at the conclusion that between 4000 and 30,000 species would be extinct by 2015 (*2*, *3*). In contrast, the IUCN Red List database of 2016 lists only 142 extinct plants; 105 of these are completely extinct, and the remaining 37 are extinct in the wild but survive in cultivation. The discrepancy between the recorded extinctions and earlier expectations cannot be explained by lower-than-expected habitat destruction. In fact, many new threats to tropical forest ecosystems have emerged since 1990, notably the expansion of industrialized agriculture driven by increased demand for soy and palm oil.

Two possible explanations present themselves. First, there may be many undocumented extinctions. It is true that extinction lists are highly conservative. Compilers have to be cautious, because even when an organism is declared extinct, there is always the possibility that it will be rediscovered. How much searching has to be done before a species that has not been seen for more than 50 years is declared extinct? And who will do the searching? Biologists generally prefer to do fieldwork in places where species survive, not degraded areas where extinction has occurred. For practical reasons, a complete list of extinct plants may be impossible to obtain. Even so, it is hard to imagine that we would miss thousands of predicted extinctions.

Second, there may be a long extinction lag time. The species-area curve is driven by equilibrium phenomena, and ecosystems may take a long time to equilibrate. Diamond has used the term "relaxation time" to describe this extinction lag (*5*). Janzen calls the species in this extinction waiting room "the living dead" (*6*). He noticed that the agricultural landscapes that replaced native forest in Costa Rica were not devoid of native trees. Forest remnants hung on at field margins and in small forest patches. However these trees could not regenerate because habitat suitable for seedlings no longer existed. The trees, although living out their physiological life, were "just as dead... as if they were in the back of a logging truck" (*6*).

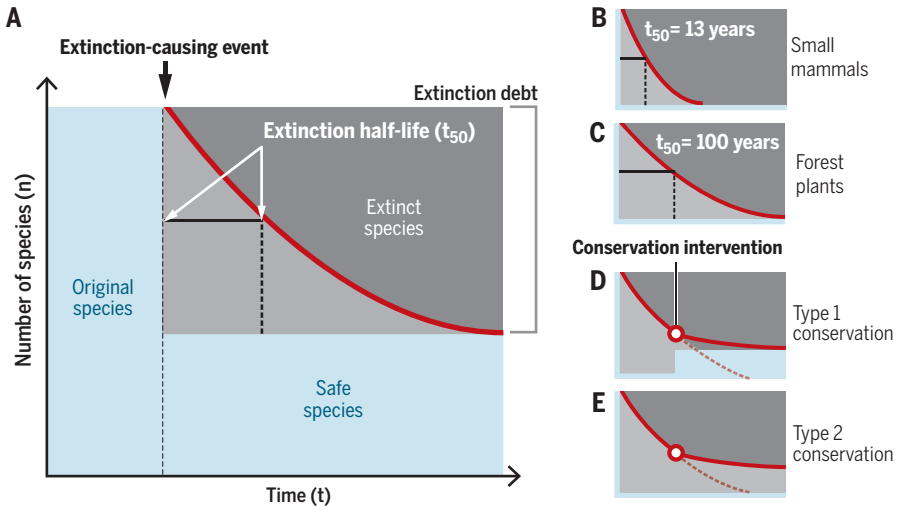
Numerous factors influence the extinction lag time (*7*). Broadly, these can be divided into those intrinsic to species (such as longevity of individuals, presence of a seed bank, and sensitivity to inbreeding depression) and extrinsic factors (such as spatial scales and patch structure). Long-lived species in large areas will have long extinction lag times and vice versa.

There are several reasons that plants should survive longer than animals as living dead. First, plants may have seed banks in the soil; until these seed banks are ex-

Beaty Biodiversity Research Centre, University of British Columbia, Vancouver, BC, Canada. Email: quentin.cronk@ubc.ca

Downloaded from http://science.sciencemag.org/ on July 28, 2016

Published by AAAS



The slow-burning fuse of plant extinction. (**A**) This conceptual scheme relates the extinction debt (the number of species expected to become extinct as the result of an extinction-causing event) to the relaxation time (the lag time to complete this process). (**B**) Small areas and fast demographic turnover promote rapid extinction and hence short persistence of the extinction debt. (**C**) Large areas or slow demographic turnover promote slow extinction and long persistence of extinction debt. (**D** and **E**) Conservation interventions can have different effects. Type 1 conservation reduces the extinction debt and thus prevents extinction (D); type 2 conservation extends the extinction lag time and thus delays extinction (E).

hausted, occasional plants may appear. Some invertebrates have stages that can diapause in lake mud for multiple years, but this strategy is generally rarer in animals than in plants. Second, few animals have life spans matching those of woody plants, which may live hundreds of years. An exception is Lonesome George, the last known Pinta tortoise (*Chelonoidis abingdoni*), who extended the living-dead phase to almost plantlike proportions by his longevity. Third, many plants can reproduce asexually or self-fertilize, and the last individual plant may therefore produce occasional successors, whereas the single last animal rarely does.

There are thus strong reasons to expect the relaxation times for plant extinction to greatly exceed that of animals. Indeed, the processes and parameters of plant extinction may be quite different from those of animals. It is therefore important to understand what happens during the relaxation time. In this vein, Downey and Richardson recently introduced the concept of a plant extinction trajectory that passes through several defined stages (*8*).

How long can plant relaxation times be? The South Atlantic island of St. Helena provides an interesting case study. The Portuguese navigators who discovered it in 1502 quickly introduced goats. Without predators, the goats multiplied into huge flocks. Most vegetation was destroyed, and plants became extinct. What is remarkable, however, is the tenacity of the living dead. For instance, the St. Helena olive (*Nesiota elliptica*) fell to an unsustainable population level of 12 to 15 plants in the mid-19th century (*9*) but only became extinct in 2003. It was arguably just as extinct with a population of less than 10 in 1900 as it is now. The extinction lag times for woody plants on St. Helena are thus measured in many centuries. Studies on temperate forest herbs similarly indicate lag times of more than 100 years (*10*), whereas small mammals in tropical forest fragments have median extinction lag times of only 13 years (*11*).

This slow-burn extinction in plants raises a number of questions. The first is a practical one. If human actions over the past 25 years have set in train a mass extinction that will take 100 years or more to play out, then how do we identify the living dead and what should be our response? At the very least, the long plant relaxation time allows us to sequence the whole genomes of the rarest plants, so that we will know a little more about the organisms we lose (and understand, or even address, some of the genetic problems they face). As sequencing costs drop, a coordinated global program of rarity genomics is something that can be considered.

The second question is whether we can use the relaxation time as a window of opportunity for conservation. Can we drive the equilibrium back to a state that retains more species? The answer is probably a cautious yes. Another way of expressing the difference between functional extinction (that is, the living dead) and census extinction (where no individuals survive) is through the concept of "extinction debt," a term coined by Tilman *et al.* from metapopulation dynamics (*12*). Extinction debt is the number of extinctions expected to result, sooner or later, from an extinction-causing event. Facing the slippery problem of quantifying census extinction, extinction debt may be a more useful approach (*13*). It may be possible, by smart ecological restoration and reserve selection, to pump "species credit" into ecosystems to reduce extinction debt (*14*).

There are some hopeful stories of species brought back from the brink sustainably. An example of a critically rare species that has possibly been moved into the sustainably safe zone is the Mauritius kestrel, which was made almost extinct by antimalarial DDT use in the 1950s and 1960s, but intensive management from 1974 worked (*15*). The kestrel escaped irreversible genetic problems only because of the very short duration of its bottleneck and the total cessation of DDT use in 1970. The success of conservation projects will depend on whether they merely prolong the extinction lag time or whether they reduce the extinction debt by dealing with fundamental ecosystem and genetic problems, moving species into the sustainably safe zone (see the figure).

At this juncture, rather than estimating census extinction, it is important that scientists develop better models for assessing global extinction debt and maximizing species credit. If the high 1990s estimates of plant extinction by 2015 are accurate estimates of extinction debt, then we are facing slow-creeping biodiversity loss on a large scale. Failing to notice this because the time scale is too long would not be smart. ■

REFERENCES AND NOTES

1. Royal Botanic Gardens, Kew, *The State of the World's Plants* (Royal Botanic Gardens, Kew, UK, 2016).
2. M. Jenkins, in *Global Biodiversity: Status of the Earth's Living Resources* (World Conservation Monitoring Centre, Cambridge, UK, 1992); http://dx.doi.org/10.5962/bhl.title.44956.
3. W. V. Reid, in *Tropical Deforestation and Species Extinction*, T. C. Whitmore, J. A. Sayer, Eds. (Chapman Hall, London, UK, 1992), pp. 55–73.
4. F. He, S. Hubbell, *Ecology* **94**, 1905 (2013).
5. J. M. Diamond, *Proc. Natl. Acad. Sci. U.S.A.* **69**, 3199 (1972).
6. D. H. Janzen, *Encyclopedia of Biodiversity* **4**, 590 (2001).
7. K. Hylander, J. Ehrlén, *Trends Ecol. Evol.* **28**, 341 (2013).
8. P. O. Downey, D. M. Richardson, *AoB Plants* 10.1093/aobpla/plw047 (2016).
9. Q. B. C. Cronk, *The Endemic Flora of St Helena* (Nelson, Oswestry, 2000).
10. M. Vellend *et al.*, *Ecology* **87**, 542 (2006).
11. L. Gibson *et al.*, *Science* **341**, 1508 (2013).
12. D. Tilman *et al.*, *Nature* **371**, 65 (1994).
13. O. R. Wearn *et al.*, *Science* **337**, 228 (2012).
14. I. Hanski, *Ann. Zool. Fennici* **37**, 271 (2000).
15. J. J. Groombridge *et al.*, *J. Anim. Ecol.* **70**, 401 (2001).

ACKNOWLEDGMENTS

I thank the organizers and participants of the State of the World's Plants Symposium at Royal Botanic Gardens, Kew (May 2016) for helpful discussion. Research in the author's laboratory is funded by the Natural Sciences and Engineering Research Council of Canada (NSERC) Discovery Grants Program (grant no. RGPIN-2014-05820).

10.1126/science.aag1794

GRAPHIC: K. SUTLIFF/*SCIENCE*

Downloaded from http://science.sciencemag.org/ on July 28, 2016

Published by AAAS



POLICY FORUM

BIOMEDICAL RESEARCH

Countering imprecision in precision medicine

Better coordination is needed to study complex interventions

By **Spencer Phillips Hey** *and* **Aaron S. Kesselheim**

The goal of precision medicine (PM) is to "ensure that the right treatment is delivered to the right patient at the right time" (*1*). Predictive biomarker diagnostics are critical to this effort. Yet despite substantial promise, PM has been plagued with problems (*2*). Many commercially available biomarker diagnostics have not been adequately validated (*3*); the scientific literature is flooded with low-quality and unreliable reports (*2*); and even ostensibly successful PMs, such as trastuzumab (Herceptin) chemotherapy in HER2-expressing breast cancer, have been characterized by uncertainty about how to use and interpret diagnostic test results (*4*). These disappointing features of PM research can be explained by three obstacles inherent in the science: (i) Biological theories play a central role in the testing methodology; therefore, pivotal trials of PMs cannot be agnostic about underlying mechanisms. (ii) Interventions are complex with many components and degrees of uncertainty that need to be resolved before clinical use. (iii) No single stakeholder controls the biomarkers or coordinates the research program. Although some new regulatory (*5*) and evidence synthesis (*6*) efforts are designed to address these problems, we believe that meaningful progress in PM requires new mechanisms of scientific oversight.

Program On Regulation, Therapeutics, and Law (PORTAL), Division of Pharmacoepidemiology and Pharmacoeconomics, Department of Medicine, Brigham and Women's Hospital and Harvard Medical School, Boston, MA 02120, USA, and Center for Bioethics, Harvard Medical School, Boston, MA 02115, USA. Email: akesselheim@partners.org

THEORY-DRIVEN RESEARCH

The gold standard for evaluating the efficacy of an experimental drug is a two-arm randomized controlled trial (RCT). One virtue of this method is its agnosticism about underlying biological theory. An RCT can decisively test the clinical hypothesis "treatment T is effective for condition C" without needing a theoretical explanation for why T is effective.

Most PM has a more ambitious aim: to discover and harness a true biological explanation for why a drug will work for an individual patient. Hypotheses take the form: "Treatment T is effective for condition C, as defined by testing positive for biomarker B, where B is determined by diagnostic assay A." Additional assumptions—why A is a reliable test for B; why B should predict activity of T against C—are now "built into" the hypothesis, so decisive tests of PM cannot be agnostic about underlying theory. If the theory is wrong, and we are not careful about testing it, the result will be systematic misclassification and worse patient outcomes—exactly what PM intends to avoid. This does not mean that etiological theories must be perfect, but we do need to actually test the underlying hypotheses before PMs are unleashed into the clinic.

Using biomarkers as outcomes in clinical trials requires more attention to validation.

Although various experimental modalities can provide some evidence of biomarker validity (e.g., retrospective designs, enrichment designs), a decisive test of a biomarker hypothesis requires that participants are prospectively stratified according to both biomarker status and treatment assignment (*7*). Unfortunately, this only rarely happens in PM development (*8*).

COMPLEX INTERVENTIONS

Although the unit of clinical translation in traditional drug development is a single therapeutic agent, the unit in PM is a "biomarker ensemble": (i) a biomarker, hypothesized to play a crucial role in the disease pathway; (ii) a diagnostic assay, used to determine a patient's biomarker status; and (iii) a therapeutic agent, intended to be more effective for patients who are "biomarker-positive." This increased complexity, with uncertainties about each component of the ensemble, means that there are more threats to the validity of a PM trial. When biomarker or assay misclassification rates are not known or not reported—which happens frequently (*9*)—the study results are difficult to interpret. In the case of a negative result: Was the therapy ineffective, the biomarker a poor predictor of therapeutic response, or the diagnostic unable to accurately classify patients according to their true biomarker status? Was it some combination of these factors?

This problem of underdetermination frustrates efficient falsification of biomarker theories (*10*). The front-loading and multiplying of clinical uncertainties combined with deficiencies in theory testing can explain why physicians have been reluctant to trust PM, insurers have been reluctant to reimburse for diagnostics, and companies have been less willing to invest (*2*).

CONTROL AND COORDINATION

Unlike a drug, a biomarker is not manufactured or controlled by a single entity. Much biomarker research operates under an "open science" model, which permits relatively free access to testing and development of biomarkers and allows individual stakeholders to make independent judgments about the state of evidence and the allocation of research resources. This also means that there is no single stakeholder with authority or responsibility for directing the scientific research effort surrounding a particular biomarker, which can lead to inefficiencies at the research system level.

These represent potentially wasteful and inefficient activities. An open science model has many attractive features, but it does not

Downloaded from http://science.sciencemag.org/ on July 28, 2016

PHOTO: DRA_SCHWARTZ/ISTOCKPHOTO.COM

Published by AAAS

have mechanisms to restrict stakeholders from pursuing a hypothesis or a particular method, even when many in the community judge that it is no longer valuable or reasonable to do so. A stakeholder's judgment about why a candidate PM or a driving theory has failed may not resonate throughout the scientific community in an efficient way.

The lingering controversy about the appropriate assay or cut-off score for distinguishing HER2-positive from HER2-negative breast cancers illustrates how greater oversight is needed for what should count as a successful PM validation (*4*). Despite the wide use of HER2 testing in the clinic, uncertainty remains about how to test for the biomarker and interpret the results. Trials designed to resolve these uncertainties are under way, but ideally, these issues should have been resolved before the test was widely adopted in clinical practice. Until the optimal biomarker ensemble is identified, patients are being systematically misclassified and harmed as a result.

ETHICS AND POLICY

Failure to conduct scientifically valid research programs undermines public support for the medical research enterprise and fails to protect the interests of patient-subjects. The ethics of medical research demands that patient-subject burdens are redeemed by gains in generalizable knowledge. Many human and material resources have been expended in pursuit of PMs (*1, 2*). Unfortunately, these costs are often not adequately redeemed by scientific gains. For example, the Evaluation of Genomic Applications in Practice and Prevention (EGAPP) initiative, which provides systematic summaries and recommendations for clinicians and health payers about the utility of particular genomic tests, has most often found that there is "insufficient evidence" to support genetic testing (*6*).

This suggests that existing social mechanisms, such as peer review, the commercial market, and broad public-funding priorities—which are responsible for "passively" coordinating medical research activities under an open science model—are inadequate to efficiently resolve the many uncertainties in PM. It may also indicate that institutional review boards (IRBs) lack the authority and access to information about the total biomarker research portfolio necessary to safeguard patient and public interests. Therefore, we believe new policy interventions are needed.

The Food and Drug Administration (FDA) has already issued draft guidance on biomarker trials that acknowledges the dangers of failing to test the driving biomarker theories (*11*) and is contemplating formal regulation of biomarker tests (*5*). We support these efforts and recommend that regulators, health care providers, and insurers explicitly demand rigorous, biomarker-stratified trials for all PMs and companion diagnostics before licensure, clinical uptake, and reimbursement.

For their part, researchers need to adhere to existing reporting guidelines (*9*) and to participate in biomarker study registration platforms (*12*). It is impossible for the scientific community to account for the complexity of biomarker ensembles if reports of previous research are inadequate or unreliable. Journal editors and research funders will need to enforce compliance more strictly with these measures as conditions of publication and funding.

However, to overcome obstacles to scientific coordination stemming from the lack of centralized control and oversight over biomarker research, we believe more radical change in the mechanisms of scientific oversight is needed. President Obama's Precision Medicine Initiative is a promising development in this respect, but it is not clear that its focus on developing a large patient cohort to produce new knowledge about disease etiology and management will substantially affect the inefficiencies with clinical translation.

"Existing social mechanisms ... are inadequate to efficiently resolve the many uncertainties in PM."

Large U.S. research institutions, such as the National Human Genome Research Institute and National Cancer Institute, already play a central role in setting national research priorities. But the coordinating capacity of these institutions is dependent on the applications submitted to them by investigators, and insofar as the overall research portfolio is not transparent, waste and inefficiency remain likely.

We therefore propose that the major research institutions should combine their efforts with regulatory bodies and explicitly take on the responsibility for coordinating and evaluating PM research activities. Once a promising PM biomarker is identified, these institutions should prospectively map out the parameter space of the biomarker ensemble and then track the accumulating state of evidence (*10*). Unlike existing evidence synthesis efforts, which provide a recommendation based on a snapshot of the total evidence at some point in time, a centrally hosted, publicly accessible, and dynamic portfolio map would help the scientific community to efficiently communicate and to coordinate its activities in real time.

Specific advantages of this approach would include the following: (i) Funding agencies could award responsibility for specific regions of the parameter space through their grants, which would mitigate research redundancy and waste; (ii) research teams would not have to sift through the literature or wait for systematic reviews but could instead immediately identify combinations of biomarker parameters needing replication and validation, as well as combinations that have been neglected, which indicate a gap in testing the theory; (iii) IRBs would have access to broader knowledge about the total state of evidence, which would allow them to make more informed judgments of social and scientific value.

This approach would complement and extend the evidence-grading schemes for PMs (*13*) and would reveal the patterns of research activities that warrant more or less attention. It would also help elucidate a much-needed standard for when a decisive test of a biomarker's clinical utility is possible. When the parameter space for a biomarker ensemble has been well-explored and the optimal ensemble has been identified, only then are the biomarker and its underlying theory ready for a pivotal trial.

Obstacles to efficient resolution of PM uncertainties are not going to go away and will require us to acknowledge and face the scientific difficulty with an appropriate methodology. The approach to PM inquiry we have outlined, which should be led by public research institutions, will help achieve the promise that the field offers. ■

REFERENCES AND NOTES

1. National Academies of Sciences, Engineering, and Medicine, *Biomarker Tests For Molecularly Targeted Therapies: Key to Unlocking Precision Medicine* (National Academies Press, Washington, DC, 2016).
2. D. F. Hayes *et al.*, *Sci. Transl. Med.* **5**, 196cm6 (2013).
3. A. de Gramont *et al.*, *Nat. Rev. Clin. Oncol.* **12**, 197 (2015).
4. C. Schmidt, *J. Natl. Cancer Inst.* **103**, 87 (2011).
5. Office of Public Health Strategy and Analysis, FDA, *The Public Health Evidence for FDA Oversight of Laboratory Developed Tests: 20 Case Studies* (FDA, Silver Spring, MD, 2015).
6. EGAPP Recommendations (2016); www.egappreviews.org.
7. D. J. Sargent *et al.*, *J. Clin. Oncol.* **23**, 2020 (2005).
8. K. V. Ballman, *J. Clin. Oncol.* **63**, 3651 (2015).
9. S. Mallett *et al.*, *Br. J. Cancer* **102**, 173 (2010).
10. S. P. Hey, *Theoria* **30**, no. 2 (2015).
11. FDA, *Guidance for Industry: Enrichment Strategies for Clinical Trials to Support Approval of Human Drugs and Biological Products* (FDA, Washington, DC, 2012).
12. F. Andre *et al.*, *Nat. Rev. Clin. Oncol.* **8**, 171 (2011).
13. P. G. Febbo *et al.*, *J. Natl. Compr. Canc. Netw.* **9** (suppl. 5), S1 (2011).

ACKNOWLEDGMENTS

A. S. K. is a Greenwall Faculty Scholar and is funded by the Laura and John Arnold Foundation and the Harvard Program in Therapeutic Science. S. P. H. received support under the PACEOMICS project, funded by Genome Canada, Genome Quebec, Genome Alberta, and the Canadian Institutes for Health Research (CIHR).

10.1126/science.aaf5101

Downloaded from http://science.sciencemag.org/ on July 28, 2016

Published by AAAS



Although they evolved independently, ant-eating mammals—including the pangolin (shown), armadillos, and aardvarks—all possess similar gut microbes.

MICROBIOME

Living in a microbial world

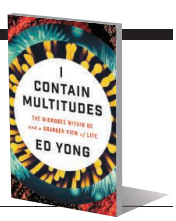
Microbes take center stage in a charming tour of Earth's microscopic menagerie

By **Susan Perkins**

Once you've experienced "the transformation," you never look at the world in the same way. For me, it occurred over 3 years of curating a public exhibit on the human microbiome at the American Museum of Natural History. After totally immersing myself in the topic, I viewed every bite of food, every handshake, every scratch of a dog's head through a different lens. How was this action shaping my microbiome—the community of trillions of microorganisms that called my body home? Ed Yong, the author of the new book *I Contain Multitudes: The Microbes Within Us and a Grander View of Life*, also experienced this transformation, and he's written a delightful, witty book that will surely be a pathway for his readers to do the same.

For most of human history, we were unaware of microbes. Then in the 1670s, the clever Dutch drapemaker Antonie van Leeuwenhoek crafted a handheld contraption that could magnify objects more than 250 times. He used it to explore pond water, insect guts, and samples taken from his own body, observing tiny "animalcules"—the first glimpses of living bacteria and protozoa.

I Contain Multitudes
The Microbes Within Us and a Grander View of Life
Ed Yong
HarperCollins, 2016. 363 pp.



In the ensuing decades, new discoveries linked microbes to human health and showed that certain ones were responsible for specific ailments. This "germ theory" of disease has been the prevailing view in medicine ever since.

With better culturing methods and early DNA sequencing efforts, the census of the microbial menagerie that calls our planet—and our bodies—home began to expand. Next-generation sequencing methods have turbocharged that discovery and revealed a previously unimaginable diversity of novel microbes.

Each one of us has a different pattern of microbial diversity that can correspond to variations in metabolism, disease, and even behavior. This discovery promises to be transformative for medicine and biotechnology. Acknowledging the growing momentum in this field, the White House Office of Science and Technology Policy recently announced the creation of the National Microbiome Initiative, a collaborative effort of federal, public, and private entities to accelerate microbiome science.

In 10 chapters, Yong vividly describes the intricate alliances forged by microbes with every other organism on the planet. He guides us on a historical journey, showing how key discoveries of symbioses, such as early work on the microbes that inhabit termite guts, have been crucial for opening up the "microbiome universe" to scientists. We learn how bacteria allow the Hawaiian bobtail squid to glow, how they permit pea aphids to subsist on nothing but plant sap, and how the wood rat has coopted them so it can digest otherwise toxic creosote. We also learn a lot about parasitic bacteria called *Wolbachia* that infect insects all over the globe, manipulating their behavior and reproductive fitness. As Yong reveals, these particular bacteria may be useful as a vector control strategy in our fight against disease-bearing hosts like mosquitos.

Any book on microbiomes would be remiss if it did not discuss dysbiosis—a condition in which microbes and host fall out of balance—and Yong does not disappoint, talking about things like emerging *Clostridium difficile* infections and the collapse of coral reef ecosystems. But he wisely never falls into the trap of labeling any microbes as inherently "good" or "bad" and stops short of predicting how conditions like obesity, infections, and allergies will soon be a thing of the past (as less rigorous journalists have been known to do when writing about this burgeoning field).

The most delightful part of Yong's book is that he does not just tell the stories of microbiomes, he also introduces readers to dozens of the scientists studying them. He visited their labs, met their germ-free mice, and made field trips to the zoo with them. He probed them with questions and captures their motivations and personalities perfectly. Their stories and conversations radiate the excitement of unlocking new secrets, putting a human face on the science.

The title of the book comes from Walt Whitman's classic poem *Song of Myself*, in which he rejoices in humanity's role in the great ecosystem of Earth. In 1855, Whitman could hardly appreciate the extent of the microbial world, but Yong deftly weaves it into the poet's ode. As Whitman writes: "I am the mate and companion of people, all just as immortal and fathomless as myself."

The reviewer is at the Sackler Institute for Comparative Genomics, American Museum of Natural History, 200 Central Park West, New York, NY 10024, USA. Email: perkins@amnh.org

10.1126/science.aag1515

PHOTO: © EPA EUROPEAN PRESSPHOTO AGENCY CREATIVE ACCOUNT/ALAMY STOCK PHOTO

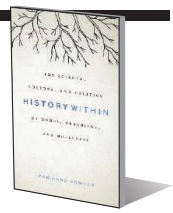
Downloaded from http://science.sciencemag.org/ on July 28, 2016

Published by AAAS

HISTORY OF SCIENCE

Interpreting evolution

A probing history sheds light on the social and cultural biases that have shaped the study of human origins



History Within
The Science, Culture, and Politics of Bones, Organisms, and Molecules
Marianne Sommer
University of Chicago Press, 2016. 552 pp.

By **Maurizio Meloni**

During one of the most dramatic waves of racist and eugenic ideas in the early 20th century, the great paleontologist George Gaylord Simpson astutely observed that there was no way to avoid a transfer of knowledge from biology to "social evolution": "Whether or not they are really pertinent, biological theories are being used in this field, and the biologist necessarily has a part in the discussion" (*1*). Such fluxes of knowledge from biology to the wider society and their implications are the focus of Marianne Sommer's *History Within: The Science, Culture, and Politics of Bones, Organisms, and Molecules*.

The book's subtitle refers to the tripartite structure of the book. The section entitled "History in Bones" focuses on the work of American paleontologist Henry Fairfield Osborn (1857–1935) at the American Museum of Natural History (AMNH), "History in Organisms" centers around the British evolutionist Julian Huxley (1887–1975) and his work at the London Zoo and other facilities, and "History in Molecules" centers on the Italian-born, Stanford-based geneticist Luigi Luca Cavalli-Sforza (b. 1922) and his contributions to the Human Genome Diversity Project.



Despite efforts to remain objective, scientific narratives about human evolution are often laden with value judgments.

What these three scientists have in common is easy to see: a passion and even a mission to transfer biological knowledge and provide "meaning and orientation" to the wider public. Across more than 500 pages, Sommer capably conveys the complexity of their lives, particularly the contestations and accusations that their projects provoked.

Osborn, who served as president of the AMNH from 1908 to 1933, transformed the museum into a preeminent site for exhibition, attracting millions of visitors during his tenure. However, he also subscribed to a linear, nonrandom view of evolution in which those of "Caucasian stock" (i.e., European) were positioned at the apex. Osborn, who presided over the Second International Congress on Eugenics in 1921 and collaborated extensively with Nordic supremacist Madison Grant, contributed to the perception of a deterioration of the "best strains of Old American stock" that ultimately culminated in the 1924 Immigration Act.

Huxley subscribed to the so-called "modern synthesis" (his term) of Darwinism and genetics. An active critic of the extreme racism of conservative and Nazi eugenics, he was nonetheless a lifelong eugenicist. From his work with the United Nations Educational, Scientific, and Cultural Organization (UNESCO)—of which he was the first director—to his popular writings and interviews on eugenics, demographic control, and transhumanism, Huxley's enduring influence on the public's ideas about evolution in the 20th century is second to none.

Cavalli-Sforza belongs to a different scientific and cultural context. His pioneering work in human population genetics focused on DNA sequences as the "fundamental objects for the reconstruction of human history." Working in an epoch less inclined to progressionist views, Cavalli-Sforza nonetheless presented his scientific project as endowed with a moral goal: using genetic data to demonstrate a unified human history as a way to combat racism. His efforts to collect genetic material from indigenous populations, however, resulted in accusations of colonialism and imposition of outsider knowledge.

The book centers around the idea of knowledge in continuous transit through society, negotiated between different stakeholders. The three scientists here described were undoubtedly a key source of knowledge. However, if one thinks of how much Osborn imbued his science with the racism typical of the conservative elite of which he was part, if one considers how much Huxley adopted and rebranded language from the eugenics movement (*2*), and if one assesses some of the naïve sociological and anthropological assumptions behind Cavalli-Sforza's work (*3*), it becomes clear how much these scientists were profoundly shaped by the wider social values and cognitive styles of their own times.

Sommer's book is very much about making sense of various layers of biological data in the context of human history. But the book stops at the work of a population geneticist (Cavalli-Sforza), whose turn-of-the-century Human Genome Diversity Project aimed to translate long-term historical processes such as human migrations into DNA sequences.

In subsequent years, new postgenomic approaches with even more ambitious goals have emerged. The epigenome, for instance, is no longer thought of as just an archive of epochal events like mass migrations. Something more immediate is sought in it: a microhistory made of local and even tiny events, such as diet (famine, obesity), habit (smoking, alcohol), stress and trauma, and general lifestyle of our most direct ancestors. It is as yet too early to say whether disciplines like social and environmental epigenetics will fulfill their ambitious task, but their practitioners would do well to heed lessons learned from past attempts to read human history into biology.

The reviewer is the author of Political Biology: Science and Social Values in Human Heredity from Eugenics to Epigenetics *(Palgrave, Basingstoke, UK, 2016). Email: m.meloni@sheffield.ac.uk*

PHOTO: SHANNON STAPLETON

REFERENCES

1. G. G. Simpson, *J. Wash. Acad. Sci.* **31**, 1 (1941).
2. P. Weindling, *J. Mod. Euro. Hist.* **10**, 480 (2012).
3. J. Reardon, *Race to the Finish: Identity and Governance in an Age of Genomics* (Princeton Univ. Press, Princeton, NJ, 2005).

10.1126/science.aag2125

Downloaded from http://science.sciencemag.org/ on July 28, 2016

Published by AAAS

LETTERS

Edited by **Jennifer Sills**

Clarifying samples in Zika analyses

IN RESPONSE TO the Zika outbreak and putatively related microcephaly cases in Brazil, many research groups in Brazil, North America, and Europe are studying the virus ("Evidence grows for Zika virus as pregnancy danger," G. Vogel, In Depth, 11 March, p. 1123). The simultaneous efforts to address this urgent matter have led to the use of some samples in multiple studies. There is no clear leadership or protocol to regulate access to patients, some of whom are also participants in studies of potential microcephaly causes unrelated to Zika, such as cytomegalovirus and genetic inbreeding (*1*). Some studies are reporting different results for the same set of samples. For example, Calvet *et al.* (*2*) and Oliveira Melo *et al.* (*3*) acknowledge overlap in the methods section. It is difficult to assess studies if we cannot determine whether, or to what degree, the cohorts are independent. Such confusion has already necessitated clarification of similar studies from different groups (*4*).

To address this problem, the World Health Organization could create a universal code for each baby with confirmed microcephaly and Zika infection, to be used by all research groups working with these data. The codes should include unique identifiers, generated by a competent government agency, that indicate the country and institution of diagnosis as well as a serial number for each patient. The World Health Organization could also provide a public database for Zika cases that would include the Zika codes as well as epidemiological information. These steps would allow individual cases to be identified in multiple studies while protecting privacy.

João R. M. de Oliveira* and Denis A. P. Moura

Laboratório de Imunopatologia Keizo Asami, Federal University of Pernambuco, Recife, Pernambuco, 50670-901, Brazil.

*Corresponding author. Email: joao.ricardo@ufpe.br

REFERENCES

1. G. França *et al.*, *The Lancet* (2016); http://dx.doi.org/10.1016/S0140-6736(16)30902-3.
2. G. Calvet *et al.*, *Lancet Infect. Dis.* **16**, 653 (2016).
3. A. S. Oliveira Melo *et al.*, *Ultrasound Obstet. Gynecol.* **47**, 6 (2016).
4. M. de Fatima Vasco Aragao, *BMJ* **353**, i2444 (2016).

10.1126/science.aah3733



Researchers studying Zika and microcephaly are using overlapping sets of data.

Animal-based antibodies: Obsolete

THE GLOBAL ANTIBODY industry produces an indispensable resource for biological, molecular, and cell scientists. Antibodies are harvested from immunized animals. The animals suffer side effects from the immunizations (*1*) and are, in some cases, mistreated (*2*). It is no longer necessary to compromise animal welfare: Since the mid-1990s, animals have not been required for antibody production (*3*). It is long past time to replace the use of animal-generated antibodies with nonimmunized recombinant antibodies.

Animal-Friendly Affinity reagents (AFAs) are antibodies that are generated by using recombinant technology in viruses or yeasts. The technology allows cloning of immunoglobulin gene segments, to produce antibody libraries with high diversity from which antibodies with desired specificities can be chosen. These are translated on the surfaces of cells or phage particles, and exposed to the target antigen, which selects a highly specific antibody, after which production can be scaled up within cell culture. AFAs are commercially available and can also be developed in individual laboratories. They have wide-ranging applicability as well as specificity and affinity—equal or greater to their animal-generated counterparts—to a huge repertoire of antigens. They also give researchers greater control over antibody properties, generation time, and cost (*4*). Thanks to AFAs, the use of animals has become obsolete.

EU Directive 2010/63/EU (*5*) requires the replacement of animals used in scientific procedures when alternatives exist. Yet, despite the maturation of a growing number of techniques to produce AFAs, antibody production using animals continues to be authorized. Twenty years ago, EU Member States were advised that "in the near future," antibody production "without prior immunization of [animals would] avoid the need to use living animals" (*6*). That prediction was correct. It is incomprehensible that such needless animal use continues.

There is little clarity about how many animals are used to produce antibodies. Only two EU Member State countries have published antibody production numbers. In 2013, the United Kingdom reported use of 9522 animals (*7*), and The Netherlands reported the use of 25,697 animals (*8*). The numbers do not include animals used to produce antibodies that were imported into those countries. Neither country has published the number of animals used for this purpose since 2013.

We recommend the following actions: Antibody production methods that use animal immunization should be replaced in EU Member States. Manufacturers outside the European Union should be required to adhere to European standards to qualify for import to Member States. An expert working group should be established to set up a roadmap for replacement. Programs should be implemented to ensure that animal-friendly antibody producers are fully supported. Subsequent reports from the Commission to the Council and the European Parliament on the statistics on the number of animals used for experimental and other scientific purposes should include data on the use of animals for antibody production as an independent category. These actions should be reinforced through international cooperation and national agencies that can execute government regulation and prevent outsourcing to regions where animal welfare is less well regulated.

A. C. Gray,[1]* S. S. Sidhu,[2] P. C. Chandrasekera,[3] C. F. M. Hendriksen,[4] C. A. K. Borrebaeck[5]

[1]AFABILITY, 74110, Morzine, France. [2]The Donnelly Centre, University of Toronto, Toronto, ON M5S 3E1, Canada. [3]CM Scientia—Life Sciences Consulting, Harrow, ON NOR 1GO, Canada. [4]Faculty of Veterinary Medicine, Utrecht University, 3584 CL Utrecht, Netherlands. [5]CREATE Health Cancer Center, Department of Immunotechnology, Lund University, S-223 81, Lund, Sweden.

*Corresponding author. Email: draligray@live.com

REFERENCES

1. P. P. Leenaars *et al.*, *Lab Anim.* **32**, 387 (1998).
2. S. Reardon, *Nature News* 10.1038/nature.2016.19958 (2016).
3. C. Borebaeck, Ed., *Antibody Engineering, 2nd Edition* (Oxford Univ. Press, 1995).
4. S. Dübel *et al.*, *Trends Biotechnol.* **28**, 333 (2010).
5. Directive 2010/63/EU (http://eur-lex.europa.eu/legal-content/EN/TXT/?uri=celex%3A32010L0063).
6. U. Marx *et al.*, *ATLA* **25**, 121 (1997).
7. Home Office, Annual Statistics of Scientific Procedures on

PHOTO: RAFAEL FABRES/PICTURE-ALLIANCE/DPA/AP IMAGES

Downloaded from http://science.sciencemag.org/ on July 28, 2016

Published by AAAS

Living Animals Great Britain 2013 (2014) ; www.gov.uk/government/uploads/system/uploads/attachment_data/file/327854/spanimals13.pdf.
8. Nederlandse Voedsel- en Warenautoriteit, Zo doende 2013: Jaaroverzicht over dierproeven en proefdiere (2014) ; www.nvwa.nl/actueel/inspectieresultaten/bestand/2207546/zo-doende-2013-jaarover-zicht-over-dierproeven-en-proefdieren [in German].

10.1126/science.aag3305

The line between science and politics

M. ENSERINK'S NEWS Feature "Peace of mind" (3 June, p. 1158) described Mohammad Herzallah's effort to establish a research oasis in the West Bank. Such a research center could benefit not only the Palestinians in the region, but the development of science throughout the Middle East. Enserink rightly highlighted the physical difficulties of getting such an oasis off the ground given barriers such as checkpoints and securities walls. However, he crossed the line into politics when he wrote, "Some hilltops are crowned with the modern contours of Israeli settlements, a major obstacle in the quest for peace."

Whether you agree with this statement or not, it does not belong in an article about establishing a new scientific endeavor.

Mel Weintraub

Skokie, IL 60076, USA. Email: melwein7@gmail.com

10.1126/science.aah3551

TECHNICAL COMMENT ABSTRACTS

Comment on "Multiple repressive mechanisms in the hippocampus during memory formation"

Rebecca S. Mathew, Hillary Mullan, Jan Krzysztof Blusztajn, Maria K. Lehtinen

Cho *et al.* (Reports, 2 October 2015, p. 82) report that gene repression after contextual fear conditioning regulates hippocampal memory formation. We observe low levels of expression for many of the top candidate genes in the hippocampus and robust expression in the choroid plexus, as well as repression at 4 hours after contextual fear conditioning, suggesting the inclusion of choroid plexus messenger RNAs in Cho *et al.* hippocampal samples.

Full text at http://dx.doi.org/10.1126/science.aaf1288

Response to Comment on "Multiple repressive mechanisms in the hippocampus during memory formation"

Jun Cho, Nam-Kyung Yu, V. Narry Kim, Bong-Kiun Kaang

Mathew *et al.* propose that many candidate genes identified in our study may reflect the events in the choroid plexus (ChP) potentially included in hippocampal samples. We reanalyze our data and find that the ChP inclusion is unlikely to affect our major conclusions regarding the basal suppression of translational machinery or the early translational repression (at 5 to 10 minutes). As Mathew *et al.* examined for a subset of genes at 4 hours, we agree that the late suppression may partly reflect the events in the ChP. Although the precise contribution of anatomical sources remains to be clarified, our behavioral analyses indicate that the late-phase suppression of these genes may contribute to memory formation.

Full text at http://dx.doi.org/10.1126/science.aaf2081

Downloaded from http://science.sciencemag.org/ on July 28, 2016

TECHNICAL RESPONSE

MEMORY MECHANISMS

Response to Comment on "Multiple repressive mechanisms in the hippocampus during memory formation"

Jun Cho,[1,2]* Nam-Kyung Yu,[2]* V. Narry Kim,[1,2]† Bong-Kiun Kaang[2]†

Mathew *et al*. propose that many candidate genes identified in our study may reflect the events in the choroid plexus (ChP) potentially included in hippocampal samples. We reanalyze our data and find that the ChP inclusion is unlikely to affect our major conclusions regarding the basal suppression of translational machinery or the early translational repression (at 5 to 10 minutes). As Mathew *et al*. examined for a subset of genes at 4 hours, we agree that the late suppression may partly reflect the events in the ChP. Although the precise contribution of anatomical sources remains to be clarified, our behavioral analyses indicate that the late-phase suppression of these genes may contribute to memory formation.

We have previously identified numerous regulatory mechanisms during long-term memory formation by analyzing transcriptome and translatome in mouse hippocampus. In particular, we found three types of repressive events: basal translational suppression of ribosomal biogenesis, learning-induced early translational repression of genes such as Nrsn1 (at 5 to 10 min after learning), and late transcriptional suppression of a subset of genes in the estrogen receptor signaling pathway (at 30 min to 4 hours after learning).

Mathew *et al*. (*1*) performed reverse transcription polymerase chain reaction (RT-PCR) on the several candidate genes at the 4-hour time point and proposed that choroid plexus (ChP) might have been included in our hippocampal samples and that the ChP inclusion might affect the changes detected at 4 hours (*2*). It is important to note that an immediate and speedy isolation of the hippocampi at specific time points was crucial for us to minimize perturbation of gene networks in the tissue because RNA in neuronal tissues is known to degrade rapidly after death. Our protocol enabled us to perform an accurate time course study with short time intervals using ribosome profiling (RPF) and RNA sequencing (RNA-seq). As Mathew *et al*. and another recent study (*3*) indicate, this conventional method of simple and quick isolation inevitably involves the inclusion of the ChP that is closely attached to the hippocampus (*3*).

So as to evaluate the effect of ChP inclusion on our transcriptome (RNA-seq) and translatome (RPF) data, we sought to examine the expression patterns of the genes that are enriched in the ChP and depleted in the hippocampus. To our knowledge, the transcriptome of the ChP has not been profiled in direct comparison with that of the hippocampus, so it is actually impossible to properly define the "ChP signature genes." Therefore, first, we examined the genes reported to be expressed relatively highly in ChP cells—compared with neurons, oligodendrocytes, and astrocytes—by in situ hybridization experiments (*4*) (categorized here as "ChP cell signature," 109 genes). We determined their relative abundance ranks among the genes detected in our RNA-seq data from hippocampal tissue and primary culture, and those in the published ChP transcriptome data, independently (*5*) (deposited in Gene Expression Omnibus, GSE66312). These genes showed strong enrichment in the ChP transcriptome, whereas they were expressed at relatively low levels in hippocampal primary culture (Fig. 1, A and B).

In our previous study, we observed a low level of translation efficiency of the ribosomal protein-coding genes from hippocampal primary culture as well as hippocampal tissue (*2*). Considering that the ribosome protein-coding genes are repressed translationally in the ChP cell-depleted culture, the basal regulation observed in our findings is unlikely to be affected by ChP inclusion.

Although the ChP cell signature genes were detected at very low levels in the hippocampal primary culture, they showed a relatively moderate level of RNA expression in hippocampal tissue (Fig. 1, A and B). These results indicate that, as Mathew *et al*. and another study pointed out (*3*), there might be a chance of inadvertent ChP inclusion in hippocampal tissue preparation. Even though the relative proportion of the adjacent ChP is tiny compared to that of the hippocampus as the source for the libraries, several genes that are highly expressed in the ChP may influence the transcriptome and translatome data.

To further evaluate the contribution of the transcripts abundant in the ChP, we generated another list of genes that are expressed highly in the ChP transcriptome (top 15%) and expressed at low levels in the primary culture transcriptome (below 50%) [dubbed as "ChP enriched (vs Hippo PC)", 369 genes]. We then examined how many differentially expressed genes (DEGs) that we identified at different time points belong to the two ChP-specific signature sets. Only one gene (*Dnah6*) of the "ChP enriched (vs Hippo PC)" and none of the "ChP cell signature" genes was included among the DEGs at early phases (among 25 DEGs at 5 min and 16 DEGs at 10 min) (Fig. 1C). Notably, *Nrsn1*, which we investigated as an example of the early repressed genes, is not highly expressed in ChP. We previously showed that *Nrsn1* was down-regulated by neuronal activity in hippocampal primary culture and that the mice with *Nrsn1* overexpression in hippocampal neurons exhibited deficits in long-term memory formation (*2*). Therefore, most of the significant changes detected at early phases are likely to be solely attributed to the hippocampus. Furthermore, behavioral results revealed the functional significance of an early repressed gene in hippocampal neurons.

Unlike the early events, the DEGs at 30 min and at 4 hours after learning included many genes that belong to the two ChP-specific signature sets. Especially, a large proportion of the DEGs that showed transcriptional repression were members of either one or both of the sets (24 out of 42 DEGs at 30 min and 37 genes out of 55 DEGs at 4 hours) (Fig. 1C), whereas none of the activated DEGs are enriched in the ChP. We therefore do not exclude the possibility that the late persistent down-regulation may reflect at least partly the changes in the ChP rather than those in the hippocampus.

However, Mathew *et al*. show that seven out of the nine ChP abundant genes they tested by qRT-PCR were down-regulated in the hippocampus as well as in the ChP. Four of them reached statistical significance, which is the same number of significantly decreased genes in the ChP. Among the down-regulated DEGs at 4 hours, many genes were also previously identified as repressed genes in the hippocampus after learning (*6*). These reports, including ours, consistently show the gene repression after conditioning in the hippocampal transcriptomes. To conclusively clarify whether the learning-induced gene regulatory events occur in the hippocampus or the ChP or both, we must await subsequent studies using advanced methods.

Last, one of the fundamental purposes of our recent study was to find and suggest unknown mechanisms that are important for long-term memory formation. Our behavioral analysis upon the activation of ESR1, a potent upstream regulator

[1]Center for RNA Research, Institute for Basic Science, Seoul 08826, Korea. [2]Department of Biological Sciences, College of Natural Sciences, Seoul National University, Seoul 08826, Korea.
*These authors contributed equally to this work. †Corresponding author. Email: narry@snu.ac.kr (V.N.K.), kaang@snu.ac.kr (B.-K.K.)

Downloaded from http://science.sciencemag.org/ on July 28, 2016

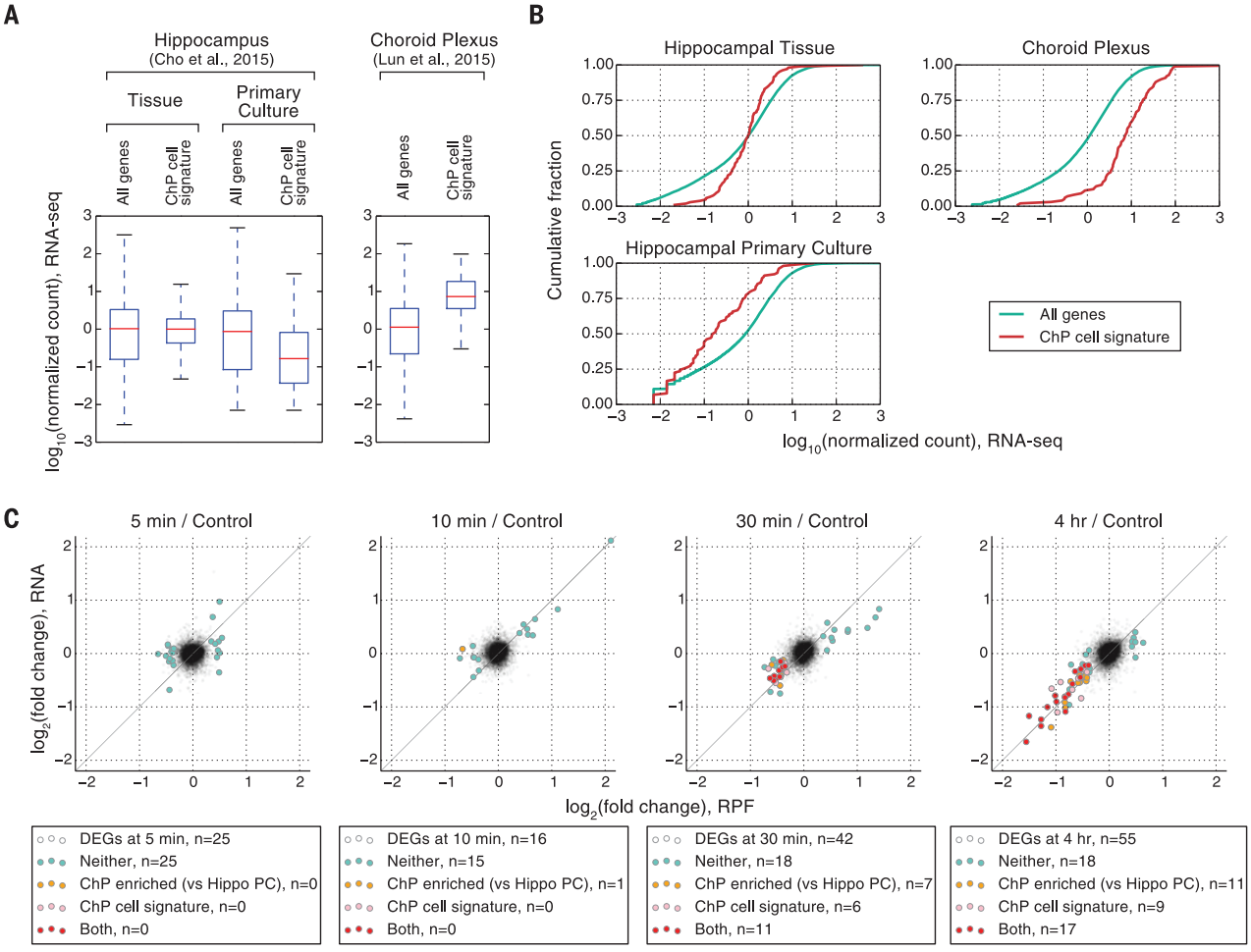


Fig. 1. Analysis of transcriptional and translational alteration of ChP-specific genes after contextual fear conditioning. (**A**) Box plot showing the normalized sequencing tag counts of all genes and ChP cell signature genes (*4*) (109 genes) in the RNA-seq libraries from hippocampal tissues and primary cultures (GSE72064) and ChP (GSE66312). (**B**) Cumulative distribution of the normalized tag counts of all genes and ChP cell signatures [alternative representation of (A)]. (**C**) Scatter plots showing relative changes of whole genes (small gray dots) and DEGs (large dots edged with thick lines). The different colors indicate whether a DEG belongs to neither of the two ChP-specific sets (cyan), to either set (yellow or pink), or to both sets (red).

for a large portion (about half) of the repressed DEGs at late phase, underpins the importance of the late persistent down-regulation of these genes for long-term memory formation: We have validated that a large number of DEGs at 4 hours are under the control of the ESR1 signaling pathway and that ESR1 agonist injection into the hippocampus impaired hippocampus-dependent memory formation in an object location task with nonstressful training, as well as contextual fear conditioning (*2*). ESR1 agonist may have directly acted on the hippocampus, but we cannot exclude the possibility that the agonist affected the ChP cells by diffusion via cerebrospinal fluid or blood vessels. However, regardless of the routes of ESR1 agonist action, these results indicate the functional importance of ESR1 signaling-mediated repression in memory formation. The possible involvement of the ChP leads to an intriguing hypothesis that the altered transcriptomic changes in the ChP may affect the composition of the cerebrospinal fluid, eventually regulating the hippocampal plasticity during memory formation, which remains to be investigated.

To summarize, a small amount of ChP could have been included in our hippocampal samples, because it is technically very difficult to perfectly separate the two regions in a short time by using the widely used dissection method. Given that much research on hippocampal transcriptome to date has shared the common isolation method we used (*2*), we agree that Mathew *et al.* raised an important issue to be addressed in future studies. However, our data set is a rich source of valuable information on transcriptomic and translatomic changes after learning. Most of the gene expression changes reflect the response from the hippocampus, which constitutes most of the sample volume unless the genes are highly specific to the ChP. The potential inclusion of the ChP does not affect our major conclusions regarding the basal translational suppression of translation machineries or the early translational repression of specific genes after learning. For some of the down-regulated genes at the late phase after contextual fear conditioning, we should consider the possibility that their changes in the transcriptomes may have been affected by ChP inclusion. Further analysis may be required to determine whether these regulations occur in the hippocampus, ChP, or both, and which event is critical for long-term memory formation.

REFERENCES

1. R. S. Mathew, H. Mullan, J. K. Blusztajn, M. K. Lehtinen, *Science* **353**, 453 (2016).
2. J. Cho *et al.*, *Science* **350**, 82–87 (2015).
3. A. M. Stankiewicz, J. Goscik, A. Majewska, A. H. Swiergiel, G. R. Juszczak, *PLOS ONE* **10**, e0142195 (2015).
4. E. S. Lein *et al.*, *Nature* **445**, 168–176 (2007).
5. M. P. Lun *et al.*, *J. Neurosci.* **35**, 4903–4916 (2015).
6. A. Sirri *et al.*, *Brain Res.* **1308**, 14–23 (2010).

20 January 2016; accepted 17 June 2016
10.1126/science.aaf2081

Downloaded from http://science.sciencemag.org/ on July 28, 2016



Some species of mussels are affected by rising temperatures and acidity levels in the ocean, two symptoms of climate change.

CREDIT: © BOB GIBBONS/ALAMY STOCK PHOTO

AAAS Pacific Division explores climate-change communication

Annual meeting symposium considers multidisciplinary approaches

By **Andrea Korte**

Organizations that have studied climate-change education efforts—including AAAS, the National Science Foundation, the National Oceanic and Atmospheric Administration, NASA, and others—have found that simply providing scientific data is not spurring the necessary public and political responses. To connect with audiences about the science of climate change and its wide-ranging human impacts, new approaches that draw from across the sciences—and the humanities—are necessary, said experts at the AAAS Pacific Division annual meeting.

"The world around us is seeing the impacts of climate change, and it's important for us to explain what's going on," said Michel Boudrias, department chair of environmental and ocean sciences at the University of San Diego. Boudrias advocates an approach to communicating about climate change that can "bring in other disciplines and other dimensions to get the message across," he said.

> ***"It's important to emphasize how climate change affects people here and now."***
>
> **Tiffany Lohwater,** AAAS

The science of climate change—and its effects on western North America—was a recurring subject at the Pacific Division meeting, held 14–17 June at the University of San Diego. In several symposia and lectures, scientists presented new findings, including about the effects of rising ocean temperatures on sea creatures in the Pacific Ocean and the presence of aerosol particles in San Diego's atmosphere. The 2016 meeting, which marked 100 years since the Pacific Division's first official gathering, drew hundreds of researchers, educators, and students from a diverse range of fields.

AAAS has long been a home for interdisciplinary collaboration, said Rush Holt, AAAS CEO and executive publisher of the *Science* family of journals, at a 15 June town hall meeting for the Pacific Division. AAAS sees "all disciplines represented," and it supports scientific work that may not fall within traditional boundaries, Holt said. The association's interdisciplinary emphasis dates to its founding in 1848, Holt said, when its organizers disbanded their scientific societies focused on individual disciplines to form AAAS to advance science as a whole.

Robert Louis Chianese—professor emeritus of English at California State University, Northridge, and, with Boudrias, an organizer and presenter of the symposium on innovative methods for communicating climate change—recommended grounding climate-change communication in the humanities and centering it on narrative. "Make it personal," said Chianese, who has explored the role that storytelling, documentary, and personal confessions can have in spurring action. Chianese recounted his encounter with a fishing-boat captain turned environmentalist who gave up fishing after witnessing too much waste—and bringing in fewer and fewer full-size creatures. "It moved me because of the teller's transformation," Chianese said of the captain's tale. "Such stories have a way of drawing us in, tying us to the specifics of the character and the situation in a way that media coverage of abuses against nature often does not. Hearing stories of personal confessions of transgressions against nature can prompt others to reevaluate their relationship to the natural world."

The captain's tale echoes an example from literature of the power of confessional storytelling, Chianese said: Samuel Taylor Coleridge's 18th-century poem, "The Rime of the Ancient Mariner." After a thoughtless sailor kills an albatross, his guilt prompts him to tell his tale and impart environmental wisdom, Chianese said.

Downloaded from http://science.sciencemag.org/ on July 28, 2016

Published by AAAS



AAAS Pacific Division Executive Director Roger Christianson (left) and Rush Holt

Tom Fehrenbacher, a teacher at a San Diego high school, also sees a role for the humanities in conveying the science of climate change. "Science is lame without the humanities, and humanities without the sciences are blind," he said, recasting a quote from Albert Einstein on the connection between science and religion. "Humanities bring value to the discussion," Fehrenbacher added, "but we need to have our values informed by fact."

Gathering and interpreting the facts also requires broad collaboration, said Nilmini Silva-Send, assistant director of the Energy Policy Initiatives Center at the University of San Diego. Data gathered from different disciplines is crucial for crafting local, state, and federal policies that address climate change and its effects, she said. Assessing greenhouse gas emissions, for instance, requires information from experts in energy, policy, engineering, planning, and law.

"We need to talk across all disciplines," she said.

Boudrias detailed the multidisciplinary work of the Climate Education Partners, which brings together a team of climate and environmental scientists, educators, social psychologists focused on the study of learning, and experts in communications, policy, and the law. The group, of which Boudrias is a principal investigator, developed a report to help San Diego–area leaders make informed decisions in response to climate change and its effects.

"The science is there," said Boudrias of the report, called *San Diego, 2050 Is Calling. How Will We Answer?* Scientific evidence in the report is bolstered by input from other fields to help experts best connect with their audience of local leaders in government, business, the transportation sector, the public health field, the region's American Indian tribes, and its robust Latino community.

The report is grounded in social psychology concepts that empower local decision-makers to take action, Boudrias said. The report does more than just convey what scientists expect for San Diego's climate—it provides concrete steps for local leaders to "answer the call" and address, according to a community's needs, climate-change effects like dwindling water resources, longer wildfire seasons, and coastal flooding. It also uses infographics to depict climate-change effects and deliberately chosen language, such as presenting temperature increases in Fahrenheit, rather than in scientist-approved Celsius.

The report leverages people's concern for future generations—their top priority, according to the group's research. This perspective also helped to inform the timeline of the report, which looks ahead to 2050, rather than hewing to the 100-year models that many climate scientists study. Looking toward the near-term future taps into people's concern for the next generation, thereby providing a "tighter connection emotionally," Boudrias said.

According to Tiffany Lohwater of AAAS, the session at the Pacific Division meeting presented useful case studies in local climate-change communication. "To effectively connect with your audience, research demonstrates that it's important to emphasize how climate change affects people here and now, and right where they live," said Lohwater. As deputy chief communications officer and director of AAAS meetings and public engagement, Lohwater heads up the association's Communicating Science workshops and the Alan I. Leshner Leadership Institute for Public Engagement with Science, which last year named 15 fellows to promote science-society dialogue about climate change and to be role models for their peers. "It's encouraging to see AAAS division leaders working to convey the science of climate change in their own communities."



IMMUNOLOGY JOURNAL DEBUTS

Science Immunology, the latest addition to the *Science* family of journals, unveiled its inaugural content on 14 July, featuring research that overturned previous thinking about transplant rejection mechanisms, insights into how different animal species have evolved to recognize and defend against an array of elements toxic to the immune system, and much more. A second issue featured research that might help bring scientists closer to developing novel therapies for diseases like type 1 diabetes, rheumatoid arthritis, and multiple sclerosis. Through the end of 2016, the subscription-based journal, which features interdisciplinary research in immunology, drawing from studies in all organisms and model systems, including humans, will be made freely available. Through a partnership with the Federation of Clinical Immunology Societies (FOCIS), leaders of that organization will serve on the new journal's editorial advisory board, and FOCIS members will have continued access to the journal. "Innate and adaptive immune cells contribute to diverse inflammatory disorders—fibrosis, cardiovascular and metabolic diseases, and even neurodegenerative diseases such as Alzheimer's and Parkinson's," *Science Immunology* Editor Angela C. Colmone wrote in a first-ever editorial, with Chief Scientific Advisors Abul K. Abbas, M.D., and Federica Sallusto. Showcasing immunology studies across disciplines and technologies "will encourage collaborative and innovative research," they wrote. Another new journal, *Science Robotics*, will debut later this year. See www.scienceimmunology.org.

PHOTO: ANDREA KORTE/AAAS

Downloaded from http://science.sciencemag.org/ on July 28, 2016

Published by AAAS

Innovation competition empowers young entrepreneurs

Science, technology, and local concerns fuel ideas from the developing world

By **Juan David Romero**

Clarisse Uwineza was only 8 years old when both of her parents were killed in the 1994 Rwandan genocide. She was the second-oldest child, and it fell on her to look after four younger siblings. Despite her heavy burden and all that she had suffered, she managed to attend school. In a country where, at least at the time, girls often left school before earning a diploma, Uwineza continued to study.

Today, at age 28, Uwineza has her Bachelor of Science degree in environmental chemistry and is the founder/CEO of her own company, Environmental Protection and Organics. One of her projects, which is aimed at converting bio-waste into clean organic fertilizer, took her as far as Stanford University in late June, where she was one of 29 entrepreneurs from the developing world who showcased start-up companies at the sixth Global Innovation through Science and Technology (GIST) Tech-I Competition. There, she mingled with fellow scientists, entrepreneurs, and potential investors and received coaching and mentorship, while vying for important networking relationships and seed capital.



Clarisse Uwineza

PHOTO: GIST TECH-I

Uwineza said that participating in GIST gave her an amazing opportunity.

"It was my first time in the United States, my first time pitching my project in front of people, my first time meeting hundreds of entrepreneurs and mentors, my first time doing what most people call networking, my first time in a competition like this—and I say, wow, thank you, God," Uwineza said.

The GIST initiative was launched in 2011 by the U.S. Department of State to provide mentorship and networks to aspiring entrepreneurs from developing nations, to equip them with the tools to impact their communities. This year's GIST Tech-I Competition was the third AAAS has administered, coordinating the selection and organization of participants and providing experienced mentors to work with the young entrepreneurs.

"At AAAS, we believe the power of curiosity and creativity can benefit communities and improve lives everywhere," said Rush Holt, AAAS CEO and executive publisher of the *Science* family of journals, at the competition's award ceremony, "and the Tech-I program is a representation of that."

Lisa Brodey, the State Department's executive director for GIST, explained the importance of the program in furthering innovation and delivering economic benefits.

"When young innovators have the skills and mentoring that they need, they are more likely to take the risks that can turn ideas into startups and ultimately into successful businesses," she said.

From year to year, the program has seen increased participation among women. Among this year's 29 finalists, 12 were female.

The finalists this year were selected from more than 1,000 applicants from 104 emerging economies.

"They're all in different stages," said Kellye Eversole, a GIST mentor and president of a technology consulting firm. "Some of them have not really formed their business plans yet, but the education they got [during the 22–24 June competition in Silicon Valley] is going to help them do that. Others are ready to launch, and what they need is some short-term capital investment to try to do the final stages of development before they go to market."

The contestants were selected based on scores from an expert review panel convened by AAAS, who reviewed applicant materials including promotional pitch videos. Top scorers went on to a public vote. After being selected, the finalists received support to attend the 2016 Global Entrepreneurship Summit (GES) at Stanford, along with the two-day entrepreneurship workshop with successful entrepreneurs, scientists, and investors, which preceded a pitch competition offering $70,000 in prize money.

Charles Dunlap is the program director for the AAAS Research Competitiveness Program (RCP), which leads the GIST Tech-I project for AAAS. He said that the spirit and goals of entrepreneurship should be promoted because they tie into the State Department's diplomatic goals, "and for AAAS, they tie into our goals to see science have full impact in society and economic development."

For Uwineza, her commitment to helping improve people's lives is stronger than ever.

"I will do everything until I have great positive impact in society, not only in my country, Rwanda, but also in Africa and even the entire world," she said.

Workshops focus on female entrepreneurs

Focusing on female innovators' access to entrepreneurship, a series of Women's Village Workshops held this year in Côte d'Ivoire, Mozambique, and Nigeria taught strategies for expanding business networks and propelling science and technology innovations toward the market.

Each workshop, organized and managed by AAAS's Research Competitiveness Program (RCP), brought together 25 local entrepreneurs from an array of fields, including information technology, health, telecommunications, and agriculture. A majority of the participants were women.

The program is just one element of the U.S. Department of State's Global Innovation through Science and Technology (GIST) initiative, which helps young innovators from around the world with startup companies that tackle economic and development challenges.

To accelerate the workshop participants' entrepreneurship, each was challenged to reach "60 in 6": to expand her network by 60 people over the course of the next 6 months using the strategies learned at the workshop.

"After the workshop, I put into practice what I have learned, and my network continues to grow," said Jessyca Esther Houenou, a software and web developer who has cofounded an organization to promote Côte d'Ivoire's natural wealth. Houenou also said that she has shared digital marketing techniques from the workshop with other women who were interested in reaching new customers.

Cultivating leadership among participants is a key benefit of the workshops, said Charles Dunlap, director of RCP.

"We see all of those things as capacity-building—we want to see our participants pass on knowledge," he said.

Participant Safoura Fadiga, also of Côte d'Ivoire, said that the workshop she attended was structured to promote collaboration.

"I liked the communication techniques used," she said, explaining that participants moved around the room to interact with one another, rather than remaining seated. An engineer, teacher, and entrepreneur, Fadiga leads IST-DUBASS, a private, French-English bilingual college that aims to train more young people—particularly girls—in science, technology, engineering, and mathematics. —*Andrea Korte*

Downloaded from http://science.sciencemag.org/ on July 28, 2016

Published by AAAS

REVIEW SUMMARY

APPLIED PHYSICS

2D materials and van der Waals heterostructures

K. S. Novoselov,* A. Mishchenko, A. Carvalho, A. H. Castro Neto*

BACKGROUND: Materials by design is an appealing idea that is very hard to realize in practice. Combining the best of different ingredients in one ultimate material is a task for which we currently have no general solution. However, we do have some successful examples to draw upon: Composite materials and III-V heterostructures have revolutionized many aspects of our lives. Still, we need a general strategy to solve the problem of mixing and matching crystals with different properties, creating combinations with predetermined attributes and functionalities.

ADVANCES: Two-dimensional (2D) materials offer a platform that allows creation of heterostructures with a variety of properties. One-atom-thick crystals now comprise a large family of these materials, collectively covering a very broad range of properties. The first material to be included was graphene, a zero-overlap semimetal. The family of 2D crystals has grown to includes metals (e.g., $NbSe_2$), semiconductors (e.g., MoS_2), and insulators [e.g., hexagonal boron nitride (hBN)]. Many of these materials are stable at ambient conditions, and we have come up with strategies for handling those that are not. Surprisingly, the properties of such 2D materials are often very different from those of their 3D counterparts. Furthermore, even the study of familiar phenomena (like superconductivity or ferromagnetism) in the 2D case, where there is no long-range order, raises many thought-provoking questions.

A plethora of opportunities appear when we start to combine several 2D crystals in one vertical stack. Held together by van der Waals forces (the same forces that hold layered materials together), such heterostructures allow a far greater number of combinations than any traditional growth method. As the family of 2D crystals is expanding day by day, so too is the complexity of the heterostructures that could be created with atomic precision.

When stacking different crystals together, the synergetic effects become very important. In the first-order approximation, charge redistribution might occur between the neighboring (and even more distant) crystals in the stack. Neighboring crystals can also induce structural changes in each other. Furthermore, such changes can be controlled by adjusting the relative orientation between the individual elements.

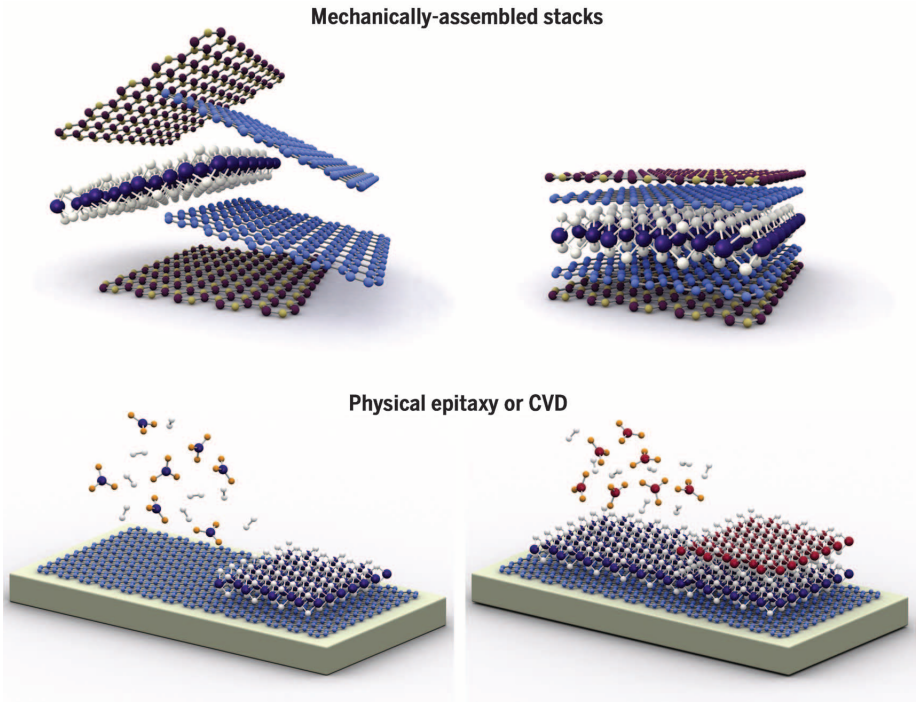
ON OUR WEBSITE

Read the full article at http://dx.doi.org/10.1126/science.aac9439

Such heterostructures have already led to the observation of numerous exciting physical phenomena. Thus, spectrum reconstruction in graphene interacting with hBN allowed several groups to study the Hofstadter butterfly effect and topological currents in such a system. The possibility of positioning crystals in very close (but controlled) proximity to one another allows for the study of tunneling and drag effects. The use of semiconducting monolayers leads to the creation of optically active heterostructures.

The extended range of functionalities of such heterostructures yields a range of possible applications. Now the highest-mobility graphene transistors are achieved by encapsulating graphene with hBN. Photovoltaic and light-emitting devices have been demonstrated by combining optically active semiconducting layers and graphene as transparent electrodes.

OUTLOOK: Currently, most 2D heterostructures are composed by direct stacking of individual monolayer flakes of different materials. Although this method allows ultimate flexibility, it is slow and cumbersome. Thus, techniques involving transfer of large-area crystals grown by chemical vapor deposition (CVD), direct growth of heterostructures by CVD or physical epitaxy, or one-step growth in solution are being developed. Currently, we are at the same level as we were with graphene 10 years ago: plenty of interesting science and unclear prospects for mass production. Given the fast progress of graphene technology over the past few years, we can expect similar advances in the production of the heterostructures, making the science and applications more achievable. ■



Production of van der Waals heterostructures. Owing to a large number of 2D crystals available today, many functional van der Waals heterostructures can be created. What started with mechanically assembled stacks (**top**) has now evolved to large-scale growth by CVD or physical epitaxy (**bottom**).

The list of author affiliations is available in the full article online.
*Corresponding author. Email: kostya@manchester.ac.uk (K.S.N.); phycastr@nus.edu.sg (A.H.C.N.)
Cite this article as K. S. Novoselov *et al.*, *Science* 353, aac9439 (2016). DOI: 10.1126/science.aac9439

Downloaded from http://science.sciencemag.org/ on July 28, 2016

REVIEW

APPLIED PHYSICS

2D materials and van der Waals heterostructures

K. S. Novoselov,[1,2]* A. Mishchenko,[1,2] A. Carvalho,[3] A. H. Castro Neto[3]*

The physics of two-dimensional (2D) materials and heterostructures based on such crystals has been developing extremely fast. With these new materials, truly 2D physics has begun to appear (for instance, the absence of long-range order, 2D excitons, commensurate-incommensurate transition, etc.). Novel heterostructure devices—such as tunneling transistors, resonant tunneling diodes, and light-emitting diodes—are also starting to emerge. Composed from individual 2D crystals, such devices use the properties of those materials to create functionalities that are not accessible in other heterostructures. Here we review the properties of novel 2D crystals and examine how their properties are used in new heterostructure devices.

The family of two-dimensional (2D) materials (*1*) has grown appreciably since the first isolation of graphene (*2*). The emergence of each new material brings excitement and puzzles, as the properties of these materials are usually very different from those of their 3D counterparts. Furthermore, 2D materials offer great flexibility in terms of tuning their electronic properties. Thus, band-gap engineering can be carried out by changing the number of layers in a given material (*3*, *4*). Even more interesting is the specific 2D physics observed in such materials [for instance, Kosterlitz-Thouless (KT) behavior, characterized by the emergence of topological order, resulting from the pairing of vortices and antivortices below a critical temperature]. Crystals with transition metals in their chemical composition are particularly prone to many-body instabilities such as superconductivity, charge density waves (CDWs), and spin density waves (SDWs). Such effects can also be induced by proximity if such crystals are sandwiched with other 2D materials.

Not only do heterostructures of 2D materials offer a way to study these phenomena, they also present unprecedented possibilities of combining them for technological use. Such stacks are very different from the traditional 3D semiconductor heterostructures, as each layer acts simultaneously as the bulk material and the interface, reducing the amount of charge displacement within each layer. Still, the charge transfers between the layers can be very large, inducing large electric fields and offering interesting possibilities in band-structure engineering.

[1]School of Physics and Astronomy, University of Manchester, Oxford Road, Manchester M13 9PL, UK. [2]National Graphene Institute, University of Manchester, Manchester M13 9PL, UK. [3]Centre for Advanced 2D Materials and Graphene Research Centre, National University of Singapore, 2 Science Drive 3, Singapore 117542.
*Corresponding author. Email: kostya@manchester.ac.uk (K.S.N.); phycastr@nus.edu.sg (A.H.C.N.)

Among the tools for band-structure engineering in van der Waals heterostructures are the relative alignment between the neighboring crystals, surface reconstruction, charge transfer, and proximity effects (when one material can borrow the property of another by contact via quantum tunneling or by Coulomb interactions). Thus, a moiré structure for graphene on hexagonal boron nitride (hBN) leads to the formation of secondary Dirac points (*5*–*9*), commensurate-incommensurate transition in the same system leads to surface reconstruction (*10*) and gap opening in the electron spectrum (*8*), and spin-orbit interaction can be enhanced in graphene by neighboring transition metal dichalcogenides (TMDCs) (*11*, *12*).

Here we provide a review of 2D materials, analyzing the physics that can be observed in such crystals. We discuss how these properties are put to use in new heterostructure devices.

Transition metal dichalcogenides

Transition metal dichalcogenides, with the formula MX_2 (where M is a transition metal and X is a chalcogen), offer a broad range of electronic properties, from insulating or semiconducting (e.g., Ti, Hf, Zr, Mo, and W dichalcogenides) to metallic or semimetallic (V, Nb, and Ta dichalcogenides). The different electronic behavior arises from the progressive filling of the nonbonding d bands by the transition metal electrons. The evolution of the electronic density of states (DOS) is shown in Fig. 1 [adapted from (*13*–*17*)] for the most stable phase of each of the dichalcogenides.

All TMDCs have a hexagonal structure, with each monolayer comprising three stacked layers (X-M-X). The two most common polytypes of the monolayers are trigonal prismatic (e.g., MoS_2 and WS_2) and octahedral (e.g., TiS_2); these terms refer to the coordination of the transition metal atom. Inversion symmetry is broken in the former, giving rise to piezoelectricity and having important consequences for the electronic structure. In addition, many of the tellurides, TcS_2, ReS_2, and other dichalcogenides adopt lower-symmetry structures in which the metal atom is displaced away from the center of the coordination unit.

Metallic TMDCs

As shown in Fig. 1, the DOS of metallic TMDCs has two main properties: (i) The Fermi level of the undoped material is always crossing a band with d-orbital character, implying that the electrons move mostly in the metal layers, and (ii) the DOS at the Fermi level is usually quite high, which hints at a common explanation for the phase transitions observed in these materials (*18*).

The interest in these materials comes from the existence of CDWs and superconductivity in their phase diagrams (*19*). Whereas the CDW phase has clear insulating tendency (opening a gap and suppressing the DOS at the Fermi level), the superconducting phase needs finite DOS to exist, resulting in a direct competition between the two many-body states. This competition leads to a complex phase diagram with the presence of inhomogeneous electronic and structural patterns, which have been observed in electron microscopy and neutron scattering in the 3D parent compound. Measurements of specific heat and magnetic susceptibility in 3D samples have shown partial gapping of the Fermi surface. In some cases (e.g., TaS_2), the CDW transition leads to the decoupling of the unit cells along the axis perpendicular to the planes, with an enormous increase in transverse resistivity.

These unusual properties of metal TMDCs have been the subject of intense theoretical debate, but no consensus has been reached. The mechanism for the CDW transition does not fit standard weak-coupling mean field theories such as Fermi surface nesting or transitions induced by van Hove singularities. Many angle-resolved photoemission experiments have been performed in 3D samples with contradictory results (*20*). The existence of several Fermi surface sheets and the partial gapping of the Fermi surface make the theoretical interpretation of the experimental data quite difficult. Furthermore, the coexistence of CDWs and superconductivity (clearly seen in local probes) (*21*) indicates that many-body effects play a very important role in these materials.

Critical information can be obtained from transport data in these materials, when transport measurements are performed in conjunction with the application of electric and magnetic fields. External electric field changes the Fermi energy and the carrier concentration in the 2D material, without the need for chemical doping (which was the case in 3D materials and which introduces appreciable disorder).

In a recent experiment on 1T-$TiSe_2$, a 2D film was encapsulated by hBN and subjected to transverse electric and magnetic fields (*22*). By applying an external electric field to change the carrier density, it was possible to tune the CDW transition temperature from 170 to 40 K and, concomitantly, the superconducting transition temperature from 0 to 3 K. Controlling the transition temperatures using an electric field allows the critical exponents for the phase transition to be determined

Downloaded from http://science.sciencemag.org/ on July 28, 2016

with high accuracy. Moreover, applying an external transverse magnetic field at the same time reveals novel physical phenomena associated with periodic motion of the Cooper pairs in the superconducting phase. Such behavior seems to be tied up with the formation of discommensurations between different CDW domains—namely, the electronic system broke down in perfectly ordered superconducting and CDW domains.

Phase transitions in 2D materials

Electrons in a solid are characterized by several quantum numbers that include charge and spin. Due to electron-electron or electron-ion interactions, electrons can organize themselves in phases characterized by an order parameter that is associated with these degrees of freedom. In a CDW state, as in the case of TMDCs, the order parameter is the local electron density $\rho(\mathbf{r})$, where $\mathbf{r}$ is the position vector, which orders with a well-defined periodicity. This periodicity implies that the Fourier transform of the density, $\rho(\mathbf{Q})$, where $\mathbf{Q}$ is the so-called ordering wave vector of the CDW, acquires a finite expectation value. For a CDW, the expectation value of $\rho(\mathbf{Q})$ is the order parameter, which is zero in the disordered (or normal) phase and finite in the ordered phase. The transition between these phases can be driven by external forces such as electric, mechanical, and thermal.

Two-dimensional systems play a particular role in the physics of phase transitions. For a system with a continuous order parameter, it is not possible to have true long-range order in less than three dimensions at any finite temperature T, implying that even minute thermal fluctuations can destroy order (*23*). In two dimensions, long-range order is possible only at strictly zero temperature. At $T = 0$, it is also possible for a system to be disordered if one varies an external parameter such as pressure or electric field, E (Fig. 2). The point at which a system becomes ordered at $T = 0$ is called the quantum critical point, and the transitions are called quantum phase transitions. In this case, it is not thermal motion that drives the system from order to disorder but quantum fluctuations. In this type of transition, the scale at which order is created is characterized by a correlation length ξ, which diverges at the phase transition as

$$\xi(E) \sim 1/|E - E_c|^{\nu}$$

where E_c is the critical field and ν is the critical exponent. Fluctuations of the order parameter at different points in space decay exponentially with ξ. Variations in length scales lead to fluctuations in energy scales as well. In a second-order phase transition, the characteristic energy scale, Δ, associated with the particular order (that is, the energy gap in the system) vanishes at the phase transition with another dynamical exponent, z, as

$$\Delta(E) \sim 1/\xi^{z} \sim |E - E_c|^{z\nu}$$

The simplest theory for understanding the effect of critical fluctuations close to a phase transition assumes that the order parameter (SDW, CDW, etc.) couples locally with the relevant degree of freedom (spin, charge, etc.). The resistivity is then given by the standard de Gennes–Friedel formula, in which the electron mean free path scales with the differential scattering cross section of the order parameter fluctuations.

In a classical phase transition, the behavior is driven by thermal fluctuations. The resistivity has the same kind of singularity as internal energy, implying that the critical behavior of the derivative of the resistivity is the same as the specific heat at the phase transition. This indicates that in a classical phase transition the critical behavior is marked by an inflection point in the resistivity at T_c.

Even though, for a 2D system, long-range order is not possible at any finite temperature, the

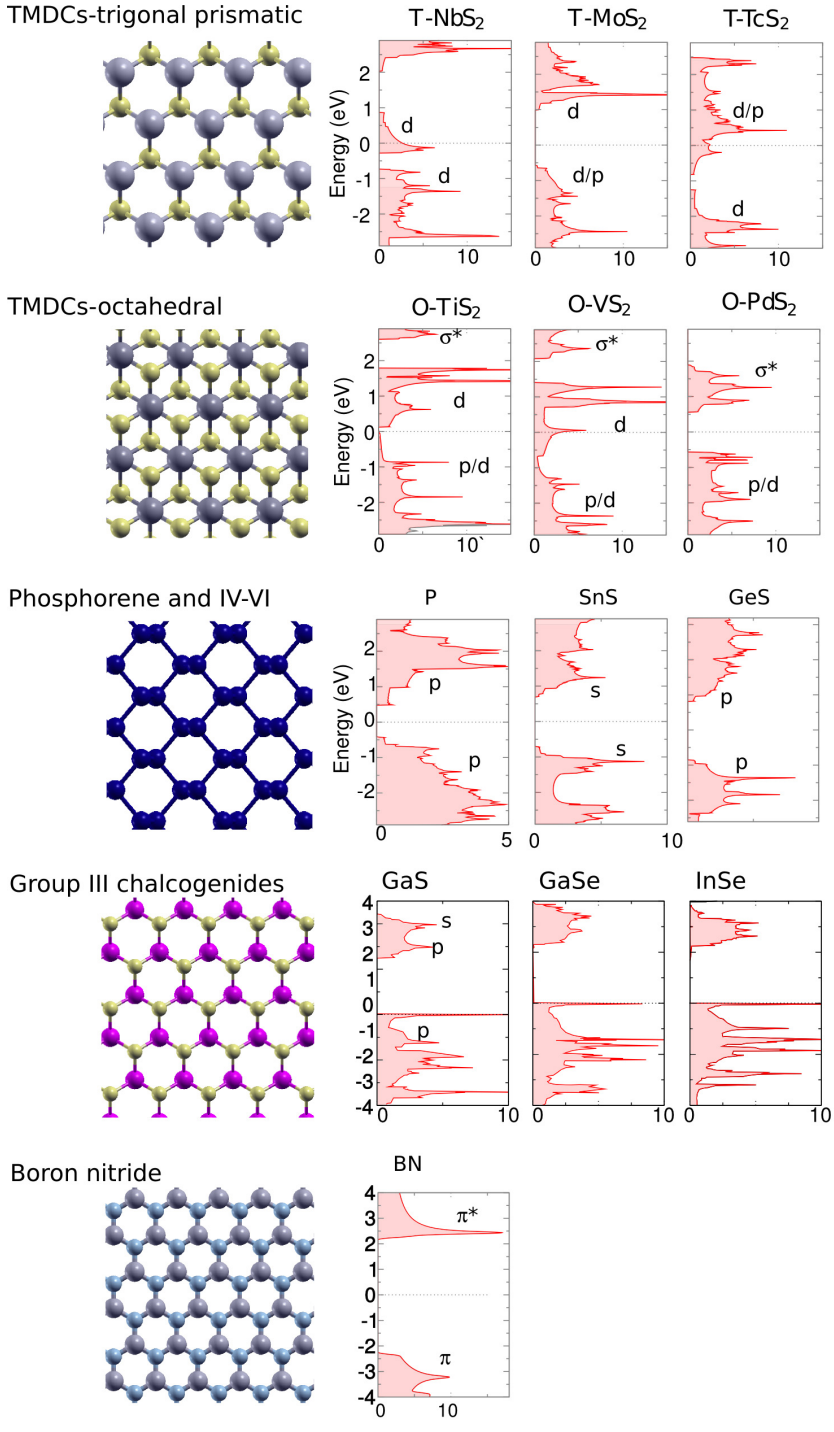


Fig. 1. Electronic properties of different classes of 2D materials. The Fermi level is set to the zero of the energy scale. The DOS is given in states per electron volt per cell.

Downloaded from http://science.sciencemag.org/ on July 28, 2016

system can undergo a transition to quasi–long-range order (KT transition) with the presence of vortex-antivortex pairs (*24*). In this case, the order parameter correlation length obeys the exponential dependence with temperature T

$$\xi(T) \sim a \exp(b/|T - T_{KT}|^{1/2}),$$

where a and b are constants and $T_{KT}(E)$ is the KT transition temperature, which is a function of the external tuning parameter E. The resistivity scales with some power of the inverse correlation length and hence is supposed to have an exponential dependence with temperature.

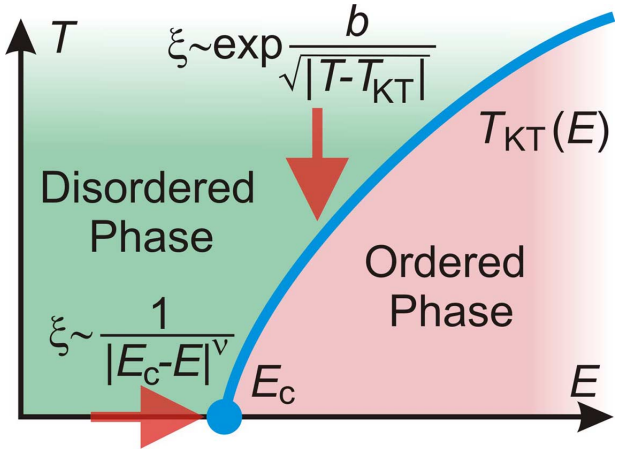


Fig. 2. Phase diagram for a 2D material with a quantum phase transition.

Semiconducting group-VIB dichalcogenides

Because of the charge confinement and reduced dielectric screening, the optical properties of semiconducting 2D materials are dominated by excitonic effects. The optical spectra of MoS_2, one of the most studied TMDCs, is characterized by three main transitions, named the A, B, and C peaks. The A exciton is the lowest energy corresponding to the fundamental optical gap of the material. The corresponding exciton binding energy is ~1 eV, according to theory. The B exciton also corresponds to a transition at the K point but for opposite spin. The C peak is of a different nature, as it has contributions from excitons from a large, annular-shaped region of the k-space with nearly identical transition energies. In nearly neutral monolayer samples, other quasiparticles have been observed, including positively and negatively charged excitons (i.e., trions) and biexcitons (*25*–*27*). The large trion binding energies (20 to 30 meV) have no parallel in traditional semiconductors and allow for these quasi-particles to be observed even at room temperature.

The series of Rydberg exciton states above the 1-s (A) exciton of WS_2 reveals an exciton series that deviates considerably from the hydrogen model (*28*, *29*). Not only do the 1s, 2s, 3s, … ns states have a closer spacing for small n, reflecting a weaker screening at short range (~log$r$, where r is the electron-hole separation) (*28*), they also have an entirely different dependence on the angular momentum. Ab initio GW calculations show that the states in the same shell but with higher angular momentum are at lower energy levels—that is, 3d, 3p, and 3s are in order of increasing energy.

From the technological point of view, however, the most relevant transitions are those close to the fundamental gap at $K(K')$ points of the Brillouin zone, which can be used for manipulating quantum information stored as spin and momentum (valley index) of individual electrons, holes, or excitons. The selection rule for optical transitions is valley-dependent, with the $K(K')$ valley coupling exclusively to right (left) circularly polarized light. Thus, the valley index, or pseudospin, can be controlled coherently by using polarized light. Because the two valleys have nonzero and symmetrical Berry curvature, in the presence of in-plane electric field they give rise to Hall currents with sign depending on the valley index, an effect known as the valley Hall effect. The orbital magnetic moment is also valley-dependent, which allows for coupling with magnetic fields (*30*–*36*).

Quantum dots of TMDCs inherit the valley properties of the monolayer and therefore are appealing for valleytronics due to the possibility of controlling spin and valley states of single confined electrons or holes—for example, via interaction with propagating single photons. Quantum dots can be created by growing finite islands on a monolayer substrate or by applying confinement potentials using patterned electrodes.

Phosphorene and group-IV monochalcogenides

Phosphorene, a monolayer of black phosphorus, is a monoelemental 2D material. Monolayer, few-layer, and bulk black phosphorus are all semiconducting materials, with a direct or nearly direct band gap (*4*). Additionally, phosphorene has a very high mobility that can reach 1000 $cm^2/V{\cdot}s$ for devices of ~10-nm thickness at room temperature (*37*). This exceeds the carrier mobility of TMDCs. According to theoretical predictions, the phonon-limited hole mobilities can reach 10,000 to 26,000 $cm^2/V{\cdot}s$ for the monolayer (zigzag direction) (*38*).

Both the optical and transport properties of phosphorene are highly anisotropic, as a consequence of this material's orthorhombic, wavelike structure. Optical selection rules dictate that the absorption threshold is lower for linear polarized light along the armchair direction than along the perpendicular direction. Optical conductivity and Raman spectra are also anisotropic, providing a fast way to determine phosphorene's lattice orientation. In addition to its optical and electronic properties, fundamental research in phosphorene has unraveled a growing number of physical phenomena, including superconductivity, high thermoelectric figure of merit (*39*), birefringence, and colossal ultraviolet (UV) absorption.

The group-IV monochalcogenides SnS, GeS, SnSe, and GeSe are isoelectronic with phosphorene and share its orthorhombic structure, but the two-atom types break the inversion symmetry of the monolayer. As a consequence, they feature spin-orbit splitting (19 to 86 meV) (*40*) and piezoelectricity with large coupling between deformation and polarization change in plane (with piezoelectric coefficients e_{33} ranging from 7×10^{-10} to 23×10^{-10} C/m, largely exceeding those of MoS_2 and hBN) (*41*).

SnS, SnSe, and GeSe are semiconductors, with gap energies covering part of the infrared and visible range for different numbers of layers (*40*). Even though the indirect band gap (in most cases) makes these materials less attractive for optical applications, the existence of two pairs of twofold degenerate valence and conduction band valleys, each placed on one principal axis of the Brillouin zone, makes them suitable for valleytronics applications. In this case, the symmetry is orthorhombic and, thus, the valley manipulation processes are different from those for TMDCs. Valley pairs can be selected using linear rather than circularly polarized light. Furthermore, there is no valley Hall effect, so the transverse valley current under an electric field is a second-order effect. Group-IV monochalcogenides are more stable against oxidation than phosphorene, can be grown by chemical vapor deposition (CVD), and have been recently exfoliated down to their bilayers.

Gallium and indium monochalcogenides

GaX and InX (where X is a chalcogen, like S, Se, or Te) are additional members of the family of hexagonal 2D materials. In this case, each layer can be viewed as a double layer of metal M = Ga, intercalated between two layers of chalcogen (X-M-M-X). The band structure of monolayers of such materials is rather unusual, having a "Mexican hat" dispersion at the top of the valence band, leading to a high DOS (*42*, *43*) (bulk materials are most probably direct band-gap semiconductors). Thus, these materials have high and fast photoresponsibility (*44*, *45*) and large second-harmonic generation and have attracted attention mostly due to their optical properties. If the Fermi level is close to this singularity in p-doped materials, a ferromagnetic instability arises (*46*).

Hexagonal boron nitride

Layers of hBN consist of hexagonal rings of alternating B and N atoms, with strong covalent sp^2 bonds and a lattice constant nearly identical to that of graphite. hBN is very resistant both to mechanical manipulation and chemical interactions and also has a large band gap in the UV range. For these reasons, hBN is a material of choice as an encapsulating layer or substrate for 2D stacked devices, providing an atomically smooth surface free of dangling bonds and charge traps. hBN substrates leave the band structure of graphene near the Dirac point virtually unperturbed (if crystallographic orientations of the two crystals are misaligned) and dramatically improve the mobility of graphene devices (*47*, *48*).

Downloaded from http://science.sciencemag.org/ on July 28, 2016

Oxide layers and other insulators

Many oxides have layered structures and can therefore be seen as a source for new 2D materials. These include lead oxide and lead salts [PbO, $Pb_2O(SO_4)$, Na_2PbO_2, etc.], phosphorus oxides and phosphates, molybdenum and vanadium oxides, and other transition metal oxides. In these materials, the layers are often connected by weak covalent bonds, oxygen bridges, or intercalating elements and are normally nonstoichiometric (due to the presence of oxygen vacancies). Further, layered oxides are normally polycrystalline, and mechanical exfoliation methods are usually limited to those available in higher-quality crystals. For the chemical means of production of such monolayers, intercalation with bulky guest species (such as tetrabutylammonium ions) has been used. Some of these layered oxides have been studied due to their importance as battery cathode materials (e.g., MoO_3, V_2O_5, and other Mo and V oxides), superconductors (e.g., copper and cobalt layered oxides) (*49*, *50*), passivating layers (phosphorus oxide) (*51*, *52*), and other areas of technological interest. Layered oxides allow for alloying, combination of different layers, and intercalation of ions and molecules; the possibilities of materials design are immense.

Among the most studied 2D insulators are hybrid perovskites, which are noteworthy for their high optical absorption coefficient within the solar spectrum and strong luminescence. Thin-film perovskite-based solar cells have emerged with a 20% power conversion efficiency, a notable value for a new technology (*53*). A hybrid perovskite is formed by layers of a metal halide intercalated with layers of organic chains. The high solar cell efficiency is thought to be greatly attributable to the confinement of excitons to the layers. Few-layer hybrid perovskites have been isolated by mechanical exfoliation and found to be stable in air in a time scale of minutes.

Novel van der Waals heterostructures

Two-dimensional crystals can be assembled into heterostructures (*54*), where the monolayers are held together by van der Waals forces. Considering that a large number of 2D crystals is currently available, it should be possible to create a substantial variety of heterostructures. However, the assembly technique currently in use (micromechanical stacking), allows only certain combinations of the interfaces. At the same time, an alternative technique, which potentially allows mass production of such structures (i.e., sequential growth of monolayers) comes with its own limitations and is presently in its infancy. Nevertheless, a large variety of novel experiments and prototypes have already been carried out with van der Waals heterostructures, which indicates that these materials are versatile and practical tools for future experiments and applications.

Assembly techniques

Currently, the most versatile technique for heterostructure assembly is direct mechanical assembly. This technique flourished starting in 2010 with Dean *et al.*'s work, which demonstrated the very high performance of graphene devices placed on an hBN substrate (*47*).

The technique used in the early works is based on preparing a flake of 2D crystal (Fig. 3, A to F) on a sacrificial membrane, aligning and placing it on another flake, and then removing the membrane. The process is then repeated to deposit further layers. Although the crystals are exposed to sacrificial membrane and solvents, which can contaminate the interface, annealing allows one to remove the contaminants and achieve very high interface quality (*55*), reaching high mobility (~10^6 $cm^2/V{\cdot}s$) in graphene devices prepared this way.

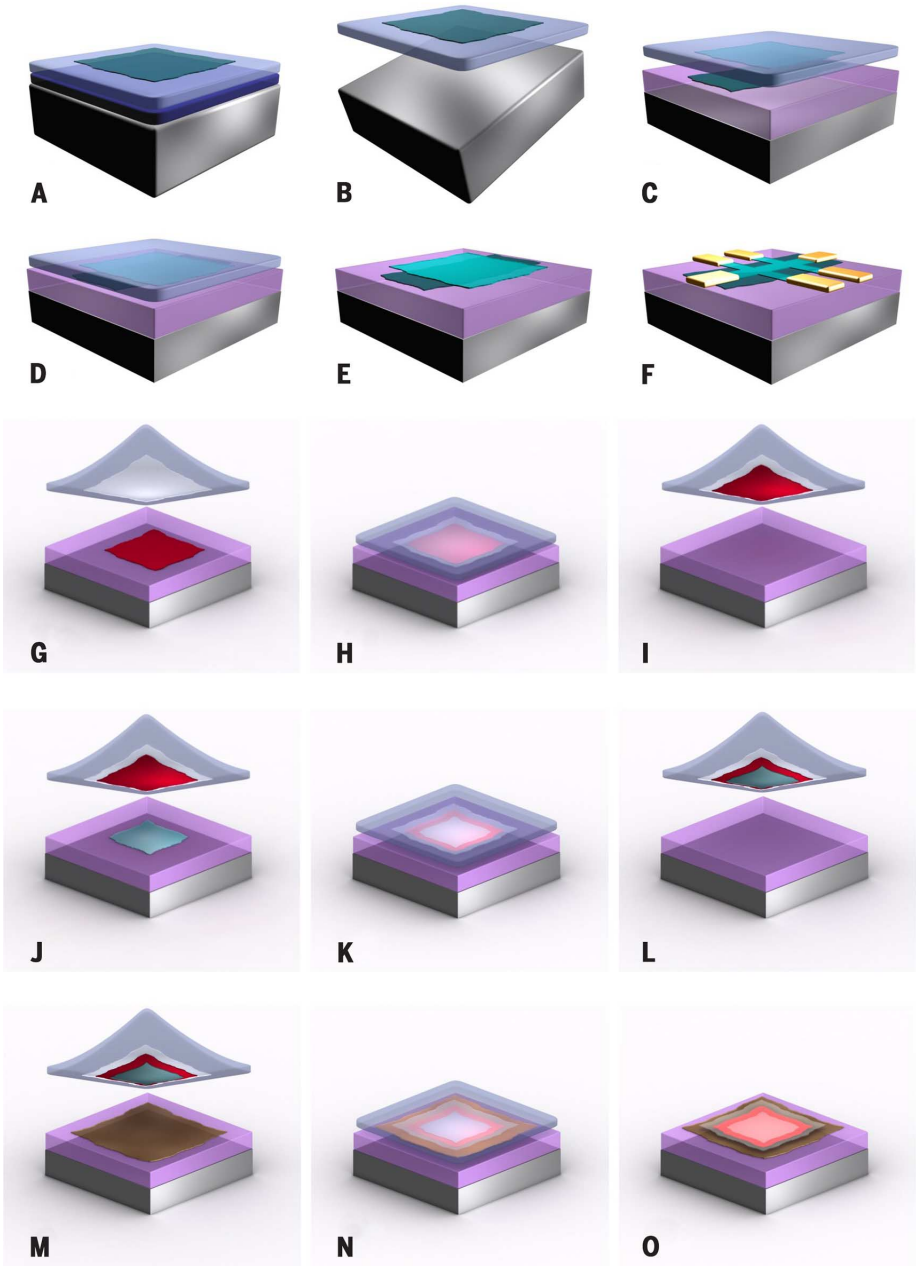


Fig. 3. Wet-transfer and pick-and-lift techniques for assembly of van der Waals heterostructures. (**A** to **F**) Wet-transfer technique. A 2D crystal prepared on a double sacrificial layer (A) is lifted on one layer by dissolving another (B). The crystal is then aligned (C) and placed (D) on top of another 2D material. Upon the removal of the membrane (E), a set of contacts and mesa can be formed (F). This process could be repeated to add more layers on top. (**G** to **O**) Pick-and-lift technique. A 2D crystal on a membrane [see (B)] is aligned (G) and then placed atop another 2D crystal (H). Depending on the relative size of the two crystals, it is possible to lift both flakes on the same membrane (I). By repeating the process, it is possible to then lift additional crystals [(J) to (L)]. Finally, the whole stack is placed on the crystal, which will serve as the substrate [(M) and (N)], and the membrane is dissolved, exposing the entire stack (O).

Downloaded from http://science.sciencemag.org/ on July 28, 2016

A substantially cleaner method (dubbed the "pick-and-lift" method) is based on strong van der Waals interactions that exist between the crystals. When the membrane with a 2D crystal on it is brought into contact with another 2D crystal, it is not dissolved but rather is lifted up (Fig. 3, G to O); then there is a chance that the second crystal will stick to the first and will be lifted together with it. The process can be repeated several times. This technique results in clean interfaces over large areas and yet higher electron mobility (*56*). Further advances could be achieved by transferring the whole process into a glovebox with a controllable atmosphere.

1D contacts

The later method (Fig. 3, G to O) has one particular disadvantage: Having a completely assembled stack would prohibit one to make contacts to the inner layer. Luckily, it has been demonstrated that one can achieve various profiles of the edges of such a stack by reactive plasma etching. Thus, it is possible to etch the edge of the stack in such a way that the desired layer becomes exposed and can be contacted by metal evaporation (*56*) (Fig. 4A). The contact resistance for graphene can be as low as 35 ohm·μm.

Self-cleansing mechanism

The transmission electron microscopy (TEM) studies (*55*) demonstrate that interfaces can be atomically flat and free of any contamination [Fig. 4, B to D; adopted from (*55*)]. The reason for such behavior is the so-called "self-cleansing" mechanism (*57*). If the affinity between the two 2D crystals is larger than the affinity between the crystals and the contaminants, then the energetically favorable situation is when the two crystals have the largest possible common interface. To achieve this condition, the contaminants are pushed away. This explains the observation of bubbles under transferred 2D crystals: Those are the pockets of contamination pushed from the rest of the interface [Fig. 4, E to J; adapted from (*57*)]. This self-cleansing mechanism works only on certain pairs of crystals (Fig. 4, E to G).

Surface reconstruction

Potentially, the van der Waals interaction between two 2D crystals might lead to surface reconstruction. The most suitable candidates for the observation of such effects are crystals with similar lattice constants, such as graphene on hBN. The lattice constant of hBN is only 1.8% larger than that of graphene, which leads to the formation of a moiré pattern (*5*).

It has been demonstrated that the most favorable configuration for graphene on hBN is when boron atoms lay on top of one of the sublattices in graphene and nitrogen is situated at the center of the hexagon (*58*). Then, by stretching itself to match the interatomic spacing of hBN, graphene tries to increase the area where the favorable configuration is achieved. Owing to the high Young modulus of graphene, such perfect stacking cannot be achieved across the whole interface (unless the hBN can contract, as the loss in elastic energy would not be compensated by the gain in the van der Waals interaction). Thus, such stretching of graphene can only be local, and the stretched regions would be separated by areas where the graphene lattice is not commensurate with hBN (Fig. 4, K and L).

This effect has been observed for graphene on hBN when the crystallographic orientations of the two crystals are practically aligned (*10*). In this case, the large regions of the moiré pattern where the two crystals are commensurate are separated by areas where the graphene lattice is relaxed. This effect disappears when the graphene is misoriented with respect to hBN. Such commensurate-incommensurate transition happens at a critical angle, which is given by the crystal mismatch (*10*).

Stacks of several other 2D crystals—including MoS_2 and $MoSe_2$ (*59*), MoS_2 and WS_2 (*60*), fluorographene and MoS_2 (*61*), and many others—have been investigated for electronic properties (*62*) and possible surface reconstruction. Thus, layer-breathing phonon modes have been observed by means of Raman spectroscopy for $MoSe_2/MoS_2$ heterobilayers (*63*). However, because the lattice-constant mismatch for those pairs is usually above 2%, the surface reconstruction would be hard to observe. It has been experimentally detected for silicene on MoS_2, where vertical buckling of silicene allows perfect stacking between the two crystals (*64*).

Spectrum reconstruction for graphene on hBN

Moiré patterns in graphene on hBN provide periodic scattering potential for electrons. This leads to the reconstruction of the electronic spectrum in graphene at the wave vectors determined by the

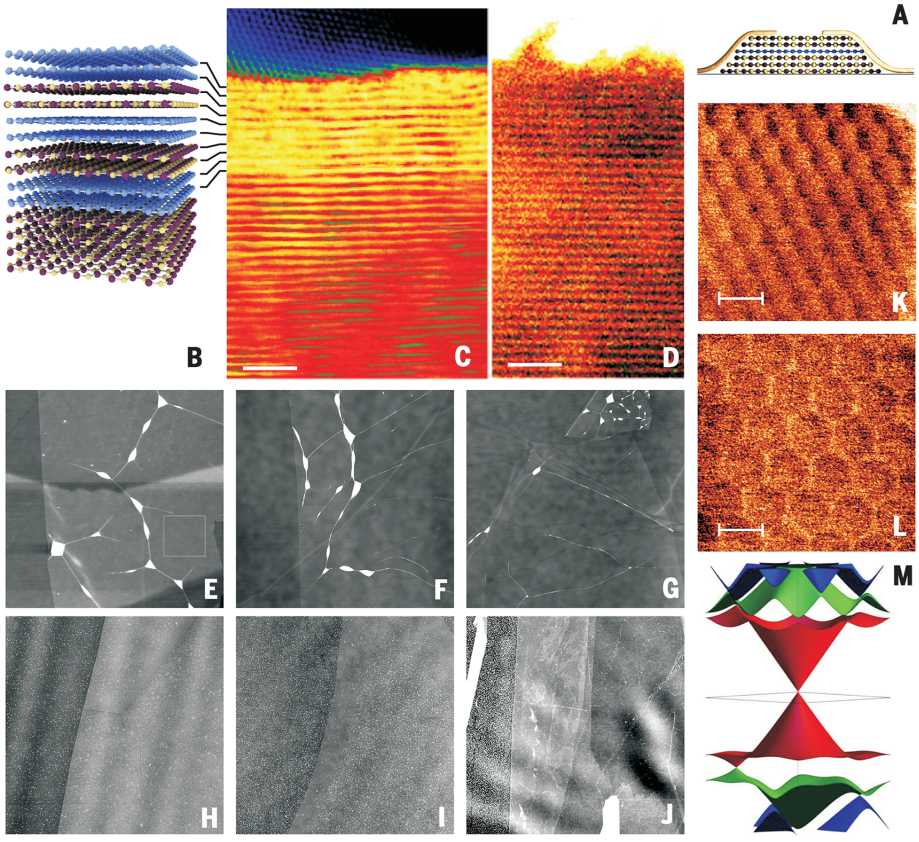


Fig. 4. Morphology of the van der Waals heterostructures. (**A**) 1D contacts to van der Waals heterostructures. Etching mesa in van der Waals heterostructures exposes the edges of the crystals inside the stack, which allows formation of 1D contacts. Here, carbon atoms are represented by blue spheres, boron is shown in yellow, and nitrogen is in purple. (**B** to **D**) TEM cross section of a graphene/hBN heterostructure. (B and C) Scanning TEM image (C) of the structure schematically presented in (B). In (B), atom coloring is the same as in (A). (D) High-angle annular dark-field image of the same stack. Scale bars in (C) and (D), 2 nm. (**E** to **J**) Atomic force microscopy (AFM) images of graphene transferred on other 2D crystals. A self-cleansing mechanism pushes contamination (hydrocarbons) away from graphene on hBN (E), MoS_2 (F), and WS_2 (G) interfaces, forcing the contamination to gather in bubbles. Instead, on the substrates with poor adhesion to graphene—such as mica (H), BSCCO (I), and V_2O_5 (J)—contamination is spread uniformly across the whole interface. Images in (E) to (J) are 15 μm by 15 μm, with a *z* scale of 4 nm. (**K** and **L**) Local Young modulus for graphene on hBN for misorientation angles of 3° (K) and 0° (L). Note the sharp domain walls in (L). Scale bars, 14 nm. (**M**) Reconstructed electronic energy spectrum for graphene aligned on hBN.

Downloaded from http://science.sciencemag.org/ on July 28, 2016

periodicity of the moiré structure, as has been observed in scanning tunneling microscopy (5) and, later, in transport (6–8) and capacitance (9) measurements. Secondary Dirac points appear in the electronic spectrum, in both the valence and conduction bands [Fig. 4M; adapted from (65)]. The energy range where the spectrum is reconstructed is given by the strength of the van der Waals interaction between graphene and hBN and is estimated to be on the order of 50 meV. Furthermore, the surface reconstruction leads to the strong asymmetry between the sublattices in graphene, which opens a gap in the graphene spectrum.

Capacitively coupled van der Waals heterostructures

Conceptually, the simplest devices based on van der Waals heterostructures are those for capacitance measurements. hBN is an ideal insulator that can sustain large electric fields (0.5 V per layer and above), allowing the preparation of capacitors with a very thin dielectric. The use of a thin dielectric ensures a large contribution of the quantum capacitance, which is directly proportional to the DOS in the electrode, making capacitance measurements a viable tool to study both single-particle and interaction phenomena in 2D materials. A number of systems have been investigated so far, including quantum capacitance in graphene (66), various sandwiches of graphene with TMDCs (57), and black phosphorus (67).

Capacitive coupling between two graphene layers through a thin layer of hBN can also lead to a number of noteworthy phenomena. This method allows for very-high-quality Coulomb drag devices, where two graphene layers, separated galvanically, interact through Coulomb forces between the charge carriers in the two layers (68). Because it is an atomically flat crystal with a very large gap in the electronic spectrum, hBN allows very thin barriers (on the order of a few nanometers) before any tunneling kicks in, bringing the two graphene layers closer than the characteristic distance between electrons in each of the layers (10 nm for a characteristic density of 10^{12} cm^{-2}). This opens the new regime of effective zero-layer separation in Coulomb drag experiments.

Tunneling devices

Graphene can be combined with semiconductor and insulating 2D crystals to create a tunnel junction (69). The use of hBN as a tunneling barrier is particularly attractive due to its large band gap (~6 eV), low number of impurity states within the barrier, and high breakdown field. Because the position of the Fermi energy and the DOS in graphene can be varied by external gate, the same applies for the tunneling current, which allows such structures to be used as field-effect tunneling transistors (FETTs) (70).

The architecture of FETTs enables tunneling spectroscopy to probe DOS in graphene, as well as to observe impurity- and phonon-assisted tunneling (71). Elastic tunneling through impurities gives peaks in dI/dV_b (I, current; V_b, bias voltage); peak positions depend on both bias and gate voltages (Fig. 5C). On the other hand, inelastic phonon-assisted tunneling is characterized by a set of plateaus in dI/dV_b, independent of gate voltage (71) [more pronounced in d^2I/dV_b^2 (Fig. 5B)]. When the bias voltage is large enough to emit a phonon ($eV_b = \hbar\omega_{ph}$, where e is the electron charge, $\hbar$ is Planck's constant h divided by 2π, and ω_{ph} is the frequency of the emitted phonon), an additional channel opens for electron tunneling, which increases transmission probability and, hence, tunnel conductance. Tunneling through impurities and with the phonon emission is especially visible if the crystallographic lattices of the two graphene electrodes are strongly misoriented with respect to each other, which prohibits direct electron tunneling because it is impossible to fulfill the momentum conservation requirements.

If the crystallographic lattices of the two graphene electrodes are aligned, momentum conservation for tunneling electrons can be achieved without impurity or phonon scattering. Rotational misalignment of the two graphene crystals corresponds to a relative rotation of the two graphene Brillouin zones in the reciprocal space. If the misalignment is small enough (<2°), then the momentum difference between the electronic states in the top and bottom graphene layers can be compensated electrostatically by applying bias and gate voltages (72), leading to the resonant tunneling and observation of the negative differential resistance (72) (Fig. 5D). A sharp negative differential resistance feature allows one to build a tunable radio-frequency oscillator with the potential to reach subterahertz frequencies.

The highest on-off ratio for FETTs can be achieved if the changes in the Fermi energy in graphene are comparable with the gap in the tunneling barrier—the situation achieved if hBN is replaced with WS_2 (on-off ratio of 10^6) (73) or MoS_2 (on-off ratio of 10^3 to 10^4, probably because of the presence of impurity bands) (70). In addition to logic applications, tunneling in van der Waals heterostructures was exploited for memory devices (74) with a floating gate, logic circuits (75), radio-frequency oscillators (72), and resonant tunneling diodes (76).

Interaction with light

Optoelectronic devices based on graphene (77) as well as other 2D materials (78) have been studied intensively. However, graphene photodetectors typically have low responsivity, which is a consequence of low adsorption coefficient. Such issues are eliminated when other 2D materials are used for such purposes. Thus, TMDCs (78), GaS (79), InSe (80), black phosphorus (81), and other materials (82) have been used as photodetectors (83) in photodiode or photoconductor regimes. The advantages of using such materials are the large DOS (which guarantees large optical adsorption), the materials' flexibility, and the possibility of local gating, which allows the creation of p-n junctions (84). Furthermore, the band gap in such materials often depends on the number of layers (3), which allows one to control the spectral response in such devices.

Van der Waals heterostructures for photovoltaic applications

Still, even larger opportunities open up when such materials are combined. Combinations of graphene (as a channel material) and TMDCs (as light-sensitive material, where trapped charges are controlled by illumination) allow creation of simple and efficient phototransistors (85).

Combining materials with different work functions can lead to photoexcited electrons and holes accumulated in different layers, giving rise to indirect excitons [e.g., as has been observed for the pairs MoS_2/WSe_2 (86) and $MoSe_2/WSe_2$ (87) (Fig. 5, E and F)]. Such excitons typically have long lifetimes, and their binding energy could be tuned by controlling the distance between the semiconductor layers.

If p- and n-doped materials are used in such devices, then atomically sharp p-n junctions can be created (88, 89). Such devices are extremely efficient in carrier separation, so they demonstrate very high quantum efficiency [for instance, GaTe/MoS_2 devices had external quantum efficiencies of >60% (88)]. Furthermore, their performance can be tuned externally by gate voltage, as has been demonstrated for black phosphorus/MoS_2 heterostructures (90).

Even more efficient photovoltaic devices can be created by combining thin layers of TMDCs (91) or metal chalcogenides (92) with graphene. By sandwiching the photosensitive material between graphene electrodes, one can achieve very efficient photocarrier extraction from the device into graphene electrodes (which typically form good ohmic contacts with the TMDCs and serve as a transparent electrode as well). Because these structures are typically symmetric (Fig. 5G), one needs to create an electric field inside the TMDC to produce efficient carrier separation by bias, external gating (because the electric field is not fully screened by graphene due to its low DOS), or different doping of the two graphene layers.

Light-emitting diodes

The p-n junctions described above can be operated in the regime of electrical injection of the charge carriers, which leads to electron-hole recombination and light emission (89). However, such arrangement is limited by the requirements of synthesizing p- and n-type materials, which have not yet been demonstrated for all 2D crystals. Furthermore, the resistance of the junction is comparable to the resistances of the p and n electrodes, which makes it hard to control the current distribution.

A more straightforward arrangement is the carrier injection from highly conductive transparent electrodes directly into the 2D material in a vertical structure. Such a scheme, however, requires careful control of the dwell time of the injected electrons and holes in the semiconductor crystal, because photoemission is a slow process in comparison with the characteristic time required to penetrate the junction between graphene and the semiconductor. The dwell time can be controlled by introducing additional tunnel barriers (Fig. 5H). Thus, two to three layers of hBN have

Downloaded from http://science.sciencemag.org/ on July 28, 2016

been used (*93*) to increase the time electrons and holes spend inside the monolayer TMDC, allowing their radiative recombination. Devices based on WSe_2 are particularly efficient: Their quantum efficiency increases with increasing temperature and injection current, reaching 20% at room temperature (*94*). One can increase the quantum efficiency of such structures by placing several layers of TMDCs in series (*93*) (Fig. 5I).

Plasmonic devices

Plasmons in graphene attract a lot of attention because it is possible to tune their frequency by changing the carrier concentration and, thus, the plasmonic frequency (*95*). Simultaneously, plasmonic and phonon-polaritonic properties have been studied in other 2D materials. For instance, hBN has polar dielectric properties, so it supports surface phonon polaritons with very low optical losses (*96*).

A number of new polaritonic effects can be seen in van der Waals heterostructures. Encapsulation of graphene with hBN allows one to eliminate the scattering of graphene plasmons with impurities, increasing their inverse damping ratio by a factor of 5 in comparison with bare graphene (*97*). By sandwiching several graphene layers separated by hBN spacers, one can hybridize plasmonic modes in such multilayers, which can be further controlled with external gate voltage (*98*).

In such heterostructures, it is possible to enter a regime where the plasmon polaritons in graphene and the phonon polaritons in hBN coexist [Fig. 5, J to L; adapted from (*99*)]. Strong coupling between the two leads to formation of the new collective modes: plasmon-phonon polaritons (*100*). Both the amplitude and the wavelength of the new collective modes can be controlled by gating graphene.

In aligned graphene/hBN heterostructures, the formation of the moiré pattern provides further modification of the graphene plasmonic spectrum. Zone folding results in the formation of the secondary Dirac points (*5*–*8*, *65*) (Fig. 4M), which allows a new type of vertical optical transition. Such transitions are immediately reflected in the modified damping factor, which exhibits a maximum at such Fermi energies (*101*). It has also

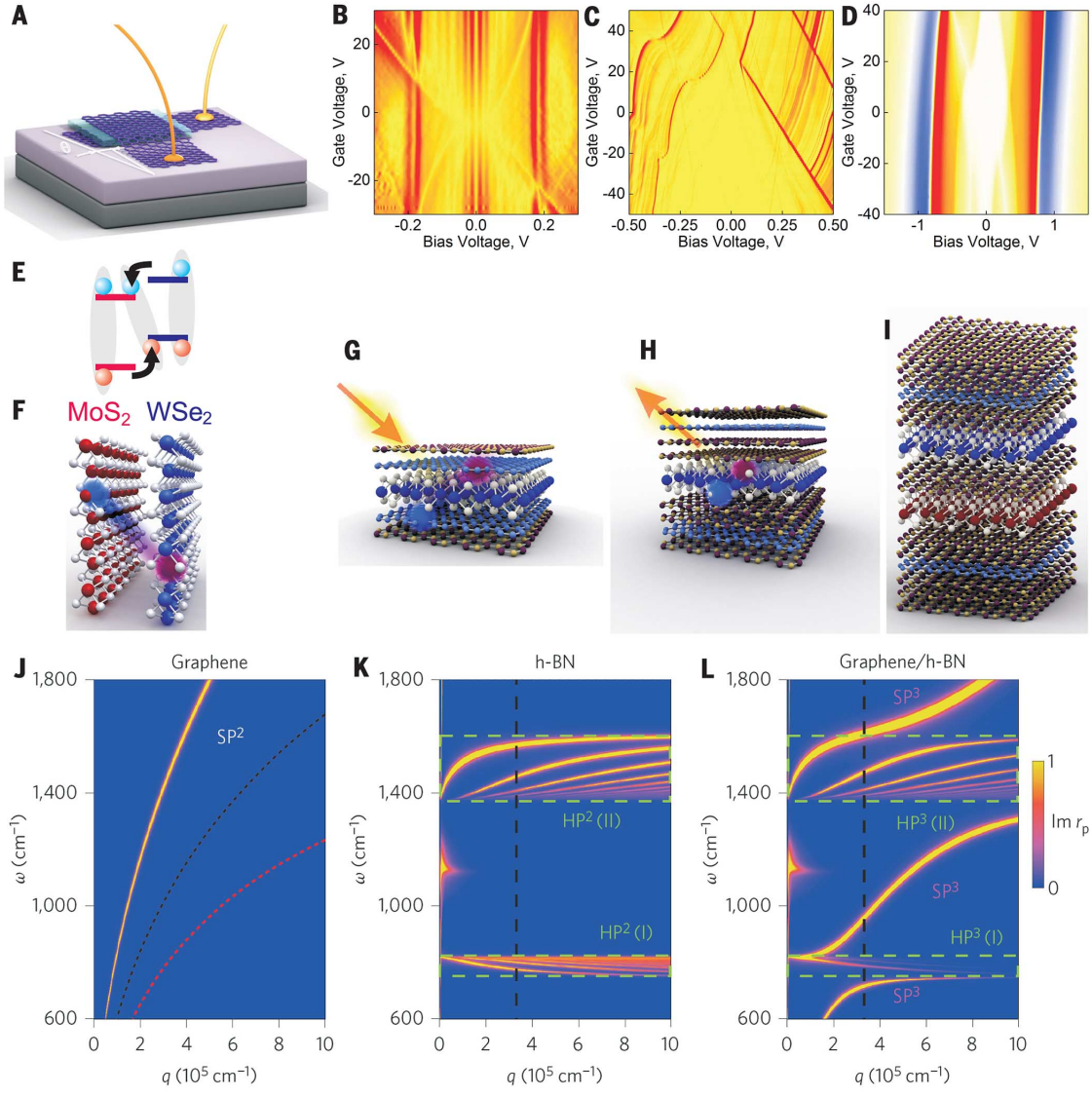


Fig. 5. Electronic and optoelectronic applications of van der Waals heterostructures. (**A** to **D**) Tunneling in graphene/hBN/graphene tunnel transistors. (A) Schematic representation of a graphene tunneling device. Graphene electrodes are shown in dark purple, and the hBN tunneling barrier is light blue. The electrodes can be aligned with respect to each other. (B) d^2I/dV_b^2 map of phonon-assisted tunneling. Color scale: yellow to red corresponds to 0 to 3.8×10^{-5} ohm^{-1} V^{-1}. (C) dI/dV_b map of resonant tunneling due to the presence of impurities in the hBN tunnel layer. Color scale: yellow to red corresponds to 0 to 7×10^{-8} ohm^{-1}. (D) dI/dV_b map of resonant tunneling with momentum conservation due to crystallographic alignment of two graphene electrodes. Blue coloring denotes the range of voltages where the negative differential conductivity is observed. Color scale: blue to white to red corresponds to -6×10^{-6} to 0 to 6×10^{-6} ohm^{-1}. (**E** and **F**) Indirect excitons in a MoS_2/WSe_2 heterostructure. Photoexcited electrons from WSe_2 are accumulated in MoS_2. Photoexcited holes from MoS_2 are accumulated in WSe_2. (**G**) TMDCs (large blue and white spheres) sandwiched between two graphene electrodes (small light-blue spheres) for photovoltaic applications. Photocarriers generated in TMDCs are separated into the opposite graphene electrodes due to an electric field created by external gating (not shown). The structure can be encapsulated in hBN (purple and yellow spheres). (**H** and **I**) Vertical light-emitting diode heterostructures. hBN barriers increase the dwell time of the electron and hole in the TMDC, allowing their radiative recombination. Multiple quantum wells, formed by different materials, can be used in such structures (I). Coloring of the atoms is the same as in (F) and (G). (**J** to **L**) Polaritonic dispersions of graphene, hBN, and a graphene/hBN heterostructure. q, polariton momentum; ω, polariton frequency; r_p, the imaginary part of the reflectivity.

Downloaded from http://science.sciencemag.org/ on July 28, 2016

been predicted that new plasmonic modes with carrier density dependence characteristic of parabolic electronic bands should appear in the vicinity of the van Hove singularities of the reconstructed spectrum (*101*) (Fig. 4M).

Assembling van der Waals heterostructures in liquid and from liquid-phase–exfoliated 2D materials

A very powerful method of preparing graphene, which can also be extended to other materials, is liquid-phase exfoliation (*102*). Ink formulation based on such suspensions led to the development of graphene-based printed electronics (*103*). However, many applications would strongly benefit from properties beyond the capabilities of graphene inks. Thus, high thermal conductivity combined with dielectric property can be delivered by hBN, and optoelectronic capabilities can be delivered by inks of 2D semiconductors.

The ability to print combinations of such materials opens the door for low-cost fabrication of various devices (*104*). Planar (*105*) and vertical (*106*) photovoltaic devices based on TMDCs, as well as planar (*107*) and tunneling transistors (*106*) based on graphene and hBN, have recently been demonstrated.

By solution synthesis of 2D crystals or by controlling the charge on individual flakes in suspensions, heterostructures can be formed directly in the liquid phase (*108*) and can be used for energy applications. For instance, $MoSe_2$/graphene structures have been used for Li-ion battery applications (*109*). Similar heterostructures have also been used for catalytic applications (*110*).

Growing van der Waals heterostructures

Direct growth methods such as CVD are promising techniques for scalable manufacturing of van der Waals heterostructures (*111*). Such techniques can be grouped as follows: (i) sequential CVD growth of 2D crystals on top of mechanically transferred or grown 2D materials, (ii) direct growth of TMDC heterostructures by vapor-solid reactions, and (iii) van der Waals epitaxy. State-of-the-art CVD, direct growth, and van der Waals epitaxy methods have already enabled the growth of many vertical heterostructures, such as graphene/hBN (*112*–*116*), MoS_2/graphene (*117*–*120*), GaSe/graphene (*121*), MoS_2/hBN (*122*, *123*), WS_2/hBN (*124*), $MoTe_2/MoS_2$ (*125*), WS_2/MoS_2 (*126*), $VSe_2/GeSe_2$ (*127*), $MoSe_2/Bi_2Se_3$ (*128*), $MoSe_2/HfSe_2$ (*129*), MoS_2/WSe_2/graphene, and $WSe_2/MoSe_2$/graphene (*76*).

In situ CVD growth of encapsulated graphene in a hBN/graphene/hBN heterostructure was an important achievement because it demonstrated the scalability of high-mobility graphene-based field-effect transistors (*116*). Also, some of the TMDC heterostructures can be grown directly in a single-step process: A WS_2/MoS_2 heterobilayer was grown on a SiO_2/Si substrate at 850°C from precursors (W, S, MoO_3) placed in the growth tube [Fig. 6A; adapted from (*126*)]. Because of the difference in the growth rates of MoS_2 and WS_2, the formation of a $Mo_xW_{1-x}S_2$ alloy is suppressed. A clean interface enabled a band alignment of

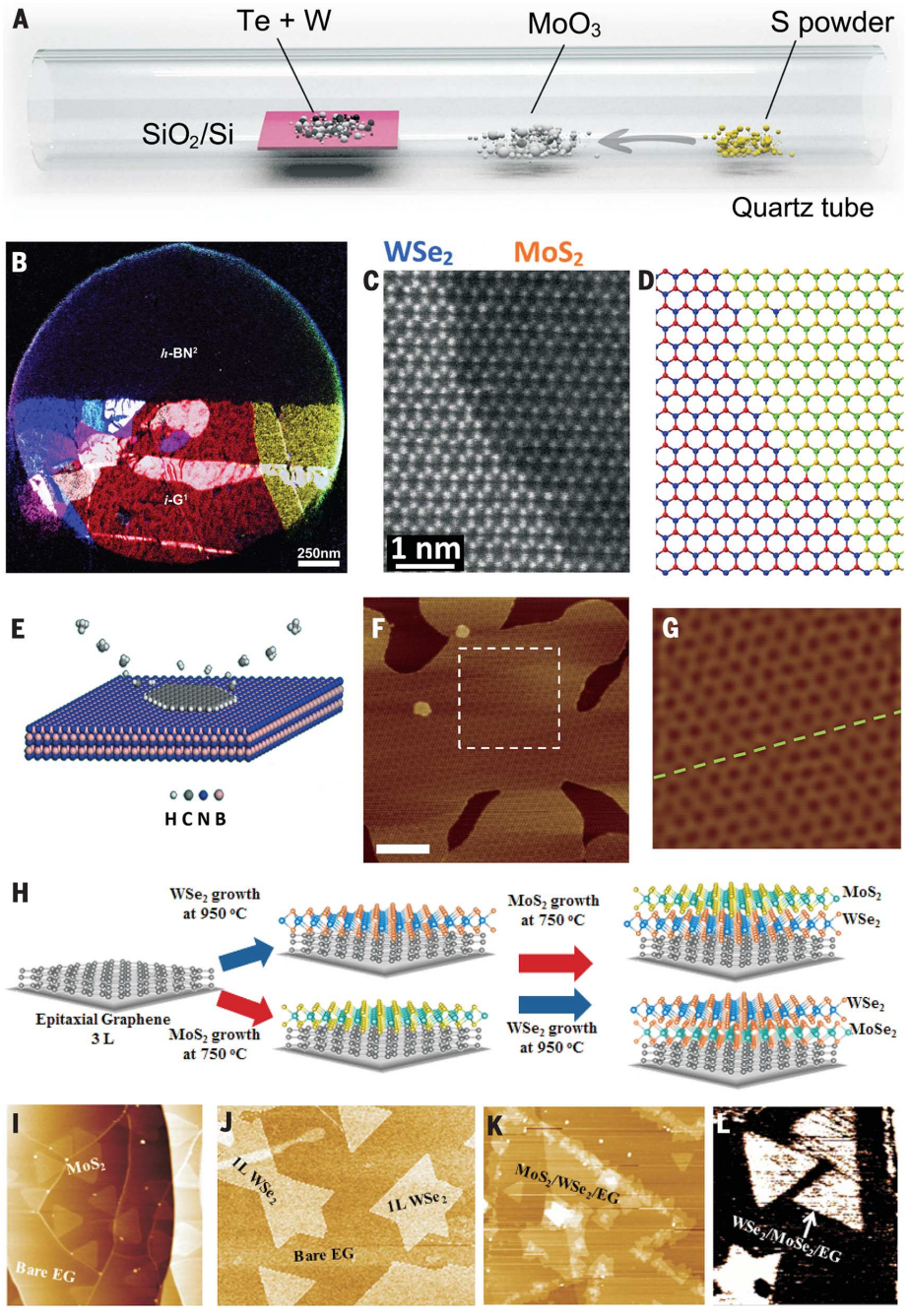


Fig. 6. Van der Waals epitaxy of vertical and in-plane heterostructures. (**A**) Schematic of the growth process of vertically stacked and in-plane WS_2/MoS_2 heterostructures. (**B**) False-color dark-field TEM image of a suspended hBN/graphene in-plane heterostructure. (**C** and **D**) High-resolution scanning transmission electron microscopy image and an atomic model of a WSe_2/MoS_2 in-plane heterostructure. (**E**) Schematics of vertical van der Waals heteroepitaxy of graphene on hBN. (**F** and **G**) (F) Moiré pattern of a graphene/hBN heterostructure as observed in tapping-mode AFM and (G) high-pass–filtered inverse fast Fourier transform of the dashed square region in (F). Scale bar in (F), 100 nm. (**H**) Schematics of the growth of MoS_2/WSe_2/graphene (top) and $WSe_2/MoSe_2$/graphene (bottom). Synthesis of both three-component heterostructures begins by growing three layers (3L) of epitaxial graphene (EG), followed by metal-organic CVD growth of either MoS_2 (I) or WSe_2 (J). Then, another TMDC layer is grown by vapor transfer of either MoS_2 (K) or WSe_2 (L). (**I** to **K**) AFM images of MoS_2/graphene, WSe_2/graphene, and MoS_2/WSe_2/graphene vertical heterostructures, respectively. (**L**) Conductive AFM image of a $WSe_2/MoSe_2$/graphene heterostructure. Color scale: black to white corresponds to 0 to 100 pA. Due to Se-S ion exchange, a layer of $MoSe_2$ forms from the original MoS_2 layer.

Downloaded from http://science.sciencemag.org/ on July 28, 2016

the two constituent layers, which led to the observation of indirect excitons in the WS_2/MoS_2 heterostructure.

Van der Waals epitaxy

Van der Waals epitaxy was introduced more than 30 years ago with the growth of a $NbSe_2$ monolayer on a cleaved face of MoS_2 bulk crystal (*130*). This work also led to the successful growth of monolayer $MoSe_2$ on SnS_2 (*131*), as well as growth of a two-component heterostructure of monolayer $NbSe_2$/trilayer $MoSe_2$ on mica (*132*).

To grow graphene on hBN, Yang *et al.* used plasma to break down precursor methane molecules (*48*), after which growth occurred at 500°C over the course of 2 to 3 hours on hBN crystals mechanically exfoliated on a SiO_2/Si substrate. Van der Waals interactions during epitaxial growth defined the preferential growth directions so that graphene crystals were aligned to the hBN substrate [Fig. 6, E to G; adapted from (*48*)].

Mechanically exfoliated hBN has also served as a substrate for CVD-based van der Waals epitaxy of a rotationally commensurate MoS_2/hBN heterostructure (*122*). Another example of van der Waals epitaxy is the growth of high-quality wafer-scale $MoSe_2/Bi_2Se_3$ heterostructures on the low-cost dielectric substrate AlN/Si in ultrahigh vacuum conditions (*128*).

Graphene is also a good substrate for van der Waals epitaxy: Grown WSe_2/graphene heterostructures show an atomically sharp interface and nearly perfect crystallographic orientation between graphene and WSe_2, despite a large (23%) lattice mismatch (*133*). Few-layer MoS_2 and hBN structures were also grown using epitaxial graphene as a growth substrate (*117*, *134*). Recently, monolayers of WSe_2 and MoS_2 were grown on free-standing CVD graphene (*135*). TMDC crystals were also explored as substrates for epitaxy when a $MoTe_2$ monolayer was grown on a bulk MoS_2 substrate (*125*).

Finally, van der Waals epitaxy can be repeated several times to grow complex multicomponent heterostructures, such as atomically thin resonant tunneling diodes based on MoS_2/WSe_2/graphene and $WSe_2/MoSe_2$/graphene [Fig. 6, H to L; adapted from (*76*)]. To this end, an epitaxial graphene trilayer was used as a substrate to grow monolayers of either MoS_2 (at 750°C) or WSe_2 (at 850°C) via powder vaporization or metal-organic CVD processes. Subsequently, a second TMDC layer (WSe_2 or MoS_2) was grown on top of the initially grown heterostructure.

Lateral heterostructures

Lateral heterostructures can also be grown by a variety of methods. Thus, CVD-grown graphene was lithographically patterned and etched away, and hBN was grown via CVD, forming lateral 1D heterojunctions [Fig. 6B; adapted from (*136*)]. Beyond graphene and hBN, lateral heterostructures based on 2D TMDCs can be disruptive for integrated optoelectronic devices. Although direct growth favors TMDC alloys because of a similar chemistry and a small lattice mismatch between different TMDCs (*137*), two-step epitaxial growth of a MoS_2/WSe_2 lateral heterostructure was recently demonstrated [Fig. 6, C and D; adapted from (*138*)]. To avoid alloying during growth, two separate temperature regimes were used (*138*). The atomically sharp WSe_2/MoS_2 heterojunction has a depletion width of ≈300 nm due to the potential difference between the MoS_2 and WSe_2 regions.

Lateral heterostructures of MoS_2/WS_2 and $WSe_2/MoSe_2$ were grown directly by controlling the growth temperature at ~650°C (*126*). Growth at relatively low temperatures was facilitated by either introducing tellurium into the CVD process (*126*) or using perylene-based growth promotors (*139*). The use of growth-promoting perylene-based aromatic molecules was recently extended to stitch together largely dissimilar 2D materials.

Conclusion

The family of 2D crystals is continuously growing, both in terms of variety and number of materials, and it looks like this process is only beginning. Almost every new 2D material possesses unusual physical properties. The 2D physics (e.g., KT transitions) in such materials is just starting to emerge. Still, we argue that the most interesting phenomena can be realized in van der Waals heterostructures, which now can be mechanically assembled or grown by a variety of techniques. Among the unsolved problems is the control of surface reconstruction, charge transfers, and built-in electric fields in such heterostructures. The standard band diagrams with quasi-electric fields are not a useful concept in 2D heterostructures; therefore, a new framework must be developed.

REFERENCES AND NOTES

1. K. S. Novoselov *et al.*, Two-dimensional atomic crystals. *Proc. Natl. Acad. Sci. U.S.A.* **102**, 10451–10453 (2005). doi: 10.1073/pnas.0502848102; pmid: 16027370
2. K. S. Novoselov *et al.*, Electric field effect in atomically thin carbon films. *Science* **306**, 666–669 (2004). doi: 10.1126/science.1102896; pmid: 15499015
3. K. F. Mak, C. Lee, J. Hone, J. Shan, T. F. Heinz, Atomically thin MoS_2: A new direct-gap semiconductor. *Phys. Rev. Lett.* **105**, 136805 (2010). doi: 10.1103/PhysRevLett.105.136805; pmid: 21230799
4. H. Liu *et al.*, Phosphorene: An unexplored 2D semiconductor with a high hole mobility. *ACS Nano* **8**, 4033–4041 (2014). doi: 10.1021/nn501226z; pmid: 24655084
5. M. Yankowitz *et al.*, Emergence of superlattice Dirac points in graphene on hexagonal boron nitride. *Nat. Phys.* **8**, 382–386 (2012). doi: 10.1038/nphys2272
6. L. A. Ponomarenko *et al.*, Cloning of Dirac fermions in graphene superlattices. *Nature* **497**, 594–597 (2013). doi: 10.1038/nature12187; pmid: 23676678
7. C. R. Dean *et al.*, Hofstadter's butterfly and the fractal quantum Hall effect in moiré superlattices. *Nature* **497**, 598–602 (2013). doi: 10.1038/nature12186; pmid: 23676673
8. B. Hunt *et al.*, Massive Dirac fermions and Hofstadter butterfly in a van der Waals heterostructure. *Science* **340**, 1427–1430 (2013). doi: 10.1126/science.1237240; pmid: 23686343
9. G. L. Yu *et al.*, Hierarchy of Hofstadter states and replica quantum Hall ferromagnetism in graphene superlattices. *Nat. Phys.* **10**, 525–529 (2014). doi: 10.1038/nphys2979
10. C. R. Woods *et al.*, Commensurate–incommensurate transition in graphene on hexagonal boron nitride. *Nat. Phys.* **10**, 451–456 (2014). doi: 10.1038/nphys2954
11. A. Avsar *et al.*, Spin-orbit proximity effect in graphene. *Nat. Commun.* **5**, 4875 (2014). doi: 10.1038/ncomms5875; pmid: 25255743
12. Z. Wang *et al.*, Strong interface-induced spin-orbit interaction in graphene on WS_2. *Nat. Commun.* **6**, 8339 (2015). doi: 10.1038/ncomms9339; pmid: 26391068
13. A. Carvalho, R. M. Ribeiro, A. H. Castro Neto, Band nesting and the optical response of two-dimensional semiconducting transition metal dichalcogenides. *Phys. Rev. B* **88**, 115205 (2013). doi: 10.1103/PhysRevB.88.115205
14. A. S. Rodin, L. C. Gomes, A. Carvalho, A. H. Castro Neto, Valley physics in tin (II) sulfide. *Phys. Rev. B* **93**, 045431 (2016). doi: 10.1103/PhysRevB.93.045431
15. L. C. Gomes, S. S. Alexandre, H. Chacham, R. W. Nunes, Stability of edges and extended defects on boron nitride and graphene monolayers: The role of chemical environment. *J. Phys. Chem. C* **117**, 11770–11779 (2013). doi: 10.1021/jp400420m
16. H. Chen, Y. Li, L. Huang, J. B. Li, Intrinsic defects in gallium sulfide monolayer: A first-principles study. *RSC Advances* **5**, 50883–50889 (2015). doi: 10.1039/C5RA08329J
17. D. V. Rybkovskiy, A. V. Osadchy, E. D. Obraztsova, Transition from parabolic to ring-shaped valence band maximum in few-layer GaS, GaSe, and InSe. *Phys. Rev. B* **90**, 235302 (2014). doi: 10.1103/PhysRevB.90.235302
18. J. A. Wilson, A. D. Yoffe, The transition metal dichalcogenides discussion and interpretation of the observed optical, electrical and structural properties. *Adv. Phys.* **18**, 193–335 (1969). doi: 10.1080/00018736900101307
19. A. H. Castro Neto, Charge density wave, superconductivity, and anomalous metallic behavior in 2D transition metal dichalcogenides. *Phys. Rev. Lett.* **86**, 4382–4385 (2001). doi: 10.1103/PhysRevLett.86.4382; pmid: 11328180
20. T. Valla *et al.*, Charge-density-wave-induced modifications to the quasiparticle self-energy in 2H- $TaSe_2$. *Phys. Rev. Lett.* **85**, 4759–4762 (2000). doi: 10.1103/PhysRevLett.85.4759; pmid: 11082645
21. H. F. Hess, R. B. Robinson, J. V. Waszczak, STM spectroscopy of vortex cores and the flux lattice. *Physica B* **169**, 422–431 (1991). doi: 10.1016/0921-4526(91)90262-D
22. L. J. Li *et al.*, Controlling many-body states by the electric-field effect in a two-dimensional material. *Nature* **529**, 185–189 (2016). doi: 10.1038/nature16175; pmid: 26700810
23. P. C. Hohenberg, Existence of long-range order in one and two dimensions. *Phys. Rev.* **158**, 383–386 (1967). doi: 10.1103/PhysRev.158.383
24. P. Minnhagen, The two-dimensional Coulomb gas, vortex unbinding, and superfluid-superconducting films. *Rev. Mod. Phys.* **59**, 1001–1066 (1987). doi: 10.1103/RevModPhys.59.1001
25. J. Shang *et al.*, Observation of excitonic fine structure in a 2D transition-metal dichalcogenide semiconductor. *ACS Nano* **9**, 647–655 (2015). doi: 10.1021/nn5059908; pmid: 25560634
26. K. F. Mak *et al.*, Tightly bound trions in monolayer MoS_2. *Nat. Mater.* **12**, 207–211 (2013). doi: 10.1038/nmat3505; pmid: 23202371
27. B. Zhu, X. Chen, X. Cui, Exciton binding energy of monolayer WS_2. *Sci. Rep.* **5**, 9218 (2015). doi: 10.1038/srep09218; pmid: 25783023
28. A. Chernikov *et al.*, Exciton binding energy and nonhydrogenic Rydberg series in monolayer WS_2. *Phys. Rev. Lett.* **113**, 076802 (2014). doi: 10.1103/PhysRevLett.113.076802; pmid: 25170725
29. Z. Ye *et al.*, Probing excitonic dark states in single-layer tungsten disulphide. *Nature* **513**, 214–218 (2014). doi: 10.1038/nature13734; pmid: 25162523
30. D. Xiao, G.-B. Liu, W. Feng, X. Xu, W. Yao, Coupled spin and valley physics in monolayers of MoS_2 and other group-VI dichalcogenides. *Phys. Rev. Lett.* **108**, 196802 (2012). doi: 10.1103/PhysRevLett.108.196802; pmid: 23003071
31. H. Zeng, J. Dai, W. Yao, D. Xiao, X. Cui, Valley polarization in MoS_2 monolayers by optical pumping. *Nat. Nanotechnol.* **7**, 490–493 (2012). doi: 10.1038/nnano.2012.95; pmid: 22706701
32. T. Cao *et al.*, Valley-selective circular dichroism of monolayer molybdenum disulphide. *Nat. Commun.* **3**, 887 (2012). doi: 10.1038/ncomms1882; pmid: 22673914
33. K. F. Mak, K. He, J. Shan, T. F. Heinz, Control of valley polarization in monolayer MoS_2 by optical helicity. *Nat. Nanotechnol.* **7**, 494–498 (2012). doi: 10.1038/nnano.2012.96; pmid: 22706698
34. A. M. Jones *et al.*, Optical generation of excitonic valley coherence in monolayer WSe_2. *Nat. Nanotechnol.* **8**, 634–638 (2013). doi: 10.1038/nnano.2013.151; pmid: 23934096
35. D. Xiao, W. Yao, Q. Niu, Valley-contrasting physics in graphene: Magnetic moment and topological transport.

Downloaded from http://science.sciencemag.org/ on July 28, 2016

Phys. Rev. Lett. **99**, 236809 (2007). doi: 10.1103/PhysRevLett.99.236809; pmid: 18233399

36. K. F. Mak, K. L. McGill, J. Park, P. L. McEuen, The valley Hall effect in MoS_2 transistors. *Science* **344**, 1489–1492 (2014). doi: 10.1126/science.1250140; pmid: 24970080
37. L. Li *et al*., Black phosphorus field-effect transistors. *Nat. Nanotechnol.* **9**, 372–377 (2014). doi: 10.1038/nnano.2014.35; pmid: 24584274
38. J. Qiao, X. Kong, Z. X. Hu, F. Yang, W. Ji, High-mobility transport anisotropy and linear dichroism in few-layer black phosphorus. *Nat. Commun.* **5**, 4475 (2014). doi: 10.1038/ncomms5475; pmid: 25042376
39. R. Fei *et al*., Enhanced thermoelectric efficiency via orthogonal electrical and thermal conductances in phosphorene. *Nano Lett.* **14**, 6393–6399 (2014). doi: 10.1021/nl502865s; pmid: 25254626
40. L. C. Gomes, A. Carvalho, Phosphorene analogues: Isoelectronic two-dimensional group-IV monochalcogenides with orthorhombic structure. *Phys. Rev. B* **92**, 085406 (2015). doi: 10.1103/PhysRevB.92.085406
41. L. C. Gomes, A. Carvalho, A. H. Castro Neto, Enhanced piezoelectricity and modified dielectric screening of two-dimensional group-IV monochalcogenides. *Phys. Rev. B* **92**, 214103 (2015). doi: 10.1103/PhysRevB.92.214103
42. V. Zólyomi, N. D. Drummond, V. I. Fal'ko, Band structure and optical transitions in atomic layers of hexagonal gallium chalcogenides. *Phys. Rev. B* **87**, 195403 (2013). doi: 10.1103/PhysRevB.87.195403
43. V. Zólyomi, N. D. Drummond, V. I. Fal'ko, Electrons and phonons in single layers of hexagonal indium chalcogenides from ab initio calculations. *Phys. Rev. B* **89**, 205416 (2014). doi: 10.1103/PhysRevB.89.205416
44. D. J. Late *et al*., GaS and GaSe ultrathin layer transistors. *Adv. Mater.* **24**, 3549–3554 (2012). doi: 10.1002/adma.201201361; pmid: 22678832
45. P. Hu, Z. Wen, L. Wang, P. Tan, K. Xiao, Synthesis of few-layer GaSe nanosheets for high performance photodetectors. *ACS Nano* **6**, 5988–5994 (2012). doi: 10.1021/nn300889c; pmid: 22676041
46. S. Wu *et al*., http://arxiv.org/abs/1409.4733 (2014).
47. C. R. Dean *et al*., Boron nitride substrates for high-quality graphene electronics. *Nat. Nanotechnol.* **5**, 722–726 (2010). doi: 10.1038/nnano.2010.172; pmid: 20729834
48. W. Yang *et al*., Epitaxial growth of single-domain graphene on hexagonal boron nitride. *Nat. Mater.* **12**, 792–797 (2013). doi: 10.1038/nmat3695; pmid: 23852399
49. R. J. Cava *et al*., Superconductivity near 70 K in a new family of layered copper oxides. *Nature* **336**, 211–214 (1988). doi: 10.1038/336211a0
50. K. Takada *et al*., Superconductivity in two-dimensional CoO_2 layers. *Nature* **422**, 53–55 (2003). doi: 10.1038/nature01450; pmid: 12621429
51. A. Ziletti *et al*., Phosphorene oxides: Bandgap engineering of phosphorene by oxidation. *Phys. Rev. B* **91**, 085407 (2015). doi: 10.1103/PhysRevB.91.085407
52. J. Lu *et al*., Bandgap engineering of phosphorene by laser oxidation toward functional 2D materials. *ACS Nano* **9**, 10411–10421 (2015). doi: 10.1021/acsnano.5b04623; pmid: 26364647
53. M. A. Green, A. Ho-Baillie, H. J. Snaith, The emergence of perovskite solar cells. *Nat. Photonics* **8**, 506–514 (2014). doi: 10.1038/nphoton.2014.134
54. A. K. Geim, I. V. Grigorieva, van der Waals heterostructures. *Nature* **499**, 419–425 (2013). doi: 10.1038/nature12385; pmid: 23887427
55. S. J. Haigh *et al*., Cross-sectional imaging of individual layers and buried interfaces of graphene-based heterostructures and superlattices. *Nat. Mater.* **11**, 764–767 (2012). doi: 10.1038/nmat3386; pmid: 22842512
56. L. Wang *et al*., One-dimensional electrical contact to a two-dimensional material. *Science* **342**, 614–617 (2013). doi: 10.1126/science.1244358; pmid: 24179223
57. A. V. Kretinin *et al*., Electronic properties of graphene encapsulated with different two-dimensional atomic crystals. *Nano Lett.* **14**, 3270–3276 (2014). doi: 10.1021/nl5006542; pmid: 24844319
58. G. Giovannetti, P. A. Khomyakov, G. Brocks, P. J. Kelly, J. van den Brink, Substrate-induced band gap in graphene on hexagonal boron nitride: Ab initio density functional calculations. *Phys. Rev. B* **76**, 073103 (2007). doi: 10.1103/PhysRevB.76.073103
59. J. Kang, J. Li, S. S. Li, J. B. Xia, L. W. Wang, Electronic structural Moiré pattern effects on MoS_2/$MoSe_2$ 2D heterostructures. *Nano Lett.* **13**, 5485–5490 (2013). doi: 10.1021/nl4030648; pmid: 24079953
60. S. Tongay *et al*., Tuning interlayer coupling in large-area heterostructures with CVD-grown MoS_2 and WS_2 monolayers. *Nano Lett.* **14**, 3185–3190 (2014). doi: 10.1021/nl500515q; pmid: 24845201
61. L. F. Wang *et al*., Superlubricity of two-dimensional fluorographene/MoS_2 heterostructure: A first-principles study. *Nanotechnology* **25**, 385701 (2014). doi: 10.1088/0957-4484/25/38/385701; pmid: 25180979
62. H. Terrones, F. López-Urías, M. Terrones, Novel hetero-layered materials with tunable direct band gaps by sandwiching different metal disulfides and diselenides. *Sci. Rep.* **3**, 1549 (2013). doi: 10.1038/srep01549; pmid: 23528957
63. C. H. Lui *et al*., Observation of interlayer phonon modes in van der Waals heterostructures. *Phys. Rev. B* **91**, 165403 (2015). doi: 10.1103/PhysRevB.91.165403
64. L. Y. Li, M. W. Zhao, Structures, energetics, and electronic properties of multifarious stacking patterns for high-buckled and low-buckled silicene on the MoS_2 substrate. *J. Phys. Chem. C* **118**, 19129–19138 (2014). doi: 10.1021/jp5043359
65. J. R. Wallbank, A. A. Patel, M. Mucha-Kruczynski, A. K. Geim, V. I. Falko, Generic miniband structure of graphene on a hexagonal substrate. *Phys. Rev. B* **87**, 245408 (2013). doi: 10.1103/PhysRevB.87.245408
66. G. L. Yu *et al*., Interaction phenomena in graphene seen through quantum capacitance. *Proc. Natl. Acad. Sci. U.S.A.* **110**, 3282–3286 (2013). doi: 10.1073/pnas.1300599110; pmid: 23401538
67. M. Kuiri *et al*., Probing 2D black phosphorus by quantum capacitance measurements. *Nanotechnology* **26**, 485704 (2015). doi: 10.1088/0957-4484/26/48/485704; pmid: 26559656
68. R. V. Gorbachev *et al*., Strong Coulomb drag and broken symmetry in double-layer graphene. *Nat. Phys.* **8**, 896–901 (2012). doi: 10.1038/nphys2441
69. G. H. Lee *et al*., Electron tunneling through atomically flat and ultrathin hexagonal boron nitride. *Appl. Phys. Lett.* **99**, 243114 (2011). doi: 10.1063/1.3662043
70. L. Britnell *et al*., Field-effect tunneling transistor based on vertical graphene heterostructures. *Science* **335**, 947–950 (2012). doi: 10.1126/science.1218461; pmid: 22300848
71. F. Amet *et al*., Tunneling spectroscopy of graphene-boron-nitride heterostructures. *Phys. Rev. B* **85**, 073405 (2012). doi: 10.1103/PhysRevB.85.073405
72. A. Mishchenko *et al*., Twist-controlled resonant tunnelling in graphene/boron nitride/graphene heterostructures. *Nat. Nanotechnol.* **9**, 808–813 (2014). doi: 10.1038/nnano.2014.187; pmid: 25194946
73. T. Georgiou *et al*., Vertical field-effect transistor based on graphene-WS_2 heterostructures for flexible and transparent electronics. *Nat. Nanotechnol.* **8**, 100–103 (2013). doi: 10.1038/nnano.2012.224; pmid: 23263726
74. M. S. Choi *et al*., Controlled charge trapping by molybdenum disulphide and graphene in ultrathin heterostructured memory devices. *Nat. Commun.* **4**, 1624 (2013). doi: 10.1038/ncomms2652; pmid: 23535645
75. H. Yang *et al*., Graphene barristor, a triode device with a gate-controlled Schottky barrier. *Science* **336**, 1140–1143 (2012). doi: 10.1126/science.1220527; pmid: 22604723
76. Y.-C. Lin *et al*., Atomically thin resonant tunnel diodes built from synthetic van der Waals heterostructures. *Nat. Commun.* **6**, 7311 (2015). doi: 10.1038/ncomms8311; pmid: 26088295
77. F. Bonaccorso, Z. Sun, T. Hasan, A. C. Ferrari, Graphene photonics and optoelectronics. *Nat. Photonics* **4**, 611–622 (2010). doi: 10.1038/nphoton.2010.186
78. Q. H. Wang, K. Kalantar-Zadeh, A. Kis, J. N. Coleman, M. S. Strano, Electronics and optoelectronics of two-dimensional transition metal dichalcogenides. *Nat. Nanotechnol.* **7**, 699–712 (2012). doi: 10.1038/nnano.2012.193; pmid: 23132225
79. P. Hu *et al*., Highly responsive ultrathin GaS nanosheet photodetectors on rigid and flexible substrates. *Nano Lett.* **13**, 1649–1654 (2013). doi: 10.1021/nl400107k; pmid: 23465066
80. S. R. Tamalampudi *et al*., High performance and bendable few-layered InSe photodetectors with broad spectral response. *Nano Lett.* **14**, 2800–2806 (2014). doi: 10.1021/nl500817g; pmid: 24742243
81. M. Buscema *et al*., Fast and broadband photoresponse of few-layer black phosphorus field-effect transistors. *Nano Lett.* **14**, 3347–3352 (2014). doi: 10.1021/nl5008085; pmid: 24821381
82. F. N. Xia, H. Wang, D. Xiao, M. Dubey, A. Ramasubramaniam, Two-dimensional material nanophotonics. *Nat. Photonics* **8**, 899–907 (2014). doi: 10.1038/nphoton.2014.271
83. F. H. L. Koppens *et al*., Photodetectors based on graphene, other two-dimensional materials and hybrid systems. *Nat. Nanotechnol.* **9**, 780–793 (2014). doi: 10.1038/nnano.2014.215; pmid: 25286273
84. B. W. H. Baugher, H. O. H. Churchill, Y. Yang, P. Jarillo-Herrero, Optoelectronic devices based on electrically tunable p-n diodes in a monolayer dichalcogenide. *Nat. Nanotechnol.* **9**, 262–267 (2014). doi: 10.1038/nnano.2014.25; pmid: 24608231
85. K. Roy *et al*., Graphene-MoS_2 hybrid structures for multifunctional photoresponsive memory devices. *Nat. Nanotechnol.* **8**, 826–830 (2013). doi: 10.1038/nnano.2013.206; pmid: 24141541
86. H. Fang *et al*., Strong interlayer coupling in van der Waals heterostructures built from single-layer chalcogenides. *Proc. Natl. Acad. Sci. U.S.A.* **111**, 6198–6202 (2014). doi: 10.1073/pnas.1405435111; pmid: 24733906
87. P. Rivera *et al*., Observation of long-lived interlayer excitons in monolayer $MoSe_2$-WSe_2 heterostructures. *Nat. Commun.* **6**, 6242 (2015). doi: 10.1038/ncomms7242; pmid: 25708612
88. F. Wang *et al*., Tunable GaTe-MoS_2 van der Waals p-n Junctions with novel optoelectronic performance. *Nano Lett.* **15**, 7558–7566 (2015). doi: 10.1021/acs.nanolett.5b03291; pmid: 26469092
89. R. Cheng *et al*., Electroluminescence and photocurrent generation from atomically sharp WSe_2/MoS_2 heterojunction p-n diodes. *Nano Lett.* **14**, 5590–5597 (2014). doi: 10.1021/nl502075n; pmid: 25157588
90. Y. Deng *et al*., Black phosphorus-monolayer MoS_2 van der Waals heterojunction p-n diode. *ACS Nano* **8**, 8292–8299 (2014). doi: 10.1021/nn5027388; pmid: 25019534
91. L. Britnell *et al*., Strong light-matter interactions in heterostructures of atomically thin films. *Science* **340**, 1311–1314 (2013). doi: 10.1126/science.1235547; pmid: 23641062
92. G. W. Mudd *et al*., High broad-band photoresponsivity of mechanically formed InSe-graphene van der Waals heterostructures. *Adv. Mater.* **27**, 3760–3766 (2015). doi: 10.1002/adma.201500889; pmid: 25981798
93. F. Withers *et al*., Light-emitting diodes by band-structure engineering in van der Waals heterostructures. *Nat. Mater.* **14**, 301–306 (2015). doi: 10.1038/nmat4205; pmid: 25643033
94. F. Withers *et al*., WSe_2 light-emitting tunneling transistors with enhanced brightness at room temperature. *Nano Lett.* **15**, 8223–8228 (2015). doi: 10.1021/acs.nanolett.5b03740; pmid: 26555037
95. A. N. Grigorenko, M. Polini, K. S. Novoselov, Graphene plasmonics. *Nat. Photonics* **6**, 749–758 (2012). doi: 10.1038/nphoton.2012.262
96. S. Dai *et al*., Tunable phonon polaritons in atomically thin van der Waals crystals of boron nitride. *Science* **343**, 1125–1129 (2014). doi: 10.1126/science.1246833; pmid: 24604197
97. A. Woessner *et al*., Highly confined low-loss plasmons in graphene-boron nitride heterostructures. *Nat. Mater.* **14**, 421–425 (2015). doi: 10.1038/nmat4169; pmid: 25532073
98. K. Zhang *et al*., Large scale graphene/hexagonal boron nitride heterostructure for tunable plasmonics. *Adv. Funct. Mater.* **24**, 731–738 (2014). doi: 10.1002/adfm.201302009
99. S. Dai *et al*., Graphene on hexagonal boron nitride as a tunable hyperbolic metamaterial. *Nat. Nanotechnol.* **10**, 682–686 (2015). doi: 10.1038/nnano.2015.131; pmid: 26098228
100. V. W. Brar *et al*., Hybrid surface-phonon-plasmon polariton modes in graphene/monolayer h-BN heterostructures. *Nano Lett.* **14**, 3876–3880 (2014). doi: 10.1021/nl501096s; pmid: 24874205
101. A. Tomadin, F. Guinea, M. Polini, Generation and morphing of plasmons in graphene superlattices. *Phys. Rev. B* **90**, 161406 (2014). doi: 10.1103/PhysRevB.90.161406
102. J. N. Coleman *et al*., Two-dimensional nanosheets produced by liquid exfoliation of layered materials. *Science* **331**, 568–571 (2011). doi: 10.1126/science.1194975; pmid: 21292974
103. F. Torrisi *et al*., Inkjet-printed graphene electronics. *ACS Nano* **6**, 2992–3006 (2012). doi: 10.1021/nn2044609; pmid: 22449258

Downloaded from http://science.sciencemag.org/ on July 28, 2016

104. E. B. Secor, M. C. Hersam, Emerging carbon and post-carbon nanomaterial inks for printed electronics. *J. Phys. Chem. Lett.* **6**, 620–626 (2015). doi: 10.1021/jz502431r; pmid: 26262476
105. D. J. Finn *et al*., Inkjet deposition of liquid-exfoliated graphene and MoS_2 nanosheets for printed device applications. *J. Mater. Chem. C* **2**, 925–932 (2014). doi: 10.1039/C3TC31993H
106. F. Withers *et al*., Heterostructures produced from nanosheet-based inks. *Nano Lett.* **14**, 3987–3992 (2014). doi: 10.1021/nl501355j; pmid: 24871927
107. J. Zhu *et al*., Solution-processed dielectrics based on thickness-sorted two-dimensional hexagonal boron nitride nanosheets. *Nano Lett.* **15**, 7029–7036 (2015). doi: 10.1021/acs.nanolett.5b03075; pmid: 26348822
108. X. Cai *et al*., Tuning the surface charge of 2D oxide nanosheets and the bulk-scale production of superlatticelike composites. *J. Am. Chem. Soc.* **137**, 2844–2847 (2015). doi: 10.1021/jacs.5b00317; pmid: 25686203
109. L. Ma *et al*., Ultrathin few-layered molybdenum selenide/graphene hybrid with superior electrochemical Li-storage performance. *J. Power Sources* **285**, 274–280 (2015). doi: 10.1016/j.jpowsour.2015.03.120
110. D. Deng *et al*., Catalysis with two-dimensional materials and their heterostructures. *Nat. Nanotechnol.* **11**, 218–230 (2016). doi: 10.1038/nnano.2015.340; pmid: 26936816
111. J. A. Robinson, Growing vertical in the flatland. *ACS Nano* **10**, 42–45 (2016). doi: 10.1021/acsnano.5b08117; pmid: 26762232
112. Z. Liu *et al*., Direct growth of graphene/hexagonal boron nitride stacked layers. *Nano Lett.* **11**, 2032–2037 (2011). doi: 10.1021/nl200464j; pmid: 21488689
113. W. Gannett *et al*., Boron nitride substrates for high mobility chemical vapor deposited graphene. *Appl. Phys. Lett.* **98**, 242105 (2011). doi: 10.1063/1.3599708
114. Z. G. Xu, R. J. Zheng, A. Khanaki, Z. Zuo, J. L. Liu, Direct growth of graphene on in situ epitaxial hexagonal boron nitride flakes by plasma-assisted molecular beam epitaxy. *Appl. Phys. Lett.* **107**, 213103 (2015). doi: 10.1063/1.4936378
115. C. Zhang *et al*., Direct growth of large-area graphene and boron nitride heterostructures by a co-segregation method. *Nat. Commun.* **6**, 6519 (2015). doi: 10.1038/ncomms7519; pmid: 25735443
116. Q. Wu *et al*., In situ synthesis of a large area boron nitride/graphene monolayer/boron nitride film by chemical vapor deposition. *Nanoscale* **7**, 7574–7579 (2015). doi: 10.1039/C5NR00889A; pmid: 25864409
117. J. A. Miwa *et al*., van der Waals epitaxy of two-dimensional MoS_2-graphene heterostructures in ultrahigh vacuum. *ACS Nano* **9**, 6502–6510 (2015). doi: 10.1021/acsnano.5b02345; pmid: 26039108
118. Y. Shi *et al*., van der Waals epitaxy of MoS_2 layers using graphene as growth templates. *Nano Lett.* **12**, 2784–2791 (2012). doi: 10.1021/nl204562j; pmid: 22642717
119. Y. C. Lin *et al*., Direct synthesis of van der Waals solids. *ACS Nano* **8**, 3715–3723 (2014). doi: 10.1021/nn5003858; pmid: 24641706
120. L. Yu *et al*., Graphene/MoS_2 hybrid technology for large-scale two-dimensional electronics. *Nano Lett.* **14**, 3055–3063 (2014). doi: 10.1021/nl404795z; pmid: 24810658
121. X. Li *et al*., van der Waals epitaxial growth of two-dimensional single-crystalline GaSe domains on graphene. *ACS Nano* **9**, 8078–8088 (2015). doi: 10.1021/acsnano.5b01943; pmid: 26202730
122. A. Yan *et al*., Direct growth of single- and few-layer MoS_2 on h-BN with preferred relative rotation angles. *Nano Lett.* **15**, 6324–6331 (2015). doi: 10.1021/acs.nanolett.5b01311; pmid: 26317240
123. S. Wang, X. Wang, J. H. Warner, All chemical vapor deposition growth of MoS_2:h-BN vertical van der Waals heterostructures. *ACS Nano* **9**, 5246–5254 (2015). doi: 10.1021/acsnano.5b00655; pmid: 25895108
124. M. Cattelan *et al*., New strategy for the growth of complex heterostructures based on different 2D materials. *Chem. Mater.* **27**, 4105–4113 (2015). doi: 10.1021/acs.chemmater.5b01170
125. H. C. Diaz, R. Chaghi, Y. J. Ma, M. Batzill, Molecular beam epitaxy of the van der Waals heterostructure $MoTe_2$ on MoS_2: Phase, thermal, and chemical stability. *2D Mater.* **2**, 044010 (2015). doi: 10.1088/2053-1583/2/4/044010
126. Y. Gong *et al*., Vertical and in-plane heterostructures from WS_2/MoS_2 monolayers. *Nat. Mater.* **13**, 1135–1142 (2014). doi: 10.1038/nmat4091; pmid: 25262094
127. M. B. Alemayehu *et al*., Designed synthesis of van der Waals heterostructures: The power of kinetic control. *Angew. Chem. Int. Ed.* **54**, 15468–15472 (2015). doi: 10.1002/anie.201506152
128. E. Xenogiannopoulou *et al*., High-quality, large-area $MoSe_2$ and $MoSe_2$/$Bi2Se_3$ heterostructures on AlN(0001)/Si(111) substrates by molecular beam epitaxy. *Nanoscale* **7**, 7896–7905 (2015). doi: 10.1039/C4NR06874B; pmid: 25856730
129. K. E. Aretouli *et al*., Two-dimensional semiconductor $HfSe_2$ and $MoSe_2$/$HfSe_2$ van der Waals heterostructures by molecular beam epitaxy. *Appl. Phys. Lett.* **106**, 143105 (2015). doi: 10.1063/1.4917422
130. A. Koma, K. Sunouchi, T. Miyajima, Fabrication of ultrathin heterostructures with van der Waals epitaxy. *J. Vac. Sci. Technol. B* **3**, 724 (1985). doi: 10.1116/1.583125
131. F. S. Ohuchi, B. A. Parkinson, K. Ueno, A. Koma, van der Waals epitaxial growth and characterization of $MoSe_2$ thin films on SnS_2. *J. Appl. Phys.* **68**, 2168–2175 (1990). doi: 10.1063/1.346574
132. K. Ueno, K. Saiki, T. Shimada, A. Koma, Epitaxial growth of transition metal dichalcogenides on cleaved faces of mica. *J. Vac. Sci. Technol. A* **8**, 68–72 (1990). doi: 10.1116/1.576983
133. Y. C. Lin *et al*., Atomically thin heterostructures based on single-layer tungsten diselenide and graphene. *Nano Lett.* **14**, 6936–6941 (2014). doi: 10.1021/nl503144a; pmid: 25383798
134. X. Liu *et al*., Rotationally commensurate growth of MoS_2 on epitaxial graphene. *ACS Nano* **10**, 1067–1075 (2016). doi: 10.1021/acsnano.5b06398; pmid: 26565112
135. A. Azizi *et al*., Freestanding van der Waals heterostructures of graphene and transition metal dichalcogenides. *ACS Nano* **9**, 4882–4890 (2015). doi: 10.1021/acsnano.5b01677; pmid: 25885122
136. M. P. Levendorf *et al*., Graphene and boron nitride lateral heterostructures for atomically thin circuitry. *Nature* **488**, 627–632 (2012). doi: 10.1038/nature11408; pmid: 22932386
137. C. Huang *et al*., Lateral heterojunctions within monolayer $MoSe_2$-WSe_2 semiconductors. *Nat. Mater.* **13**, 1096–1101 (2014). doi: 10.1038/nmat4064; pmid: 25150560
138. M. Y. Li *et al*., Epitaxial growth of a monolayer WSe_2-MoS_2 lateral p-n junction with an atomically sharp interface. *Science* **349**, 524–528 (2015). doi: 10.1126/science.aab4097; pmid: 26228146
139. X. Q. Zhang, C. H. Lin, Y. W. Tseng, K. H. Huang, Y. H. Lee, Synthesis of lateral heterostructures of semiconducting atomic layers. *Nano Lett.* **15**, 410–415 (2015). doi: 10.1021/nl503744f; pmid: 25494614

ACKNOWLEDGMENTS

This work was supported by the European Union FP7 Graphene Flagship Project 604391, European Research Council Synergy Grant, Hetero2D, Engineering and Physical Sciences Research Council (EPSRC) (Toward Engineering Grand Challenges), the Royal Society, U.S. Army Research Office, U.S. Navy Research Office, and U.S. Airforce Research Office. A.M. acknowledges support of EPSRC Early Career Fellowship EP/N007131/1. A.H.C.N. and A.C. acknowledge the National Research Foundation of Singapore under the Prime Minister's Office for Financial support under the Mid Size Centre Grant. We thank A. K. Geim, I. V. Grigorieva, V. I. Fal'ko, R. V. Gorbachev, F. Withers, A. V. Kretinin, C. Gesner, and S. J. Haigh.

10.1126/science.aac9439

Downloaded from http://science.sciencemag.org/ on July 28, 2016



2D materials and van der Waals heterostructures
K. S. Novoselov, A. Mishchenko, A. Carvalho and A. H. Castro Neto (July 28, 2016)
Science **353** (6298), . [doi: 10.1126/science.aac9439]

Editor's Summary

This copy is for your personal, non-commercial use only.

Article Tools Visit the online version of this article to access the personalization and article tools:
http://science.sciencemag.org/content/353/6298/aac9439

Permissions Obtain information about reproducing this article:
http://www.sciencemag.org/about/permissions.dtl

Science (print ISSN 0036-8075; online ISSN 1095-9203) is published weekly, except the last week in December, by the American Association for the Advancement of Science, 1200 New York Avenue NW, Washington, DC 20005. Copyright 2016 by the American Association for the Advancement of Science; all rights reserved. The title *Science* is a registered trademark of AAAS.

Downloaded from http://science.sciencemag.org/ on July 28, 2016

RESEARCH ARTICLE SUMMARY

CELL LINEAGE TRACING

Whole-organism lineage tracing by combinatorial and cumulative genome editing

Aaron McKenna,* Gregory M. Findlay,* James A. Gagnon,* Marshall S. Horwitz, Alexander F. Schier,† Jay Shendure†

INTRODUCTION: The developmental path by which a fertilized egg gives rise to the cells of a multicellular organism is termed the cell lineage. In 1983, John Sulston and colleagues documented the invariant cell lineage of the roundworm *Caenorhabditis elegans* as determined by visual observation. However, tracing cell lineage in nearly all other multicellular organisms is vastly more challenging. Contemporary methods rely on genetic markers or somatic mutations, but these approaches have limitations that preclude their application at the level of a whole, complex organism.

RATIONALE: For a technology to comprehensively trace cell lineages in a complex multicellular system, it must uniquely and incrementally mark cells and their descendants over many divisions and in a way that does not interfere with normal development. These unique marks must also accumulate irreversibly over time, allowing the reconstruction of lineage trees. Finally, the full set of marks must be read out from each of many single cells. We hypothesized that genome editing, which introduces diverse, irreversible edits in a highly programmable fashion, could be repurposed for cell lineage tracing in a way that realizes these characteristics.

To this end, we developed a method termed genome editing of synthetic target arrays for lineage tracing (GESTALT). This method uses genome editing to generate a combinatorial diversity of mutations that accumulate over many cell divisions within a compact DNA barcode consisting of multiple clustered regularly interspaced short palindromic repeats (CRISPR)/Cas9 target sites. Lineage relationships can be readily queried by sequencing the edited barcodes and relating the patterns of edits observed.

RESULTS: We first developed this approach in cell culture, editing synthetic arrays of 9 to 12 CRISPR/Cas9 target sites to generate thousands of unique derivative barcodes. We show that edited barcodes can be read by targeted sequencing of either DNA or RNA. In addition, the rates and patterns of barcode editing are tunable and the diverse edits accumulate over successive divisions in a way that is informative of cell lineage.

We then applied GESTALT to the zebrafish *Danio rerio* by injecting fertilized eggs with editing reagents that target a genomic barcode bearing 10 target sites. Across dozens of embryos, we demonstrate the accumulation of hundreds to thousands of uniquely edited barcodes per animal, from which lineage relationships can be inferred on the basis of shared mutations. In adult zebrafish, we evaluated the edited barcodes from ~200,000 cells and observed that the majority of cells in each organ are derived from a small number of progenitor cells. Furthermore, ancestral progenitors, inferred on the basis of shared mutations among subsets of cells, can contribute to different germ layers and organ systems.

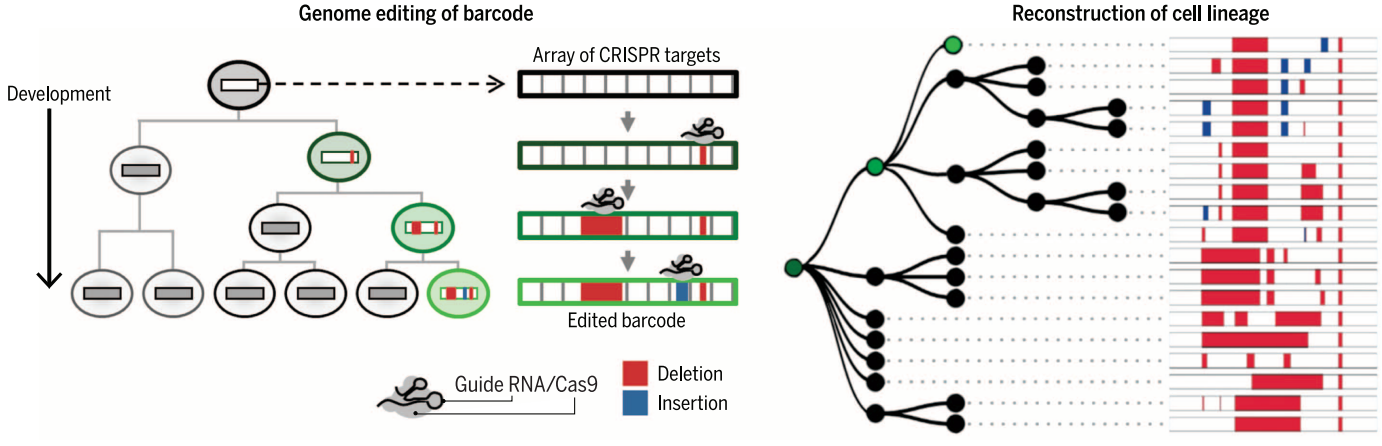
CONCLUSION: Our proof-of-principle experiments show that combinatorial, cumulative genome editing of a compact barcode can be used to record lineage information in multicellular systems. Further optimization of GESTALT will enable mapping of the complete cell lineage in diverse organisms. This method could also be adapted to link cell lineage information to molecular profiles of the same cells. In the long term, we envision that rich, systematically generated maps of organismal development—wherein lineage, epigenetic, transcriptional, and positional information are concurrently captured at single-cell resolution—will advance our understanding of development in both healthy and disease states. More broadly, cumulative and combinatorial genome editing could stably record other types of biological information and history in living cells. ■

ON OUR WEBSITE

Read the full article at http://dx.doi.org/10.1126/science.aaf7907

The list of author affiliations is available in the full article online.
*These authors contributed equally to this work.
†Corresponding author. Email: shendure@uw.edu (J.S.); schier@fas.harvard.edu (A.F.S.)
Cite this article as A. McKenna *et al.*, *Science* **353**, aaf7907 (2016). DOI: 10.1126/science.aaf7907

GESTALT. (**Left**) A barcode of CRISPR/Cas9 target sites is progressively edited over many cell divisions. (**Right**) Edited barcode sequences are related to one another on the basis of shared mutations in order to reconstruct lineage trees.



Downloaded from http://science.sciencemag.org/ on July 28, 2016

RESEARCH ARTICLE

CELL LINEAGE TRACING

Whole-organism lineage tracing by combinatorial and cumulative genome editing

Aaron McKenna,[1]* Gregory M. Findlay,[1]* James A. Gagnon,[2]* Marshall S. Horwitz,[1,3] Alexander F. Schier,[2,4,5,6]† Jay Shendure[1,7]†

Multicellular systems develop from single cells through distinct lineages. However, current lineage-tracing approaches scale poorly to whole, complex organisms. Here, we use genome editing to progressively introduce and accumulate diverse mutations in a DNA barcode over multiple rounds of cell division. The barcode, an array of clustered regularly interspaced short palindromic repeats (CRISPR)/Cas9 target sites, marks cells and enables the elucidation of lineage relationships via the patterns of mutations shared between cells. In cell culture and zebrafish, we show that rates and patterns of editing are tunable and that thousands of lineage-informative barcode alleles can be generated. By sampling hundreds of thousands of cells from individual zebrafish, we find that most cells in adult organs derive from relatively few embryonic progenitors. In future analyses, genome editing of synthetic target arrays for lineage tracing (GESTALT) can be used to generate large-scale maps of cell lineage in multicellular systems for normal development and disease.

The tracing of cell lineages was pioneered in nematodes by Whitman in the 1870s, at a time of controversy surrounding Haeckel's theory of recapitulation, which argued that embryological development paralleled evolutionary history (*1*). This line of work culminated a century later in the complete description of mitotic divisions in the roundworm *Caenorhabditis elegans*—a tour de force facilitated by its visual transparency as well as the modest size and invariant nature of this nematode's cell lineage (*2*).

Over the past century, a variety of creative methods have been developed for tracing cell lineage in developmentally complex organisms (*3*). In general, subsets of cells are marked and their descendants followed as development progresses. The ways in which cell marking has been achieved include dyes and enzymes (*4*–*6*), cross-species transplantation (*7*), recombinase-mediated activation of reporter gene expression (*8*, *9*), insertion of foreign DNA (*10*–*12*), and naturally occurring somatic mutations (*13*–*15*). However, despite many powerful applications, these methods have limitations for the large-scale reconstruction of cell lineages in multicellular systems. For example, dye and reporter gene–based cell marking are uninformative with respect to the lineage relationships between descendant cells. Furthermore, when two or more cells are independently but equivalently marked, the resulting multitude of clades cannot be readily distinguished from one another. Although these limitations can be overcome in part with combinatorial labeling systems (*16*, *17*) or through the introduction of diverse DNA barcodes (*10*–*12*), these strategies fall short of a system for inferring lineage relationships throughout an organism and across developmental time. In contrast, methods based on somatic mutations have this potential, as they can identify lineages and sublineages within single organisms (*13*, *18*). However, somatic mutations are distributed throughout the genome, necessitating whole-genome sequencing (*14*, *15*), which is expensive to scale beyond small numbers of cells and not readily compatible with in situ readouts (*19*, *20*).

What are the requirements for a system for comprehensively tracing cell lineages in a complex multicellular system? First, it must uniquely and incrementally mark cells and their descendants over many divisions and in a way that does not interfere with normal development. Second, these unique marks must accumulate irreversibly over time, allowing the reconstruction of lineage trees. Finally, the full set of marks must be easily read out in each of many single cells.

We hypothesized that genome editing, which introduces diverse, irreversible edits in a highly programmable fashion (*21*), could be repurposed for cell lineage tracing in a way that realizes these requirements. To this end, we developed genome editing of synthetic target arrays for lineage tracing (GESTALT), a method that uses clustered regularly interspaced short palindromic repeats (CRISPR)/Cas9 genome editing to accumulate combinatorial sequence diversity to a compact, multitarget, densely informative barcode. Edited barcodes can be efficiently queried by a single sequencing read from each of many single cells (Fig. 1A). In both cell culture and in the zebrafish *Danio rerio*, we demonstrate the generation of thousands of uniquely edited barcodes that can be related to one another to reconstruct cell lineage relationships. In adult zebrafish, we observe that the majority of cells of each organ are derived from a small number of progenitor cells. Furthermore, ancestral progenitors, inferred on the basis of shared edits among subsets of derived alleles, make highly nonuniform contributions to germ layers and organ systems.

Results

Combinatorial and cumulative editing of a compact genomic barcode in cultured cells

To investigate whether genome editing can be used to generate a combinatorial diversity of mutations within a compact region, we synthesized a contiguous array of 10 CRISPR/Cas9 targets separated by three base-pair (bp) linkers (total length of 257 bp). The first target perfectly matched one single-guide RNA (sgRNA), whereas the remainder were off-target sites for the same sgRNA, ordered from highest to lowest activity (*22*). This array of targets (v1 barcode) was cloned downstream of an enhanced green fluorescent protein (EGFP) reporter in a lentiviral construct (*23*). We then transduced human embryonic kidney (HEK) 293T cells with lentivirus and used fluorescence-activated cell sorting (FACS) to purify an EGFP-v1–positive population. To edit the barcode, we cotransfected these cells with a plasmid expressing Cas9 and the sgRNA and a vector expressing Discosoma red fluorescent protein (DsRed). Cells were sorted 3 days after transfection for high DsRed expression, and genomic DNA (gDNA) was harvested on day 7. The v1 barcode was polymerase chain reaction (PCR) amplified, and the resulting amplicons were subjected to deep sequencing.

To minimize confounding sequencing errors, which are primarily substitutions, we analyzed edited barcodes for only insertion-deletion changes relative to the wild-type v1 barcode. In this first experiment, we observed 1650 uniquely edited barcodes (each observed in ≥25 reads), with diverse edits concentrated at the expected Cas9 cleavage sites, predominantly intertarget deletions involving sites 1, 3, and 5 or focal edits of sites 1 and 3 (Fig. 1, B and C, and table S1). These results show that combinatorial editing of the barcode can give rise to a large number of unique sequences, i.e., alleles.

To evaluate reproducibility, we transfected the same editing reagents to cultures expanded from three independent EGFP-v1–positive clones. Targeted reverse transcription PCR (RT-PCR) and sequencing of EGFP-v1 RNA showed similar distributions of edits to the v1 barcode in the transcript pool, between replicates as well as in comparison to

[1]Department of Genome Sciences, University of Washington, Seattle, WA, USA. [2]Department of Molecular and Cellular Biology, Harvard University, Cambridge, MA, USA. [3]Department of Pathology, University of Washington, Seattle, WA, USA. [4]Center for Brain Science, Harvard University, Cambridge, MA, USA. [5]The Broad Institute of Harvard and MIT, Cambridge, MA, USA. [6]FAS Center for Systems Biology, Harvard University, Cambridge, MA, USA. [7]Howard Hughes Medical Institute, Seattle, WA, USA.
*These authors contributed equally to this work. †Corresponding author. Email: shendure@uw.edu (J.S.); schier@fas.harvard.edu (A.F.S.)

Downloaded from http://science.sciencemag.org/ on July 28, 2016

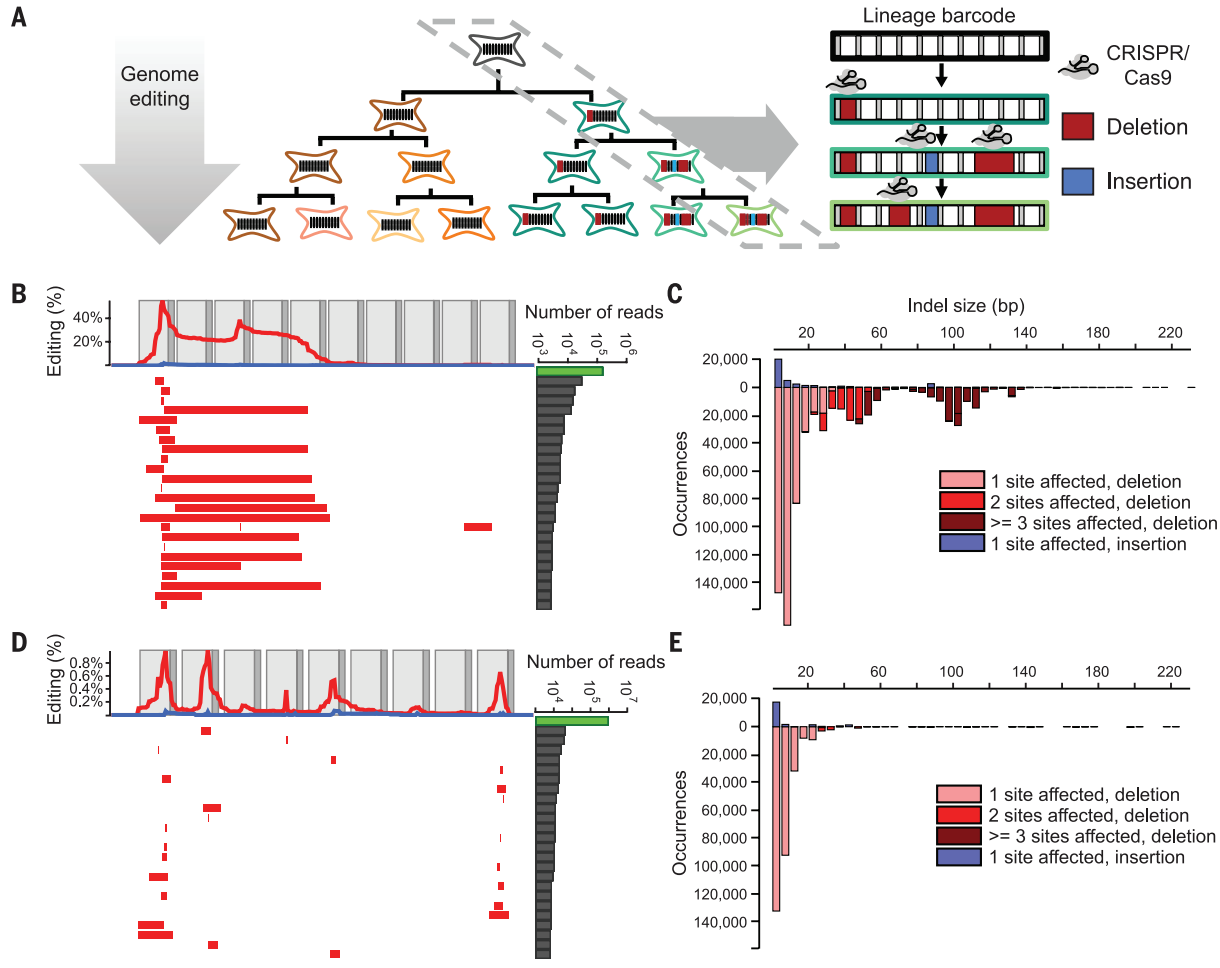


Fig. 1. GESTALT. (**A**) An unmodified array of CRISPR/Cas9 target sites (i.e., a barcode) is engineered into a genome (gray cell). Editing reagents are introduced during expansion of cell culture or in vivo development of an organism, resulting in a unique pattern of insertions and deletions (right) that are stably accumulated in specific lineages (green cell lineage). The lineage relationships of alleles that differ in sequence can often be inferred on the basis of these accumulated edits. (**B**) The 25 most frequent alleles from the edited v1 barcode are shown. Each row corresponds to a unique sequence, with red bars indicating deleted regions and blue bars indicating insertion positions. Blue bars begin at the insertion site, with their width proportional to the size of the insertion, which will rarely obscure immediately adjacent deletions. The number of reads observed for each allele is plotted at the right (log10 scale; the green bar corresponds to the unedited allele). The frequency at which each base is deleted (red) or flanks an insertion (blue) is plotted at the top. Light gray boxes indicate the location of CRISPR protospacers, and dark gray boxes indicate protospacer adjacent motif (PAM) sites. For the v1 array, intertarget deletions involving sites 1, 3, and 5 or focal (single target) edits of sites 1 and 3 were observed predominantly. (**C**) A histogram of the size distribution of insertion (top) and deletion (bottom) edits to the v1 array is shown. The colors indicate the number of target sites affected. Although most edits are short and affect a single target, a substantial proportion of edits are intertarget deletions. (**D**) We tested three array designs in addition to v1, each comprising 9 to 10 weaker off-target sites for the same sgRNA (v2 to v4) (*22*). Editing of the v2 array is shown with layout as described in (B). Editing of the v3 and v4 arrays is shown in fig. S3, A and B. The weaker sites within these alternative designs exhibit lower rates of editing than the v1 array but also a much lower proportion of intertarget deletions. (**E**) A histogram of the size distribution of insertion (top) and deletion (bottom) edits to the v2 array is shown. In contrast with the v1 array, almost all edits affect only a single target.

the previous experiment (fig. S1). These results show that the observed editing patterns are largely independent of the site of integration and that edited barcodes can be queried from either RNA or DNA.

To evaluate how editing outcomes vary as a function of Cas9 expression, we cotransfected EGFP-v1–positive cells with a plasmid expressing Cas9 and the sgRNA, as well as a DsRed vector, and after 4 days we sorted cells into low, medium, and high DsRed bins and harvested gDNA. Overall editing rates matched DsRed expression (frequency of non–wild-type barcodes: low DsRed = 40%; medium DsRed = 69%; high DsRed = 91%). The profile of edits observed remained similar, but there were fewer intertarget deletions in the lower DsRed bins (fig. S2). These results show that adjusting expression levels of editing reagents can be used to modify the rates and patterns of barcode editing.

We also synthesized and tested three barcodes (v2 to v4) with nine or ten weaker off-target sites for the same sgRNA as used for v1 (*22*). Genome editing resulted in derivative barcodes with substantially fewer edits than seen with the v1 barcode, but a much greater proportion of these edits were to a single target site—i.e., fewer intertarget deletions were observed (Fig. 1, D and E, and fig. S3, A and B). As only a few targets were substantially edited in designs v1 to v4, we combined the most highly active targets to a new, 12-target barcode (v5). This barcode exhibited more uniform usage of constituent targets, but with relative activities still ranging over two orders of magnitude (fig. S3C and table S1). These results illustrate the potential value of iterative barcode design.

To determine whether the means of editing reagent delivery influences patterns of barcode editing, we introduced a lentiviral vector expressing Cas9 and the same sgRNA to cells containing the v5 barcode (*24*). After 2 weeks of culturing a population

Downloaded from http://science.sciencemag.org/ on July 28, 2016

bottlenecked to 200 cells by FACS, we observed diverse barcode alleles, but with substantially fewer intertarget deletions than with episomal delivery of editing reagents (fig. S3D). This finding demonstrates that the allelic spectrum can also be modulated by the delivery mode of editing reagents.

Taken together, these results show that editing multiple target sites within a compact barcode can generate a combinatorial diversity of alleles, and also that these alleles can be read out by single sequencing reads derived from either DNA or RNA. Rates and patterns of barcode editing are tunable by using targets with different activities, and/or off-target sequences, by iteratively recombining targets to new barcode designs and by modulating the concentration and means of delivery of editing reagents.

Reconstruction of lineage relationships in cultured cells

To determine whether GESTALT could be used to reconstruct lineage relationships, we applied it to a designed lineage in cell culture (Fig. 2). A monoclonal population of EGFP-v1–positive cells was transfected with editing reagents to induce a first round of mutations in the v1 barcode. Clones derived from single cells were expanded, sampled, split, and retransfected with editing reagents to induce a second round of mutations of the v1 barcode. For each clonal population, two 100-cell samples of the re-edited populations were expanded and harvested for gDNA. In these experiments, we began incorporating unique molecular identifiers (UMIs) (10 bp) during amplification of barcodes by a single round of polymerase extension (fig. S4A). Each UMI tags the single barcode present within each single cell, thereby allowing for correction of subsequent PCR amplification bias and enabling each UMI-barcode combination to be interpreted as deriving from a single cell (*25*).

Seven of 12 clonal populations we isolated contained mutations in the v1 barcode that were unambiguously introduced during the first round of editing (Fig. 2A). Additional edits accumulated in re-edited cells but generally did not disrupt the early edits (Fig. 2B and fig. S5). We next sought to reconstruct the lineage relationships between all alleles observed in the experiment using a maximum parsimony approach (fig. S4B) (*26*). The resultant tree contained major clades that were defined by the early edits present in each lineage (Fig. 2C). Four clonal populations (nos. 3, 5, 7, and 8) were cleanly separated upon lineage reconstruction, with >99.7% of cells accurately placed into each lineage's major clade. Two lineages (nos. 1 and 6) were mixed because they shared identical mutations from the first round of editing. These most likely represent the recurrence of the same editing event across multiple lineages but could also have been daughter cells subsequent to a single, early editing event prior to isolating clones. Consequently, 99.9% of cells of these two lineages were assigned to a single clade (Fig. 2C, blue). One clonal population (no. 4) appears to have derived from two independent cells, one of which harbored an unedited barcode. Later editing of these barcodes confounded the assignment of this lineage on the tree. Overall, however, these results demonstrate that GESTALT can be used to capture and reconstruct cell lineage relationships in cultured cells.

Combinatorial and cumulative editing of a compact genomic barcode in zebrafish

To determine the potential of GESTALT for in vivo lineage tracing in a complex multicellular organism, we turned to the zebrafish *D. rerio*. We designed two new barcodes, v6 and v7, each with 10 sgRNA target sites that are absent from the zebrafish genome and predicted to be highly editable (see the supplementary materials). In contrast to v1 to v5, in which the target sites are variably editable by one sgRNA, the targets within v6 or v7 are designed to be edited by distinct sgRNAs. We generated transgenic zebrafish that harbor each barcode in the 3′ UTR of DsRed driven by the ubiquitin promoter (*27*, *28*) and a GFP marker that is expressed in the cardiomyocytes of the heart (fig. S6) (*29*). To evaluate whether diverse alleles could be generated by in vivo genome editing, we injected Cas9 and 10 different sgRNAs with perfect complementarity to the barcode target sites into single-cell v6 embryos (Fig. 3A). Editing of integrated barcodes had no noticeable effects on development (fig. S7). To characterize barcode editing in vivo, we extracted gDNA from a series of single 30-hours-post-fertilization (hpf) embryos, and UMI-tagged, amplified, and sequenced the v6 barcode. In control embryos ($Cas9^-$) (n = 2), all 4488 captured barcodes were unedited. In contrast, in edited embryos ($Cas9^+$) (n = 8), fewer than 1% of captured barcodes were unedited. We recovered barcodes from hundreds of cells per embryo (median 943; range 257 to 2832) and identified dozens to hundreds of alleles per embryo (median 225; range 86 to 1323). Within single embryos 41 ± 10% of alleles were observed recurrently, most likely reflecting alleles that were generated in a progenitor of two or more cells. Fewer than 0.01% of alleles were shared in pairwise comparisons of embryos, revealing the highly stochastic nature of editing in different embryos. These results demonstrate that GESTALT can generate very high allelic diversity in vivo.

Reconstruction of lineage relationships in embryos

To evaluate whether lineage relationships can be reconstructed using edited barcodes, we focused on the v6 embryo with the lowest rates of intertarget deletions and edited target sites (Fig. 3B; avg. 58% ± 27% of target sites no longer a perfect match to the unedited target, compared to 87% ± 21% for all other 30 hpf v6 embryos). Application of our parsimony approach (fig. S4B) to the 1,961 cells in which we observed 1,323 distinct alleles generated the large tree shown in Fig. 4. 1,307 of the 1,323 (98%) alleles could be related to at least one other allele by one or more shared edits, 85% by two or more shared edits, and 56% by three or more shared edits. These results illustrate the principle of using patterns of shared edits between distinct barcode alleles to reconstruct their lineage relationships in vivo.

Developmental timing of barcode editing

To determine the developmental timing of barcode editing, we injected Cas9 and 10 sgRNAs into one-cell stage v7 transgenic embryos and harvested genomic DNA before gastrulation (dome stage, 4.3 hpf; n = 10 embryos), after gastrulation (90% epiboly/bud stage, 9 hpf; n = 11 embryos), at pharyngula stage (30 hpf; n = 12 embryos), and from early larvae (72 hpf; n = 12 embryos) (Fig. 3A). We recovered barcode sequences from a median of 8785 cells per embryo (range 461 to 31,640; total of 45 embryos), comprising a median of 1223 alleles per embryo (range 15 to 4195) (Fig. 3C). Within single embryos, 65 ± 6% of alleles were observed recurrently, whereas in pairwise comparisons of embryos only 2 ± 5% of alleles were observed recurrently. The abundances of alleles were well correlated between technical replicates for each of two 72-hpf embryos (fig. S8, A and B), and alleles containing many edits were more likely to be unique to an embryo than those with few edits (fig. S8C). To assess when editing begins, we analyzed the proportions of the most common editing events across all barcodes sequenced in a given embryo, reasoning that the earliest edits would be the most frequent. Across 8 v6 and 45 v7 embryos, we never observed an edit that was present in 100% of cells. This observation indicates that no permanent edits were introduced at the one-cell stage. In nearly all embryos, we observed that the most common edit is present in >10% of cells, and in some cases in ~50% of cells (Fig. 3D and fig. S9). This observation also holds in ~4000-cell dome-stage embryos, which result from ~12 rounds of largely synchronous division unaccompanied by cell death. Most of these edits are rare or absent in other embryos, suggesting that they are unlikely to have arisen recurrently within each lineage. These results suggest that the edits present in ~50% of cells were introduced at the two-cell stage and that the edits present in >10% of cells were introduced before the 16-cell stage.

How long does barcode editing persist? Two aspects of the data suggest that it tapers relatively early in development. First, in dome-stage embryos (4.3 hpf), we captured barcodes from a median of 2086 cells, in which a median of 4.8 targets were edited. Although the number of cells and alleles that we were able to sample increased at the later developmental stages, the proportion of edited sites appeared relatively stable (Fig. 3C). If editing were occurring throughout this time course, we would instead expect the proportion of edited sites to increase substantially. Second, the number of unique alleles appears to saturate early, never exceeding 4200 (Fig. 3E). For example, only 4195 alleles were observed in a 72-hpf embryo in which we sampled the highest number of cells (n = 31,639). These results suggest that the majority of editing events occurred before dome stage.

Editing diversity in adult organs

To evaluate whether barcodes edited during embryogenesis can be recovered in adults, we dissected

Downloaded from http://science.sciencemag.org/ on July 28, 2016

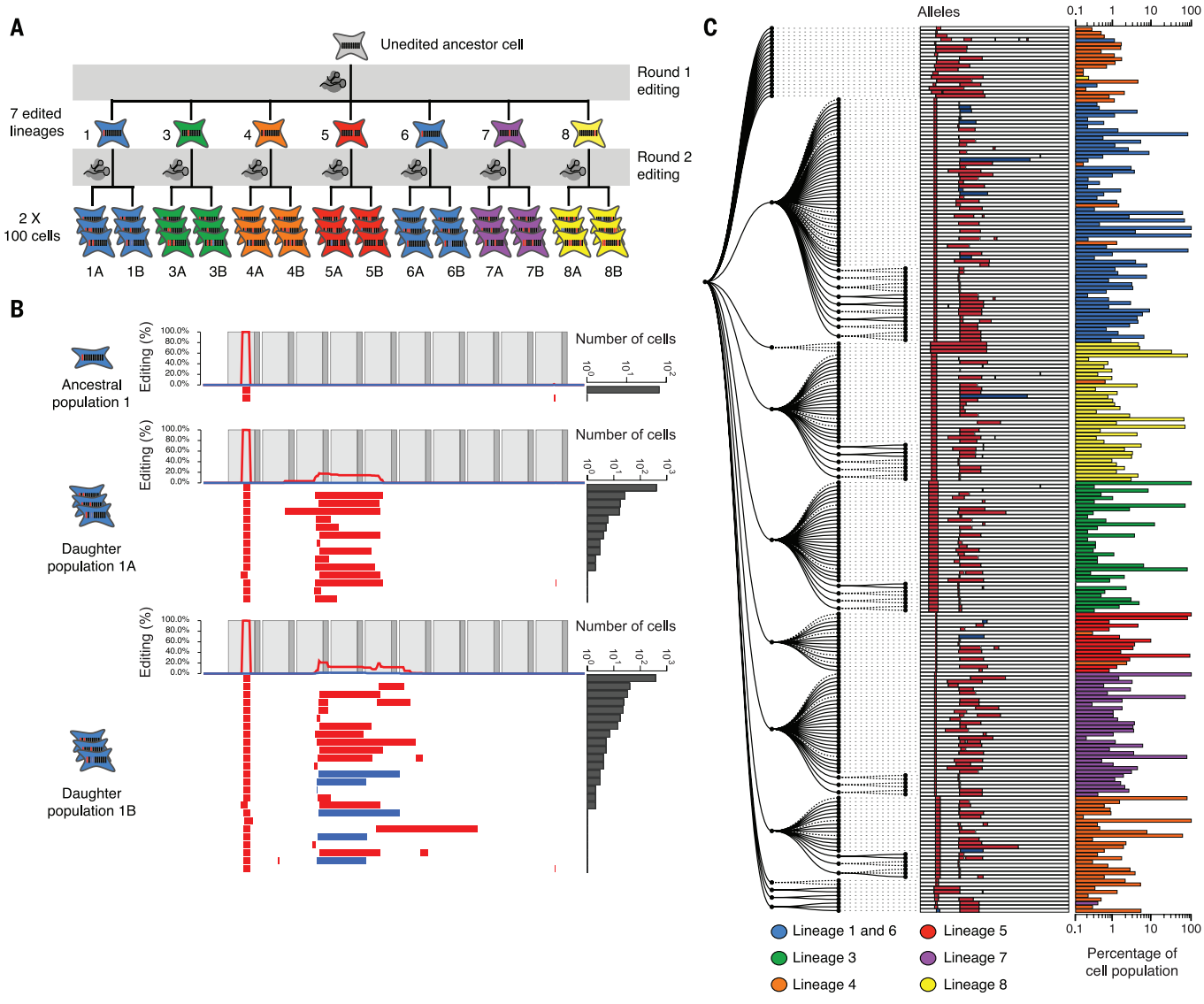


Fig. 2. Reconstruction of a synthetic lineage based on genome editing and targeted sequencing of edited barcodes. (**A**) A monoclonal population of cells was subjected to editing of the v1 array. Single cells were expanded, sampled (nos. 1 to 12), retransfected to induce a second round of barcode editing, and then expanded and sampled from 100-cell subpopulations (1a and 1b to 12a and 12b). For clarity, the five clones where the original population was unedited are not shown. (**B**) Alleles observed in the synthetic lineage experiment are shown, with layout as described in the Fig. 1B legend. Cell population 1 represents sampling of cells that had been subjected to only the first round of editing; virtually all cells contain a shared edit to the first target. Populations 1a and 1b are derived from 1 but are subjected to a second round of editing prior to sampling. These retain the edit to the first target, but subpopulations bear additional edits to other targets. (**C**) Maximum parsimony reconstruction using PHYLIP Mix (see Materials and Methods and fig. S4B) from alleles seen two or more times in the seven cell lineages represented in (A). Lineage membership and abundance of each allele are shown on the right. Progenitor cell lineage 4 (orange) appears to be derived from two cells, one edited and the other wild-type. Only 62% of lineage 4 falls into a single clade, consistent with the proportion (64%) of the lineage edited after the first round. We assume that cells unedited in the first round either accrued edits matching other lineages (thus causing mixing) or accrued different edits (thus remaining outside the major clades).

two edited 4-month-old v7 transgenic zebrafish (ADR1 and ADR2) (Fig. 5A). We collected organs representing all germ layers: the brain and both eyes (ectodermal), the intestinal bulb and posterior intestine (endodermal), the heart and blood (mesodermal), and the gills (neural crest, with contributions from other germ layers). We further divided the heart into four samples: a piece of heart tissue, dissociated unsorted cells (DHCs), FACS-sorted GFP$^+$ cardiomyocytes, and noncardiomyocyte heart cells (NCs) (fig. S10). We isolated genomic DNA from each sample, amplified and sequenced edited barcodes with high technical reproducibility (fig. S11), and observed barcode editing rates akin to those in embryos (fig. S12). For zebrafish ADR1, we captured barcodes from between 776 and 44,239 cells from each tissue sample (median 17,335), corresponding to a total of 197,461 cells and 1138 alleles. For zebrafish ADR2, we captured barcodes from between 84 and 52,984 cells from each tissue sample (median 20,973), corresponding to a total of 217,763 cells and 2016 alleles. These results show that edits introduced to the barcode during embryogenesis are inherited through development and tissue homeostasis and can be detected in adult organs.

Differential contribution of embryonic progenitors to adult organs

To analyze the contribution of diverse alleles to different organs, we compared the frequency of edited barcodes within and between organs. We first examined blood [of note, zebrafish erythrocytes

Downloaded from http://science.sciencemag.org/ on July 28, 2016

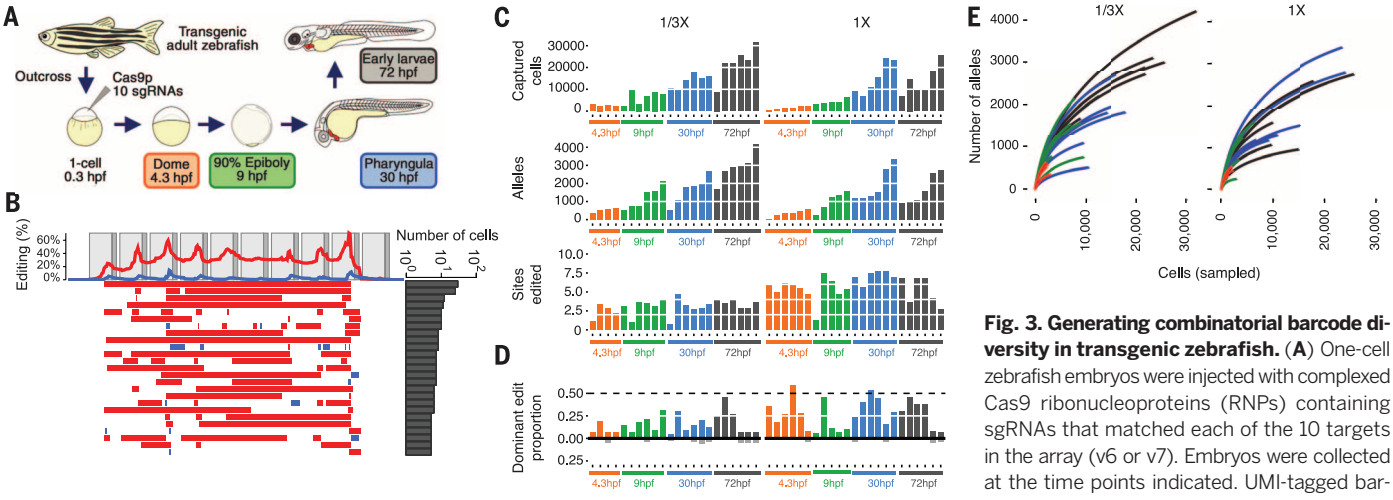


Fig. 3. Generating combinatorial barcode diversity in transgenic zebrafish. (**A**) One-cell zebrafish embryos were injected with complexed Cas9 ribonucleoproteins (RNPs) containing sgRNAs that matched each of the 10 targets in the array (v6 or v7). Embryos were collected at the time points indicated. UMI-tagged barcodes were amplified and sequenced from genomic DNA. (**B**) Patterns of editing in alleles recovered from a 30-hpf v6 embryo, with layout as described in the Fig. 1B legend. (**C**) Bar plots show the number of cells sampled (top), unique alleles observed (middle), and the average number of sites edited (bottom) for 45 v7 embryos collected at four developmental time points and two levels of Cas9 RNP (1/3x and 1x). Colors correspond to stages shown in (A). Although more alleles are observed with sampling of larger numbers of cells at later time points, the proportion of target sites edited remains relatively constant. (**D**) Bar plots show the proportion of edited barcodes containing the most common editing event in a given embryo. Six of 45 embryos had the most common edit in approximately 50% of cells (dashed line), consistent with this edit having occurred at the two-cell stage (see fig. S8A for example). Colors correspond to stages shown in (A). These same edits are rarer or absent in other embryos (gray bars below). (**E**) For each of the 45 v7 embryos, all barcodes observed were sampled without replacement. The cumulative number of unique alleles observed as a function of the number of cells sampled is shown (average of the 500 iterations shown per embryo; two levels of Cas9 RNP: 1/3x on left, 1x on right). The number of unique alleles observed, even in later developmental stages where we are sampling much larger numbers of cells, appears to saturate, and there is no consistent pattern supporting substantially greater diversity in later time points, consistent with the bottom row of (C) in supporting the conclusion that the majority of editing occurs before dome stage.

are nucleated (*30*)]. Only five alleles defined over 98% of cells in the ADR1 blood sample (Fig. 5B), suggesting highly clonal origins of the adult zebrafish blood system from a few embryonic progenitors. Consistent with the presence of blood in all dissected organs, these common blood alleles were also observed in all organs (10 to 40%) (Fig. 5C) but largely absent from cardiomyocytes isolated by flow sorting (0.5%). Furthermore, the relative proportions of these five alleles remained largely constant in all dissected organs, suggesting that they primarily mark the blood and do not substantially contribute to nonblood lineages (Fig. 5D). In performing similar analyses of clonality across all organs (while excluding the five most common blood alleles), we observed that a small subset of alleles dominates each organ (Fig. 5E). Indeed, for all dissected organs, fewer than 7 alleles comprised >50% of cells (median 4, range 2 to 6), and, with the exception of the brain, fewer than 25 alleles comprised >90% of cells (median 19, range 4 to 38). Most of these dominant alleles were organ-specific—i.e., although they were found rarely in other organs, they tended to be dominant in only one organ (Fig. 5F). For example, the most frequent allele observed in the intestinal bulb comprised 13.6% of captured nonblood cells observed in that organ but <0.01% of cells observed in any other organ. There are exceptions, however. For example, one allele is observed in 24.7% of sorted cardiomyocytes, 13.4% of the intestinal bulb, and at lower abundances in all other organs. Similar results were observed in ADR2 (fig. S13). These results indicate that the majority of cells in diverse adult organs are descended from a few differentially edited embryonic precursors.

Reconstructing lineage relationships in adult organs

To reconstruct the lineage relationships between cells both within and across organs on the basis of shared edits, we again relied on maximum parsimony methods (fig. S4B). The resulting trees for ADR1 and ADR2 are shown in Fig. 6 and fig. S14, respectively. We observed clades of alleles that shared specific edits. For example, ADR1 had eight major clades, each defined by "ancestral" edits that are shared by all captured cells assigned to that clade (Fig. 7A; also indicated by colors in the tree shown in Fig. 6). Collectively, these clades comprised 49% of alleles and 90% of the 197,461 cells sampled from ADR1 (Fig. 7A). Blood was contributed to by three major clades (nos. 3, 6, and 7) (Fig. 7B). After reallocating the five dominant blood alleles from the composition of individual organs back to blood (Fig. 5B and fig. S15), we observed that all major clades made highly nonuniform contributions across organs. For example, clade 3 contributed almost exclusively to mesodermal and endodermal organs, while clade 5 contributed almost exclusively to ectodermal organs. These results reveal that GESTALT can be used to infer the contributions of inferred ancestral progenitors to adult organs.

Although some ancestral clades appear to contribute to all germ layers, we find that subclades, defined by additional shared edits within a clade, exhibit greater specificity. For example, although clade 1 contributes substantially to all organs except blood, additional edits divide clade 1 into three subclades with greater tissue restriction (Fig. 7, C and D). The 1+A subclade primarily contributes to mesendodermal organs (heart and both gastrointestinal organs), whereas the 1+C subclade primarily contributes to neuroectodermal organs (brain, left eye, and gills). Similar patterns are observed for clade 2 (Fig. 7, E and F), where the 2+A subclade contributes primarily to mesendodermal organs, the 2+B subclade to the heart, and the 2+C subclade to neuroectodermal organs. Additional edits divide these subclades into further tissue-specific sub-subclades. For example, whereas the 2+A subclade is predominantly mesendoderm, additional edits define 2+A+D (heart, primarily cardiomyocytes), 2+A+E (heart and posterior intestine), and 2+A+F (intestinal bulb). All of the major clades exhibit similar patterns of increasing restriction with additional edits (Fig. 7, C to F, and fig. S16). Similar observations were made in fish ADR2 (fig. S17). These results indicate that GESTALT can record lineage relationships across many cell divisions and capture information both before and during tissue restriction.

Discussion

We describe a method, GESTALT, which uses combinatorial and cumulative genome editing to record cell lineage information in a highly multiplexed fashion. We successfully applied this method to both artificial lineages (cell culture) as well as to a whole organism (zebrafish). Full-tree reconstructions for cell culture, zebrafish embryo, and zebrafish adult experiments are provided at http://gestalt.gs.washington.edu.

Downloaded from http://science.sciencemag.org/ on July 28, 2016

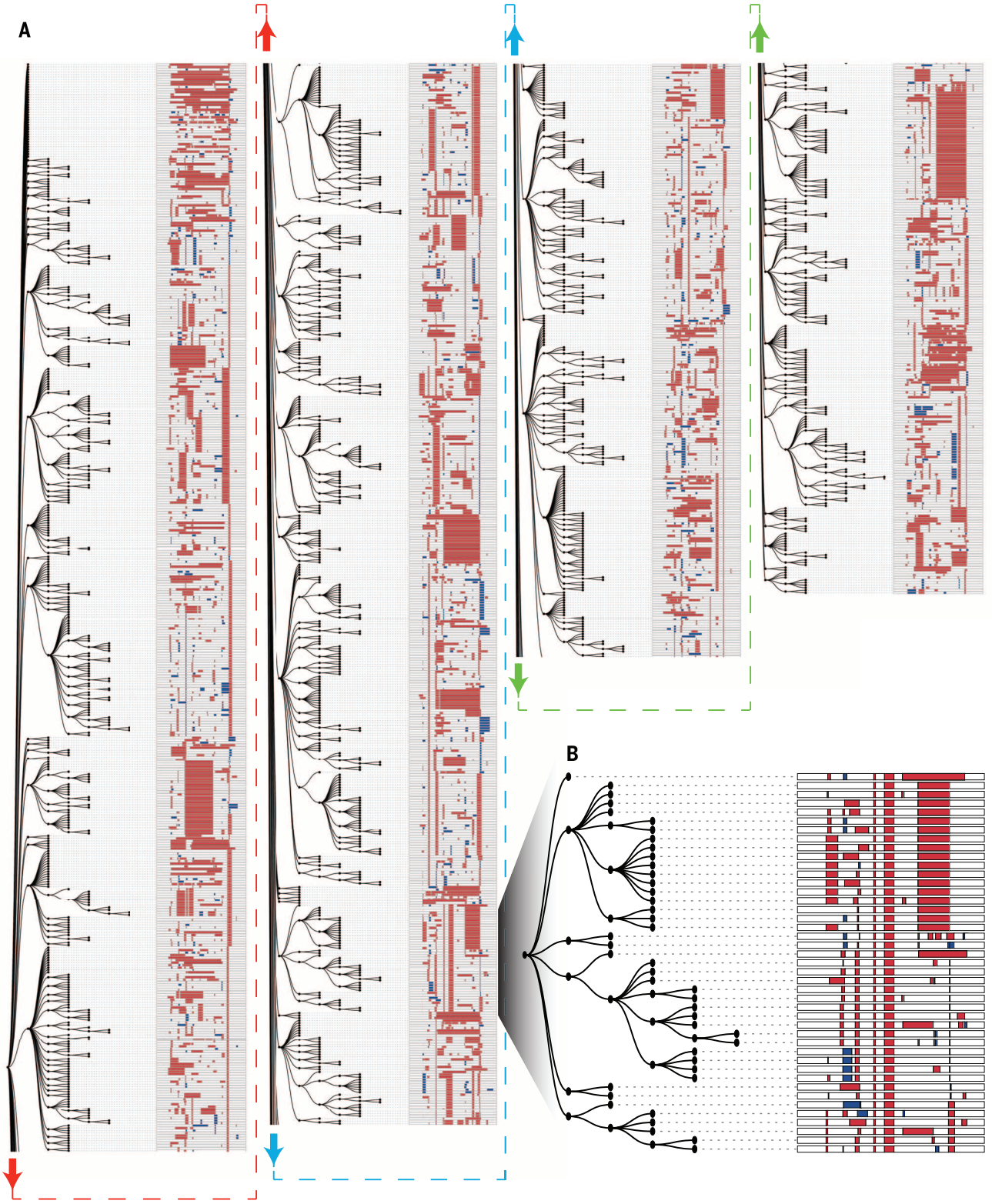


Fig. 4. Lineage reconstruction of an edited zebrafish embryo. (**A**) A lineage reconstruction of 1323 alleles recovered from the v6 embryo also represented in Fig. 3B, generated by a maximum parsimony approach implemented in the PHYLIP Mix package (see Materials and Methods and fig. S4B). A dendrogram to the left of each column represents the lineage relationships, and the alleles are represented on the right. Each row represents a unique allele. Matched colored arrows and dashed lines connect subsections of the tree together. There are many large clades of alleles sharing specific edits, as well as subclades defined by "dependent" edits. These dependent edits occur within a clade defined by a more frequent edit but are rare or absent elsewhere in the tree. (**B**) A portion of the tree is shown at higher resolution. Two edits are shared by all alleles in this clade. Six independent edits define descendant subclades within this clade, and further edits define additional sub-subclades within the clade.

Downloaded from http://science.sciencemag.org/ on July 28, 2016

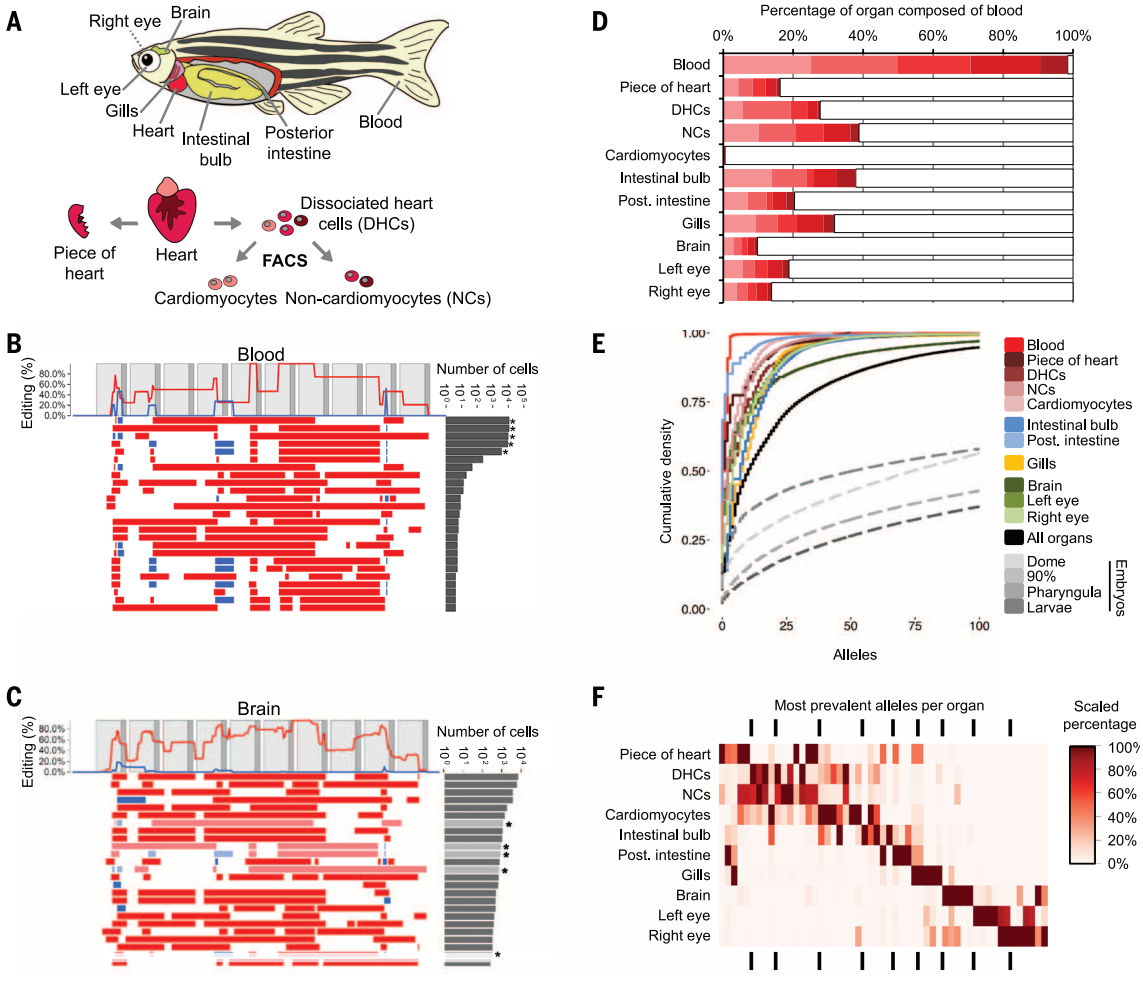


Fig. 5. Organ-specific progenitor cell dominance. (**A**) The indicated organs were dissected from a single adult v7 transgenic edited zebrafish (ADR1). A blood sample was collected as described in the Methods. The heart was further split into the four samples shown (fig. S10). (**B**) Patterns of editing in the most prevalent 25 alleles (out of 135 total) recovered from the blood sample. Layout as described in the Fig. 1B legend. The most prevalent five alleles (indicated by asterisks) comprise >98% of observed cells. (**C**) Patterns of editing in the most prevalent 25 alleles (out of 399 total) recovered from brain. Layout as described in the Fig. 1B legend. Alleles that have identical editing patterns compared with the most prevalent blood alleles are indicated by asterisks and light shading. (**D**) The five dominant blood alleles (shades of red) are present in varying proportions (10 to 40%) in all intact organs except the FACS-sorted cardiomyocyte population (0.5%). All other alleles are summed in gray. (**E**) The cumulative proportion of cells (*y* axis) represented by the most frequent alleles (*x* axis) for each adult organ of ADR1 is shown, as well as the adult organs in aggregate. In all adult organs except blood, the five dominant blood alleles are excluded. All organs exhibit dominance of sampled cells by a small number of progenitors, with fewer than seven alleles comprising the majority of cells. For comparison, a similar plot for the median embryo (dashed line) from each time point of the developmental time course experiment is also shown. (**F**) The distribution of the most prevalent alleles for each organ, after removal of the five dominant blood alleles, across all organs. The most prevalent alleles were defined as being at >5% abundance in a given organ (median 5 alleles, range 4 to 7). Organ proportions were normalized by column and colored as shown in the legend. Underlying data are presented in table S2.

The strengths of GESTALT include (i) the combinatorial diversity of mutations that can be generated within a dense array of CRISPR/Cas9 target sites; (ii) the potential for informative mutations to accumulate across many cell divisions and throughout an organism's developmental history; (iii) the ability to scalably query lineage information from at least hundreds of thousands of cells and with a single sequencing read per single cell; and (iv) the likely applicability of GESTALT to any organism, from bacteria and plants to vertebrates, that allows genome editing, as well as human cells (e.g., tumor xenografts). Even in organisms in which transgenesis is not established, lineage tracing by genome editing may be feasible by expressing editing reagents to densely mutate an endogenous, nonessential genomic sequence.

Our experiments also highlight several remaining technical challenges. Chief among these are (i) the chance recurrence of identical edits or similar patterns of edits in distantly related cells can confound lineage inference; (ii) nonuniform editing efficiencies and intertarget deletions within the barcode contribute to suboptimal sequence diversity and loss of information, respectively; (iii) the transient means by which Cas9 and sgRNAs are introduced likely restrict editing to early embryogenesis; (iv) the computational challenge of precisely defining the multiple editing events that give rise to different alleles complicates the unequivocal reconstruction of lineage trees; and (v) the difficulty of isolating tissues without contamination by blood and other cells can hinder the assignment of alleles to specific organs. A broader set of challenges includes the lack of information about the precise anatomical location and exact cell type of each queried cell, the fact that genome editing events are not directly coupled to the cell cycle, and the failure to recover all cells. These challenges currently hinder the reconstruction of a lineage tree as complete and precise as the one that Sulston and colleagues described for *C. elegans* (*2*). Despite these limitations, our proof-of-principle study shows that GESTALT can inform developmental biology by richly defining lineage relationships among vast numbers of cells recovered from an organism.

The current challenges highlight the need for further optimization of the design of targets and arrays, as well as the delivery of editing reagents. For example, an array containing twice as many targets as used here could fit within a single read on contemporary sequencing platforms, thus yielding more lineage information per cell without sacrificing throughput. Also, as we have shown, adjustments to the target sequences and dosages of editing reagents can be used to fine-tune mutation rates and to minimize undesirable intertarget deletions. Finally, sgRNA sequences and lengths (*31*), Cas9 cleavage activity and target preferences (*32*, *33*), and the means by which Cas9 and sgRNA(s) are expressed [e.g., transient, constitutive (*34*), or

Downloaded from http://science.sciencemag.org/ on July 28, 2016

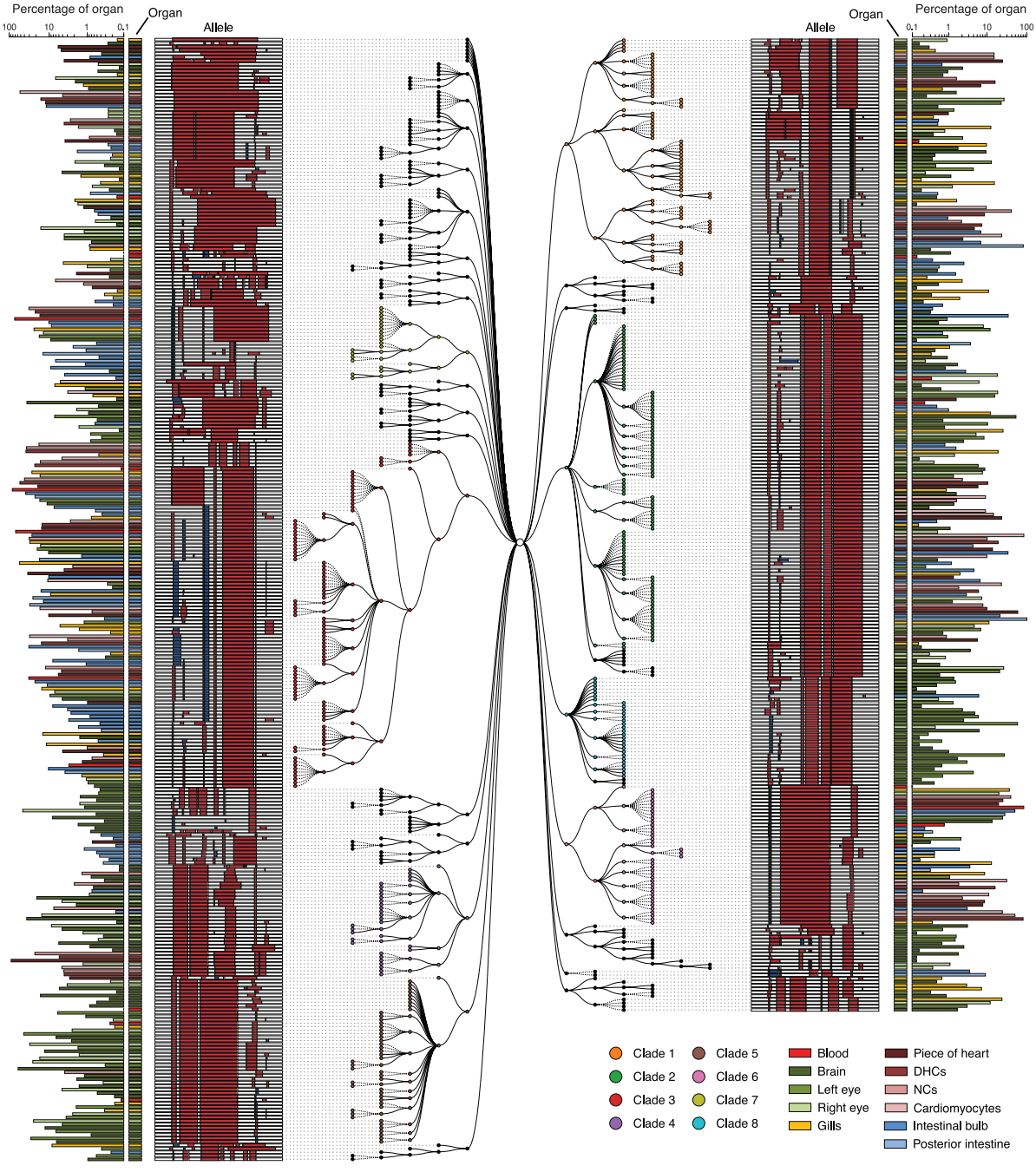


Fig. 6. Lineage reconstruction for adult zebrafish ADR1. Unique alleles sequenced from adult zebrafish organs can be related to one another using a maximum parsimony approach implemented in the PHYLIP Mix package (see Materials and Methods and fig. S4B). For reasons of space, we show a tree reconstructed from the 601 ADR1 alleles observed at least five times in individual organs. Eight major clades are displayed with colored nodes, each defined by "ancestral" edits that are shared by all alleles assigned to that clade (shown in Fig. 7A). Editing patterns in individual alleles are represented as shown previously. Alleles observed in multiple organs are plotted on separate lines per organ and are connected with stippled branches. Two sets of bars outside the alleles identify the organ in which the allele was observed and the proportion of cells in that organ represented by that allele (log10 scale).

induced (*35*, *36*)], can be altered to control the pace, temporal window, and tissue(s) at which the barcodes are mutated. For example, coupling editing to cell cycle progression might enable higher resolution reconstruction of lineage relationships throughout development.

Our application of GESTALT to a vertebrate model organism, zebrafish, demonstrates its potential to yield insights into developmental biology. First, our results suggest that relatively few embryonic progenitor cells give rise to the majority of cells of many adult zebrafish organs, reminiscent of clonal dominance (*37*, *38*). For example, only 5 of the 1138 alleles observed in ADR1 gave rise to >98% of blood cells, and for all dissected organs, fewer than 7 alleles comprised >50% of cells. There are several mechanisms by which such dominance can emerge—e.g., by uneven starting populations in the embryo, drift, competition, interference, unequal cell proliferation or death, or a combination of these mechanisms (*39*–*42*). Controlling the temporal and spatial induction of edits and isolating defined cell types from diverse organs should help resolve the

Downloaded from http://science.sciencemag.org/ on July 28, 2016

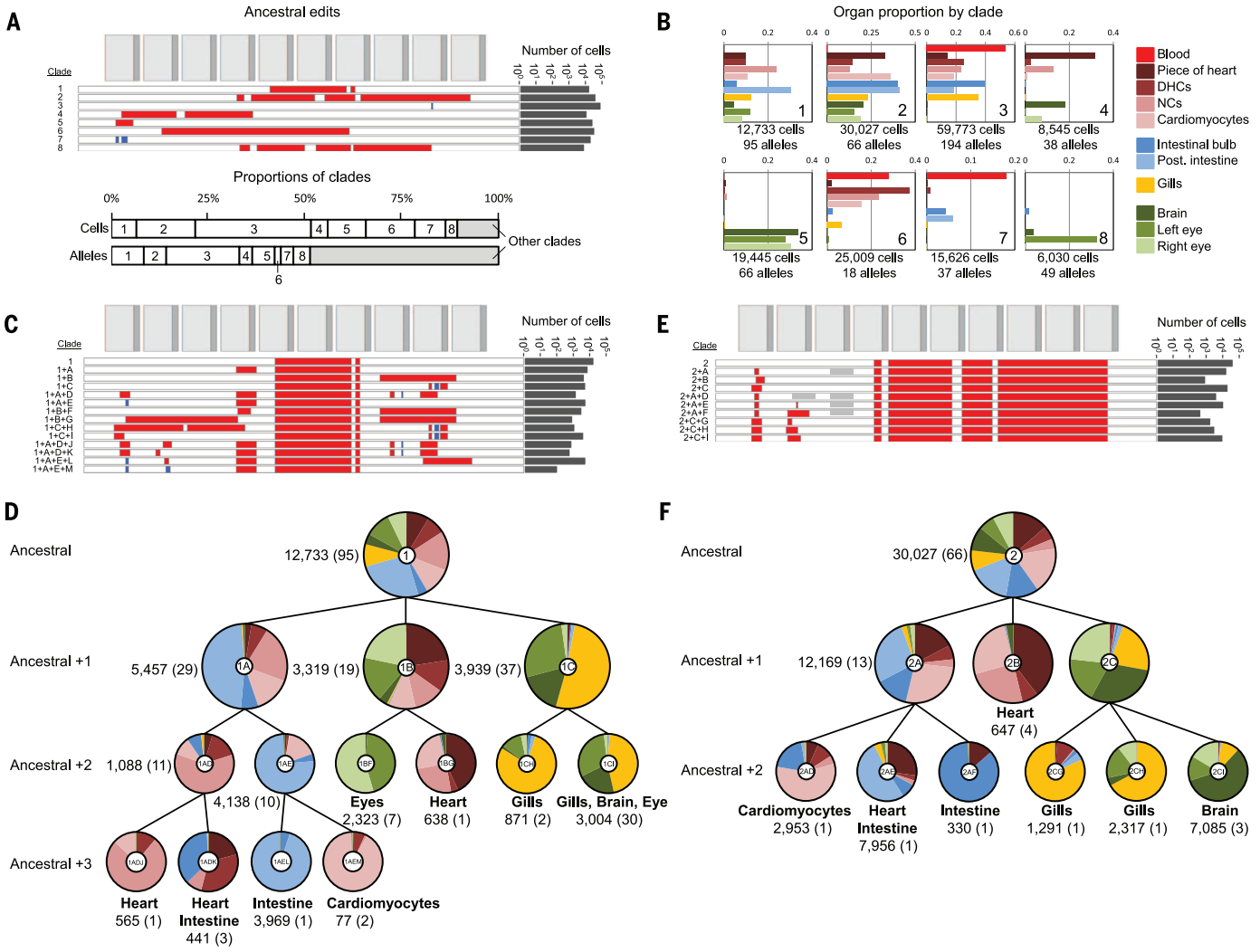


Fig. 7. Clades and subclades corresponding to inferred progenitors exhibit increasing levels of organ restriction. (**A**) (Top) The parsimony-inferred ancestral edits that define eight major clades of ADR1 are shown, with the total number of cells in which these are observed indicated on the right. (Bottom) Contributions of the eight major clades to all cells or all alleles. Nineteen alleles (out of 1138 total) that contained ancestral edits from more than one clade were excluded from assignment to any clade and from any further lineage analysis. (**B**) Contributions of each of the eight major clades to each organ, displayed as a proportion of each organ. To accurately display the contributions of the eight major clades to each organ, we first reassigned the five dominant blood alleles from other organs back to the blood. The total number of cells and alleles within a given major clade are listed below. The clade contributions of all clades and subclades are presented in table S3. For heart subsamples: piece of heart, a piece of heart tissue; DHCs, dissociated unsorted cells; cardiomyocytes, FACS-sorted GFP^{+} cardiomyocytes; and NCs, noncardiomyocyte heart cells. (**C** and **E**) Edits that define subclades of clade 1 (C) and clade 2 (E), with the total number of cells in which these are observed indicated on the right. A gray box indicates an unedited site or sites, distinguishing it from related alleles that contain an edit at this location. (**D** and **F**) Lineage trees corresponding to subclades of clade 1 (D) and clade 2 (F) that show how dependent edits are associated with increasing lineage restriction. The pie chart at each node indicates the organ distribution within a clade or subclade. Ratios of cell proportions are plotted, a normalization that accounts for differential depth of sampling between organs. Labels in the center of each pie chart correspond to the subclade labels in (C) and (E). Alleles present in a clade but not assigned to a descendant subclade (either they have no additional lineage restriction or are at low abundance) are not plotted for clarity. The number of cells (and the number of unique alleles) are also listed, and terminal nodes also list major organ restriction(s), i.e., those comprising >25% of a subclade by proportion.

mechanisms by which different embryonic progenitors come to dominate different adult organs.

Second, we show that GESTALT can inform the lineage relationships among thousands of differentiated cells. For example, following the accumulation of edits from ancestral to more complex reveals the progressive restriction of progenitors to germ layers and then organs. Cells within an organ can both share and differ in their alleles, revealing additional information about organ development. Future studies will need to determine whether such lineages reflect distinct cell fates (e.g., blood sublineages or neuronal subpopulations), because the anatomical resolution at which we queried alleles was restricted to grossly dissected organs and tissues. Because edited barcodes are expressed as RNA, we envision that combining our system with other platforms will permit much greater levels of anatomical resolution without sacrificing throughput. For example, in situ RNA sequencing (RNA-seq) of barcodes would provide explicit spatial and histological context to lineage reconstructions (*19*, *20*). Also, capturing richly informative lineage markers in single-cell RNA-seq or assay for transposase-accessible chromatin (ATAC)–seq data sets may inform the interpretation of those molecular phenotypes, while also adding cell type resolution to studies of lineage (*43*, *44*). Such integration may be particularly relevant to efforts to

Downloaded from http://science.sciencemag.org/ on July 28, 2016

build comprehensive atlases of cell types. Because these single-cell methods generate many reads per single cell, this would also facilitate using multiple, unlinked target arrays. In principle, the combined diversity of the barcodes queried from single cells could be engineered to uniquely identify every cell in a complex organism. In addition, orthogonal imaging-based lineage tracing approaches in fixed and live samples [e.g., Brainbow and related methods (*16*, *29*)] and longitudinal whole-animal imaging approaches (*45*, *46*) might be used in parallel to validate and complement lineages resolved by GESTALT.

Although further work is required to optimize GESTALT toward enabling spatiotemporally complete maps of cell lineage, our proof-of-principle experiments show that using multiplex in vivo genome editing to record lineage information to a compact barcode at an organism-wide scale will be a powerful tool for developmental biology. This approach is not limited to normal development but can also be applied to animal models of developmental disorders, as well as to investigate the origins and progression of cancer. Our study also supports the notion that, although its most widespread application has been to modify endogenous biological circuits, genome editing can also be used to stably record biological information (*47*), analogous to recombinase-based memories but with considerably greater flexibility and scalability. For example, coupling editing activity to external stimuli or physiological changes could record the history of exposure to intrinsic or extrinsic signals. In the long term, we envision that rich, systematically generated maps of organismal development, wherein lineage, epigenetic, transcriptional, and positional information are concurrently captured at single-cell resolution, will advance our understanding of normal development, inherited diseases, and cancer.

REFERENCES AND NOTES

1. G. S. Stent, Developmental cell lineage. *Int. J. Dev. Biol.* **42**, 237–241 (1998); pmid: 9654003
2. J. E. Sulston, E. Schierenberg, J. G. White, J. N. Thomson, The embryonic cell lineage of the nematode *Caenorhabditis elegans*. *Dev. Biol.* **100**, 64–119 (1983). doi: 10.1016/0012-1606(83)90201-4; pmid: 6684600
3. K. Kretzschmar, F. M. Watt, Lineage tracing. *Cell* **148**, 33–45 (2012). doi: 10.1016/j.cell.2012.01.002; pmid: 22265400
4. C. B. Kimmel, R. D. Law, Cell lineage of zebrafish blastomeres. III. Clonal analyses of the blastula and gastrula stages. *Dev. Biol.* **108**, 94–101 (1985). doi: 10.1016/0012-1606(85)90012-0; pmid: 3972184
5. R. E. Keller, Vital dye mapping of the gastrula and neurula of *Xenopus laevis*. I. Prospective areas and morphogenetic movements of the superficial layer. *Dev. Biol.* **42**, 222–241 (1975). doi: 10.1016/0012-1606(75)90331-0; pmid: 46836
6. D. A. Weisblat, R. T. Sawyer, G. S. Stent, Cell lineage analysis by intracellular injection of a tracer enzyme. *Science* **202**, 1295–1298 (1978). doi: 10.1126/science.725606; pmid: 725606
7. N. M. Le Douarin, M. A. Teillet, Experimental analysis of the migration and differentiation of neuroblasts of the autonomic nervous system and of neurectodermal mesenchymal derivatives, using a biological cell marking technique. *Dev. Biol.* **41**, 162–184 (1974). doi: 10.1016/0012-1606(74)90291-7; pmid: 4140118
8. S. M. Dymecki, H. Tomasiewicz, Using Flp-recombinase to characterize expansion of Wnt1-expressing neural progenitors in the mouse. *Dev. Biol.* **201**, 57–65 (1998). doi: 10.1006/dbio.1998.8971; pmid: 9733573
9. D. L. Zinyk, E. H. Mercer, E. Harris, D. J. Anderson, A. L. Joyner, Fate mapping of the mouse midbrain-hindbrain constriction using a site-specific recombination system. *Curr. Biol.* **8**, 665–672 (1998). doi: 10.1016/S0960-9822(98)70255-6; pmid: 9635195
10. C. Walsh, C. L. Cepko, Widespread dispersion of neuronal clones across functional regions of the cerebral cortex. *Science* **255**, 434–440 (1992). doi: 10.1126/science.1734520; pmid: 1734520
11. R. Lu, N. F. Neff, S. R. Quake, I. L. Weissman, Tracking single hematopoietic stem cells in vivo using high-throughput sequencing in conjunction with viral genetic barcoding. *Nat. Biotechnol.* **29**, 928–933 (2011). doi: 10.1038/nbt.1977; pmid: 21964413
12. S. N. Porter, L. C. Baker, D. Mittelman, M. H. Porteus, Lentiviral and targeted cellular barcoding reveals ongoing clonal dynamics of cell lines in vitro and in vivo. *Genome Biol.* **15**, R75 (2014). doi: 10.1186/gb-2014-15-5-r75; pmid: 24886633
13. S. J. Salipante, M. S. Horwitz, Phylogenetic fate mapping. *Proc. Natl. Acad. Sci. U.S.A.* **103**, 5448–5453 (2006). doi: 10.1073/pnas.0601265103; pmid: 16569691
14. S. Behjati *et al.*, Genome sequencing of normal cells reveals developmental lineages and mutational processes. *Nature* **513**, 422–425 (2014). doi: 10.1038/nature13448; pmid: 25043003
15. M. A. Lodato *et al.*, Somatic mutation in single human neurons tracks developmental and transcriptional history. *Science* **350**, 94–98 (2015). doi: 10.1126/science.aab1785; pmid: 26430121
16. J. Livet *et al.*, Transgenic strategies for combinatorial expression of fluorescent proteins in the nervous system. *Nature* **450**, 56–62 (2007). doi: 10.1038/nature06293; pmid: 17972876
17. G. M. Church, J. Shendure, Nucleic acid memory device. President and Fellows of Harvard College, assignee. Patent US 20030228611. (2003).
18. C. A. Carlson *et al.*, Decoding cell lineage from acquired mutations using arbitrary deep sequencing. *Nat. Methods* **9**, 78–80 (2011). doi: 10.1038/nmeth.1781; pmid: 22120468
19. J.-H. Lee *et al.*, Highly multiplexed subcellular RNA sequencing in situ. *Science* **343**, 1360–1363 (2014). doi: 10.1126/science.1250212; pmid: 24578530
20. R. Ke *et al.*, In situ sequencing for RNA analysis in preserved tissue and cells. *Nat. Methods* **10**, 857–860 (2013). doi: 10.1038/nmeth.2563; pmid: 23852452
21. J. A. Doudna, E. Charpentier, The new frontier of genome engineering with CRISPR-Cas9. *Science* **346**, 1258096–1258096 (2014). doi: 10.1126/science.1258096; pmid: 25430774
22. S. Q. Tsai *et al.*, GUIDE-seq enables genome-wide profiling of off-target cleavage by CRISPR-Cas nucleases. *Nat. Biotechnol.* **33**, 187–197 (2015). doi: 10.1038/nbt.3117; pmid: 25513782
23. Y. Sancak *et al.*, The Rag GTPases bind raptor and mediate amino acid signaling to mTORC1. *Science* **320**, 1496–1501 (2008). doi: 10.1126/science.1157535; pmid: 18497260
24. N. E. Sanjana, O. Shalem, F. Zhang, Improved vectors and genome-wide libraries for CRISPR screening. *Nat. Methods* **11**, 783–784 (2014). doi: 10.1038/nmeth.3047; pmid: 25075903
25. B. E. Miner, R. J. Stöger, A. F. Burden, C. D. Laird, R. S. Hansen, Molecular barcodes detect redundancy and contamination in hairpin-bisulfite PCR. *Nucleic Acids Res.* **32**, e135–e135 (2004). doi: 10.1093/nar/gnh132; pmid: 15459281
26. J. Felsenstein, PHYLIP - Phylogeny Inference Package (Version 3.2). *Cladistics* **5**, 164–166 (1989).
27. K. Kawakami, Tol2: A versatile gene transfer vector in vertebrates. *Genome Biol.* **8** (Suppl 1), S7 (2007). doi: 10.1186/gb-2007-8-s1-s7; pmid: 18047699
28. S. N. Porter, L. C. Baker, D. Mittelman, M. H. Porteus, Lentiviral and targeted cellular barcoding reveals ongoing clonal dynamics of cell lines in vitro and in vivo. *Genome Biol.* **15**, R75 (2014). doi: 10.1186/gb-2014-15-5-r75; pmid: 24886633
29. Y. A. Pan *et al.*, Zebrabow: Multispectral cell labeling for cell tracing and lineage analysis in zebrafish. *Development* **140**, 2835–2846 (2013). doi: 10.1242/dev.094631; pmid: 23757414
30. C. Thisse, L. I. Zon, Organogenesis—heart and blood formation from the zebrafish point of view. *Science* **295**, 457–462 (2002). doi: 10.1126/science.1063654; pmid: 11799232
31. Y. Fu, J. D. Sander, D. Reyon, V. M. Cascio, J. K. Joung, Improving CRISPR-Cas nuclease specificity using truncated guide RNAs. *Nat. Biotechnol.* **32**, 279–284 (2014). doi: 10.1038/nbt.2808; pmid: 24463574
32. B. P. Kleinstiver *et al.*, Engineered CRISPR-Cas9 nucleases with altered PAM specificities. *Nature* **523**, 481–485 (2015). doi: 10.1038/nature14592; pmid: 26098369
33. I. M. Slaymaker *et al.*, Rationally engineered Cas9 nucleases with improved specificity. *Science* **351**, 84–88 (2016). doi: 10.1126/science.aad5227; pmid: 26628643
34. R. J. Platt *et al.*, CRISPR-Cas9 knockin mice for genome editing and cancer modeling. *Cell* **159**, 440–455 (2014); pmid: 25263330
35. J. Ablain, E. M. Durand, S. Yang, Y. Zhou, L. I. Zon, A CRISPR/Cas9 vector system for tissue-specific gene disruption in zebrafish. *Dev. Cell* **32**, 756–764 (2015). doi: 10.1016/j.devcel.2015.01.032; pmid: 25752963
36. L. Yin *et al.*, Multiplex conditional mutagenesis using transgenic expression of Cas9 and sgRNAs. *Genetics* **200**, 431–441 (2015). doi: 10.1534/genetics.115.176917; pmid: 25855067
37. V. Gupta, K. D. Poss, Clonally dominant cardiomyocytes direct heart morphogenesis. *Nature* **484**, 479–484 (2012). doi: 10.1038/nature11045; pmid: 22538609
38. H. J. Snippert *et al.*, Intestinal crypt homeostasis results from neutral competition between symmetrically dividing Lgr5 stem cells. *Cell* **143**, 134–144 (2010). doi: 10.1016/j.cell.2010.09.016; pmid: 20887898
39. A. M. Klein, B. D. Simons, Universal patterns of stem cell fate in cycling adult tissues. *Development* **138**, 3103–3111 (2011). doi: 10.1242/dev.060103; pmid: 21750026
40. C. Blanpain, B. D. Simons, Unravelling stem cell dynamics by lineage tracing. *Nat. Rev. Mol. Cell Biol.* **14**, 489–502 (2013). doi: 10.1038/nrm3625; pmid: 23860235
41. P. M. Henson, D. A. Hume, Apoptotic cell removal in development and tissue homeostasis. *Trends Immunol.* **27**, 244–250 (2006). doi: 10.1016/j.it.2006.03.005; pmid: 16584921
42. J. Pellettieri, A. Sánchez Alvarado, Cell turnover and adult tissue homeostasis: From humans to planarians. *Annu. Rev. Genet.* **41**, 83–105 (2007). doi: 10.1146/annurev.genet.41.110306.130244; pmid: 18076325
43. R. Satija, J. A. Farrell, D. Gennert, A. F. Schier, A. Regev, Spatial reconstruction of single-cell gene expression data. *Nat. Biotechnol.* **33**, 495–502 (2015). doi: 10.1038/nbt.3192; pmid: 25867923
44. D. A. Cusanovich *et al.*, Multiplex single-cell profiling of chromatin accessibility by combinatorial cellular indexing. *Science* **348**, 910–914 (2015). doi: 10.1126/science.aab1601; pmid: 25953818
45. S. G. Megason, S. E. Fraser, Imaging in systems biology. *Cell* **130**, 784–795 (2007). doi: 10.1016/j.cell.2007.08.031; pmid: 17803903
46. Z. Liu, P. J. Keller, Emerging imaging and genomic tools for developmental systems biology. *Dev. Cell* **36**, 597–610 (2016). doi: 10.1016/j.devcel.2016.02.016; pmid: 27003934
47. F. Farzadfard, T. K. Lu, Genomically encoded analog memory with precise in vivo DNA writing in living cell populations. *Science* **346**, 1256272–1256272 (2014). doi: 10.1126/science.1256272; pmid: 25395541

ACKNOWLEDGMENTS

For discussion and advice, we thank J. Felsenstein, M. Kuhner, M. Rossmann, E. Fast, C. Burns, R. Ben-Yair, S. Salipante; members of the Shendure laboratory, particularly M. Snyder; members of the Schier laboratory, particularly J. Farrell, B. Raj, M. Norris, and N. Lord; and members of the Horwitz laboratory, particularly D. Anderson. We thank G. Church for work on predecessors of this concept with J.S. in 2000. We thank M. Desai, R. Losick, A. Murray, and L. Zon for comments on the manuscript. We also thank the Bauer Core FACS Facility, the

Downloaded from http://science.sciencemag.org/ on July 28, 2016

staff of the zebrafish facility, and L. Pieper for technical support. Data associated with this paper are archived at Dryad and can be downloaded from doi:10.5061/dryad.478t9. This work was supported by grants from the Paul G. Allen Family Foundation (J.S. and M.S.H.), an NIH Director's Pioneer Award (J.S.; DP1HG007811), NIH/NIGMS (A.F.S.; GM056211), NIH/NICHD (A.F.S.; HD085905), and NIH/NIMH (A.F.S.; MH105960). J.A.G. was supported by a fellowship from the American Cancer Society. A.M. was supported by a fellowship from the NIH/NHLBI (T32HL007312). J.S. is an investigator of the Howard Hughes Medical Institute. J.S., A.M., G.M.F., J.A.G., and A.F.S. have filed a provisional patent application (62/332,896) that relates to genome editing of synthetic target arrays for lineage tracing. Author contributions: G.M.F., A.M., and J.S. developed the initial concept. G.M.F. led the cell culture experiments and developed the UMI protocol, with assistance from A.M. J.A.G. led the fish experiments, with assistance from A.M. and G.M.F. A.M. led development of the analysis pipeline. A.M., G.M.F., and J.A.G. processed and analyzed the data. A.M., G.M.F., J.A.G., A.F.S., and J.S. designed experiments and interpreted the data. M.S.H. provided critical early insight. A.M., G.M.F., J.A.G., A.F.S., and J.S. wrote the manuscript.

SUPPLEMENTARY MATERIALS

www.sciencemag.org/content/353/6298/aaf7907/suppl/DC1
Materials and Methods
Figs. S1 to S17
Tables S1 to S4
References (*48*–*56*)

30 March 2016; accepted 20 May 2016
Published online 26 May 2016
10.1126/science.aaf7907

Downloaded from http://science.sciencemag.org/ on July 28, 2016

RESEARCH ARTICLE SUMMARY

SYNTHETIC BIOLOGY

Molecular recordings by directed CRISPR spacer acquisition

Seth L. Shipman,* Jeff Nivala,* Jeffrey D. Macklis, George M. Church†

INTRODUCTION: Although recent advances in DNA synthesis and sequencing technologies have made practical the writing and readout of arbitrary data in the form of synthetic DNA, still lacking are the robust tools necessary to generate a dynamic record of such information within the genomes of living cells. An in vivo system, built out of biological parts with large storage capacity, would enable the recording of defined biological events into stable genetic memory and facilitate the tracking of long molecular and cellular histories.

RATIONALE: The CRISPR (clustered regularly interspaced short palindromic repeats)–Cas system is a prokaryotic type of immunological memory. Foreign DNA sequences originating from viral infections are stored within genome-based arrays in the form of short sequences—called spacers—that confer sequence-specific resistance to the invading nucleic acids. These arrays not only preserve the spacer sequences but also record the order in which the sequences are acquired, generating a temporal record of acquisition events. We harnessed this system to record arbitrary DNA sequences into a genomic CRISPR array in the form of spacers acquired from synthetic oligonucleotides electroporated into a population of cells overexpressing the CRISPR adaptation proteins Cas1 and Cas2. This enabled the recording of defined molecular events into a stable genomic locus over time and the storage of arbitrary information across a population of cells.

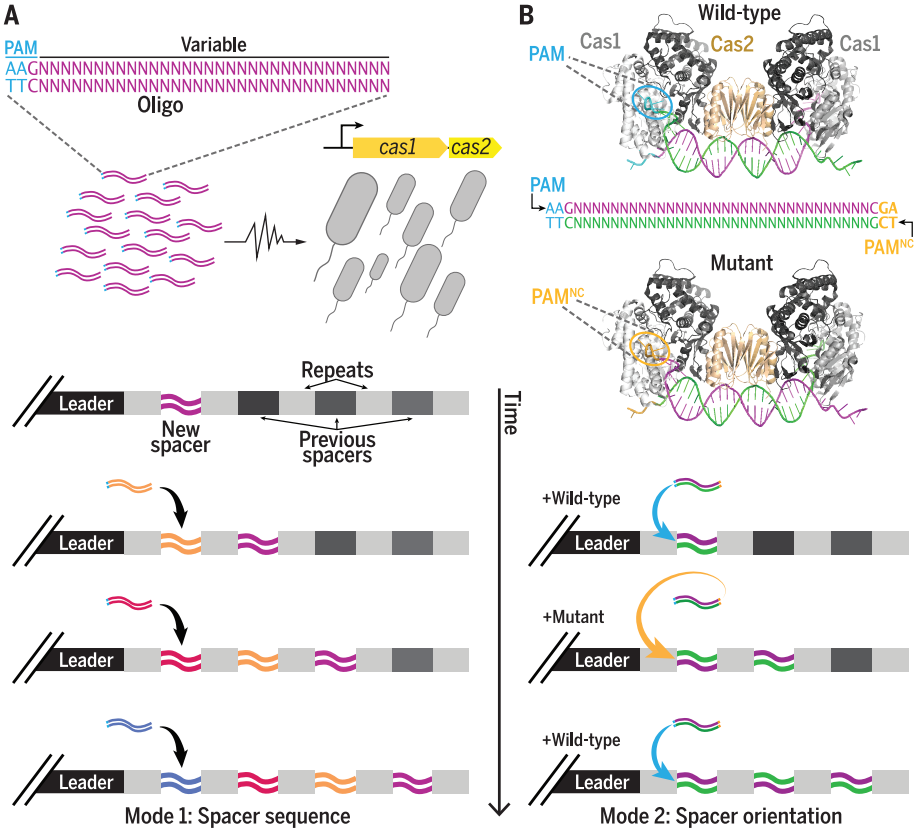
RESULTS: We show that the Cas1-Cas2 complex can be used in vivo to integrate synthetic DNA of a defined sequence into the *Escherichia coli* genome. We used this feature to examine the type I-E CRISPR-Cas spacer acquisition process and optimized the synthetic spacer design to achieve higher acquisition efficiency and specific integration orientation through the addition of an AAG protospacer adjacent motif (PAM). We then generated stable genomic recordings of multiple molecular events by electroporating sets of oligonucleotides over several days. These molecular records were read out with high-throughput sequencing and then decoded with a program that identified and faithfully reconstructed the temporal event order.

ON OUR WEBSITE

Read the full article at http://dx.doi.org/10.1126/science.aaf1175

Last, we used directed evolution to generate many Cas1-Cas2 mutants with modified PAM specificity (PAM^{NC}). By modulating expression of these mutant and wild-type Cas1-Cas2 complexes, we could dynamically control the orientation of spacer integration. This enabled us to record acquisition events in multiple modes. That is, information was encoded in both the temporal order of the spacers and the orientation in which they were integrated.

CONCLUSION: Our results establish a recording system that uses the nucleotide content, temporal ordering, and orientation of defined DNA sequences within a CRISPR array in order to encode arbitrary information within the genomes of a population of cells. Because information can be encoded in spacer nucleotide space (up to two bits per base) and in alternate modes, the system has the potential to record and permanently store higher capacities of information than any other synthetic biological system to date. This lays the foundation for an in vivo recording device that could be coupled with diverse molecular phenomena and used for applications that require tracing of long molecular histories. We also demonstrate that delivery of synthetic DNA substrates to a CRISPR-Cas adaptation system in vivo is a practical method to probe and adapt the system. ■



Two modes of encoding information into the CRISPR locus. (**A**) Oligonucleotides containing an AAG PAM and 32 variable bases were electroporated into cells overexpressing Cas1-Cas2 and inserted into the genomic CRISPR array. Delivery of oligos with distinct sequence over time generates a molecular record. (**B**) Cas1-Cas2 mutants identified through directed evolution alter the orientation of acquisition. Varying expression ratios of wild-type and mutant Cas1-Cas2 over time generates a record encoded in spacer orientation.

The list of author affiliations is available in the full article online.
*These authors contributed equally to this work.
†Corresponding author. Email: gchurch@genetics.med.harvard.edu
Cite this article as S. L. Shipman *et al.*, *Science* 353, aaf1175 (2016). DOI: 10.1126/science.aaf1175

Downloaded from http://science.sciencemag.org/ on July 28, 2016

RESEARCH ARTICLE

SYNTHETIC BIOLOGY

Molecular recordings by directed CRISPR spacer acquisition

Seth L. Shipman,[1,2,3]* Jeff Nivala,[1,3]* Jeffrey D. Macklis,[2] George M. Church[1,3]†

The ability to write a stable record of identified molecular events into a specific genomic locus would enable the examination of long cellular histories and have many applications, ranging from developmental biology to synthetic devices. We show that the type I-E CRISPR (clustered regularly interspaced short palindromic repeats)–Cas system of *Escherichia coli* can mediate acquisition of defined pieces of synthetic DNA. We harnessed this feature to generate records of specific DNA sequences into a population of bacterial genomes. We then applied directed evolution so as to alter the recognition of a protospacer adjacent motif by the Cas1-Cas2 complex, which enabled recording in two modes simultaneously. We used this system to reveal aspects of spacer acquisition, fundamental to the CRISPR-Cas adaptation process. These results lay the foundations of a multimodal intracellular recording device.

DNA has the potential to encode, preserve, and propagate information (*1*). The precipitous drop in DNA sequencing cost has now made it practical to read out this information with high throughput (*2*). However, the ability to write arbitrary information into DNA, in particular within the genomes of living cells, has been restrained by a lack of biologically compatible recording systems that can exploit anything close to the full encoding capacity of nucleic acid space.

A number of approaches aimed at recording information within cells have been explored (*3*). These systems can be broadly divided into those that alter transcription through feedback loops and toggles (*4*–*14*) and those that encode information permanently into the genome, most often using recombinases to store information via the orientation of DNA segments (*15*–*19*). Although the majority of these systems are effectively binary, efforts have also been made toward analog recording systems (*20*) and digital counters (*21*). Despite these efforts, the recording and genetic storage of little more than a single byte of information (*18*) has remained out of reach.

Immunological memory is essential to an organism's adaptive immune response and hence must be an efficient and robust form of recording molecular events in living cells. The CRISPR-Cas system is a recently understood form of adaptive immunity used by bacteria and archaea (*22*). This system records past infections by storing short sequences of viral DNA within a genomic array. These acquired sequences are referred to as protospacers in their native viral context and as spacers once they are inserted into the CRISPR (clustered regularly interspaced short palindromic repeats) array. New spacers are integrated into the CRISPR array ahead of older spacers (*23*). Over time, a long record of spacer sequences can be stored in the genomic array, arranged in the order in which they were acquired. Thus, the CRISPR array functions as a high-capacity temporal memory bank of invading nucleic acids.

We harnessed the CRISPR-Cas system to record specific and arbitrary DNA sequences into a bacterial genome. We could generate a record of defined sequences, recorded over many days and in multiple modalities. In exploring this system, we also elucidated fundamental aspects of native CRISPR-Cas spacer acquisition and leveraged this knowledge to enhance the recording system.

A type I-E CRISPR-Cas system accepts synthetic spacers in vivo

Overexpression of the *Escherichia coli* type I-E CRISPR-Cas proteins Cas1 and Cas2 is sufficient to drive acquisition of new spacers in a strain containing two genomic CRISPR arrays but lacking endogenous Cas proteins (BL21-AI) (*23*). We replicated this result (Fig. 1A) and similarly found that new spacers were consistently integrated into the first position of array I directly adjacent to the leader with a consistent size of 33 bases (fig. S1, A and B). These spacers were drawn in roughly equal number from the cell's own genome and from the plasmid used to overexpress Cas1 and Cas2 (Fig. 1B). Considering the overall DNA content of the cell, this ratio of genome-to-plasmid–derived spacers represents a substantial bias toward the plasmid as a protospacer source (*24*). Despite this bias, new spacers were drawn from a diverse range of sites around the genome and plasmid (Fig. 1C) and, besides the overrepresentation of a 5′ AAG protospacer adjacent motif (PAM), there was no way to predict a priori the full sequence of a new spacer without sequencing the expanded array.

To extend the function of the CRISPR acquisition system into a synthetic device for recording molecular events, it is necessary to direct the system to capture spacers of specific, defined sequence. In vitro, Cas1 and Cas2 can mediate integration of synthetic 33–base pair (bp) DNA oligos into plasmid-based arrays (*25*). We reasoned that similarly supplying an exogenous source of protospacers to the system within a cell might direct sequence-specific spacer acquisition in vivo. We therefore passaged an overnight culture of *E. coli* BL21-AI containing arabinose- and isopropyl β-D-1-thiogalactopyranoside (IPTG)–inducible Cas1 and Cas2 genes with or without arabinose and IPTG for 2 hours. We then electroporated the cells with a complementary pair of 33-base oligos (protospacer ps33), which matched the sequence of the most abundant M13-derived spacer found after phage infection of a native type I-E system (*26*). After incubating the cells for another 2 hours after transformation, we checked the genomic array for expansion and specific integration of the synthetic protospacer into the array by means of polymerase chain reaction (PCR) (Fig. 1D). By using the reverse sequence of the supplied oligo as the reverse primer, we also observed amplification of specifically sized PCR products that confirmed acquisition of the oligo-supplied sequence when Cas1 and Cas2 were induced or (more weakly) uninduced, but never for the case in which the oligos were not supplied. We confirmed that the specific ps33 nucleotide sequence was present within a fraction of the expanded arrays by means of Sanger sequencing. These results demonstrate that the CRISPR-Cas system acquired a sequence-specific spacer.

To better understand both the properties of this synthetic system as well as the fundamental properties of Cas1-Cas2–mediated spacer acquisition, we altered the oligos that we provided via electroporation. The system required both complementary strands for acquisition, and the double-stranded protospacer could insert in either direction (Fig. 1E). We modified the 5′ ends of the oligos with phosphorothioate bonds to help resist degradation by cellular nucleases but found no differences in acquisition efficiency (Fig. 1E). We tested whether RNA could serve as a protospacer by supplying either one or both of the oligo strands as RNA but detected no sequence-specific integration of RNA oligos (fig. S1D).

To investigate these results more quantitatively, we performed a PCR across the array (as in Fig. 1D) and subjected the resulting amplicon to high-throughput sequencing on an Illumina MiSeq platform. We quantified the percentage of all arrays that were expanded at the completion of an experiment, as well as the spacer source. Coupled with quantitative PCR, we generated a time course of spacer acquisition (Fig. 1F). Sequence-specific acquisitions occurred as early as 20 min after electroporation, reaching ~4% of all arrays by 2 hours.

[1]Department of Genetics, Harvard Medical School, 77 Avenue Louis Pasteur, Boston, MA 02115, USA. [2]Department of Stem Cell and Regenerative Biology, Center for Brain Science, and Harvard Stem Cell Institute, Harvard University, Bauer Laboratory 103, Cambridge, MA 02138, USA. [3]Wyss Institute for Biologically Inspired Engineering, Harvard University, Cambridge, MA 02138, USA.
*These authors contributed equally to this work. †Corresponding author. Email: gchurch@genetics.med.harvard.edu

Downloaded from http://science.sciencemag.org/ on July 28, 2016

The oligo concentration required to achieve spacer acquisition was determined by testing a twofold dilution series (Fig. 1G and fig. S1E). Whether oligos were delivered or acquired as spacers had no effect on the genome- or plasmid-derived spacers. Thus, protospacer availability in the cell may be a limiting factor in spacer acquisition. On the other hand, the addition of an additional CRISPR array on the expression plasmid had little to no effect on the acquisition frequency of new spacers into the endogenous genomic array (Fig. 1G). Like genome- and plasmid-derived spacers, the synthetic spacers were inserted into the first (or occasionally first and second) positions of the array, and the great majority were of 33 bases (Fig. 1, H and I). Loss of previously acquired spacers has been reported both in the presence (*27*, *28*) and absence (*29*, *30*) of selective pressure. Although our analysis was restricted to the leader-proximal spacers, we did find rare instances in which the previous first spacer was deleted (0.096% of arrays sequenced ±0.012 SEM).

PAMs modify the efficiency and directionality of spacer acquisition

Data from sequencing millions of expanded arrays showed that genome- and plasmid-derived protospacers were drawn in equivalent numbers from the forward and reverse strands overall, with the only apparent bias being toward the genomic origin of replication (Fig. 2A). Similarly, oligo-derived protospacers were found in equal proportions in the forward and reverse orientation in the array (Fig. 2B). When we further examined the context of the genomic- and plasmid-derived protospacers, we found strong evidence for a PAM on the 5′ end of the protospacer consisting of two adenines at positions −2 and −1 from the spacer and a strong bias for a guanine as the first spacer base (Fig. 2C). This is largely consistent with previous characterizations of the *E. coli* type I-E system (*31*, *32*). An interior sequence motif at the 3′ end of the spacer termed the acquisition-affecting motif (AAM) has also been reported for this system (*31*). We found spacer sequences that are consistent with the presence of this interior motif, but the frequency of its occurrence is minor compared with the 5′ PAM.

Although there is no bias in forward- or reverse-strand–derived protospacers from the genome or plasmid on the whole, a sharper picture emerged at the level of individual nucleotides. For example, examining one small stretch of the plasmid (~550 bases), asymmetric peaks of spacer coverage—that is, the cumulative count of each time a given nucleotide was observed within an acquired spacer—emerged (Fig. 2D). Plotting the forward and reverse PAMs along the same stretch of plasmid revealed that in addition to biasing toward specific sequences for acquisition, the PAM also

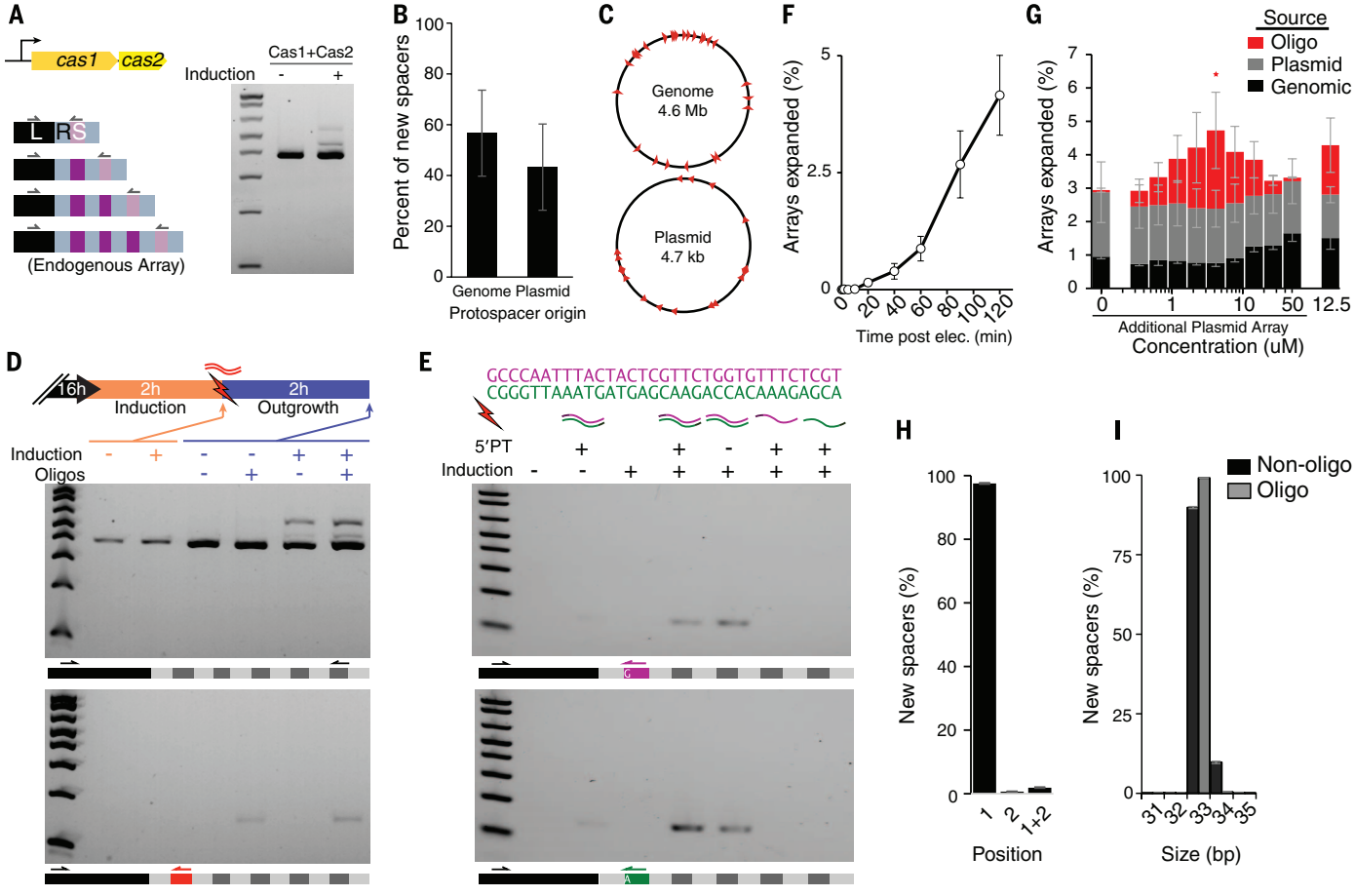


Fig. 1. Acquisition of synthetic spacers. (**A**) Schematic of the minimal elements of the type I-E CRISPR acquisition system used, including Cas1, Cas2, and array with leader (L), repeat (R), and spacer (S) along with PCR detection of an expanded array after the overnight induction of Cas1-Cas2. (**B**) Origin of new spacers (plasmid or genome), mean ± SEM. (**C**) Genome- and plasmid-derived spacers after overnight induction are mapped back to the approximate location of their protospacer (marked in red). (**D**) Array expansion (top) and specific acquisition of synthetic oligo protospacer (bottom) after electroporation. Top schematic shows the experimental outline. Schematics under each gel show specific PCR strategy. (**E**) Sequence-specific acquisition in either the forward (top) or reverse (bottom) orientation after electroporation with various single- and double-stranded oligos. 5′PT indicates phosphorothioate modifications to the oligos at the 5′ ends. (**F**) Time course of expansion after electroporation, mean ± SEM. (**G**) Percent of arrays expanded by spacer source as a function of electroporated oligo concentration, mean ± SEM. (**H**) Position of new spacers relative to the leader, mean ± SEM. (**I**) Size of new spacers in base pairs, mean ± SEM. All gels are representative of ≥3 biological replicates; * $P <$ 0.05. Additional statistical details are provided in table S1.

Downloaded from http://science.sciencemag.org/ on July 28, 2016

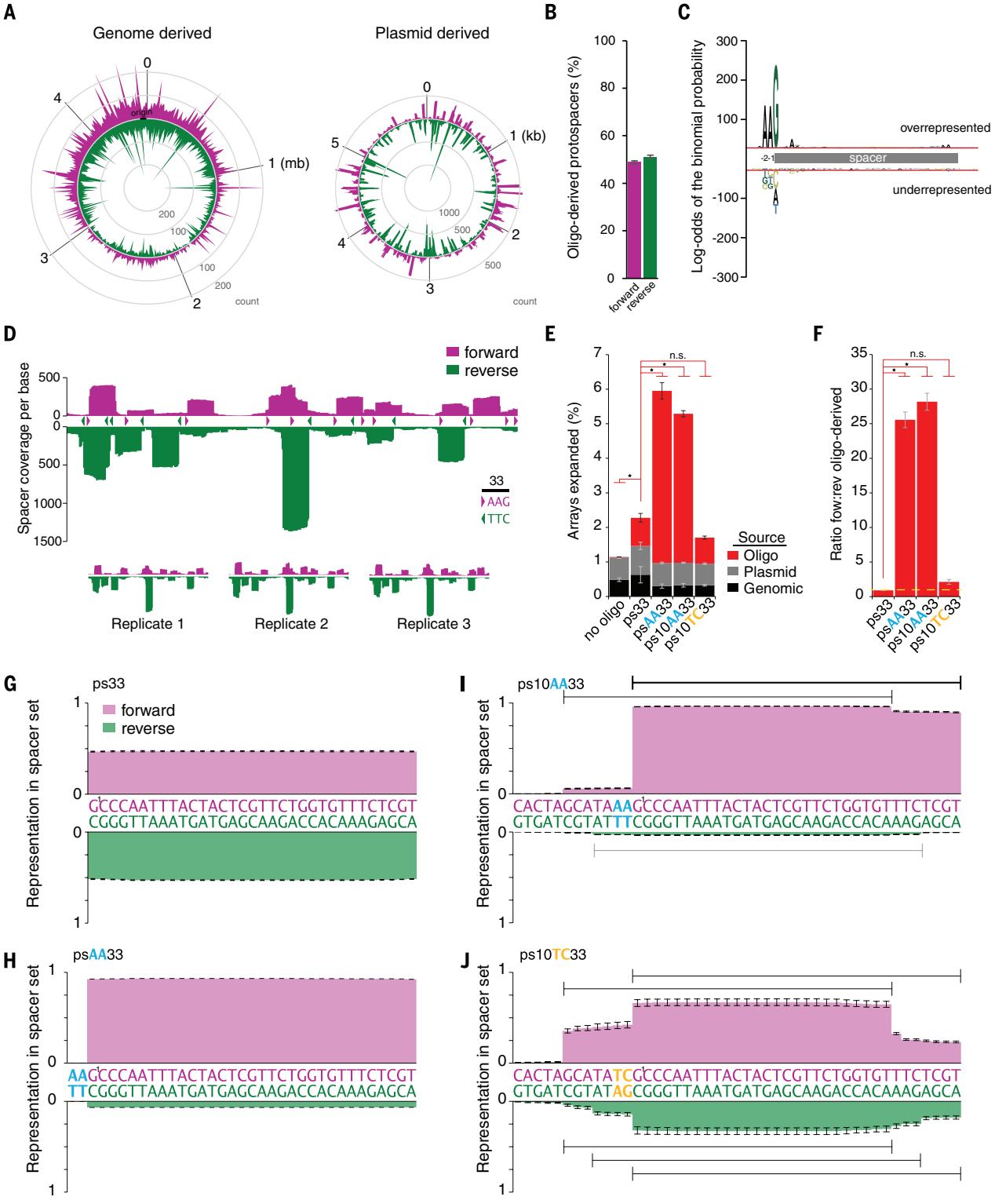


Fig. 2. PAMs modify the efficiency and orientation of spacer acquisition. (**A**) Genome-derived (count/10 kb) and plasmid-derived (coverage/base) spacers mapped to their protospacer location on the forward (purple) or reverse (green) strands. (**B**) Direction of oligo-derived spacers in the forward (purple) or reverse (green) orientation, mean ± SEM. (**C**) Representative sequence pLOGO (*46*) generated based on 896 distinct genome- and plasmid-derived protospacers. Five bases of the protospacer are included at each end of the spacer. (**D**) Plot of the summed spacer coverage mapped to the plasmid among three replicates at each nucleotide for a 553-nucleotide stretch. Carrots demarcate canonical PAMs on the forward (purple) or reverse (green) strand. Scale bar, 33 bases. Individual replicates are shown below. (**E**) Percent of arrays expanded by spacer source for different oligo protospacers, mean ± SEM. (**F**) Ratio of oligo-derived spacers acquired in the forward versus reverse orientation for different oligo protospacers, mean ± SEM. (**G** to **J**) Normalized representation of oligo-derived spacers by base acquired in the forward and reverse direction for each oligo. Bars in (I) and (J) are 33 bases long to show dominant and minority spacers drawn from the oligo protospacers. For all panels, * $P < 0.05$. Additional statistical details are provided in table S1.

Downloaded from http://science.sciencemag.org/ on July 28, 2016

specified the orientation of integration into the array. Although nearly every protospacer that contained a PAM was acquired as a spacer, not all were acquired at the same frequency (Fig. 2D).

The presence of Chi sites—an eight-base motif in which double-strand break repair is more likely to occur—within a genome or plasmid biases the frequency of protospacer acquisitions (*24*). However, we wondered whether the sequence of the protospacer itself might also bias acquisition frequency. We ranked every PAM (AAG)–containing potential protospacer in the plasmid according to the frequency at which it was acquired into the genomic array (fig. S2A). We searched for characteristics among protospacers, including GC percentage and free energy, that might explain the difference in acquisition frequency, but failed to identify a correlation (fig. S2, B and C). For a direct test, we selected and synthesized three protospacer sequences (including their 15-bp flanking regions): one each from the high (psH), middle (psM), and low (psL) end of the frequency spectrum (fig. S2A). We then electroporated each of these oligo protospacers into cells expressing Cas1-Cas2 from an alternate plasmid that did not include these particular sequences. psL was acquired much less frequently than psH or psM (fig. S2F). To determine whether this was caused by the sequence of the spacer itself or a flanking region, we swapped the 15-bp flanking regions of psH with those of psL and vice versa (psH/L and psL/H, respectively). Again, the psL/H spacer was acquired at a lower frequency than was psH/L, independent of the flanking regions. These results indicate that the sequence of the protospacer itself influences the efficiency of acquisition. We do not know, however, the mechanism of this effect, whether by a direct effect on the acquisition process itself or by indirect effects such as sequence-dependent interactions with endogenous nucleotides, competing proteins, or degradation.

Given that spacers are selected from the genome and plasmid according to an adjacent sequence, we wondered whether the inclusion of a PAM in our synthetic protospacer ps33 would alter acquisition frequency. We designed three additional oligo protospacers: psAA33, in which two adenines were included at the 5′ end of ps33 to create the entire canonical AAG PAM; ps10AA33, which includes an additional 10 5′ nucleotides; and ps10TC33, in which the AA of the PAM was mutated to TC to create a noncanonical PAM (PAM^{NC}). Using these oligos, we found that the inclusion of a PAM greatly increased the efficiency of sequence-specific acquisition (Fig. 2E). Whether preceded by 10 extra nucleotides or not, oligos with the AAG PAM (psAA33 and ps10AA33) were acquired at greater than five times the frequency of those that did not include a PAM (ps33). Conversely, including the TCG PAM^{NC} did not change acquisition frequency relative to ps33 (Fig. 2E).

In line with what has been previously observed for the PAM motif in CRISPR adaptation—that it is consistently localized to the leading rather than trailing end of the integrated spacer (*24*, *31*, *33*–*36*)—the inclusion of a PAM also altered the orientation frequency of oligo-derived spacer acquisition. Whereas ps33 and ps10TC33 were acquired equally in both orientations, psAA33 and ps10AA33 were acquired almost exclusively in the forward orientation (Fig. 2, F to J, and fig. S3A). Consistent with the type I-E preference for an AAG PAM, psAA33 and ps10AA33 were consistently inserted with nucleotide G^1 as the first base of the spacer (Fig. 2, H and I). In contrast, ps10TC33 lacked a single dominant spacer product and was inserted at several different $PAMs^{NC}$ (Fig. 2J). We verified that both Cas1 and Cas2 were necessary for synthetic spacer integration, whereas Cas2 nuclease activity was not required (fig. S3, B and C) (*25*). Therefore, the inclusion of a PAM in synthetic protospacers dictates both the efficiency and orientation of the spacer that is acquired by the Cas1-Cas2 complex.

A molecular recording over time

We tested whether we could harness the acquisition of specific spacer sequences to record a series of synthetic spacers into a population of cells over time. As an initial test, we recorded three unique elements (1 × 3) into a single culture of *E. coli* by sequentially electroporating a series of three different oligo protospacer sequences into the culture, over a period of 3 days (one protospacer each day) (fig. S4A). After sequencing a population of the arrays on day 3, we could reconstruct the order in which the spacers were delivered (fig. S4, B and C, and materials and methods). To further probe the limits of this system, we recorded 15 distinct elements (3 × 5): three sets of five protospacers, electroporated three at a time over 5 days (Fig. 3A). The analysis of both the 1 × 3 and 3 × 5 recordings are conceptually similar, so we will discuss the latter in detail (fig. S4B and Fig. 3B, respectively).

For the 3 × 5 recording, all oligo protospacers consisted of 35 nucleotides, beginning with a 5′ AAG PAM followed by a five-base barcode (specific to each of the three sets) and 27 more bases (specific to each of the 15 protospacers). At the end of the 3 × 5 recording, nearly a quarter of all arrays in the cell population contained at least one oligo-derived spacer, with spacers from each round of electroporation represented in roughly equivalent proportions (Fig. 3, C and D). Individual variations among the spacer acquisition frequency were more heavily driven by spacer nucleotide sequence than by the round in which they were acquired (Fig. 3E), whereas loss of recorded spacers after acquisition was rare (0.076% ± 0.182 SEM).

Because of the low probability of acquiring spacers from every round in any single array (Fig. 3D), successful readout of the recording required analysis of a population of arrays. Therefore, we sequenced the first three spacers of each array (moving in from the leader) and considered only the order of pairs of newly acquired spacers (Fig. 3B). For any given synthetic spacer pair within the same set, the order should follow a predictable rule: Among all arrays that contain any two new spacers, a spacer electroporated in an earlier round will always be found further from the leader than a spacer introduced at a later round. We also gained information by considering the arrangement of oligo-derived spacers in relation to newly acquired genome- and plasmid-derived spacers. Because the endogenous spacers will accumulate over time, synthetic spacers from an earlier round will be paired more often with a new genome/plasmid spacer in one direction (toward the leader) than in the other (relative to the synthetic spacer), and vice versa for oligo-derived spacers from a later round. With five possible spacers (in each set), we considered all possible pairwise comparisons and generated 15 ordering rules from which we can reconstruct the order of the entire set (Fig. 3B). We took the sequences of arrays after the completion of the 3 × 5 recording and passed them through an algorithm that, with the only sequence-based input being the sequence of the CRISPR repeat, would predict all oligo-derived spacer sequences, assign them to a set according to the barcodes, and then test all possible permutations of the sequence against the 15 ordering rules. For each set, only one permutation satisfied all 15 ordering rules, and in every case, that permutation matched the actual order of electroporated oligos (Fig. 3F). Although we analyzed ~2 million reads for each replicate, we found that order could be correctly reconstructed in most cases with 20,000 reads or fewer. Thus, we could reliably record and read out the 15-element recording.

Cas1-Cas2 PAM recognition can be modified

The ability to control not only the sequence of new spacers but also the orientation of new spacer integration would enable recording of information in multiple modalities simultaneously. Because the addition of a 5′ AAG PAM on our synthetic spacers controlled the orientation of new acquisitions (Fig. 2F), we sought to modify integration orientation by altering PAM recognition of Cas1-Cas2. To do this, we performed the directed evolution approach shown in Fig. 4A. First, we generated a large library of random Cas1-Cas2 mutants by means of error-prone PCR (fig. S5, A and B) and inserted this library into a plasmid upstream of a minimal CRISPR array. After cloning the plasmid library into BL21-AI, we induced and transformed mutants with a protospacer bearing the canonical 5′ AAG PAM on the forward strand and a noncanonical 5′ TCG PAM^{NC} on the reverse strand. After outgrowth, we selected mutants using a forward primer ahead of the Cas1-Cas2 mutant genes and a reverse primer matching the PAM^{NC} spacer sequence in order to yield specific amplification of only those mutants that had acquired the spacer in the (reverse) PAM^{NC} orientation. A subset of these selected mutants were then tested for PAM specificity, and a separate subset were subjected to another round of selection for refinement before testing. For testing, individually selected mutant clones were induced overnight, and their expanded arrays were analyzed by means of sequencing. Specifically, we analyzed the PAMs of the all genome- and plasmid-derived spacers to determine what, if any, PAM specificity remained. Wild-type Cas1-Cas2 acquires spacers from AAG PAM protospacers at nearly the

Downloaded from http://science.sciencemag.org/ on July 28, 2016

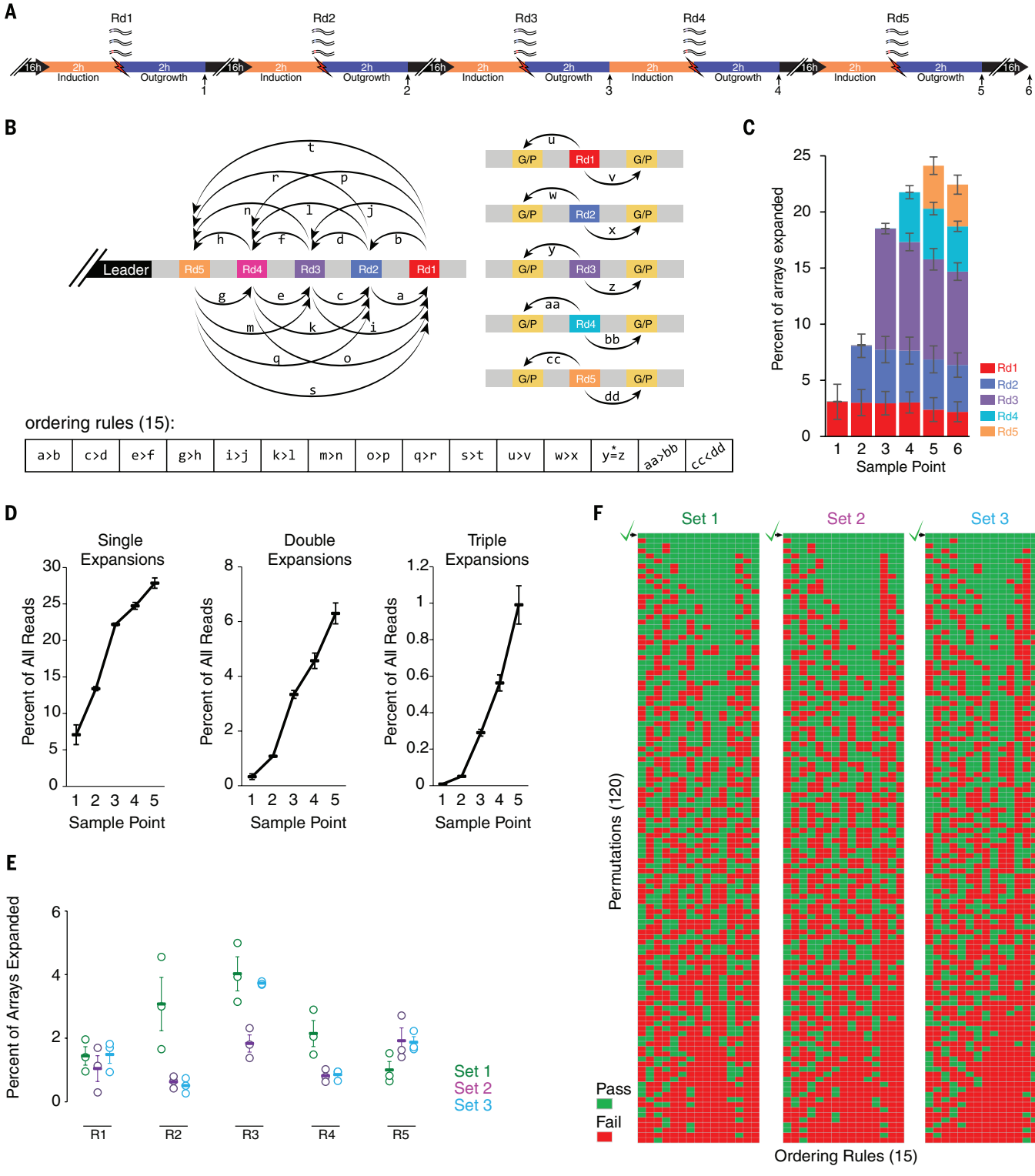


Fig. 3. A molecular recording over time. (**A**) Experimental outline of the 3 × 5 recording. Over 5 days, three sets of five oligo protospacers (15 elements) were electroporated (one protospacer from each of the three sets each day) into cells expressing Cas1-Cas2. Time points at which cells were sampled for sequencing are numbered 1 to 6. (**B**) Schematic illustrating all possible pairwise ordering of new spacers. G/P denotes a spacer derived from the genome or plasmid. Ordering rules are shown below. In the case of $y = z$, asterisk indicates a tolerance within ±20% of the mean of both values. (**C**) At each of the six sample points [marked in (A)], percent of all arrays expanded with synthetic spacers from each of the indicated rounds, mean ± SEM. (**D**) Single, double, and triple expansions for each round, mean ± SEM. (**E**) Percent of all expansions at sample point six, broken down by electroporation round and set. Open circles are individual replicates; filled bars are mean ± SEM. (**F**) Results of ordering rule analysis for one replicate across each set. For all 120 permutations, results of the tested rule are shown (green indicates pass, red indicates fail). For all sets, only one permutation passed all rules and in every case that permutation matched the actual order in which the oligos were electroporated (as indicated by check mark). Additional statistical details are provided in table S1.

Downloaded from http://science.sciencemag.org/ on July 28, 2016

same frequency as from all other (non-AAG) PAM protospacers combined (Fig. 4B). In contrast, the majority of mutants we selected acquired non-AAG protospacers at a greater frequency than that of AAG protospacers (Fig. 4B). There was no gain in non-AAG acquisition frequency from the extra step of refinement (fig. S5C), so mutants from both subsets are shown together (Fig. 4B and fig. S5D).

To visualize shifts in PAM specificity, we plotted a heat map showing the normalized frequency of observed PAMs among all potential PAMs for wild-type Cas1-Cas2 and several selected mutants (Fig. 4C). Wild-type Cas1-Cas2 had strong selectivity for the canonical AAG PAM. A minority of mutants also retained (m-24) or even increased (m-27) this preference. However, many more mutants showed reduced or, in the case of the three mutants shown (m-74, m-80, and m-89), nearly no specificity for the canonical PAM. From the sequence of these selected mutants, we chose a subset of single-point mutations for follow-up analysis on the basis of repeated observations in the data set or location in the crystal structure of the Cas1-Cas2 complex (Fig. 4E and table S3) (*37*–*39*). Most of the single-point mutants tested in isolation also reduced the PAM specificity compared with that of wild type (Fig. 4D and fig. S5D). These results demonstrate that PAM recognition by the Cas1-Cas2 complex can be modified by many different mutations without drastically reducing spacer acquisition efficiency.

Recording in a second modality

As a proof of concept, we selected a PAM^{NC} Cas1-Cas2 mutant (m-89) (Fig. 4C and fig. S5D) to add an extra modality to the 1 × 3 recording (fig. S4). We subjected bacteria to three sequential rounds of electroporation, with each oligo protospacer

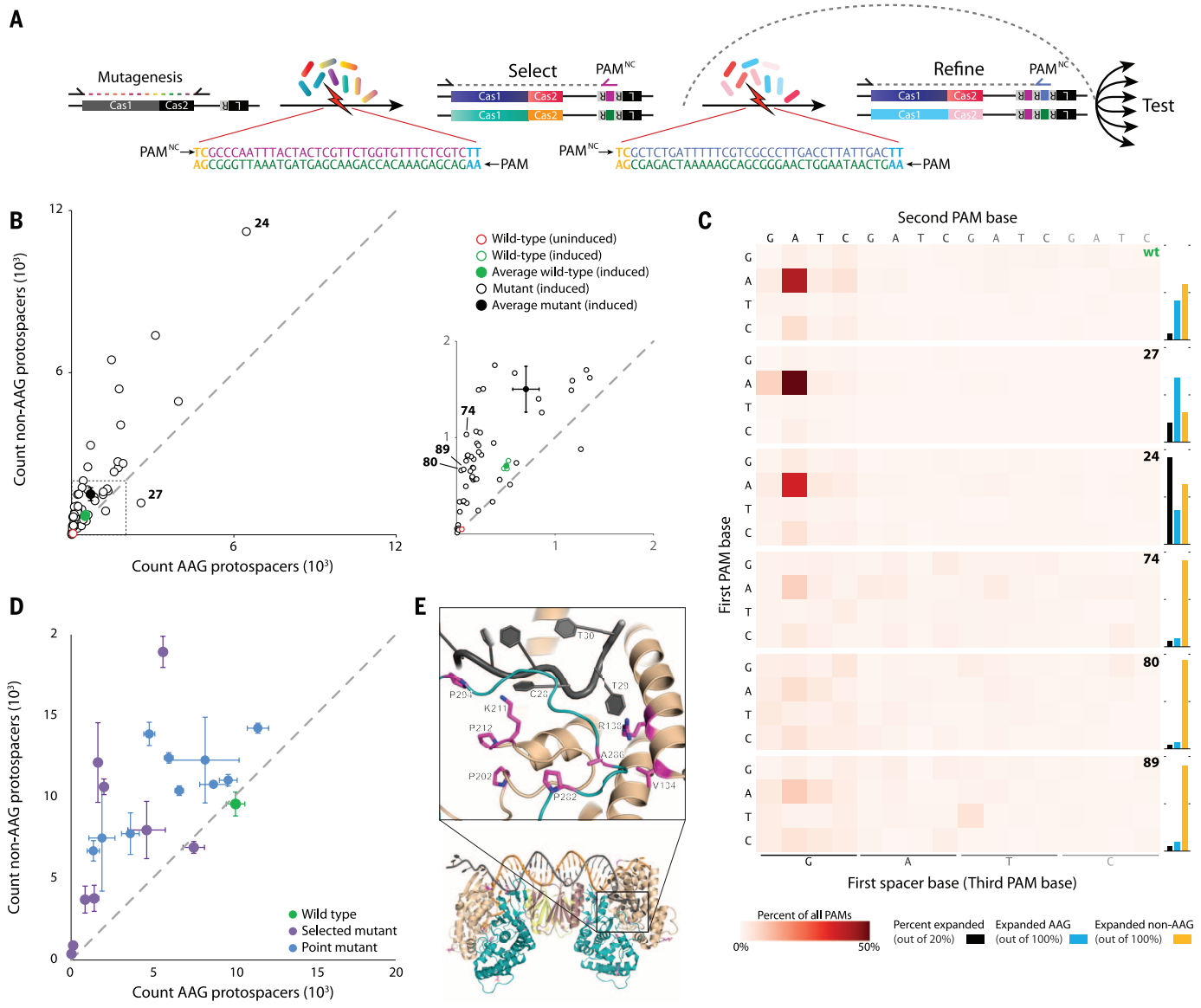


Fig. 4. Directed evolution of PAM recognition. (**A**) Schematic of the directed evolution. (**B**) Testing of selected mutants, plotting 5′ AAG versus non-AAG PAM protospacers normalized to count per 100,000 sequences. Scatter plot shows 65 induced mutants (open black circles), three induced wild-type replicates (open green circles), an uninduced wild type (open red circle), the average of the induced mutants (filled black circle), and the average of the induced wild types (filled green circle) ± SEM. Scatter plot to the right is an inset of the larger plot. (**C**) Heatmap of protospacer PAM frequency over the entire sequence space for wild-type Cas1-Cas2 (wt), mutants that increase or maintain AAG PAM specificity (m-27 and m-24), and mutants that lose AAG PAM specificity (m-74, m-80, and m-89). Numbers at top right correlate to numbers in (B). (**D**) A subset of selected mutants reassayed in triplicate as well as a subset of single-point mutants chosen from the original selection. All points are the average of three replicates ± SEM. (**E**) Crystal structure of Cas1-Cas2 complex bound to a protospacer (*38*). Inset highlights, in purple, residues in the Cas1 active site that (when mutated) decrease PAM specificity. The protospacer PAM complementary sequence (T30 T29 C28, numbering as in PDB ID 5DQZ) is also noted. Additional statistical details are provided in table S1.

Downloaded from http://science.sciencemag.org/ on July 28, 2016

containing a 5′ AAG PAM on the forward strand and a 5′ TCG PAM^{NC} on the reverse (Fig. 5A). We controlled expression of wild-type Cas1-Cas2 and m-89 using different inducible promoters (pLTetO and pT7*lac*, respectively) on the same plasmid (Fig. 5B). We split the bacteria between two conditions, each alternating between T7*lac* and tet induction from round to round. We found that cells of both conditions acquired spacers from each round at similar frequencies, indicating that transcription and integration activity of the wild-type and m-89 Cas1-Cas2 were both adequate (Fig. 5C). At the completion of the recording, we compared the orientation of each spacer between the two conditions. The ratio of forward- to reverse-oriented spacers shifted toward PAM^{NC} (reverse) during tet induction (Fig. 5, D and F). After normalization for the total spacer orientation ratio for each spacer, we could clearly discriminate which cultures had been exposed to each inducer at each time point on the basis of only the direction of integration (Fig. 5G). Thus, this system can simultaneously record in two modalities.

Discussion

We developed a CRISPR-Cas–based system to record molecular events into a genome in the form of essentially arbitrary synthetic DNA sequences. Although the information is only partially encoded within any given cell, the complete record remains distributed across a population of cells. To read out the recordings, we used high-throughput sequencing and only considered the pairwise order of any two new spacer sequences within single CRISPR arrays. From these many binary comparisons, a complete record of events could then be assembled, faithfully decoding the distributed memory fully preserved within the cell population. An important consideration of this system is that despite the necessary destruction of cells for readout at the end of the recording, the encoding process is not destructive. Thus, as

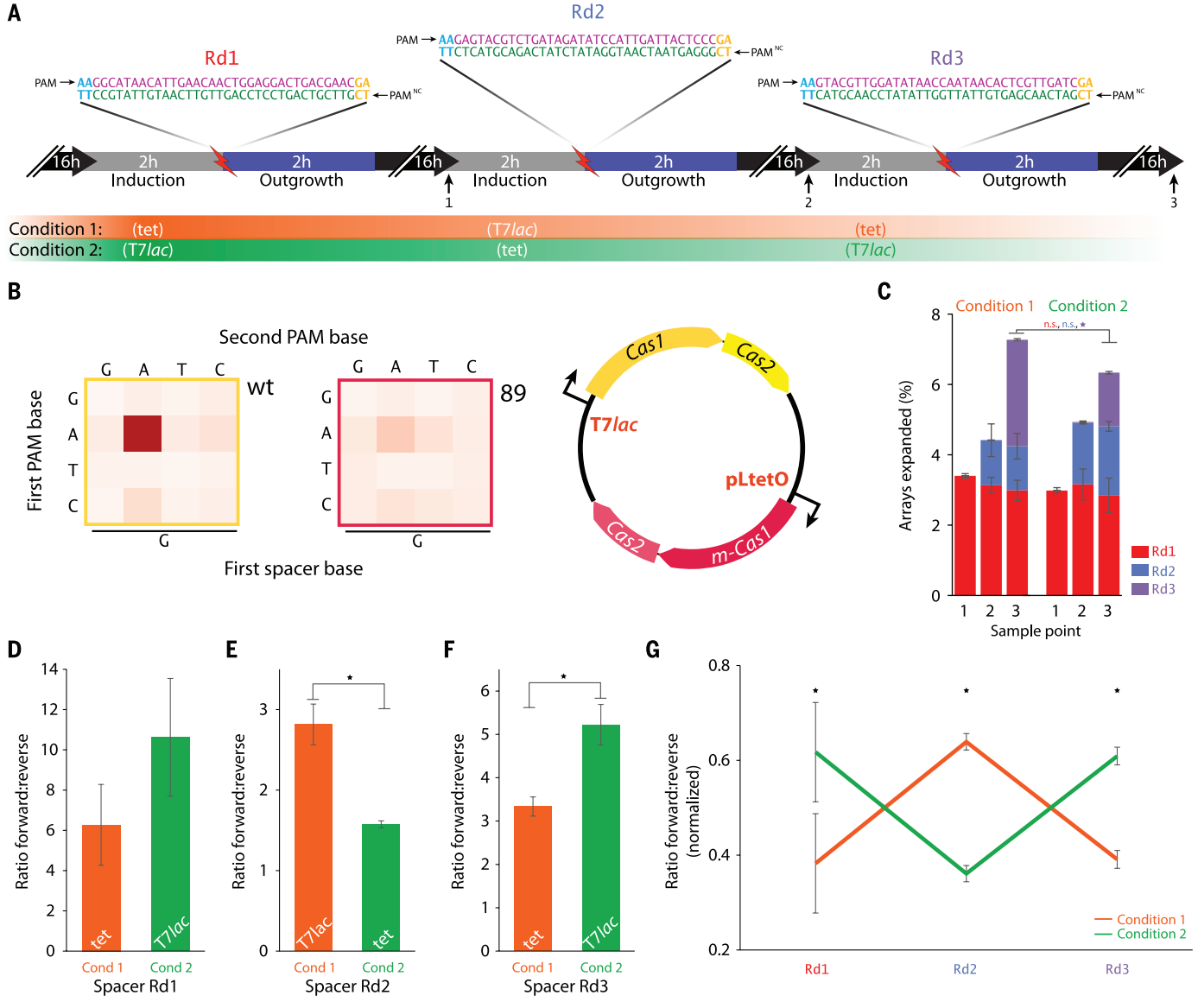


Fig. 5. Recording in an additional mode. (**A**) Outline of the recording process. Three different synthetic protospacers (each containing a 5′ AAG PAM on the forward strand and a 5′ TCG PAM on the reverse) were electroporated over 3 days (one protospacer each day) into two bacterial cultures under different induction conditions (shown below timeline). Sampling time points are numbered 1 to 3. (**B**) Schematic of the plasmid construct used, showing wild-type and PAM^{NC} mutant (m-89) Cas1-Cas2 driven by independently inducible promoters (T7lac and pLtetO, respectively). The heatmap shows 5′ PAM specificity for wild type (boxed in yellow) and mutant m-89 (boxed in red). (**C**) At each of the three sample points [marked in (B)], percent of expanded arrays with spacers from each of the indicated rounds for the two conditions, mean ± SEM. (**D** to **F**) Ratio of synthetic spacers acquired in the forward versus reverse orientation for each round under each condition, mean ± SEM. (**G**) Ratio of forward to reverse integrations normalized to the sum of both possible orientations for each of the two conditions, mean ± SEM. For all panels, *P < 0.05. Additional statistical details are provided in table S1.

Downloaded from http://science.sciencemag.org/ on July 28, 2016

opposed to sequential sampling of a population to generate a record of events, the current approach does not require that cells be destroyed while the experiment is ongoing. Moreover, because the recording is distributed across a population, only a fraction of the population needs to be sampled to retrieve the recording.

We uncovered details of the native CRISPR-Cas adaptation system. Integration of synthetic oligo sequences in vivo by the Cas1-Cas2 protein complex enabled us to directly assess detailed aspects of protospacer acquisition. Because the frequency of spacers acquired from the genome and plasmid is largely unaltered in the presence of oligo-derived acquisition (Figs. 1G and 2E), we conclude that the availability of adequate protospacers is likely one limiting aspect of the adaptation system. The presence of a 5′ AAG PAM modulated both the frequency and orientation of spacer acquisition, and the interior sequence of the protospacer influenced acquisition efficiency.

Directed evolution allowed us to experimentally modify PAM recognition of the Cas1-Cas2 complex, which enabled us to generate a record in multiple modalities simultaneously. This directed evolution method required no structural information and should be generally applicable to evolving other activities of CRISPR-Cas proteins by coupling them to the spacer acquisition process (for example, modifying target site specificity).

There are challenges to directly comparing between different cellular recording approaches. For instance, some are rewritable (*4*–*7*, *9*–*14*, *17*, *20*, *21*), whereas others, similar to our system, create permanent records (*15*, *17*–*21*). To date, the highest permanent storage capacity of a synthetic in vivo recording device was achieved by using 11 orthogonal recombinases, capable of 2^{11} (2,048) distinct states, capturing 1.375 bytes of information within a single cell (*18*). In our 3 × 5 recording, we encoded 15 individual elements within a population of cells. However, because this system can record arbitrary defined sequences, the number of possible states is expanded dramatically. With an invariable G at the beginning of the spacer and a five-base set identifier, 27 bases remain that could encode information, yielding 4^{27} possible distinct sequences per spacer. It was possible to encode the order within each set to at least five elements, resulting in a specific state capacity for each set based on the permutation $P(4^{27},5)$ = 1.9×10^{81}, or 5.7×10^{81} combining the three sets and assuming set independence. If we include interdependence between each set, total distinct states would rise to $(4^{27})^{15}$ or $\sim 7 \times 10^{243}$. As a point of comparison, the number of atoms in the observable universe is estimated at 1×10^{80}.

Moving from theoretical to practical considerations, the information capacity of a given recording in our system depends on the degree to which the sequence of the protospacer is constrained. If there are no sequence constraints on the protospacer, and thus any arbitrary sequence is available, then the 15 recorded spacers (in the 3 × 5 recording paradigm) each contain 27 bases of recording potential at four bases per byte, yielding 101.25 bytes per recording. Throughout our experiments, we were able to vary the nucleotide identity at every one of these 27 positions in our oligo protospacers. However, we have not explicitly tested, nor is it practical to test, all possible protospacers for viability. Moreover, we have shown that the sequence of the protospacer can influence acquisition frequency, so it is reasonable to assume that not all possible sequences will be suitable protospacers.

We can set an absolute lower limit on the information capacity of the 3 × 5 recording presented here by assuming that the particular sequences that we used in the recording are the only possible sequences that could be used. In that case, we can encode information only in the order of the sequences recorded in three sets of five possible spacers, disallowing repetition. In this case, the bits per set is given by $\log_2[P(5,5)]$ = ~6.9 bits or ~2.59 bytes, summing all three sets.

However, to assume that no other sequences are allowable is conservative. For instance, considering just the new spacers that were observed in this work, there were 48,773 genome-derived, 186 plasmid-derived, and 23 oligo-derived spacers of 33 bases that included an AAG PAM in their protospacer context. Using this pool of validated sequences in our recording paradigm would yield $\log_2[P(48982,5)]$ = ~77.9 bits per set, or ~29.21 bytes of potential encoding capacity for all three sets. Again, this estimation is certainly overconstrained because these sequences are drawn from an incredibly small subset of all possible sequences. Nonetheless, in the interest of being cautious, we can say that the recording capacity of the 3 × 5 paradigm is not less than 2.59 bytes nor more than 101.25 bytes and likely falls somewhere between 29.21 and 101.25 bytes. By also considering the ability to control spacer orientation (an extra modality), we could potentially encode an additional 5 bits per set. Of course, this only reflects the information of our current recordings, which we arbitrarily limited to 15 spacers. Native species have been found with as many as 458 spacers in a single cell (*S. tokodaii*) (*40*). This illustrates the potential space to encode complex biological phenomena, such as the transcriptional time course of many genes in a cell by means of reverse transcription of mRNA protospacers (*41*). We anticipate that such a recording system will be valuable in applications that require tracing long histories of in vivo cellular activity, including development, lineage, and activity in the brain (*42*, *43*).

Materials and methods

Bacterial strains and culturing conditions

Expression and new spacer acquisition were carried out in BL21-AI cells. Unless otherwise specified, cells were grown in Luria Broth (LB) shaking (240 rpm) at 37°C. Genes expressed from the T7lac promoter were induced using L-arabinose (Sigma-Aldrich) at a final concentration of 0.2% (w/w) from a 20% stock solution in water and isopropyl-beta-D-thiogalactopyranoside (IPTG; Sigma-Aldrich) at a final concentration of 1mM from a 100mM stock solution in water. Cas mutants expressed from the pLtetO promoter were induced via anhydrotetracycline (aTc; Clontech) at a final concentration of 214nM from a 214μM stock in 50% ethanol. While expressing from the pLtetO promoter, 0.2% glucose was added to reduce unintended background expression from the T7lac promoter. For new spacer acquisition experiments not involving oligo-derived spacers, cells were induced and grown overnight (16h). All cloning was performed using NEB5α cells.

Cloning and library construction

Plasmid containing Cas1 and Cas2 under the expression of a T7lac promoter (pWUR 1+2) was a generous gift of Udi Qimron (*23*). A variant of this plasmid was created harboring an additional CRISPR array based on an array found in the K12 strain. This additional array was synthesized and cloned into pWUR 1+2 to generate pWUKI 1+2. Cas1+2 were cloned into pRSF-DUET for a different plasmid context (pRSF-DUET 1/2). Cas1 and Cas2 were extracted from pWUR 1+2 by PCR and re-cloned into the same plasmid separately. In the case of Cas1, the selection was also changed in this step from spectinomycin to ampicillin to create pWURA Cas1 and pWUR Cas2. The point mutation E9Q was introduced into Cas2 by PCR to generate pWUKI Cas1+Cas2 E9Q. Similarly, point mutants of Cas1+2 based on mutants from the directed evolution experiment were created by PCR. Mutant 89 from the directed evolution experiment was cloned into pWUR 1+2 along with a terminator, pLtetO, and the tetR repressor from pJKR-H-tetR (*44*) to create pWUR 1+2 tetO mut89. Mutant library was created via error-prone PCR using GeneMorph II Random Mutagenesis Kit (Agilent) and cloned into ElectroTen-Blue ultracompetent cells (Agilent) before being transferred to the expression strain (BL21-AI). For additional details see plasmid table (table S2).

Oligo protospacer electroporation

For spacer acquisition experiments involving oligo-derived spacers, cells were first grown overnight from individual plated clones. In the morning, 100μl of the overnight culture was diluted into 3ml of LB, with induction components as dictated by the experiment. Cells were grown with inducers for 2h. For an individual experimental condition, 1ml of this culture was pelleted and re-suspended in water. Cells were further washed by two additional pelleting and re-suspension steps, then pelleted a final time and re-suspended in 50μl of a 3.125μM solution of double stranded oligonucleotides (unless otherwise noted) synthesized by IDT (Integrated DNA Technologies). All pelleting steps were via centrifugation at 13,000xg for 1 min and the entire process from the first pelleting to the final resuspension was carried out at 4°C. Finally, the cell-oligo mixture was transferred to a 1mm gap cuvette and electroporated using a Bio-Rad gene pulser set to 1.8 kV and 25 μF with pulse controller at 200 Ω. Only those conditions with an electroporation time constant > 4.0 ms were carried through to analysis. Immediately after electroporation, cells were transferred into a culture tube containing 3ml of LB and grown for 2h (unless

Downloaded from http://science.sciencemag.org/ on July 28, 2016

otherwise noted). At this time, 50µl of the culture was lysed by heating to 95°C for 5 min, cooled, then either used directly for analysis or saved for later analysis at -20°C. For multi-day recordings, 50ul of the culture was used to inoculate an overnight culture (in the absence of inducers) to restart the process the next day.

Analysis of spacer acquisition

Qualitative assessment of new spacer acquisition was achieved by PCR across the array (for all expansions) or PCR from either side of the array with the opposite primer matching the oligo that was electroporated (for sequence-specific acquisition). New spacer sequences were assigned to their origin in initial experiments by TOPO cloning (ThermoFisher) the expanded amplicons, followed by Sanger sequencing of the resulting colonies. For the majority of experiments, however, acquisition events were assessed by sequencing a library of all expanded and unexpanded arrays for a given condition using an Illumina MiSeq sequencer. Libraries were created from an initial PCR across the genomic array, then single- or dual-indexed using NEBNext Multiplex Oligos (NEB). Up to 96 conditions were run per flow cell. A list of oligo protospacers used can be found in table S4.

Processing and analysis of MiSeq data

Sequences were analyzed using custom written software (Python). Briefly, spacer sequences were extracted from reads based on their arrangement between identifiable repeat sequences (four mismatches permitted in the repeat to allow for errors in sequencing), then compared against the sequences of spacers that populated the array prior to the experiment (five mismatches allowed against old spacers) to identify new spacers. At this time, metrics were collected as to the number of expanded versus unexpanded arrays, the number of expansions in each array, the position of new expansions, and the length of new spacers. The sequences of new spacers were then blasted (NCBI, blastn) against a database containing the genome, plasmid, and any electroporated oligo sequences. From this, origin and orientation were determined as was the protospacer flanking sequence for PAM analysis. To analyze the recordings over time, all reads containing double and triple expansions were analyzed. Oligo-derived sequences were identified based on their frequency among all new spacers, then, if applicable, set identifiers were extracted based on their known location in the sequences and sets of oligo-derived sequences were assembled. The order of all oligo-derived spacers relative to each other and genome- or plasmid-derived spacers in pairwise comparisons in all double and triple expanded arrays was assessed. Then, those values were used to test all ordered permutations of the oligo-derived across each of the ordering rules. Sets were analyzed independently. An estimate of the time course of spacer acquisition was inferred by relative qPCR Ct values at all time points, referenced to a quantitative analysis of expansions by MiSeq at the two-hour time point. Library sizes for various mutant libraries were estimated by sequencing of fragmented mutant amplicons on a MiSeq sequencer. Sequence diversity was estimated as $S_1 = S_{obs} + \frac{F_1^2}{2F_2}$, where S_{obs} is the number of observed unique sequences in the sample, F1 is the number of sequences with a single occurrence and F2 is the number of sequences with exactly two occurrences (*45*).

Statistics

See table S1.

REFERENCES AND NOTES

1. G. M. Church, Y. Gao, S. Kosuri, Next-generation digital information storage in DNA. *Science* **337**, 1628 (2012). doi: 10.1126/science.1226355; pmid: 22903519
2. J. Shendure, H. Ji, Next-generation DNA sequencing. *Nat. Biotechnol.* **26**, 1135–1145 (2008). doi: 10.1038/nbt1486; pmid: 18846087
3. D. R. Burrill, P. A. Silver, Making cellular memories. *Cell* **140**, 13–18 (2010). doi: 10.1016/j.cell.2009.12.034; pmid: 20085698
4. N. T. Ingolia, A. W. Murray, Positive-feedback loops as a flexible biological module. *Curr. Biol.* **17**, 668–677 (2007). doi: 10.1016/j.cub.2007.03.016; pmid: 17398098
5. C. M. Ajo-Franklin *et al*., Rational design of memory in eukaryotic cells. *Genes Dev.* **21**, 2271–2276 (2007). doi: 10.1101/gad.1586107; pmid: 17875664
6. D. R. Burrill, M. C. Inniss, P. M. Boyle, P. A. Silver, Synthetic memory circuits for tracking human cell fate. *Genes Dev.* **26**, 1486–1497 (2012). doi: 10.1101/gad.189035.112; pmid: 22751502
7. T. S. Gardner, C. R. Cantor, J. J. Collins, Construction of a genetic toggle switch in *Escherichia coli*. *Nature* **403**, 339–342 (2000). doi: 10.1038/35002131; pmid: 10659857
8. D. Greber, M. D. El-Baba, M. Fussenegger, Intronically encoded siRNAs improve dynamic range of mammalian gene regulation systems and toggle switch. *Nucleic Acids Res.* **36**, e101 (2008). doi: 10.1093/nar/gkn443; pmid: 18632760
9. M. R. Atkinson, M. A. Savageau, J. T. Myers, A. J. Ninfa, Development of genetic circuitry exhibiting toggle switch or oscillatory behavior in *Escherichia coli*. *Cell* **113**, 597–607 (2003). doi: 10.1016/S0092-8674(03)00346-5; pmid: 12787501
10. H. Kobayashi *et al*., Programmable cells: Interfacing natural and engineered gene networks. *Proc. Natl. Acad. Sci. U.S.A.* **101**, 8414–8419 (2004). doi: 10.1073/pnas.0402940101; pmid: 15159530
11. N. Vilaboa, M. Fenna, J. Munson, S. M. Roberts, R. Voellmy, Novel gene switches for targeted and timed expression of proteins of interest. *Mol. Ther.* **12**, 290–298 (2005). doi: 10.1016/j.ymthe.2005.03.029; pmid: 15925546
12. B. P. Kramer, M. Fussenegger, Hysteresis in a synthetic mammalian gene network. *Proc. Natl. Acad. Sci. U.S.A.* **102**, 9517–9522 (2005). doi: 10.1073/pnas.0500345102; pmid: 15972812
13. D. R. Burrill, P. A. Silver, Synthetic circuit identifies subpopulations with sustained memory of DNA damage. *Genes Dev.* **25**, 434–439 (2011). doi: 10.1101/gad.1994911; pmid: 21363961
14. M. Wu *et al*., Engineering of regulated stochastic cell fate determination. *Proc. Natl. Acad. Sci. U.S.A.* **110**, 10610–10615 (2013). doi: 10.1073/pnas.1305423110; pmid: 23754391
15. T. S. Ham, S. K. Lee, J. D. Keasling, A. P. Arkin, Design and construction of a double inversion recombination switch for heritable sequential genetic memory. *PLOS ONE* **3**, e2815 (2008). doi: 10.1371/journal.pone.0002815; pmid: 18665232
16. T. S. Moon *et al*., Construction of a genetic multiplexer to toggle between chemosensory pathways in *Escherichia coli*. *J. Mol. Biol.* **406**, 215–227 (2011). doi: 10.1016/j.jmb.2010.12.019; pmid: 21185306
17. J. Bonnet, P. Subsoontorn, D. Endy, Rewritable digital data storage in live cells via engineered control of recombination directionality. *Proc. Natl. Acad. Sci. U.S.A.* **109**, 8884–8889 (2012). doi: 10.1073/pnas.1202344109; pmid: 22615351
18. L. Yang *et al*., Permanent genetic memory with >1-byte capacity. *Nat. Methods* **11**, 1261–1266 (2014). doi: 10.1038/nmeth.3147; pmid: 25344638
19. P. Siuti, J. Yazbek, T. K. Lu, Synthetic circuits integrating logic and memory in living cells. *Nat. Biotechnol.* **31**, 448–452 (2013). doi: 10.1038/nbt.2510; pmid: 23396014
20. F. Farzadfard, T. K. Lu, Genomically encoded analog memory with precise in vivo DNA writing in living cell populations. *Science* **346**, 1256272 (2014). doi: 10.1126/science.1256272; pmid: 25395541
21. A. E. Friedland *et al*., Synthetic gene networks that count. *Science* **324**, 1199–1202 (2009). doi: 10.1126/science.1172005; pmid: 19478183
22. R. Barrangou *et al*., CRISPR provides acquired resistance against viruses in prokaryotes. *Science* **315**, 1709–1712 (2007). doi: 10.1126/science.1138140; pmid: 17379808
23. I. Yosef, M. G. Goren, U. Qimron, Proteins and DNA elements essential for the CRISPR adaptation process in *Escherichia coli*. *Nucleic Acids Res.* **40**, 5569–5576 (2012). doi: 10.1093/nar/gks216; pmid: 22402487
24. A. Levy *et al*., CRISPR adaptation biases explain preference for acquisition of foreign DNA. *Nature* **520**, 505–510 (2015). doi: 10.1038/nature14302; pmid: 25874675
25. J. K. Nuñez, A. S. Lee, A. Engelman, J. A. Doudna, Integrase-mediated spacer acquisition during CRISPR-Cas adaptive immunity. *Nature* **519**, 193–198 (2015). doi: 10.1038/nature14237; pmid: 25707795
26. K. A. Datsenko *et al*., Molecular memory of prior infections activates the CRISPR/Cas adaptive bacterial immunity system. *Nat. Commun.* **3**, 945 (2012). doi: 10.1038/ncomms1937; pmid: 22781758
27. M. J. Lopez-Sanchez *et al*., The highly dynamic CRISPR1 system of *Streptococcus agalactiae* controls the diversity of its mobilome. *Mol. Microbiol.* **85**, 1057–1071 (2012). doi: 10.1111/j.1365-2958.2012.08172.x; pmid: 22834929
28. N. F. Delaney *et al*., Ultrafast evolution and loss of CRISPRs following a host shift in a novel wildlife pathogen, Mycoplasma gallisepticum. *PLOS Genet.* **8**, e1002511 (2012). doi: 10.1371/journal.pgen.1002511; pmid: 22346765
29. P. Horvath *et al*., Diversity, activity, and evolution of CRISPR loci in *Streptococcus thermophilus*. *J. Bacteriol.* **190**, 1401–1412 (2008). doi: 10.1128/JB.01415-07; pmid: 18065539
30. S. Gudbergsdottir *et al*., Dynamic properties of the Sulfolobus CRISPR/Cas and CRISPR/Cmr systems when challenged with vector-borne viral and plasmid genes and protospacers. *Mol. Microbiol.* **79**, 35–49 (2011). doi: 10.1111/j.1365-2958.2010.07452.x; pmid: 21166892
31. I. Yosef *et al*., DNA motifs determining the efficiency of adaptation into the *Escherichia coli* CRISPR array. *Proc. Natl. Acad. Sci. U.S.A.* **110**, 14396–14401 (2013). doi: 10.1073/pnas.1300108110; pmid: 23940313
32. E. Savitskaya, E. Semenova, V. Dedkov, A. Metlitskaya, K. Severinov, High-throughput analysis of type I-E CRISPR/Cas spacer acquisition in *E. coli*. *RNA Biol.* **10**, 716–725 (2013). doi: 10.4161/rna.24325; pmid: 23619643
33. F. J. M. Mojica, C. Díez-Villaseñor, J. García-Martínez, C. Almendros, Short motif sequences determine the targets of the prokaryotic CRISPR defence system. *Microbiology* **155**, 733–740 (2009). doi: 10.1099/mic.0.023960-0; pmid: 19246744
34. C. Rollie, S. Schneider, A. S. Brinkmann, E. L. Bolt, M. F. White, Intrinsic sequence specificity of the Cas1 integrase directs new spacer acquisition. *eLife* **4**, e08716 (2015). doi: 10.7554/eLife.08716; pmid: 26284603
35. S. Shmakov *et al*., Pervasive generation of oppositely oriented spacers during CRISPR adaptation. *Nucleic Acids Res.* **42**, 5907–5916 (2014). doi: 10.1093/nar/gku226; pmid: 24728991
36. J. van der Oost, E. R. Westra, R. N. Jackson, B. Wiedenheft, Unravelling the structural and mechanistic basis of CRISPR-Cas systems. *Nat. Rev. Microbiol.* **12**, 479–492 (2014). doi: 10.1038/nrmicro3279; pmid: 24909109
37. J. K. Nuñez *et al*., Cas1-Cas2 complex formation mediates spacer acquisition during CRISPR-Cas adaptive immunity. *Nat. Struct. Mol. Biol.* **21**, 528–534 (2014). doi: 10.1038/nsmb.2820; pmid: 24793649
38. J. Wang *et al*., Structural and mechanistic basis of PAM-dependent spacer acquisition in CRISPR-Cas systems. *Cell* **163**, 840–853 (2015). doi: 10.1016/j.cell.2015.10.008; pmid: 26478180
39. J. K. Nuñez, L. B. Harrington, P. J. Kranzusch, A. N. Engelman, J. A. Doudna, Foreign DNA capture during CRISPR-Cas adaptive immunity. *Nature* **527**, 535–538 (2015). doi: 10.1038/nature15760; pmid: 26503043

Downloaded from http://science.sciencemag.org/ on July 28, 2016

40. C. Rousseau, M. Gonnet, M. Le Romancer, J. Nicolas, CRISPI: A CRISPR interactive database. *Bioinformatics* **25**, 3317–3318 (2009). doi: 10.1093/bioinformatics/btp586; pmid: 19846435
41. S. Silas *et al*., Direct CRISPR spacer acquisition from RNA by a natural reverse transcriptase-Cas1 fusion protein. *Science* **351**, aad4234 (2016). doi: 10.1126/science.aad4234; pmid: 26917774
42. A. H. Marblestone *et al*., Physical principles for scalable neural recording. *Front. Comput. Neurosci.* **7**, 137 (2013). doi: 10.3389/fncom.2013.00137; pmid: 24187539
43. A. P. Alivisatos *et al*., Nanotools for neuroscience and brain activity mapping. *ACS Nano* **7**, 1850–1866 (2013). doi: 10.1021/nn4012847; pmid: 23514423
44. J. K. Rogers *et al*., Synthetic biosensors for precise gene control and real-time monitoring of metabolites. *Nucleic Acids Res.* **43**, 7648–7660 (2015). doi: 10.1093/nar/gkv616; pmid: 26152303
45. R. K. Colwell, J. A. Coddington, Estimating terrestrial biodiversity through extrapolation. *Philos. Trans. R. Soc. London B Biol. Sci.* **345**, 101–118 (1994). doi: 10.1098/rstb.1994.0091; pmid: 7972351
46. J. P. O'Shea *et al*., pLogo: A probabilistic approach to visualizing sequence motifs. *Nat. Methods* **10**, 1211–1212 (2013). doi: 10.1038/nmeth.2646; pmid: 24097270

ACKNOWLEDGMENTS

S.L.S., J.N., J.D.M, and G.M.C. are inventors on a provisional patent (62/296,812) filed by the President and Fellows of Harvard College that covers the work in this manuscript. S.L.S is a Shurl and Kay Curci Foundation Fellow of the Life Sciences Research Foundation and received additional support from the National Institute on Aging (grant 5T32AG000222). The project was supported by grants from the National Institute of Mental Health (grant 5R01MH103910) and National Human Genome Research Institute (grant 5P50HG005550) to G.M.C., the National Institute of Neurological Disorders and Stroke (grant 5R01NS045523) to J.D.M., and an Allen Distinguished Investigator Award from the Paul G. Allen Family Foundation to J.D.M. Sequence data will be deposited into the National Center for Biotechnology Information Sequence Read Archive database as appropriate, and plasmids will be available under a materials transfer agreement with Addgene.

SUPPLEMENTARY MATERIALS

www.sciencemag.org/content/353/6298/aaf1175/suppl/DC1
Supplementary Text
Figs. S1 to S5
Tables S1 to S4

18 December 2015; accepted 22 May 2016
Published online 9 June 2016
10.1126/science.aaf1175

Downloaded from http://science.sciencemag.org/ on July 28, 2016

REPORTS

OPTICS

Orbital angular momentum microlaser

Pei Miao,[1]* Zhifeng Zhang,[1]* Jingbo Sun,[1]* Wiktor Walasik,[1] Stefano Longhi,[2] Natalia M. Litchinitser,[1]† Liang Feng[1]†

Structured light provides an additional degree of freedom for modern optics and practical applications. The effective generation of orbital angular momentum (OAM) lasing, especially at a micro- and nanoscale, could address the growing demand for information capacity. By exploiting the emerging non-Hermitian photonics design at an exceptional point, we demonstrate a microring laser producing a single-mode OAM vortex lasing with the ability to precisely define the topological charge of the OAM mode. The polarization associated with OAM lasing can be further manipulated on demand, creating a radially polarized vortex emission. Our OAM microlaser could find applications in the next generation of integrated optoelectronic devices for optical communications in both quantum and classical regimes.

Light typically consists of a stream of linearly polarized photons, traveling in a straight line and carrying a linear momentum. However, it was recognized that beyond the linear momentum, circularly polarized light carries angular momentum (*1*). The angular momentum associated with the polarization degree of freedom, or spin angular momentum (SAM), can take only one of two values $\pm\hbar$. In addition to the SAM, it was also demonstrated that a light beam can carry orbital angular momentum (OAM) (*2*). Such beams possess helical phase fronts so that the Poynting vector within the beam is twisted with respect to the principal axis. This fundamental discovery of an OAM opened a new branch of optical physics, facilitating studies ranging from rotary photon drag (*3*), angular uncertainty relationships (*4*), and rotational frequency shifts (*5*), to spin-orbital coupling (*6*). The OAM degree of freedom has enabled technological advances, for example, edge-enhanced microscopy (*7*). Moreover, in contrast to the SAM that can take only two values, the OAM is unbounded. OAM beams are thus being considered as potential candidates for encoding information in both quantum and classical systems. The combined use of spin and orbital angular momenta is expected to enable the implementation of entirely new high-speed secure optical communication and quantum teleportation systems in a multidimensional space (*8*), satisfying the exponentially growing demand worldwide for network capacity.

To date, most of the light sources only produce relatively simple light beams with spatially homogeneous polarization and planar wavefront. Generation of the complex OAM beams usually relies on either bulk devices, such as spiral phase plates, spatial light modulators, and computer-generated holograms (*1*), or recently developed planar optical components, including phase modulation–based metasurfaces (*9*–*14*), q-plates (*15*), and silicon resonators (*16*). Although the science of the OAM light beams on the micro- and nanoscale is still in its early days, it is likely to advance our knowledge of light interaction with conventional and artificial atoms (e.g., quantum dots) provided that the OAM beam is focused to subwavelength dimensions (*17*), facilitating on-chip functionalities for micromanipulation and microfluidics. Nevertheless, it remains a grand challenge to integrate the existing approaches for OAM microlasers on-a-chip. For an ultimate miniaturized optical communication platform, there is a necessity of independent micro- and nanoscale laser sources (*18*) emitting complex vector beams carrying the OAM information.

One approach to creating an OAM laser (*19*) is based on combining a conventional bulk laser with additional phase-front shaping components. Despite being straightforward, this approach relies on rather different device technologies and material platforms, and therefore it is not easily scalable and integratable. On the contrary, here we integrate the advantages of semiconductor microlasers with the pronounced changes in light propagation at the exceptional point to realize a fundamentally new, compact, active OAM source on a complementary metal-oxide-semiconductor (CMOS) compatible platform. We consider a microring cavity that supports whispering gallery modes (WGMs). These modes circulate inside the cavity and carry large OAM. However, because of the mirror symmetry of a ring cavity, clockwise and counterclockwise eigen-WGMs can be simultaneously excited, and their carried OAMs consequently cancel each other. This is evidenced by the quantized phase, taking values of either 0 or π, azimuthally distributed in the ring, which results from the interference between two counterpropagating WGMs (fig. S1) (*20*). To observe the OAM of an individual WGM, it is essential to

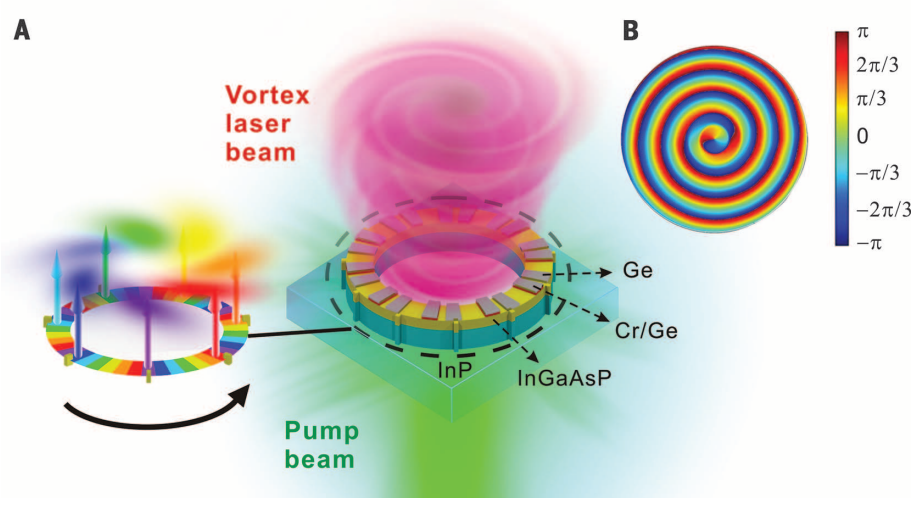


Fig. 1. Design of OAM microlaser. (**A**) Schematic of the OAM microlaser on an InP substrate. The diameter of the microring resonator is 9 μm, the width is 1.1 μm, and the height is 1.5 μm (500 nm of InGaAsP and 1 μm of InP). Thirteen-nanometer Ge single-layer and 5-nm Cr/11-nm Ge bilayer structures are periodically arranged in the azimuthal direction on top of the InGaAsP/InP microring, mimicking real index and gain/loss parts of an EP modulation at $n' = n'' = 0.01$ to support unidirectional power circulation. The designed azimuthal order is $N = 56$ at the resonant wavelength of 1472 nm. Equidistant sidewall scatters with a total number of $M = 57$ are introduced to couple the lasing emission upward, creating an OAM vortex emission with a helical wavefront. Its topological charge is defined by $l = N - M = -1$. (**B**) Simulated phase distribution of emitted light. A spiral phase map for an OAM charge-one vortex is clearly demonstrated.

[1]Department of Electrical Engineering, The State University of New York at Buffalo, Buffalo, NY 14260, USA. [2]Dipartimento di Fisica, Politecnico di Milano and Istituto di Fotonica e Nanotecnologie del Consiglio Nazionale delle Ricerche, Piazza L. da Vinci 32, Milano I-20133, Italy. *These authors contributed equally to this work. †Corresponding author. Email: fengl@buffalo.edu (L.F.); natashal@buffalo.edu (N.M.L.)

Downloaded from http://science.sciencemag.org/ on July 28, 2016

introduce a mechanism of robust selection of either clockwise or counterclockwise mode. In conventional bulk optics, unidirectional ring lasers have been demonstrated by implementing a nonreciprocal isolator in the light path. The optical isolator breaks the reciprocity between counterpropagating waves, facilitating the desired unidirectional flow. This approach, however, is not feasible at the micro- and nanoscale, as the realization of micrometer-sized isolators is extremely challenging.

To overcome this fundamental limitation, we realize the unidirectional power circulation by introducing complex refractive-index modulations to form an exceptional point (EP) (Fig. 1A). Driven by non-Hermiticity (i.e., gain and loss in optics) (*21*, *22*), an EP occurs when multiple eigenstates coalesce into one (*23*–*26*). In our device, EP operation is essential to obtaining OAM laser emission (*20*). The microring laser resonator is designed with 500-nm-thick InGaAsP multiple quantum wells on an InP substrate. The complex refractive-index grating is achieved by placing on top of InGaAsP along the azimuthal direction (θ) periodically alternate single-layer Ge and bilayer Cr/Ge structures, corresponding to the refractive index (n') and gain/loss (n'') in the cavity, respectively:

$$\Delta n = \begin{cases} in'' \text{ for } 2\pi p/N < \theta < 2\pi\left(p+\frac{1}{4}\right)/N \\ n' \text{ for } 2\pi\left(p+\frac{3}{8}\right)/N < \theta < 2\pi\left(p+\frac{5}{8}\right)/N \end{cases} \quad (1)$$

where N denotes the azimuthal number of the targeted WGM and p takes integer values from the set $\{0, N-1\}$. An EP is obtained when the amplitudes of index and gain/loss gratings are set equal (i.e., $n' = n''$). At EP, the Fourier transform of the complex refractive-index modulation is one-sided, yielding one-way distributed feedback (*27*–*29*) and robust unidirectional laser emission above threshold, as shown by a detailed semiconductor rate equation analysis (*20*). As a result, the counterclockwise WGM unidirectionally circulates in the cavity carrying large OAM through the azimuthally continuous phase evolution (figs. S2 and S3) (*20*).

The OAM associated with the unidirectional power flow is extracted upward into free space by introducing sidewall modulations periodically arranged along the microring perimeter (*16*). The azimuthal phase dependence of the targeted unidirectional Nth WGM is given by $\varphi = N\theta$. The sidewall modulations coherently scatter light, with the phase continuously varying in azimuthal direction, defined by the locations of the scatters (Fig. 1A, inset). For M equidistant scatters, the locations of the scatters are given by $\theta_s = 2\pi s/M$, where $s \in \{0, M-1\}$, resulting in the extracted phase $\theta_s = 2\pi sN/M$ that carries OAM. Because the physically meaningful phase is measured modulo 2π, we can subtract $2\pi s$ from each of the extracted phases and derive

$$\varphi_s = 2\pi s(N-M)/M \quad (2)$$

Equation 2 shows that the extracted phase increases linearly from 0 to $2\pi(N-M)$, thereby creating a vortex beam with topological charge $l = N - M$. Figure 1B shows the modeling result of the vortex laser emission from our OAM microlaser, where $N = 56$ and $M = 57$. The phase of

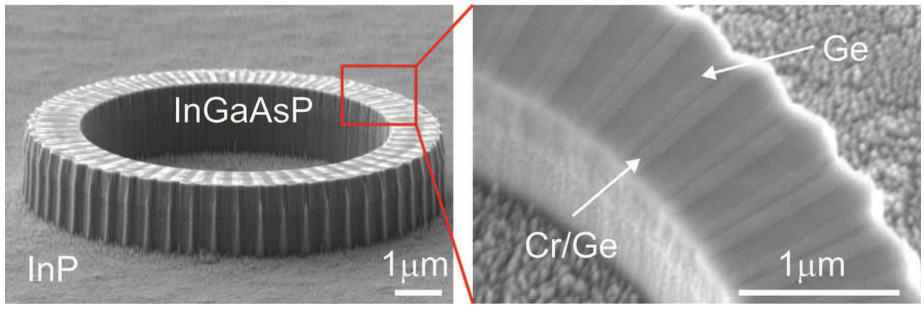


Fig. 2. Scanning electron microscope images of OAM microlaser. The OAM microlaser was fabricated on the InGaAsP/InP platform. Alternating Cr/Ge bilayer and Ge single-layer structures were periodically implemented in the azimuthal direction on top of the microring, presenting, respectively, the gain/loss and index modulations required for unidirectional power circulation.

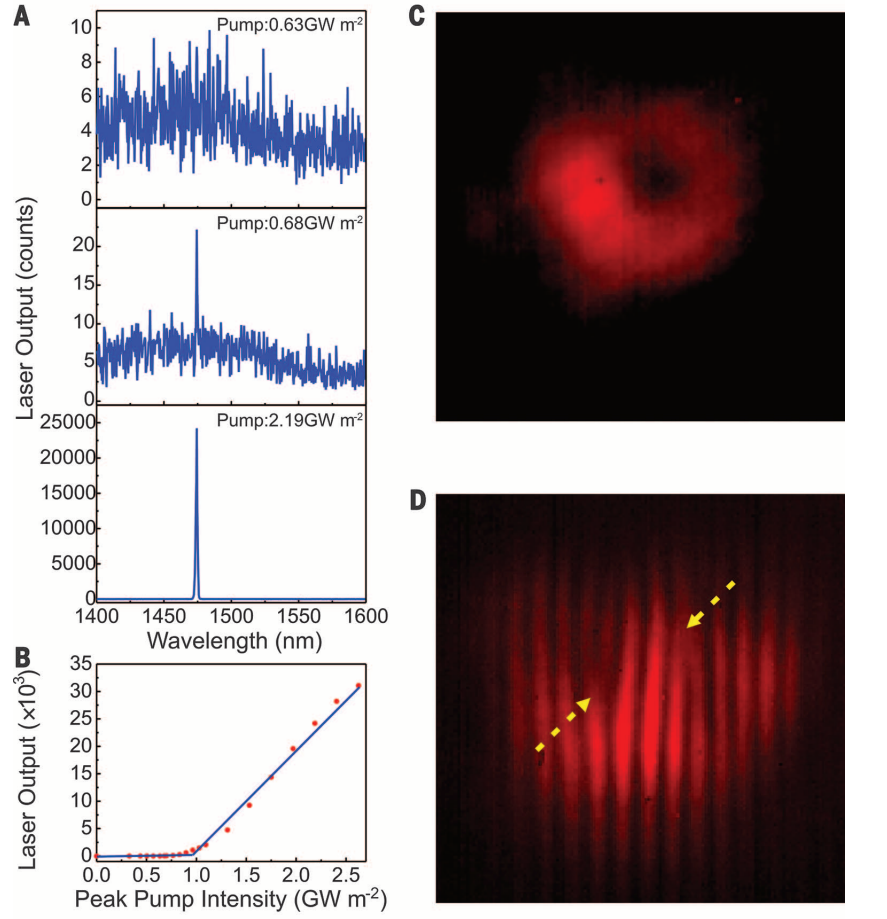


Fig. 3. Characterization of OAM lasing. (**A**) Evolution of the light emission spectrum from PL, to ASE, and to lasing at 1474 nm, as the peak power density of pump light was increased from 0.63, to 0.68, to 2.19 GW m^{-2}, respectively. (**B**) Input-output laser curve, showing a lasing threshold of ~1 GW m^{-2}. (**C**) Far-field intensity distribution of the laser emission exhibiting a doughnut-shaped profile, where the central dark core is due to the phase singularity at the center of the OAM vortex radiation. (**D**) Off-center self-interference of the OAM lasing radiation, showing two inverted forks (marked with arrows) located at two phase singularities. Originating from the superposition of central helical and outer quasiplanar phases intrinsically associated with OAM, the double-fork pattern confirms the OAM vortex nature of the laser radiation.

Downloaded from http://science.sciencemag.org/ on July 28, 2016

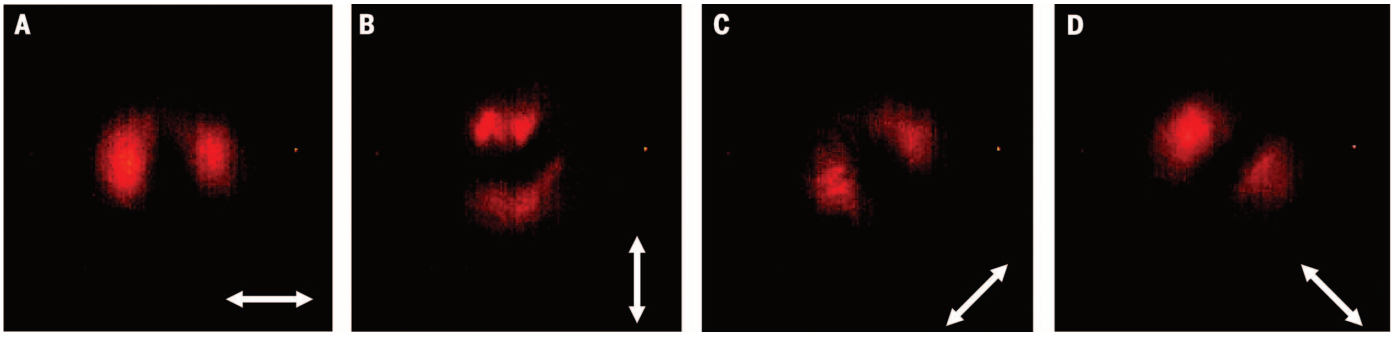


Fig. 4. Polarization state of OAM lasing. Measured intensity distributions of the OAM lasing radiation passing through a linear polarizer with different polarization orientations indicated by arrows: (**A**) 0°, (**B**) 90°, (**C**) 45°, and (**D**) −45°. The two-lobe structure rotated with the rotation of the polarizer in the same fashion, confirming radially polarized OAM lasing.

the electric field changes by 2π upon one full circle around the center of the vortex. The phase is continuous everywhere except for the center of the emission path, presenting a topological phase singularity point at the beam axis. The topological charge of the vortex emission can be viewed as the number of twists done by the wavefront in one wavelength, exhibiting OAM lasing of charge $l = -1$.

The OAM microlaser with the EP modulation by periodically arranged Ge and Cr/Ge (Fig. 2) was fabricated by means of overlay electron beam lithography (*20*). The unidirectional power flow oscillating in the cavity eliminates the undesired spatial hole-burning effect that would be created by the interference pattern of two counterpropagating WGMs. The preferential gain saturation in the antinodes of the interference pattern would cause spatial gain inhomogeneity, leading to a decrease in the laser slope efficiency, multilongitudinal mode operation, and unstable laser emission. In our OAM microlaser, unidirectional power flow forced at the EP modulation (fig. S3) (*20*) enables efficient and stable single-mode lasing with a sideband suppression ratio of ~40 dB (Fig. 3A). In the transition from broadband photoluminescence (PL), to amplified spontaneous emission (ASE), and finally to lasing (Fig. 3, A and B), the emission peak stabilized at the same resonant wavelength, demonstrating the avoidance of multimode oscillation typically existing in a microring cavity. The OAM characteristics, such as the vortex nature and the phase singularity, were characterized by analyzing the spatial intensity profile of lasing emission and its self-interference (fig. S4) (*20*). In the far field, we observed the intensity of lasing emission spatially distributed in a doughnut shape with a dark core in the center (Fig. 3C). The observed dark center is due to the topological phase singularity at the beam axis where the phase becomes discontinuous, as predicted in Fig. 1B. The presence of the OAM was then validated by the self-interference of two doughnut-shaped beams split from the same lasing emission. In each doughnut beam, because of its OAM, optical phase varies more markedly with a helical phase front close to the central singularity area, whereas the outer doughnut area is of a relatively uniform quasiplanar phase front. At the observation plane, we intentionally created a horizontal offset between two doughnut beams, so that the dark center of one beam overlapped with the bright doughnut area of the other, and vice versa. The resulting interference patterns between the helical and quasiplanar phase fronts revealed two inverted forks (Fig. 3D), as the quasiplanar and helical phases were reversed at the centers of two doughnuts. For both of them, the single fringe split into two at the fork dislocation, evidently confirming that the radiation from our OAM laser was an optical vortex of topological charge $l = -1$.

The polarization properties of the demonstrated OAM microlaser can be designed on demand. In particular, radially polarized beams, characterized by a nonuniform spatial distribution of their polarization vector, have enabled unique functionalities, such as high–spatial resolution microscopy by their sharp focusing (*30*). Although the conventional schemes require external optical components, such as geometric phase–based diffraction elements (*9*), radially polarized beams can be directly produced from our OAM microlaser. In a microring cavity, the resonant mode can be designed to be either quasi–transverse magnetic (TM) or quasi–transverse electric (TE). The radially polarized component of the quasi-TM mode is tightly confined at the microring perimeter and sensitive to sidewall modulations, facilitating the outcoupling of this mode from the laser (fig. S5) (*20*). Therefore, in our microring cavity, the dominant oscillating mode is designed to be a quasi-TM mode, and its scattering by the sidewall modulation results in the radially polarized OAM lasing. In experiments, the polarization state of the OAM lasing was validated. After transmission through a linear polarizer, the doughnut profile splits into two lobes aligned along the orientation of the polarizer (Fig. 4). The two lobes remained parallel to the polarization axis regardless of the rotation of the polarizer, manifesting pure radially polarized OAM lasing. Additionally, in contrast to linearly polarized OAM modes that are not compatible with optical fibers, fibers can support radially polarized OAM eigenmodes.

We have demonstrated a microring OAM laser producing an optical vortex beam with an on-demand topological charge and vector polarization states. This is enabled through combined index and gain/loss modulations at an EP, which breaks the mirror symmetry in the lasing generation dynamics and facilitates the unidirectional power oscillation. Finally, OAM vector laser beams might offer novel degrees of freedom for the next generation of optical communications in both classical and quantum regimes.

REFERENCES AND NOTES

1. A. M. Yao, M. J. Padgett, *Adv. Opt. Photonics* **3**, 161 (2011).
2. L. Allen, M. W. Beijersbergen, R. J. C. Spreeuw, J. P. Woerdman, *Phys. Rev. A* **45**, 8185–8189 (1992).
3. S. Franke-Arnold, G. Gibson, R. W. Boyd, M. J. Padgett, *Science* **333**, 65–67 (2011).
4. S. Franke-Arnold *et al.*, *New J. Phys.* **6**, 103 (2004).
5. J. Courtial, D. Robertson, K. Dholakia, L. Allen, M. Padgett, *Phys. Rev. Lett.* **81**, 4828–4830 (1998).
6. Q. Guo, W. Gao, J. Chen, Y. Liu, S. Zhang, *Phys. Rev. Lett.* **115**, 067402 (2015).
7. C. Maurer, A. Jesacher, S. Bernet, M. Ritsch-Marte, *Laser Photonics Rev.* **5**, 81–101 (2011).
8. N. Bozinovic *et al.*, *Science* **340**, 1545–1548 (2013).
9. Z. Bomzon, G. Biener, V. Kleiner, E. Hasman, *Opt. Lett.* **27**, 1141–1143 (2002).
10. N. Yu *et al.*, *Science* **334**, 333–337 (2011).
11. D. Lin, P. Fan, E. Hasman, M. L. Brongersma, *Science* **345**, 298–302 (2014).
12. K. E. Chong *et al.*, *Nano Lett.* **15**, 5369–5374 (2015).
13. M. I. Shalaev *et al.*, *Nano Lett.* **15**, 6261–6266 (2015).
14. G. Knöner *et al.*, *Opt. Express* **15**, 5521–5530 (2007).
15. E. Karimi, B. Piccirillo, E. Nagali, L. Marrucci, E. Santamato, *Appl. Phys. Lett.* **94**, 231124 (2009).
16. X. Cai *et al.*, *Science* **338**, 363–366 (2012).
17. R. W. Heeres, V. Zwiller, *Nano Lett.* **14**, 4598–4601 (2014).
18. M. A. Noginov *et al.*, *Nature* **460**, 1110–1112 (2009).
19. D. Naidoo *et al.*, *Nat. Photonics* **10**, 327–332 (2016).
20. Materials and methods are available as supplementary materials on *Science* Online.
21. K. G. Makris, R. El-Ganainy, D. N. Christodoulides, Z. H. Musslimani, *Phys. Rev. Lett.* **100**, 103904 (2008).
22. C. E. Rüter *et al.*, *Nat. Phys.* **6**, 192–195 (2010).
23. J. Wiersig, S. W. Kim, M. Hentschel, *Phys. Rev. A* **78**, 053809 (2008).
24. B. Peng *et al.*, *Nat. Phys.* **10**, 394–398 (2014).
25. H. Schomerus, *Phys. Rev. Lett.* **104**, 233601 (2010).
26. M. Brandstetter *et al.*, *Nat. Commun.* **5**, 4034 (2014).
27. Z. Lin *et al.*, *Phys. Rev. Lett.* **106**, 213901 (2011).
28. A. Regensburger *et al.*, *Nature* **488**, 167–171 (2012).
29. L. Feng *et al.*, *Nat. Mater.* **12**, 108–113 (2013).
30. R. Dorn, S. Quabis, G. Leuchs, *Phys. Rev. Lett.* **91**, 233901 (2003).

Downloaded from http://science.sciencemag.org/ on July 28, 2016

ACKNOWLEDGMENTS

We acknowledge funding from the U.S. Army Research Office Award (W911NF-15-1-0152) that enabled the design, modeling, and topological charge characterization of the EP-based OAM laser, Department of Energy Award (DE-SC0014485) that was used to perform the analysis and characterization of the spectral properties of OAM lasing, and National Science Foundation Award (DMR-1506884) that facilitated the fabrication of the device and optimization of the EP modulation.

SUPPLEMENTARY MATERIALS

www.sciencemag.org/content/353/6298/464/suppl/DC1
Supplementary Text
Figs. S1 to S5
References (*31*–*34*)

10 April 2016; accepted 30 June 2016
10.1126/science.aaf8533

ELECTROCHEMISTRY

Nanostructured transition metal dichalcogenide electrocatalysts for CO_2 reduction in ionic liquid

Mohammad Asadi,[1] Kibum Kim,[1,2]* Cong Liu,[3]* Aditya Venkata Addepalli,[1] Pedram Abbasi,[1] Poya Yasaei,[1] Patrick Phillips,[4] Amirhossein Behranginia,[1] José M. Cerrato,[5] Richard Haasch,[6] Peter Zapol,[3] Bijandra Kumar,[1,7] Robert F. Klie,[4] Jeremiah Abiade,[1] Larry A. Curtiss,[3]† Amin Salehi-Khojin[1]†

Conversion of carbon dioxide (CO_2) into fuels is an attractive solution to many energy and environmental challenges. However, the chemical inertness of CO_2 renders many electrochemical and photochemical conversion processes inefficient. We report a transition metal dichalcogenide nanoarchitecture for catalytic electrochemical CO_2 conversion to carbon monoxide (CO) in an ionic liquid. We found that tungsten diselenide nanoflakes show a current density of 18.95 milliamperes per square centimeter, CO faradaic efficiency of 24%, and CO formation turnover frequency of 0.28 per second at a low overpotential of 54 millivolts. We also applied this catalyst in a light-harvesting artificial leaf platform that concurrently oxidized water in the absence of any external potential.

Electrochemical or photochemical reduction of carbon dioxide (CO_2) could in principle conveniently recycle the greenhouse gas back into fuels (*1*–*6*). However, existing catalysts are too inefficient in practice (*7*–*11*): Either weak binding interactions between the reaction intermediates and the catalyst give rise to high overpotentials, or slow electron transfer kinetics result in low exchange current densities. Both of these metrics depend not only on the intrinsic electronic properties of the catalyst, but also on the solvent and the catalyst morphology. Recently, we reported that three-dimensional (3D) bulk molybdenum disulfide (MoS_2) catalyzes CO_2 reduction to CO at an extremely low overpotential (54 mV) (*12*) in an ionic liquid (IL). Here, we report 2D nanoflake (NF) architectures of this and other transition metal dichalcogenides (TMDCs) that manifest much higher performance for electrocatalytic CO_2 reduction in the IL 1-ethyl-3-methylimidazolium tetrafluoroborate (EMIM-BF_4).

[1]Department of Mechanical and Industrial Engineering, University of Illinois, Chicago, IL 60607, USA. [2]Department of Mechanical Engineering, Chungbuk National University, Cheongju 361-763, South Korea. [3]Materials Science Division, Argonne National Laboratory, Argonne, IL 60439, USA. [4]Department of Physics, University of Illinois at Chicago, Chicago, IL 60607, USA. [5]Department of Civil Engineering, University of New Mexico, Albuquerque, NM 87131, USA. [6]Materials Research Laboratory, University of Illinois at Urbana-Champaign, Urbana, IL 61801, USA. [7]Conn Center for Renewable Energy Research, University of Louisville, Louisville, KY 40292, USA.
*These authors equally contributed to this work. **†Corresponding author. Email: salehikh@uic.edu (A.S.-K.); curtiss@anl.gov (L.A.C.)**

CO_2 reduction activities of similarly sized (~100 nm) TMDC NFs including MoS_2, WS_2, $MoSe_2$, and WSe_2 were tested using a rotating disc electrode. All TMDCs were grown using a chemical vapor transport technique (*13*). Figure 1A shows cyclic voltammetry (CV) results of WSe_2 NFs, and bulk MoS_2 as well as Ag nanoparticles (Ag NPs) and bulk Ag as a representative noble-metal catalyst. All experiments were performed inside a two-compartment, three-electrode electrochemical cell (fig. S6) using an electrolyte of 50 volume percent (vol %) EMIM-BF_4 and 50 vol % deionized water; this composition gives the maximum CO_2 reduction activity (*13*). The polarization curves of all studied catalysts were obtained by sweeping potential between +0.8 and −0.764 V versus RHE (reversible hydrogen electrode; all potentials reported here are based on RHE) with a scan rate of 50 mV s^{-1} (Fig. 1A and fig. S8). We also performed chronoamperometry at different applied potentials for WSe_2 NFs. The results indicate that the obtained current densities for all applied potentials are 10 to 20% less than the CV results with 50 mV/s scan rate (fig. S9). The difference is attributed to the charging current (capacitive behavior) in the CV measurements.

The CO_2 reduction began at −0.164 V (overpotential of 54 mV) for WSe_2 NFs, as confirmed by faradaic efficiency (FE) measurements (Fig. 1B). At this potential (overpotential of 54 mV), a current density of 18.95 mA/cm^2 (normalized on the basis of geometrical surface area) was obtained for WSe_2 NFs; by comparison, current densities were 0.19 mA/cm^2 for bulk Ag, 1.57 mA/cm^2 for Ag NPs, and 3.4 mA/cm^2 for bulk MoS_2. The CO formation FEs for WSe_2 NFs (Fig. 1B) and bulk MoS_2 (*12*) were 24% and 3%, respectively. However, the Ag NPs and bulk Ag did not reduce CO_2 at this overpotential. At −0.764 V potential, the recorded current density for WSe_2 NFs was 330 mA cm^{-2}, versus 3.3 mA cm^{-2} for bulk Ag, 11 mA cm^{-2} for Ag NPs, and 65 mA cm^{-2} for bulk MoS_2. The CO formation turnover frequency (TOF) (Fig. 1C) (*13*), a measure of per-site activity of catalysts to produce CO, was 0.28 s^{-1} for WSe_2 NFs versus 0.016 s^{-1} for bulk MoS_2. However, this value was zero for Ag NPs, as they could not produce CO at this overpotential (54 mV). Figure 1C also shows that the CO formation TOF of WSe_2 was approximately three orders of magnitude higher than that of Ag NPs in the overpotential range of 150 to 650 mV.

Gas chromatography and differential electrochemical mass spectroscopy analyses indicated that CO and H_2 were the only gas-phase products (*5*, *11*, *12*, *14*–*16*) in the potential range of 0 to −0.764 V (*13*). The measured FE for WSe_2 NFs/IL (Fig. 1B) showed that this system is highly selective for CO formation at high potentials (−0.2 to −0.764 V). However, at smaller potentials (−0.164 to −0.2 V), it produces a mixture of CO and H_2 (synthesis gas). Figure S13 shows the selectivity (FE) results of all TMDCs tested in this study (*13*).

The catalytic performance of TMDC NFs was compared with that of other reported catalysts (Fig. 1D) by multiplying current density (activity) by CO formation FE (selectivity). At 100 mV overpotential, the performance of WSe_2 NFs exceeded that of bulk MoS_2 and Ag NPs tested under identical conditions in an ionic liquid by a factor of nearly 60. The performance of WSe_2 NFs also exceeds those of Au NPs (*17*) and Cu NPs (*18*) by three orders of magnitude. Additionally, at this overpotential, the performance of WSe_2 exceeded that of WS_2 and $MoSe_2$ NFs by factors of 3 and 2, respectively (Fig. 1D). We also performed chronoamperometry experiments to examine the electrochemical stability of WSe_2 NFs in 50:50 vol % IL/deionized water. At the applied potential of −0.364 V (0.254 V overpotential), a small decay (10%) was observed after 27 hours of continuous operation of the three-electrode two-compartment cell (fig. S14) (*13*).

The photochemical performance of WSe_2/IL was also studied using a custom-built wireless setup. This artificial leaf mimics the photosynthesis process in the absence of any external applied potential. The cell (Fig. 2A) (*13*) is composed of three major segments: (i) two amorphous silicon triple-junction photovoltaic (PV-a-si-3jn) cells in series to harvest light, (ii) the WSe_2/IL cocatalyst

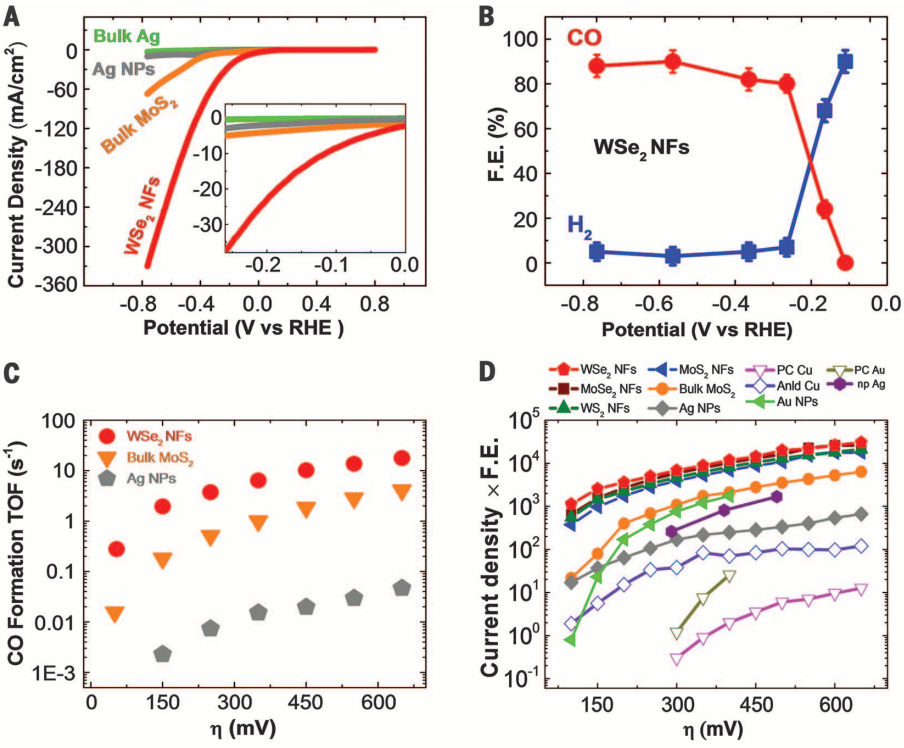


Fig. 1. CO_2 reduction performance of the TMDC catalysts, Ag NPs, and bulk Ag in the EMIM-BF_4 solution. (**A**) Cyclic voltammetry (CV) curves for WSe_2 NFs, bulk MoS_2, Ag nanoparticles (Ag NPs), and bulk Ag in CO_2 environment. Inset shows the current densities in low overpotentials. (**B**) CO and H_2 overall faradaic efficiency (FE) at different applied potentials for WSe_2 NFs. The error bars represent SD of four measurements. (**C**) CO formation TOF of WSe_2 NFs, bulk MoS_2, and Ag NPs in IL electrolyte at overpotentials of 54 to 650 mV. At 54 mV overpotential, Ag NPs' result is zero. (**D**) Overview of different catalysts' performance at different overpotentials (η). All TMDC and Ag NP data were obtained from chronoamperometry experiments under identical conditions. Data for other catalysts are from (*12*).

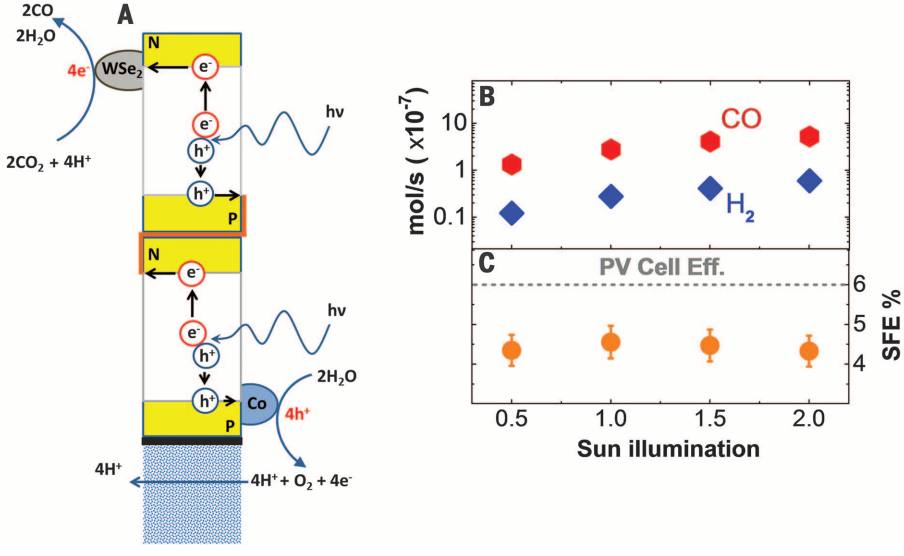


Fig. 2. Artificial leaf. (**A**) Schematic of the cell design. (**B**) Rate of product formation (mol/s) with respect to different Sun illuminations. (**C**) Calculated solar-to-fuel efficiency (SFE) of photochemical process using the WSe_2/IL cocatalyst system. Our calculation indicates ~4.6% SFE, which is limited by the maximum efficiency of PV-a-si-3jn (~6.0%). Error bars indicate uncertainty in the calculated SFE (table S5) (*13*).

system on the cathode side for CO_2 reduction, and (iii) cobalt (Co^{II}) oxide/hydroxide in potassium phosphate pH = 7.0 (KPi) electrolyte on the anode side to catalyze the oxygen evolution reaction (*19*–*21*). Because the CO_2 reduction and oxygen evolution reactions in the artificial leaf system are electrically coupled together through the photovoltaic, the production and consumption rates of electrons and protons are equal on the anode and cathode sides of the cell. When the reaction starts, proton (H^+) generation is initiated in the KPi solution (anode side) through the oxygen evolution reaction (decreasing the initial pH of 7); on the IL electrolyte (cathode side), the CO_2 reduction reaction consumes H^+ available in the IL electrolyte (increasing the initial pH of ~3.2). During this transient period, diffusion of the K^+ ions through the proton exchange membrane from the anode to the cathode side compensates the charge imbalance to achieve charge neutrality (fig. S17) (*13*). However, after this period (~5 min), the pH in the KPi solution and the IL approaches ~3.4, where the operation of the artificial leaf system reaches steady state and H^+ diffuses in place of K^+. Our measurements indicate that 1.43×10^{-4} M K^+ diffuses to the IL in the transient stage and that its concentration remains constant under steady-state operation. This quantification is consistent with the change in the H^+ concentration (1.52×10^{-4} M) on the cathode side. The PV-a-si-3jn cell can function continuously for 5 hours (fig. S18) before corrosion of the transparent indium tin oxide layer on the anode inhibits operation (fig. S19) (*13*). However, replacing the PV-a-si-3jn cells restores performance to its previous level.

To test the stability of ionic liquid (50 vol % EMIM-BF_4 in water) and KPi electrolytes, we replaced the PV-a-si-3jn cells every 4 hours for a cumulative time of 100 hours. Results shown in table S3 (*13*) indicate that, within error margins, the same molar quantities of CO and H_2 were produced during each 4-hour period of the 100-hour-long operation of the artificial leaf, confirming the durability of both anode (KPi) and cathode (50/50 vol% IL/water) electrolytes. We also observed no significant change in the pH of the solution after 100 hours (*13*). Moreover, our calculations (*13*) indicate that a negligible amount of water (~0.018 ml/hour) is produced during the CO_2 reduction reaction on the cathode side relative to the total volume of electrolyte (100 ml of IL/water) used in our experiment.

Figure 2B shows the molar rates of product formation with respect to simulated solar illumination (number of Suns). The respective yields of CO and H_2 measured by GC follow an approximately 10:1 ratio for the entire range of illuminations. This result is consistent with our FE measurements obtained at higher overpotentials in the three-electrode electrochemical setup. We also calculated the solar-to-fuel conversion efficiency (SFE) for our photochemical process (Fig. 2C), obtaining a value of ~4.6% limited by the maximum efficiency of the PV-a-si-3jn cell (~6.0%) (*13*, *20*). This SFE is higher than that of

the water-splitting reaction (~2.5%) previously measured using an identical triple-junction photovoltaic (PV-a-si-3jn) cell (*20*). Our measurements indicate that the SFE of the system remains stable for 5 hours of continuous operation (fig. S20) (*13*). The SFEs of the artificial leaf during 100 hours of operation (with successive PV-a-si-3jn replacements) are shown in table S6.

Next, we performed electrochemical impedance spectroscopy (EIS) at 150 mV overpotential to measure the charge transfer resistance (R_{ct}) for WSe_2 NFs, bulk MoS_2, and Ag NPs catalysts (*13*, *22*–*24*). A charge transfer resistance is correlated to the number of electrons transferred from the catalyst surface to the reactant (*25*–*27*) as well as intermediate formation inside the double layer (*22*, *23*). Our experimental results (Fig. 3) indicate that the R_{ct} of WSe_2 is ~180 ohms, versus ~420 ohms for bulk MoS_2 and ~550 ohms for Ag NPs.

Additionally, we measured the work function of WSe_2 and the other TMDCs by ultraviolet photoelectron spectroscopy (UPS) (*11*, *13*) (fig. S22). Our results indicate a considerably lower work function of WSe_2 NFs (3.52 eV) compared to bulk MoS_2 (3.99 eV) (*12*) and Ag NPs (4.38 eV), confirming the EIS data. These results provide evidence that the superior electronic properties of W edge atoms result in a faster electron transfer and consequently higher catalytic activity during CO_2 reduction.

To characterize the atomic arrangement of edge atoms, we performed scanning transmission electron microscopy (STEM) analysis on several liquid-exfoliated monolayers and multiple layers of WSe_2 NFs (fig. S23A) (*13*). The line intensity profile of single-layer WSe_2 NF (fig. S23B) indicates that the edges of the nanoflakes are W-terminated. Moreover, STEM analysis on the edge atoms after 27 hours of chronoamperometry (fig. S14) indicates a stable atomic structure of W edge sites (fig. S23, C and D). These results suggest that transition metals with d-orbital electrons on the edge sites mainly contribute to the CO_2 reduction without any evidence of instability over time. X-ray photoelectron spectroscopy data further verified the long-term stability of the catalyst (fig. S24, A to D) (*12*, *13*).

Density functional theory (DFT) calculations were performed to gain insight into the catalytic properties of the TMDC NFs (*13*). The calculated reaction free energies of the $CO_2 \rightarrow CO$ pathway using a computational hydrogen electron approach at zero potential (*28*) show that the formation of COOH* is highly endergonic and is the rate-limiting step for both Ag(111) and the Ag_{55} cluster (Fig. 4A). The Ag_{55} cluster requires less energy than Ag(111) to form COOH* because of the presence of undercoordinated Ag atoms of the cluster. This result explains the lower overpotential of Ag nanoparticles relative to bulk Ag, in agreement with other studies (*7*). COOH* formation is similarly endergonic on other metal surfaces such as Pd, Au, and Cu (*7*, *29*, *30*). However, on the metallic edges of the TMDC NFs, COOH* formation is exergonic because of strong binding to the TMDC metal edge sites. The CO* is also much more stable on the TMDC NFs than on Ag, residing at lower energy than COOH*. This energetic ordering suggests that the formation of CO* from CO_2 is kinetically more favorable on the TMDC NFs than on Ag (Fig. 4A) resulting in lower overpotentials. In addition, the calculated projected density of states of the edge metal atom (Mo or W) reveals that the d-band centers of these metal edges (Fig. 4, B and C, and fig. S26, A to D) (*13*) are much closer to the Fermi level than those of the Ag(111) surface, further supporting the strong binding interactions of the adsorbed intermediates with the TMDC NFs (*31*, *32*). However, the strong binding of CO on the TMDCs also inhibits desorption of CO, which becomes the rate-limiting step in the TMDC systems. Previous studies have indicated that the coverage of the adsorbed intermediates significantly affects the binding energies (*33*, *34*). We further investigated the effect of CO coverage on the metal edge of the TMDCs and found that each metal atom on the TMDC edge can bind up to two CO molecules ($\theta_{CO} \leq 2$ ML) (*13*). The binding energy per CO on a metal atom (when $\theta_{CO} = 1$ ML) ranges from 0.8 to 1.1 eV (Fig. 4A), whereas the binding energy per second CO on a metal atom (when $\theta_{CO} = 2$ ML) decreases to 0.3 to 0.5 eV. This finding suggests that the metal edges of the TMDCs likely have high CO coverage ($\theta_{CO} > 1$ ML) during the catalytic reaction to maintain a high turnover rate.

We also calculated the work functions of the monolayers of the four TMDCs (fig. S27). Our calculations show a trend of $MoS_2 > WS_2 > MoSe_2 > WSe_2$, consistent with experimental measurements of the work functions (fig. S22) (*13*). This trend of work functions correlates with the trend of the experimental activities as measured by current densities of the four TMDCs, suggesting that the electron transfer properties of the TMDCs play an important role in the electrochemical reduction of CO_2. In this case, WSe_2 has the lowest work function and is the best TMDC for CO_2 activation among the tested materials.

The ionic liquid also plays an important role in the CO_2 electrochemical reduction. Our previous study suggested that the $EMIM^+$ ion helps transport CO_2 to the catalyst surface by complexation under acidic conditions (*12*). Overall, we attribute the exceptional performance of the present catalysts to a combination of low overpotentials and efficient electron transfer properties of the TMDC NFs and the IL-enhanced local CO_2 concentration.

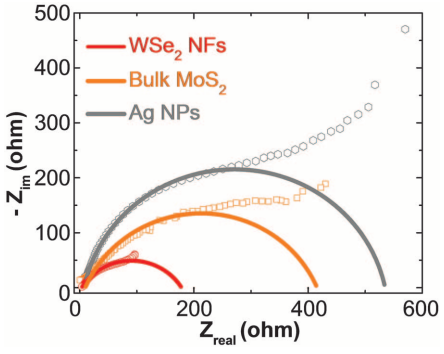


Fig. 3. Electrochemical impedance spectroscopy of CO_2 reduction using WSe_2 NFs, bulk MoS_2, and Ag NPs at 150 mV overpotential.

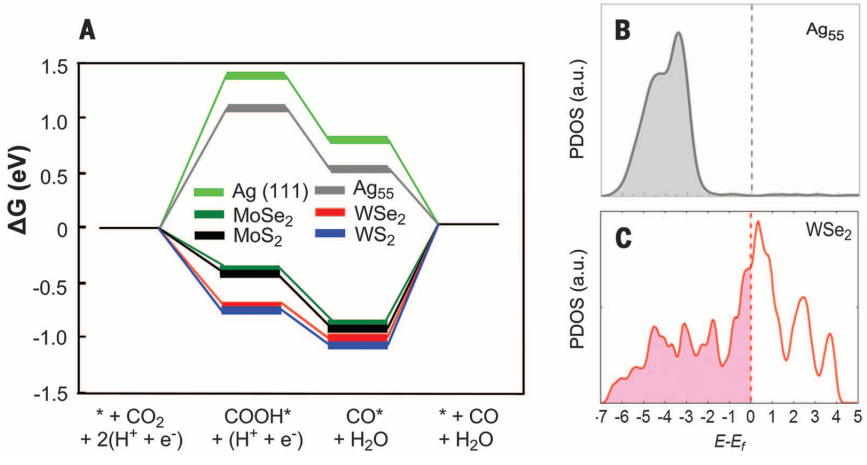


Fig. 4. Density functional theory analysis. (**A**) Calculated free energy diagrams for CO_2 electroreduction to CO on Ag(111), Ag_{55} NPs, MoS_2, WS_2, $MoSe_2$, and WSe_2 NFs at 0 V RHE. (**B**) Calculated partial density of states of the d band (spin-up) of the surface Ag atom of Ag_{55}. (**C**) Calculated partial density of states of the surface bare metal edge atom (W) of the WSe_2 NFs. The calculations of the Ag systems are at CO coverage of 1/16 ML; those of the TMDC systems are at CO coverage of 1 ML. See (*13*) for details of the coverage effects in the TMDC systems.

REFERENCES AND NOTES

1. R. Angamuthu, P. Byers, M. Lutz, A. L. Spek, E. Bouwman, *Science* **327**, 313–315 (2010).
2. J. Hawecker, J.-M. Lehn, R. Ziessel, *Helv. Chim. Acta* **69**, 1990–2012 (1986).
3. J. Medina-Ramos, J. L. DiMeglio, J. Rosenthal, *J. Am. Chem. Soc.* **136**, 8361–8367 (2014).

4. R. D. Richardson, E. J. Holland, B. K. Carpenter, *Nat. Chem.* **3**, 301–303 (2011).
5. B. A. Rosen *et al.*, *Science* **334**, 643–644 (2011).
6. L. Zhang, D. Zhu, G. M. Nathanson, R. J. Hamers, *Angew. Chem. Int. Ed.* **53**, 9746–9750 (2014).
7. D. Gao *et al.*, *J. Am. Chem. Soc.* **137**, 4288–4291 (2015).
8. H. Mistry *et al.*, *J. Am. Chem. Soc.* **136**, 16473–16476 (2014).
9. R. Reske, H. Mistry, F. Behafarid, B. Roldan Cuenya, P. Strasser, *J. Am. Chem. Soc.* **136**, 6978–6986 (2014).
10. W. Zhu *et al.*, *J. Am. Chem. Soc.* **135**, 16833–16836 (2013).
11. A. Salehi-Khojin *et al.*, *J. Phys. Chem. C* **117**, 1627–1632 (2013).
12. M. Asadi *et al.*, *Nat. Commun.* **5**, 4470 (2014).
13. See supplementary materials on *Science* Online.
14. J. L. DiMeglio, J. Rosenthal, *J. Am. Chem. Soc.* **135**, 8798–8801 (2013).
15. B. Kumar *et al.*, *Nat. Commun.* **4**, 2819 (2013).
16. B. A. Rosen, W. Zhu, G. Kaul, A. Salehi-Khojin, R. I. Masel, *J. Electrochem. Soc.* **160**, H138–H141 (2012).
17. Y. Chen, C. W. Li, M. W. Kanan, *J. Am. Chem. Soc.* **134**, 19969–19972 (2012).
18. C. W. Li, M. W. Kanan, *J. Am. Chem. Soc.* **134**, 7231–7234 (2012).
19. D. A. Lutterman, Y. Surendranath, D. G. Nocera, *J. Am. Chem. Soc.* **131**, 3838–3839 (2009).
20. S. Y. Reece *et al.*, *Science* **334**, 645–648 (2011).
21. M. W. Kanan, D. G. Nocera, *Science* **321**, 1072–1075 (2008).
22. Y. Tan *et al.*, *Adv. Mater.* **26**, 8023–8028 (2014).
23. D. J. Li *et al.*, *Nano Lett.* **14**, 1228–1233 (2014).
24. J. Kibsgaard, Z. Chen, B. N. Reinecke, T. F. Jaramillo, *Nat. Mater.* **11**, 963–969 (2012).
25. G. Fishman, D. Calecki, *Phys. Rev. Lett.* **62**, 1302–1305 (1989).
26. T. Fujita *et al.*, *Phys. Rev. Lett.* **101**, 166601 (2008).
27. C. Gong *et al.*, *ACS Nano* **7**, 11350–11357 (2013).
28. J. K. Nørskov *et al.*, *J. Phys. Chem. B* **108**, 17886–17892 (2004).
29. H. A. Hansen, J. B. Varley, A. A. Peterson, J. K. Nørskov, *J. Phys. Chem. Lett.* **4**, 388–392 (2013).
30. A. A. Peterson *et al.*, *Energy Environ. Sci.* **3**, 1311 (2010).
31. B. Hammer, J. K. Nørskov, *Adv. Catal.* **45**, 71–129 (2000).
32. B. Hammer, J. K. Norskov, *Nature* **376**, 238–240 (1995).
33. C. Tsai, F. Abild-Pedersen, J. K. Nørskov, *Nano Lett.* **14**, 1381–1387 (2014).
34. C. Tsai, K. Chan, F. Abild-Pedersen, J. K. Nørskov, *Phys. Chem. Chem. Phys.* **16**, 13156–13164 (2014).

ACKNOWLEDGMENTS

Supported by NSF grant CBET-1512647 (A.S.-K.); the MRSEC Materials Preparation and Measurement Laboratory shared user facility at the University of Chicago (grant NSF-DMR-1420709); the EPIC facility (NUANCE Center–Northwestern University), which has received support from the MRSEC program (grant NSF-DMR-1121262) at the Materials Research Center; the Nanoscale Science and Engineering Center (NSF EEC-0647560) at the International Institute for Nanotechnology; and the State of Illinois through the International Institute for Nanotechnology. The work at Argonne National Laboratory was supported by the U.S. Department of Energy under contract DE-AC0206CH11357 from the Division of Materials Science and Engineering, Basic Energy Science (P.Z., C.L., and L.A.C.). The authors also acknowledge Analytical Chemistry Laboratory of the Earth and Planetary Sciences Department, University of New Mexico. Author contributions: A.S.-K., M.A., and B.K. conceived the idea; A.S.-K., M.A., K.K., and A.V.A. performed the electrochemical experiments; M.A., P.A., and A.B. grew and synthesized the TMDC flakes; M.A., B.K., and P.Y. did the characterizations; C.L., P.Z., and L.C. performed DFT calculations; P.P. and R.K. carried out STEM and electron energy loss spectroscopy; R.H. performed UPS experiments; J.M.C. performed elemental analysis measurement; J.A. and A.S.K. jointly supervised M.A.'s efforts; and all authors contributed to the manuscript before submission. A.S.-K., M.A., and B.K. have filed a provisional patent application. The other authors declare no competing financial interests.

SUPPLEMENTARY MATERIALS

www.sciencemag.org/content/353/6298/467/suppl/DC1
Materials and Methods
Figs. S1 to S27
Tables S1 to S7
References (*35*–*53*)

14 February 2016; accepted 1 July 2016
10.1126/science.aaf4767

PALEOCEANOGRAPHY

North Atlantic ocean circulation and abrupt climate change during the last glaciation

L. G. Henry,[1]* J. F. McManus,[1] W. B. Curry,[2,3] N. L. Roberts,[4] A. M. Piotrowski,[4] L. D. Keigwin[2]

The most recent ice age was characterized by rapid and hemispherically asynchronous climate oscillations, whose origin remains unresolved. Variations in oceanic meridional heat transport may contribute to these repeated climate changes, which were most pronounced during marine isotope stage 3, the glacial interval 25 thousand to 60 thousand years ago. We examined climate and ocean circulation proxies throughout this interval at high resolution in a deep North Atlantic sediment core, combining the kinematic tracer protactinium/thorium (Pa/Th) with the deep water-mass tracer, epibenthic $\delta^{13}C$. These indicators suggest reduced Atlantic overturning circulation during every cool northern stadial, with the greatest reductions during episodic Hudson Strait iceberg discharges, while sharp northern warming followed reinvigorated overturning. These results provide direct evidence for the ocean's persistent, central role in abrupt glacial climate change.

Unlike the relatively stable preindustrial climate of the past 10 thousand years, glacial climate was characterized by repeated millennial oscillations (*1*). These alternating cold stadial and warm interstadial events were most abrupt and pronounced on Greenland and across much of the northern hemisphere, with the most extreme regional conditions during several Heinrich (H) events (*2*), catastrophic iceberg discharges into the subpolar North Atlantic Ocean. These abrupt events not only had an impact on global climate but also are associated with widespread reorganizations of the planet's ecosystems (*3*). Geochemical fingerprinting of the ice-rafted detritus (IRD) associated with the most pronounced of these events consistently indicates a source in the Hudson Strait (HS) (*4*), so we abbreviate this subset of H events as HS events and their following cool periods as HS stadials. During northern stadials, ice cores show that Antarctica warmed, and each subsequent rapid northern hemisphere warming was followed shortly by cooling at high southern latitudes (*5*). Explanations for the rapidity and asynchrony of these climate changes require a mechanism for partitioning heat on a planetary scale, initiated either through reorganization of atmospheric structure (*6*) or the ocean's thermohaline circulation, particularly the Atlantic meridional overturning circulation (AMOC) (*7*–*10*). Coupled climate models have successfully used each of these mechanisms to generate time series that replicate climate variability observed in paleoclimate archives (*9*, *11*). We investigated the relationship between Northern Hemispheric climate as recorded in Greenland ice cores and marine sediments, along with isotopic deep-sea paleoproxies sensitive to changes in North Atlantic Deep Water (NADW) production and AMOC transport during marine isotope stage three (MIS3). Throughout that time, when global climate was neither as warm as today nor as cold as the last glacial maximum (LGM), ice sheets of intermediate size blanketed much of the northern hemisphere, and large millennial stadial-interstadial climate swings (*6*, *8*) provide a wide dynamic range that allows examination of the ocean's role in abrupt change.

Sediment samples were taken from the long (35 m) core KNR191-CDH19—recovered from the Bermuda Rise (33° 41.443' N; 57° 34.559' W, 4541 m water depth) in the northwestern Atlantic Ocean (Fig. 1), near previous seafloor sampling at Integrated Ocean Drilling Program (IODP) site 1063—and coring sites KNR31 GPC-5, EN120 GGC-1, MD95-2036, OCE326-GGC5, and others. Because this region of the deep North Atlantic is characterized by steep lateral gradients in tracers of NADW and Antarctic Bottom Water (AABW), the Bermuda Rise has been intensively used to explore the connection between changes in ocean circulation and climate (*7*, *12*). In this study, we measured the radioisotopes ^{231}Pa and ^{230}Th in bulk sediment, age-corrected to the time of deposition, along with stable carbon ($\delta^{13}C$) and oxygen ($\delta^{18}O$) isotope ratios in the microfossil shells of both epibenthic foraminifera (*Cibicidoides wuellerstorfi* and *Nuttallides umbonifera*) and planktonic foraminifera (*Globigerinoides ruber*), respectively, yielding inferences on relative residence times and the origin of deep water masses on centennial time scales.

Isotopes of protactinium and thorium, ^{231}Pa and ^{230}Th, are produced from the decay of ^{235}U and ^{234}U, respectively, dissolved in seawater. This activity of ^{231}Pa and ^{230}Th in excess of the amount

[1]Lamont-Doherty Earth Observatory (LDEO), Columbia University, Palisades, NY 10964, USA. [2]Woods Hole Oceanographic Institution, Woods Hole, MA 02543, USA. [3]Bermuda Institute of Ocean Sciences, St. George's, Bermuda. [4]University of Cambridge, Department of Earth Sciences, Cambridge CB2 3EQ, UK.
*Corresponding author. Email: lhenry@ldeo.columbia.edu

Downloaded from http://science.sciencemag.org/ on July 28, 2016

supported by the decay of uranium within the crystal lattice of the sediment's mineral grains is denoted by $^{231}Pa_{xs}$ and $^{230}Th_{xs}$. Because the parent U isotopes have long residence times, U is well mixed throughout the ocean. This yields a $^{231}Pa_{xs}/^{230}Th_{xs}$ (hereafter Pa/Th) production ratio (Pa/Th = 0.093) that is constant and uniformly distributed (*13*, *14*). Both daughter isotopes are removed by adsorption onto settling particles, with Th more efficiently scavenged than Pa. The residence time of $^{231}Pa_{xs}$ (τ_{res} = ~200 years) in seawater is thus greater than that of $^{230}Th_{xs}$ (τ_{res} = ~30 years), allowing $^{231}Pa_{xs}$ to be redistributed laterally by changes in basin-scale circulation before deposition (*7*, *14*–*16*), with the additional potential influence of removal because of changes in particle rain associated with biological productivity (*17*). Settling particles (*18*) and surface sediments throughout the basin reveal a deficit in $^{231}Pa_{xs}$ burial that is consistent with large-scale export by the deep circulation (Fig. 1) (*19*).

The downcore Pa/Th in core CDH-19 ranges from ~0.05 to slightly above the production ratio of 0.093, with a series of well-defined variations throughout MIS3 (Fig. 2). In sediments deposited during Greenland interstadial intervals (*1*), Pa/Th ratios average 0.0609 ± 0.0074 (2σ), which is substantially below the production ratio (Fig. 2) and only 10% higher than the mean value (Pa/Th = 0.055) of the Holocene, a time of relatively vigorous AMOC (*7*). Because $^{230}Th_{xs}$ is buried in near balance with its production (*20*), the relatively low Pa/Th indicates a substantial lateral export of $^{231}Pa_{xs}$, which is consistent with relatively vigorous AMOC during interstadials, although the vertical integration through the water column of this deficit does not distinguish whether this export occurred at deep or intermediate levels. Epibenthic $\delta^{13}C$ ($\delta^{13}C_{BF}$) data allow discrimination between these two possibilities and display increased values during each interstadial, implying a greater contribution of the isotopically more positive North Atlantic end member (Fig. 2). During these intervals, this positive isotopic signal suggests that a deeper overturning cell was established, rather than a shallower, yet more vigorous one. This confirms a previous suggestion of intervals of relatively strong AMOC within the most recent ice age (*21*, *22*), although Pa/Th and $\delta^{13}C_{BF}$ adjusted for whole-ocean inventory changes (*23*) rarely reach early Holocene values.

Pa/Th increases within each Greenland stadial interval, for a mean duration of 0.531 ± 0.303 thousand years to a Pa/Th value of 0.0797 ± 0.0154, which indicates decreased lateral export of $^{231}Pa_{xs}$ and is consistent with a shallower or reduced overturning cell in the North Atlantic. During these

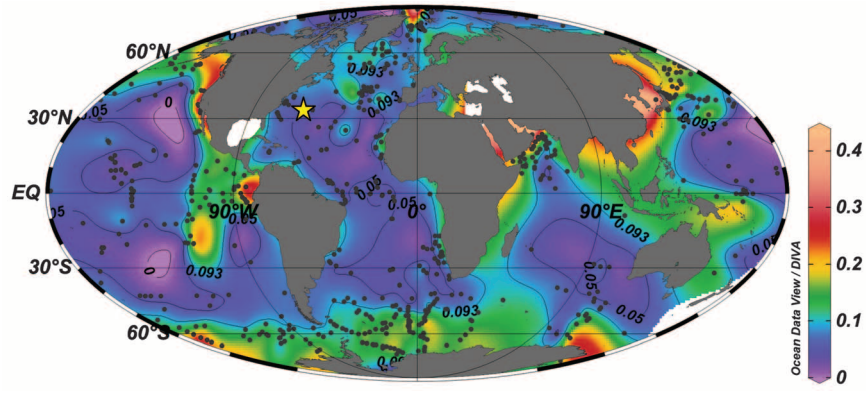


Fig. 1. Study core location and coretop distribution of Pa/Th. Location sediment core CDH19 indicated with a star (33° 41.443' N; 57° 34.559' W, 4541-m water depth), with Pa/Th ratios (black dots) in core top sediments used with Ocean Data View Data-Interpolating Variational Analysis gridding to produce the color contours. White areas contain no data.

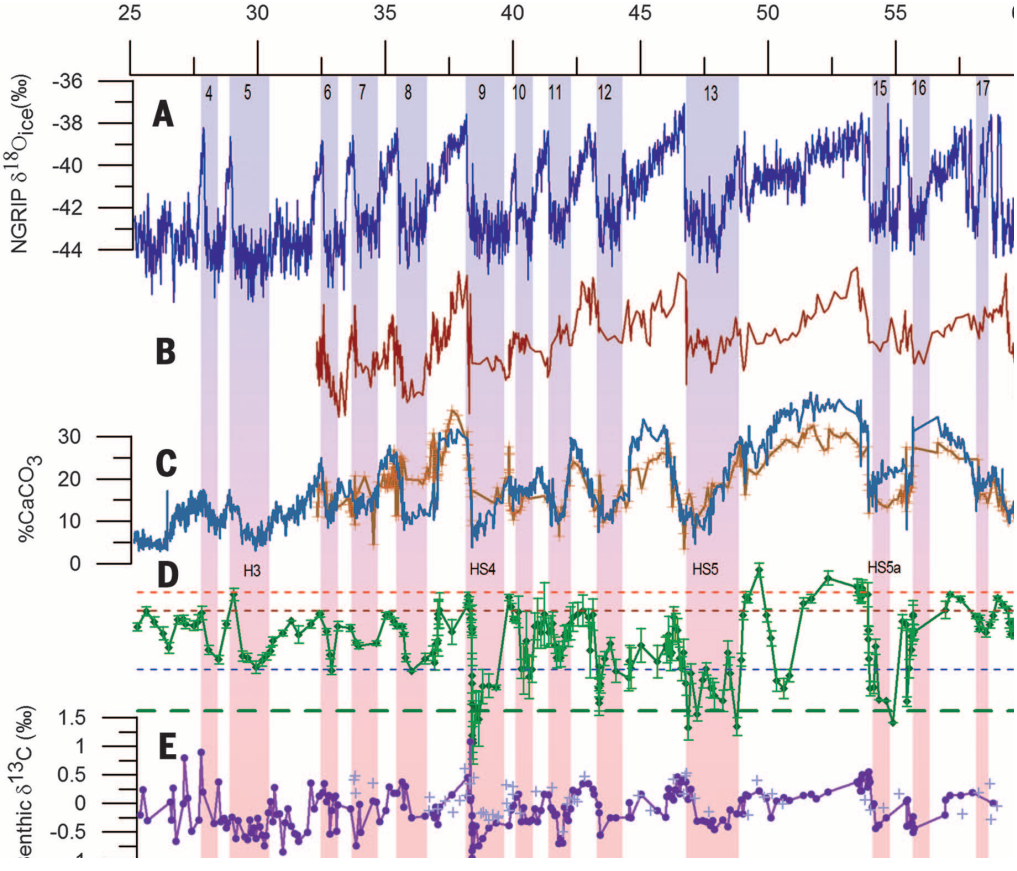


Fig. 2. Climate and circulation indices through MIS3. Stadials are numbered with vertical bars. (**A**) NGRIP ice core $\delta^{18}O_{ice}$ 75.1°N, 42.32°W (*35*). (**B**) SST (°C) from MD95-2036, 33° 41.444'N, 57° 34.548'W, 4462 m (*31*). (**C**) Calcium x-ray fluorescence (orange) from core CDH19 (this study) mapped to %$CaCO_3$, with calibration r^2 = 0.87 (S.1), with spectral reflectance (blue) from core MD95-2036 (*36*). (**D**) Pa/Th from bulk sediment (green) taken from core CDH19. (**E**) $\delta^{13}C_{BF}$ from core CDH19 (purple) alternates between values consistent with southern and northern sourced $\delta^{13}C_{BF}$ end members.

Downloaded from http://science.sciencemag.org/ on July 28, 2016

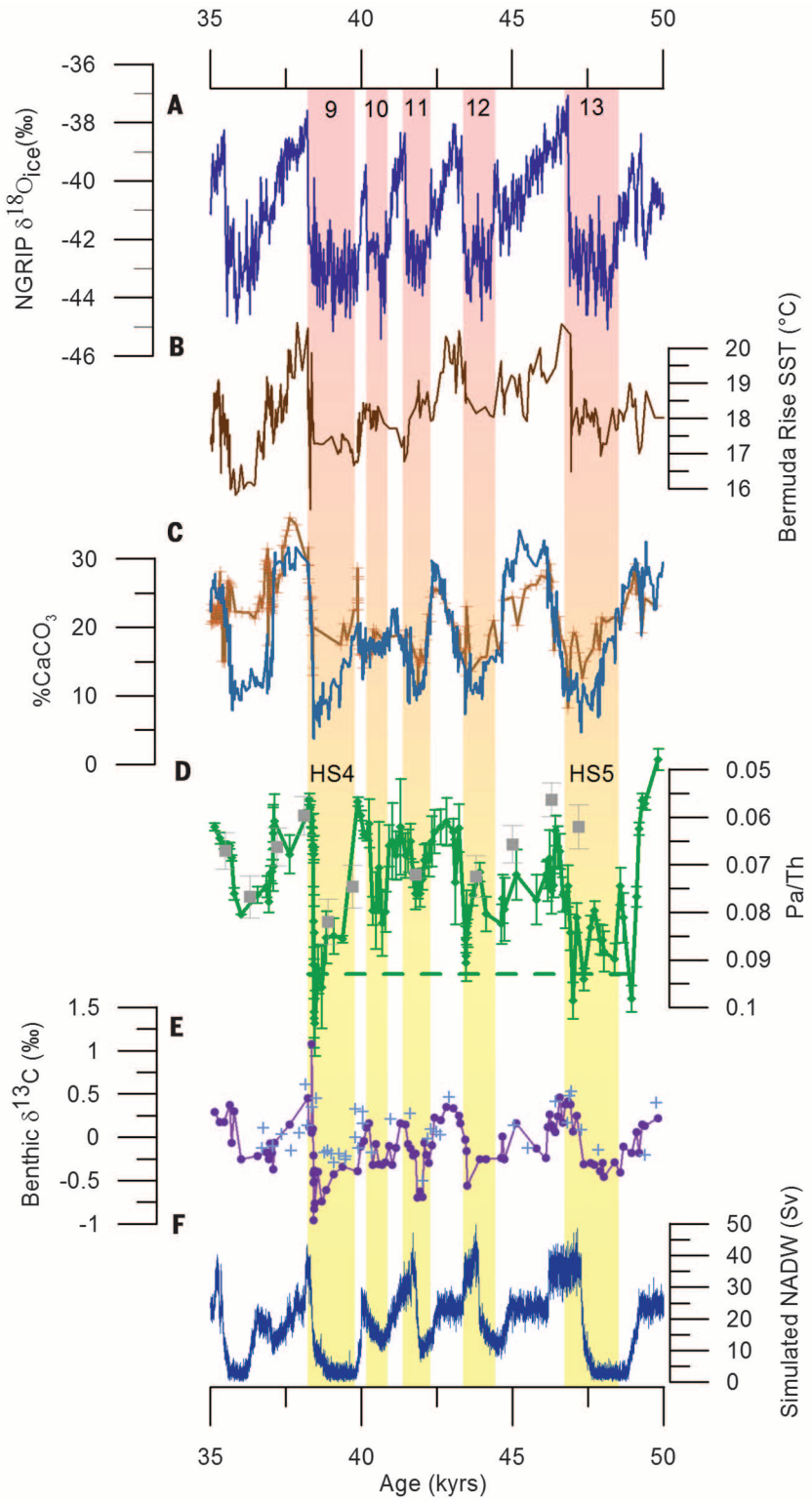


Fig. 3. Detail of millennial cyclicity in glacial climate and the deep ocean. (**A**) through (**E**) are as in Fig. 2, A to E. (**F**) Simulated NADW (Sv) in a coupled ocean/atmosphere model (*11*), with (D) published Pa/Th (gray squares) (*21*) and $\delta^{13}C_{BF}$ data (blue crosses) (*12*).

stadials, $\delta^{13}C_{BF}$ decreases substantially to negative values [−0.2 per mill (‰) to −0.5‰], suggesting greater influence of the glacial equivalent of modern Antarctic Bottom Water (AABW), an isotopic result that is consistent with reduced AMOC from a coupled climate model (*10*). Although the northern and southern water mass end members are not well known throughout the last glaciation, deep waters in the Atlantic during the LGM ranged from less than −0.5‰ in the south to greater than 1.5‰ in the north (*23*). If these values prevailed throughout MIS3, then the low $\delta^{13}C_{BF}$ indicates a dominant stadial influence of southern waters and substantial northward retreat or shoaling of the AABW/NADW mixing zone, which is consistent with the deep water mass configuration that has previously been reconstructed for the LGM (*23*, *24*), although not for millennial-scale stadial intervals within the glaciation.

The mean Pa/Th of both stadials and interstadials is consistent with export of $^{231}Pa_{xs}$ from the subtropical North Atlantic during most of MIS3. During peak interstadials, when low Pa/Th indicates the local burial of approximately half of $^{231}Pa_{xs}$ production, the remaining half would have been exported. In contrast, the substantial decrease in the lateral export of $^{231}Pa_{xs}$ evident in higher Pa/Th, along with lower $\delta^{13}C_{BF}$ during each stadial interval, points to repeated reductions in AMOC and its attendant northward heat transport throughout MIS3. The contrast between apparent deep, vigorous overturning during interstadials and shallower (*25*), weaker overturning during stadials is most pronounced in conjunction with all HS stadials (Fig. 2), when catastrophic discharge of melting icebergs from Canada flooded the subpolar North Atlantic (*4*).

Sediments deposited during HS stadials are characterized by a mean duration of 1.65 ± 0.545 thousand years and an average Pa/Th of 0.095 ± 0.016, which is indistinguishable from the production ratio. These results therefore indicate no net export of $^{231}Pa_{xs}$ from the subtropical North Atlantic during these events sourced from the Hudson Strait. This balance between seawater radiometric production and underlying sedimentary burial would be expected under conditions with a substantial reduction in AMOC or other lateral transport and might imply a near cessation of $^{231}Pa_{xs}$ export through deep circulation. Although variable scavenging may also contribute to sedimentary Pa/Th, values throughout MIS3 bear only a weak relationship with bulk and opal fluxes [coefficient of determination (r^2) = 0.19] (*19*), which therefore constitute secondary influences.

These new results reveal that AMOC variations were associated with every MIS3 stadial-interstadial oscillation, with the largest reductions during HS stadials. The well-resolved interval 35 thousand to 50 thousand years ago provides a good example (Fig. 3). This iconic interval contains H4, H5, and the intervening series of oscillations that have served as a basis for conceptual and computer models seeking to explain such variability (*8*–*11*, *26*, *27*). A previous Pa/Th record (*21*) covering this interval captured much of the overall amplitude, and the new data resolve each stadial increase in Pa/Th, indicating that only HS4 and HS5 reach the production ratio of 0.093. Because the interstadial values are similar to each other, the subsequent abrupt increases in AMOC and regional warming are also the greatest and occur

Downloaded from http://science.sciencemag.org/ on July 28, 2016

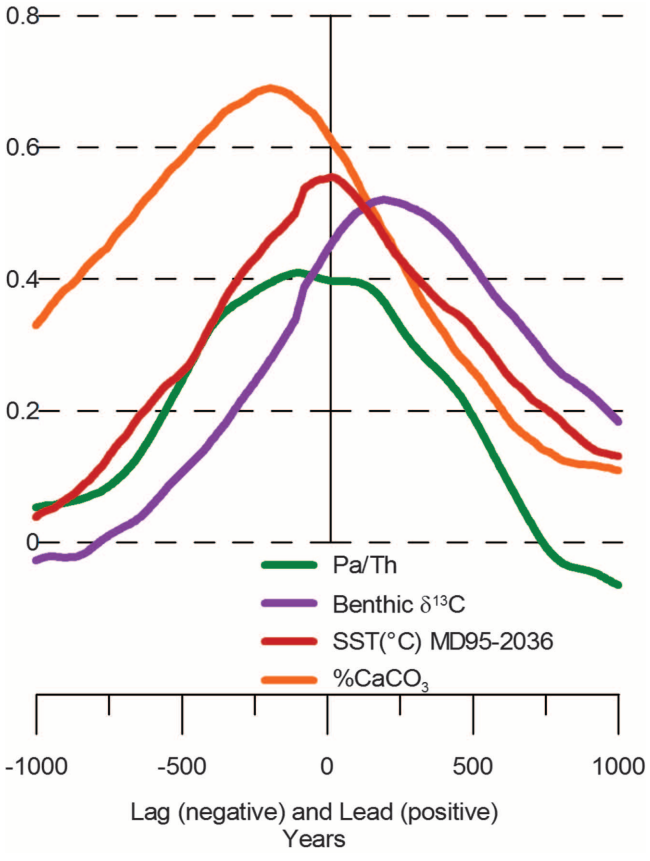


Fig. 4 Phasing lag correlations. Correlation of NGRIP ice core $\delta^{18}O$ with CDH19 $CaCO_3$ flux (blue), Pa/Th of bulk sediment from CDH19 (green), $\delta^{13}C_{BF}$ from CDH19 (purple), and SST °C from MD95-2036 (*31*) (red).

within the century-scale response time of Pa/Th. Throughout the records, the Pa/Th and $\delta^{13}C_{BF}$ bear a striking similarity to model output forced by freshwater anomalies (*11*).

Combined with previous investigations (*7*, *28*), these new results confirm that all HS events of the past 60 thousand years were associated with a dramatic increase in Pa/Th and are evidence for major reduction in AMOC in association with the largest IRD events (*29*). In contrast, H3, the sole Heinrich event stadial that fails to reach the production ratio (peak Pa/Th = 0.079), displays smaller IRD fluxes across the subpolar Atlantic (*29*), with provenance inconsistent with a Hudson Strait source (*4*). This muted result for H3 is consistent with evidence from the Florida Straits (*30*) showing a smaller reduction at that time in the northward flow of near-surface waters that feed the overturning circulation. As with all stadials, the HS events are characterized by lower $\delta^{13}C_{BF}$, suggesting diminished influence of NADW and proportionately greater AABW on Bermuda Rise. Combined Pa/Th and $\delta^{13}C_{BF}$ results therefore indicate a persistent pattern of stadial weakening and interstadial strengthening, with a repeatedly largest reduction in AMOC associated with all HS events. Although these observations are consistent with a number of numerical model simulations (*11*, *27*) as well as conceptual models for the mechanisms of abrupt change, they have previously been difficult to document and fully resolve.

Recent data from the Western Antarctic ice sheet provide compelling evidence for a robust lead of Greenland climate over Antarctica (*5*). That analysis revealed a Northern Hemisphere lead of 208 ± 96 years, indicating that the interhemispheric teleconnection propagates from north to south on time scales consistent with basin-scale ocean circulation. To ascertain whether Northern Hemisphere climate is forced or reinforced by changes in AMOC, we investigated the phase relationship between surface and deep-sea properties. Cross-correlations were performed on each of $\delta^{13}C_{BF}$, Pa/Th, sea surface temperature (SST), and $CaCO_3$ with North Greenland Ice Core Project (NGRIP) $\delta^{18}O$ from both sediment cores CDH19 and MD95-2036 from the Bermuda Rise. The optimal correlation of $\delta^{13}C_{BF}$ leads NGRIP $\delta^{18}O$ by approximately 2 centuries (Fig. 4). This lead is corroborated by Pa/Th phasing, which when considering the century-scale response time of the proxy (*13*, *14*) is consistent with AMOC changes indicated by $\delta^{13}C_{BF}$. The SST reconstruction from MD95-2036 was aligned with Greenland $\delta^{18}O$, yielding a correlation of $r^2 = 0.83$ (*31*). SST and Pa/Th are synchronous with NGRIP to within the estimated bioturbation error of 8 cm within the core, displaying correlations with Greenland of $r^2 = 0.47$ for Pa/Th and $r^2 = 0.65$ for SST. The optimal correlation of $\%CaCO_3$, $r^2 = 0.64$, lags NGRIP $\delta^{18}O$ by nearly 200 years.

The consistent lead of variations in $\delta^{13}C_{BF}$ before SST and Greenland temperatures, repeated over multiple millennial cycles, indicates the potential influence of AMOC on NH climate and confirms that the Bermuda Rise is exposed to shifts in deep-water mass mixing. Initially, deep circulation changes, which is evidenced overall by the timing of $\delta^{13}C_{BF}$. Pa/Th shifts are essentially in tandem with regional temperature when circulation accelerates, and soon thereafter as it responds to weakening AMOC (*19*). Given the response time of Pa/Th to instantaneous shifts in North Atlantic overturning (*13*, *14*), this also suggests that changes in AMOC precede regional temperature change, although the exact timing may have differed during cooling and warming phases. Both SST and Greenland temperature proxies lag the ocean circulation in a consistent fashion, and in turn, these northern changes have been demonstrated to lead Antarctic temperatures (*5*). Calcium-carbonate concentration is the last of the proxies to respond to AMOC change, which is consistent with the longer time scale of preservation, dissolution, and dilution in the deep ocean.

The relative timing of the observed AMOC changes has important implications for regional and global climate. Whereas numerous computer simulations suggest that melting icebergs and other freshwater input associated with H events may have shut down NADW production (*9*, *11*, *27*), recent results examining the phasing of North Atlantic SST and IRD suggest that stadial conditions began to develop before ice-rafting (*32*). The evidence here nevertheless indicates that the greatest AMOC reduction and the coldest stadial intervals accompanied the largest iceberg discharges. This suggests that the iceberg discharges may have provided a positive feedback mechanism to accelerate the initial cooling within each multimillennial climate cycle. In addition, the extended H-stadial reductions in AMOC observed in this study coincide with intervals of rising atmospheric CO_2 (*33*), whereas CO_2 declined when AMOC increased during the subsequent sharp transitions to northern interstadials, supporting a potential influence on the atmosphere by the deep circulation on millennial time scales (*34*).

The robust relationship of reductions in export of northern deep waters evident in reduced $^{231}Pa_{xs}$ export and decreased $\delta^{13}C_{BF}$ before and during stadial periods, and the dramatic increases in both during interstadials, provide direct evidence for the role of AMOC in abrupt glacial climate change. The sequence of marked circulation changes and northern hemisphere climate detailed here, combined with the demonstrated lag of Antarctic temperature variations (*5*), strongly implicates changes in meridional heat transport by the ocean as a trigger for abrupt northern hemisphere warming and the tipping of the "bipolar seesaw" (*26*).

REFERENCES AND NOTES

1. W. Dansgaard *et al.*, *Nature* **364**, 218–220 (1993).
2. W. Broecker, G. Bond, M. Klas, E. Clark, J. McManus, *Clim. Dyn.* **6**, 265–273 (1992).
3. M. Yasuhara, T. M. Cronin, P. B. Demenocal, H. Okahashi, B. K. Linsley, *Proc. Natl. Acad. Sci. U.S.A.* **105**, 1556–1560 (2008).
4. S. R. Hemming, *Rev. Geophys.* **42**, RG1005 (2004).
5. C. Buizert *et al.*, *Nature* **520**, 661–665 (2015).
6. X. Zhang, G. Lohmann, G. Knorr, C. Purcell, *Nature* **512**, 290–294 (2014).
7. J. F. McManus, R. Francois, J. M. Gherardi, L. D. Keigwin, S. Brown-Leger, *Nature* **428**, 834–837 (2004).
8. R. B. Alley, P. Clark, L. Keigwin, R. Webb, *Geophys. Monog. Ser.* **112**, 385–394 (1999).
9. S. Rahmstorf, *Nature* **419**, 207–214 (2002).
10. A. Schmittner, D. C. Lund, *Clim. Past* **11**, 135–152 (2015).
11. L. Menviel, A. Timmermann, T. Friedrich, M. H. England, *Clim. Past* **10**, 63–77 (2014).
12. L. Keigwin, E. Boyle, *Paleoceanography* **14**, 164–170 (1999).
13. G. M. Henderson, R. F. Anderson, *Rev. Mineral. Geochem.* **52**, 493–531 (2003).
14. E. F. Yu, R. Francois, M. P. Bacon, *Nature* **379**, 689–694 (1996).
15. C. Negre *et al.*, *Nature* **468**, 84–88 (2010).

Downloaded from http://science.sciencemag.org/ on July 28, 2016

16. J. M. Gherardi *et al.*, *Paleoceanography* **24**, PA2204 (2009).
17. R. F. Anderson *et al.*, *Science* **323**, 1443–1448 (2009).
18. C. Hayes *et al.*, *Mar. Chem.* **170**, 49–60 (2015).
19. Materials and methods are available as supplementary materials on *Science* Online.
20. G. M. Henderson, C. Heinze, R. F. Anderson, A. M. E. Winguth, *Deep Sea Res. Part I Oceanogr. Res. Pap.* **46**, 1861–1893 (1999).
21. E. Böhm *et al.*, *Nature* **517**, 73–76 (2015).
22. J. Gottschalk *et al.*, *Nat. Geosci.* **8**, 950–954 (2015).
23. W. B. Curry, D. W. Oppo, *Paleoceanography* **20**, PA1017 (2005).
24. J. F. Adkins, *Paleoceanography* **28**, 539–561 (2013).
25. R. Zahn, A. Stüber, *Earth Planet. Sci. Lett.* **200**, 191–205 (2002).
26. W. Broecker, *Paleoceanography* **13**, 119–121 (1998).
27. A. Ganopolski, S. Rahmstorf, *Nature* **409**, 153–158 (2001).
28. J. Lippold *et al.*, *Geophys. Res. Lett.* **36**, L12601 (2009).
29. J. F. McManus, R. F. Anderson, W. S. Broecker, M. Q. Fleisher, S. M. Higgins, *Earth Planet. Sci. Lett.* **155**, 29–43 (1998).
30. J. Lynch-Stieglitz *et al.*, *Nat. Geosci.* **7**, 144–150 (2014).
31. J. P. Sachs, S. J. Lehman, *Science* **286**, 756–759 (1999).
32. S. Barker *et al.*, *Nature* **520**, 333–336 (2015).
33. J. Ahn, E. J. Brook, *Science* **322**, 83–85 (2008).
34. A. Schmittner, E. D. Galbraith, *Nature* **456**, 373–376 (2008).
35. A. Svensson *et al.*, *Clim. Past* **4**, 47–57 (2008).
36. E. A. Boyle, *Proc. Natl. Acad. Sci. U.S.A.* **94**, 8300–8307 (1997).

ACKNOWLEDGMENTS

Data are available at www.ncdc.noaa.gov/paleo/study/20248. This research was supported in part by a NSF Graduate Research Fellowship to L.G.H., by awards from the Comer Science and Education Foundation and NSF grant ATM-0936496 to J.F.M., and an award from the LDEO Climate Center to L.G.H. and J.F.M. L.D.K. and W.B.C. were supported by NSF grant ATM-0836472, and L.D.K. was supported by NSF grant AGS-1548160. We thank M. Jeglinski and K. Rose for technical support. The authors thank R. Anderson, S. Hemming, and C. Hayes for constructive discussion leading to improvement of the manuscript; R. Anderson for unpublished data included in the Fig. 1 map; and M. Fleisher for analytical support.

SUPPLEMENTARY MATERIALS

www.sciencemag.org/content/353/6298/470/suppl/DC1
Materials and Methods
SupplementaryText
Figs. S1 to S7
References (*37*–*55*)
Database S1

29 February 2016; accepted 20 June 2016
10.1126/science.aaf5529

EDUCATION

Teaching accreditation exams reveal grading biases favor women in male-dominated disciplines in France

Thomas Breda[1,2]*† and Mélina Hillion[1,3]†

Discrimination against women is seen as one of the possible causes behind their underrepresentation in certain STEM (science, technology, engineering, and mathematics) subjects. We show that this is not the case for the competitive exams used to recruit almost all French secondary and postsecondary teachers and professors. Comparisons of oral non–gender-blind tests with written gender-blind tests for about 100,000 individuals observed in 11 different fields over the period 2006–2013 reveal a bias in favor of women that is strongly increasing with the extent of a field's male-domination. This bias turns from 3 to 5 percentile ranks for men in literature and foreign languages to about 10 percentile ranks for women in math, physics, or philosophy. These findings have implications for the debate over what interventions are appropriate to increase the representation of women in fields in which they are currently underrepresented.

Why are women underrepresented in most areas of science, technology, engineering, and mathematics (STEM)? One of the most common explanations is that a hiring bias against women exists in those fields (*1*–*4*). This explanation is supported by a few older experiments (*5*–*7*), a recent one with fictitious resumes (*8*), and a recent lab experiment (*9*), which suggest that the phenomenon still prevails.

However, some scholars have challenged this view (*10*, *11*), and another recent experiment with fictitious resumes finds a bias in favor of women in academic recruitment (*12*). Studies based on actual hiring also find that when women apply to tenure-track STEM positions, they are more likely to be hired (*13*–*18*). However, those studies do not control for applicants' quality and a frequent claim is that their results simply reflect that only the best female Ph.D.'s apply to these positions, whereas a larger fraction of males do so (*11*, *13*). A study by one of us did partly control for applicants' quality and reported a bias in favor of women in male-dominated fields (*19*). However, it has limited external validity because it relies on only 3000 candidates who took the French Ecole Normale Supérieure entrance exam.

The present analysis is based on a natural experiment involving >100,000 individuals who participated in competitive exams used to hire French primary, secondary, and college or university teachers over the period 2006–2013. It has two distinct advantages over all previous studies. First, it provides large-scale real-world evidence of gender biases in evaluation-based hiring in several fields. Second, it shows that those biases against or in favor of women are strongly shaped by the actual degree of female underrepresentation in the field in which the evaluation takes place, which partly reconciles existing studies.

Carefully taking into account the extent of underrepresentation of women in 11 academic fields allowed us to extend the analysis beyond the STEM distinction. As pointed out recently (*11*, *12*, *19*, *20*), the focus on STEM versus non-STEM fields can be misleading for understanding female underrepresentation in academia, as some STEM fields are not dominated by men [e.g., 54% of U.S. Ph.D.'s in molecular biology are women (*21*)], whereas some non-STEM fields, including humanities, are male-dominated [e.g., only 31% of U.S. Ph.D.'s in philosophy are women (*21*)]. A better predictor of this underrepresentation, some have argued, is the belief that innate raw talent is the main requirement to succeed in the field (*20*).

To study how female underrepresentation can shape skills assessment, we exploit the two-stage design of the three national exams used in France to recruit virtually all primary-school teachers, CRPE middle- and high-school teachers, CAPES and Agrégation; as well as a large share of graduate school and university teachers, who also take the Agrégation (*22*). A college degree is necessary to take part in those competitive exams [table S1 in (*22*)]. Except for the lower level (CRPE), each exam is subject-specific and typically includes two or three written tests. The best candidates after those written tests (tables S2 and S3) are eligible for typically two or three oral tests taken no later than 3 months after the written tests (*22*). Note that oral tests are not general recruiting interviews: Depending on the subject, they include exercises, questions, or text discussions designed to assess candidates' fundamental skills, exactly as written tests. Teachers or professors who have specialized in the subject grade all the tests. At the highest-level exam (Agrégation), 80% of evaluators are either full-time researchers or university professors in French academia. The corresponding statistic is 30% for the medium-level exam (CAPES).

Our strategy exploits the "blinding" of the written tests (candidates' name and gender are not known by the professors who grade these tests), whereas the oral tests are not blinded. If one assumes that female handwriting cannot be easily detected—which we discuss later—written tests

[1]Paris School of Economics, 48 Boulevard Jourdan, Paris 75014, France. [2]CNRS, UMR8545, Paris-Jourdan Sciences-Economiques, 48 Boulevard Jourdan, Paris 75014, France. [3]Center for Research in Economics and Statistics (CREST), 15 Boulevard Gabriel Péri, Malakoff 92245, France.
*The authors contributed equally to this work. †**Corresponding author. Email: thomas.breda@ens.fr (T.B.); melina.hillion@gmail.com (M.H.)**

Downloaded from http://science.sciencemag.org/ on July 28, 2016

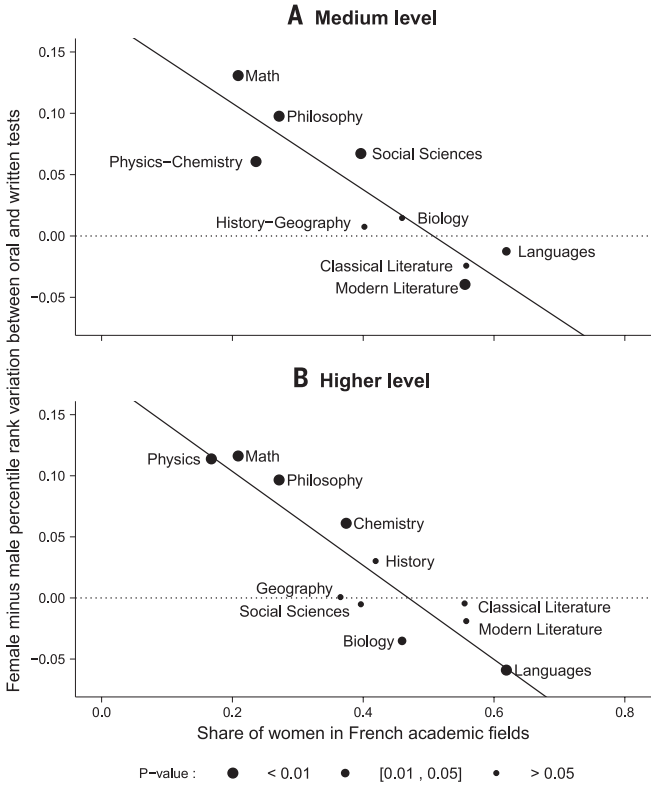


Fig. 1. Female evaluation advantage or disadvantage and fields' extent of male-domination. (**A** and **B**) The gap between females' average percentile rank on nonblind oral tests and blind written tests, minus the same gap for men is shown on the *y* axis. It is computed for each field-specific exam at the high and medium level. The size of each point indicates the extent to which it is different from 0 (*P* value from Student's *t* test). Fields' extent of (non–)male-domination (*x* axis) measured by the share of women academics in each field [see (*22*) for alternative measures].

provide a counterfactual measure of students' cognitive ability in each subject.

The French evaluation data offer unique advantages over previously published experiments; they provide real-world test scores for a large group of individuals. Thus, they avoid the usual problem of experiments' limited external validity. At the same time, these data present a compelling "experiment of nature" in which naturally occurring variations can be leveraged to provide controls. A final advantage is being able to draw on very rich administrative data that allow numerous statistical controls to be applied and comparisons to be made across levels of evaluation, from lower-level (primary and secondary teaching) to college or university hiring.

To assess gender bias in evaluation, we focused on candidates who took all oral and written tests, and we ranked them according to their total score on either written or oral tests. We then compared the variation of women's mean percentile rank between written and oral tests to the same variation for men. This standardized measure is bounded between −1 and 1, and it is independent of the share of females among the total pool of applicants. It is equal to 1 if all women are below the men on written tests and above them on oral tests [see (*22*) for additional explanations]. For each subject-specific exam, we computed this measure and its statistical significance using a linear regression model—named DD1 in (*22*)—of the type $\Delta Rank_i = a + bF_i + \varepsilon_i$. $\Delta Rank_i$ is the variation in rank between oral and written tests of candidate i, F_i is an indicator variable equal to 1 for female candidates and 0 for males, ε_i is an error term, and b is the measure of interest.

In fields in which women are underrepresented (mathematics, physics, chemistry, and philosophy), oral tests favor women over men both on the higher-level exams (professorial and high-school teaching) and medium-level exams (secondary school teaching only) (Fig. 1) (Ps < 0.01 in all cases, see sample sizes and detailed results in table S4). In contrast, oral tests in fields in which women are well-represented (literature and foreign languages) favor men over women, but the differences are smaller and not always significantly different from 0 at the 5% statistical level (Fig. 1 and table S4). In history, geography, and social sciences, there are only small gender differences between oral and written tests. Those differences are not significantly different from 0 at the 5% statistical level. In biology, a bias against women is found on the high-level exam only. With the exception of social sciences at the medium-level exam (*22*), all results are robust to the inclusion of control variables and to the use of a more general econometric model that allows for different returns to candidates' fundamental skills between oral and written tests [see models DD2 and DD3+IV in (*22*)].

A simple explanation for these results would be that examiners on oral tests try to lower the gender difference in ability observed on written tests. This is not always the case (Fig. 2): The oral tests sometimes fully invert a significant ranking gap between women and men on written tests (physics at the highest level, math at the medium level).

A clear pattern emerges from Fig. 1: The more male-dominated a field is, the higher the bonus for women on the nonblinded oral tests. To formally capture this pattern, we study how the bonus b on oral tests varies with the share of women s among assistant professors and senior professors in the French academy [see (*22*) for statistical details and other measures of fields' feminization, e.g., table S5]. We find a significant negative relation at both the higher- and medium-level exams (see table S6) ($b = 0.25 - 0.53\,s$ at the high-level exam; $b = 0.13 - 0.28\,s$ at the medium-level exam, with $P < 0.02$ for both slopes and intercepts of the fitted lines).

The relation between the extent of a field's male-dominance and female bonuses on oral tests at the highest-level exams (for high-school teachers and professorial) is about 150% of that at the medium-level exams. At the highest level, switching from a subject as feminine as foreign languages ($s = 0.62$) to a subject as masculine as math ($s = 0.21$) leads female candidates to gain, on average, 17 percentile ranks on oral tests with respects to written tests. To avoid sample-selection bias, this comparison between the medium- and the high-level exam is made on a subsample of about 3500 individuals who have taken both exams in the same subject the same year [(*22*), fig. S2, and table S6].

Finally, the statistical analysis suggests an absence of large significant gender biases on oral tests for the lower-level teaching exam (*22*). Note that this exam is not subject-specific. However, since 2011, all applicants have been required to take both an oral and a written test in math and literature, which makes it possible to study the bonus on oral tests for women in those two subjects. We find a small premium of around 3 percentile ranks for women on oral tests, both in math and literature, with no clear difference between those two subjects (see table S7). This finding should, however, be considered with prudence because it can only be established with the more general econometric specification [see model DD3+IV in (*22*)].

The differences between written and oral tests on the specialized medium- and high-level exams have implications for the gender composition of newly recruited secondary and postsecondary teachers. Oral tests give the gender in the minority better chances of being hired (fig. S1) and, therefore, induce a rebalancing of gender ratios between teachers hired in male- and female-dominated fields (table S8). We also find that the gender gaps between oral and written tests are very stable across the written test score distribution in all fields for the medium- and high-level exams (table S9).

Should the differences between written and oral test scores be interpreted as evaluation biases? In natural experiments, the researcher does not have full control on the research design; thus, the results usually need to be interpreted with caution. The setting we exploit has three potential issues: (i) gender may be inferred on written tests from handwriting; (ii) there might be gender differences in the types of abilities that are required on oral and written tests; and (iii) the way candidates self-select in a given field may depend on their gender.

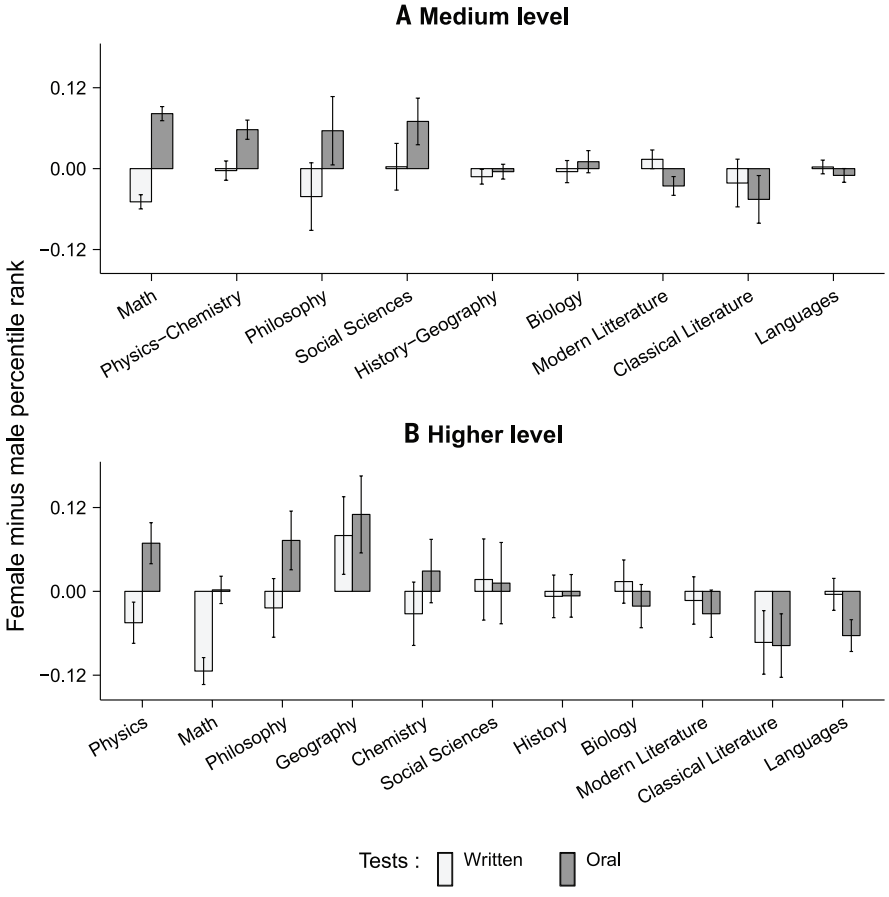


Fig. 2. Average rank difference between women and men on oral and written tests in each subject-specific exam at the high and medium level. (**A** and **B**) Error bars indicate 95% confidence intervals from Student's *t* test.

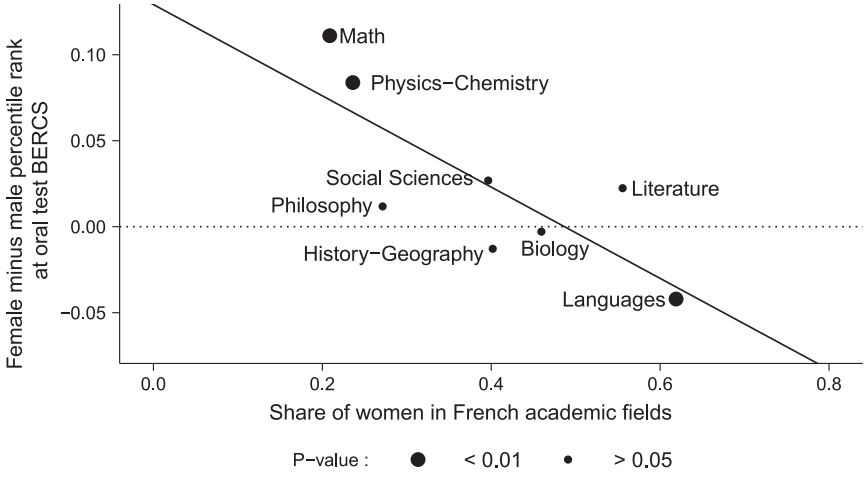


Fig. 3. Female advantage or disadvantage on an oral test which is identical in all fields. The difference between women's and men's average rank on the oral test "Behave as an ethical and responsible civil servant" in the different subject-specific medium-level exams (*y* axis). The size of each point indicates the extent to which it is different from 0 (*P* value from Student's *t* test). Any fields' extent of (non−)male-domination measured by the share of women academics in each field (*x* axis).

Tests that we previously conducted have shown that the rate of success in guessing gender from handwritten anonymous exam sheets is, on average, 68.6% (*19*). This suggests that examiners are rarely certain about the candidates' gender from written tests [see additional details in (*22*)]. Their limited ability to detect the gender of candidates from the written tests would be truly problematic for the interpretation of our results if and only if those examiners were biased in opposite directions on the written and oral tests. This assumption cannot be tested empirically but seems unlikely, given that the same examiners usually evaluate both the written and oral tests (*22*). Moreover, examiners' bias is likely to be smaller when they face presumably female or male handwriting than when they are exposed to an actual female or male candidate during an oral test. Therefore, partial gender detection on written tests should, if anything, only attenuate the magnitude of the estimated biases, which would keep their direction identified.

A more fundamental issue is that the gap between a candidate's oral and written test score in a given subject can capture the effect of gender-related attributes visible only from oral or written tests, such as the quality of handwriting, elocution, or emotional intelligence [see (*23*–*26*) for surveys on possible sex differences in cognitive abilities, including verbal fluency].

The first defense against those interpretations is that our key result is not the absolute gender gap in the oral versus written test scores in a given subject, but the variation—and even reversal—of this gap across subjects according to a regular pattern. If there are gender-specific differences in abilities required specifically for oral or written tests, these differences need to vary between male-dominated and other subjects to explain our results. For example, handwriting quality or elocution would both need to differ across gender and to be more rewarded for some subjects than for others. This could be true if the oral tests in the most male-dominated subjects are framed in a way that makes more visible the qualities that are more prevalent among women.

To overcome these issues and a possible handwriting detection problem, we exploit a remarkable feature of the teaching exams: since 2011, all of them have included an oral test entitled "Behave as an ethical and responsible civil servant" (BERCS). At the medium- and high-level exams, BERCS is the only test that is not subject- specific (*27*). This oral interview is a subpart of an oral test that otherwise attempts to evaluate the competence in the exam core subject. It is consequently graded by teachers or professors specialized in the exam core subject.

We have data on detailed scores for the BERCS test for the lower- and medium-level exams (*22*). Comparisons of gender differences in performance on this oral test across subjects for the medium-level exam reveals that women systematically get better grades, and that this bonus b' decreases with the share of women s in the exam's overall subject area (Fig. 3, $b' = 0.12 - 0.25\,s$, with $P < 0.0001$ for both the slope and the intercept, clustering by subjects). This pattern is similar to what is observed in Fig. 1 when comparing blind and nonblind subject-specific tests. However, the comparison across fields now relies on a single oral test that is identical in all exams. Consequently, the pattern in Fig. 3

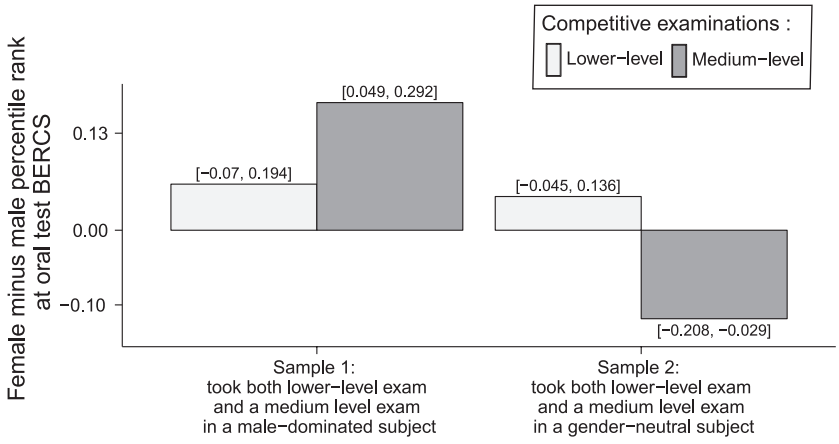


Fig. 4. Female advantage or disadvantage on the BERCS test for candidates taking both the lower-level exam and a medium level exam in either a male-dominated or a gender-neutral field. Rank difference between women and men on the oral test "Behave as an ethical and responsible civil servant" at the lower-level exam and at the medium-level exam among two samples of candidates: those who took both the lower- and medium-level exams in a strongly male-dominated subject (math, physics, or philosophy, left side, N = 60), and those who took both the lower- and medium-level exams in a more gender neutral subject (social sciences, history, geography, biology, literature, or foreign languages, right side, N = 120). To control for selection, ranks at the tests have been computed within each sample, ignoring other candidates that are not in the sample. Confidence intervals at the 90% level are given in square brackets.

cannot be influenced by (i) handwriting detection or by (ii) the fact that the oral and written tests evaluate different skills. Figure 3 also suggests that examiners favor women who chose to specialize in male-dominated subjects no matter what they are tested on.

A last reason why our results could reflect skill differences is that (iii) the populations tested in the different subjects are not the same and are self-selecting. The women who decided to study math and take the math exams might be especially confident in math and perform better on oral tests for this reason, whereas the same happens for men in literature. Selection may also explain the results of the BERCS test: Women enrolled in the more male-dominated exams may have better aptitude for that particular oral test.

We can first reject that sample selection drives our results in a specific case: at the medium-level exam in physics-chemistry, the same candidates have to take the oral and written tests in both physics-chemistry. Among those candidates, the bonus for women on oral tests is 9 percentile points greater in physics than in chemistry, a subject that is less male-dominated according to all indicators. The idea that sample selection does not drive the general pattern in Fig. 1 is also confirmed by a previous analysis that is entirely based on identical samples of candidates being tested in different subjects (*19*).

To control for sample selection in the BERCS test, we exploited a pattern(?) of test-taking over the period 2011–2013: A few candidates took both the lower-level exam and the medium-level exam in a specific subject. We used the grade obtained from the BERCS test for the lower-level exam (where this test is also mandatory and graded as a subpart of the literature test) as a counterfactual measure of ability. As the lower-level exam is not subject-specific, it offers a counterfactual measure in a gender-neutral context. Among the small group of candidates who took both exams and took the medium-level exam in a less male-dominated subject (social sciences, history, geography, biology, literature, or foreign languages), men get an advantage over women on the oral test BERCS that is significantly higher at the 5% level for the medium-level exam than for the lower-level exam (Fig. 4, P = 0.04, N = 120 candidates). The reverse is true (however, not statistically significant) among the group that took the medium-level exam in a male-dominated subject (math, physics-chemistry, or philosophy, N = 60). As both the test subject and the sample of candidates are held constant in this last experiment, observed differences almost surely reflect examiners' bias according to the extent of male-domination in the candidates' field of specialization.

In total, the various empirical checks provided here imply with high confidence that our results for the medium- and higher-level exams reflect evaluation biases rather than differences in candidates' abilities. These biases rebalance gender asymmetries in academic fields by favoring the minority gender. For women, this runs counter to the claim of negative discrimination in recruitment of professors into math-based fields. If anything, women appear to be advantaged in those fields. In contrast, men appear to be advantaged in recruitment into the most feminized fields. Those behaviors are stronger on the highest-level exams, where candidates are more skilled, and where initial gender imbalances between the different fields are largest (see table S2).

Our results are compatible with two main mechanisms. First, evaluators may have different beliefs about female and male applicants in the different fields and may statistically discriminate accordingly. For example, females who have mastered the curriculum, and who apply for highly skilled jobs in male-dominated fields may signal that they do not elicit the general stereotypes associating quantitative ability with men. This may induce a rational belief reversal regarding the motivation or ability of those female applicants (*28*), or a so-called "boomerang effect" (*29*) that modifies the attitudes toward them. Experimental evidence provides support for this theory by showing that gender biases are lower or even inverted when information clearly indicates high competence of those being evaluated (*29*, *30*). Second, evaluators may simply have a preference for gender diversity, either conscious (e.g., political reasons) or unconscious. Evidence shows that evaluation biases in favor of the minority gender in a given field are larger in years where this gender performs more poorly at written tests (table S10). This result, which should not be overinterpreted (*22*), tends to reject the first explanation and is consistent with the second one.

Finally, for the math medium-level exam [the only one for which we have data on jury composition (table S11)], we find no evidence that male (with respect to female) examiners systematically favor female (with respect to male) candidates (table S12). This result is in line with previous research (*12*, *19*, *31*) and suggests that context effects (surrounding gender stereotypes) are more important than examiners' gender in explaining gender biases in evaluation. It excludes that between-fields variation in panel composition drives our results. We also checked (on the subsample for which we have detailed information) that examiners' teaching levels do not affect their preferences and conclude that the higher proportion of assistant professors and professors who judge the higher-level exam cannot explain the stronger bonus obtained by the minority gender at that level.

Even without being fully conclusive on the underlying mechanisms, the presented analyses shed light on the possible causes of the underrepresentation of women in many academic fields. They confirm evidence from a recent experiment with fictitious resumes (*12*) that women can be favored in male-dominated fields at high recruiting levels (from secondary school teaching to professorial hiring), once they have already specialized and heavily invested in those fields (candidates on teaching exams hold at least a college or a master's degree) (*32*). In contrast, the study of the recruiting process for primary schoolteachers suggests that prowomen biases in male-dominated fields may disappear in less prestigious and less selective hiring exams, where candidates are not necessarily specialized. Perhaps the bias in favor of women in male-dominated fields would even reverse at lower recruiting levels, as in experiments done with medium-skilled applicants (*8*, *9*). Discrimination may

then still impair women's chances to pursue a career in quantitative science (or philosophy), but only at the early stages of the curriculum, before or just as they enter the pipeline that leads to a Ph.D. or a professorial position.

Nevertheless, there is no compelling evidence of hiring discrimination against individuals who have already decided against social norms to pursue an academic or a teaching career in a field where their own gender is in the minority. This result has three consequences for policy. First, active policies aimed at counteracting stereotypes and discrimination should probably focus on students at early ages, before educational choices are made. Second, nonblind evaluation and hiring should be favored over blind-evaluation in order to reduce gender imbalances across academic fields. In particular, policies that impose anonymous curricula vitae in the first stage of academic hiring are likely to have effects opposite to those expected. Third, many women may shy away from male-dominated fields at early ages because they believe that they would suffer from discrimination. Advertising that they have at least as good—or even better—opportunities as their male counterparts at the levels of secondary school teaching and professorial recruiting could encourage talented young women to study in those fields.

REFERENCES AND NOTES

1. J. M. Sheltzer, J. C. Smith, *Proc. Natl. Acad. Sci. U.S.A.* **111**, 10107–10112 (2014).
2. C. Hill, C. Corbett, A. St. Rose, *Why So Few? Women in Science, Technology, Engineering, and Mathematics* (American Association of University Women, Washington, DC, 2010).
3. National Academy of Sciences, National Academy of Engineering, and Institute of Medicine, *Beyond Bias and Barriers: Fulfilling the Potential of Women in Academic Science and Engineering* (The National Academies Press, Washington, DC, 2007).
4. M. S. West, J. W. Curtiss, *AAUP Gender Equity Indicators 2006* (American Association of University Professors, Washington, DC, 2006).
5. M. Foschi, L. Lai, K. Sigerson, *Soc. Psychol. Q.* **57**, 326–339 (1994).
6. R. Steinpreis, K. Anders, D. Ritzke, *Sex Roles* **41**, 509–528 (1999).
7. J. Swim, E. Borgida, G. Maruyama, D. G. Myers, *Psychol. Bull.* **105**, 409–429 (1989).
8. C. A. Moss-Racusin, J. F. Dovidio, V. L. Brescoll, M. J. Graham, J. Handelsman, *Proc. Natl. Acad. Sci. U.S.A.* **109**, 16474–16479 (2012).
9. E. Reuben, P. Sapienza, L. Zingales, *Proc. Natl. Acad. Sci. U.S.A.* **111**, 4403–4408 (2014).
10. S. J. Ceci, W. M. Williams, *Proc. Natl. Acad. Sci. U.S.A.* **108**, 3157–3162 (2011).
11. S. J. Ceci, D. K. Ginther, S. Kahn, W. M. Williams, *Psychol. Sci. Public Interest* **15**, 75–141 (2014).
12. W. M. Williams, S. J. Ceci, *Proc. Natl. Acad. Sci. U.S.A.* **112**, 5360–5365 (2015).
13. National Research Council, *Gender Differences at Critical Transitions in the Careers of Science, Engineering, and Mathematics Faculty* (National Academies Press, Washington, DC, 2009).
14. N. H. Wolfinger, M. A. Mason, M. Goulden, *J. Higher Educ.* **79**, 388–405 (2008).
15. C. Glass, K. Minnotte, *J. Divers. High. Educ.* **3**, 218–229 (2010).
16. A. D. Irvine, *Dialogue* **35**, 255–292 (1996).
17. D. Kimura, "Preferential hiring of women" (University of British Columbia Reports, 2002); www.safs.ca/april2002/hiring.html.
18. C. Seligman, Summary of Recruitment Activity for All Full-Time Faculty at the University of Western Ontario by Sex and Year (The Society for Academic Freedom and Scholarship, Halifax, Nova Scotia, Canada, 2001); www.safs.ca/april2001/recruitment.html.
19. T. Breda, S. T. Ly, *Am. Econ. J. Appl. Econ.* **7**, 53–75 (2015).
20. S. J. Leslie, A. Cimpian, M. Meyer, E. Freeland, *Science* **347**, 262–265 (2015).
21. National Science Foundation, Survey of Earned Doctorates (NSF, Alexandria, VA, 2011); www.nsf.gov/statistics/srvydoctorates/.
22. Materials and methods are available as supplementary materials on *Science* Online.
23. A. H. Eagly, *Am. Psychol.* **50**, 145–158 (1995).
24. D. Halpern, *Sex Differences in Cognitive Abilities* (Erlbaum, Mahwah, NJ, ed. 3, 2000).
25. E. S. Spelke, *Am. Psychol.* **60**, 950–958 (2005).
26. J. S. Hyde, *Am. Psychol.* **60**, 581–592 (2005).
27. We checked that candidates' score on the test, "Behave as an ethical and responsible civil servant," for the computation of candidates' rank on oral tests do not affect the main results. To do this, we restricted the analysis to the period before it was implemented in 2011. We also replicated the analysis by keeping only one oral and one written test in each of the medium- and high-level exams. We kept the pairs of tests that match the most closely in terms of the subtopic or test program on which they were based. Results are virtually unchanged (fig. S3 and table S12).
28. R. G. Fryer Jr., *J. Public Econ.* **91**, 1151–1166 (2007).
29. M. Heilman, R. Martell, M. Simon, *Organ. Behav. Hum. Decis. Process.* **41**, 98–110 (1988).
30. A. J. Koch, S. D. D'Mello, P. R. Sackett, *J. Appl. Psychol.* **100**, 128–161 (2015).
31. M. Bagues, M. Sylos-Labini, N. Zinovyeva, "Does the gender composition of scientific committees matter?" [Social Science Research Network 2628176, IZA Discussion Paper No. 9199, Institute for the Study of Labor (IZA), Bonn, Germany, 2015].
32. The higher-level teaching exam has been passed by a substantial fraction of researchers and may in some cases accelerate a career in French academia. In that sense, results obtained on this exam can be seen as more closely related to the specific debate on the underrepresentation of women scientists in academia.

ACKNOWLEDGMENTS

We thank S. Ceci for his amazing feedback and advice, as well as P. Askenazy, X. D'Hautefeuille, S. Georges-Kot, A. Marguerie, F. Kramarz, H. Omer, G. Piaton, T. Piketty, J. Rothstein, and D. Skandalis. We also thank colleagues and seminar participants at Paris School of Economics, CREST, and IZA, as well as three anonymous reviewers for their comments. The data necessary to reproduce most of this study are available at http://dx.doi.org/10.3886/E81536V1. The initial data are property of the French Ministry of Education. Preliminary agreement is necessary to access the data for research purposes (we thank people in Office A2 at DEPP and Xavier Sorbe for giving us access). Summary statistics on sample sizes and female average rank at each test are given in the supplementary materials.

SUPPLEMENTARY MATERIALS

www.sciencemag.org/content/353/6298/474/suppl/DC1
Materials and Methods
Supplementary Text
Figs. S1 to S3
Tables S1 to S14
References (*33*–*38*)

13 March 2016; accepted 29 June 2016
10.1126/science.aaf4372

PARASITIC PLANTS

Detection of the plant parasite *Cuscuta reflexa* by a tomato cell surface receptor

Volker Hegenauer,[1]* Ursula Fürst,[1]* Bettina Kaiser,[1]* Matthew Smoker,[2] Cyril Zipfel,[2] Georg Felix,[1] Mark Stahl,[1] Markus Albert[1]†

Parasitic plants are a constraint on agriculture worldwide. *Cuscuta reflexa* is a stem holoparasite that infests most dicotyledonous plants. One exception is tomato, which is resistant to *C. reflexa*. We discovered that tomato responds to a small peptide factor occurring in *Cuscuta* spp. with immune responses typically activated after perception of microbe-associated molecular patterns. We identified the cell surface receptor-like protein CUSCUTA RECEPTOR 1 (CuRe1) as essential for the perception of this parasite-associated molecular pattern. CuRe1 is sufficient to confer responsiveness to the Cuscuta factor and increased resistance to parasitic *C. reflexa* when heterologously expressed in otherwise susceptible host plants. Our findings reveal that plants recognize parasitic plants in a manner similar to perception of microbial pathogens.

Along with microbial pathogens and herbivorous arthropods, parasitic plants represent an additional class of threat to crops (*1*). As many as 4000 species, belonging to more than 20 plant families, have been classified as parasitic plants; hence, the switch to a parasitic lifestyle occurred independently and on several occasions during evolution (*2*).

The plant genus *Cuscuta* (dodder) comprises about 200 species, all of which live as obligate stem holoparasites with broad host spectra (*3*–*6*). Germinating *Cuscuta* seedlings sense plant volatiles and direct their growth toward their host (*7*). Initial contact induces the formation of haustoria (*8*), specialized structures that attach, penetrate, and connect to the vascular bundles of their hosts. Once connected, *Cuscuta* parasites withdraw water, nutrients, and carbohydrates (*5*, *9*–*11*) from host plants, and also exchange macromolecules such as proteins and RNAs, as well as viruses, in a bidirectional manner (*12*–*17*).

Most susceptible plants lack efficient defense systems to ward off *C. reflexa*. However, the cultivated tomato (*Solanum lycopersicum*) is resistant to *C. reflexa* and exhibits a hypersensitive response to attempted penetration by *C. reflexa* haustoria (*18*–*21*) (Fig. 1A). We asked whether tomato might detect and respond to molecular signals associated with the parasitic plant in a

[1]Center for Plant Molecular Biology, University of Tübingen, 72076 Tübingen, Germany. [2]The Sainsbury Laboratory, Norwich Research Park, Norwich NR4 7UH, UK.
*These authors contributed equally to this work. **†Corresponding author. Email: markus.albert@zmbp.uni-tuebingen.de**

manner comparable to the response of plants to microbe-associated molecular patterns (MAMPs). We tested extracts of *C. reflexa* for their ability to induce release of reactive oxygen species (ROS) and to trigger synthesis of the stress-related phytohormone ethylene. Indeed, *C. reflexa* extract triggered both responses in *S. lycopersicum* but not in susceptible plants, including the related Solanaceae *Nicotiana tabacum*, *N. benthamiana*, *S. tuberosum*, and the wild tomato species *S. pennellii* (Fig. 1B and fig. S1).

Initial characterization showed that the factor present in the *C. reflexa* extract is heat-stable at 95°C but is sensitive to treatment with proteases (Fig. 1C). Checking for putative secondary modifications, we observed that enzymatic de-N-glycosylation had no influence on its activity, whereas treatment with ammonia, a procedure known to remove ester-type modifications such as sugar side chains from peptide backbones (*22*), led to a loss of functionality (Fig. 1D). The Cuscuta factor appeared to be constitutively present in all parts of *C. reflexa*, including shoot tips, stems, haustoria, and, at lower levels, in flowers (fig. S2A), indicating that this factor is not produced only at certain developmental or infectious stages. Activity was apparently associated with the cell walls of the parasite, from which it could be released by acidic conditions (fig. S2B).

We observed induction of ethylene production in *S. lyopersicum* with extracts from six different *Cuscuta* species but not with extracts from *A. thaliana*, *N. benthamiana*, or *S. lycopersicum* (Fig. 1E). Also inactive were extracts from *Calystegia sepium* (hedge bindweed), a nonparasitic species of the Convolvulaceae related to *Cuscuta*, and *Rhinanthus alectorolophus*, a hemiparasitic flowering plant of the Orobanchaceae, which infects roots of many herbaceous plants (Fig. 1E). Thus, the active factor seems to be common to *Cuscuta* species but absent from plants outside this genus.

To purify and identify the Cuscuta factor, we established a purification scheme involving sequential separation steps (fig. S3A). Prepurified *C. reflexa* extract was first separated by cation exchange chromatography, where activity eluted as several peaks indicating heterogeneity with respect to charge (fig. S3B). Active fractions of "peak 2" (fig. S3B) were pooled and further purified by reversed-phase chromatography (RPC) on C18 material using different pH conditions. This activity further split into different peaks and fractions (fig. S3C); this indicates that the activity, rather than representing a single defined molecule, is associated with a range of physicochemically heterogeneous compounds present in the *Cuscuta* extract. Although this heterogeneity dispersed activity to numerous subfractions, we succeeded in purifying a single molecule with a molecular mass of 2262.79 Da that correlated with activity in elution from the final RPC used for liquid chromatography–mass spectrometry (MS) analysis (fig. S3D). However, we did not obtain conclusive fragmentation patterns from tandem MS/MS analysis of this molecule in several attempts (fig. S4). Apart from the low amount of this particular form of the Cuscuta factor, this might be attributable to the yet unidentified modification present on the peptide. Nonetheless, our data suggest that the Cuscuta factor is associated with a small, potentially modified (e.g., O-glycosylated) peptide that is characteristically present in extracts from *Cuscuta* spp.

We exploited the natural variation between susceptible *S. pennellii* (*23*) and resistant *S. lycopersicum* to identify the receptor for the Cuscuta factor. We used an introgression library of *S. lycopersicum* × *S. pennellii* (*24*) to map genomic regions essential for the differential response to the Cuscuta factor. The collection of 49 introgression lines (ILs) included chromosome fragments of *S. pennellii* covering ~98% of the tomato genome (*25*). Only line IL8-1 was unresponsive to the Cuscuta factor (Fig. 2A). Further mapping with sublines IL8-1-1 and IL8-1-5 (*24*) (Fig. 2B) identified a chromosome region termed bin d8-B (Fig. 2C) (*25*), which has 822 annotated genes. Only five of these genes are predicted to encode cell surface receptor–type proteins (*25*) that could perceive the Cuscuta factor. We individually expressed these candidate genes,

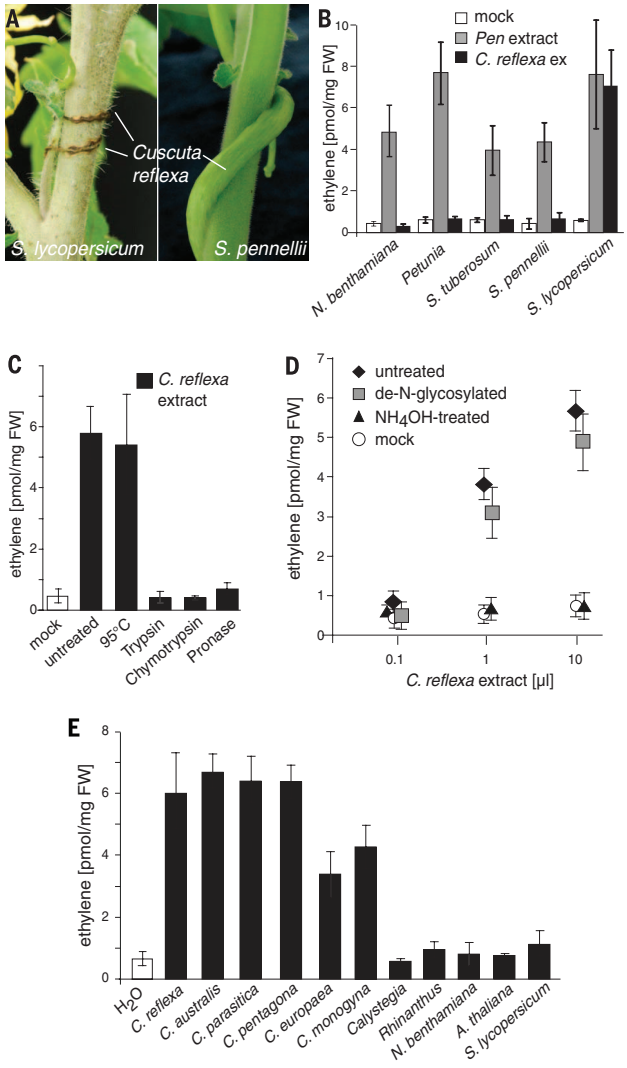


Fig. 1. *S. lycopersicum* (cultivated tomato) shows defense responses to *C. reflexa* and to extracts thereof. (**A**) Left: *C. reflexa* cannot form connections to *S. lycopersicum* and dies off. Right: *C. reflexa* on the susceptible host *S. pennellii*. Photos were taken ~14 days after parasite onset. (**B**) *C. reflexa* extract triggers ethylene biosynthesis in *S. lycopersicum* but not in other plant species. Bovine serum albumin (BSA) buffer in 25 mM MES buffer, pH 5.7 (0.01 mg/ml) was added as mock control; *Penicillium* extract (0.05 mg/ml) served as positive control (*38*). FW, fresh weight. (**C** and **D**) Characteristics of the Cuscuta factor present in the *C. reflexa* extract. (C) Ethylene biosynthesis of tomato leaf pieces to *C. reflexa* extract, to boiled extract (95°C, 30 min), or to extract pretreated with the proteases indicated. (D) Ethylene response to different doses of the Cuscuta factor after enzymatic de-N-glycosylation or to Cuscuta factor treated with 20% NH_4OH (45°C, 16 hours), respectively. (**E**) Ethylene response of tomato leaf pieces triggered by extracts of other *Cuscuta* species or by extracts of other plants. In (B) to (E), ethylene measurements show means of three technical replicates; error bars denote SD. All experiments were repeated more than three times.

Downloaded from http://science.sciencemag.org/ on July 28, 2016

which encode three leucine-rich repeat receptor-like proteins (LRR-RLPs) and two receptor-like kinases (RLKs), in *N. benthamiana*, a species lacking an endogenous detection system for the Cuscuta factor (Fig. 1B and fig. S1). Four of these candidates had no effect, but *N. benthamiana* leaves expressing Solyc08g016270 responded to the Cuscuta factor with increased ethylene biosynthesis (Fig. 2D) and an oxidative burst (Fig. 3A). Dose dependence of response (Fig. 3B) showed half-maximal stimulation with Cuscuta factor at an estimated concentration of <0.3 nM. Thus, the protein encoded by Solyc08g016270 is sufficient to confer sensitive responsiveness specific for the Cuscuta factor, and we termed it CuRe1 (Cuscuta receptor 1). To corroborate its function as a genuine receptor that directly interacts with the Cuscuta factor as a ligand, we tested whether immunoprecipitates of CuRe1 could specifically retain Cuscuta factor when incubated with *Cuscuta* extract. As controls, we used similar immunoprecipitates obtained from *N. benthamiana* leaves expressing the receptor kinase EFR (*26*) and the LRR-RLP AtRLP23 (*27*) from *Arabidopsis*. Cuscuta factor, assayed by the ethylene induction assay in tissue expressing CuRe1, was reproducibly detected in immunoprecipitates with CuRe1 but not with control receptors or empty beads (Fig. 3C).

Because activity in *Cuscuta* extracts separates into distinct subfractions during purification (fig. S3B), we tested these different forms of the Cuscuta factor for bioactivity in CuRe1-expressing *N. benthamiana* plants. Samples from all subfractions (fig. S3B) induced clear ethylene responses in a CuRe1-dependent manner, indicating that the Cuscuta factor, although heterogeneous in structure, triggers CuRe1 via a common active principle. Similarly, we confirmed that the extracts of other *Cuscuta* species (Fig. 1E) also induced ethylene biosynthesis via CuRe1 (fig. S5B).

CuRe1 encodes a typical LRR-RLP that comprises an N-terminal signal peptide for export via the endoplasmic reticulum, a large LRR ectodomain with 30 to 32 LRRs and 18 potential N-glycosylation sites, a single transmembrane helix, and a short cytoplasmic tail (fig. S6). Full-length *CuRe1* is represented in *S. lycopersicum* genomic DNA and cDNA but is absent from *S. pennellii* and from IL8-1-1 (fig. S7). This is in accordance with available genomic sequencing data showing that only truncated forms of *CuRe1*—annotated as Sopen08g00656 and Sopen08g006740—are present in *S. pennellii* (*28*). The closest relatives of *CuRe1* in *S. lycopersicum*, with amino acid sequence identities of 82% and 72%, respectively (Solyc08g016210 and Solyc08g016310), were found to be in close proximity to *CuRe1* on chromosome 8 but were unable to initiate ethylene production in response to the Cuscuta factor when transiently expressed in *N. benthamiana* (Fig. 2D). CuRe1-like sequences with similar amino acid sequence identities of ~70 to 80% can also be found in other Solanaceae but not in species outside this family. However, the CuRe1-related genes present in *N. benthamiana* and *S. tuberosum* seem not to be sufficient to confer responsiveness to the Cuscuta factor in these species (Fig. 1B and fig. S1).

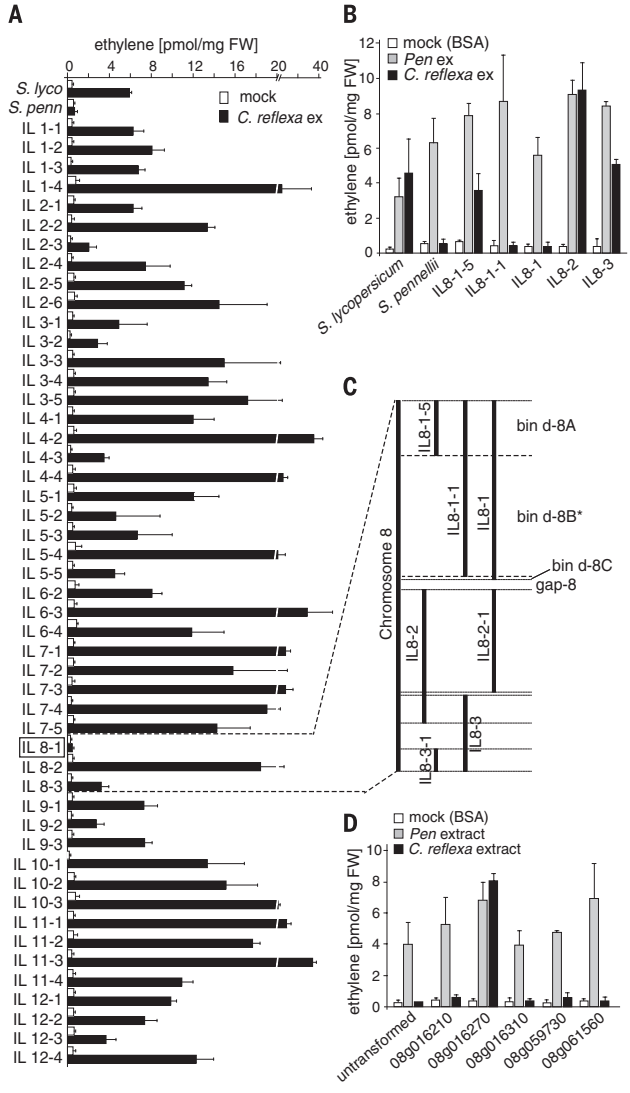


Fig. 2. Mapping of responsiveness to *C. reflexa* extracts in tomato. (**A**) Tomato introgression lines of *S. lycopersicum* × *S. pennellii* were screened for ethylene production in response to *C. reflexa* extract; BSA/buffer was used as mock control. (**B**) Ethylene response of additional ILs related to tomato chromosome 8. (**C**) Graphical scheme of the mapped chromosome region bin d8-B as modified from (*25*). (**D**) Receptor candidate genes encoded within bin d8-B were expressed in *N. benthamiana*. Ethylene production was measured after treatment with *C. reflexa* extract, *Penicillium* extract, or BSA as indicated. Data are means ± SD of $n = 3$ replicates.

Plant receptor-like proteins lack cytoplasmic kinase domains for signaling output and, in general, seem to depend on adaptor kinases of the SOBIR1 (suppressor of BAK1-interacting receptor kinase) type (*27*, *29*–*33*). Coimmunoprecipitation analysis with tagged versions of CuRe1 and SlSOBIR1 or SlSOBIR1-like from *S. lycopersicum* (tomato) showed constitutive interaction of CuRe1 with both of these adaptor kinases (Fig. 3D). As for other RLPs, such as tomato Cf-9 and Cf-4 or *A. thaliana* AtRLP23, AtRLP30, and ReMax/AtRLP1 (*27*, *29*, *30*, *33*, *34*), formation of the complex between CuRe1 and SlSOBIR1 occurred irrespective of the presence or absence of the Cuscuta factor as stimulus (Fig. 3D).

To check for the biological function of CuRe1, we stably transformed *CuRe1* constructs into *S. pennellii* and *N. benthamiana*, which are usually insensitive to the Cuscuta factor and susceptible to *C. reflexa* attack (Fig. 1B and fig. S1) (*23*, *35*). Transformed lines of *S. pennellii* and *N. benthamiana* plants gained responsiveness to Cuscuta factor (figs. S8 and S9) and exhibited increased resistance to *C. reflexa* infestation (Fig. 3, E and F). Thereby, the process of parasite ingrowth seems disturbed, as hypersensitive response symptoms were visible at haustoria penetration sites on the host (fig. S10). Thus, CuRe1 from tomato improves resistance to *C. reflexa* attack in both the closely related species *S. pennellii* and the more distant species *N. benthamiana*.

Full resistance of tomato against *C. reflexa* seems to require more than CuRe1 and perception

Downloaded from http://science.sciencemag.org/ on July 28, 2016

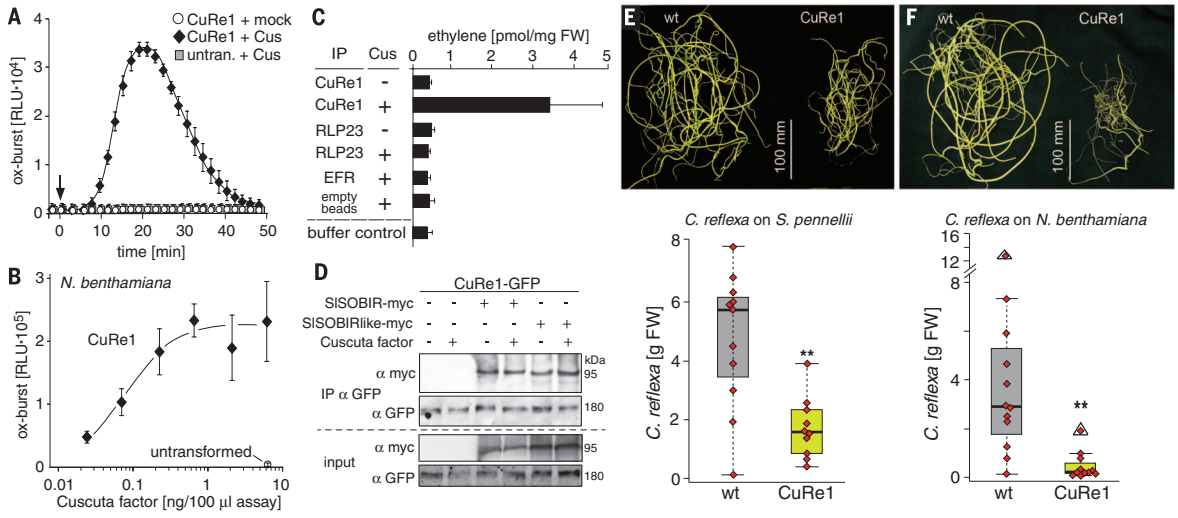


Fig. 3. CuRe1 exhibits properties as pattern recognition receptor for the Cuscuta factor. (**A**) *N. benthamiana* leaves expressing CuRe1 respond with rapid induction of an oxidative burst to treatment with the Cuscuta factor. Data are means ± SD of $n = 5$ replicates. RLU, relative light units. (**B**) Dose dependence of oxidative burst induction by purified Cuscuta factor. Assuming the preparation contains only Cuscuta factor (~2 kDa), this allows estimation of a half-maximal effective concentration $EC_{50} < 0.3$ nM. Values show maxima of oxidative burst (mean ± SD of three measurements). (**C**) Binding of Cuscuta factor (Cus) to immunoprecipitates (IP) of CuRe1; EFR, AtRLP23, or empty beads were used as controls. Ethylene production of *N. benthamiana* leaf tissue expressing CuRe1 and treated with the elutions derived from the receptor IPs indicated; data are means ± SD of $n = 3$ replicates. The experiment was independently repeated >3 times. (**D**) CuRe1 forms a complex with SOBIR1-type adaptor kinases. Immunoblots of SlSOBIR1-myc and SlSOBIR1-like–myc, coimmunoprecipitated with CuRe1; pulldown against the C-terminal green fluorescent protein tag present at CuRe1. Proteins were coexpressed in *N. benthamiana*, and samples were treated with Cuscuta factor (+; 1:100 diluted in water) or water alone (−) as control. (**E**) Growth of *C. reflexa* shoots on *S. pennellii* plants transformed with CuRe1 (T_1 generation) or nontransformed wild-type (wt) controls during 14 days of infestation with one *C. reflexa* shoot [15 cm in length, ~0.6 g FW] per host plant. Red diamonds represent weight of individual *C. reflexa* shoots. Box plots show median values of $n = 12$ replicates. $^{**}P_{adj} = 0.0015$ (Tukey honestly significant difference test). (**F**) Growth of *C. reflexa* shoots on *N. benthamiana* plants stably transformed with CuRe1 (homozygous T_2 generation) or nontransformed wild-type controls during 21 days of *C. reflexa* infestation. Experimental conditions and data evaluation were as in (E). Triangles mark outliers not included in analysis. $^{**}P \leq 0.005$ (Student t test). Data presented in (E) and (F) are representative of three independent repetitions, each with different lines of transformants.

of the Cuscuta factor alone. This is evident from the observation that the two introgression lines that lack CuRe1 (IL8-1 and IL8-1-1) (fig. S8) still showed HR symptoms and proved fully resistant to *C. reflexa* (fig. S11). Immunity against *C. reflexa* in tomato may be a process with layers additional to CuRe1, much like defense systems against microbial pathogens where MAMP-triggered immunity (MTI) and effector-triggered immunity (ETI) act as two perception layers of the plant immune system (*36*, *37*). Nonetheless, our data show that the MTI type of responses stimulated by the Cuscuta factor via the pattern recognition receptor CuRe1 significantly contribute to protection of host plants against *C. reflexa*. Identification of CuRe1 thus provides a starting point for studying and managing parasitic plant infestations.

REFERENCES AND NOTES

1. T. Spallek, M. Mutuku, K. Shirasu, *Mol. Plant Pathol.* **14**, 861–869 (2013).
2. J. H. Westwood, J. I. Yoder, M. P. Timko, C. W. dePamphilis, *Trends Plant Sci.* **15**, 227–235 (2010).
3. H. T. Funk, S. Berg, K. Krupinska, U. G. Maier, K. Krause, *BMC Plant Biol.* **7**, 45 (2007).
4. M. A. García, M. Costea, M. Kuzmina, S. Stefanović, *Am. J. Bot.* **101**, 670–690 (2014).
5. J. M. Hibberd *et al.*, *Planta* **205**, 506–513 (1998).
6. J. R. McNeal, K. Arumugunathan, J. V. Kuehl, J. L. Boore, C. W. Depamphilis, *BMC Biol.* **5**, 55 (2007).
7. J. B. Runyon, M. C. Mescher, C. M. De Moraes, *Science* **313**, 1964–1967 (2006).
8. J. H. M. Dawson, *Weed Sci.* **6**, 265 (1994).
9. C. C. Davis, Z. Xi, *Curr. Opin. Plant Biol.* **26**, 14–19 (2015).
10. J. M. Hibberd, W. P. Quick, M. C. Press, J. D. Scholes, W. D. Jeschke, *Plant Cell Environ.* **22**, 937–947 (1999).
11. W. D. Jeschke, A. Hilpert, *Plant Cell Environ.* **20**, 47–56 (1997).
12. S. Haupt, K. J. Oparka, N. Sauer, S. Neumann, *J. Exp. Bot.* **52**, 173–177 (2001).
13. G. Kim, J. H. Westwood, *Curr. Opin. Plant Biol.* **26**, 20–25 (2015).
14. A. Alakonya *et al.*, *Plant Cell* **24**, 3153–3166 (2012).
15. R. David-Schwartz, S. Runo, B. Townsley, J. Machuka, N. Sinha, *New Phytol.* **179**, 1133–1141 (2008).
16. J. K. Roney, P. A. Khatibi, J. H. Westwood, *Plant Physiol.* **143**, 1037–1043 (2007).
17. G. Kim, M. L. LeBlanc, E. K. Wafula, C. W. dePamphilis, J. H. Westwood, *Science* **345**, 808–811 (2014).
18. M. Albert, X. Belastegui-Macadam, R. Kaldenhoff, *Plant J.* **48**, 548–556 (2006).
19. B. Ihl, N. Tutakhil, A. Hagen, F. Jacob, *Flora* **181**, 383 (1988).
20. M. Werner, N. Uehlein, P. Proksch, R. Kaldenhoff, *Planta* **213**, 550–555 (2001).
21. B. Kaiser, G. Vogg, U. B. Fürst, M. Albert, *Front. Plant Sci.* **6**, 45 (2015).
22. F. G. Hanisch, M. Jovanovic, J. Peter-Katalinic, *Anal. Biochem.* **290**, 47–59 (2001).
23. H. R. Johnsen *et al.*, *New Phytol.* **207**, 805–816 (2015).
24. Y. Eshed, D. Zamir, *Genetics* **141**, 1147–1162 (1995).
25. D. H. Chitwood *et al.*, *Plant Cell* **25**, 2465–2481 (2013).
26. C. Zipfel *et al.*, *Cell* **125**, 749–760 (2006).
27. I. Albert *et al.*, *Nat. Plants* **1**, 15140 (2015).
28. Sol Genomics Network; https://solgenomics.net/jbrowse/current/?data=data%2Fjson%2Fspenn&loc=Spenn-ch08%3A7569001.8078000&tracks=DNA%2Cgene_models&highlight=.
29. T. W. Liebrand *et al.*, *Proc. Natl. Acad. Sci. U.S.A.* **110**, 10010–10015 (2013).
30. W. Zhang *et al.*, *Plant Cell* **25**, 4227–4241 (2013).
31. A. A. Gust, G. Felix, *Curr. Opin. Plant Biol.* **21**, 104–111 (2014).
32. T. W. Liebrand, H. A. van den Burg, M. H. Joosten, *Trends Plant Sci.* **19**, 123–132 (2014).
33. J. Postma *et al.*, *New Phytol.* **210**, 627–642 (2016).
34. A. K. Jehle *et al.*, *Plant Cell* **25**, 2330–2340 (2013).
35. M. Bleischwitz, M. Albert, H. L. Fuchsbauer, R. Kaldenhoff, *BMC Plant Biol.* **10**, 227 (2010).
36. J. D. Jones, J. L. Dangl, *Nature* **444**, 323–329 (2006).
37. P. N. Dodds, J. P. Rathjen, *Nat. Rev. Genet.* **11**, 539–548(2010).
38. B. Thuerig, G. Felix, A. Binder, T. Boller, L. Tamm, *Physiol. Mol. Plant Pathol.* **67**, 180–193 (2005).

ACKNOWLEDGMENTS

We thank the Tomato Genetics Resource Center (University of California, Davis) for providing seeds of the tomato introgression lines; N. Sinha and M. Farhi for providing *C. pentagona* material and seeds; M. H. A. J. Joosten and S. Robatzek for SlSOBIR and SlSOBIR-like constructs; and P. Neumann and I. Bock for technical assistance; and N. Holton and I. Albert for critical reading of the manuscript before submission. Supported by Deutsche Forschungsgemeinschaft (DFG) grant AL1426/1-1 (M.A.), DFG grant AL1426/1-2 (V.H., U.F., and B.K.), the German Federal Ministry of Education (BMBF-KBBE project 031A328 36) (U.F.), and DFG grant CRC 1101 (M.S. and G.F.). Research at the C.Z. laboratory is funded by the Gatsby Charitable Foundation. The authors do not have any competing interests. Supplement contains additional data.

SUPPLEMENTARY MATERIALS

www.sciencemag.org/content/353/6298/478/suppl/DC1
Figs. S1 to S11
Materials and Methods
References (*39*–*43*)

3 February 2016; accepted 18 May 2016
10.1126/science.aaf3919

Downloaded from http://science.sciencemag.org/ on July 28, 2016

PLANT ECOLOGY

Rapid evolution accelerates plant population spread in fragmented experimental landscapes

Jennifer L. Williams,[1]* Bruce E. Kendall,[2] Jonathan M. Levine[3]

Predicting the speed of biological invasions and native species migrations requires an understanding of the ecological and evolutionary dynamics of spreading populations. Theory predicts that evolution can accelerate species' spread velocity, but how landscape patchiness—an important control over traits under selection—influences this process is unknown. We manipulated the response to selection in populations of a model plant species spreading through replicated experimental landscapes of varying patchiness. After six generations of change, evolving populations spread 11% farther than nonevolving populations in continuously favorable landscapes and 200% farther in the most fragmented landscapes. The greater effect of evolution on spread in patchier landscapes was consistent with the evolution of dispersal and competitive ability. Accounting for evolutionary change may be critical when predicting the velocity of range expansions.

In an era of global environmental change, biological invasions and the movement of species ranges with climate change present two of the greatest disruptions to natural and managed ecosystems (*1*, *2*). At the core of each dynamic is the spread of populations across landscapes fragmented by natural and anthropogenic barriers to movement. It has long been appreciated that habitat fragmentation slows the velocity of spread (*3*, *4*), but its influence on the potential for evolution to increase population expansion is unknown (*5*). Theory shows that natural selection at the low-density front of populations expanding through continuously favorable landscapes, coupled with the spatial sorting of offspring, favors traits contributing to fecundity and dispersal, both of which accelerate the invasion velocity (*6*–*10*). Whether this eco-evolutionary process operates similarly in systems fragmented by unsuitable habitat is uncertain because spread in these systems depends on the buildup of high-density populations capable of dispersing over gaps (*5*, *11*). Although any factor that alters selection on an expanding population can influence spread, whether evolution operating through selection or genetic drift predictably affects spread velocity on the rapid time scale of ecological dynamics remains to be determined. Answering questions about how evolution affects population expansion has important implications for predicting the future spread of biological invasions and climate change migrants, based on currently measured rates.

[1]Department of Geography and Biodiversity Research Centre, University of British Columbia, 1984 West Mall, Vancouver, British Columbia V6T 1Z2, Canada. [2]Bren School of Environmental Science and Management, University of California, Santa Barbara, Santa Barbara, CA 93106-5131, USA. [3]Institute of Integrative Biology, ETH Zurich, Universitätstrasse 16, 8092 Zurich, Switzerland.
*Corresponding author. Email: jennifer.williams@geog.ubc.ca

Empirical progress toward understanding evolution in populations spreading through fragmented landscapes is limited, largely because the process occurs over many generations and at geographic spatial scales. Due to these constraints, nearly all empirical evidence for evolution affecting spread comes from a few retrospective, observational analyses (*12*–*16*). The spread velocity of cane toads, for example, increased by a factor of 5 after the species was introduced to Australia, consistent with evolved changes in dispersal (*14*, *17*, *18*). Nonetheless, with stochastic events contributing to the ecological and evolutionary trajectories of spreading populations (*5*, *19*–*21*), replicated, controlled studies are necessary for understanding the predictability of this eco-evolutionary dynamic (*15*). Given the challenges of replicating invasions in the field and doing so in landscapes of varying fragmentation, model laboratory systems present an excellent opportunity to evaluate how evolution affects the speed at which populations expand through habitats of varying patchiness.

We manipulated evolution in populations of the model plant *Arabidopsis thaliana* spreading through continuous and fragmented landscapes, each consisting of a linear array of rectangular pots (Fig. 1A) (*22*). We initiated each replicate invasion in the leftmost pot of the array by sowing equal fractions of 14 genotypes (recombinant inbred lines), which varied in spread-relevant traits. Due to nearly complete self-pollination of *A. thaliana* (*23*), the 14 genotypes can be treated as clones (*24*), facilitating our measurements of evolutionary change. In evolving populations, the resulting plants produced seeds, which dispersed across the array (assisted via a simulated rain event), constituting the next generation of the population (Fig. 1B). In nonevolving treatments, germinants emerging in the next generation were replaced with individuals randomly drawn from the initial seed pool, thus maintaining population dynamics while eliminating any change in the frequency or spatial sorting of genotypes. We manipulated habitat patchiness by separating individual pots of suitable habitat by gaps that were 0 (continuous landscapes), 4, 8, or 12 times the mean dispersal distance. This protocol was repeated over six generations of spread, at which point individuals at the leading edge and back of the invasions were genotyped, and traits of all 14 genotypes were measured.

We found that after six generations of spread in continuous landscapes, evolving populations spread a modest 11% farther than nonevolving populations (Fig. 2A), a difference that was only marginally significant ($t_{13.5}$ = −2.05, P = 0.060). By contrast, in experimental landscapes with gaps 12 times the mean dispersal distance, evolving populations spread three times as far as their nonevolving counterparts (Fig. 2D) ($t_{10.4}$ = −3.36, P = 0.007), leading to a significant gap size by evolution interaction ($F_{1,72}$ = 10.77, P = 0.002). The effects of evolutionary change were so strong in patchy landscapes that evolving populations showed no significant reduction in velocity as the size of gaps increased from 4 to 8 to 12 times the mean dispersal distance (generation-six location of dark green line in Fig. 2, B to D) ($F_{1,25}$ = 0.014, P = 0.908), even as velocity slowed in the nonevolving populations ($F_{1,28}$ = 8.52, P = 0.007). Patchiness and evolutionary change also influenced the among-replicate variability in expansion

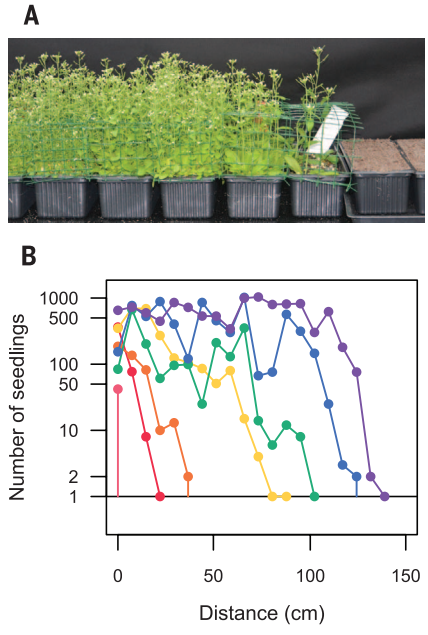


Fig. 1. Spread of *A. thaliana* in experimental greenhouse arrays. (**A**) Leading edge of an invasion of a continuous landscape. (**B**) Spread in a continuous landscape for one replicate in the evolving treatment. Each colored line represents a successive generation (pink, founding population; red to purple from left to right, first to sixth generation of spread). Points show abundance in the individual pots that make up the arrays.

Downloaded from http://science.sciencemag.org/ on July 28, 2016

velocity (Fig. 2). The coefficient of variation for spread was four times greater in the patchiest landscapes than in the continuous ones (fig. S1), consistent with a spread process driven by infrequent long-distance dispersal events in fragmented systems. We also found that evolving populations showed significantly less among-replicate variation in spread than nonevolving populations (fig. S1). Thus, despite the theoretical expectation for greater genetic drift at the leading edge of spreading populations (*25*), invasion speed was more predictable in evolving populations.

One explanation for the greater effects of evolutionary change on spread velocity in patchier landscapes might be faster evolution due to stronger selection in these systems. However, the extent of genotypic change did not differ significantly with gap size (fig. S2 and table S1; Fig. 3 shows the initial and final genotypic compositions), and the extent of trait change increased only marginally with increasing gap size (Fig. 3, fig. S2, and table S1). In fact, trait and genotypic change occurred in populations spreading through all landscape types, irrespective of whether evolution enhanced the spread velocity (significant intercepts in the fitted models of table S1). These evolutionary changes reflect the combined effects of selection and drift. In the continuously favorable landscapes in particular, we found more among-replicate variation in the genotypic composition of leading individuals than expected by chance (fig. S3), consistent with spatial priority effects where genotypes that initially got ahead due to chance dispersal were able to stay ahead (*5*, *25*).

Despite similarities in the extent of trait and genotypic change across gap sizes, landscape patchiness affected the direction of evolution. Height and the average distance of the farthest dispersed seed, traits correlated with one another (Spearman rank correlation coefficient $r_s = 0.55$, $P = 0.046$), increased with landscape patchiness (backward and rightward shift of the replicates with increasing patchiness in Fig. 3; $P = 0.008$ and 0.060, respectively, Table 1). These trait changes were associated with changes in the genotypic composition of the leading individuals with increasing patchiness (Fig. 3) ($F_{1,34} = 2.54$, $P = 0.042$). Considering theory showing that greater dispersal increases the invasion velocity (*6*–*10*), the evolution of greater height and dispersal in patchier systems is consistent with the greater effects of evolution on spread in these landscapes. Nevertheless, whether landscape patchiness selected directly for better dispersal or indirectly via unmeasured traits that are correlated with dispersal remains an open question.

Increased competitive ability probably also contributed to the greater effects of evolutionary change on spread velocity in patchier systems. Although competitive ability evolved to the same extent regardless of gap size [upward shift of replicates (Fig. 3 and Table 1); a similar result was found for seed mass (Table 1)], theory (*5*, *11*) predicts that increasing competitive ability will have a greater effect on spread in fragmented versus continuously favorable landscapes (fig. S4 shows this result applied to our system). In fragmented habitats, individuals often compete at crowded invasion fronts, enabling genotypes that make more offspring at high density (i.e., better competitors) to spread faster (*5*, *11*) (fig. S4). Though weaker, this effect also emerges in models of finite populations in continuously favorable landscapes (fig. S4) (*26*), consistent with the evolving populations moving modestly farther than the nonevolving populations in continuous landscapes (Fig. 2A).

Extrapolating our results to wild populations requires care for several reasons. First, the focal populations were effectively asexual, meaning that trait variation was not continuous and traits were perfectly linked. Nonetheless, it is not clear how more continuous variation or less linkage between traits would influence the effect of evolutionary change on spread velocity. Second, although we manipulated genetic change in this experiment, we cannot rule out the influence of maternal and epigenetic effects on our results. Third, we explored the effects of fragmentation, assuming it has no influence on the initial pool of genetic variation. If fragmentation in the nonspreading portion of a species range was to select for reduced dispersal (*16*, *27*), then populations that spread from such sources might have less genetic variation in dispersal-related traits, limiting the response to selection. Related to this point, the effects of evolution in our study arose through drift and selection on standing variation; our results do not bear on the rates of evolution resulting from the rise of novel mutations.

Our results demonstrate that evolution on ecological time scales can increase the speed of advance in spreading populations, and markedly so in the most patchy landscapes. However, further studies are needed to evaluate whether patchiness per se generally selects for traits that increase spread (*24*). Our results for less patchy landscapes show that large evolutionary changes in spreading populations can have little or no consequence for spread velocity. More generally, our findings add a more process-focused perspective to past work that has shown either accelerating invasion fronts consistent with evolution (*13*–*15*, *17*) or trait differences between individuals at the front and back of spreading populations (*18*, *28*, *29*). We conclude that accounting for evolutionary change on ecological time scales may be critical when predicting the rate at which biological invasions and climate change migrants reach new locations.

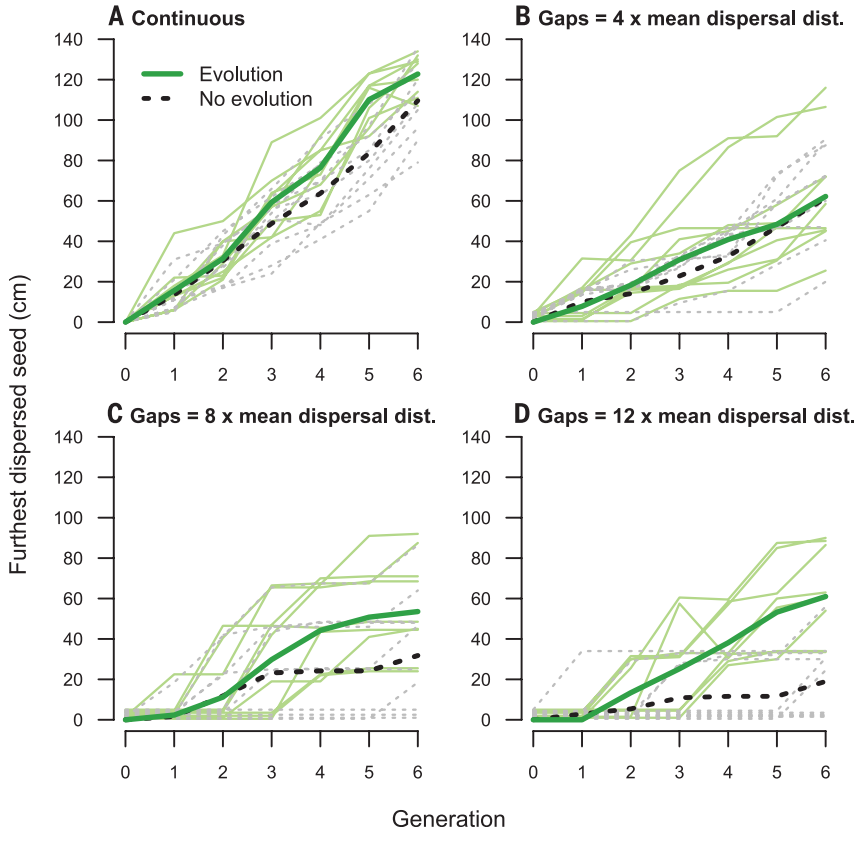


Fig. 2. Farthest distance colonized in each generation. Distance moved by evolving (thin green solid lines) and nonevolving (thin gray dashed lines) replicate invasions and their mean values (thick green and black lines, respectively) in landscapes that are (**A**) continuous or separated by gaps that are (**B**) 4, (**C**) 8, and (**D**) 12 times the mean dispersal distance. Lines in the three patchy landscapes are jittered for visibility.

Downloaded from http://science.sciencemag.org/ on July 28, 2016

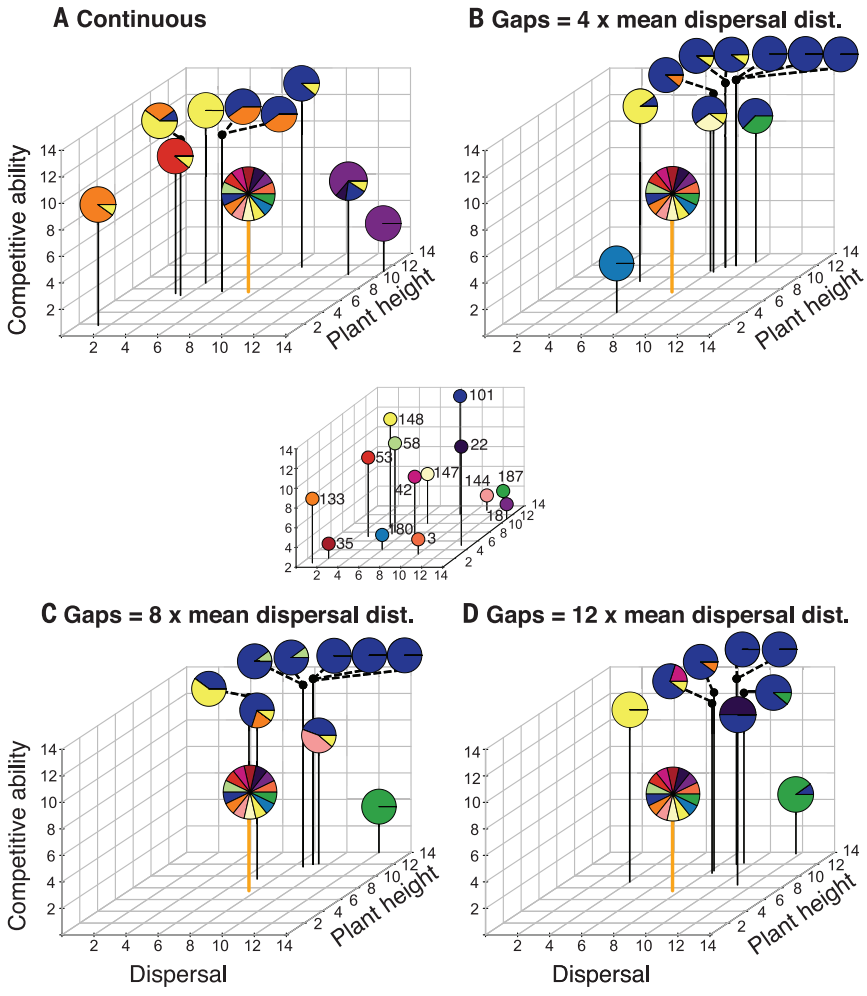


Fig. 3. Genotypes and traits at the invasion fronts. The central pinwheel of each panel depicts the equal frequency of genotypes in the founding population and is located at the mean trait rank for three spread-relevant traits: competitive ability (dominance in nonspreading context), dispersal (average distance of farthest dispersed seed from a solitary individual), and plant height. Pies show the genotypic composition of the 10 leading individuals for each replicate invasion after six generations of spread through landscapes that are (**A**) continuous or separated by gaps that are (**B**) 4, (**C**) 8, and (**D**) 12 times the mean dispersal distance. The location of each replicate is given by the genotype-weighted trait rank mean (*22*). A fourth trait, seed mass, also evolved, but its evolution did not vary with landscape patchiness and is not shown here. The central panel shows trait ranks of the 14 genotypes; numbers indicate genotype identity.

Table 1. Evolution of spread-relevant traits as a function of landscape patchiness. Results of linear models examining the change in height, dispersal, competitive ability, and seed mass at the invasion front after six generations of evolution as a function of landscape patchiness (size of gaps between suitable habitat). Trait change was measured as the difference between the genotype-weighted trait rank for each replicate ($N = 36$) and 7.5 – the mean trait rank of 14 genotypes in the founding population. Significant slopes indicate that the amount of change in the trait increased with increasing gap size (units of mean dispersal distance). Significant intercepts indicate that the trait changed significantly from the founding population, even in continuous landscapes. For competitive ability and seed mass, two traits with nonsignificant slopes, zero-slope models yielded highly significant intercepts ($P \leq 0.001$). Est., estimated value.

Change in genotype weighted trait rank of	Intercept			Slope		
	Est.	*t*	*P*	Est.	*t*	*P*
Plant height	1.45	2.25	0.031	0.25	2.83	0.008
Dispersal	−0.64	−0.88	0.386	0.19	1.95	0.060
Competitive ability	3.36	3.74	<0.001	0.15	1.17	0.250
Seed mass	1.29	2.25	0.031	−0.02	−0.24	0.814

REFERENCES AND NOTES

1. M. H. Williamson, *Biological Invasions* (Chapman & Hall, 1996).
2. C. Parmesan, G. Yohe, *Nature* **421**, 37–42 (2003).
3. D. B. Lindenmayer, J. Fischer, *Habitat Fragmentation and Landscape Change: An Ecological and Conservation Synthesis* (Island Press, 2013).
4. N. Shigesada, K. Kawasaki, E. Teramoto, *Theor. Popul. Biol.* **30**, 143–160 (1986).
5. J. L. Williams, R. E. Snyder, J. M. Levine, *Am. Nat.* **188**, 15–26 (2016).
6. O. J. Burton, B. L. Phillips, J. M. J. Travis, *Ecol. Lett.* **13**, 1210–1220 (2010).
7. R. Shine, G. P. Brown, B. L. Phillips, *Proc. Natl. Acad. Sci. U.S.A.* **108**, 5708–5711 (2011).
8. M. Kot, M. A. Lewis, P. van den Driessche, *Ecology* **77**, 2027–2042 (1996).
9. A. Hastings *et al.*, *Ecol. Lett.* **8**, 91–101 (2005).
10. B. L. Phillips, G. P. Brown, J. M. J. Travis, R. Shine, *Am. Nat.* **172** (suppl. 1), S34–S48 (2008).
11. E. Pachepsky, J. M. Levine, *Am. Nat.* **177**, 18–28 (2011).
12. A. D. Simmons, C. D. Thomas, *Am. Nat.* **164**, 378–395 (2004).
13. C. D. Thomas *et al.*, *Nature* **411**, 577–581 (2001).
14. B. L. Phillips, G. P. Brown, J. K. Webb, R. Shine, *Nature* **439**, 803 (2006).
15. E. A. Fronhofer, F. Altermatt, *Nat. Commun.* **6**, 6844 (2015).
16. C. L. Hughes, C. Dytham, J. K. Hill, *Ecol. Entomol.* **32**, 437–445 (2007).
17. B. L. Phillips, G. P. Brown, R. Shine, *J. Evol. Biol.* **23**, 2595–2601 (2010).
18. T. A. Perkins, B. L. Phillips, M. L. Baskett, A. Hastings, *Ecol. Lett.* **16**, 1079–1087 (2013).
19. B. A. Melbourne, A. Hastings, *Science* **325**, 1536–1539 (2009).
20. T. E. X. Miller, B. D. Inouye, *Ecol. Lett.* **16**, 354–361 (2013).
21. B. L. Phillips, *Biol. Invasions* **17**, 1949–1960 (2015).
22. Materials and methods are available as supplementary materials on *Science* Online.
23. R. J. Abbott, M. F. Gomes, *Heredity* **62**, 411–418 (1989).
24. S. Fakheran *et al.*, *Proc. Natl. Acad. Sci. U.S.A.* **107**, 19120–19125 (2010).
25. L. Excoffier, M. Foll, R. J. Petit, *Annu. Rev. Ecol. Evol. Syst.* **40**, 481–501 (2009).
26. R. E. Snyder, *Ecology* **84**, 1333–1339 (2003).
27. J. M. J. Travis, H. S. Smith, S. M. W. Ranwala, *Divers. Distrib.* **16**, 690–702 (2010).
28. A. Chuang, C. R. Peterson, *Global Change Biol.* **22**, 494–512 (2016).
29. F. F. Kilkenny, L. F. Galloway, *Evolution* **67**, 722–731 (2013).

Downloaded from http://science.sciencemag.org/ on July 28, 2016

ACKNOWLEDGMENTS

We thank S. Giovanettina, R. Guidon, A. Bieger, M. Clerc, and other members of the ETH Zurich Plant Ecology group for help with performing the experiments and F. Altermatt, A. Angert, T. Miller, and the Plant Ecology group for providing comments on the manuscript. J.M.L., J.L.W., and B.E.K. acknowledge support from the Swiss National Science Foundation (grants 31003A_141025 and IZK0Z3_163497), B.E.K. from the U.S. NSF (grant DEB-1120865), and J.L.W. from the Natural Sciences and Engineering Research Council of Canada. Data described in the paper are available from the Dryad Digital Repository: http://dx.doi.org/10.5061/dryad.q7605.

SUPPLEMENTARY MATERIALS

www.sciencemag.org/content/353/6298/482/suppl/DC1
Materials and Methods
Figs. S1 to S4
Tables S1 to S3
References (*30*–*43*)

8 March 2016; accepted 4 July 2016
10.1126/science.aaf6268

PLANT DEVELOPMENT

Arabidopsis transcriptional repressor VAL1 triggers Polycomb silencing at *FLC* during vernalization

Julia I. Qüesta,[1] Jie Song,[1,2]* Nuno Geraldo,[1] Hailong An,[1]† Caroline Dean[1]‡

The determinants that specify the genomic targets of Polycomb silencing complexes are still unclear. Polycomb silencing of *Arabidopsis FLOWERING LOCUS C* (*FLC*) accelerates flowering and involves a cold-dependent epigenetic switch. Here we identify a single point mutation at an intragenic nucleation site within *FLC* that prevents this epigenetic switch from taking place. The mutation blocks nucleation of plant homeodomain–Polycomb repressive complex 2 (PHD-PRC2) and indicates a role for the transcriptional repressor VAL1 in the silencing mechanism. VAL1 localizes to the nucleation region in vivo, promoting histone deacetylation and *FLC* transcriptional silencing, and interacts with components of the conserved apoptosis- and splicing-associated protein (ASAP) complex. Sequence-specific targeting of transcriptional repressors thus recruits the machinery for PHD-PRC2 nucleation and epigenetic silencing.

In *Arabidopsis thaliana*, prolonged cold exposure during winter promotes flowering through epigenetic silencing of *FLOWERING LOCUS C* (*FLC*) in a process called vernalization (*1*, *2*). Cold exposure induces expression of antisense transcripts to *FLC* (collectively known as COOLAIR) (*3*) and a plant homeodomain (PHD) protein called VERNALIZATION INSENSITIVE 3 (VIN3) (*4*). COOLAIR facilitates *FLC* transcriptional silencing and coordinates the switching between chromatin states (*5*). VIN3 associates with a homologous PHD protein, VERNALIZATION 5 (VRN5), and a vernalization-specific Polycomb repressive complex 2 (PRC2) (*6*, *7*), which accumulates at an intragenic nucleation region covering the first exon and part of the first intron of *FLC*. Quantitative accumulation of H3K27me3 at the nucleation region during cold exposure, and over the whole locus after cold exposure, reflects a cell-autonomous epigenetic switch affecting an increasing proportion of cells (*8*). The recruitment of PHD-PRC2 to the nucleation region is, therefore, a key step in the silencing process. In *Drosophila*, Polycomb response elements (PRE) have been identified as cis sites for PRC2 recruitment and provide sequence-specific "memory" modules for the activity of linked enhancers (*9*). In contrast, in mammals, CpG islands facilitate targeting of Polycomb machinery, with Polycomb complexes "sampling" chromatin to determine transcriptional states (*10*). In *Arabidopsis*, PRE-like elements have been identified (*11*), but whether they recruit Polycomb complexes has been unclear. We sought to determine what targets PHD-PRC2 to the nucleation region of *FLC*.

A forward genetic screen for impaired *FLC-LUCIFERASE* (*FLC-LUC*) silencing (*12*) identified *vrn8* mutant (Fig. 1A and fig. S1, A to C). The progenitor plants showed characteristic cold-induced silencing of both the endogenous *FLC* and the *FLC-LUC* transgene (Fig. 1, B and C, and fig. S1A). In contrast, the *FLC-LUC* transgene expression remained high in *vrn8* after cold exposure, whereas expression of the endogenous *FLC* was reduced as normal (Fig. 1, B and C, and fig. S1A). The different behavior of the two copies suggests that *vrn8* does not encode a trans factor involved in vernalization.

The *vrn8* mutation was a cytosine-to-thymine change in intron 1 of the *FLC-LUC* transgene, at position +585 downstream of the transcriptional start site (hereafter, we term this mutation *C585T*; Fig. 1D and fig. S1D). *C585T* maps to the first of a pair of RY cis elements (TGCATG, RY-1 and RY-2; R, purine; Y, pyrimidine), which are recognized by B3 DNA binding domains (*13*). Alignment of *FLC* intronic sequences from different species of *Arabidopsis* and *Brassica* shows 100% sequence conservation of both RY motifs (Fig. 1D). To confirm the effect, we regenerated the *C585T* mutation and compared plants carrying wild-type (*FLC-WT*) and mutated (*FLC-C585T*) transgenes (fig. S2A). Cold-induced repression of *FLC* was impaired in *FLC-C585T* transgenic lines (Fig. 1E and fig. S2B), and the plants flowered later (fig. S2C). The proximity of the *C585T* change to the PHD-PRC2 nucleation region prompted an analysis of cold-induced chromatin changes in *FLC-C585T*. The quantitative increase in H3K27me3 and equivalent decrease in H3K36me3 at *FLC-WT* (Fig. 1F and fig. S2D) (*14*) were not found at *FLC-C585T* (Fig. 1G and fig. S2E), suggesting that the *C585T* mutation prevents PHD-PRC2 nucleation.

Identification of the *C585T* mutation raised the question of what bound to the RY elements. Potential candidates included the B3 transcriptional regulators belonging to the LAV family (*13*): LEAFY COTYLEDON 2 (LEC2), ABSCISIC ACID INSENSITIVE 3 (ABI3), FUSCA3 (FUS3), and the VIVIPAROUS1/ABI3-LIKE factors (VAL1, VAL2, and VAL3). The low levels of expression of *ABI3*, *LEC2*, *FUS3*, and *VAL3* in 10-day-old seedlings (fig. S3, A and B) argued against a function of the corresponding transcriptional regulators in *FLC* silencing during vernalization. In contrast, *VAL1* and *VAL2* were expressed at higher levels than other LAV family genes in seedlings (fig. S3A) and continued to be expressed during vernalization (fig. S3, C and D). VAL proteins repress late seed maturation genes and promote the switch from embryonic to vegetative development. *val1 val2* double-mutant seedlings express many embryonic-specific transcripts and also show synergistically increased expression of *FLC* compared with each single mutant alone (*15*). We crossed *val1* and *val2* single mutants with the Columbia *FRIGIDA* (Col *FRI*) line to assess whether VAL genes are required for *FLC* regulation during vernalization. *val1 FRI* mutants flowered later than Col *FRI* and *val2 FRI* plants (Fig. 2A and fig. S4A), and this was reflected in higher *FLC* expression levels before and during cold exposure (Fig. 2B). *val1 FRI* mutants also showed reduced sensitivity to vernalization. The cold-induced reduction in nonspliced *FLC* transcript (probably reflecting transcription; figs. S4B and S5A) and *FLC* mRNA (Fig. 2C) was slower in *val1 FRI* than in wild-type plants, but COOLAIR induction was unaffected (fig. S5B). The mutant phenotype was complemented by expression of a hemagglutinin (HA)–tagged VAL1 (fig. S6). VAL1 not only modulated *FLC* transcriptional shutdown but also appeared to influence the *FLC* homologs *MADS AFFECTING FLOWERING 1* and *2* (*MAF1* and *MAF2;* fig. S4, C and D). Loss of VAL1 also attenuated the

[1]Department of Cell and Developmental Biology, John Innes Centre, Norwich Research Park, Norwich NR4 7UH, UK. [2]Department of Life Sciences, Imperial College London, London SW7 2AZ, UK.
*Present address: Department of Life Sciences, Imperial College London, London SW7 2AZ, UK. †Present address: State Key Laboratory of Crop Biology, Shandong Agricultural University, Tai'an 271018, China. ‡Corresponding author. Email: caroline.dean@jic.ac.uk

Downloaded from http://science.sciencemag.org/ on July 28, 2016

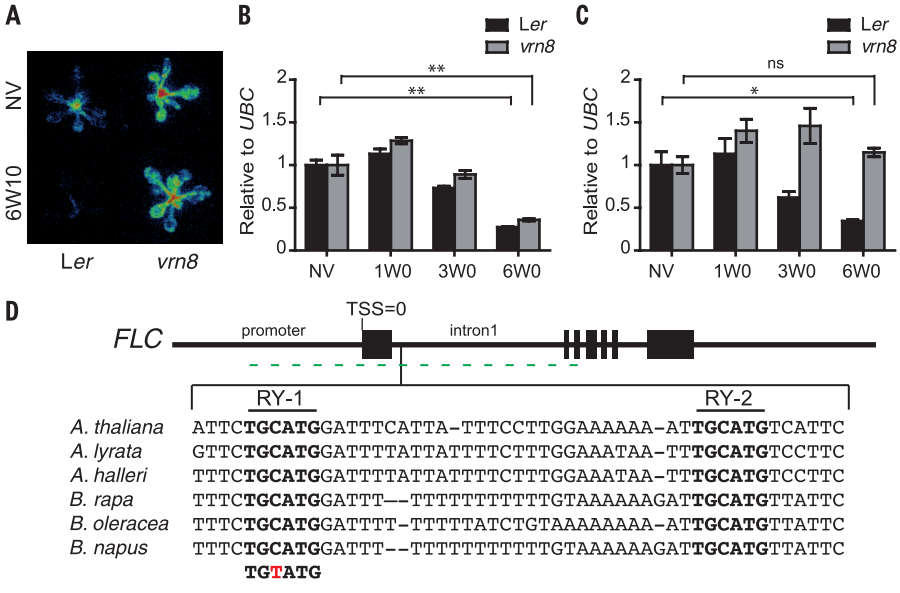


Fig. 1. *vrn8* disrupts an intronic RY element that is required for *FLC* silencing. (**A**) The *vrn8* mutant fails to silence *FLC-LUC* after cold exposure. Luciferase activity is depicted with false color from least (blue) to most intense (red). Ler, Landsberg *erecta* accession. (**B** and **C**) Expression of endogenous Ler *FLC* (B) and *FLC-LUC* transgene (C). The data are abundances relative to *UBIQUITIN-CONJUGATING ENZYME 21* (*UBC*) and standardized to nonvernalized (NV) conditions. Numeral-W-numeral, number of weeks (W) of cold treatment followed by number of days of growth at 22°C. (**D**) Schematic representation of *FLC* genomic locus. Black boxes represent exons. The green dashed line represents the region analyzed in (F) and (G). Alignment of *FLC* intronic sequences from different species of Brassicaceae is shown below; RY motifs are in bold. The single nucleotide change in *vrn8* is indicated (*C585T*, red). TSS, transcriptional start site. (**E**) Spliced *FLC* expression in *FLC-WT* and *FLC-C585T* transgenic lines. (**F** and **G**) ChIP analysis of H3K27me3 accumulation at the *FLC* locus in *FLC-WT* (F) and *FLC-C585T* (G) plants. Numbers on the *x* axes are distances to the TSS (TSS = 0). Throughout this figure, values are means ± SEM of three biological replicates. $^{**}P < 0.01$; $^{*}P < 0.05$; ns, not significant.

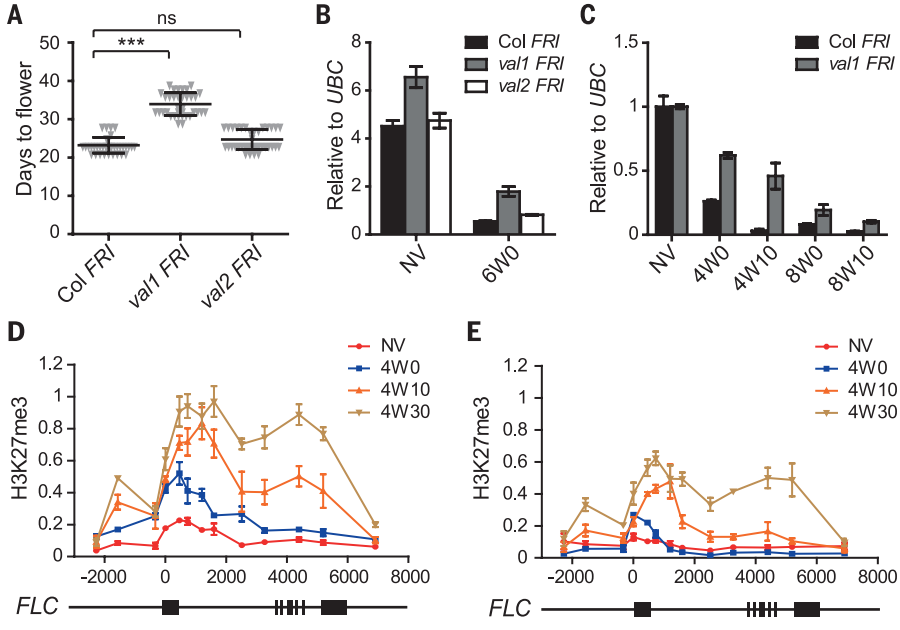


Fig. 2. VAL1 is a component of the vernalization mechanism. (**A**) Flowering time after 6 weeks of cold. Each gray triangle represents a single plant ($n = 36$); means (black horizontal lines) ± SD (error bars) are shown. $^{***}P < 0.001$. (**B**) Spliced *FLC* expression in *val1 FRI*, Col *FRI*, and *val2 FRI* plants before (NV) and during (6W0) cold exposure. (**C**) Dynamics of spliced *FLC* down-regulation during vernalization. Data in (B) and (C) are abundances, expressed as in Fig. 1. (**D** and **E**) H3K27me3 accumulation (from ChIP analysis) along the *FLC* locus in Col *FRI* (D) and *val1 FRI* (E) plants. Numbers on the *x* axes are distances to the TSS (TSS = 0). The schematic of the *FLC* locus is shown below each panel. Values in (B) to (E) are means ± SEM of three biological replicates.

cold-induced H3K27me3 accumulation at *FLC*: Starting levels before cold exposure were lower and failed to reach wild-type levels after 4 weeks of cold (Fig. 2, D and E). The nonreactivation of *FLC* after cold exposure in *val1 FRI* (Fig. 2C and fig. S4B) implies that nucleation is defective (Fig. 2E) but that the components of the longer-term Polycomb memory are not perturbed. The phenotype of *val1 FRI* (Fig. 2E) was not as strong as that caused by *C585T* (Fig. 1G), which is consistent with VAL1 and VAL2 functioning redundantly in *FLC* regulation (*15*).

ABI3, FUS3, and LEC2 bind in a sequence-specific manner to RY elements in vitro (*16*–*18*). This is also the case for the VAL1 B3 domain, which binds in vitro to the *FLC* RY-1 element (Fig. 3A), with the *C585T* mutation sufficient to disrupt binding. Competition experiments showed specificity of VAL1 B3 binding to the *FLC* RY motif (fig. S7, A and B) and not to a different B3 binding cis element (RAV) (*19*). VAL1 B3 can also bind to the second RY site (RY-2) that occurs just

Downloaded from http://science.sciencemag.org/ on July 28, 2016

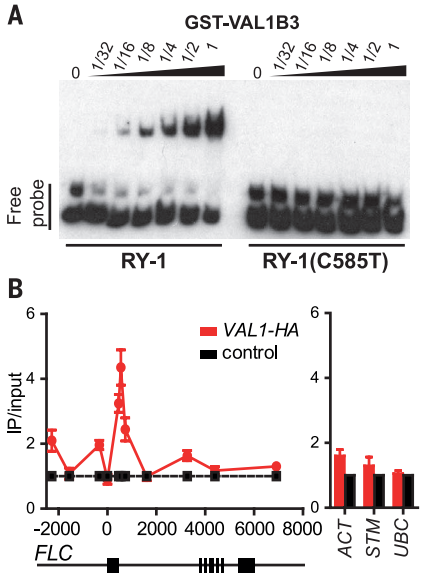


Fig. 3. VAL1 binds to the *FLC* nucleation region. (**A**) Electrophoretic mobility shift assay testing GST-VAL1B3 binding to an RY *cis* element (GST, glutathione *S*-transferase). Wild-type (RY-1) or mutated [RY-1(*C585T*)] RY probes were combined with increasing amounts of GST-VAL1B3 (1 = 25 ng/μl). (**B**) ChIP–quantitative polymerase chain reaction of VAL1-HA binding along *FLC*. *ACTIN2 (ACT)*, *UBC*, and *SHOOT MERISTEMLESS (STM)* were used as negative controls. The schematic of the *FLC* locus is shown below. Values are means ± SEM of one biological replicate for samples from six independent transgenic lines.

A

Identified Protein	Accession no.	Mol. Mass (kDa)	No. of Protein Matched Peptides				Sequence Coverage (%)			
			IP1	IP2	IP3	IP4	IP1	IP2	IP3	IP4
VAL1	At2g30470	87	34	29	15	14	48	39	20	20
AtBMI1A	At2g30580	47	10	8	6	5	13	12	7	7
AtSAP18	At2g45640	17	10	0	8	6	60	0	43	36
ACINUS	At4g39680	69	0	11	13	10	0	15	28	15
AtSR45	At1g16610	45	0	0	5	3	0	0	7	8

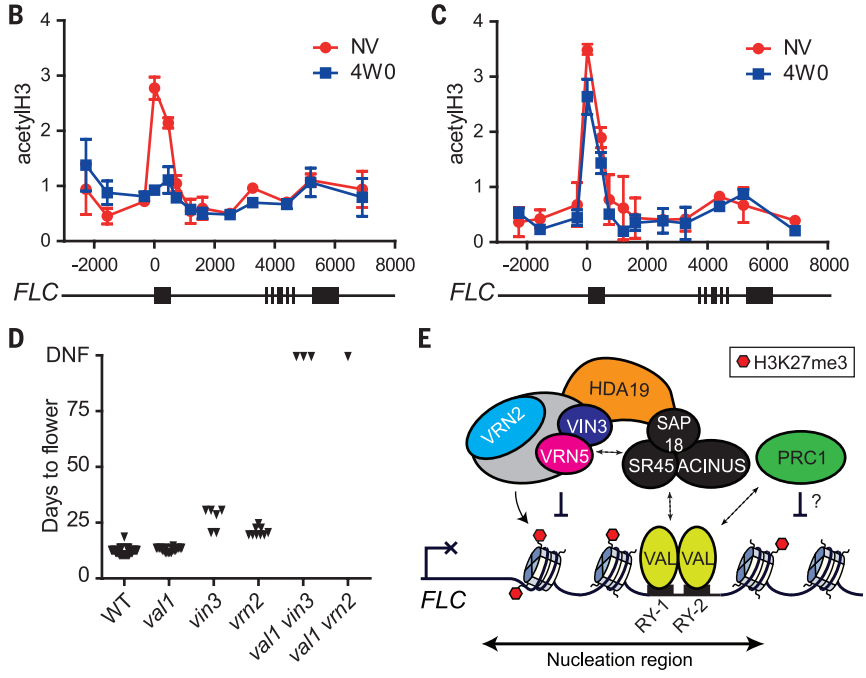


Fig. 4. VAL1 nucleates silencing at the *FLC* locus. (**A**) List of proteins identified by VAL1-HA (IP1 and IP2) and GFP-VAL1 (IP3 and IP4) affinity purification (IP, immunoprecipitation). (**B** and **C**) ChIP analysis of histone H3 acetylation (acetylH3) along the *FLC* locus in Col *FRI* (B) and *val1 FRI* (C). Numbers on the *x* axes are distances to the TSS (TSS = 0) and correspond to the schematic below each panel. (**D**) Days to flower after 12 weeks of vernalization for F2 plants from *val1 FRI* crosses with *vin3 FRI* and *vrn2 FRI* (table S6). WT indicates at least one functional allele for *VAL1*, *VRN2*, and *VIN3*. Lowercase indicates that both alleles are nonfunctional (*val1*, *vin3*, and *vrn2*). All F2 individuals are in *FRI* background. DNF, did not flower. (**E**) Schematic depicting sequence-specific binding of VAL proteins to the *FLC* nucleation region, targeting ASAP, HDA19, and potentially PRC1 activities to shut down transcription and thereby enable PHD-PRC2 nucleation. After this process, H3K27me3 covers the *FLC* locus to help maintain epigenetic silencing. Small double arrows indicate protein interactions identified in this work.

downstream of RY-1; competition experiments revealed that mutation of both RY elements is required to block VAL1 B3 binding to the nucleation region in vitro (fig. S7C). Consistent with this, in vivo mutation of RY-2 also attenuated *FLC* silencing (fig. S7D), suggesting that both RY elements contribute functionally. Chromatin immunoprecipitation (ChIP) confirmed in vivo binding of VAL1-HA to the *FLC* nucleation region during cold exposure (Fig. 3B). These data raise interesting parallels with the cooperative binding of auxin response factors (ARFs) to tandem binding sites in vivo (*20*).

The association of VAL1 with the nucleation region as a prerequisite for PHD-PRC2 activity at the locus raised two questions. First, how does VAL1 binding within intron 1 repress *FLC* transcription? Second, what is the link between VAL1 and PHD-PRC2? Affinity purification of HA- and green fluorescent protein (GFP)–tagged VAL1 from *Arabidopsis* seedlings revealed VAL1 in vivo interactors: the PRC1 RING finger homolog AtBMI1A, the co-repressor SIN3-associated protein SAP18 (AtSAP18), and its two partners, the RNA-binding protein SR45 and the SAP-domain protein ACINUS (Fig. 4A, fig. S6D, and tables S1 and S2) (*21*). AtBMI1A has previously been found to interact with VAL1 to repress seed maturation genes through H2A lysine 121 ubiquitination (H2Aub) (*22*). We therefore tested accumulation of H2Aub at *FLC* during vernalization. Although H2Aub was detected at *FLC* after 4 weeks of cold, there was no difference between Col *FRI* and *val1 FRI* (fig. S8). However, H2Aub is not always required for efficient PRC1 repression (*23*), which can directly repress genes by triggering chromatin compaction (*24*).

SAP18 is a component of the SIN3–histone deacetylase complex (HDAC) that in humans is required to enhance SIN3-mediated repression of transcription (*25*). VAL1 contains a plant-specific ethylene-responsive element binding factor–associated amphiphilic repression (EAR) motif that can physically interact with AtSAP18 to mediate histone deacetylase 19 (HDA19) recruitment (*26*). We hypothesized that VAL1 could bring HDA19 activity to the *FLC* locus. H3 acetylation is reduced at the *FLC* nucleation region during cold exposure (Fig. 4B) (*27*); this reduction was blocked in *val1 FRI* (Fig. 4C), as has been observed in *vin3* (*27*). SAP18 has also been linked to RNA processing and degradation (*28*) and is a subunit of the conserved apoptosis- and splicing-associated protein (ASAP) complex, together with SR45 and ACINUS (*21*). Affinity purification of GFP-AtSAP18 from *Arabidopsis* confirmed association with AtSR45 and ACINUS (table S3). This suggests that the conserved function of ASAP and HDA19 is required for VAL1-mediated *FLC* silencing. Accordingly, *hda19* and *sr45* mutants, and to a lesser extent *sap18* mutants, showed *FLC* up-regulation (fig. S9). Importantly, AtSAP18, AtSR45, and HDA19 were immunopurified with both VRN5-GFP (table S4) and VIN3-GFP (table S5), linking VAL1 association with a specific DNA sequence to Polycomb silencing. Combination of *val1 FRI* with mutants with loss of function in *VRN2* (*vrn2 FRI*) and *VIN3* (*vin3 FRI*)

Downloaded from http://science.sciencemag.org/ on July 28, 2016

confirmed the close functionality of VAL1 and PHD-PRC2. *val1 vin3* and *val1 vrn2* plants were very delayed in flowering (Fig. 4D; table S6; and fig. S10, A to D) after 12 and 18 weeks of cold, and *FLC* expression remained high (fig. S10, E and F). This synergistic interaction is best explained by VAL1-VAL2 redundancy, with both proteins functioning through PHD-PRC2.

We propose that VAL1 binds sequence-specifically, probably as a homodimer, but potentially as a heterodimer with VAL2, to the RY motifs in the *FLC* nucleation region (Fig. 4E). This recruits the ASAP complex and potentially PRC1, resulting in the shutdown of transcription and reduced histone acetylation. In turn, these activities allow PHD-PRC2 nucleation and long-term epigenetic silencing of the locus. We cannot exclude the possibility of effects of VAL1 and VAL2 on *FLC* expression that are independent of the binding to *FLC* intron 1. The association of HDA19 with the PHD proteins suggests that it has multiple roles in the process, potentially interacting with VAL1 through SAP18 (*26*) for transcriptional repression and with VIN3 (and VRN5) to facilitate +1 nucleosome stabilization (*27*). It will now be important to investigate which components confer the switchlike on-off property that has been proposed for the nucleation event (*29*).

REFERENCES AND NOTES

1. S. D. Michaels, R. M. Amasino, *Plant Cell* **11**, 949–956 (1999).
2. C. C. Sheldon, D. T. Rouse, E. J. Finnegan, W. J. Peacock, E. S. Dennis, *Proc. Natl. Acad. Sci. U.S.A.* **97**, 3753–3758 (2000).
3. S. Swiezewski, F. Liu, A. Magusin, C. Dean, *Nature* **462**, 799–802 (2009).
4. S. Sung, R. M. Amasino, *Nature* **427**, 159–164 (2004).
5. T. Csorba, J. I. Questa, Q. Sun, C. Dean, *Proc. Natl. Acad. Sci. U.S.A.* **111**, 16160–16165 (2014).
6. M. Derkacheva, L. Hennig, *J. Exp. Bot.* **65**, 2769–2784 (2014).
7. A. R. Gendall, Y. Y. Levy, A. Wilson, C. Dean, *Cell* **107**, 525–535 (2001).
8. A. Angel, J. Song, C. Dean, M. Howard, *Nature* **476**, 105–108 (2011).
9. P. A. Steffen, L. Ringrose, *Nat. Rev. Mol. Cell Biol.* **15**, 340–356 (2014).
10. N. P. Blackledge, N. R. Rose, R. J. Klose, *Nat. Rev. Mol. Cell Biol.* **16**, 643–649 (2015).
11. B. Sun *et al.*, *Science* **343**, 1248559 (2014).
12. J. Mylne, T. Greb, C. Lister, C. Dean, *Cold Spring Harb. Symp. Quant. Biol.* **69**, 457–464 (2004).
13. K. Swaminathan, K. Peterson, T. Jack, *Trends Plant Sci.* **13**, 647–655 (2008).
14. H. Yang, M. Howard, C. Dean, *Curr. Biol.* **24**, 1793–1797 (2014).
15. M. Suzuki, H. H. Wang, D. R. McCarty, *Plant Physiol.* **143**, 902–911 (2007).
16. R. Nag, M. K. Maity, M. Dasgupta, *Plant Mol. Biol.* **59**, 821–838 (2005).
17. S. A. Braybrook *et al.*, *Proc. Natl. Acad. Sci. U.S.A.* **103**, 3468–3473 (2006).
18. W. Reidt *et al.*, *Plant J.* **21**, 401–408 (2000).
19. Y. Kagaya, K. Ohmiya, T. Hattori, *Nucleic Acids Res.* **27**, 470–478 (1999).
20. D. R. Boer *et al.*, *Cell* **156**, 577–589 (2014).
21. C. Schwerk *et al.*, *Mol. Cell. Biol.* **23**, 2981–2990 (2003).
22. C. Yang *et al.*, *Curr. Biol.* **23**, 1324–1329 (2013).
23. A. R. Pengelly, R. Kalb, K. Finkl, J. Müller, *Genes Dev.* **29**, 1487–1492 (2015).
24. N. J. Francis, R. E. Kingston, C. L. Woodcock, *Science* **306**, 1574–1577 (2004).
25. Y. Zhang, R. Iratni, H. Erdjument-Bromage, P. Tempst, D. Reinberg, *Cell* **89**, 357–364 (1997).
26. K. Hill, H. Wang, S. E. Perry, *Plant J.* **53**, 172–185 (2008).
27. E. Jean Finnegan, *Plant J.* **84**, 875–885 (2015).
28. K. K. Singh *et al.*, *RNA* **16**, 2442–2454 (2010).
29. A. Angel *et al.*, *Proc. Natl. Acad. Sci. U.S.A.* **112**, 4146–4151 (2015).

ACKNOWLEDGMENTS

We thank all members of the Dean and Howard research groups for discussions. We are grateful to G. Saalbach for assistance with mass spectrometry, M. Suzuki for providing *val1* and *val2* lines, J. Irwin for the *Brassica FLC* sequences, J. Long for the *hda19-1* line, and A. Pendle for the 35S::GFP-AtSAP18 plasmid. We thank V. Coustham, B. Rutjens, and J. Mylne for contributions at the early phase of this project. The Dean laboratory is supported by the UK Biotechnology and Biological Sciences Research Council and a European Research Council Advanced Investigator grant. The supplementary materials contain additional data.

SUPPLEMENTARY MATERIALS

www.sciencemag.org/content/353/6298/485/suppl/DC1
Materials and Methods
Figs. S1 to S10
Tables S1 to S7
References (*30*–*39*)

22 March 2016; accepted 1 July 2016
10.1126/science.aaf7354

SYMBIOSIS

Basidiomycete yeasts in the cortex of ascomycete macrolichens

Toby Spribille,[1,2]* Veera Tuovinen,[3,4] Philipp Resl,[1] Dan Vanderpool,[2] Heimo Wolinski,[5] M. Catherine Aime,[6] Kevin Schneider,[1]† Edith Stabentheiner,[1] Merje Toome-Heller,[6]‡ Göran Thor,[4] Helmut Mayrhofer,[1] Hanna Johannesson,[3] John P. McCutcheon[2,7]

For over 140 years, lichens have been regarded as a symbiosis between a single fungus, usually an ascomycete, and a photosynthesizing partner. Other fungi have long been known to occur as occasional parasites or endophytes, but the one lichen–one fungus paradigm has seldom been questioned. Here we show that many common lichens are composed of the known ascomycete, the photosynthesizing partner, and, unexpectedly, specific basidiomycete yeasts. These yeasts are embedded in the cortex, and their abundance correlates with previously unexplained variations in phenotype. Basidiomycete lineages maintain close associations with specific lichen species over large geographical distances and have been found on six continents. The structurally important lichen cortex, long treated as a zone of differentiated ascomycete cells, appears to consistently contain two unrelated fungi.

Most definitions of the lichen symbiosis emphasize its dual nature: the mutualism of a single fungus and single photosynthesizing symbiont, occasionally supplemented by a second photosynthesizing symbiont in modified structures (*1*–*4*). Together, these organisms form stratified, often leafy or shrubby body plans (thalli) that resemble none of the symbionts in isolation, a feature thought to be unique among symbioses (*1*). Attempts to synthesize lichen thalli from the accepted two components in axenic conditions, however, have seldom produced structures that resemble natural thalli (*5*, *6*). Notably, a critical structural feature of stratified lichens, the cortex, typically remains rudimentary in laboratory-generated symbioses (*5*). Recently, it has been suggested that microbial players, especially bacteria, may play a role in forming complete, functioning lichen thalli (*7*). However, although culturing and amplicon sequencing have revealed rich communities of microbes (*7*, *8*), including other fungi (*8*–*10*), no new stably associated symbiotic partners have been found.

The recalcitrance of lichens to form thalli in vitro means that characterizing symbiont gene activity (e.g., through transcriptomics) requires an approach that works with natural thalli. We used metatranscriptomics to better understand the factors involved in forming two macrolichen symbioses, *Bryoria fremontii* and *B. tortuosa*. These two species have been distinguished for 90 years by the thallus-wide production of the toxic substance vulpinic acid in *B. tortuosa*, causing it to appear yellowish, in contrast to *B. fremontii*, which is dark brown (*11*). Recent phylogenetic analyses have failed to detect any fixed sequence differences between the two species in either the mycobiont (Ascomycota, Lecanoromycetes, *Bryoria*) or the photobiont (Viridiplantae, *Trebouxia simplex*) when considering four and two loci, respectively (*12*, *13*). We hypothesized that differential gene expression might account for the

[1]Institute of Plant Sciences, NAWI Graz, University of Graz, 8010 Graz, Austria. [2]Division of Biological Sciences, University of Montana, Missoula, MT 59812, USA. [3]Department of Organismal Biology, Uppsala University, Norbyvägen 18D, 752 36 Uppsala, Sweden. [4]Department of Ecology, Swedish University of Agricultural Sciences, Post Office Box 7044, SE-75007 Uppsala, Sweden. [5]Institute of Molecular Biosciences, BioTechMed-Graz, University of Graz, 8010 Graz, Austria. [6]Department of Botany and Plant Pathology, Purdue University, West Lafayette, IN 47907, USA. [7]Program in Integrated Microbial Biodiversity, Canadian Institute for Advanced Research, Toronto, Ontario, Canada.
***Corresponding author. Email: toby.spribille@mso.umt.edu**
†Present address: Institute of Biodiversity, Animal Health and Comparative Medicine, College of Medical, Veterinary and Life Sciences, University of Glasgow, Glasgow G12 8QQ, UK. ‡Present address: Plant Health and Environmental Laboratory, Ministry for Primary Industries, Auckland, New Zealand.

Downloaded from http://science.sciencemag.org/ on July 28, 2016

increased production of vulpinic acid in *B. tortuosa*.

We first selected 15 thalli (six from *B. fremontii* and nine from *B. tortuosa*, all free from visible parasitic infection) from sites across western Montana, USA, for mRNA transcriptome sequencing. An initial transcriptome-wide analysis of single-nucleotide polymorphisms (SNPs) for Ascomycota and Viridiplantae transcript subsets showed no correlation between genotype and phenotype in *B. fremontii* and *B. tortuosa*, confirming previous results (*12*, *13*) (Fig. 1, A and B). Next, we estimated transcript abundances by mapping raw reads back to a single, pooled metatranscriptome assembly and binning by taxon. Restricting our analyses to Ascomycota and Viridiplantae revealed little differential transcript abundance associated with phenotype (Fig. 1, C and E). Taken together, these analyses confirm previous conclusions that the two lichen species are nomenclatural synonyms (*12*) but still provide no explanation for the underlying phenotypes (which we shall continue to refer to by their species names for convenience). However, by expanding the taxonomic range to consider all Fungi, we found 506 contigs with significantly higher abundances in vulpinic acid–rich *B. tortuosa* thalli. A majority of these contigs were annotated as Basidiomycota (Fig. 1D). These data suggested that a previously unrecognized basidiomycete was present in thalli of both species but was more abundant whenever vulpinic acid was present in large amounts.

We next sought to determine whether this uncharacterized basidiomycete was specific to the studied *Bryoria* species or could be found in other lichens. From metatranscriptome contigs containing ribosomal RNA (rRNA) basidiomycete sequences, we designed specific primers for ribosomal DNA [rDNA; 18*S*, internal transcribed spacer (ITS), and D1D2 domains of 28*S*) to screen lichens growing physically adjacent to *Bryoria* in Montana forests. Each assayed lichen species carried a genetically distinct strain of the basidiomycete, indicating a high degree of specificity. Furthermore, we found that *Letharia vulpina*, a common lichen species growing intermixed with *Bryoria*, maintained basidiomycete genotypes that were distinct from those in *Bryoria*, not only in Montana but also in northern Europe (fig. S1). When assaying for the basidiomycete across the seven main radiations of macrolichens in the class Lecanoromycetes, we found related basidiomycete lineages associated with 52 lichen genera from six continents, including in 42 of 56 sampled genera of the family Parmeliaceae (fig. S2). As a whole, these data indicate that basidiomycete fungi are ubiquitous and global associates of the world's most speciose radiation (*14*) of macrolichens.

To place the basidiomycete lineages in a phylogenetic context, we generated a 349-locus phylogenomic tree by using gene sequences inferred from our transcriptome data set and other available genomes (table S1). This analysis placed the basidiomycete as sister to *Cystobasidium minutum* (class Cystobasidiomycetes, subphylum Pucciniomycotina) with high support (Fig. 2A). The only previously known lichen-associated members of Cystobasidiomycetes are two species of *Cyphobasidium*, which is hypothesized to cause galls on species of Parmeliaceae (*15*). When incorporated into a broader sample of published cystobasidiomycete rDNA sequence data (*16*–*18*), the majority of our lichen-derived sequences form a strongly supported monophyletic clade with *Cyphobasidium* (Fig. 2B). Using current classification criteria (*18*), the lichen-associated lineages would include numerous new family-level lineages, and we recognize this set of subclades as the new order Cyphobasidiales (*19*). Applying a relaxed molecular clock to our phylogenomic tree

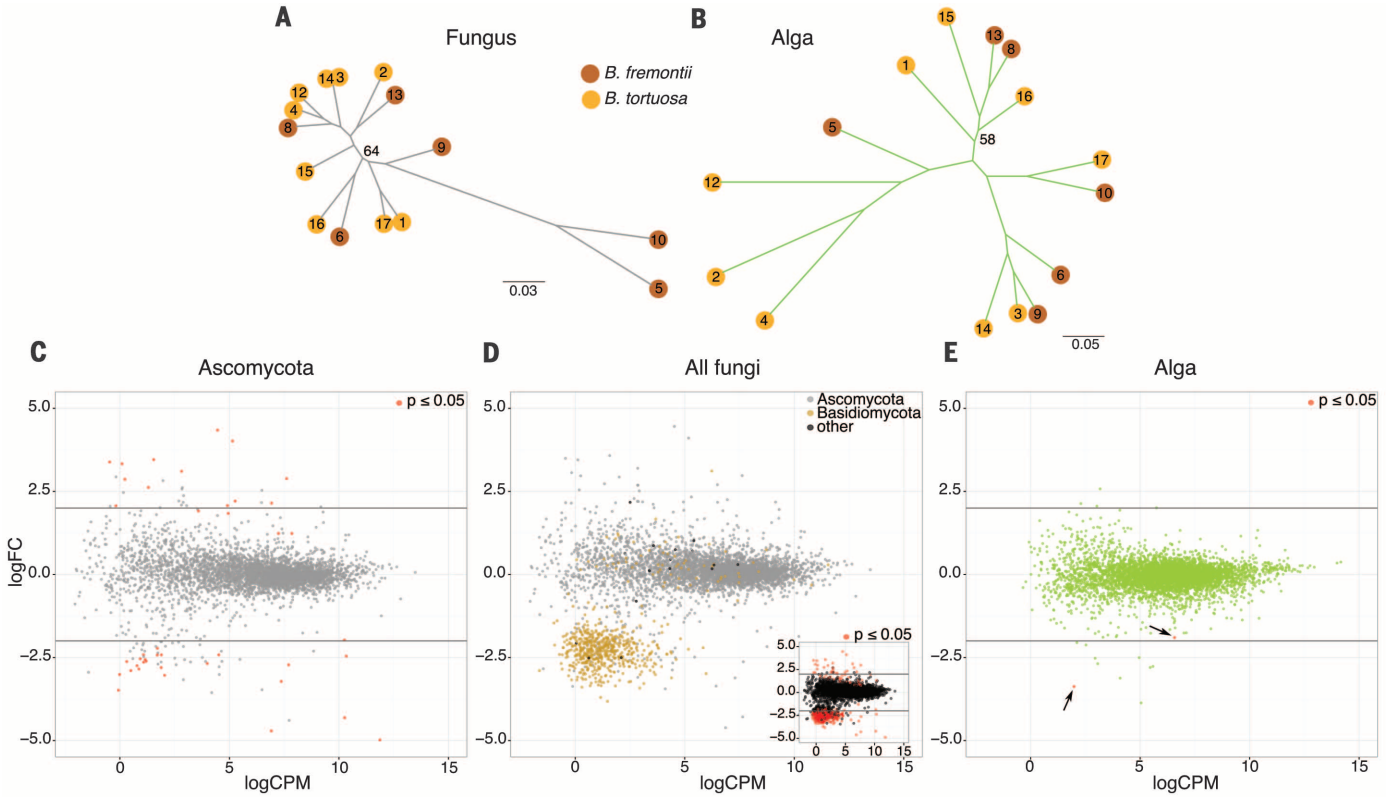


Fig. 1. Genome-wide divergence and transcript abundance of fungi and algae, based on symbiont subsets extracted from wild *Bryoria* metatranscriptomes. (**A** and **B**) Unrooted maximum likelihood topologies for (A) the Ascomycota member (lecanoromycete) and (B) the Viridiplantae member (alga) within the lichen pair *B. fremontii* and *B. tortuosa*, based on 30,001 and 25,788 SNPs, respectively. Numbers refer to metatranscriptome sample IDs (table S2). Scale bars indicate the average number of substitutions per site (**C** to **E**) Logarithm of the fold change (logFC) between vulpinic acid–deficient (*B. fremontii*) and vulpinic acid–rich (*B. tortuosa*) phenotypes in 15 *Bryoria* metatranscriptomes, plotted against transcript abundance (logCPM, logarithm of counts per million reads). Only transcripts found in all 15 samples were included. Ascomycota transcripts only are shown in (C). All fungal transcripts are shown in (D), with taxonomic assignments superimposed; a plot with statistically significant transcript differential abundance is shown as an inset. Viridiplantae transcripts are shown in (E). Red dots indicate a log fold change with $P < 0.05$ in (C), the inset of (D), and (E) (highlighted with arrows).

Downloaded from http://science.sciencemag.org/ on July 28, 2016

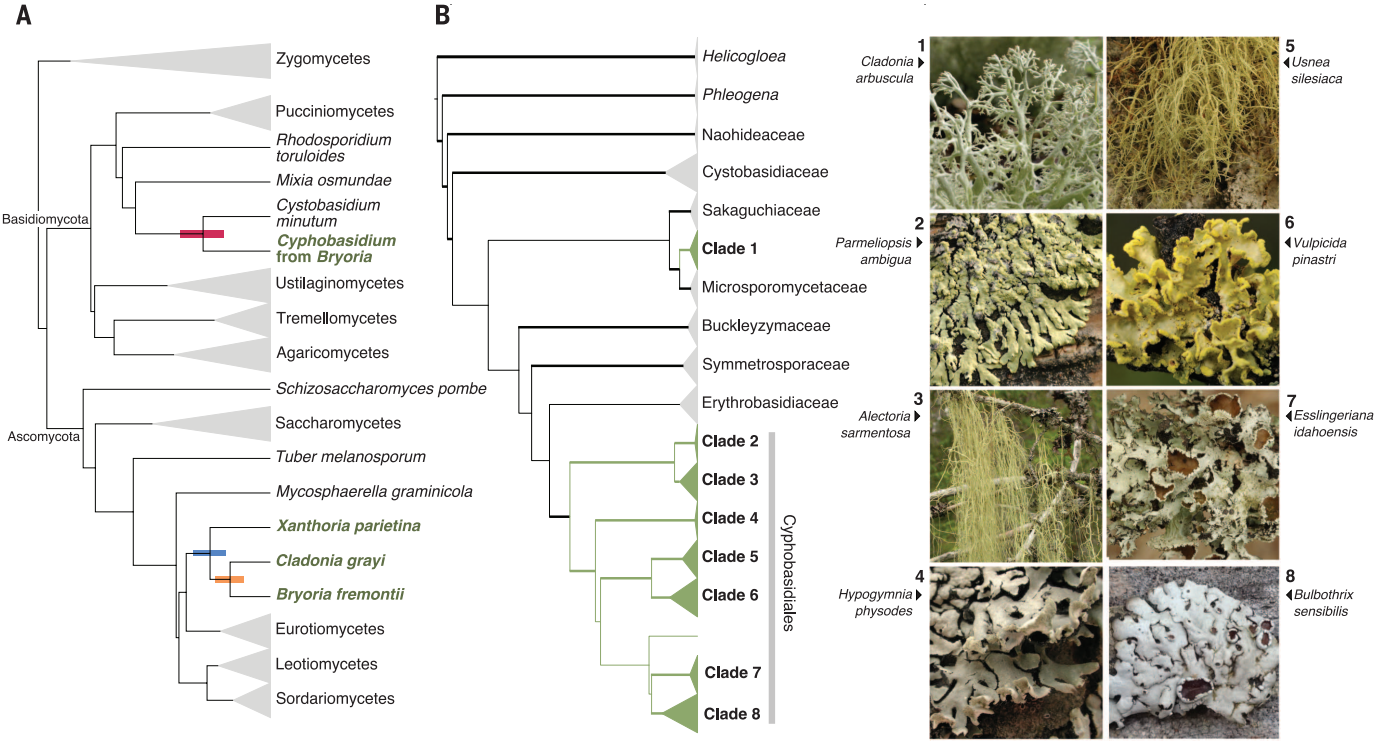


Fig. 2. Placement of Cyphobasidiales members and their diversity within lichens. (**A**) Maximum likelihood phylogenomic tree based on 39 fungal proteomes and 349 single-copy orthologous loci. Dating based on a 58-locus subsample shows relative splits between Cyphobasidiales and *Cystobasidium minutum* and splits leading to the lecanoromycete genera *Xanthoria*, *Cladonia*, and *Bryoria* (colored bars indicate 95% confidence intervals; fungi occurring in lichens are shown in green). (**B**) Maximum likelihood rDNA phylogeny of the class Cystobasidiomycetes, with images of representative lichen species from which sequences were obtained in each clade; thick branches indicate bootstrap support >70%. Shaded triangles are scaled to the earliest branch splits of underlying sequence divergence in each clade. Full versions of the trees are shown in fig. S3.

(Fig. 2A) shows the *Cystobasidium-Cyphobasidium* split occurring around the same time as the origin of three of the main groups of lecanoromycete macrolichens in which Cyphobasidiales species occur, suggesting a long, shared evolutionary history. Two fossil calibrations place this split at around 200 million years before the present (figs. S4 and S5).

Our initial microscopic imaging failed to reveal any cells that we could assign to Basidiomycetes with certainty. Furthermore, attempts to culture the basidiomycete from fresh thalli were unsuccessful. We therefore developed protocols for fluorescent in situ hybridization (FISH) targeting specific ascomycete and cystobasidiomycete rRNA sequences. Cystobasidiomycete-specific FISH probes unambiguously hybridized round, ~3- to 4-μm-diameter cells embedded in the peripheral cortex of both *B. fremontii* and *B. tortuosa* (Fig. 3 and movie S1). Consistent with the transcript abundance data, these cells were more abundant in thalli of *B. tortuosa* (Fig. 3), where they were embedded in secondary metabolite residues (movie S1). Imaging of other lichen species likewise revealed cells of similar morphology in the peripheral cortex (fig. S6). Composite three-dimensional FISH images from *B. capillaris* show the cells occurring in a zone exterior to the lecanoromycete (Fig. 4 and movie S2) and embedded in polysaccharides (Fig. 4C), explaining why these cells are not observed in scanning electron microscopy (Fig. 4A). In some species, such as *L. vulpina*, the abundance of hybridized living cells was low, but selective removal of the polysaccharide layer through washing revealed high densities of collapsed, apparently dead cells within the cortex (fig. S7). These dead cells may explain the paucity of the FISH signal in some experiments. The mononucleate single cells (fig. S8C), evidence of budding, and absence of hyphae or clamp connections are consistent with an anamorphic or yeast state in Cystobasidiomycetes. FISH imaging of *Cyphobasidium* galls on the lichen *Hypogymnia physodes*, obtained from Norway, confirmed the link to the sexual or teleomorphic state (fig. S8), which appears to develop rarely (*15*). These data suggest that the gall-inducing form of *Cyphobasidium* completes its life cycle entirely within lichens.

It is remarkable that *Cyphobasidium* yeasts have evaded detection in lichens until now, despite decades of molecular and microscopic studies of the Parmeliaceae (*20*–*22*). It seems likely that the failure to detect *Cyphobasidium* in both Sanger and amplicon sequencing studies (*8*) is due to multitemplate polymerase chain reaction bias. The most widespread clade of *Cyphobasidium* possesses a 595–base pair group I intron inserted downstream of the primer binding site ITS1F, doubling the template length of ITS, a popular fungal barcode (*23*). This, combined with low background abundance, can push a template below detection thresholds (*24*). Also, we cannot rule out that *Cyphobasidium* yeasts have actually been sequenced and discarded as presumed contaminants.

The lichen cortex layer has long been considered to be key for structural stabilization of macrolichens, as well as for water and nutrient transfer into the thallus interior (*6*, *25*). Most macrolichens possess a basic two-layer cortex scheme consisting of conglutinated internal hyphae and a thin, polysaccharide-rich peripheral layer (*25*). However, the internal cellular structure is not uniform across lichens (*26*), and the composition of extracellular polysaccharides is poorly known (*27*). In *Bryoria*, the layer in which *Cyphobasidium* yeasts occur has not been recognized as distinct from the cortex (*11*), although in other parmelioid lichens, a seemingly homologous layer has sometimes been referred to as the "epicortex" (*20*). The discovery of ubiquitous yeasts embedded in the cortex raises the prospect that more than one fungus may be involved in its construction, and it could explain why lichens synthesized in vitro from axenically grown ascomycete and algal cultures develop only rudimentary cortex layers (*5*).

In many lichens, the peripheral cortex layer in which *Cyphobasidium* yeasts are embedded is enriched with specific secondary metabolites (*25*), the production of which often does not correlate with the lecanoromycete phylogeny (*28*).

Downloaded from http://science.sciencemag.org/ on July 28, 2016

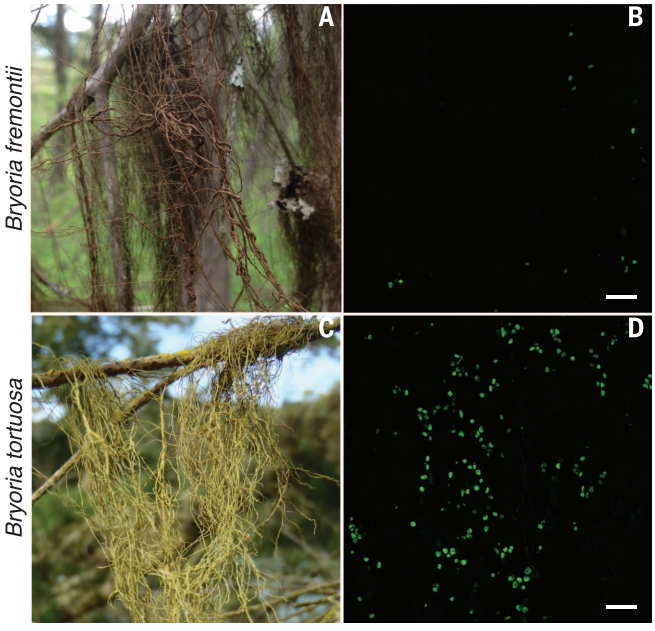


Fig. 3. Differential abundance of Cyphobasidiales yeasts in *B. fremontii* and *B. tortuosa*. (**A**) *B. fremontii*, with (**B**) few FISH-hybridized live yeast cells at the level of the cortex. (**C**) *B. tortuosa*, with (**D**) abundant FISH-hybridized cortical yeast cells (scale bars, 20 μm).

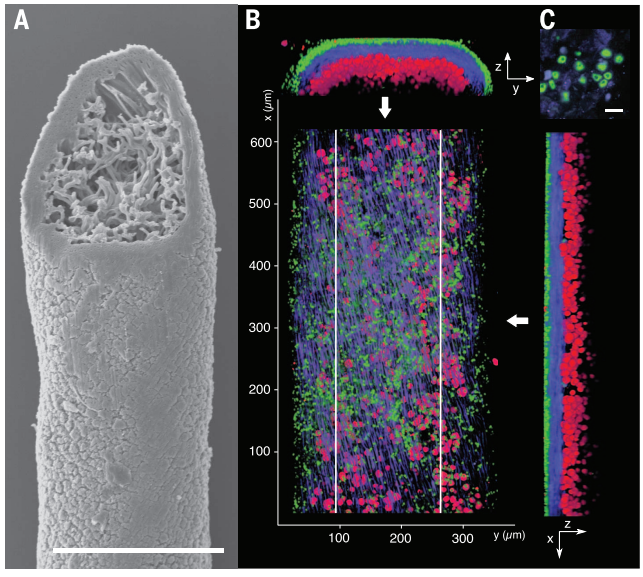


Fig. 4. Fluorescent cell imaging of dual fungal elements in lichen thalli. (**A**) Scanning electron microscopy image of a thallus filament of *B. capillaris* (scale bar, 200 μm). (**B**) FISH hybridization of *B. capillaris* thallus, showing Cyphobasidiales yeasts (green) and the lecanoromycete (blue) with algal chlorophyll A autofluorescence (red). The volume within the two vertical lines is visualized on the right; the unclipped frontal view is shown at the top. Movie S2 shows an animation of the three-dimensional ~100-μm z-stack. (**C**) Detail of yeast cells (scale bar, 5 μm).

The assumption that these substances are exclusively synthesized by the lecanoromycete must now be considered untested. In *B. tortuosa,* differential transcript and cell abundance data, along with physical adjacency to crystalline residues, implicate *Cyphobasidium* in the production of vulpinic acid, either directly or by inducing its synthesis by the lecanoromycete. Confirming a link by using transcriptome or genome data is impossible until the enzymatic synthesis pathway of vulpinic acid is described. However, related pulvinic acid derivatives are synthesized by other members of Basidiomycota (*29*).

The assumption that stratified lichens are constructed by a single fungus with differentiated cell types is so central to the definition of the lichen symbiosis that it has been codified into lichen nomenclature (*30*). This definition has brought order to the field but may also have constrained it by forcing untested assumptions about the true nature of the symbiosis. We suggest that the discovery of *Cyphobasidium* yeasts should change expectations about the potential diversity and ubiquity of organisms involved in one of the oldest known and most recognizable symbioses in science.

REFERENCES AND NOTES

1. A. De Bary, *Die Erscheinung der Symbiose* (Verlag Karl Trübner, 1879).
2. A. Gargas, P. T. DePriest, M. Grube, A. Tehler, *Science* **268**, 1492–1495 (1995).
3. F. Lutzoni, M. Pagel, V. Reeb, *Nature* **411**, 937–940 (2001).
4. D. L. Hawksworth, *Bot. J. Linn. Soc.* **96**, 3–20 (1988).
5. V. Ahmadjian, *The Lichen Symbiosis* (John Wiley & Sons, 1993).
6. R. Honegger, *New Phytol.* **125**, 659–677 (1993).
7. I. A. Aschenbrenner, T. Cernava, G. Berg, M. Grube, *Front. Microbiol.* **7**, 180 (2016).
8. S. T. Bates *et al.*, *Lichenologist* **44**, 137–146 (2012).
9. O. Petrini, U. Hake, M. M. Dreyfuss, *Mycologia* **82**, 444–451 (1990).
10. J. M. U'Ren, F. Lutzoni, J. Miadlikowska, A. E. Arnold, *Microb. Ecol.* **60**, 340–353 (2010).
11. I. M. Brodo, D. L. Hawksworth, *Opera Bot.* **42**, 1–164 (1977).
12. S. Velmala, L. Myllys, P. Halonen, T. Goward, T. Ahti, *Lichenologist* **41**, 231–242 (2009).
13. H. Lindgren *et al.*, *Lichenologist* **46**, 681–695 (2014).
14. G. Amo de Paz, P. Cubas, P. K. Divakar, H. T. Lumbsch, A. Crespo, *PLOS ONE* **6**, e28161 (2011).
15. A. M. Millanes, P. Diederich, M. Wedin, *Fungal Biol.* 10.1016/j.funbio.2015.12.003 (2015).
16. M. C. Aime *et al.*, *Mycologia* **98**, 896–905 (2006).
17. Q.-M. Wang *et al.*, *Stud. Mycol.* **81**, 27–53 (2015).
18. Q.-M. Wang *et al.*, *Stud. Mycol.* **81**, 149–189 (2015).
19. Cyphobasidiales T. Sprib. & H. Mayrhofer, ord. nov. (MB 816120); diagnosis is the same as type family Cyphobasidiaceae T. Sprib. & H. Mayrhofer, fam. nov. (MB 816119); embedded in lichen thalli; teleomorph filamentous, rarely observed; when fertile, basidia develop thick-walled probasidium and thin-walled, cylindrical meiosporangium; anamorph is the prevalent known form, consisting of budding yeast with round, thin-walled cells, 2.5 to 4.5 μm in diameter, embedded in the upper cortex of lichens, especially Parmeliaceae; exogenous compound utilization not characterized; cell wall constituents unknown. Type genus, *Cyphobasidium* Millanes, Diederich, and Wedin, *Fungal Biology* doi:10.1016/j.funbio.2015.12.003, p. 4 (2015).
20. M. E. Hale Jr., *Lichenologist* **13**, 1–10 (1981).
21. A. Thell *et al.*, *Nord. J. Bot.* **30**, 641–664 (2012).
22. A. Crespo *et al.*, *Taxon* **59**, 1735–1753 (2010).
23. C. L. Schoch *et al.*, *Proc. Natl. Acad. Sci. U.S.A.* **109**, 6241–6246 (2012).
24. E. Kalle, M. Kubista, C. Rensing, *Biomol. Detect. Quantif.* **2**, 11–29 (2014).
25. R. Honegger, "The symbiotic phenotype of lichen-forming ascomycetes and their endo- and epibionts," in *Fungal Associations*, B. Hock, Ed., vol. IX of *The Mycota*, K. Esser, Ed. (Springer, ed. 2, 2012), pp. 287–339.
26. D. Anglesea, C. Veltkamp, G. H. Greenhalgh, *Lichenologist* **14**, 29–38 (1982).
27. E. S. Olafsdottir, K. Ingólfsdottir, *Planta Med.* **67**, 199–208 (2001).
28. C. G. Boluda, V. J. Rico, A. Crespo, P. K. Divakar, D. L. Hawksworth, *Lichenologist* **47**, 279–286 (2015).
29. N. Arnold, W. Steglich, H. Besl, *Z. Mykol.* **62**, 69–73 (1996).
30. W. L. Culberson, *Taxon* **10**, 161–165 (1961).

ACKNOWLEDGMENTS

This project was supported by an incubation grant from the University of Montana to J.P.M. and T.S.; by an Austrian Science Fund grant (P25237) to T.S., H.M., and P.R.; by NSF (IOS-1256680, IOS-1553529, and EPSCoR award NSF-IIA-1443108) and NASA Astrobiology Institute (NNA15BB04A) grants to J.P.M.; by a NSF Graduate Research Fellowship (DGE-1313190) to D.V.; by a grant from the Swedish University of Agricultural Sciences Council for Ph.D. Education (2014.3.2.5-5149) to V.T.; and by a grant (DO2011-0022) from Stiftelsen Oscar och Lili Lamms minne to G.T. Specimens from Glacier Bay National Park, Alaska, were collected with the support of the U.S. National Park Service as part of CESU (Cooperative Ecosystem Studies Units) project P11AC90513. We thank D. Armaleo and F. Lutzoni of Duke University for allowing us to use unpublished data from the *Cladonia grayi* proteome, as well as P. Dyer, P. Crittenden, and D. Archer (University of Nottingham, UK) for access to unpublished data from the *Xanthoria parietina* genome project, which is conducted together with the U.S. Department of Energy Joint Genome Institute (supported by the Office of Science of the U.S. Department of Energy under contract no. DE-AC02-05CH11231). We thank T. Goward, M. Grube, P. Lukasik, J. T. Van Leuven, F. Fernández-Mendoza, A. Millanes, V. Wagner, and M. Wedin for discussions and L. Bergström, C. Gueidan, J. Hermansson, H. Holien, B. Kanz, E. Lagostina, S. Leavitt, B. McCune, J. Nascimbene, C. Printzen, T. Wheeler, and D. Winston for field support and fresh material. C. Björk, S. Gunnarsson, L. Herritt, M. Hiltunen, W. Obermayer, A. de los Ríos, and E. Timdal provided technical help, advice, and photos. We acknowledge the Purdue University Genomic Core Facility for generating transcriptomic data for

Downloaded from http://science.sciencemag.org/ on July 28, 2016

Cystobasidium minutum and the Institute of Molecular Biosciences–Graz Microscopy Core Facility and S. Kohlwein for providing infrastructural support for imaging. Data are available under accession numbers SRP076577 and SRP073687 in the National Center for Biotechnology Information (NCBI) Sequence Read Archive (transcriptomes), NCBI nucleotide accession numbers KU948728 to KU948928 (single-locus DNA sequences), and the Dryad digital repository at http://dx.doi.org/10.5061/dryad.7qv72 (alignments, scripts, and tree files).

SUPPLEMENTARY MATERIALS

www.sciencemag.org/content/353/6298/488/suppl/DC1
Materials and Methods
Figs. S1 to S16
Tables S1 to S12
References (*31*–*74*)
Movies S1 and S2

6 April 2016; accepted 22 June 2016
Published online 21 July 2016
10.1126/science.aaf8287

INFECTION

Increased plasmid copy number is essential for *Yersinia* T3SS function and virulence

He Wang,[1,2] Kemal Avican,[1,2] Anna Fahlgren,[1] Saskia F. Erttmann,[1,2] Aaron M. Nuss,[3] Petra Dersch,[3] Maria Fallman,[1,2] Tomas Edgren,[1]*† Hans Wolf-Watz[1,2]*†

Pathogenic bacteria have evolved numerous virulence mechanisms that are essential for establishing infections. The enterobacterium *Yersinia* uses a type III secretion system (T3SS) encoded by a 70-kilobase, low-copy, IncFII-class virulence plasmid. We report a novel virulence strategy in *Y. pseudotuberculosis* in which this pathogen up-regulates the plasmid copy number during infection. We found that an increased dose of plasmid-encoded genes is indispensable for virulence and substantially elevates the expression and function of the T3SS. Remarkably, we observed direct, tight coupling between plasmid replication and T3SS function. This regulatory pathway provides a framework for further exploration of the environmental sensing mechanisms of pathogenic bacteria.

Three human pathogenic *Yersinia* strains—*Y. pestis*, *Y. enterocolitica*, and *Y. pseudotuberculosis*—share a common 70-kb virulence plasmid (IncFII) that encodes a set of virulence proteins called Yops (*Yersinia* outer proteins) (*1*, *2*). These bacterial toxins are secreted by a plasmid-encoded organelle, the *ysc/yop* type III secretion system (T3SS) (*3*–*5*). The T3SS comprises ~20 proteins that span the inner and outer bacterial membranes (*6*, *7*). Upon contact with eukaryotic cells, *Yersinia* deploys the T3SS to translocate Yops into the cytoplasm of target cells via a translocon formed in the cell membrane (*8*, *9*). This process is strictly regulated, and Yop expression and secretion increase after the bacterium establishes intimate contact with the eukaryotic target cell (*10*). This cell contact–dependent regulation can be mimicked in vitro at 37°C by depleting Ca^{2+} from the growth medium (*11*).

Incubation of *Yersinia* at 37°C in Ca^{2+}-deficient medium leads to T3SS induction and growth restriction after approximately two generations (*4*). Growth arrest may be due to the metabolic burden caused by excess expression of plasmid-encoded T3SS proteins (*12*). Thus, the function of the T3SS is paradoxical, because conditions that promote Yop secretion result in bacterial growth restriction. This feature is incompatible with infection; consequently, we reasoned that *Yersinia* must have evolved a mechanism to circumvent this problem. We observed that increased amounts of virulence plasmid DNA were recovered from wild-type *Y. pseudotuberculosis* cells grown under T3SS-inductive conditions relative to bacteria grown under T3SS-repressive conditions (fig. S1B). Therefore, we hypothesized that *Yersinia* may undergo rapid changes in gene expression by increasing and decreasing virulence plasmid copy numbers. Rapid changes in gene dose could adjust the T3SS output to trade off virulence costs and the pathogen's metabolic capacity to optimize growth.

To explore a potential connection between virulence and plasmid copy number, we first determined plasmid (pIBX) copy numbers in *Y. pseudotuberculosis* YpIII (YpIII/pIBX) (*13*) cultures under different conditions with a polymerase chain reaction (PCR)–free whole-genome sequencing approach (*14*). The depth of coverage (the number of times a nucleotide is read during the sequencing process) reflects the concentrations of chromosomal DNA and plasmid DNA molecules in the sample. We found that the pIBX copy number increased from ~1 to ~3 per chromosomal equivalent when conditions were repressive (26°C) or inductive (37°C, Ca^{2+}-free), respectively, to T3SS activity (Fig. 1A). At 37°C in the presence of Ca^{2+} (T3SS-repressive conditions), the copy number increased only modestly (1.6 per chromosomal equivalent). Similar differences in plasmid

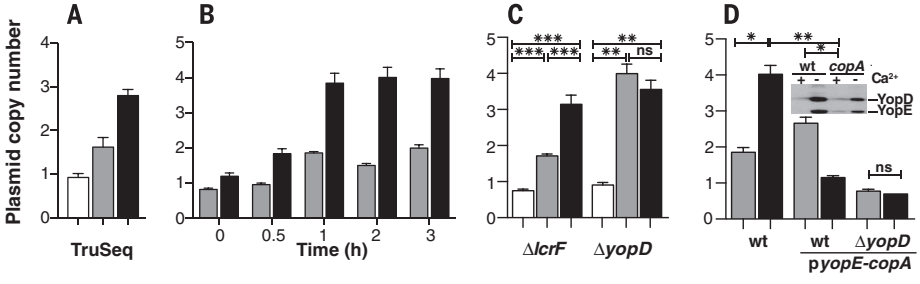


Fig. 1. *Y. pseudotuberculosis* differentially regulates virulence plasmid copy number in vitro. (**A**) Virulence plasmid copy numbers in DNA isolated from *Y. pseudotuberculosis* YpIII/pIBX grown for 3 hours under different conditions [white, 26°C; gray, 37°C under T3SS-repressive conditions (Ca^{2+}); black, 37°C under T3SS-inductive conditions] as determined by whole-genome sequencing (TruSeq). Copy number was calculated as the ratio of average depth of plasmid DNA coverage to chromosomal DNA coverage (N = 2). (**B**) Time course of plasmid copy number increase determined by qPCR. At time zero, *Y. pseudotuberculosis* cultures were shifted from 26° to 37°C under T3SS-repressive (gray) and T3SS-inductive (black) conditions. Plasmid copy number is defined as the number of plasmid equivalents per chromosome (N = 6). (**C**) Plasmid copy number changes in YpIII/pIB73 (Δ*lcrF*) and YpIII/pIB621 (Δ*yopD*) determined by qPCR after 3 hours of growth under the same conditions as in (A) (N = 6). (**D**) qPCR results showing plasmid copy numbers in YpIII/pIBX (wt) and a YpIII/pIB621 (Δ*yopD*) overexpressing the antisense *copA* RNA fused to the *yopE* promoter in cis (p*yopE-copA*) after 3 hours of growth at 37°C under T3SS-repressive (gray) and T3SS-inductive (black) conditions. Copy numbers in YpIII/pIBX (wt) are shown as control (N = 4). Inset: Immunoblot of whole-cell lysates from the indicated strains probed with antibodies to Yops. Data are means ± SEM (*$P \le 0.05$, **$P \le 0.01$, ***$P \le 0.001$, Mann-Whitney U test; ns, not significant).

[1]Umeå Centre for Microbial Research (UCMR), Department of Molecular Biology, Umeå University, SE-901 87 Umeå, Sweden. [2]Laboratory for Molecular Infection Medicine Sweden (MIMS), Department of Molecular Biology, Umeå University, SE-901 87 Umeå, Sweden. [3]Department of Molecular Infection Biology, Helmholtz Centre for Infection Research, Braunschweig, Germany.
***Corresponding author. Email: tomas.edgren@umu.se (T.E.); hans.wolf-watz@umu.se (H.W.-W.)** †These authors contributed equally to this work.

Downloaded from http://science.sciencemag.org/ on July 28, 2016

copy numbers were found with quantitative real-time PCR (qPCR) (fig. S1A) and Southern blot analysis (fig. S1B).

We used qPCR to determine the time course of pIBX copy number variations. We found that the copy number increased and plateaued 1 hour after the temperature shift to T3SS-inductive conditions (Fig. 1B). Bacteria grown at 37°C under T3SS-repressive conditions plateaued at ~2 chromosome equivalents (Fig. 1B). These results confirmed that the plasmid copy number increased in *Y. pseudotuberculosis* under T3SS-inductive conditions.

To analyze the control of plasmid copy number in *Yersinia*, we investigated copy number changes in T3SS regulatory mutants. Earlier studies have shown that both Ca^{2+} and temperature regulate the T3SS in *Yersinia* (*15*, *16*). The T3SS transcriptional activator LcrF activates transcription of the T3SS regulon in response to elevated temperature (37°C) and low Ca^{2+}; *lcrF* mutants lack Yop expression and growth is not restricted in Ca^{2+}-depleted medium at 37°C (*16*). In contrast, *yopD* mutants display Ca^{2+}-insensitive Yop expression and restricted growth at 37°C, irrespective of Ca^{2+} concentration (*17*). Thus, YopD is involved in a negative-feedback regulatory pathway controlling T3SS expression (*18*). We found that plasmid copy number control was not affected in a Δ*lcrF* mutant (YpIII/pIB73) (Fig. 1C). In contrast, in a Δ*yopD* mutant (YpIII/pIB621), the plasmid copy number was elevated at 37°C under T3SS-repressive conditions (gray bars, Fig. 1C). Thus, YopD directly or indirectly inhibits a default temperature-regulated plasmid copy number increase in *Yersinia*.

The plasmid replication initiation protein RepA initiates IncFII plasmid replication. The level of RepA is controlled at the translational level by the antisense RNA CopA (*19*). To investigate whether the IncFII replicon per se is responsible for increased virulence plasmid copy number, we expressed *Yersinia copA* (*20*) under control of the *yopE* promoter. This should increase CopA levels and consequently reduce the rate of initiation of virulence plasmid replication under T3SS-inductive conditions. This construct was integrated in cis into the virulence plasmids of wild-type *Yersinia* and a Δ*yopD* mutant. CopA overexpression resulted in reduced plasmid copy numbers under T3SS-inductive conditions in both strains (Fig. 1D). This shows that the IncFII replicon, per se, is essential for the T3SS-regulated copy number increase. Furthermore, the reduced plasmid copy number in the CopA-overexpressing strains suppressed T3SS-related growth defects and reduced Yop expression under T3SS-inductive conditions (Fig. 1D, inset, and fig. S2). This indicates that *Yersinia* has evolved a T3SS-dependent mechanism to down-regulate the copy number of its virulence plasmid, and that this mechanism is likely to counteract the metabolic burden associated with induction of the T3SS.

To investigate whether increased plasmid copy number is involved in virulence, we designed a mutant strain that could not change virulence plasmid copy number during infection. This was achieved by inserting pIBX, without the replication function ($IncFII^-$), into the chromosome of *Y. pseudotuberculosis* (Fig. 2A). The final mutant, YpIII:$(cIBX)_{n=1}$, contained one copy of the replication-deficient pIBX inserted into the chromosomal gene *YPK_3687* (Fig. 2A). *YPK_3687* was previously shown to be redundant for *Y. pseudotuberculosis* virulence (*21*). Insertion of a single copy of the replication-deficient pIBX plasmid, $(cIBX)_{n=1}$, into *YPK_3687* was verified by DNA sequencing and qPCR (Fig. 2B and fig. S3). As expected, the mutant strain was unable to change the gene dose of plasmid-encoded genes in response to T3SS activity (fig. S3). Secretion analysis showed that YpIII:$(cIBX)_{n=1}$ retained temperature- and Ca^{2+}-dependent regulation of Yop expression and secretion, but Yop levels were severely reduced by comparison with the wild type (Fig. 2C). Yop translocation experiments showed that YpIII:$(cIBX)_{n=1}$ could translocate the reporter protein $YopH_{1\text{-}99}$-Bla (*22*) into HeLa cells in a dose-dependent manner, but less than the parental YPIII/pIBX wild-type strain (Fig. 3A). The YpIII:$(cIBX)_{n=1}$ mutant was severely attenuated in an oral BALB/c mouse infection model. YpIII:$(cIBX)_{n=1}$ initially colonized Peyer's patches (PP), cecum, and mesenteric lymph nodes (MLNs; Fig. 3B and fig. S4) but all infected mice survived and recovered their initial body weight (Fig. 3B, inset), showing that the YpIII:$(cIBX)_{n=1}$ strain is avirulent.

To confirm whether the reduced virulence of YpIII:$(cIBX)_{n=1}$ was a result of a reduced gene dose of virulence plasmid–encoded genes, we amplified the integrated virulence plasmid in the mutant. This was achieved by selecting for a gene dose–dependent increase in chloramphenicol resistance conferred by the *cat* gene

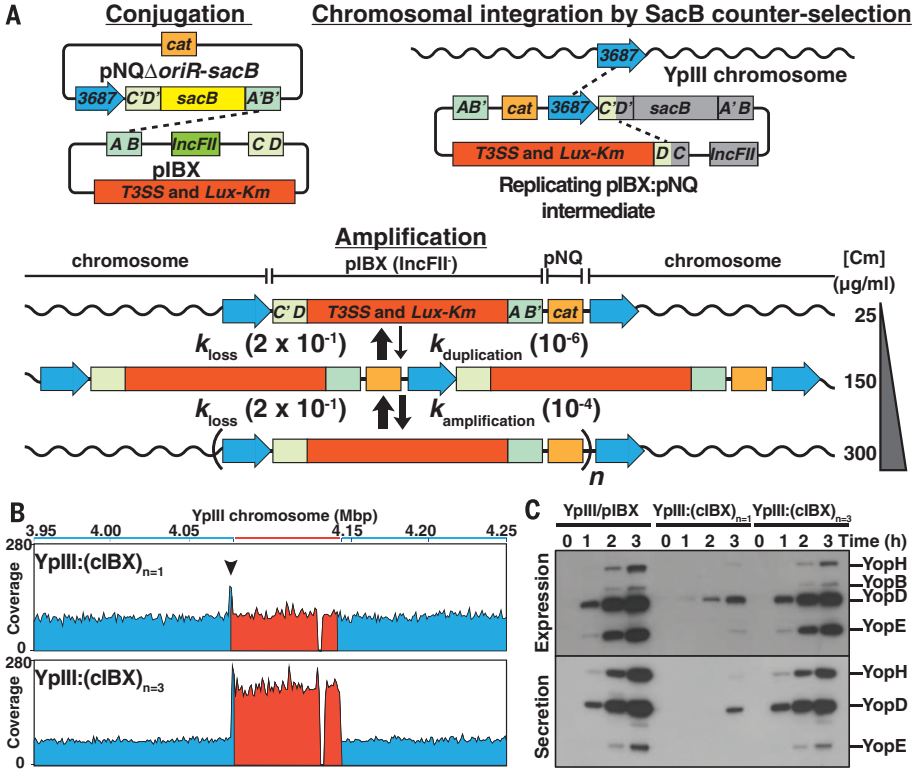


Fig. 2. Integration of the pIBX ($IncFII^-$) amplicon into the chromosome. (**A**) Homologous recombination of pNQΔ*oriR1-sacB* (Cm^r) into pIBX (Km^r) results in a replicating pIBX:pNQΔ*oriR1-sacB* intermediate (Cm^r, Km^r, $sacB^+$). SacB counterselection in the presence of Km and Cm, selects for $sacB^-$ clones where the pIBX:pNQ plasmid (Cm^r, Km^r) has been integrated into the chromosome. The final Cm^r, Km^r, $sacB^-$ strain results from the deletion of 3426 bp encoding the native pIBX IncFII replicon and *sacB* (gray). Dashed lines indicate homologous recombination events. The integrated construct, flanked by duplicated *YPK_3687* sequences (blue arrows), can be amplified by selecting for gene dose–dependent increase in Cm^r conferred by the *cat* gene (orange box). Black arrows and corresponding numbers denote the experimentally derived frequencies of indicated genetic events. (**B**) Number of reads of pIBX and chromosome sequences determined by whole-genome DNA sequencing. Red, pIBX sequences; blue, chromosomal sequences. Gap in the plasmid sequence alignments shows the 3426-bp deletion of the IncFII replicon. Arrowhead indicates increased *YPK_3687* coverage after gene duplication/multimerization. The figure is a composite where the pIBX reads have been inserted into the correct location in the chromosome. (**C**) Western blot analysis of Yop expression and secretion by T3SS-induced *Y. pseudotuberculosis* cultures (without Ca^{2+}). Whole-cell samples (upper panel) and proteins secreted into the culture medium (lower panel) were collected at the indicated times after a shift from 26°C to 37°C.

Downloaded from http://science.sciencemag.org/ on July 28, 2016

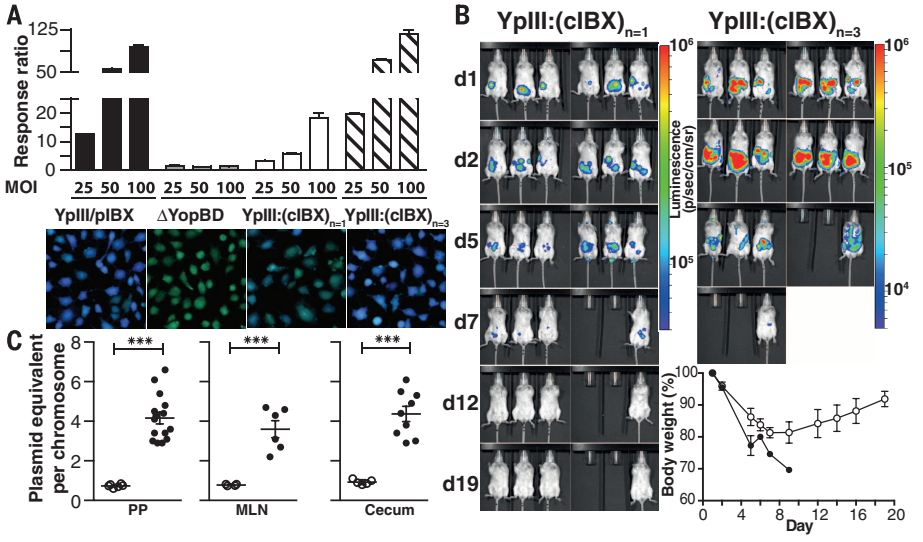


Fig. 3. Increased gene dose of plasmid-encoded genes is essential for *Yersinia* virulence. (**A**) Translocation of $YopH_{1-99}$-Bla into HeLa cells after 90 min. Histograms represent mean ± SEM of a representative experiment. Translocation-deficient Δ*yopBD* mutant (YpIII/pIB219) expressing $YopH_{1-99}$-Bla is included as a negative control. Response ratio: blue/green ratio divided by background ratio. Lower panel shows representative micrographs of cells infected at a multiplicity of infection (MOI) of 50. (**B**) In vivo images showing anesthetized mice infected with YpIII:$(cIBX)_{n=1}$ (left) or YpIII:$(cIBX)_{n=3}$ (right). Colors indicate levels of light emitted by bioluminescent bacteria. Inset: Changes in average body weight of infected mice over time [open symbols, YpIII:$(cIBX)_{n=1}$; solid symbols, YpIII:$(cIBX)_{n=3}$]. (**C**) Virulence plasmid gene dose measured in bacterial colonies isolated from Peyer's patches (PP), mesenteric lymph node (MLN), and cecum from infected mice 2 days after infection. Each point represents the virulence plasmid copy number per chromosome of a single colony determined by qPCR [open symbols, YpIII:$(cIBX)_{n=1}$; solid symbols, YpIII:$(cIBX)_{n=3}$]. Data are means ± SEM (***$P \le 0.001$, Mann-Whitney *U* test).

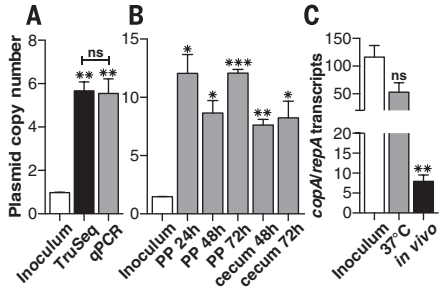


Fig. 4. *Yersinia* virulence plasmid copy number increases during infection in mice. (**A**) Virulence plasmid copy number of wild-type YpIII/pIBX in total DNA extracted from infected Peyer's patches (PP) 48 hours after infection, determined by whole-genome sequencing (TruSeq) (table S1) and by qPCR. Plasmid copy number of infecting inoculum determined by qPCR is shown as control ($N = 4$). (**B**) Plasmid copy numbers of wild-type YpIII/pIBX in lysates from homogenates from indicated organs determined by qPCR. Plasmid copy number of infecting inoculum is shown as control ($N \ge 3$). (**C**) The ratio of *copA*:*repA* RNA decreases in *Yersinia* during infection. The *copA*:*repA* ratio was calculated as reads per kilobase of transcript per million mapped reads (RPKM) of *copA* and *repA* (table S2) from bacteria grown at 25°C (inoculum), 37°C, and infected PP (in vivo) ($N = 3$). Data are means ± SEM; *$P \le 0.05$, **$P \le 0.01$, ***$P \le 0.001$ (difference between control and the respective conditions; unpaired *t* test).

encoded by the integrated construct (Fig. 2A) (*23*, *24*). Amplification of the *cat* gene was possible through homologous recombination of the duplicated [831 base pairs (bp)] *YPK_3687* sequences flanking the integrated IncFII$^-$ pIBX plasmid (Fig. 2A). When YpIII:$(cIBX)_{n=1}$ was plated on to agar plates with different chloramphenicol concentrations, we recovered clones resistant to chloramphenicol (150 μg/ml) at a frequency of 1×10^{-6} and found duplication of the integrated virulence plasmid. After initial duplication, further amplification was achieved after selection on plates with chloramphenicol (300 μg/ml) at a frequency of 1×10^{-4}. As expected, in the absence of selective pressure (*23*), the amplified virulence plasmid-containing clones were unstable and reverted to the original single-copy genotype at a frequency of 2×10^{-1}. These revertants showed the same phenotype as the original YpIII:$(cIBX)_{n=1}$ variant.

A clone with three copies of the plasmid [YpIII:$(cIBX)_{n=3}$] was selected for further analysis of T3SS function and virulence. We verified the high- and low-copy genotypes of YpIII:$(cIBX)_{n=1}$ and YpIII:$(cIBX)_{n=3}$, respectively, by whole-genome sequencing and qPCR (Fig. 2B and fig. S3). YpIII:$(cIBX)_{n=3}$ showed Yop expression, secretion, and translocation profiles similar to those of the wild-type strain (Fig. 2C and Fig. 3A). Whereas the YpIII:$(cIBX)_{n=1}$ strain showed a growth rate similar to that of the plasmid-cured YpIII (T3SS$^-$) strain, the YpIII:$(cIBX)_{n=3}$ strain showed reduced growth at 37°C under T3SS-inductive conditions similar to that of the wild-type strain (fig. S5). YpIII:$(cIBX)_{n=3}$ was virulent in an oral BALB/c mouse infection model (Fig. 3B).

All infected mice developed a systemic infection and were consequently killed. Bacterial loads 2 days after infection were higher in homogenized PPs from animals infected with virulent YpIII:$(cIBX)_{n=3}$ than in those infected with avirulent YpIII:$(cIBX)_{n=1}$ by two orders of magnitude (fig. S4). The high- and low-copy genotypes of bacterial strains were retained after passage through the mouse. YpIII:$(cIBX)_{n=3}$ colonies recovered from PPs, MLNs, and cecum 2 days after infection showed variable numbers of virulence plasmid equivalents (Fig. 3C). Remarkably, several isolated colonies possessed greater plasmid equivalents than the original three, indicating that the integrated plasmid was under selective pressure for further amplification. Collectively, the observed gene dose–dependent virulence of YpIII:$(cIBX)_{n=1}$ and YpIII:$(cIBX)_{n=3}$ indicates that plasmid copy number amplification is essential for *Yersinia* virulence.

To determine whether the plasmid copy number increases during infection, we isolated total DNA from PPs of mice after infection with wild-type YpIII/pIBX. The copy number of pIBX was determined by whole-genome DNA sequencing and qPCR in the complex DNA sample. Both independent methods showed a factor of 6 increase in virulence plasmid copy number in the PPs relative to the infecting inoculum (Fig. 4A). Increased virulence plasmid copy number during infection was verified by qPCR of lysates prepared from animal tissues recovered at different times after oral infections with wild-type YPIII/pIBX (Fig. 4B). We observed substantial increases in virulence plasmid copy numbers in all infected samples analyzed.

Reduced amounts of *copA* antisense RNA relative to *repA* mRNA have been shown to lead to elevated RepA levels and thus to an increase in plasmid replication initiation (*19*). Analysis of *copA* and *repA* transcript levels in *Yersinia* during infection showed that the ratio of *copA* RNA to *repA* RNA decreased significantly during PP colonization relative to bacteria grown in vitro (Fig. 4C), corroborating the findings presented above. Our results show that T3SS-related copy number regulation affects the stability or transcription of both RNA species (table S2 and fig. S6). Taking into account the actual gene dose of plasmid-encoded genes under the different conditions, we found that the major change was a marked decrease in *copA* levels while the *repA* mRNA levels per plasmid copy remained basically unchanged (table S2 and fig. S6). Such a finding favors a model in which T3SS-related copy number regulation operates via a change in *copA* antisense RNA levels.

Our results show that an increased dose of plasmid-encoded genes is essential for *Yersinia* virulence. One copy of the virulence plasmid that encodes the T3SS regulon is insufficient to establish

Downloaded from http://science.sciencemag.org/ on July 28, 2016

a systemic infection in mice; thus, *Yersinia* has evolved a mechanism to rapidly increase the copy number during an infection. Our results also show that, despite the increased metabolic burden caused by three T3SS regulon copies, there was selective pressure during infection to increase the T3SS gene dose. Moreover, the secreted protein, YopD, is involved in regulation of the copy number. This feature indicates that the system is tightly controlled, linking external sensors to T3SS activity and the plasmid copy number.

In *Yersinia*, high T3SS activity is deleterious for growth in vitro. Yet T3SS expression is essential for successful infection and proliferation in hosts. We found an inverse correlation between virulence plasmid gene dose and growth rate under T3SS-inductive conditions. Therefore, we propose that *Yersinia* maintains the entire T3SS virulence system in a plasmid, which enables rapid adjustments in T3SS expression in response to prevailing environmental conditions. This basic regulatory tactic is likely to apply to any plasmid-encoded genes by analogous mechanisms. Our findings provide a framework for further functional investigations of the regulatory pathways that allow pathogens to respond to environmental cues, and plasmid copy number regulation may be important in bacterial antibiotic resistance.

REFERENCES AND NOTES

1. D. A. Portnoy, H. Wolf-Watz, I. Bolin, A. B. Beeder, S. Falkow, *Infect. Immun.* **43**, 108–114 (1984).
2. I. Bölin, D. A. Portnoy, H. Wolf-Watz, *Infect. Immun.* **48**, 234–240 (1985).
3. T. Michiels, P. Wattiau, R. Brasseur, J. M. Ruysschaert, G. Cornelis, *Infect. Immun.* **58**, 2840–2849 (1990).
4. S. C. Straley, G. V. Plano, E. Skrzypek, P. L. Haddix, K. A. Fields, *Mol. Microbiol.* **8**, 1005–1010 (1993).
5. T. Bergman, K. Erickson, E. Galyov, C. Persson, H. Wolf-Watz, *J. Bacteriol.* **176**, 2619–2626 (1994).
6. T. Kubori *et al.*, *Science* **280**, 602–605 (1998).
7. J. E. Galán, H. Wolf-Watz, *Nature* **444**, 567–573 (2006).
8. R. Rosqvist, K. E. Magnusson, H. Wolf-Watz, *EMBO J.* **13**, 964–972 (1994).
9. S. Håkansson *et al.*, *EMBO J.* **15**, 5812–5823 (1996).
10. J. Pettersson *et al.*, *Science* **273**, 1231–1233 (1996).
11. G. R. Cornelis, H. Wolf-Watz, *Mol. Microbiol.* **23**, 861–867 (1997).
12. R. R. Brubaker, *Rev. Infect. Dis.* **5** (suppl. 4), S748–S758 (1983).
13. A. Fahlgren, K. Avican, L. Westermark, R. Nordfelth, M. Fällman, *Infect. Immun.* **82**, 3471–3482 (2014).
14. See supplementary materials on *Science* Online.
15. A. Forsberg, H. Wolf-Watz, *Mol. Microbiol.* **2**, 121–133 (1988).
16. G. R. Cornelis *et al.*, *Mol. Microbiol.* **3**, 1455–1459 (1989).
17. M. S. Francis, H. Wolf-Watz, *Mol. Microbiol.* **29**, 799–813 (1998).
18. A. W. Williams, S. C. Straley, *J. Bacteriol.* **180**, 350–358 (1998).
19. K. Nordström, *Plasmid* **55**, 1–26 (2006).
20. A. M. Nuss *et al.*, *PLOS Genet.* **11**, e1005087 (2015).
21. A. A. Amer *et al.*, *PLOS ONE* **8**, e77767 (2013).
22. K. Akopyan *et al.*, *Proc. Natl. Acad. Sci. U.S.A.* **108**, 1639–1644 (2011).
23. L. Sandegren, D. I. Andersson, *Nat. Rev. Microbiol.* **7**, 578–588 (2009).
24. J. Meyer, S. Iida, *Mol. Gen. Genet.* **176**, 209–219 (1979).

ACKNOWLEDGMENTS

Sequence data used in this study have been deposited in the European Nucleotide Archive with accession number PRJEB13406. Supported by Stiftelsen JC Kempes Minnes Stipendiefond (H.W.-W.), EMBO grant ALTF 1629-2011 (H.W.), the Swedish Research Council (grant 2015-02874, H.W.-W.; grant 2011-4937, T.E.; grant K2014-56X-11222-20-5, M.F.), Carl Tryggers Stiftelse för Naturvetenskaplig Forskning (T.E.), and the German Center for Infection Research (P.D.). This work traces back to Kurt Nordström (mentor to H.W.-W.), to whom this paper is dedicated.

SUPPLEMENTARY MATERIALS

www.sciencemag.org/content/353/6298/492/suppl/DC1
Materials and Methods
Figs. S1 to S7
Tables S1 to S4
References (*25*–*35*)

24 March 2016; accepted 22 June 2016
Published online 30 June 2016
10.1126/science.aaf7501

EPIGENETICS

Early-life nutrition modulates the epigenetic state of specific rDNA genetic variants in mice

Michelle L. Holland,[1]*† Robert Lowe,[1]* Paul W. Caton,[2] Carolina Gemma,[1]‡ Guillermo Carbajosa,[1]§ Amy F. Danson,[1] Asha A. M. Carpenter,[3] Elena Loche,[3] Susan E. Ozanne,[3] Vardhman K. Rakyan[1]†

A suboptimal early-life environment, due to poor nutrition or stress during pregnancy, can influence lifelong phenotypes in the progeny. Epigenetic factors are thought to be key mediators of these effects. We show that protein restriction in mice from conception until weaning induces a linear correlation between growth restriction and DNA methylation at ribosomal DNA (rDNA). This epigenetic response remains into adulthood and is restricted to rDNA copies associated with a specific genetic variant within the promoter. Related effects are also found in models of maternal high-fat or obesogenic diets. Our work identifies environmentally induced epigenetic dynamics that are dependent on underlying genetic variation and establishes rDNA as a genomic target of nutritional insults.

Exposure to an adverse in utero environment can have a long-lasting influence on adult phenotypes in mammals, a process termed "developmental programming" (*1*, *2*). Consequently, there is great interest in identifying the molecular mechanisms that underlie developmental programming, and, in this regard, modulation of the epigenome has emerged as a potentially key contributing factor (*3*, *4*).

To explore epigenetic mechanisms involved in developmental programming, we employed a maternal protein restriction model (*5*). Inbred C57BL/6J mice were mated, and G0 females were assigned to either a protein-restricted diet (PR) (8% protein) or a control diet (C) (20% protein) (table S1) until their G1 offspring were weaned. Only male G1s were studied in detail (n = 146). From weaning onward, both G1-PR and G1-C mice were kept on a control diet until they were killed at 16 to 20 weeks. Consistent with previous work, G1-PR males were ~25% lighter than G1-C at weaning (*5*) (Fig. 1A) ($P = 2 \times 10^{-6}$). PRs also displayed reduced spontaneous locomotor activity (fig. S1) and reduced glucose-stimulated insulin secretion (fig. S2).

Several studies have shown that developmental programming can perturb DNA methylation profiles (*1*). We used reduced representation bisulfite sequencing (RRBS) to generate genome-scale, single-base resolution DNA methylomes for eight G1-PR and eight G1-C mice, initially focusing on sperm, because it can be isolated to a high degree of purity. After genome-wide correction, we identified a single 1916–base pair (bp) differentially methylated region (DMR) hypermethylated in G1-PR males that mapped to *Rn45s* on chromosome 17 (mm10) (table S2). Further analysis revealed that *Rn45s* displays 98% homology to the 973- to 2883-bp region of the ribosomal DNA (rDNA) consensus (Fig. 1B). rDNA is excluded from genome assemblies because of its multicopy nature. We therefore remapped the RRBS data to the consensus sequence for mouse rDNA (BK000964) and confirmed extensive hypermethylation in PR sperm across the entire promoter and coding regions (~13.5 kb) (Fig. 1B). Directly correlating weaning weight with rDNA methylation levels revealed that G1-PR displayed a significantly greater negative correlation between weaning weight and

[1]The Blizard Institute, Barts, and The London School of Medicine and Dentistry, Queen Mary University of London, London E1 2AT, UK. [2]Division of Diabetes and Nutritional Sciences, King's College London, 150 Stamford Street, London SE1 9NH, UK. [3]University of Cambridge Metabolic Research Laboratories and MRC Metabolic Diseases Unit, Institute of Metabolic Science, Addenbrookes Hospital, Cambridge, CB2 0QQ, UK.
*These authors contributed equally to this work. **†Corresponding author. Email: m.holland@qmul.ac.uk (M.L.H.); v.rakyan@qmul.ac.uk (V.K.R.)** ‡Present address: Department of Surgery and Cancer, Imperial College London, Hammersmith Hospital Campus, London, UK. §Present address: Institute of Psychiatry, Psychology and Neuroscience, King's College London, UK.

Downloaded from http://science.sciencemag.org/ on July 28, 2016

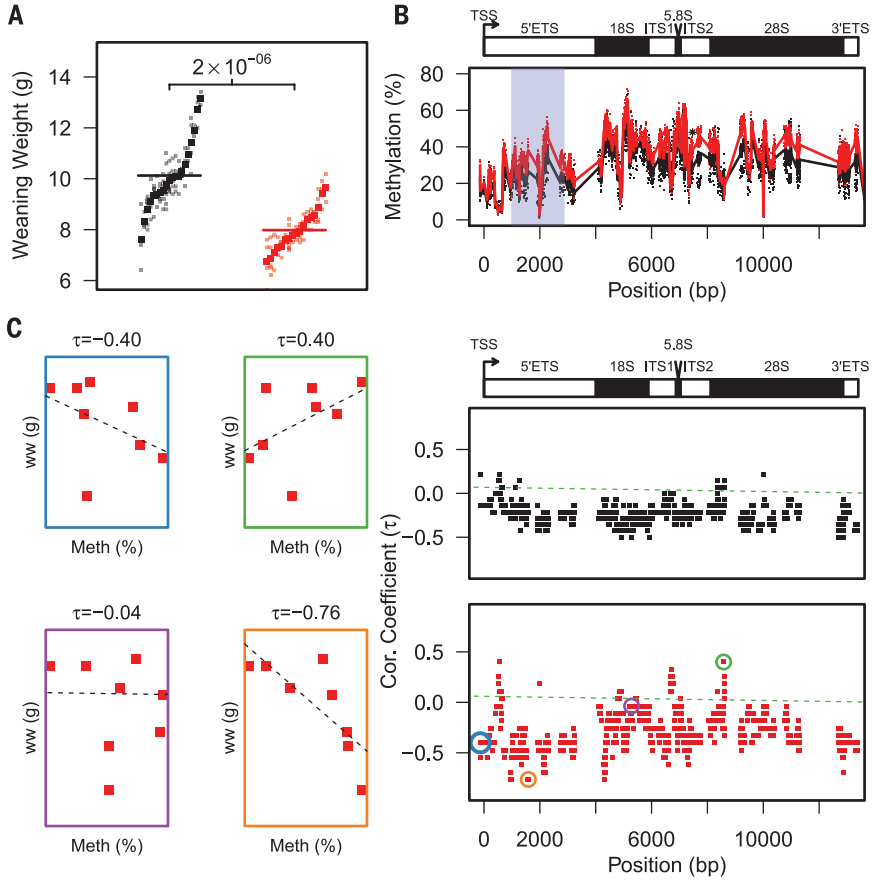


Fig. 1. Maternal PR induces a correlation between rDNA methylation and weaning weight. (**A**) Weaning weight of G1-PR males (red; 62 individual mice from 17 different litters) was reduced compared with G1-C (black; 84 individual males from 20 different litters) (*t* test, $P = 2 \times 10^{-6}$ using litter means, and $P < 2.2 \times 10^{-6}$ using individual mice). Small points represent individual mice; larger squares represent the mean of a given G1 litter. (**B**) RRBS analysis of rDNA in G1 sperm shows that PRs ($n = 8$) are hypermethylated compared to controls ($n = 8$). The line represents mean methylation, and points represent individual mice. The rDNA schematic shows the rRNA subunits, transcriptional start site (TSS), external transcribed spacer (ETS), and internal transcribed spacer (ITS). The *Rn45S* regions identified in the initial RRBS analysis is 98% homologous to the region shaded blue. (**C**) The correlation coefficient (τ) between weaning weight (ww) and DNA methylation across the rDNA. Highlighted are examples of a positive correlation (green), close to zero (purple), and negative (orange). CpG-133 is circled in blue.

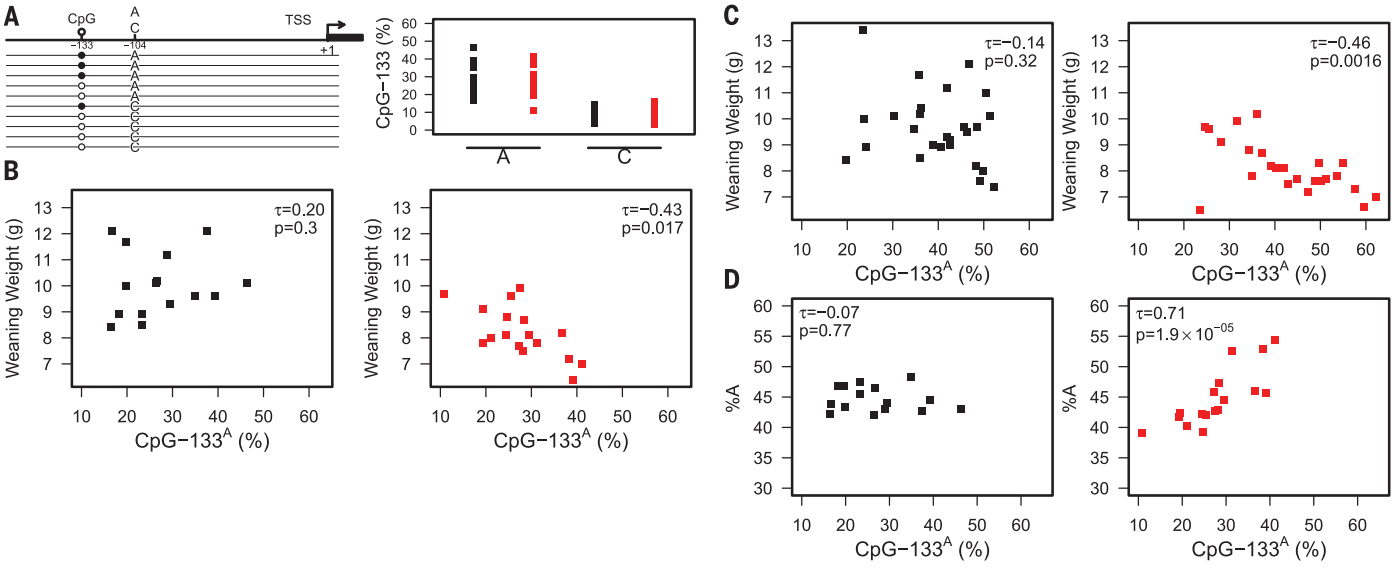


Fig. 2. Diet-induced methylation dynamics are restricted to a specific genetic variant of rDNA. (**A**) BisPCR-seq amplicons were generated to simultaneously analyze methylation at CpG-133 (methylation indicated by black circle) and genetic variation at position −104 (A or C) (left panel). CpG-133 methylation levels in sperm for each genetic variant is shown for G1-C (black; $n = 15$), and G1-PR (red; $n = 17$). (**B**) In sperm, methylation levels at A-variant–associated CpG-133 sites (CpG-133^A) and weaning weight are not correlated in G1-C (black; $n = 15$, $\tau = 0.20$, $P = 0.30$) but are negatively correlated in G1-PR (red; $n = 17$, $\tau = -0.43$, $P = 0.017$). (**C**) In liver, CpG-133^A methylation levels and weaning weight are not correlated in G1-C (black; $n = 26$, $\tau = -0.14$, $P = 0.32$) but are negatively correlated in G1-PR (red; $n = 24$, $\tau = -0.46$, $P = 0.0016$). (**D**) In sperm, CpG-133^A methylation levels are uncorrelated with the percentage of total rDNA copies with an A-variant (%A) in G1-C (black; $n = 15$, $\tau = -0.07$, $P = 0.77$) but are positively correlated in G1-PR (red; $n = 17$, $\tau = 0.71$, $P = 1.9 \times 10^{-5}$).

Downloaded from http://science.sciencemag.org/ on July 28, 2016

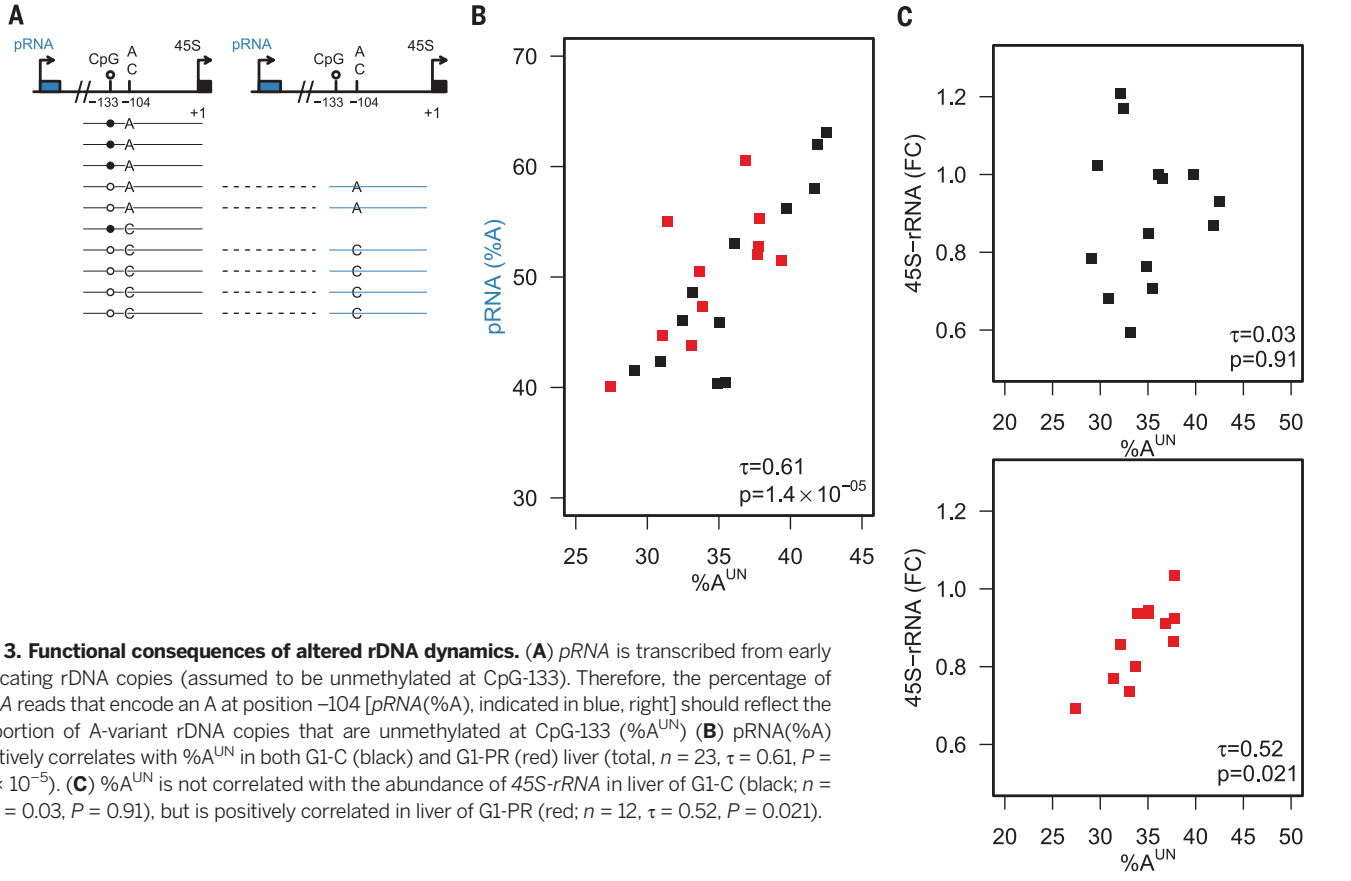


Fig. 3. Functional consequences of altered rDNA dynamics. (**A**) *pRNA* is transcribed from early replicating rDNA copies (assumed to be unmethylated at CpG-133). Therefore, the percentage of *pRNA* reads that encode an A at position –104 [*pRNA*(%A), indicated in blue, right] should reflect the proportion of A-variant rDNA copies that are unmethylated at CpG-133 (%A^{UN}) (**B**) pRNA(%A) positively correlates with %A^{UN} in both G1-C (black) and G1-PR (red) liver (total, $n = 23$, $\tau = 0.61$, $P = 1.4 \times 10^{-5}$). (**C**) %A^{UN} is not correlated with the abundance of *45S-rRNA* in liver of G1-C (black; $n = 14$, $\tau = 0.03$, $P = 0.91$), but is positively correlated in liver of G1-PR (red; $n = 12$, $\tau = 0.52$, $P = 0.021$).

DNA methylation compared with G1-C (Wilcoxon rank sum test; $P < 2.2 \times 10^{-16}$) (Fig. 1C). This correlation was not confounded by weight or age at death (fig. S3).

In the C57BL/6J genome, rDNA is composed of hundreds of copies in large arrays on chromosomes 12, 15, 18, and 19, but only a subset are actively transcribed (*6*). Silenced copies are methylated at a CpG site located 133-bp upstream of the *45S-rRNA* transcriptional start site (Fig. 1C), and this prevents binding of the transcription factor UBF (upstream binding factor) and assembly of RNA polymerase I (*7*). We therefore focused on CpG-133 in the rest of the study using high-throughput sequencing (>1000X coverage) of bisulfite polymerase chain reaction (PCR) amplicons (bisPCR-seq). BisPCR-seq analysis of the same samples profiled by RRBS revealed strong concordance between the two methods (fig. S4) ($\tau = 0.77$, $P = 1 \times 10^{-5}$).

As rDNA copies within a single genome are genetically polymorphic (*8*), we designed the bisPCR-seq amplicon targeting CpG-133 to simultaneously assay previously documented genetic variation at position –104 (C or A, Fig. 2A). (Note that this variant does not overlap a CpG site) (*9*). CpG-133 methylation levels were substantially lower for the C-variant relative to the A-variant (Fig. 2A), and there was no interaction between C-variant–associated CpG-133 methylation and weaning weight in G1-PR or G1-C sperm (fig. S5). On the other hand, CpG-133 methylation levels of A-variant rDNA (which we denote as CpG-133^{A}) were negatively correlated with weaning weight (Fig. 2B) ($\tau = -0.43$, $P = 0.017$). Figure 2B incorporates additional males (nine G1-PR and seven G1-C from litters not represented in the RRBS data), reinforcing the negative correlation between weaning weight and total CpG-133 methylation observed in the RRBS data set. BisPCR-seq analysis of in vitro methylated samples confirmed that there was no amplification bias associated with either variant (fig. S6). We also confirmed sperm purity by analysis of several parentally imprinted regions (fig. S7). Analysis of liver using BisPCR-seq revealed a strong correlation with sperm within individual G1-C (fig. S8) ($\tau = 0.72$, $P = 0.00028$) or G1-PR animals (fig. S8) ($\tau = 0.54$, $P = 0.0041$). Liver CpG-133^{A} methylation was negatively correlated with weaning weight in G1-PR ($\tau = -0.46$, $n = 24$, $P = 0.0016$) but not in G1-C ($n = 26$) (Fig. 2C). Collectively, these data demonstrate that PR exposure induces not just rDNA hypermethylation but also a linear relationship between a phenotypic outcome (weaning weight) and CpG-133^{A} methylation in sperm and liver, which is maintained into adulthood.

Further exploration of the bisPCR-seq data revealed interindividual variation in the relative copy number of rDNA harboring the A-variant at position –104, even in an inbred genetic background. This underlying copy number variation (which we denote as %A, i.e., the percentage of A-variant reads relative to total coverage for this amplicon) was positively correlated between sperm and liver of both G1-C (fig. S9) ($\tau = 0.77$, $P = 7 \times 10^{-5}$) and G1-PR animals (fig. S9) ($\tau = 0.73$, $P = 3.7 \times 10^{-5}$). The accuracy of the bisPCR-seq–derived estimates of %A were confirmed by whole-genome resequencing of six mice (fig. S10) ($\tau = 1$, $P = 0.0028$). Furthermore, CpG-133^{A} methylation correlated positively with %A in G1-PR sperm (Fig. 2D) ($\tau = 0.71$, $P = 1.9 \times 10^{-5}$) and liver (fig. S11) ($\tau = 0.31$, $P = 0.034$) but not in G1-C sperm (Fig. 2D) or liver (fig. S11). Therefore, early-life PR induces an interdependence between underlying variation in the relative abundance of a specific genetic variant of rDNA and methylation state of this variant at a functionally relevant CpG site.

rDNA copies that lack methylation at CpG-133 have the potential to be transcriptionally active (*7*). As most methylation is localized to A-variant rDNA, both the level of methylation at CpG-133^{A} and the relative abundance of this variant (i.e., %A) will contribute toward transcriptional competency. This interaction can be represented as the percentage of total rDNA copies that are both A-variant and unmethylated at CpG-133 (which we denote as %A^{UN}). (Note that %A^{UN} is different from simply considering the percentage of CpG-133^{A} that is unmethylated.) As expected, %A^{UN} correlates between the sperm and liver of G1-C and G1-PR mice (fig. S12). To confirm the functional importance of %A^{UN}, we analyzed a regulatory noncoding RNA [promoter-associated RNA (*pRNA*)] that spans the rDNA promoter (Fig. 3A). *pRNA* is transcribed from early replicating and unmethylated rDNA copies (*10*). It functions in trans to recruit nucleolar chromatin remodeling complex and DNA methyltransferase to silenced rDNA copies

Downloaded from http://science.sciencemag.org/ on July 28, 2016

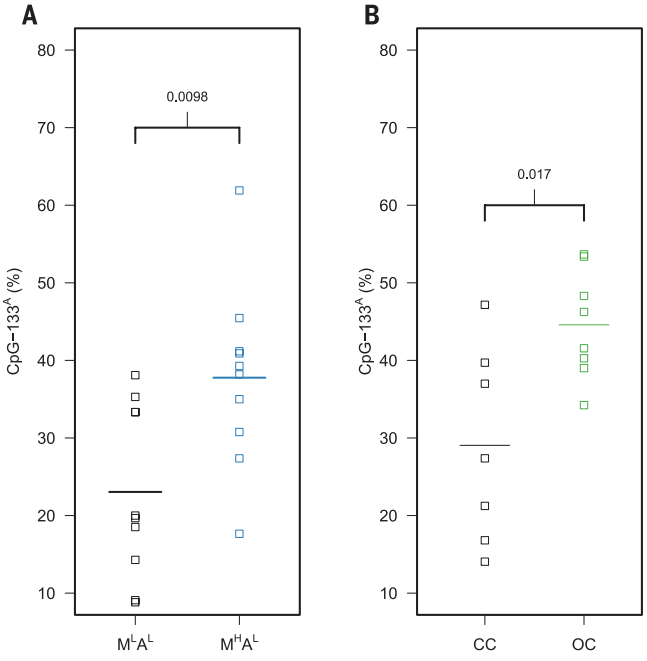


Fig. 4. Maternal high-fat or obesogenic diet induces hypermethylation at CpG-133^{A}. (**A**) RRBS raw sequencing reads [obtained from (*14*)] were mapped to the rDNA consensus. G0 dams that were fed either a low- (M^{L}) or high-fat (M^{H}) diet before conception and up until the G1s were weaned. Data shown here are from the livers of 9-week-old G1 males that were placed on a low-fat diet from weaning up until they were killed. n = 10 mice per group. We only reanalyzed data from (*14*) for the dietary groups analogous to the design of our PR model (**B**) G0 dams were fed either a control (C) or obesogenic (O) diet 6 weeks before conception and up until the G1s were weaned. bsPCR-seq data shown here are from the livers of 6-month-old G1 males that were placed on a control diet from weaning until they were killed (CC, n = 7; OC, n = 8).

(*11*). Using reverse transcription quantitative PCR (RT-qPCR), we generated a *pRNA*-derived amplicon spanning the genetic polymorphism at position –104 and determined the percentage of A-variant reads after high-throughput sequencing [pRNA(%A)]. The pRNA(%A) reads in liver were consistently and positively correlated with %A^{UN} (Fig. 3B) but not %A (fig. S13). Therefore, %A^{UN} is indicative of transcriptional competency at rDNA.

The *45S-rRNA* is cotranscriptionally cleaved at position +650 within the 5′ external transcribed spacer, and the first 650 nucleotides (nt) are then rapidly degraded (*12*). We assessed the abundance of the nascent, uncleaved *45S-rRNA* precursor via RT-qPCR targeting the first 650 nt. In the liver of G1-C, *45S-rRNA* abundance did not correlate with CpG-133^{A} methylation, %A, or %A^{UN} (Fig. 3C and fig. S14). In PR males, *45S-rRNA* levels did not correlate with CpG-133^{A} methylation or %A but correlated positively with %A^{UN} (Fig. 3C) (τ = 0.52, P = 0.021) (fig. S14). Therefore, PR exposure induces a correlation between transcriptional competency and *45S-rRNA* levels.

Because rDNA expression is sensitive to nutrient availability (*13*), the types of effects we describe could be a conserved feature of other nutritional developmental programming models. We identified a recent study in which the authors fed C57BL/6J G0 females a low-fat (LF) or high-fat (HF) diet from 3 weeks before pregnancy until the male G1 offspring were weaned at 3 weeks onto a LF diet until they were killed at 9 weeks (*14*). Their RRBS analysis of G1 liver did not identify any maternal diet–induced DNA methylation differences. We mapped their raw sequencing reads to rDNA and found that early-life exposure to HF induces CpG-133^{A} hypermethylation in the G1s (Fig. 4A) (P = 0.0098); again, CpG-133^{C} showed lower methylation levels that were not affected by diet. Unfortunately, there were insufficient mice to examine correlations between %A and methylation or weaning weight. Next, we generated bisPCR-seq data for G1 male C57BL/6J mice from a model of maternal obesogenic diet (*15*) (elevated fat and sugar content). G0 females were fed either control or obesogenic diet 6 weeks before mating until the G1 offspring were weaned at 3 weeks onto a control diet and killed at 6 months. G1 males exposed in utero to obesogenic diet showed hypermethylation at CpG-133^{A} (Fig. 4B) (P = 0.017).

Recently, Shea *et al.* reported a study in which they exposed male C57BL/6J mice to one of three different diets (PR, HF, or caloric restriction) postweaning (*16*). They identified substantial interindividual genetic and methylomic variability at rDNA but no consistent diet-induced effects. Although part of the reason for the discrepant conclusions could be that they did not discriminate between the A or C genetic variants, the more likely explanation is differences in developmental timing of the dietary insults because we analyzed exposures spanning only the period between conception and weaning. Previous human epidemiological and animal studies suggest that early life is a critical time when exposures can have long-term phenotypic effects on the offspring (*17*).

In summary, we have described an example of a mammalian "epiallele" whose epigenetic state is influenced by an interaction between the underlying genotype and early-life environment, and this correlates with transcriptional and phenotypic outcomes. A schematic model of the effects we describe is presented in fig. S15. Our work, in combination with previous demonstrations in flies and yeast (*18*, *19*), identifies rDNA as a genomic target of various nutritional insults that is conserved among nonmammalian and mammalian models. Exploration of such interactions at rDNA in humans could provide novel insights into the molecular basis of some complex phenotypes and diseases.

REFERENCES AND NOTES

1. D. S. Fernandez-Twinn, M. Constância, S. E. Ozanne, *Semin. Cell Dev. Biol.* **43**, 85–95 (2015).
2. M. A. Hanson, P. D. Gluckman, *Physiol. Rev.* **94**, 1027–1076 (2014).
3. E. W. Tobi *et al.*, *Nat. Commun.* **5**, 5592 (2014).
4. E. J. Radford *et al.*, *Science* **345**, 1255903 (2014).
5. Z. Vucetic *et al.*, *Neuroscience* **168**, 359–370 (2010).
6. V. G. Dev, R. Tantravahi, D. A. Miller, O. J. Miller, *Genetics* **86**, 389–398 (1977).
7. R. Santoro, I. Grummt, *Mol. Cell* **8**, 719–725 (2001).
8. H. Tseng *et al.*, *PLOS ONE* **3**, e1843 (2008).
9. Y. H. Shiao *et al.*, *PLOS ONE* **6**, e22266 (2011).
10. C. Mayer, K. M. Schmitz, J. Li, I. Grummt, R. Santoro, *Mol. Cell* **22**, 351–361 (2006).
11. R. Santoro, K. M. Schmitz, J. Sandoval, I. Grummt, *EMBO Rep.* **11**, 52–58 (2010).
12. S. Kass, N. Craig, B. Sollner-Webb, *Mol. Cell. Biol.* **7**, 2891–2898 (1987).
13. A. Murayama *et al.*, *Cell* **133**, 627–639 (2008).
14. M. V. Cannon *et al.*, *PLOS ONE* **9**, e90335 (2014).
15. C. E. Aiken, J. L. Tarry-Adkins, N. C. Penfold, L. Dearden, S. E. Ozanne, *FASEB J.* **30**, 1548–1556 (2016).
16. J. M. Shea *et al.*, *Dev. Cell* **35**, 750–758 (2015).
17. N. El Hajj, E. Schneider, H. Lehnen, T. Haaf, *Reproduction* **148**, R111–R120 (2014).
18. C. V. Jack *et al.*, *Proc. Natl. Acad. Sci. U.S.A.* **112**, 9674–9679 (2015).
19. J. C. Aldrich, K. A. Maggert, *PLOS Genet.* **11**, e1005148 (2015).

ACKNOWLEDGMENTS

This work was supported by the following grants and fellowships: Biotechnology and Biological Sciences Research Council, UK (BB/M012494/1) to V.K.R. and (BB/G00711/X/1) to V.K.R. and C.G.; and a Research Council UK Academic Fellowship to M.L.H. R.L. is supported by EU-FP7 BLUEPRINT. S.E.O. is supported by the British Heart Foundation (FS/12/64/30001) and the Medical Research Council (MC_UU_12012/4). This research used Queen Mary's MidPlus computational facilities, supported by Queen Mary University of London Research-IT and funded by *Engineering and Physical Sciences Research Council* grant EP/K000128/1. We thank King's College London FWB Genomics Centre and Barts and The London Genome Centre for performing high-throughput sequencing. Author contributions: M.L.H., C.G., P.W.C., V.K.R., A.A.M.C., and E.L. performed all experiments. R.L. and G.C. conducted the bioinformatic analyses. V.K.R. and S.E.O. provided reagents and contributed to experimental design. M.L.H., R.L., and V.K.R. conceived the study and prepared the manuscript. All authors discussed the results and interpretation and approved the final manuscript. Data deposition statement: Whole-genome sequencing data and pRNA sequencing were submitted to BioProject under ID PRJNA293403. RRBS and BisPCR-seq were all submitted to the National Center for Biotechnology Information's Gene Expression Omnibus under accession GSE72610. All data will be linked under the BioProject ID. Competing interest declaration: The authors declare no conflict of interest.

SUPPLEMENTARY MATERIALS

www.sciencemag.org/content/353/6298/495/suppl/DC1
Materials and Methods
Figs. S1 to S15
Tables S1 to S4
References (*20*–*23*)

17 March 2016; accepted 28 June 2016
Published online 7 July 2016
10.1126/science.aaf7040

Downloaded from http://science.sciencemag.org/ on July 28, 2016

HUMAN GENETICS

Early Neolithic genomes from the eastern Fertile Crescent

Farnaz Broushaki,[1] Mark G. Thomas,[2] Vivian Link,[3,4] Saioa López,[2] Lucy van Dorp,[2] Karola Kirsanow,[1] Zuzana Hofmanová,[1] Yoan Diekmann,[2] Lara M. Cassidy,[5] David Díez-del-Molino,[2,6] Athanasios Kousathanas,[3,4,7] Christian Sell,[1] Harry K. Robson,[8] Rui Martiniano,[5] Jens Blöcher,[1] Amelie Scheu,[1,5] Susanne Kreutzer,[1] Ruth Bollongino,[1] Dean Bobo,[9] Hossein Davoudi,[10] Olivia Munoz,[11] Mathias Currat,[12] Kamyar Abdi,[13] Fereidoun Biglari,[14] Oliver E. Craig,[8] Daniel G. Bradley,[5] Stephen Shennan,[15] Krishna R. Veeramah,[9] Marjan Mashkour,[16] Daniel Wegmann,[3,4*†] Garrett Hellenthal,[2*†] Joachim Burger[1*†]

We sequenced Early Neolithic genomes from the Zagros region of Iran (eastern Fertile Crescent), where some of the earliest evidence for farming is found, and identify a previously uncharacterized population that is neither ancestral to the first European farmers nor has contributed substantially to the ancestry of modern Europeans. These people are estimated to have separated from Early Neolithic farmers in Anatolia some 46,000 to 77,000 years ago and show affinities to modern-day Pakistani and Afghan populations, but particularly to Iranian Zoroastrians. We conclude that multiple, genetically differentiated hunter-gatherer populations adopted farming in southwestern Asia, that components of pre-Neolithic population structure were preserved as farming spread into neighboring regions, and that the Zagros region was the cradle of eastward expansion.

The earliest evidence for cultivation and stock-keeping is found in the Neolithic core zone of the Fertile Crescent (*1*, *2*); a region stretching north from the southern Levant through eastern Anatolia and northern Mesopotamia, then east into the Zagros Mountains on the border of modern-day Iran and Iraq (Fig. 1). From there, farming spread into surrounding regions, including Anatolia and, later, Europe, southern Asia, and parts of Arabia and North Africa. Whether the transition to agriculture was a homogeneous process across the core zone, or a mosaic of localized domestications, is unknown. Likewise, the extent to which core zone farming populations were genetically homogeneous, or exhibited structure that may have been preserved as agriculture spread into surrounding regions, is undetermined.

Ancient DNA (aDNA) studies indicate that early Aegean farmers dating to ~6500 to 6000 BCE are the main ancestors of early European farmers (*3*, *4*), although it is not known if they were predominantly descended from core zone farming populations. We sequenced four Early Neolithic (EN) genomes from Zagros, Iran, including one to 10× mean coverage from a well-preserved male sample from the central Zagros site of Wezmeh Cave [WC1, 7455 to 7082 calibrated years (cal) BCE]. The three other individuals were from Tepe Abdul Hosein and were less well preserved (genome coverage between 0.6 and 1.2×) but are around 10,000 years old, and therefore are among the earliest Neolithic human remains in the world (tables S1 and S3).

Despite a lack of a clear Neolithic context, the radiocarbon-inferred chronological age and palaeodietary data support WC1 being an early farmer (tables S1 to S3 and fig. S7). WC1 bone collagen $\delta^{13}C$ and $\delta^{15}N$ values are indistinguishable from those of a securely assigned Neolithic individual from Abdul Hosein and consistent with a diet rich in cultivated C_3 cereals rather than animal protein. Specifically, collagen from WC1 and Abdul Hosein is ^{13}C depleted compared to those from contemporaneous wild and domestic fauna from this region (*5*), which consumed C_4 plants. Crucially, WC1 and the Abdul Hosein farmers exhibit very similar genomic signatures.

The four EN Zagros genomes form a distinct cluster in the first two dimensions of a principal components analysis (PCA; Fig. 2); they plot closest to modern-day Pakistanis and Afghans and are well separated from European hunter-gatherers (HG) and other Neolithic farmers. In an outgroup *f3*-test (*6*, *7*) (figs. S17 to S20), all four Neolithic Iranian individuals are genetically more similar to each other than to any other prehistoric genome except a Chalcolithic genome from northwestern Anatolia (see below). Despite ^{14}C dates spanning around 1200 years, these data are consistent with all four genomes being sampled from a single eastern Fertile Crescent EN population.

Examination of runs of homozygosity (ROH) above 500 kb in length in WC1 demonstrated that he shared a similar ROH distribution with European and Aegean Neolithics, as well as modern-day Europeans (Fig. 3, A and B). However, of all ancient samples considered, WC1 displays the lowest total length of short ROH, suggesting that he was descended from a relatively large HG population. In contrast, the ROH distributions of the HG Kotias from Georgia, and Loschbour from Luxembourg, indicate prolonged periods of small ancestral population size (*8*).

We also developed a method to estimate heterozygosity ($\hat{\theta}$) in 1-Mb windows that takes into account postmortem damage and is unbiased even at low coverage (*9*) (Fig. 3, C and D). The mean $\hat{\theta}$ in WC1 was higher than in HG individuals (Bichon and Kotias), similar to that in Bronze Age individuals from Hungary and modern Europeans, and lower than in ancient (*10*) and modern Africans. Multidimensional scaling on a matrix of centered Spearman correlations of local $\hat{\theta}$ across the whole genome again puts WC1 closer to modern populations than to ancient foragers, indicating that both the mean and distribution of diversity over the genome are more similar to those of modern populations (Fig. 3E). However, WC1 does have an excess of long ROH segments (>1.6 Mb), relative to Aegean and European Neolithics (Fig. 3B). This includes several very long (7 to 16 Mb) ROH segments (Fig. 3A), confirmed by low $\hat{\theta}$ estimates in those regions (Fig. 3C). These regions do not show reduced coverage in WC1 nor a reduction in diversity in other samples, with the exception of the longest such segment where we find reduced diversity in modern and HG individuals, although less extended than in WC1 (*7*) (Fig. 3B). This observed excess of long segments of reduced heterozygosity could be the result of cultural practices such as consanguinity and endogamy, or demographic constraints such as a recent or ongoing bottleneck (*11*).

The extent of population genetic structure in Neolithic southwestern Asia has important implications for the origins of farming. High levels of structuring would be expected under a scenario of localized independent domestication processes by distinct populations, whereas low structure would be more consistent with a single population origin of farming or a diffuse homogeneous domestication process, perhaps

[1]Palaeogenetics Group, Johannes Gutenberg University Mainz, 55099 Mainz, Germany. [2]Department of Genetics, Evolution and Environment, University College London, London WC1E 6BT, UK. [3]Department of Biology, University of Fribourg, 1700 Fribourg, Switzerland. [4]Swiss Institute of Bioinformatics, 1015 Lausanne, Switzerland. [5]Smurfit Institute of Genetics, Trinity College Dublin, Dublin 2, Ireland. [6]Department of Bioinformatics and Genetics, Swedish Museum of Natural History, SE-10405, Stockholm, Sweden. [7]Unit of Human Evolutionary Genetics, Institut Pasteur, 75015 Paris, France. [8]BioArCh, Department of Archaeology, University of York, York YO10 5YW, UK. [9]Department of Ecology and Evolution, Stony Brook University, Stony Brook, NY 11794-5245, USA. [10]Department of Archaeology, Faculty of Humanities, Tarbiat Modares University, Tehran, Iran. [11]UMR 7041 ArScAn-VEPMO, Maison de l'Archéologie et de l'Ethnologie, 21 allée de l'Université, 92023 Nanterre, France. [12]Department of Genetics and Evolution–Anthropology Unit, University of Geneva, 1211 Geneva, Switzerland. [13]Samuel Jordan Center for Persian Studies and Culture, University of California–Irvine, Irvine, CA 92697-3370, USA. [14]Paleolithic Department, National Museum of Iran, 113617111, Tehran, Iran. [15]Institute of Archaeology, University College London, London WC1H 0PY, UK. [16]CNRS/MNHN/SUs–UMR 7209, Archéozoologie et Archéobotanique, Sociétés, Pratiques et Environnements, Département Ecologie et Gestion de la Biodiversité, 55 rue Buffon, 75005 Paris, France.
*These authors contributed equally to this work. †**Corresponding author. Email: jburger@uni-mainz.de (J.B.); g.hellenthal@ucl.ac.uk (G.H.); daniel.wegmann@unifr.ch (D.W.)**

Downloaded from http://science.sciencemag.org/ on July 28, 2016

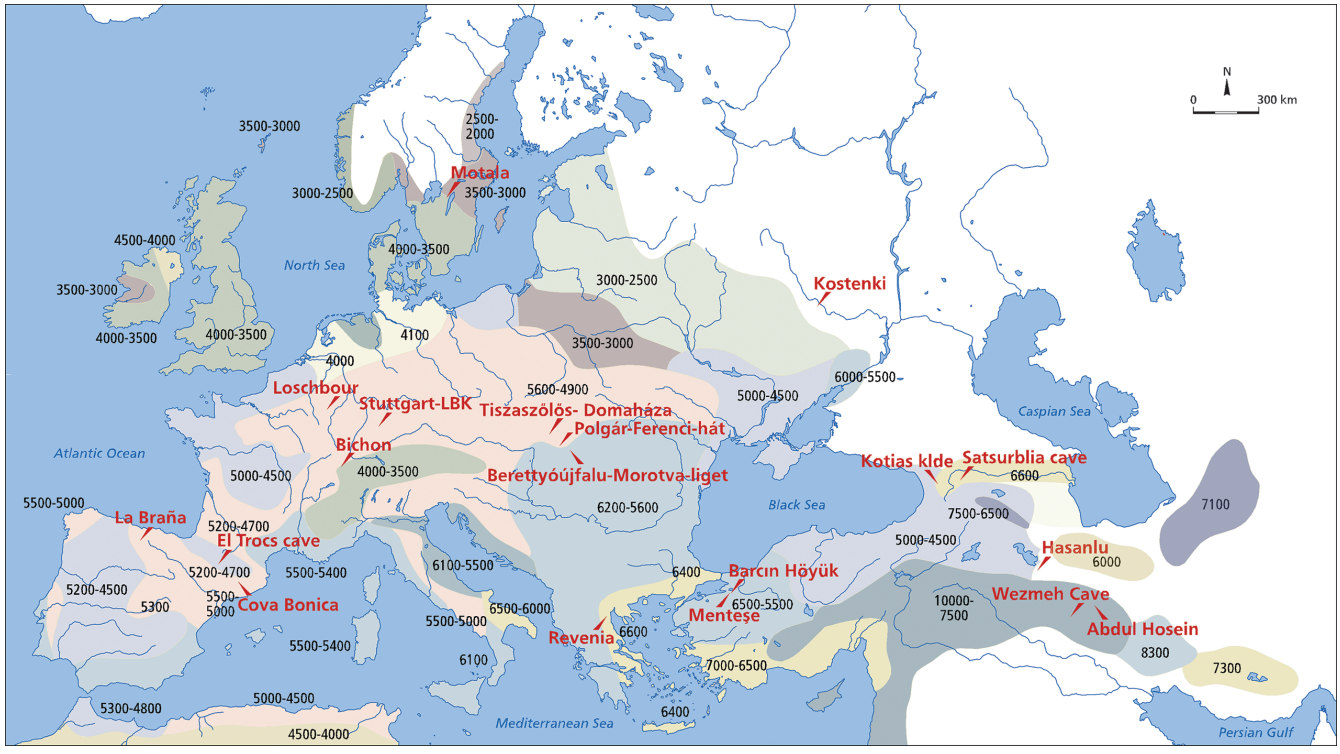


Fig. 1. Map of prehistoric Neolithic and Iron Age Zagros genome locations. Colors indicate isochrones, with numbers giving approximate arrival times of the Neolithic culture (in years BCE).

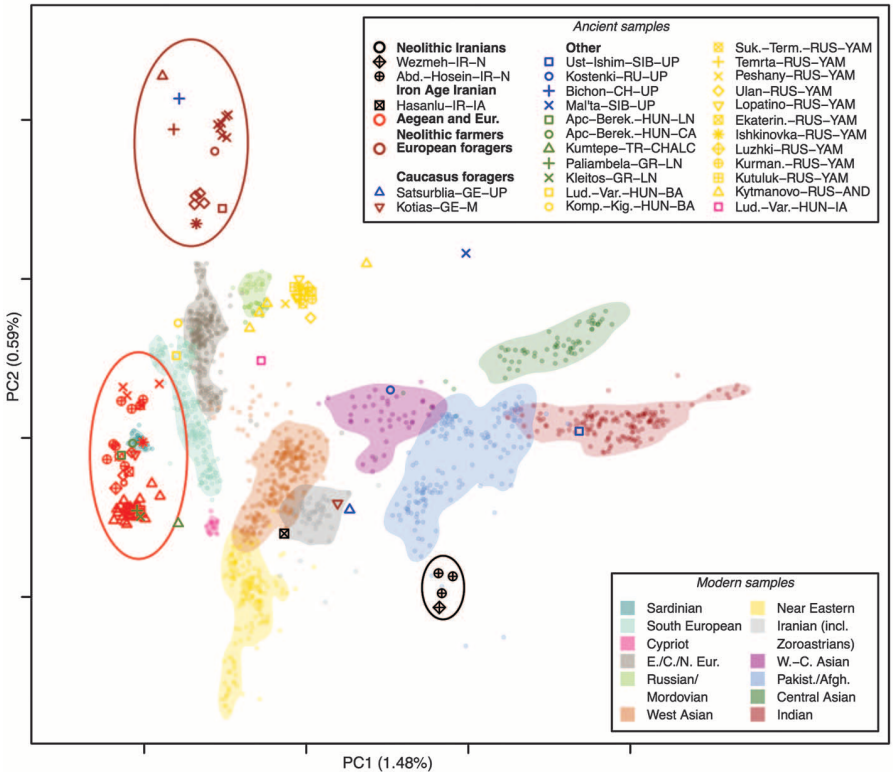


Fig. 2. PCA plot of Zagros, European, and Near and Middle Eastern ancient genomes. Comparison of ancient and modern genomes shows that Neolithic Zagros genomes form a discrete genetic cluster close to modern Pakistani and Afghan genomes but distinct from the genomes of other Neolithic farmers and European hunter-gatherers. See animation S1 for an interactive three-dimensional version of the PCA, including the third principal component.

involving high rates of gene flow across the entire Neolithic core zone. The ancient Zagros individuals show stronger affinities to Caucasus HGs (table S17.1), whereas Neolithic Aegeans showed closer affinities to other European HGs (tables S17.2 and S17.3). Formal tests of admixture of the form *f3*(Neo_Iranian, HG; Anatolia_Neolithic) were all positive with *Z*-scores above 15.78 (table S17.6), indicating that Neolithic northwestern Anatolians did not descend from a population formed by the mixing of Zagros Neolithics and known HG groups. These results suggest that Neolithic populations from northwestern Anatolia and the Zagros descended from distinct ancestral populations. Furthermore, although the Caucasus HGs are genetically closest to EN Zagros individuals, they also share unique ancestry with eastern, western, and Scandinavian European HGs (table S16.1), indicating that they are not the direct ancestors of Zagros Neolithics.

The significant differences between ancient Iranians, Anatolian/European farmers, and European HGs suggest a pre-Neolithic separation. Assuming a mutation rate of 5×10^{-10} per site per year (*12*), the inferred mean split time for Anatolian/European farmers (as represented by Bar8, 4) and European HGs (Loschbour) ranged from 33,000 to 39,000 years ago [combined 95% confidence interval (CI) 15,000 to 61,000 years ago], whereas the preceding divergence of the ancestors of Neolithic Iranians (WC1) occurred 46,000 to 77,000 years ago (combined 95% CI 38,000 to 104,000 years ago) (*13*) (fig. S48 and tables S34 and S35). Furthermore, the European

Downloaded from http://science.sciencemag.org/ on July 28, 2016

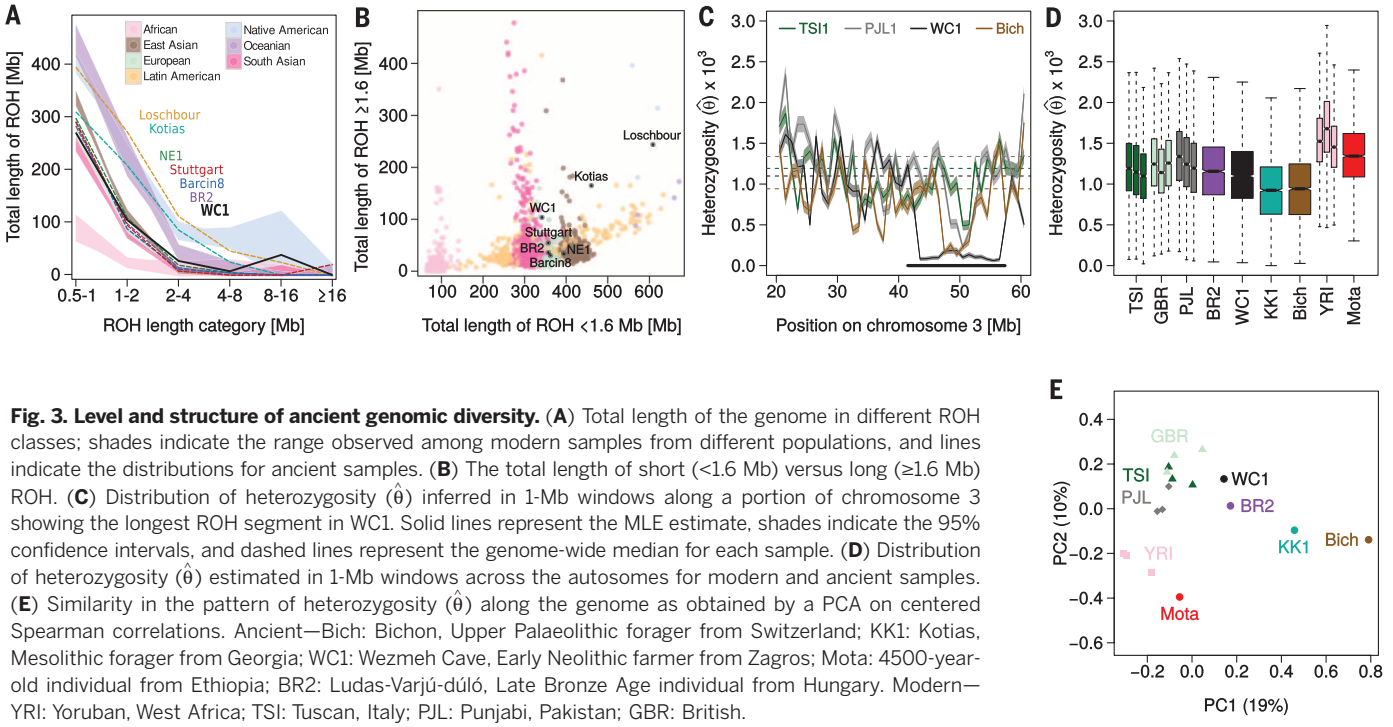


Fig. 3. Level and structure of ancient genomic diversity. (**A**) Total length of the genome in different ROH classes; shades indicate the range observed among modern samples from different populations, and lines indicate the distributions for ancient samples. (**B**) The total length of short (<1.6 Mb) versus long (≥1.6 Mb) ROH. (**C**) Distribution of heterozygosity ($\hat{\theta}$) inferred in 1-Mb windows along a portion of chromosome 3 showing the longest ROH segment in WC1. Solid lines represent the MLE estimate, shades indicate the 95% confidence intervals, and dashed lines represent the genome-wide median for each sample. (**D**) Distribution of heterozygosity ($\hat{\theta}$) estimated in 1-Mb windows across the autosomes for modern and ancient samples. (**E**) Similarity in the pattern of heterozygosity ($\hat{\theta}$) along the genome as obtained by a PCA on centered Spearman correlations. Ancient—Bich: Bichon, Upper Palaeolithic forager from Switzerland; KK1: Kotias, Mesolithic forager from Georgia; WC1: Wezmeh Cave, Early Neolithic farmer from Zagros; Mota: 4500-year-old individual from Ethiopia; BR2: Ludas-Varjú-dúló, Late Bronze Age individual from Hungary. Modern—YRI: Yoruban, West Africa; TSI: Tuscan, Italy; PJL: Punjabi, Pakistan; GBR: British.

HGs were inferred to have an effective population size (*Ne*) that was ~10 to 20% of either Neolithic farming group, consistent with the ROH and $\hat{\theta}$ analyses.

Levels of inferred Neanderthal ancestry in WC1 are low (fig. S22 and table S21), but fall within the general trend described recently in Fu *et al*. (*14*). Fu *et al*. (*14*) also inferred a basal Eurasian ancestry component in the Caucasus HG sample Satsurblia when examined within the context of a "base model" for various ancient Eurasian genomes dated from ~45,000 to 7,000 years ago. We examined this base model using ADMIXTUREGRAPH (*6*) and inferred almost twice as much basal Eurasian ancestry for WC1 as for Satsurblia (62 versus 32%) (fig. S52), with the remaining ancestry derived from a population most similar to ancient north Eurasians such as Mal`ta1 (*15*). Thus, Neolithic Iranians appear to derive predominantly from the earliest known Eurasian population branching event (*7*).

"Chromosome painting" and an analysis of recent haplotype sharing using a Bayesian mixture model (*7*) revealed that, when compared to 160 to 220 modern groups, WC1 shared a high proportion (>95%) of recent ancestry with individuals from the Middle East, Caucasus, and India. We also compared WC1's haplotype-sharing profile to that of three high-coverage Neolithic genomes from northwestern Anatolia (Bar8; Barcın, Fig. 4), Germany (LBK; Stuttgart), and Hungary (NE1; Polgár-Ferenci-hát). Unlike WC1, these Anatolian and European Neolithics shared ~60 to 100% of recent ancestry with modern groups sampled from southern Europe (figs. S24, S30, and S32 to S37; table S22).

We also examined recent haplotype sharing between each modern group and ancient Neolithic genomes from Iran (WC1) and Europe (LBK, NE1), HG genomes sampled from Luxembourg (Loschbour) and the Caucasus (KK1; Kotias), a 4500-year-old genome from Ethiopia (Mota) and Ust'-Ishim, and a 45,000-year-old genome from Siberia. Modern groups from south, central, and northwestern Europe shared haplotypes predominantly with European Neolithic samples LBK and NE1, and European HGs, whereas modern Near and Middle Eastern, as well as southern Asian samples, had higher sharing with WC1 (figs. S28 and S29). Modern Pakistani, Iranian, Armenian, Tajikistani, Uzbekistani, and Yemeni samples were inferred to share >10% of haplotypes with WC1. This was true even when modern groups from neighboring geographic regions were added as potential ancestry surrogates (figs. S26 and S27 and table S23). Iranian Zoroastrians had the highest inferred sharing with WC1 out of all modern groups (table S23). Consistent with this, outgroup *f3* statistics indicate that Iranian Zoroastrians are the most genetically similar to all four Neolithic Iranians, followed by other modern Iranians (Fars), Balochi (southeastern Iran, Pakistan, and Afghanistan), Brahui (Pakistan and Afghanistan), Kalash (Pakistan), and Georgians (figs. S12 to S15). Interestingly, WC1 most likely had brown eyes, relatively dark skin, and black hair, although Neolithic Iranians carried reduced pigmentation-associated alleles in several genes and derived alleles at 7 of the 12 loci showing the strongest signatures of selection in ancient Eurasians (*3*) (tables S29 to S33). Although there is a strong Neolithic component in these modern south Asian populations, simulation of allele sharing rejected full population continuity under plausible ancestral population sizes, indicating some population turnover in Iran since the Neolithic (*7*).

While Early Neolithic samples from eastern and western southwest Asia differ conspicuously, comparisons to genomes from Chalcolithic Anatolia and Iron Age Iran indicate a degree of subsequent homogenization. Kumtepe6, a ~6750-year-old genome from northwestern Anatolia (*16*), was more similar to Neolithic Iranians than to any other non-Iranian ancient genome (figs. S17 to S20 and table S18.1). Furthermore, our male Iron Age genome (F38; 971 to 832 BCE; sequenced to 1.9×) from Tepe Hasanlu in northwestern Iran shares greatest similarity with Kumtepe6 (fig. S21) even when compared to Neolithic Iranians (table S20). We inferred additional non-Iranian or non-Anatolian ancestry in F38 from sources such as European Neolithics and even post-Neolithic Steppe populations (table S20). Consistent with this, F38 carried a N1a subclade mitochondrial DNA (mtDNA), which is common in early European and northwestern Anatolian farmers (*3*). In contrast, his Y chromosome belongs to subhaplogroup R1b1a2a2, also found in five Yamnaya individuals (*17*) and in two individuals from the Poltavka culture (*3*). These patterns indicate that post-Neolithic homogenization in southwestern Asia involved substantial bidirectional gene flow between the east and west of the region, as well as possible gene flow from the Steppe.

Migration of people associated with the Yamnaya culture has been implicated in the spread of Indo-European languages (*17*, *18*), and some level of Near Eastern ancestry was previously inferred in southern Russian pre-Yamnaya populations (*3*). However, our analyses suggest that Neolithic Iranians were unlikely to be the main source of Near Eastern ancestry in the Steppe population

Downloaded from http://science.sciencemag.org/ on July 28, 2016

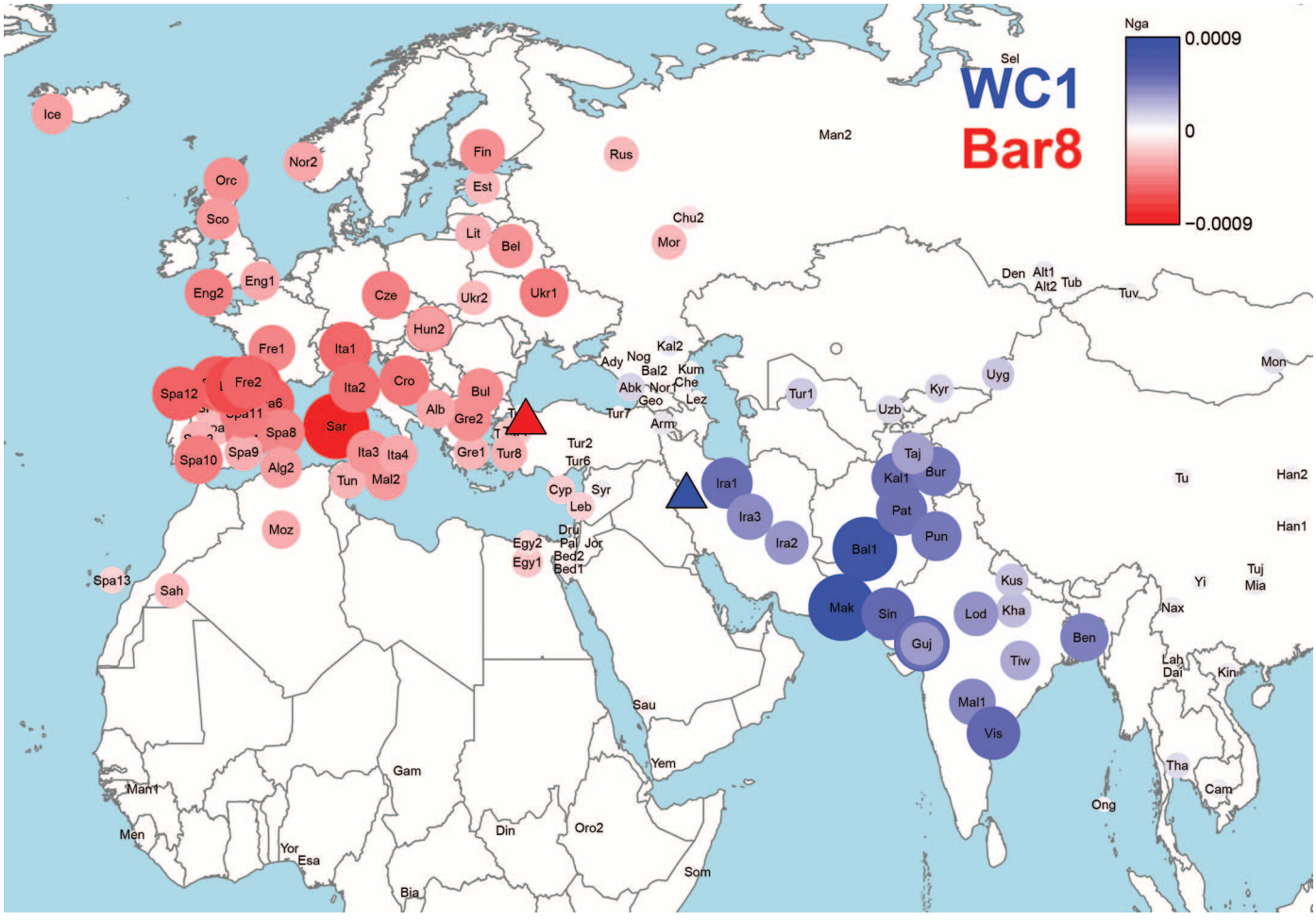


Fig. 4. Modern-day peoples with affinity to WC1. Modern groups with an increasingly higher (respectively lower) inferred proportion of haplotype sharing with the Iranian Neolithic Wezmeh Cave (WC1, 7455 to 7082 cal BCE, blue triangle) compared to the Anatolian Neolithic Barcın genome (Bar8; 6212 to 6030 cal BCE, red triangle) are depicted with an increasingly stronger blue or red color, respectively. Circle sizes illustrate the relative absolute proportion of this difference between WC1 versus Bar8. The key for the modern group labels is provided in table S24.

(table S20) and that this ancestry in pre-Yamnaya populations originated primarily in the west of southwest Asia.

We also inferred shared ancestry between Steppe and Hasanlu Iron Age genomes that was distinct from EN Iranians (table S20) (*7*). In addition, modern Middle Easterners and South Asians appear to possess mixed ancestry from ancient Iranian and Steppe populations (tables S19 and S20). However, Steppe-related ancestry may also have been acquired indirectly from other sources (*7*), and it is not clear if this is sufficient to explain the spread of Indo-European languages from a hypothesized Steppe homeland to the region where Indo-Iranian languages are spoken today. Yet the affinities of Zagros Neolithic individuals to modern populations of Pakistan, Afghanistan, Iran, and India is consistent with a spread of Indo-Iranian languages, or of Dravidian languages (which includes Brahui), from the Zagros into southern Asia, in association with farming (*19*).

The Neolithic transition in southwest Asia involved the appearance of different domestic species, particularly crops, in different parts of the Neolithic core zone, with no single center (*20*). Early evidence of plant cultivation and goat management between the 10th and the 8th millennium BCE highlights the Zagros as a key region in the Neolithization process (*1*). Given the evidence of domestic species movement from east to west across southwest Asia (*21*), it is surprising that EN human genomes from the Zagros are not closely related to those from northwestern Anatolia and Europe. Instead they represent a previously undescribed Neolithic population. Our data show that the chain of Neolithic migration into Europe does not reach back to the eastern Fertile Crescent, also raising questions about whether intermediate populations in southeastern and Central Anatolia form part of this expansion. Nevertheless, it seems probable that the Zagros region was the source of an eastern expansion of the southwestern Asian domestic plant and animal economy. Our inferred persistence of ancient Zagros genetic components in modern day south Asians lends weight to a strong demic component to this expansion.

REFERENCES AND NOTES

1. S. Riehl, M. Zeidi, N. J. Conard, *Science* **341**, 65–67 (2013).
2. R. Mattews, W. Mattews, Y. Mohammadifar, Eds., *The Earliest Neolithic of Iran: 2008 Excavations at Sheikh-e Abad and Jani Central Zagros* (Oxbow Books, Oxford, 2013), vol. 1.
3. I. Mathieson *et al.*, *Nature* **528**, 499–503 (2015).
4. Z. Hofmanová *et al.*, *Proc. Natl. Acad. Sci. U.S.A.* **113**, 6886–6891 (2016).
5. G. Müldner, Isotope analysis of animal bone, in *The Earliest Neolithic of Iran: 2008 Excavations at Sheikh-e Abad and Jani*, R. Matthews, W. Matthews, Y. Mohammadifar, Eds. (Oxbow Books, 2013).
6. N. Patterson *et al.*, *Genetics* **192**, 1065–1093 (2012).
7. Materials and methods are available as supplementary materials on *Science* Online.
8. E. R. Jones *et al.*, *Nat. Commun.* **6**, 8912 (2015).
9. A. Kousathanas *et al.*, Inferring heterozygosity from ancient and low coverage genomes. *bioRxiv* 10.1101/046748 (2016).
10. M. G. Llorente *et al.*, *Science* **350**, 820–822 (2015).
11. T. J. Pemberton *et al.*, *Am. J. Hum. Genet.* **91**, 275–292 (2012).
12. A. Kong *et al.*, *Nature* **488**, 471–475 (2012).
13. M. W. Nachman, S. L. Crowell, *Genetics* **156**, 297–304 (2000).
14. Q. Fu *et al.*, *Nature* **534**, 200–205 (2016).
15. M. Raghavan *et al.*, *Nature* **505**, 87–91 (2014).

Downloaded from http://science.sciencemag.org/ on July 28, 2016

16. A. Omrak *et al*., *Curr. Biol.* **26**, 270–275 (2016).
17. W. Haak *et al*., *Nature* **522**, 207–211 (2015).
18. M. E. Allentoft *et al*., *Nature* **522**, 167–172 (2015).
19. J. P. Mallory, D. Q. Adams, Eds., *Encyclopedia of Indo-European Culture* (Taylor & Francis, London, 1997).
20. D. Q. Fuller, G. Willcox, R. G. Allaby, *J. Exp. Bot.* **63**, 617–633 (2012).
21. A. Scheu *et al*., *BMC Genet.* **16**, 54 (2015).

ACKNOWLEDGMENTS

This paper is a product of the Palaeogenome Analysis Team (PAT). F.Br. was supported by funds of Johannes Gutenberg University Mainz given to J.Bu., Z.H., and R.M. are supported by a Marie Curie Initial Training Network (BEAN—Bridging the European and Anatolian Neolithic, GA no. 289966). C.S. was supported by the European Union (EU) SYNTHESYS–Synthesis of Systematic Resources, GA no. 226506-CP-CSA-INFRA, and Deutsche Forschungsgemeinschaft (DFG) (BO 4119/1). A.S. was supported by the EU CodeX Project no. 295729. M.C. was supported by Swiss NSF grant 31003A_156853. A.K. and D.W. were supported by Swiss NSF grant 31003A_149920. S.L. is supported by Biotechnology and Biological Sciences Research Council (grant no. BB/L009382/1). L.v.D. is supported by CoMPLEX via the Engineering and Physical Sciences Research Council (grant no. EP/F500351/1). G.H. is supported by a Sir Henry Dale Fellowship jointly funded by the Wellcome Trust and the Royal Society (grant no. 098386/Z/12/Z) and supported by the National Institute for Health Research University College London Hospitals Biomedical Research Centre. M.G.T. and Y.D. are supported by a Wellcome Trust Senior Research Fellowship awarded to M.G.T. J.Bu. is grateful for support by the high-performance computing cluster MOGON (funded by DFG; INST 247/602-1 FUGG). L.M.C. is funded by the Irish Research Council (GOIPG/2013/1219). M.M. was supported by the UMR 7209, CNRS National Museum of Natural History–Sorbonne University and ANR-14-CE03-0008-01-CNRS ANR Kharman. O.M. was supported by Institut Français de Recherche en Iran (October 2015). F.Bi., M.M., O.M., and H.D. thank the National Museum of Iran and especially J. Nokandeh, director of National Museum of Iran. We thank N. Patterson for early access to the latest version of qpgraph. Accession numbers: Mitochondrial genome sequences are deposited in GenBank (KX353757-KX353761). Genomic data are available at ENA (European Nucleotide Archive) with the accession number PRJEB14180 in BAM format. Iranian Zoroastrian and Fars genotype data are available in plink format at figshare: https://dx.doi.org/10.6084/m9.figshare.3470135.

SUPPLEMENTARY MATERIALS

www.sciencemag.org/content/353/6298/499/suppl/DC1
Materials and Methods
Figs. S1 to S52
Tables S1 to S37
References (*22*–*162*)
Animation S1

7 April 2016; accepted 5 July 2016
Published online 14 July 2016
10.1126/science.aaf7943

STRUCTURAL BIOLOGY

Crystal structure of Zika virus NS2B-NS3 protease in complex with a boronate inhibitor

Jian Lei,[1,2] Guido Hansen,[1] Christoph Nitsche,[3]* Christian D. Klein,[3] Linlin Zhang,[1,2] Rolf Hilgenfeld[1,2]†

The ongoing Zika virus (ZIKV) outbreak is linked to severe neurological disorders. ZIKV relies on its NS2B/NS3 protease for polyprotein processing; hence, this enzyme is an attractive drug target. The 2.7 angstrom crystal structure of ZIKV protease in complex with a peptidomimetic boronic acid inhibitor reveals a cyclic diester between the boronic acid and glycerol. The P2 4-aminomethylphenylalanine moiety of the inhibitor forms a salt-bridge with the nonconserved Asp^{83} of NS2B; ion-pairing between Asp^{83} and the P2 residue of the substrate likely accounts for the enzyme's high catalytic efficiency. The unusual dimer of the ZIKV protease:inhibitor complex seen in the crystal may provide a model for assemblies formed at high local concentrations of protease at the endoplasmatic reticulum membrane, the site of polyprotein processing.

Previously considered a rare and mild pathogen for humans (*1*), Zika virus (ZIKV) infection has recently been found to be responsible for neurological disorders in a substantial portion of patients. The infection can trigger Guillain-Barré syndrome (*2*), and prenatal ZIKV infection is responsible for a dramatically increased number of microcephaly cases in fetuses and newborn children (*3*). The World Health Organization (WHO) recently declared the association of ZIKV infection with these neurological disorders a Public Health Emergency of International Concern (*4*). There are no vaccines or antiviral drugs available for protection from or treatment of ZIKV infection.

ZIKV is a member of the genus *Flavivirus* in the Flaviviridae family of RNA viruses. Its ~10.7-kb single-stranded RNA genome of positive polarity encodes a single polyprotein, which, by analogy to other flaviviruses, is assumed to be cleaved by host-cell proteases (signalase and furin) and the viral NS2B/NS3 protease into three structural (C, prM/M, and E) and seven nonstructural proteins (NS1, NS2A, NS2B, NS3, NS4A, NS4B, and NS5) (fig. S1). Similar to other flavivirus proteases, such as those of dengue virus (DENV) and West Nile virus (WNV), the mature form of ZIKV protease consists of the N-terminal domain of NS3, which carries the catalytic triad Ser^{135}-His^{51}-Asp^{75}, and the membrane-bound NS2B (a sequence alignment is available in fig. S2). Crystallization of this complex has not been successful so far for any flavivirus protease, but it has been shown that a construct comprising ~40 hydrophilic residues of NS2B and ~185 residues of NS3, covalently linked via a Gly$_4$-Ser-Gly$_4$ sequence, displays strong peptidolytic activity (*5*). Crystal structures of the free form of this protease construct ("NS2B-NS3^{pro}") usually reveal an "open conformation" featuring a well-ordered NS3^{pro} core and a flexible NS2B part that shows only limited interaction with NS3^{pro}, whereas inhibitor (and presumably substrate) binding induces a pronounced conformational change of NS2B yielding a more compact, "closed" form (*6*, *7*).

We expressed in *Escherichia coli* a DNA construct corresponding to the NS2B-NS3^{pro}–coding region of the Brazilian ZIKV isolate BeH823339 (GenBank accession number KU729217.2) (*8*). This construct codes for residues 49 to 95 of ZIKV NS2B, the C terminus of which is covalently linked via Gly$_4$-Ser-Gly$_4$ to the N terminus of NS3 (residues 1 to 170). The recombinant enzyme obtained is a mixture of monomer, disulfide-linked dimer (here designated "SS-dimer") and—to a lesser extent—higher oligomers (fig. S3). The double mutant Cys^{80}Ser/Cys^{143}Ser leads to loss of the disulfide bond, which occurs between Cys^{143} residues of different polypeptide chains, as revealed by our x-ray structure. The SS-dimer and the monomer obtained by reduction with tris(2-carboxyethyl)phosphine (TCEP) (fig. S3) as well as the Cys^{80}Ser/Cys^{143}Ser mutant of ZIKV NS2B-NS3^{pro} are hyperactive against the standard flavivirus protease substrate benzoyl-norleucine-lysine-lysine-arginine 7-amino-4-methylcoumarine (Bz-Nle-Lys-Lys-Arg-AMC), with a very low Michaelis constant (K_m) and a specific catalytic efficiency (k_{cat}/K_m) more than 20 times higher than for the WNV enzyme (Table 1).

In order to elucidate the molecular basis of this hyperactivity, and to provide a starting point for structure-based drug design efforts, we have crystallized ZIKV NS2B-NS3^{pro} in the closed form and determined its x-ray structure at 2.7 Å resolution. Containing two molecules ("A" and "B") per asymmetric unit of the crystal, the structure reveals the same chymotrypsin-like fold for the NS3^{pro} domain as seen previously for other flavivirus proteases, with the NS2B polypeptide

[1]Institute of Biochemistry, Center for Structural and Cell Biology in Medicine, University of Lübeck, Ratzeburger Allee 160, 23562 Lübeck, Germany. [2]German Center for Infection Research (DZIF), Hamburg–Lübeck–Borstel–Riems Site, University of Lübeck, Germany. [3]Medicinal Chemistry, Institute of Pharmacy and Molecular Biotechnology, Heidelberg University, Im Neuenheimer Feld 364, 69120 Heidelberg, Germany.
*Present address: Research School of Chemistry, Australian National University, Canberra, ACT 2601, Australia.
†Corresponding author. Email: hilgenfeld@biochem.uni-luebeck.de

Downloaded from http://science.sciencemag.org/ on July 28, 2016

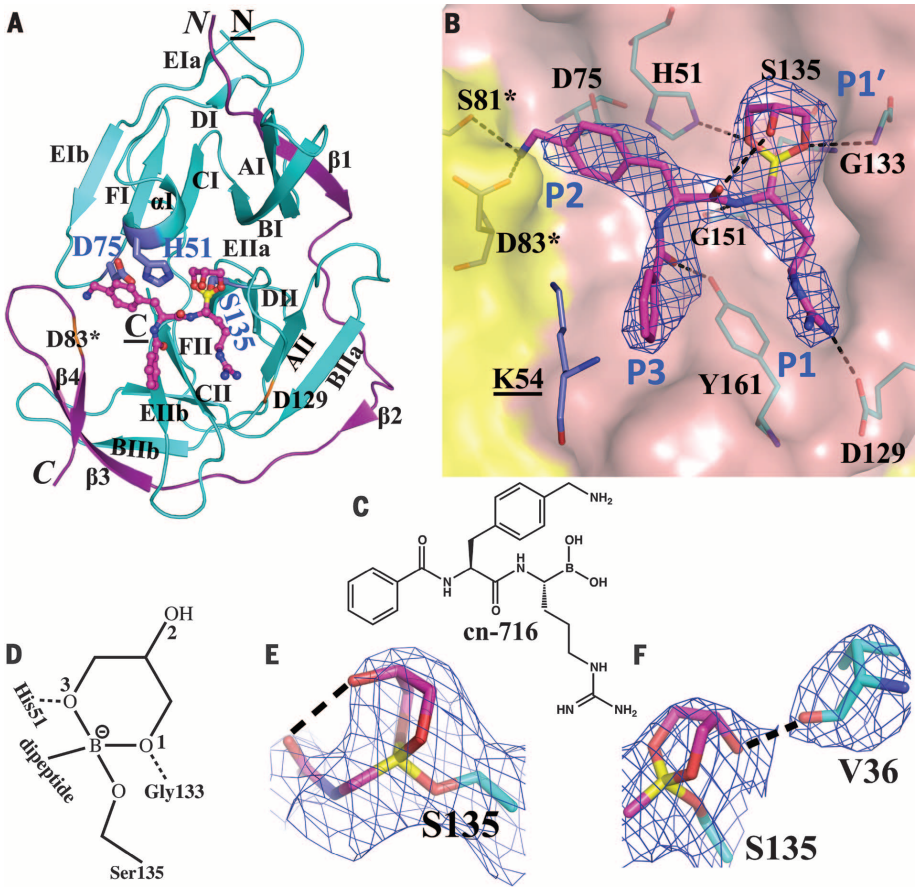


Fig. 1. Crystal structure of the ZIKV NS2B-NS3^{pro} monomer in complex with cn-716. (**A**) Overall structure of the complex. NS3^{pro} (light blue) and NS2B (purple) are shown as ribbons, with secondary-structure elements labeled. NS3^{pro} is made up by two β-barrels with strand orders AI-BI-CI-αI-DI-EIa-EIb-FI and AII-BIIa-BIIb-CII-DII-EIIa-EIIb-FII. NS2B includes β-strands β1 to β4. The N- and C-termini of NS2B and NS3^{pro} are indicated by letters in italics and nonitalics/underlined, respectively. The inhibitor cn-716 is shown with carbon atoms in purple and boron in yellow. Residues of the catalytic triad are in dark blue. Asterisk denotes residues from NS2B. (**B**) The inhibitor cn-716 is embedded in the substrate-binding site of ZIKV NS2B-NS3^{pro} [same view as in (A)]. The surfaces of NS2B and NS3^{pro} are yellow and purple, respectively. A F_{obs}-F_{calc} difference density contoured at 2.5σ is shown for cn-716. Lys^{54} from molecule B of the dimer interacts with the inhibitor and is indicated by underlined K54. (**C**) Chemical structure of cn-716. (**D**) Schematic drawing and (**E**) F_{obs}-F_{calc} difference density (2.5σ) for the cyclic diester and its environment in molecule A. (**F**) Difference density (2.5σ) for the cyclic diester and its environment in molecule B.

wrapped around the NS3^{pro}. The interaction between the two is stabilized by hydrogen bonds between β-strands β1 and AI, β2 and BIIa, as well as β3 and BIIb of NS2B and NS3^{pro}, respectively (Fig. 1A). The root mean square deviations between the ZIKV NS2B-NS3^{pro} complex and tetrapeptide aldehyde complexes of WNV and DENV-3 proteases are 0.9 to 1.1 Å [for main-chain atoms; Protein Data Bank (PDB) codes 2FP7 and 3U1I (*6*, *9*)]. The capped dipeptide boronic acid compound cn-716 (Fig. 1C) was used to obtain the closed conformation of the protease. We found this compound to reversibly inhibit ZIKV NS2B-NS3^{pro} with half maximal inhibitory concentration (IC_{50}) = 0.25 ± 0.02 μM and inhibition constant (K_i) = 0.040 ± 0.006 μM (in the presence of 20% glycerol) (fig. S4). In the structure of the complex, the boron atom is covalently linked to the side-chain Oγ of the catalytic Ser^{135} (Fig. 1, B and D to F). The structure also reveals that the boronic acid moiety forms a cyclic diester with glycerol, which was continuously present in our enzyme preparation during purification and crystallization, as well as cryoprotection of crystals. Boronic acids tend to form esters with diols and triols, especially if five- or six-membered rings can be formed (*10*). Our F_{obs}-F_{calc} (observed and calculated structure-factor amplitudes, respectively) difference density indicates that a six-membered ring has been formed by reaction of the boronic acid with the terminal hydroxyl groups of glycerol (Fig. 1, B and D to F). The six-membered ring fits neatly into the S1′ pocket of the enzyme (Fig. 1B), a site so far rarely addressed by synthetic flavivirus protease inhibitors. In the absence of glycerol, the IC_{50} for the boronic acid inhibitor was nearly unchanged (0.20 ± 0.02 μM), but through ester formation with larger, more hydrophobic diols or triols, a prodrug might be obtained that will traverse the cellular membrane more readily than will free boronic acid derivatives.

Because of the ring closure, the tetrahedral geometry of the boron is somewhat distorted. In molecule A, the six-membered ring assumes a boat-like conformation, with the middle hydroxyl group (O2) of glycerol in an axial position and donating an intramolecular hydrogen bond to the main-chain oxygen of the P2 residue of the inhibitor (Fig. 1E). In molecule B, the six-membered ring adopts a somewhat twisted half-chair conformation, and the central hydroxyl group, also in an axial position, donates a hydrogen bond to the carbonyl oxygen of Val^{36} (Fig. 1F). In molecule A, the two ring oxygens (O1 and O3) accept H-bonds respectively from the amide of Gly^{133} (from the oxyanion hole) and from the catalytic His^{51}, whereas the latter interaction is missing in molecule B. These differences between the two inhibitor molecules in the asymmetric unit of the crystal reflect the conformational variability of the cyclic boronates (*10*).

The P1-Arg residue of cn-716 forms a salt-bridge with Asp^{129}, a feature conserved in many flavivirus protease complexes. Most probably protonated, the amino group of the 4-aminomethylphenylalanyl residue in the P2 position forms a hydrogen bond with the main-chain oxygen of Ser^{81}* and a salt-bridge with Asp^{83}* of the NS2B polypeptide (Fig. 1B; residues of NS2B are denoted by an asterisk). Asp^{83}* is Asn in WNV and Ser or Thr in DENV 1–4 NS2B-NS3^{pro} (fig. S2), unable to form an ion-pair interaction with the P2 residue of the inhibitor or the substrate, Bz-Nle-Lys-Lys-Arg-AMC. The Asp^{83}*Asn mutation leads to an approximately twofold increase of K_m and a k_{cat}/K_m reduced by 55%, as compared with the wild-type (WT) enzyme (Table 1). The Asp residue in this position provides an at least partial explanation for the lower K_m and hence the much higher k_{cat}/K_m of ZIKV protease as compared with the WNV and DENV enzymes (Table 1). DENV NS2B/NS3 protease has been shown to counteract the type-I interferon response via digesting the stimulator of inferon genes (STING) in human dendritic cells (DCs) (*11*). Because ZIKV also permissively infects human DCs (*12*), we speculate that an increased catalytic activity of ZIKV NS2B/NS3^{pro} could cause more efficient cleaveage of STING, leading to an enhanced suppression of the host innate immunity.

In the crystal, ZIKV NS2B-NS3^{pro} forms an unusual dimer with noncrystallographic, quasi-twofold symmetry (Fig. 2A) that has not been seen with other flavivirus proteases. This tight dimer has to be distinguished from the labile SS-dimers seen in solution. In the tight dimer, the substrate-binding sites of the two monomers,

Downloaded from http://science.sciencemag.org/ on July 28, 2016

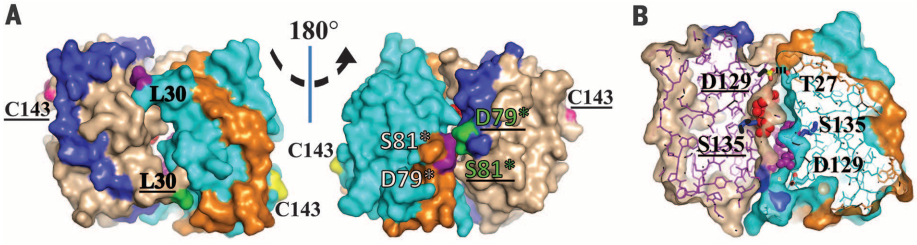


Fig. 2. The tight, noncrystallographic 2:2 dimer of quasi-twofold symmetry formed by the ZIKV NS2B-NS3^{pro}:inhibitor complex in the asymmetric unit of the crystal. (**A**) Front view and back view. The surfaces of NS2B and NS3^{pro} of molecule A are shown in light blue and orange, respectively; those of molecule B are dark blue and beige. Labels of molecule B residues are underlined. Residues of NS2B are marked by an asterisk. Residues Leu^{30} (purple/green) and Leu^{31} at the tip of the AI-BI loop (Fig. 1A) form a hook, making hydrophobic contacts with the opposing monomer. The Cys^{143} residues forming labile disulfide bonds in the SS-dimer are yellow and pink. (**B**) A slice through the interior of the dimer, showing the S135 side-chains (dark blue) covalently bound to the inhibitor molecules. The color code is the same as in (A). Inhibitor molecules are colored purple and red. A schematic illustration of the interactions across the dimer interface is provided in fig. S5.

Table 1. Kinetic parameters of variants of ZIKV NS2B-NS3 protease, in comparison to a similar WNV NS2B-NS3^{pro} construct. Data are for the cleavage of the flavivirus protease substrate Bz-Nle-Lys-Lys-Arg-AMC. "Monomer (wt)" (details, including definition of "wt", are provided in the supplementary materials), and "SS-dimer (wt)" indicate enzyme preparations corresponding to the monomer (in the presence of TCEP) and the SS-dimer fraction from gel permeation chromatography. The kinetic parameters for the ZIKV protease with Asp^{83}* replaced by Asn are also included. "WNV NS2B-NS3^{pro} (wt)" is our recombinant preparation of the WNV protease. For comparison, the k_{cat}/K_m values for WNV and DENV-2 NS2B-NS3^{pro} and with the substrate Bz-Nle-Lys-Arg-Arg-AMC reported in (*6*) are given. Dashes indicate "not reported." All values in this table are obtained at pH 8.5.

Protease	k_{cat} (s^{-1})	K_m (μM)	k_{cat}/K_m (s^{-1} M^{-1})
ZIKV NS2B-NS3^{pro}			
Monomer (wt)	44.6 ± 1.0	18.3 ± 1.6	2,440,000 ± 215,000
SS-dimer (wt)	28.5 ± 0.6	5.9 ± 0.5	4,850,000 ± 429,000
Cys^{80}Ser/Cys^{143}Ser	28.8 ± 0.5	5.1 ± 0.5	5,620,000 ± 546,000
Asp^{83}*Asn (monomer)	38.5 ± 1.4	35.3 ± 4.2	1,091,000 ± 136,000
WNV NS2B-NS3^{pro}			
wt	8.7 ± 0.1	77.4 ± 3.6	112,000 ± 5000
wt (*6*)	—	—	37,000 ± 7000
DENV-2 NS2B-NS3^{pro}			
wt (*6*)	—	—	30,000 ± 7000

along with the bound inhibitor, face each other (Fig. 2B). The dimer has openings at both sides, which upon some "breathing" would allow access of substrate to the two active sites located at the center (Fig. 2A). The tight dimer in the asymmetric unit of the crystal is connected to neighboring dimers through two labile disulfide bonds linking Cys^{143} of monomer A to the same residue of monomer B in a symmetry-related dimer, and vice versa, giving rise to disulfide-mediated polymers of tight dimers (Cys^{143} is indicated in Fig. 2A). This disulfide bond is responsible for the formation of the "SS-dimer" apparent in the SDS–polyacrylamide gel electrophoresis (fig. S3). After a few seconds of the crystal in the x-ray beam, this exposed disulfide appears to be reduced as a consequence of irradiation, although the presence of the disulfide seems to be essential for crystallization of the ZIKV NS2B-NS3^{pro}, as we failed to obtain crystals of the Cys^{80}Ser/Cys^{143}Ser variant.

Formation of the tight dimer in the asymmetric unit buries ~1240 Å^2 of the surface of each of the two monomers, and the shape complementarity (*Sc*) index (*13*) is 0.64 [for a large set of well-characterized homodimeric proteins, the mean *Sc* was 0.69 ± 0.07 (*14*)]. If we include the two inhibitor molecules in the calculation, ~1500 Å^2 of molecular surface are buried per monomer. Both the large surface area buried and the shape complementarity indicate that dimer formation is likely of biological relevance. Although we failed to observe this dimer in solutions of the ZIKV NS2B-NS3^{pro} complex with cn-716 up to a concentration of 133 μM, we detected it by means of electrospray ionization mass spectrometry in the presence but not in the absence of the boronic acid inhibitor (fig. S6). The structure suggests that the closed form of the enzyme has the potential of forming well-defined dimers at higher concentrations as they may occur (and are perhaps promoted by the membrane-embedded parts of NS2B, which are lacking in the present structure) at the endoplasmic reticulum membrane, where polyprotein processing and viral replication take place.

Peptide boronic acids have previously been tested as drugs, and the proteasome inhibitor bortezomib (Velcade) has been approved for the treatment of multiple myelomas (*15*). A tetrapeptide-boronic acid was reported as a potent inhibitor of the DENV-2 NS2B-NS3^{pro} but not studied further (*16*). Peptide boronic acids are usually not cytotoxic to Huh7 cells, which is what we observed with compound cn-716 (fig. S7). The structure presented here forms a good starting point for the design of more specific anti-ZIKV drugs.

REFERENCES AND NOTES

1. W. G. Bearcroft, *Trans. R. Soc. Trop. Med. Hyg.* **50**, 442–448 (1956).
2. V. M. Cao-Lormeau *et al.*, *Lancet* **387**, 1531–1539 (2016).
3. S. A. Rasmussen, D. J. Jamieson, M. A. Honein, L. R. Petersen, *N. Engl. J. Med.* **374**, 1981–1987 (2016).
4. D. L. Heymann *et al.*, *Lancet* **387**, 719–721 (2016).
5. D. Leung *et al.*, *J. Biol. Chem.* **276**, 45762–45771 (2001).
6. P. Erbel *et al.*, *Nat. Struct. Mol. Biol.* **13**, 372–373 (2006).
7. D. Luo, S. G. Vasudevan, J. Lescar, *Antiviral Res.* **118**, 148–158 (2015).
8. N. R. Faria *et al.*, *Science* **352**, 345–349 (2016).
9. C. G. Noble, C. C. Seh, A. T. Chao, P. Y. Shi, *J. Virol.* **86**, 438–446 (2012).
10. L. Türker, *Indian J. Chem.* **45A**, 1339–1344 (2006).
11. S. Aguirre *et al.*, *PLOS Pathog.* **8**, e1002934 (2012).
12. R. Hamel *et al.*, *J. Virol.* **89**, 8880–8896 (2015).
13. M. C. Lawrence, P. M. Colman, *J. Mol. Biol.* **234**, 946–950 (1993).
14. D. Kuroda, J. J. Gray, *Bioinformatics 10.1093/bioinformatics/btw197* (2016).
15. P. G. Richardson *et al.*, *N. Engl. J. Med.* **352**, 2487–2498 (2005).
16. Z. Yin *et al.*, *Bioorg. Med. Chem. Lett.* **16**, 36–39 (2006).

ACKNOWLEDGMENTS

We thank S. Zoske and Y. Gül for assistance, S. Anemüller for recording the mass spectra, L. Weigel for the synthesis of precursors of cn-716, and D. Graf for testing this compound for cytotoxicity. We are indebted to the staff of synchrotron beamlines BL 14.1 (BESSY, Berlin) and P11 (DESY, Hamburg) for support. The corresponding coordinates and structure factors are available from the PDB under accession code 5LC0. Funding from the German Center for Infection Research (DZIF–TTU01, grant 8011801911) is gratefully acknowledged. C.D.K. thanks the Deutsche Forschungsgemeinschaft for financial support (KL-1356/3-1).

SUPPLEMENTARY MATERIALS

www.sciencemag.org/cgi/content/353/6298/503/suppl/DC1
Materials and Methods
Figs. S1 to S7
Table S1
References (*17*–*28*)

28 May 2016; accepted 30 June 2016
Published online 7 July 2016
10.1126/science.aag2419

Downloaded from http://science.sciencemag.org/ on July 28, 2016

STRUCTURAL BIOLOGY

An atomic model of HIV-1 capsid-SP1 reveals structures regulating assembly and maturation

Florian K. M. Schur,[1,2] Martin Obr,[2,3] Wim J. H. Hagen,[1] William Wan,[1] Arjen J. Jakobi,[1,4] Joanna M. Kirkpatrick,[5*] Carsten Sachse,[1] Hans-Georg Kräusslich,[2,3] John A. G. Briggs[1,2†]

Immature HIV-1 assembles at and buds from the plasma membrane before proteolytic cleavage of the viral Gag polyprotein induces structural maturation. Maturation can be blocked by maturation inhibitors (MIs), thereby abolishing infectivity. The CA (capsid) and SP1 (spacer peptide 1) region of Gag is the key regulator of assembly and maturation and is the target of MIs. We applied optimized cryo-electron tomography and subtomogram averaging to resolve this region within assembled immature HIV-1 particles at 3.9 angstrom resolution and built an atomic model. The structure reveals a network of intra- and intermolecular interactions mediating immature HIV-1 assembly. The proteolytic cleavage site between CA and SP1 is inaccessible to protease. We suggest that MIs prevent CA-SP1 cleavage by stabilizing the structure, and MI resistance develops by destabilizing CA-SP1.

The major structural protein of HIV-1, Gag, oligomerizes at the plasma membrane of infected cells, leading to membrane bending and release of immature virus particles. Ordered cleavage of the Gag polyprotein at five sites by the viral protease (PR) then causes a dramatic structural rearrangement of the virus to produce the mature, infectious virion (fig. S1, A to C). Gag-Gag interactions in the immature virus are mediated by the adjacent CA (capsid) domain and SP1 (spacer peptide 1). After maturation, CA forms a conical core encapsulating the viral RNA-nucleoprotein complex (*1*). The final proteolytic cleavage in Gag occurs between CA and SP1. Even small remnants of uncleaved CA-SP1 have a dominant-negative effect on infectivity (*2*, *3*). Cleavage at this site is inhibited by maturation inhibitors (MIs) (fig. S1B) (*4*), and polymorphisms in this region cause resistance against the first-in-class MI bevirimat (BVM) (*5*). Other MIs inhibiting CA-SP1 cleavage are currently undergoing clinical trials, but the precise mechanisms of their inhibitory action and of resistance against them are unclear.

Unprocessed Gag is assembled into irregular curved lattices whose structures cannot be determined using conventional structural biology techniques. The best structural model for CA in the immature virus has been derived by fitting nuclear magnetic resonance and crystal structures of the folded N-terminal and C-terminal domains (CA-NTD and CA-CTD, respectively) into a structure of the immature CA lattice acquired through cryo-electron tomography and subtomogram averaging (*6*). Subtomogram averaging can resolve protein structures within complex environments ranging from cells to enveloped viruses (*7*), but it has been limited to resolutions of ~8 Å. The positions of α-helices are visible at this resolution, but those of amino acids are not. Furthermore, 8 Å resolution is not sufficient to generate ab initio structural models for unknown structures such as the Gag regions downstream of the crystallized CA-CTD, which ends at residue 220 of the 231–amino acid CA domain (fig. S1D). This downstream region consists of a sequence of amino acids that is thought to assemble into a flexible hinge, followed by a sequence that is predicted to form a six-helix bundle spanning the C-terminal residues of CA, the critical CA-SP1 cleavage site, and the N-terminal residues of SP1 (*8*). This region includes the majority of the amino acids that are essential for virus assembly (*9*–*11*). Obtaining a high-resolution structure of CA-SP1 in the immature arrangement is vital for a mechanistic understanding of HIV-1 assembly, maturation, and inhibition.

The HIV-1 Gag construct ΔMACANCSP2 (MA, matrix; NC, nucleocapsid) (*11*) assembles into immature virus-like particles (VLPs) in vitro (Fig. 1A and fig. S1C). We assembled ΔMACANCSP2 particles in the absence or presence of 100 μg/ml BVM. We also purified intact, immature HIV-1 virus particles carrying an inactivating PR mutation, D25A. For all three cases, we used an optimized data collection scheme to acquire cryo-electron tomography tilt series (table S1)

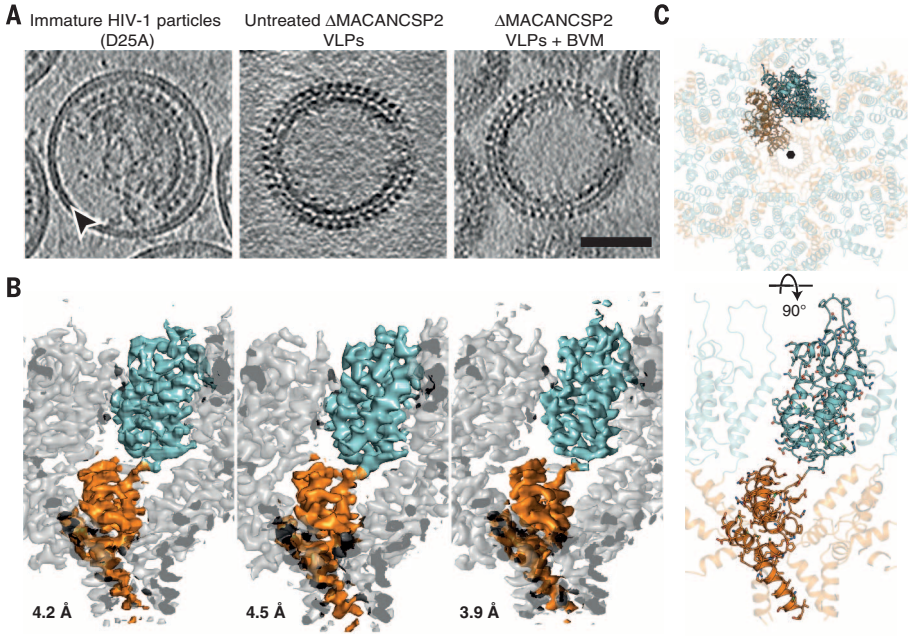


Fig. 1. Structure of the immature HIV-1 CA-SP1 lattice at 3.9 Å. (**A**) Computational slices through tomograms of immature HIV-1 (D25A mutant), untreated ΔMACANCSP2 VLPs, and BVM-treated ΔMACANCSP2 VLPs. The arrowhead marks the membrane bilayer in the left panel. Scale bar, 50 nm. (**B**) Electron densities of CA-SP1 from the samples shown in (A), viewed perpendicular to the lattice, generated by subtomogram averaging. One CA-SP1 monomer is highlighted in color, with the CA-NTD in cyan and the CA-CTD and SP1 in orange. The resolutions of the determined structures are noted. (**C**) The refined atomic model, viewed from outside of the virus (top) and rotated by 90°, shown in the same view as in (B) (bottom). The sixfold symmetry axis is indicated with a hexagon.

[1]Structural and Computational Biology Unit, European Molecular Biology Laboratory, Meyerhofstraße 1, 69117 Heidelberg, Germany. [2]Molecular Medicine Partnership Unit, European Molecular Biology Laboratory–Universitätsklinikum Heidelberg, Heidelberg, Germany. [3]Department of Infectious Diseases, Virology, Universitätsklinikum Heidelberg, Im Neuenheimer Feld 324, 69120 Heidelberg, Germany. [4]Hamburg Unit c/o DESY (Deutsches Elektronen-Synchrotron), European Molecular Biology Laboratory, Notkestraße 85, 22607 Hamburg, Germany. [5]Proteomics Core Facility, European Molecular Biology Laboratory, Meyerhofstraße 1, 69117 Heidelberg, Germany.
*Present address: Leibniz Institute on Aging–Fritz Lipmann Institute, Beutenbergstraße 11, 07745 Jena, Germany.
†Corresponding author. Email: john.briggs@embl.de

Downloaded from http://science.sciencemag.org/ on July 28, 2016

(*12*, *13*). VLPs with or without BVM were indistinguishable, showing densities for the Gag lattice that were similar to those in the immature virus particles (Fig. 1A). Subtomogram averaging was performed independently for each data set, using an optimized workflow with features including frame-based motion correction (*14*) and exposure filtering (*15*). The resolutions of the CA-SP1 layer in the final averages for untreated VLPs, BVM-treated VLPs, and immature virus particles were 4.5, 3.9, and 4.2 Å, respectively (Fig. 1B and fig. S2, A and B).

We compared the three structures and found no clear differences in the protein densities of CA or SP1; they varied only in the presence or absence of densities at the center of the hexamer near SP1 (fig. S2, C to I, and fig. S3C). Given the high degree of structural similarity between the maps, we used the 3.9 Å structure to build and refine a complete atomic model for the CA-SP1 region from Gag residues 148 to 371 (Figs. 1C and 2, figs. S3 and S4, table S2, and movies S1 and S2). Residues 356 to 371, covering the C terminus of CA and the first eight residues of SP1, assemble into a six-helix bundle.

Interactions in the CA-NTD layer are described in fig. S4A. The CA-NTD and CA-CTD contact one another in the region of E160 and E161 in the CA-NTD and Q308 in the CA-CTD. The relative positions of the two domains may also be restricted by the extended rigid linker between them, which appears to be stabilized by an interaction with R305 in helix 8. Y277, the last residue of helix 7 in a solution structure (*16*) and in the mature-like CA hexamer (*17*), is rotated out of the helix and packs against the linker at P279 (Fig. 2B). This network of interactions may allow the CA-CTD to be structurally modulated by cleavage upstream of the CA-NTD, and vice versa.

Highly conserved residues of the major homology region (MHR) in the CA-CTD abut the extended chain between the 3_{10}-helix and helix 8 (Fig. 2C). Charged residues in the 3_{10}-helix and extended chain interact with the neighboring CA-CTD molecule within the hexamer (Fig. 2, B and C). Hexamers are linked by a CA-CTD dimer interface (fig. S4B) formed by residues W316 and M317 (*6*, *18*, *19*).

Downstream of helix 11, beyond the residues that are resolved in crystal structures (*19*, *20*), the flexible hinge region (referred to here as the VGG hinge; residues 353 to 355) unexpectedly adopts a rigid structure within the lattice. P356 then marks the start of a helix (referred to here as the CA-SP1 helix) that extends down to residue 371 in SP1 (Fig. 2, A and D) before abruptly ending, indicating that residues C-terminal of 371 are disordered (movie S1). The CA-SP1 helix protrudes up into the CA-CTD layer, where the top of the helix and the VGG hinge from one Gag molecule pack tightly against the CA-CTD from the neighboring Gag molecule. The CA-CTD, VGG hinge, and CA-SP1 helix thus form a single, integrated assembly unit that defines the structure of the hexamer (Fig. 2, D and G).

This assembly unit appears to be stabilized by a three-way interaction between H358 in the CA-SP1 helix, D329 in the base of helix 10, and P356 in the CA-SP1 helix of the neighboring CA molecule (Fig. 2E). K290 in the loop upstream of helix 8 and K359 in the CA-SP1 helix protrude from above and below these residues toward the center of the six-helix bundle, where they coordinate a density, presumably a negatively

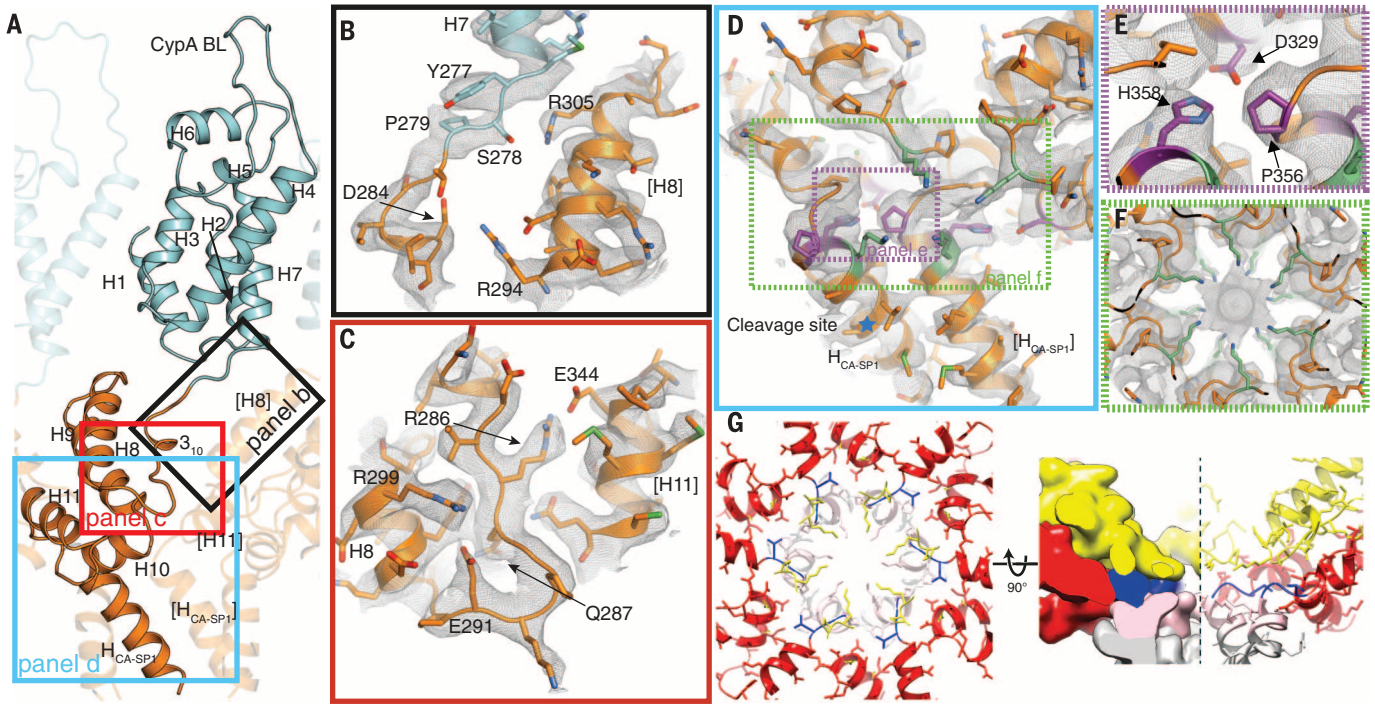


Fig. 2. Structural features in the immature CA-SP1 lattice. (**A**) A single CA-SP1 monomer, as in Fig. 1C. α-helices (H1 to H11 and H_{CA-SP1}) and the cyclophilin A binding loop (CypA BL) are labeled (α-helices from neighboring CA monomers are shown in brackets). Colored rectangles indicate regions enlarged in (B) to (D). (**B**) The CA-NTD–CA-CTD linker is in an extended conformation, with Y277 binding to the linker and S278 approaching R305. (**C**) The highly conserved residues in the MHR (Q287, E291, and R299) stabilize the linker connecting the 3_{10}-helix and helix 8. Residues in this linker can interact with an adjacent CA monomer around the hexameric ring (e.g., R286 with E344 and D284 with R294); point mutations of these residues do not abolish assembly (*22*), suggesting some redundancy in these interactions. (**D**) The CA-CTD, the VGG hinge, and the top of the CA-SP1 helix form an integrated structural assembly unit. The CA-SP1 cleavage site is marked by a blue star. Dashed rectangles indicate the approximate positions of the regions enlarged in (E) and (F). Residues are colored as in (E) and (F). (**E**) Residues D329, P356, and H358 (in purple) form a three-way linkage between two neighboring CA-SP1 helices and the base of the CA-CTD. (**F**) K290 and K359 (in green) protrude from above and below the region shown in (E) to the center of the hexamer, where they coordinate a strong density. (**G**) Horizontal (left) and vertical (right) slabs through the structure illustrate that the MHR (yellow), other residues in the CA-CTD base (red), the VGG hinge (blue), and the top of the CA-SP1 helix (pink) come together to form the hexameric assembly unit. In the vertical slab, one-half of the hexamer is represented in a surface view. Single-letter abbreviations for the amino acid residues are as follows: A, Ala; D, Asp; E, Glu; G, Gly; H, His [except when used to indicate helices, as in (A) to (D)]; K, Lys; L, Leu; M, Met; P, Pro; Q, Gln; R, Arg; S, Ser; V, Val; W, Trp; and Y, Tyr.

Downloaded from http://science.sciencemag.org/ on July 28, 2016

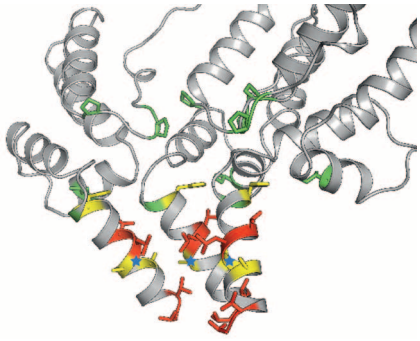


Fig. 3. Mutations that confer resistance to MIs destabilize the immature lattice. Resistance mutations or naturally occurring polymorphisms that render HIV-1 resistant to BVM (red) or PF-46396 (green) have been mapped onto the atomic model. Mutations that confer resistance for both compounds are colored yellow. The CA-SP1 cleavage site is marked by blue stars. For clarity, only three helices of the six-helix bundle are displayed.

charged ion cluster (Fig. 2F and movie S2). This arrangement is reminiscent of the six arginine residues that protrude into the center of the NTD hexamer in mature HIV CA (*17*, *21*). Twelve essential amino residues have been identified in the CA-CTD, where mutation to alanine abolishes virus assembly (*22*, *23*). These include W316 and M317 in the hydrophobic dimeric interface; V353, G354, and G355 in the VGG hinge; K290, D329, P356, H358, and K359, which together form the intricate network of interactions that defines the assembly unit; and A360 and L363, which appear to have hydrophobic interactions within the six-helix bundle. There is therefore a close correlation between the sensitivity of a residue to mutation and whether it has a role in mediating interactions in the CA-SP1 assembly unit, confirming the importance of these interactions in virus assembly.

During maturation, the final proteolytic cleavage occurs between L363 and A364. In our structure, this site is in the middle of the CA-SP1 helix bundle, where it is inaccessible to PR, which acts on extended protein chains (*24*) (Fig. 2D and movie S2). Disassembly of the immature lattice and full cleavage between CA and SP1 only take place once cleavage has occurred both between MA and CA and between SP1 and NC (*10*, *25*). Together, these observations support a model in which the final step in maturation is regulated by limiting the access of PR to its substrate: Cleavage upstream of CA and downstream of SP1 together destabilize the immature lattice and the CA-SP1 helix, thereby allowing PR to cleave between CA and SP1.

MIs block HIV infection by preventing cleavage at the CA-SP1 site (*4*, *13*, *26*) (fig. S5) and may also stabilize the immature lattice (*27*, *28*). We mapped mutations, deletions, and polymorphisms that confer resistance to BVM (*5*, *29*, *30*) and PF-46396 [another MI (*31*, *32*)] onto our structural model (Fig. 3). This revealed that the positions of resistance mutations do not map out potential drug-binding pockets. Instead, they are located at protein-protein interfaces within the CA-SP1 lattice. Together with our observation that the CA-SP1 cleavage site is inaccessible in the immature virus, this implies that the mode of action of MIs is not steric inhibition of proteolysis but, instead, stabilization of the immature Gag lattice. Our data suggest that BVM stabilizes the lattice by binding to a site in the center of the six-helix bundle (fig. S2). The reduced cleavage at the CA-SP1 boundary is a downstream effect of stabilization because cleavage of this site requires unfolding to an extended chain. HIV-1 appears to develop MI resistance by destabilizing its immature form, thus directly counteracting the stabilizing effects of MIs.

Note added in proof: In a concurrent publication, Wagner *et al.* report a crystal structure of a CA-CTD-SP1 construct that adopts a similar conformation to the structure reported here (*33*). They also report that the CA-SP1 cleavage site is within a six-helix bundle and suggest that MIs prevent proteolytic cleavage by stabilizing this structure.

REFERENCES AND NOTES

1. W. I. Sundquist, H. G. Kräusslich, *Cold Spring Harb. Perspect. Med.* **2**, a006924 (2012).
2. B. Müller *et al.*, *J. Biol. Chem.* **284**, 29692–29703 (2009).
3. M. A. Checkley, B. G. Luttge, F. Soheilian, K. Nagashima, E. O. Freed, *Virology* **400**, 137–144 (2010).
4. C. S. Adamson, K. Salzwedel, E. O. Freed, *Expert Opin. Ther. Targets* **13**, 895–908 (2009).
5. C. S. Adamson, M. Sakalian, K. Salzwedel, E. O. Freed, *Retrovirology* **7**, 36 (2010).
6. F. K. Schur *et al.*, *Nature* **517**, 505–508 (2015).
7. J. A. Briggs, *Curr. Opin. Struct. Biol.* **23**, 261–267 (2013).
8. M. A. Accola, S. Höglund, H. G. Göttlinger, *J. Virol.* **72**, 2072–2078 (1998).
9. S. A. Datta *et al.*, *J. Virol.* **85**, 4111–4121 (2011).
10. A. de Marco *et al.*, *PLOS Pathog.* **6**, e1001215 (2010).
11. I. Gross *et al.*, *EMBO J.* **19**, 103–113 (2000).
12. W. J. Hagen, W. Wan, J. A. Briggs, *J. Struct. Biol.* 10.1016/j.jsb.2016.06.007 (2016).
13. Materials and methods are available as supplementary materials on *Science* Online.
14. X. Li *et al.*, *Nat. Methods* **10**, 584–590 (2013).
15. T. Grant, N. Grigorieff, *eLife* **4**, e06980 (2015).
16. C. Tang, Y. Ndassa, M. F. Summers, *Nat. Struct. Biol.* **9**, 537–543 (2002).
17. A. T. Gres *et al.*, *Science* **349**, 99–103 (2015).
18. J. A. Briggs *et al.*, *Proc. Natl. Acad. Sci. U.S.A.* **106**, 11090–11095 (2009).
19. V. Bartonova *et al.*, *J. Biol. Chem.* **283**, 32024–32033 (2008).
20. T. R. Gamble *et al.*, *Science* **278**, 849–853 (1997).
21. O. Pornillos *et al.*, *Cell* **137**, 1282–1292 (2009).
22. U. K. von Schwedler, K. M. Stray, J. E. Garrus, W. I. Sundquist, *J. Virol.* **77**, 5439–5450 (2003).
23. D. Melamed *et al.*, *J. Virol.* **78**, 9675–9688 (2004).
24. M. Prabu-Jeyabalan, E. Nalivaika, C. A. Schiffer, *Structure* **10**, 369–381 (2002).
25. K. Wiegers *et al.*, *J. Virol.* **72**, 2846–2854 (1998).
26. M. Sakalian *et al.*, *J. Virol.* **80**, 5716–5722 (2006).
27. P. W. Keller *et al.*, *J. Virol.* **87**, 13655–13664 (2013).
28. P. W. Keller, C. S. Adamson, J. B. Heymann, E. O. Freed, A. C. Steven, *J. Virol.* **85**, 1420–1428 (2011).
29. C. S. Adamson *et al.*, *J. Virol.* **80**, 10957–10971 (2006).
30. N. A. Margot, C. S. Gibbs, M. D. Miller, *Antimicrob. Agents Chemother.* **54**, 2345–2353 (2010).
31. K. Waki *et al.*, *PLOS Pathog.* **8**, e1002997 (2012).
32. W. S. Blair *et al.*, *Antimicrob. Agents Chemother.* **53**, 5080–5087 (2009).
33. J. M. Wagner *et al.*, *eLife* **5**, e17063 (2016).

ACKNOWLEDGMENTS

The authors thank B. Glass for preparation of the immature HIV-1 (D25A) sample; J. Plitzko and D. Tegunov for providing the K2Align software; and S. Mattei, N. Hoffman, F. Thommen, A. Sonnen, and S. Dodonova for technical assistance and/or discussion. This study was supported by Deutsche Forschungsgemeinschaft grants BR 3635/2-1 (to J.A.G.B.) and KR 906/7-1 (to H.-G.K.). The Briggs laboratory acknowledges financial support from the European Molecular Biology Laboratory (EMBL) and from the Chica und Heinz Schaller Stiftung. W.W. was supported by a European Molecular Biology Organization Long-Term Fellowship (ALTF 748-2014). A.J.J. acknowledges support by the EMBL Interdisciplinary Postdoc Program under the Marie Curie Action COFUND (PCOFUND-GA-2008-229597) and by the Joachim Herz Stiftung. This study was technically supported by the EMBL information technology services unit and the EMBL Proteomics Core Facility. F.K.M.S., M.O., H.-G.K., and J.A.G.B. designed the experiments, with J.M.K. assisting in the design of those involving mass spectrometry. F.K.M.S. and M.O. prepared samples. W.J.H.H. implemented tomography acquisition schemes. F.K.M.S. and W.J.H.H. acquired the data. F.K.M.S. and W.W. processed images. F.K.M.S., A.J.J., and C.S. refined the model. F.K.M.S., M.O., and J.A.G.B. analyzed the data. F.K.M.S. and J.A.G.B. wrote the manuscript with support from all authors. Representative tomograms and the final electron microscopy structures have been deposited in the Electron Microscopy Data Bank with accession numbers EMD-4015, EMD-4016, EMD-4017, EMD-4018, EMD-4019, and EMD-4020. The refined HIV-1 CA-SP1 model has been deposited in the Protein Data Bank with accession number 5L93.

SUPPLEMENTARY MATERIALS

www.sciencemag.org/content/353/6298/506/suppl/DC1
Materials and Methods
Figs. S1 to S5
Tables S1 and S2
References (*34*–*59*)
Movies S1 and S2

26 April 2016; accepted 29 June 2016
Published online 14 July 2016
10.1126/science.aaf9620

Downloaded from http://science.sciencemag.org/ on July 28, 2016

Be Among the First to Publish in *Science Robotics*



Image: jim/AdobeStock

NOW ACCEPTING MANUSCRIPTS

ScienceRobotics.org

Science Robotics is a unique journal created to help advance the research and development of robotics for all environments. *Science Robotics* will provide a much-needed central forum to share the latest technological discoveries and to discuss the field's critical issues.

Join in the excitement for the Fall 2016 debut!

Science Robotics
AAAS

myIDP: A career plan customized for you, by you.



For your career in science, there's only one **Science**

my IDP
ScienceCareers

Recommended by leading professional societies and the NIH

Features in myIDP include:

- Exercises to help you examine your skills, interests, and values.
- A list of 20 scientific career paths with a prediction of which ones best fit your skills and interests.
- A tool for setting strategic goals for the coming year, with optional reminders to keep you on track.
- Articles and resources to guide you through the process.
- Options to save materials online and print them for further review and discussion.
- Ability to select which portion of your IDP you wish to share with advisors, mentors, or others.
- A certificate of completion for users that finish myIDP.

Visit the website and start planning today!
myIDP.sciencecareers.org

ScienceCareers In partnership with:

advancing the life sciences 1912-2012 FASEB Federation of American Societies for Experimental Biology

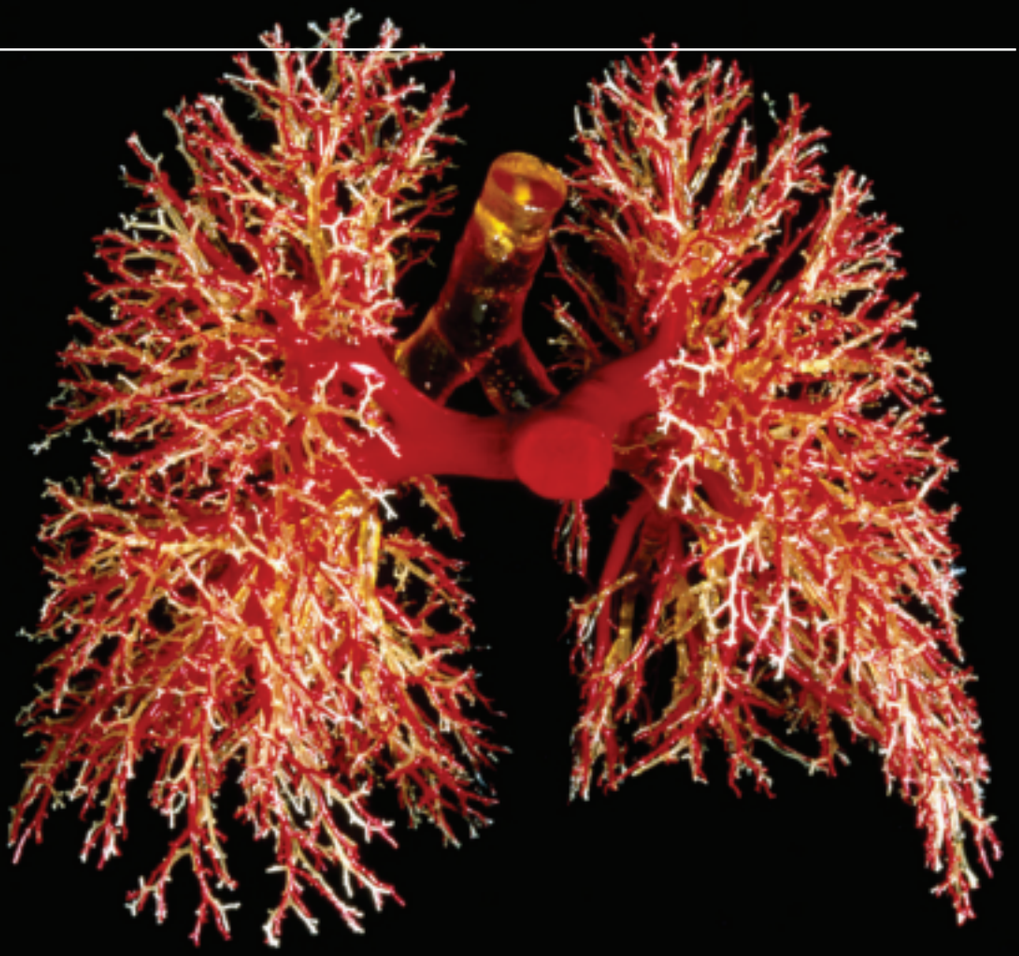
UCSF University of California San Francisco

Medical College of Wisconsin

Burroughs Wellcome Fund

0729Product.indd 423 7/20/16 8:49 AM

WILL YOUR RESEARCH LEAD TO BETTER LIVES FOR PATIENTS?



Gopinath Sutendra and Evangelos D. Michelakis, "Pulmonary Arterial Hypertension: Challenges in Translational Research and a Vision for Change", *Sci. Transl. Med.* 5, 208sr5 (2013) Credit: *Science* Source

Science Translational Medicine | AAAS

INTEGRATING SCIENCE, ENGINEERING, AND MEDICINE

Find out more about the scope of the journal and submit your research today!
ScienceTranslationalMedicine.org

Visible-Range Spectrophotometer

A new, rugged, accurate visible-range spectrophotometer is designed for lab managers and instructors looking for ease of operation and superior photometric performance in a single instrument. The GENESYS 30 visible-range spectrophotometer features a 5-in. color display and a rubber push-button keypad. It has a large sample compartment with a removable, washable liner to protect against spills. The larger sample compartment improves accessibility and flexibility, enabling labs to use a variety of standard cuvette holders and test tubes. Designed to provide fast, accurate results every time, the instrument offers rapid scanning capabilities and photometric performance usually reserved for higher-priced models. A front-facing USB port and optional snap-on thermal printer allow rapid data export for further analysis. The user interface is intuitive and guides new users through standard protocols, sample analysis, and results interpretation, minimizing the need for training.

Thermo Fisher Scientific
For info: 800-955-6288
www.thermoscientific.com/uv-vis

Vis-NIR Spectroscopy Software

Vision Air spectroscopy software is now available for visible and near-infrared (Vis-NIR) spectroscopy instruments. Designed for routine analysis measurements, this new software includes an intuitive, self-guided user interface for fast measurement and straightforward data interpretation. Its operation focuses on sample analysis parameters and trends, not spectra, increasing the information density from NIR measurements. The software saves time and guarantees reliable measurements across multiple facilities and multiple operators, by ensuring that configurations and methods are updated simultaneously. Single instrument configurations also benefit from networking functionalities, including data integrity and support. Vision Air software allows the user to develop the analysis model or use a model developed by and stored on a Metrohm server. Chemometrics expertise is no longer needed to use NIR. Customers can choose the level of support they need and deploy models using one instrument locally or hundreds of instruments globally.

Metrohm
For info: 866-638-7646
www.metrohm.com



Raman-SEM Imaging

The WITec Raman Imaging and Scanning Electron (RISE) microscopy mode for correlative Raman-scanning electron microscopy (SEM) imaging is now compatible with the SEM Zeiss MERLIN. Raman microscopy, a label-free, nondestructive technology for the identification and imaging of the molecular composition of a sample, is the perfect complement to SEM, which visualizes the surface structure of a sample, and the often-associated energy-dispersive X-ray spectroscopy that can only identify elemental constituents. The integration of both techniques into one system greatly accelerates the experimental workflow. It places both the objective and sample stage required for Raman microscopy within the SEM's vacuum chamber. The sample is simply transferred between the Raman and SEM measuring positions by a software-driven, push-button mechanism using an extremely precise scan stage. Customers benefit from high-quality, sophisticated system components for state-of-the-art research in such fields as nanotechnology, life sciences, geosciences, pharmaceutics, and materials research.

WITec
For info: +49-(0)-731-140-700
www.witec.de

Comet Assay Platform

The CometChip high-throughput GenTox platform allows a 5,000% increase in throughput over the original comet assay procedure. The comet assay is a highly sensitive, direct approach for the measurement of DNA damage and repair. However, adoption and routine use of the assay in the safety screening for drugs, cosmetics, chemicals, pesticides, fungicides, and other compounds affecting health and the environment have been hampered by technical issues including reproducibility, accuracy, and the inordinate time required for high-volume testing. If an average of 208 arrayed comets is imaged per well, the 96-well CometChip produces on average 20,000 comets per chip. With a capacity for three CometChips per electrophoresis system run, the output for just two runs per day is 120,000 comets. The Comet Analysis Software can analyze in minutes what used to take days. In this example, 120,000 comets can be analyzed, the data exported, and a report generated in under 20 minutes.

Trevigen
For info: 800-TREVIGEN
www.trevigen.com

HDx RNA Fusion Reference Standards

HDx FFPE RNA Fusion Reference Standards are available for independent analytical controls for the optimization and validation of targeted RNA sequencing, endpoint reverse transcription PCR (RT-PCR), or RT quantitative PCR (RT-qPCR) assays that detect gene fusions. Each section contains an FFPE cell line multiplex-verified to contain *EML4-ALK* (Variant 1), *CCDC6-RET*, and *SLC34A2-ROS1* fusions. *ALK* fusions of the genetic markers *ALK, RET,* and *ROS1* are found in approximately 3%–7% of lung tumors and are an important clinical marker for non-small cell lung cancer. The anticancer drug crizotinib is approved to treat certain late-stage, non-small cell lung cancers that express the abnormal anaplastic lymphoma kinase (*ALK*) gene. Accurate and reliable molecular diagnostic testing is needed prior to beginning therapy. These FFPE RNA reference standards allow end users to optimize and validate targeted RNA fusion panels. The cell lines employed in creating these standards provide a renewable source of reference material that is reproducible and consistent.

Horizon Discovery
For info: 844-655-7800
www.horizondiscovery.com

Electronically submit your new product description or product literature information! Go to www.sciencemag.org/about/new-products-section for more information.

Newly offered instrumentation, apparatus, and laboratory materials of interest to researchers in all disciplines in academic, industrial, and governmental organizations are featured in this space. Emphasis is given to purpose, chief characteristics, and availability of products and materials. Endorsement by *Science* or AAAS of any products or materials mentioned is not implied. Additional information may be obtained from the manufacturer or supplier.

0729Product.indd 509 7/25/16 10:52 AM



REVEALING AN EVER-CLEARER PICTURE OF IMAGING SCIENCE

The Welch Foundation hosts its 60th Annual Conference on Chemical Research | October 24-25, 2016, Houston, TX

Dr. Ahmed H. Zewail of Caltech welcomes the world's leading minds for a compelling program on the Frontiers of Imaging. His assembly of distinguished speakers and session leaders will explore the wide-ranging impacts and implications of breakthrough research, from molecular to cellular imaging. The research program presents an exposé of the progress made in understanding brain function, improving molecular health, and advancing materials science. Dr. Zewail is joined by three other Nobel laureates at this distinguished gathering.

Frontiers of Imaging: Visualization of Matter through Electrons and Photons

For registration information and a complete program, visit our website at www.welch1.org/conference/conference-overview

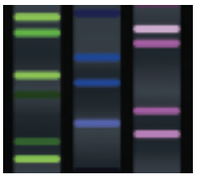
THE Welch FOUNDATION

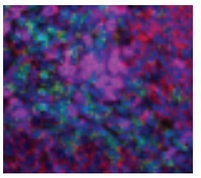
0729Product.indd 515 7/20/16 8:50 AM

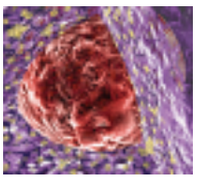
want new technologies?

antibodies
apoptosis
biomarkers
cancer
cytometry
data
diseases
DNA
epigenetics
genomics
immunotherapies
medicine
microbiomics
microfluidics
microscopy
neuroscience
proteomics
sequencing
toxicology
transcriptomics









watch our webinars

Learn about the latest breakthroughs, new technologies, and ground-breaking research in a variety of fields. Our expert speakers explain their quality research to you and answer questions submitted by live viewers.

VIEW NOW!
webinar.sciencemag.org

Science
AAAS

Brought to you by the *Science*/AAAS Custom Publishing Office

@SciMagWebinars

0729Product.indd 516 7/20/16 8:50 AM



Science Careers Advertising

For full advertising details, go to ScienceCareers.org and click For Employers, or call one of our representatives.

Tracy Holmes
Worldwide Associate Director
Science Careers
Phone: +44 (0) 1223 326525

THE AMERICAS

E-mail: advertise@sciencecareers.org
Fax: +1 (202) 289 6742

Tina Burks
Phone: +1 (202) 326 6577

Nancy Toema
Phone: +1 (202) 326 6578

Online Job Posting Questions
Phone: +1 (202) 312 6375

EUROPE / INDIA / AUSTRALIA / NEW ZEALAND / REST OF WORLD

E-mail: ads@science-int.co.uk
Fax: +44 (0) 1223 326532

Sarah Lelarge
Phone: +44 (0) 1223 326527

Kelly Grace
Phone: +44 (0) 1223 326528

Online Job Posting Questions
Phone: +44 (0) 1223 326528

JAPAN

Katsuyoshi Fukamizu (Tokyo)
E-mail: kfukamizu@aaas.org
Phone: +81 3 3219 5777

Hiroyuki Mashiki (Kyoto)
E-mail: hmashiki@aaas.org
Phone: +81 75 823 1109

CHINA / KOREA / SINGAPORE / TAIWAN / THAILAND

Ruolei Wu
E-mail: rwu@aaas.org
Phone: +86 186 0082 9345

Danny Zhao
E-mail: dzhao@aaas.org
Phone: +86 131 4114 0012

All ads submitted for publication must comply with applicable U.S. and non-U.S. laws. *Science* reserves the right to refuse any advertisement at its sole discretion for any reason, including without limitation for offensive language or inappropriate content, and all advertising is subject to publisher approval. *Science* encourages our readers to alert us to any ads that they feel may be discriminatory or offensive.

ScienceCareers
FROM THE JOURNAL SCIENCE AAAS

ScienceCareers.org



Learn more and keep your job search out of the cheap seats.

- Search thousands of job postings
- Create job alerts based on your criteria
- Get career advice from our Career Forum experts
- Download career advice articles and webinars
- Complete an individual development plan at "myIDP"

Target your job search using relevant resources on **ScienceCareers.org**.

ScienceCareers
FROM THE JOURNAL SCIENCE AAAS

BIOMOLECULAR NMR SPECTROSCOPIST

Florida State University Department of Chemistry & Biochemistry and the National High Magnetic Field Laboratory are searching for a **mid-career faculty member with research interests in biochemistry and solution NMR spectroscopy**. Preference will be given to candidates whose research represents strong arguments for spectroscopy at high magnetic fields including, but not limited to, work in intrinsically disordered proteins or macromolecular dynamics. The successful candidate will be expected to maintain an extramurally funded research program, teach both graduate and undergraduate classes, and to actively participate in the Magnet Lab's efforts to take solution NMR spectroscopy to much higher magnetic fields and to help drive the development of high frequency probes for NMR science.

Persons interested in the position can contact **Professor Timothy A. Cross** for more information. Applicants should email all application materials, including cover letter, CV, statement of research plans and teaching interests, and the names and contact information for three professional references to **nmr_search@chem.fsu.edu**. Review of applications will begin on **October 1, 2016**, and continue until the position is filled.

FSU is an Equal Opportunity/Access/Affirmative Action/Pro Disabled & Veteran Employer. FSU's Equal Opportunity Statement can be viewed at: http://www.hr.fsu.edu/PDF/Publications/diversity/EEO_Statement.pdf

South Carolina Smartstate Endowed Chair in Biofabrication Biology
Medical University of South Carolina, Department of Regenerative Medicine and Cell Biology

The Department of Regenerative Medicine and Cell Biology at the Medical University of South Carolina is seeking a leader to fill the Smartstate Endowed Chair in Biofabrication Biology at the rank of Professor or Associate Professor. This position is part of the South Carolina Advanced Tissue Biofabrication Center of Economic Excellence (http://smartstatesc.org/advanced-tissue-biofabrication). A focus of the center is to integrate basic cell biology with biofabrication to generate tissues in the laboratory that can be used to advance our understanding and treatment of human disease. The successful candidate will have a strong background in cell or developmental biology and will integrate the use of bioengineering or tissue fabrication into their research program. Candidates interested in the study of vascular, cardiovascular, or digestive disease are particularly encouraged to apply.

Candidates should have a Ph.D. or MD/Ph.D. degree (or equivalent) with credentials that are compatible with granting tenure. In addition, candidates should have extensive experience in managing a successful research laboratory, an outstanding and internationally recognized record of high impact publications, and a compelling history of extramural funding. Current research strengths in the department include pluripotent stem cell differentiation, cardiovascular development, digestive disease, and molecular biology of the cell. Research at MUSC is supported by several excellent core facilities specializing in imaging, genetically modified mice and rats, drug discovery, proteomics, genomics, and flow cytometry.

MUSC in Charleston was established in 1824 and is ranked in the upper quartile of all freestanding academic medical universities. The university has approximately 2,200 graduate and professional students that are supported by 2,000 faculty members. In 2014 total financial support topped $217 million with $100 million coming from the NIH. This includes funding that supports the NCI–designated Hollings Cancer Center as well as a Clinical and Translational Science Award.

MUSC is an Affirmative Action/Equal Opportunity Employer that strives to hire without regard to gender, race, color, national origin, sex, age, religion, disability, sexual orientation, genetic information or veteran status. MUSC takes affirmative action to hire and advance women, minorities, protected veterans and individuals with disabilities. MUSC has received a 4-year NSF ADVANCE grant to promote the recruitment, retention and advancement of women in science.

Applicants should provide curriculum vitae, research plan, and the names of three references through the MUSC employment portal: **http://careers.pageuppeople.com/756/cw/en-us/job/495349/univ-associate-professorprofessor-regenerative-medicine**

香 港 大 學
THE UNIVERSITY OF HONG KONG

Lecturer/Assistant Lecturer in Common Core Curriculum (Ref.: 201600883)

Applications are invited for appointment as Lecturer/Assistant Lecturer in the Common Core Curriculum in the Faculty of Science, from as soon as possible, on a two-year fixed-term basis, with the possibility of renewal.

The University has established a Common Core Curriculum for all undergraduates since September 2012. The Faculty of Science offers courses in the area of Scientific and Technology Literacy to students from all ten Faculties. A senior Professor in the Faculty of Science will lead the teaching of these courses and work with the Lecturer/Assistant Lecturer in the relevant area who will serve primarily as a tutor for small groups of students from multiple disciplines. The medium of instruction is English. Information about the Common Core Curriculum can be viewed at http://tl.hku.hk/common-core-curriculum.

Applicants should have a Ph.D. degree in Chemistry, Physics or Biological Sciences, and enthusiasm for and commitment to teaching. For **Lecturer**, at least 3 years of teaching experience at the university level is required. The appointee's duties include conducting small-group tutorials for two courses per semester, marking assignments/examination scripts, preparing teaching materials, supervising student work, developing new courses, and undertaking other tasks related to science education. He/She will meet regularly with the Centre for the Enhancement of Teaching and Learning to reflect on and refine the teaching activities in Common Core courses.

A globally competitive remuneration package commensurate with qualifications and experience will be offered. At current rates, salaries tax does not exceed 15% of gross income. The appointments will attract a contract-end gratuity and University contribution to a retirement benefits scheme, totalling up to 15% (Lecturer)/10% (Assistant Lecturer) of basic salary, as well as annual leave, and medical benefits. Please note that the University is not able to offer a relocation assistance package (including temporary University housing accommodation and a passage and baggage allowance) to the successful candidate recruited from overseas.

Enquiries about the specific job requirements should be sent to Professor Pauline Chiu, Faculty of Science, e-mail: sciappt@hku.hk. Applicants should send a completed application form, together with an up-to-date C.V. and a statement on teaching philosophy, which includes a portfolio of syllabi and descriptions of courses they have taught or co-taught by e-mail to sciappt@hku.hk. They should also arrange for submission of three references from senior academics who are familiar with their teaching approaches, skills and experience to sciappt@hku.hk. Please indicate clearly at which *level* they wish to be considered for and the reference number in the subject of the e-mail. Application forms (341/1111) can be downloaded at http://www.hku.hk/apptunit/form-ext.doc. Further particulars can be obtained at http://jobs.hku.hk/. **Closes August 19, 2016**.

The University thanks applicants for their interest, but advises that only candidates shortlisted for interviews will be notified of the application result.

The University is an equal opportunities employer and is committed to a Non-Smoking Policy

Assistant/Associate Professor
Dept. of Cell & Developmental Biology

The Department of Cell & Developmental Biology at SUNY Upstate Medical University in Syracuse, New York invites applications for a tenure-track position at the Assistant/Associate Professor level. Candidates must have a PhD or equivalent degree and postdoctoral experience in cell biology or a related field. Applicants with interests in all areas of cellular biology are encouraged to apply.

Candidates at the Associate Professor level should have an established track record of funding and research productivity. Successful candidates are expected to develop and maintain a vigorous extramurally funded research program and participate in the education of both medical and graduate students.

The Department provides a strong, collaborative research community with interests in developmental and disease model systems, signaling, cell motility and the cytoskeleton explored in diverse model systems. We offer excellent departmental resources to support faculty including state of the art live cell imaging facilities, newly-renovated space, competitive salaries and startup packages, in additional to outstanding institutional core facilities. Syracuse is located in central NY and provides a diverse, dynamic and affordable metropolitan environment with easy access to the outstanding recreational opportunities of the Adirondack Mountains and the Finger Lakes, while the proximity of SUNY Upstate to Syracuse University and SUNY ESF campuses fosters productive scientific interactions and provides unique collaborative funding opportunities. To learn more go to **http://www.upstate.edu/cdb/**.

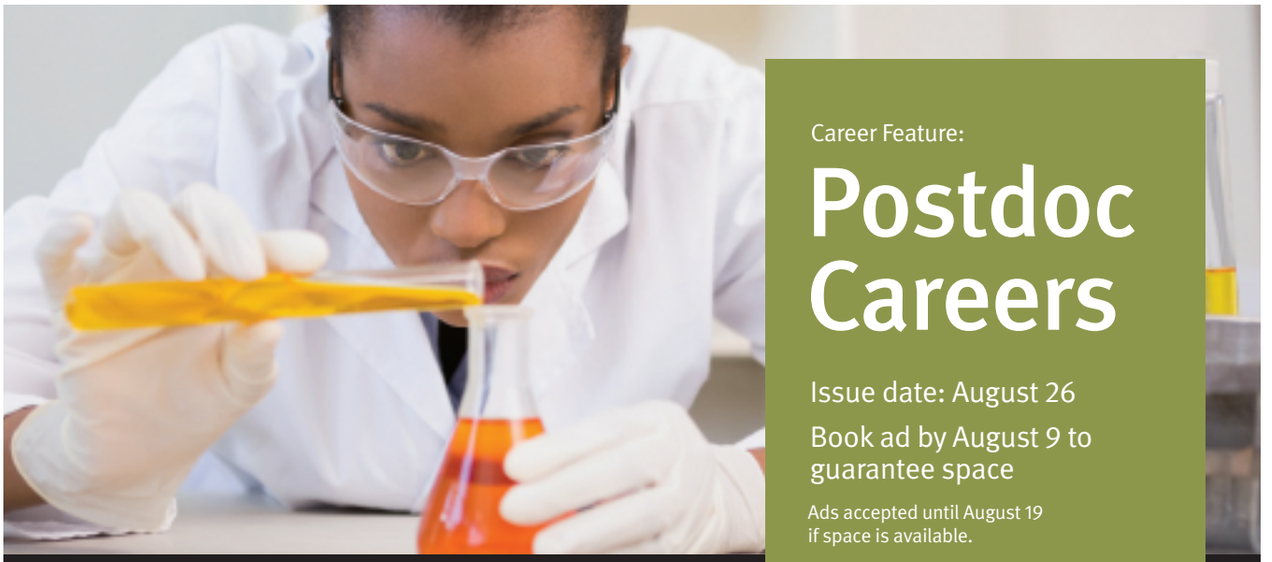
Please submit a CV and a research statement describing past accomplishments and future plans, as a single PDF file, and arrange to have three letters of recommendation sent to: **ReeshM@upstate.edu**.

Review of applications will begin October 1 and continue until the position is filled.

UPSTATE MEDICAL UNIVERSITY

At SUNY Upstate Medical University we strive to promote a professional environment that encourages varied perspectives from faculty members with diverse life experiences. A respect for diversity is one of our core values. We are committed to recruiting and supporting a rich community of outstanding faculty, staff and students. We actively seek applications from women and members of underrepresented groups to contribute to the diversity of our university community in support of our teaching, research and clinical missions.

ScienceCareers online @sciencecareers.org



Career Feature:

Postdoc Careers

Issue date: August 26

Book ad by August 9 to guarantee space

Ads accepted until August 19 if space is available.

For recruitment in science, there's only one *Science*.

Looking to fill your postdoc positions?

Scientists will be eager to learn about non-faculty career options in academia in STEM. What do these jobs involve and how can scientists prepare for them? What are the entry points and skills needed for success? Postdocs who have moved into these types of careers will share their success stories. Reach these readers and share opportunities at your university or company.

What makes *Science* the best choice for recruiting?

- Read and respected by 400,000 readers around the globe
- 78% of readers read *Science* more often than any other journal
- Your ad dollars support AAAS and its programs, which strengthens the global scientific community.

Why choose this Postdoc Feature for your advertisement?

- Relevant ads lead off the career section with a special "Postdoc" banner.

Expand your exposure by posting your print ad online:

- Link on the job board homepage directly to postdoc positions
- Dedicated landing page for postdoc positions.

Produced by the *Science*/AAAS Custom Publishing Office.

Deliver your message to a global audience of targeted, qualified scientists.

129,574
subscribers in print every week

352,966
monthly unique browsers on ScienceCareers.org

65%
of our weekly readers are Ph.D.s



SCIENCECAREERS.ORG

ScienceCareers
FROM THE JOURNAL SCIENCE AAAS

To book your ad: **advertise@sciencecareers.org**

The Americas
+202 326 6582

Japan
+81 3 3219 5777

Europe/RoW
+44(0)1223 326500

China/Korea/Singapore/Taiwan
+86 186 0082 9345

0729Recruitment_SC.indd 512 7/26/16 1:09 PM



ANNOUNCEMENTS

NOTICE
Cancellation of BoyaLife/Science Prize

Due to unforeseen circumstances the BoyaLife/Science prize has been cancelled. Science/AAAS is no longer affiliated with any prize/award that is associated with BoyaLife. If you have any questions, please e-mail your inquires to **scienceadvertising@aaas.org**

Post your jobs Fast and Easy



ScienceCareers
employers.sciencecareers.org

Columbia University Medical Center
Irving Institute for clinical and translational research

RESEARCH FELLOWSHIP IN PRECISION MEDICINE

Columbia University's Irving Institute for Clinical and Translational Research is accepting applications for a two-year Precision Medicine Fellowship with the goal of training physicians/researchers to use genomics and complex clinical data to improve clinical care and clinical outcomes by tailoring prevention, screening, and medical interventions to individual patient characteristics.

Award Amount: $200,000 ($100,000 per year).

Quantity: Up to 2 per year.

Eligibility: Applicants must have a Ph.D., M.D., D.D.S., or comparable doctoral degree from an accredited domestic or foreign institution.

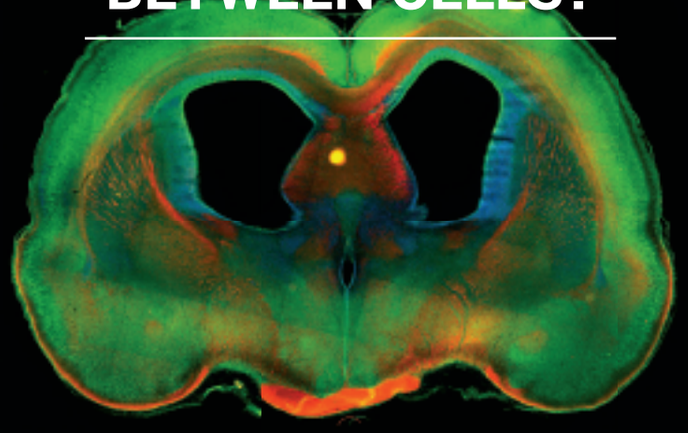
Requirements: The applicant will need to identify a faculty mentor at Columbia University and propose a research project in precision medicine to be started on July 1, 2017.

Application deadline: 5 pm EDT, September 30, 2016.

Download application form and instructions at http://www.irvinginstitute.columbia.edu/resources/precision_med.html

Columbia University is an Equal Opportunity/Affirmative Action Employer.

CALL FOR PAPERS!
DOES YOUR LAB ANALYZE THE MECHANISMS THAT MEDIATE COMMUNICATION BETWEEN CELLS?



Kong-Yan WKong-Yan Wu *et al.* (Zhen-Ge Luo), "Semaphorin 3A activates the guanosine triphosphatase Rab5 to promote growth cone collapse and organize callosal axon projections", *Sci. Signal.* 7, ra81 (2014). Rat Brain Slice. Image: Kong-Yan Wu and Zhen-Ge Luo, Chinese Academy of Sciences.

Stay on top of the latest advances in brain development and neurological disorders with *Science Signaling,* the leading online journal of cross-disciplinary cell signaling research. The journal's high-impact articles showcase basic research related to cellular and organismal regulation relevant to development, physiology, and disease as well as applied signaling research important for drug discovery and synthetic biology.

Learn more and submit your research today:
ScienceSignaling.org

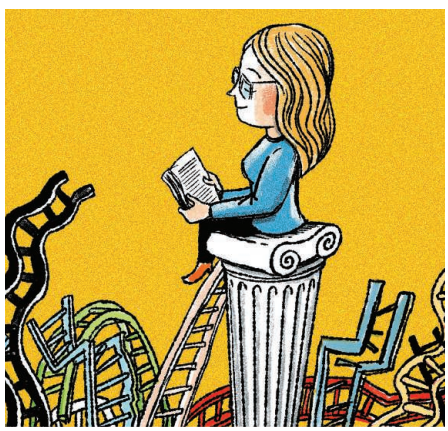
Science Signaling | AAAS
CELL SIGNALING IN PHYSIOLOGY AND DISEASE

By **Tenaya K. Vallery**

Growth from failure

Our task as scientists is to ask difficult questions until we uncover the truth—which means learning from failed experiments and trying again, undaunted. Yet, after years of honing my type A tendencies to succeed academically, I began graduate school with a fear of failure. As I searched for the truths related to my project, I struggled with failing at the bench and became frustrated and defensive. I have only recently come to respect the critical role of failure in research, and I have learned to be open when I encounter it.

In the beginning of my fifth year of grad school, I hit a rough patch in my studies—the most recent in a series of setbacks—and was not navigating the situation well. I had switched to a new project in the spring of my fourth year, but it was progressing slowly and hitting roadblocks. After 1513 days as a Ph.D. student, I could not generate the materials that I needed for my experiments. The RNA I was trying to extract from cancer cells was degrading before I could analyze it, and the virus that I once could propagate would not cooperate. I was unsure when I would publish my work and graduate, and I was feeling purposeless after 4 years of little progress.



"My role as a grad student is to learn from others—and from my mistakes."

But instead of asking my labmates and principal investigator (PI) for help, I adopted a defensive attitude, becoming closed to suggestions and hiding the extent of my difficulties. I feared that if I acknowledged my lack of progress, I would lose the respect of my PI and colleagues. At the same time, I berated myself for continual failure.

One Friday afternoon, my PI approached me about my research struggles. It was a challenging conversation. She asked how she could help, but I did not know what to tell her. Overwhelmed, I asked whether we could meet again on Monday morning. She agreed.

Coping with my shame and the criticism from my PI was difficult. After 24 hours of feeling overwhelmed with embarrassment and frustration, I finally reached out to my mom. She urged me to regain my mental focus by tackling a 1000-piece jigsaw puzzle over the weekend—which I now see as a corny but honest metaphor for piecing myself back together. Having a concrete objective helped me turn my thoughts outward in a productive way, toward what I could do to move forward. Midway through the puzzle, I decided to address my PI's concerns by making an outline of my current progress and a definitive plan for the next month.

On Monday morning, I presented the plan to my PI. I emphasized my commitment to continuing my research in spite of the failures I had experienced. In response, she implored me to ask more often for help on technical matters. When I left her office, I knew that a long path of hard work lay ahead, not only to produce results but to overcome my fear of failure. I promised myself that I would start communicating my struggles to others, asking for help more—and accepting it when it is offered.

Now, at the end of my fifth year, my research is progressing. Following a recommendation from a labmate, I overcame my RNA degradation problem by wearing smaller gloves, which reduces contamination. I am also working on a new approach to reconstituting the virus.

Looking back at that meeting with my PI, I am thankful that she approached me privately, in a direct and constructive manner. Even though her feedback was difficult to process at the time, I learned from that experience to be more open with my colleagues about my research setbacks. I have found that open discussion helps me organize my thoughts, forcing me to face my obstacles. It's still a challenge, but one thing that helps is to remind myself that my colleagues and PI only want to help, and that my role as a grad student is to learn from others—and from my mistakes.

Being a scientist requires resilience, and it always will. The open, supportive lab atmosphere my PI fosters has helped me cope with my fear of failure and become a more mature scientist. Quoting a friend, I now strive to be "type lowercase-a" instead of type A. ■

Tenaya K. Vallery is a Ph.D. candidate in the Department of Molecular Biophysics and Biochemistry at Yale University. Send your story to SciCareerEditor@aaas.org.

ILLUSTRATION: ROBERT NEUBECKER

Downloaded from http://science.sciencemag.org/ on July 28, 2016

Published by AAAS